TURBULENT FLUID JET EXCAVATION IN COHESIVE SOIL
WITH PARTICULAR APPLICATION TO JET GROUTING

Chu Eu Ho

BEng (Hons) Civil Engineering 1984
National University of Singapore, Singapore

MSc Engineering Rock Mechanics 1985
Imperial College of Science and Technology, London

DIC Engineering Rock Mechanics 1985
Imperial College of Science and Technology, London

Submitted to the Department of Civil and Environmental Engineering
in Partial Fulfillment of the Requirements for the Degree of

Doctor of Science in Geotechnical and Geoenvironmental Engineering

at the

Massachusetts Institute of Technology

June 2005

Signature of Author _____
Department of Civil and Environmental Engineering
May 6, 2005

Certified by _____
Andrew J Whittle
Professor of Civil and Environmental Engineering
Thesis Co-Supervisor

Certified by _____
John T Germaine
Principal Research Associate
Thesis Co-Supervisor

Accepted by _____
Professor Andrew J Whittle
Chairman, Department Committee on Graduate Studies

TURBULENT FLUID JET EXCAVATION IN COHESIVE SOILS WITH PARTICULAR APPLICATION TO JET GROUTING

by

Chu Eu Ho

Submitted to the Department of Civil and Environmental Engineering
on May 6, 2005 in partial fulfillment of the requirements for the degree of
Doctor of Science in the field of Geotechnical and Geoenvironmental Engineering

ABSTRACT

This thesis reviews the jet grouting methodology, and the current state of practice and research. Current methods of prediction of jet grout diameters are highly empirical and site specific, and do not take into account the jet hydrodynamics and soil properties explicitly. A rational model to describe the jet excavation mechanism for cohesive soil is presented in this thesis, with the aim of providing an improved prediction tool that can be used in jetting design.

The model is based on the assumption that the velocity distribution in the cutting jet is equivalent to that of a free jet with boundaries corresponding to the dimensions of the cavity excavated in the ground. The shape of the cavity formed depends on the erosional properties of the soil and jet expansion is limited by the resistance at the jet-soil interface. It is hypothesized that the shape of the cavity excavated follows the locus of the jet radius satisfying the condition of constant wall shear stress. The model predicts that the limit of jet penetration is reached when the dynamic pressure at the jet tip becomes equal to the ultimate soil bearing resistance.

The model was validated by laboratory jetting tests, using soil specimens manufactured from powdered kaolin clay, cement and water. Cement-soil ratios (CSR) of 2.5 to 7.5% were used to produce specimens with undrained shear strength (s_u) ranging from 5 to 45 kPa. A period of at least 3 days was allowed for the specimen to cure in the test tank before jetting was commenced. The tests were conducted using different nozzle diameters, jetting pressures, rotation speeds and soil strengths. The specimens were exhumed after completion of each test to map the shape of the cuts excavated. The insitu shear strength of the specimens was obtained using torvane and laboratory vane shear tests. Samples were also obtained for density and moisture content measurements.

The experimental results showed that the measured and predicted shapes of cut were in reasonable agreement, with the predicted jet width being conservative in most cases. A strong linear correlation was found between jet penetration, nozzle diameter, nozzle pressure difference and soil bearing capacity. It was found that a bearing capacity coefficient (N_c) of 2.4 was applicable for failure at the jet tip. This value of N_c was corroborated by field trial data. Wall shear stresses back-calculated from the experiments were much smaller than the residual soil strengths obtained from laboratory vane shear

tests and correspond more closely to the erosional strength of clays. The model enables the lift step of the jetting monitor to be computed directly.

The present research demonstrated that valuable information regarding the excavation mechanism can be obtained by careful examination of the actual cut in a soil formed by a jet. It is recommended that further work be done to investigate the erosional process at the jet-soil interface and the properties of the grouted soil, using higher jetting pressures and soils with higher shear strengths. The effect of withdrawal rate on column formation and uniformity of mix is of interest. The brittleness of the grouted product and its effect on strength and deformation behavior is also important.

Thesis Co-Supervisor: Andrew J Whittle
Title: Professor of Civil and Environmental Engineering

Thesis Co-Supervisor: Dr John T Germaine
Title: Principal Research Associate

ACKNOWLEDGMENTS

I would like to take this opportunity to thank Prof Andrew Whittle, Dr John Germaine and Prof Ole Madsen for serving on my Doctoral Thesis Committee. It has been a pleasure working with them and learning to view a problem from different perspectives. Having acquired 14 years of professional experience in industry and coming back to do a Doctoral degree has proven to be a challenging experience for me. Nevertheless, the interaction with Committee members and the experience gained in conducting research in a topic close to my heart has left an indelible impression on my mind.

I thank Prof Whittle for letting me indulge in developing my ideas on the topic of jet grouting, Dr Germaine for his arduous efforts in helping me solve unusual laboratory testing problems and Prof Madsen for his insightful discussions on the analysis of jets and soil erosion.

Pat Dixon, Cynthia Stewart, Dr. Eric Adams, Prof. Jerry Connors and Alice Kalemkiarian have been especially encouraging to me and my family throughout our time at MIT.

Finally, I am grateful to my wife Patsy and my children Ivan and Vivianne for their patience and support during my doctoral studies in the last six years. We are thankful for many who upheld us in their prayers and God's grace in seeing us through.

TABLE OF CONTENTS

CHAPTER 4. DESIGN OF LABORATORY EXPERIMENTS

CHAPTER 5. RESULTS AND INTERPRETATION OF JET EXCAVATION EXPERIMENTS

CHAPTER 6. SUMMARY, CONCLUSIONS AND RECOMMENDATIONS

APPENDICES

LIST OF TABLES

LIST OF FIGURES

CHAPTER ONE

INTRODUCTION

Jet grouting has been successfully applied to a variety of civil engineering works such as foundations and underpinning, deep excavation support, stabilization of slopes, tunneling and ground water cut-offs (Figure 1-1). This thesis is motivated by the tremendous interest in jet grouting techniques within the civil engineering industry since their development in Japan in 1970s (Miki and Nakanishi 1984), and their first application in the United States in the early 1980s (Welsh, 1998).

Jet grouting is a ground improvement process whereby the ground is disintegrated using a high velocity fluid jet and grout is simultaneously injected to mix or replace the soil. The jetting monitor is attached to a hollow rod through which fluids can be injected, with a drill bit fixed at the bottom. A borehole is initially sunk using a wash boring technique (Figure 1-2). At the desired treatment depth, fluid is injected as a high pressure jet from the side of the monitor, the monitor is rotated (at 10 to 20 rpm) and lifted simultaneously as the injection progresses (either continuously or in incremental lift steps). High capacity pumps used in these operations work at pressures of 200 to 600 bars (2900 to 8700 psi) and flow rates of 70 to 180 l/min, to produce jetting velocities ranging from 200 to 350 m/s. Nozzle diameters typically range from 1 to 5 mm. Figure 1-3 shows the typical features of the jet grouting equipment.

In comparison with other more established ground improvement techniques (permeation, compaction and fracture grouting), jet grouting has proven to be the most versatile, and has been successfully applied to a wide range of soil types from clays to

gravels (Figure 1-4). Unlike other techniques involving injection of grouts, grain size and permeability of the soil are not major factors for successful implementation of jet grouting, since a highly erosive fluid jet is used to break down the soil structure and enable the formation of a grouted soil mass without the need for permeation through the soil. The zone of soil treatment is also better controlled compared with other injection grouting techniques, where the quality of treatment is more random and less predictable.

There are three basic grouting methods that are currently employed, using single, double or triple fluid jetting systems (Figure 1-5). The single fluid system utilizes only fluid grout for both cutting and mixing. In the double fluid system, an air shroud is injected to surround the fluid grout and enhance the cutting distance. The triple fluid system uses an air shrouded water jet to cut the soil, while grout is injected separately through a second nozzle located at a lower elevation on the monitor. Typical column diameters range from 0.6 to 2 m. Vertical jet grout columns have been installed at depths exceeding 40 m.

There are two primary concerns in jet grout design; (a) the column diameter that could be achieved for a given set of operational parameters; and (b) the strength of the soilcrete columns that are formed. The latter is usually controlled by specifying the necessary cement content and water-cement ratio of the grout. It is more difficult to determine the achievable column diameters due to inherent variability of soil conditions. In general, larger diameter columns can be formed in granular soils compared with cohesive soils, due to a lack of cohesion. The current practice in the industry is to carry out full-scale field trials at shallow depths (3 to 5 m) and then exhume the jet grout columns to determine whether the operational parameters have been correctly selected to

obtain the desired column diameter. The main operational parameters are pumping pressure, P, pumping flowrate, Q, rotational speed, R_s and lift speed, L_s. The selection of operational parameters is largely based on trial-and-error, relying heavily on the specialist contractors' past experience in similar ground conditions. In many instances, production jet grouting is carried out at much greater depths than the field trials (and as-built conditions of the jet grout columns are not known). Indeed, shallow field trials are unlikely to be representative of the actual soil conditions at depth.

Schlosser (1997) describes the use of simple empirical correlations relating the hydraulic energy per unit height of treated column[1] (i.e., PQ/v_t) to the average column diameter, D (Figure 1-6). This approach is highly site specific and often correlation is good only if the soil is reasonably uniform. In particular, this empirical method ignores the hydrodynamic properties of the jet and soil strength.

This thesis is predicated on the basis that improved predictions of jet grout column diameter should be based on a more rational model of the jetting process. The research focuses on the application of a single fluid grouting system in cohesive soil. One practical advantage of choosing a cohesive material is its low hydraulic conductivity, which ensures that the boundary conditions at the jet-soil interface are well defined as there is no permeation/bleeding of the jet fluid into the surrounding soil during jetting and the soil is effectively sheared under undrained conditions.

---

[1] Energy, $E = PQt$ and height of jet grout column, $H = v_t t$, where t is the time for jetting. Hence, specific energy, $E_s = E/H = PQ/v_t$.

The following is an outline of the scope of this thesis. Chapter 2 provides a review of the current body of knowledge on jet grouting and highlights the limitations of current methods for predicting the size of jet grout columns. The basic concepts of turbulent jets as applied to jet grouting are presented in Chapter 3, together with the theoretical formulation of a proposed analytical model to describe the jet excavation process. Chapter 4 describes the design of a laboratory set-up for measuring jet excavation in cohesive soil. The chapter gives details of the test equipment specifications, the properties of the model soil and jetting fluid used, and test operational parameters for the fluid jet. The complete results of the experiments are presented in Chapter 5 together with detailed interpretation of these data and comparisons with the proposed theoretical model. The thesis concludes in Chapter 6, with a summary of results of the current work and recommendations for future research.

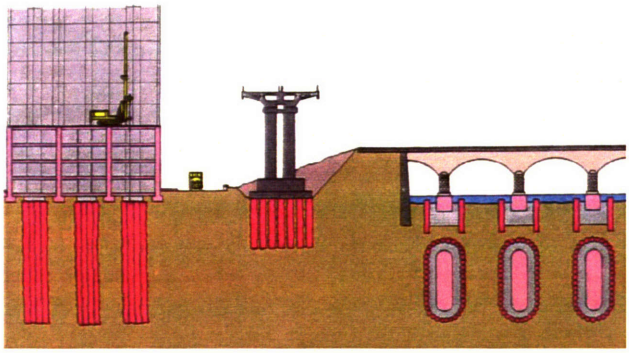

(a) Foundations and cofferdams

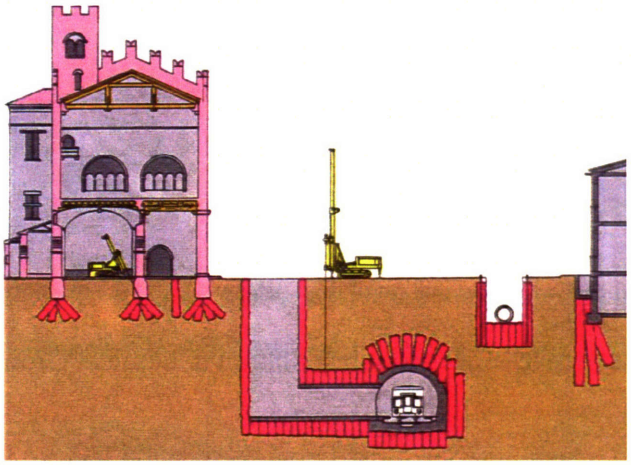

(b) Underpinning, excavations, shafts and soft ground tunneling

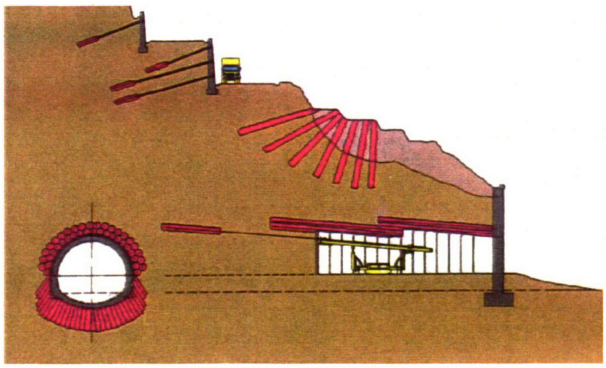

(c) Anchorages, slope stabilization and NATM tunneling

Figure 1-1. Jet grouting applications in civil engineering works
(Trevi brochure, www.trevispa.com)

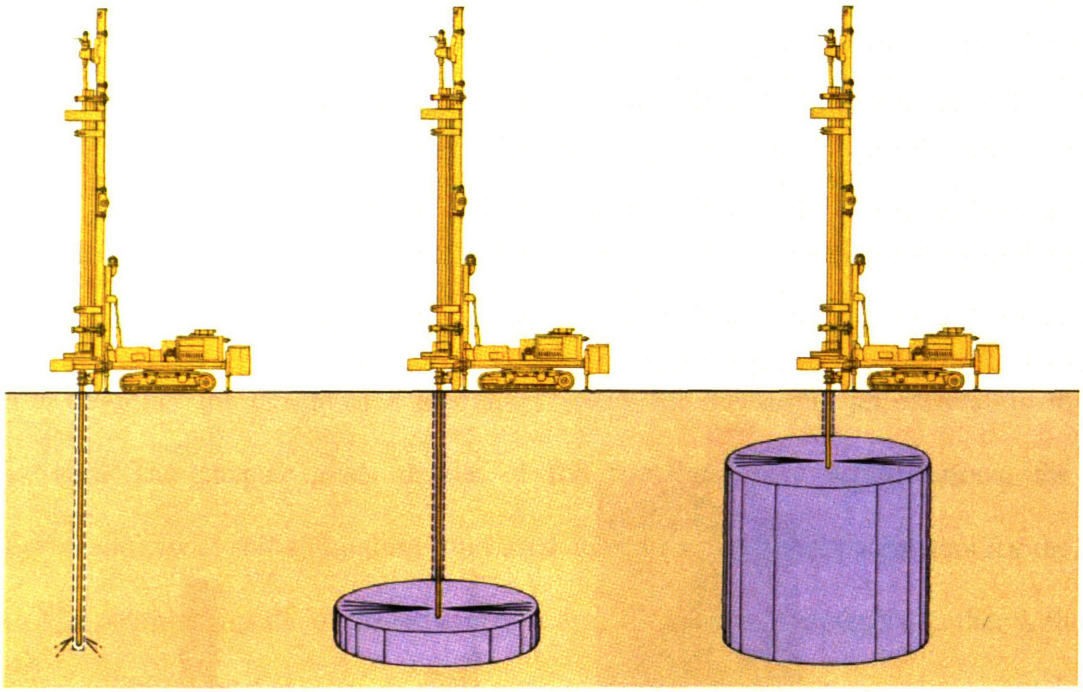

(a) drilling a borehole (b) activation of high pressure jet (c) rotation and withdrawal of rod

Figure 1-2. Sequence of jet grout installation (Chemical Grouting Co. brochure)

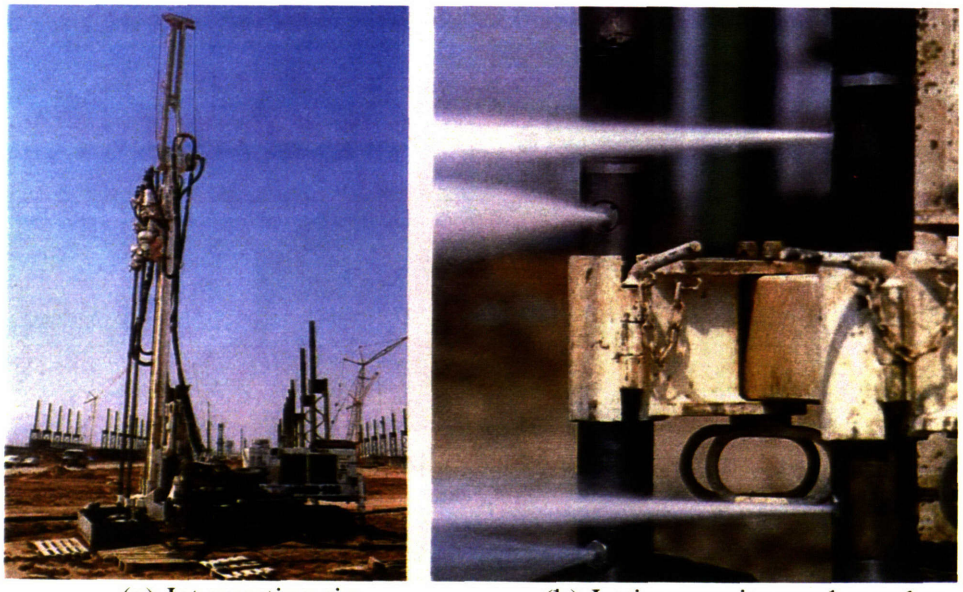

(a) Jet grouting rig (b) Jetting monitor and nozzles

Figure 1-3. Jet grouting equipment (Trevi brochure, www.trevispa.com)

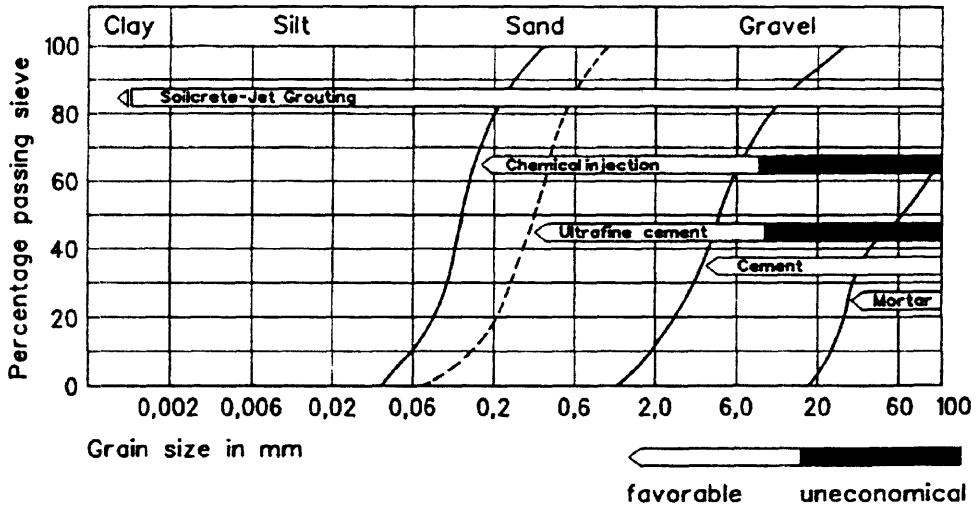

Figure 1-4. Comparison of jet grouting with other injection grouting systems (after Chambosse and Kirsch, 1995)

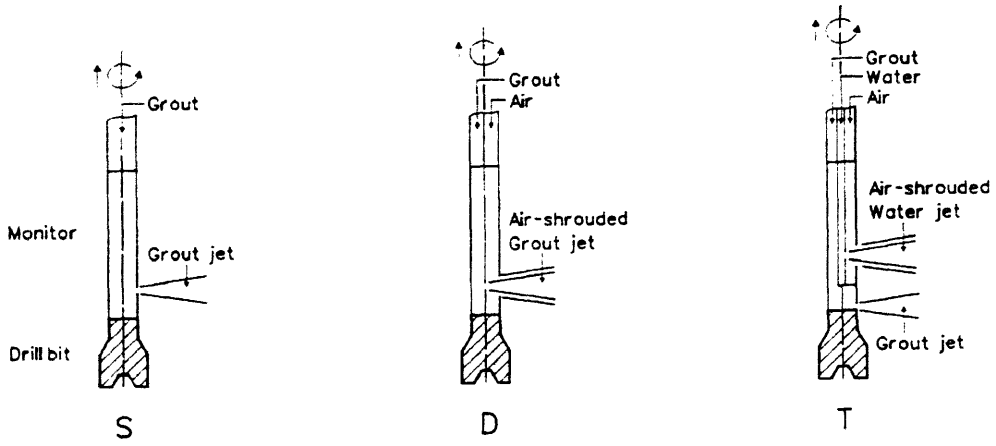

Figure 1-5. Jet grouting systems: single fluid (S), double fluid (D) and triple fluid (T) (after Chambosse and Kirsch, 1995)

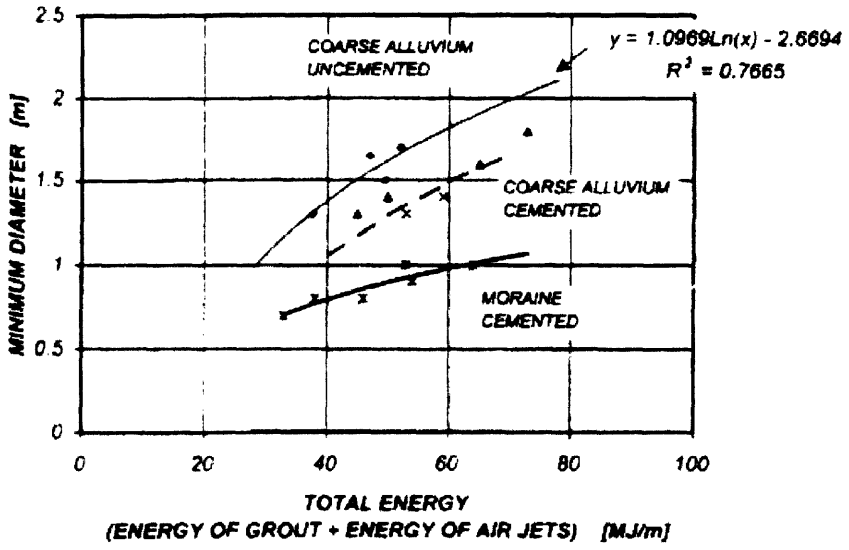

Figure 1-6. Field trial results (after Sembenelli and Sembenelli, 1999)

CHAPTER TWO

FACTORS AFFECTING JET GROUTING PERFORMANCE

2.1 Introduction

Jet grouting can be performed in a variety of soils. Successful performance is highly dependent on an appreciation of the excavation process and how the operational parameters relate to achievable column diameters. The mechanisms involved in treating cohesive soils and granular soils are different due to the permeability of the soils. This chapter reviews the factors that govern the performance of jet grouting treatment, in particular the relationship between operational parameters of the jetting system and soil properties. The current research on improvement of jetting capability and methods of predicting jet grout column diameters are presented.

2.2 Operational Parameters

The main operational variables that control the jet grouting process are nozzle pressure, flowrate, rod rotation speed and withdrawal rate. The maximum injection pressure is governed by the capacity of the pumps, which is currently limited to 400 to 600 bars (Lunardi, 1997). Chambosse and Kirsch (1995) indicated that for safety reasons, pump capacities over 500 bars are seldom used.

Jet grouting is carried out using a single nozzle or multiple nozzles at the same level diametrically spaced from one another. The nozzles are attached to the side of a jetting monitor (Figure 2-1). The number of nozzles and their diameter directly influence the flow rate of the injected fluids and determine the rate of soil excavation and grout

injection to fill the void created in the ground. The number of nozzles may vary from 1 to 4, and nozzle diameters range from 1.0 to 5.0 mm. Lunardi (1997) indicated that a high flowrate, although is desirable, will require a high capacity pump to maintain the high pressures required for excavation. Larger diameter nozzles make more efficient use of the available power offered by high capacity pumps. However, for a given delivery rate, an increase in the number of nozzles will result in a decrease in excavation performance due to greater head losses.

A traversing nozzle ensures that the jet is always directed at a new soil surface for continuous excavation. Adequate exposure time of the soil surface to the jet stream is necessary for effective jet penetration. The exposure time is a function of the strength of the soil and can be controlled by presetting the rod rotation speed. The rotation speed dictates the number of times the soil at a particular position is subjected to the jet impact. The diameter that is achievable is limited only by the resistance of the ground to the action of the jet. Lunardi (1997) indicates that there is a lower limit for the rotation speed below which "jet reflection" will occur (i.e., the jet front will overlap with the pressurized return slurry). This will cause a reduction in the excavation efficiency of the jet. When rotation speeds are too high, the exposure time is reduced and jet penetration will also be limited. The author suggests typical values of rotation speed in the range 5 to 15 rpm (single fluid) and 4 to 8 rpm (double and triple fluid).

The exposure time of the soil to the jet stream is also controlled by the withdrawal rate of the monitor. The movement of the monitor can be continuous or preset at a fixed lift and time interval. As with the rotation speed, there is a minimum rate of withdrawal below which the injected fluid will not effectively penetrate the ground due to jet

reflection and will backup the borehole (Lunardi, 1997). For a fixed rotation speed, a faster withdrawal rate will result in smaller diameters, as a result of reduced exposure time. The author indicates that typical withdrawal rates used are 15 to 100 cm/min (single fluid), 10 to 30 cm/min (double fluid) and 6 to 15 cm/min (triple fluid).

The duration for grout injection is dependent on the size and strength of the grouted soilcrete product required. A longer time of injection will result in increased grout inflow for mixing and hence, higher strength in the final product. The available injection time is determined by the rotational speed and withdrawal rate of the monitor. Therefore, the combination of rotation speed and withdrawal rate has to satisfy requirements for both grout volume inflow and excavation performance of the jet. In the case of the triple fluid jet grouting system, the separation of the grouting process from the excavation process allows greater flexibility in the choice of operating parameters.

As the soil is being excavated away, spoil and dispensed fluid from the jet are continuously being returned to the borehole along the void created adjacent to the advancing jet. This return sludge is transported up the annular space between the drill rod and the borehole wall, and is discharged at the ground surface at atmospheric pressure. The pressure of the slurry in the annular space is dependent on the net hydraulic head of the return slurry in the borehole. The ambient slurry pressure at the exit of the nozzle will increase with the depth at which the jet is operating. In order to achieve effective displacement of the slurry up the borehole, the density of the injected grout should be kept as high as possible by keeping the water-cement ratio low. Typical water-cement ratios range from 0.7 to 1.0, the lower limit being governed by workability of the grout.

The compressed air introduced in the double and triple fluid systems also assists the slurry discharge via air lifting action (Bell, 1993). Figure 2-2 shows the air hole surrounding a nozzle. In horizontal jet grouting operations, the effectiveness of air-lifting in using a compressed air shroud is negated by the adverse orientation of the borehole, which tends to trap the air bubbles. Hence the single fluid system is almost exclusively adopted in horizontal jet grouting operations (Kauschinger et al. 1992).

2.3 Effect of Soil Properties on Achievable Column Diameters

Bell (1993) indicated that sands are best suited for treatment and large columns can be formed (Figure 2-3). Erosion of individual particles requires little energy due to their lack of cohesion between particles (for uncemented materials), and the waste slurry is easily discharged to the ground surface due to its high flowability. The largest column diameters are formed in loose poorly graded soils. Relative density is usually more important than grading, especially when the uniformity coefficient ($c_u = D_{60}/D_{10}$) is high. It is observed that column diameters are not affected by grading for $D_{60}/D_{10} > 10$ (Miki 1985). Welsh et al. (1986) also indicate that particle size distribution has little effect on jet penetration in sand, or silt dominated mixtures with $D_{60}/D_{10} > 8$. Soils with lower uniformity coefficients are most easily eroded, enabling column diameters up to 3m or more at normal operating parameters.

Bell (1993) suggested that gravelly soils are usually amenable to treatment (Figure 2-4). However, highly permeable poorly graded gravels may result in loss of grout and injected fluids due to bleeding into the surrounding ground, thereby reducing intended treatment geometry and altering properties. Shadowing of the jet may occur if

cobble-sized particles or aggregations of large gravel-sized particles are effectively held in place by the surrounding soil. Welsh et al. (1986) indicated that where the proportion of larger particles (such as medium to coarse gravel, cobbles and boulders) exceeds about 50%, poor formation of jet grout columns will occur. This is due to occurrence of jet reflection when the average particle size is large in relation to the jet nozzle diameter.

Bell (1993) noted that excavation efficiency is influenced by even small amounts of cohesion in soils being treated (Figure 2-5). The diameters achieved in silty sands and silts are therefore smaller than in clean sands. This effect is much more significant in cohesive silt or clay deposits. Experience reported by Welsh et al. (1986) has shown that increased cohesion in the soil produces smaller diameters for the same jetting pressures and withdrawal rates. In order to achieve the same diameter, increased energy or decreased withdrawal rates will be required. Most of the energy is absorbed in breaking down the cohesion for soils with undrained shear strength, $s_u > 41$ kPa and column diameters larger than 1.5m are seldom achieved. Luo et al. (1997) reported that jet grout columns cannot be effectively formed in clayey silts with SPT, N = 6 to 7 blows/0.3m and s_u = 48 to 52 kPa, even with the triple fluid jetting system. This is consistent with observations by Bell (1993), which suggests that jet grouting in soils with shear strengths, $s_u > 50$ to 60 kPa are limited. Figure 2-6 shows an example of the results of treating a stiff clayey soil.

Bell (1993) indicated that because of the range of operational parameters that needs to be controlled and the complexity of natural soils, it is not surprising that no reliable theoretical relationships governing jet grouting have so far been produced. The selection of parameters often has to be guided by experience and empirical relationships.

The most comprehensive guidelines for selection of jetting parameters are given by the Japanese Jet Grouting Association (JJGA, 1995). Tables 2-1 and 2-2 provide the parameters for double fluid jet grouting in granular soil and cohesive soil respectively for depths less than 25m below ground. The operational parameters for the triple fluid system are given in Table 2-3 and 2-4. The triple fluid system allows jet grout columns to be formed at depths up to 40m. It can be seen that the limit of soil treatment for cohesive soil is N = 4 blow/0.3m for double fluid system and N = 9 blows/0.3m for triple fluid system. The corresponding limits for treating granular soil using the triple fluid system, are N = 50 blows/0.3m (double fluid) and N = 200 blows/0.3m (triple fluid). The achievable column diameters are reduced when jetting is carried out at greater depths between 30 and 40m. It can be seen that the expected range of column diameters will be 1.0 to 2.0m generally.

More recently, development of high capacity pumps in Japan has enabled the formation of much larger diameters up to 5m, using the method termed Superjet (Yoshida et al., 1996). The method is basically similar to the double fluid system, except that a much higher flowrate is employed. The operational parameters associated with the formation of such large diameters as recommended by the Japanese Superjet Research Association (JSRA, 1995) are summarized in Tables 2-5 and 2-6 for granular soil and cohesive soil respectively. The limits of treatment are reached at N = 100 blows/0.3m for sand and N = 5 blows/0.3m for clay, for the diameters specified.

2.4 Mechanism of Soil Excavation

Various authors have attempted to explain the process of soil excavation by a fluid jet. According to Yahiro and Yoshida (1973) there are three fundamental aspects of the jet grouting process that are essential for understanding the effectiveness of jet grouting:(1) the structure of a water jet, (b) the jetting energy, and (c) the excavation mechanism. They indicate that the characteristics of jet structure and its energy have been clarified through research on nozzle design. However, the process of excavating soil by high pressure fluid jets is very complex and has yet to be fully understood. Researchers have simplified the problem by considering the fluid jet as a rigid body penetrating within the soil mass. It has also been suggested that the process is a cavitation problem and can be studied as a hydrodynamic phenomenon, although the results are still not conclusive. The authors suggest that soil failure is induced by impact stress at the tip of the jet (Figure 2-7). The velocity and pressure distributions in the jet can be represented by a normal distribution function and the stress in the ground can be calculated using Boussinesq's classical elastic stress solution, giving the axial and radial stress components. The soil will fail when the resulting shear stress on the critical failure plane exceeds the shear strength of the soil.

Kanematsu (1980) suggested that the mechanism of soil disintegration by high speed water jets consist of a number of effects:-

a. hydrodynamic pressure (i.e. kinetic energy of the jet)
b. pulsation (or hammerhead) load of water jet
c. water wedge effect
d. impingement force of water mass

e. cavitation (or tensile action)

The high speed water jet accompanied by a large hydrodynamic pressure repeatedly impinges on the soil and destroys it via the impingement force and wedging effect. At the same time, negative pressures produced by the flow of water jet, act to remove the soil grains from their original positions.

Kauschinger et al. (1992) highlights the basic requirement in the jet grouting process is that there must be continuous flow of cuttings up the borehole to the ground surface where atmospheric pressure exists. This requirement ensures that the pressure head at the point of injection is only due to the static head of the return slurry in the borehole. When jet grouting is correctly executed and the condition of flow continuity is satisfied, then the process of jet grouting is basically a high velocity erosion process.

Covil and Skinner (1994) suggest that the high pressure of the jet causes a mixing of the soil and continuous systematic 'claquage' of the soil within the radius of influence of the excavating jet. This process would not give rise to any strain phenomena in the surrounding ground (and hence will not influence the insitu soil stresses outside the radius of influence). Even when operating at very high pressures, the process of injection only causes an increase in the pressure within the excavated volume.

As opposed to the notion that the process of jet grouting is mainly due to soil disintegration by the erosive action of the jet, Miki (1985) and Bell (1993) reported that in gravels, grout is observed to flow through the soil pores without destroying the soil structure, suggesting that permeation can be an important mechanism in very coarse-grained materials.

Although the above research reveals some aspects of the soil excavation process in jet grouting, there have been no attempts to observe or measure the actual process directly. The main difficulty lies in the inability to see through the soil during the process of column formation. Croce and Flora (2000) suggest that an investigation of the probable excavation mechanisms (such as permeation, erosion, mixing and replacement) has to be carried indirectly through careful examination of the physical features of jet grout columns after treatment has been performed.

2.5 Behavior of Liquid Jets

An understanding of the behavior of liquid jets is fundamental to research on jet cutting. The characteristics of water jets at high velocities have been studied by many researchers (Leach and Walker 1966, Shavlovsky 1972, Yainada 1974). Many of these studies were related to use of water jets for fragmentation of rocks or cutting of metals in the mining and metallurgical industries. Extensive experimental trials have been carried out using water jets issuing into quiescent air and impacting on a solid face. However, there is much more limited information on specific research relating used for jet grouting in soils.

The most significant contribution to jet grouting technology is attributed to Yahiro and Yoshida (1974) who studied the characteristics of water jets under a variety of simulated field conditions in the laboratory. Their research involved experiments using water jets issuing into a liquid medium, and included investigations on the effects of an air shroud and hydrostatic pressure on jet penetration. Their experimental apparatus comprised a large diameter pressure chamber (1.13m in diameter and 3m long) where the

pressure of the liquid medium could be increased to simulate effects of different operating depths of the nozzle in the ground. Pressures in the jet were measured using a pressure transducer which could be moved in the axial and radial directions. The nozzle was 2 mm in diameter, and included a 13^{o} cone angle with a 5 mm straight section. A slit 1 mm wide surrounding the nozzle allows compressed air to be introduced as a shroud around the nozzle. The outlet pressure of the jet, P_o was measured within a distance of 5mm from the nozzle.

Under normal jet grouting conditions, the jet operates under a submerged condition, hence the penetrating distance of the jet is severely attenuated. Figure 2-8 shows the influence of the ambient pressure around the jet. It is observed that jet penetration is very sensitive to small increases in the ambient pressure up to approximately 1 kg/cm^2. Further increase beyond this level does not alter the jet penetration characteristics significantly. Yahiro and Yoshida (1974) studied the effectiveness of introducing an air shroud to improve the penetration of the jet. Figure 2-9 shows that the jet penetration is increased when the air flowrate is increased, however, for flowrates above 1.0 m^3/min, there is no further influence of the compressed air on the jet penetration distance. The authors indicate that when the air flowrate is greater than 5 m^3/min, the jet becomes irregular, and hence less focused

The jet structure consists of two regions: (a) an initial core region, where the pressure at the jet centerline remains constant, and (b) the mixing region, where the pressure decays with distance from the nozzle (Figure 2-10). The mixing region can be further divided into three regions: the transitional, main and final. Table 2-7 summarizes

the demarcations of the various regions determined from the pressure distributions obtained by Yahiro and Yoshida (1974).

Figure 2-11 shows the changes in the boundaries of the different regions due to an increase in ambient pressure. It was observed that the length of the initial region ranged from x_o = 15 to 17 mm, depending on the nozzle pressure, for the base case of jetting in water (Test series I). The boundary between the transitional region and main region was observed to occur at x_1 = 46 to 53 mm, while the end of the main region varied between x_2 = 102 to 122 mm. It is observed that when an ambient pressure was applied (Test series III), the length of the initial region was only reduced by approximately 10% to x_o = 13 to 15 mm, although the lengths of the transitional and main regions were reduced much more significantly (by 71 % and 67 % respectively).

Figure 2-12 shows the changes in the diffusion regions under the influence of a compressed air shroud (Test series IV). It can be seen that the length, x_o increased by 187% when an air shroud was introduced around the water jet, producing x_o = 29 to 34 mm. The upper and downstream boundaries of the main region were correspondingly changed to x_1 = 170 to 210 mm, and x_2 = 460 to 500 mm respectively (i.e. an increase of 386 % and 425 %). Hence, the effectiveness of a compressed air shroud in extending the penetration of the jet is clearly demonstrated.

Figure 2-13 shows that there is no significant difference in the length of the initial region, x_o when jetting in a viscous medium of greater density (such as bentonite or mud slurry), although there is some indication that the main region is displaced further downstream at nozzle pressures greater than 300 kg/cm^2. However, this increase in penetration with nozzle pressure is not observed in the tests where the ambient pressure

or compressed air is used (Figures 2-14 and 2-15). Yahiro and Yoshida (1974) conclude that in general the observed pressure distributions were not significantly changed when jetting in bentonite or mud slurry.

Pressure measurements along the axis of the jet show that the centerline dynamic pressure (P_c) was reasonably constant in the initial region and was equal to the outlet pressure, P_o. Within the mixing region, the decline of the centerline dynamic pressure was observed to follow an exponential function:

$$P_c = P_o e^{n} \tag{2.1}$$

with

$$n = c_1(x-x_o)^{c_2} \tag{2.1a}$$

where x is the distance from the nozzle, x_o is the length of the initial region, and c_1 and c_2 are experimental constants which depend on the nozzle and jetting conditions. Empirical values of these coefficients range from c_1 = -0.00007 to -0.248 and c_2 = 0.956 to 2.714. The agreement of Eqn.2.1 with test measurements was reported to be very good, with a coefficient of correlation of 0.98.

The pressure distribution (P_r) in the radial direction was found to approximate to a normal distribution function:

$$P_r = P_c e^{-m} \tag{2.2}$$

where, $m = r^2/(2r_i^2)$, r is the radial distance from the jet centerline axis and r_i is the radial dimension to the inflexion point on the curve, and is a measure of the spread of the jet width. Figure 2-16 shows the typical radial pressure distribution obtained from the experiments by Yahiro and Yoshida (1974).

In most research experiments, the fluid jet is injected through a nozzle aligned with the axis of the feed line and the characteristics of the jet are studied under this condition. However, because jet grouting employs a pressurized fluid that is discharging sideways (i.e. through the nozzle on the side of the monitor), significant turbulence is generated in the fluid jet due to the abrupt change in flow direction close to the point of injection. This causes the jet to become dispersed and decreases its eroding efficiency (Yoshida et al., 1991). Recent research has been directed to enhancement of jetting performance by improving the focus of the cutting jet. The condition of flow upstream of the nozzle is critical to the performance of the jet. By reducing the curvature of the jet, when it transitions from vertical flow down the rod to horizontal flow through the nozzle, better focusing is achieved (Shibazaki et al., 2003).

Jet focusing is also improved by adopting a tapered nozzle with a short straight length just before the jet emerges from the nozzle. The nozzle design is based largely on the work of Leach and Walker (1966) for rock cutting using water jets in air. Figure 2-17(a) shows the pressure decay along the jet centerline with distance from the nozzle for different nozzle shapes, as measured in laboratory tests. As can be seen, the best performance is obtained using an included angle of 13^{o}. Figure 2-17(b) shows that, for a fixed cone angle of 13^{o}, optimum jetting condition is achieved when the length of the straight portion in the nozzle is approximately 3 times the nozzle diameter. For applications in jet grouting, Shibazaki (1997, 2003) recommends that the nozzle design be based on a 13^{o} cone angle with a straight portion of between 2.5 and 3.0 times the nozzle diameter. The material of the nozzle must be very hard, usually tungsten carbide, and the internal surface has to be highly polished. The improvement in focusing has led

to the recent development of Superjet technology to form columns with diameters up to 5m.

Recent research by Yoshida et al. (1989) emphasized the influence of the input hydraulic power on jet cutting distance. The product of the pressure and flowrate (PQ) represents the input hydraulic power, where P is the pump pressure and Q, the flowrate. Figure 2-18 shows the contours of equal power and cutting distance obtained in model sand, loosely compacted using water (SPT, N = 2 to 3 blows/300mm). It is evident that the cutting distance is closely related to the input hydraulic power, the larger the input power the greater the cutting distance. The authors suggest that flowrate has a large influence on cutting distance compared with pumping pressure. Hence, for efficiency in equipment design, a lower operating pressure and higher flowrate is desirable. Yoshida et al. (1996) recommend an operating pressure, P = 300 bars and flowrate, Q = of 600 l/min. This level of operating pressure is lower than the 400 to 600 bars commonly adopted in practice in conventional single, double and triple fluid jet grouting systems.

Yoshida et al. (1991) have also studied the effects of the number of passes of the nozzle (N_p) and rotation speed (R_s) on cutting distance, using model soil consisting of silty sand with SPT, N = 3 to 6 blows/300mm. For a given hydraulic power, the cutting distance was found to increase with the number of passes of the jet (Figure 2-19). It was observed that the rate of increment of cutting distance diminished rapidly beyond about 10 passes. In addition, for a given hydraulic power, the cutting distance decreased with increasing rotational speed of the jet (Figure 2-20). The reduction was most significant for rotational speeds less than 10 rpm.

For effective cutting, operational specifications should be based on a rotational speed of 10 rpm, with the frequency of impact limited to within 10 passes of the jet (Yoshida et al., 1996). Yoshida et al. (1991) emphasized that, in order to achieve the minimum number of passes (N_p) required for soil cutting in a given lift step (Δz), the withdrawal rate (v_t) has to be selected such that the duration of jetting (Δt) is correctly matched with the rotation speed (R_s), i.e. $\Delta t = N_p/R_s = \Delta z/v_t$.

2.6 Prediction of Jet Grout Column Diameter

Due to the complexity of the jet grouting process, empirical correlations have been developed by specialist contractors to relate column diameter with relative density or soil strength. It is common practice to correlate diameter with standard penetration test (SPT) data (which is a measure of relative density) for granular soils or undrained shear strength (s_u) for clays. Experience has shown that such simple correlations are inadequate due to the many variables that govern the jet grouting process.

For a given jet grout column diameter (D) and a withdrawal rate (v_t), the volume of soil (V) eroded per unit time is $dV/dt = (\pi D^2/4)v_t$. It is commonly assumed that, for a fixed input energy and similar soil, dV/dt is constant (Essler 1995), therefore $D \sim 1/\sqrt{v_t}$ (i.e. the column diameter is inversely proportional to the square root of the withdrawal rate). This is consistent with findings by Bell (1983) which showed that, for a fixed jetting energy and soil condition, the square of the treated diameter is inversely proportional to the withdrawal rate. This relationship has also been shown in Figure 2-21 after Coomber (1985). Alternatively, the average cross-sectional area of the jet grout column can be expressed as the grouted volume per unit height of column formed. Figure

2-22, summarizes data compiled by Covil and Skinner (1994) in this format. There is a general decreasing trend in the data, but the scatter in the measurements makes the interpretation inconclusive.

The time (Δt) for cutting the soil in each lift step (Δz) is given by $\Delta t = \Delta z/v_t$, where v_t is the withdrawal rate of the rod. Since Δt and v_t are inversely related, it would be possible to correlate the column diameter with the duration of cutting per step (Δt) directly. This is demonstrated in Figure 2-23, based on field trials in silty sand (SPT, N = 10 to 15 blows/300mm) carried out by Yoshida et al. (1996), where an approximately linear correlation between jet grout column diameter and pullout time (i.e. the time of jetting required for soil cutting in each lift step) is obtained. It can be seen that the column diameter (average D = 5.7m) is largest when $t = t_o$ (the maximum duration), decreasing linearly as the duration of jetting is shortened ($t/t_o < 1.0$). When t/t_o is reduced by half, D reduces by approximately 12 % to an average of 5 m.

Tornaghi (1989) introduced the use of specific energy (E_s) as a parameter for correlating with jet grout column diameter. E_s is defined as the energy (E) consumed in forming a unit height of jet grout column (i.e. $E_s = E/H$). The total energy supplied, $E = P_pQt$ and treated column height, $H = v_tt$, where P_p is the pressure at the pump, Q is the flowrate, v_t is the withdrawal rate and t is the duration of injection. The specific energy may be expressed in a simpler form, $E_s = PQ/v_t$. At the present state of practice, this method of correlating jet grout column diameter is widely used according to Schlosser (1997).

Paggliacci et al. (1994) indicated that the formula can be applied to single, double and triple fluid systems. In the case of single and double fluid systems, the grout jet is the

cutting jet and hence we may designate the contribution of the grout jet, $E_{sg} = P_g Q_g / v_t$. For the triple fluid system, the water jet is the cutting jet, with energy contrinution, $E_{sw} = P_w Q_w / v_t$. Tornaghi (1989) proposed that the compressed air component can be expressed by a dimensional equation, E_{sa} (in MJ/m) = $0.035 Q_a[\text{l/min}]\{(10 P_a[\text{MPa}])^{0.29} - 1\}/v_t[\text{cm/min}]$. For the double and triple fluid systems, the total specific energy for cutting (E_{st}) can be expressed as the combination of the various components, $E_{st} = (E_{sg} + E_{sa})$ and $E_{st} = (E_{sw} + E_{sa})$ respectively. Figure 2-24 shows an example of correlating the column diameter with total specific energy, E_{st}. Experience has shown that due to uncertainty of the energy losses in the jetting system and the variability of soil parameters, data plotted in this way is highly site specific. Paggliacci et al. (1994) indicates that other variables have not been accounted for in the above formulas, which are important in jet grouting treatment, such as the number of nozzles and their diameter, the depth at which jetting takes place, the density of the jetting fluid and the energy losses in the feed lines.

Croce and Flora (2000) present data suggesting that energy losses in the jetting system could be as large as 20% (Figure 2-25). To account for energy losses, the authors propose that the energy at the nozzle exit should be used to correlate with column diameter instead i.e., $E_n = \frac{1}{2} m v_o^2 / H$, where m is the mass of cutting fluid injected in a given time interval, Δt, and v_o is the nozzle exit velocity. The mass is computed as $m = \rho Q \Delta t$, where ρ and Q are the fluid mass density and flowrate of the cutting jet respectively. The exit velocity is given by $v_o = (Q/n)/A_n$, where n is the number of nozzles and A_n is the cross-sectional area of the nozzle, $A_n = \frac{1}{4} \pi d_n^2$.

However, the authors found that the correlation of column diameter with E_n is still very scattered, except for silty sands with average SPT N = 15 blows/0.3m, where an approximately linear relationship was obtained (Figure 2-26).

2.7 Concluding Remarks

The above review of the current state of practice and research suggest that the methods of predicting jet grout column diameter is still highly empirical and relies heavily on a database of field trial results to assist in the selection of operational parameters. The interaction between the jet and soil is complex, and excavation mechanisms in different soil types can be substantially different.

To date, investigation of jet cutting performance is limited to laboratory experiments and no theoretical formulation has been proposed that adequately describes the jet excavation process explicitly. In most cases, jetting experiments are carried out on model soils consisting of sand. This is probably due to the ease of preparation and handling in the laboratory. There is so far no study on jetting of cohesive soils on the scale conducted for the experiments on sand, such as those of Yahiro and Yoshida (1974) and Yoshida et al. (1989, 1991), even though jet grouting in cohesive soils are commonly carried out in the industry. The knowledge gained from experiments in granular soils may not be directly applicable to cohesive sols. It is therefore timely that research be focused on cutting of cohesive soils, so that the technological advances achieved in equipment design and operations can be fully harnessed and successfully applied to a wider range of soils.

It has been recognized that an understanding of the jet characteristics is fundamental to the study of the jet grouting process. It is proposed that the problem of jet excavation be investigated from a theoretical approach, based on fundamental principles of jet hydrodynamics and soil mechanics, so that the results can be generalized and used as a predictive tool. The following chapter presents the theory of jets and their application to the jet excavation problem in cohesive soil.

Table 2-1. Effective column diameter and operational parameters for double fluid system in granular soil (after JGGA, 1995)

SPT N value (blows/0.3m)	N<10	10<N<20	20<N<30	30<N<35	35<N<40	40<N<50
Diameter (m) 0 < Z < 25m	2.0	1.8	1.6	1.4	1.2	1.0
Withdrawal rate (min/m)	40	35	30	26	21	17
Grout flowrate (l/min)	60					
Grout pressure (bars)	200					
Air Pressure (bars)	7					

Table 2-2. Effective column diameter and operational parameters for double fluid system in cohesive soil (after JGGA, 1995)

SPT N value (blows/0.3m)	Hammer weight	0<N<1	1<N<2	2<N<3	3<N<4
Diameter (m) 0 < Z < 25m	2.0	1.8	1.6	1.4	1.2
Withdrawal rate (min/m)	30	27	23	20	16
Grout flowrate (l/min)	60				
Grout Pressure (bars)	200				
Air Pressure (bars)	7				

Table 2-3. Effective column diameter and operational parameters for triple fluid system in granular soil (after JGGA, 1995)

SPT N value (blows/0.3m)	N<30	30<N<50	50<N<100	100<N<150	150<N<175	175<N<200
Diameter (m) 0<Z<30m	2.0	2.0	1.8	1.6	1.4	1.2
Diameter (m) 30<Z<40m	1.8	1.8	1.6	1.4	1.2	1.0
Withdrawal rate (min/m)	16	20		25		
Grout flowrate (l/min)	180			140		
Grout pressure (bars)	20 to 50					
Water flowrate (l/min)	70					
Water pressure (bars)	400					
Air pressure (bars)	7					

Table 2-4.Effective column diameter and operational parameters for triple fluid system in cohesive soil (after JGGA, 1995)

SPT N value (blows/0.3m)	N<3	3<N<5	5<N<7	7<N<9
Diameter (m) 0<Z<30m	2.0	1.8	1.6	1.2
Diameter (m) 30<Z<40m	1.8	1.6	1.4	1.0
Withdrawal rate (min/m)	20		25	
Grout flowrate (l/min)	180		140	
Grout pressure (bars)	20 to 50			
Water flowrate (l/min)	70			
Water pressure (bars)	400			
Air pressure (bars)	7			

Table 2-5.Effective column diameter and operational parameters for Superjet system in granular soil (after JSRA, 1995)

SPT N value (blows/0.3m)	N<50	50<N<100	N<50	50<N<100
Diameter (m) 0 < Z < 20m	3.5	3.2	5.0	4.5
Diameter (m) Z > 20m	3.2	2.8	4.5	4.0
Withdrawal rate (min/m)	12		16	
Grout flowrate (l/min)	400		600	
Grout pressure (bars)	300			
Air Pressure (bars)	7			

Table 2-6.Effective column diameter and operational parameters for Superjet system in cohesive soil (after JSRA, 1995)

SPT N value (blows/0.3m)	N<3	3<N<5	N<3	3<N<5
Diameter (m) 0 < Z < 20m	3.5	3.2	5.0	4.5
Diameter (m) Z > 20m	3.2	2.8	4.5	4.0
Withdrawal rate (min/m)	12		16	
Grout flowrate (l/min)	400		600	
Grout pressure (bars)	300			
Air Pressure (bars)	7			

Table 2-7 Observed boundaries of diffusion regions of jet (after Yahiro and Yoshida,1974)

Test series	Test no.	Medium	Viscosity	Specific gravity	Outlet pressure	Ambient pressure	Air flowrate	Region boundaries		
			μ (cP)	G_s	P_o (kg/cm^2)	P_{am} (kg/cm^2)	Q_a (m^3/min)	x_o (mm)	x_1 (mm)	x_2 (mm)
I	1	Water			125.2			17	53	118
	2				251.6			16	46	102
	3				421.8			17	52	122
	4				125.2			15	48	107
	5				186.9			15	49	109
II	6	Bentonite	236	1.059	162.3			15	55	123
	7		352	1.067	261.8			15	50	131
	8		563	1.079	186.9			14	60	114
	9		605	1.080	348.7			15	61	160
	10		402	1.072	435.9			16	85	210
	11		98	1.055	338.3			17	72	150
	12	Mud	63	1.073	397.5			16	68	180
	13		41	1.099	279.5			16	58	170
III	15	Water			187.8	2.0		15	36	70
	16				163.4	4.0		14	38	69
	17				116.0	2.0		15	35	83
	18				98.6	4.0		13	32	74
	19				190.5	1.0		15	34	85
	20				231.5	1.0		14	37	80
	21				209.5	3.0		15	36	68
	23	Bentonite	101	1.031	172.2	2.0		15	38	80
	24		736	1.085	290.2	2.0		15	41	68
	25		135	1.040	179.5	4.0		14	33	65
	26		365	1.057	208.7	4.0		15	42	78
	27		276	1.054	414.0	3.0		16	40	87
IV	28	Water			226.6		1.0	29	180	510
	30				191.5		5.0	32	190	490
	31				284.5		1.0	32	200	500
	32				223.5		1.0	29	170	500
	34				236.1		3.0	25	190	400
	35				291.2		5.0	34	200	460
	36				194.8		5.0	29	210	460
	39	Bentonite	603	1.070	477.2		1.0	29	210	480
	40		450	1.069	425.8		3.0	30	200	480
	41		346	1.058	317.9		1.0	31	205	510
	42		804	1.087	328.8		3.0	30	220	480
V	45	Water			206.4	1.0	3.0	26	190	440
	46				209.0	3.0	1.0	28	140	370
	47				200.0	3.0	3.0	27	140	420
	48				262.9	1.0	1.0	28	150	440
	49				234.8	3.0	1.0	25	140	400
	50				252.9	1.0	3.0	28	120	450
	51				235.1	3.0	3.0	25	140	400
	52	Bentonite	233	1.051	486.7	3.0	1.0	24	130	390

Note: Results for test no.14, 22, 29, 33, 37, 38 and 43 were not reported in the paper.

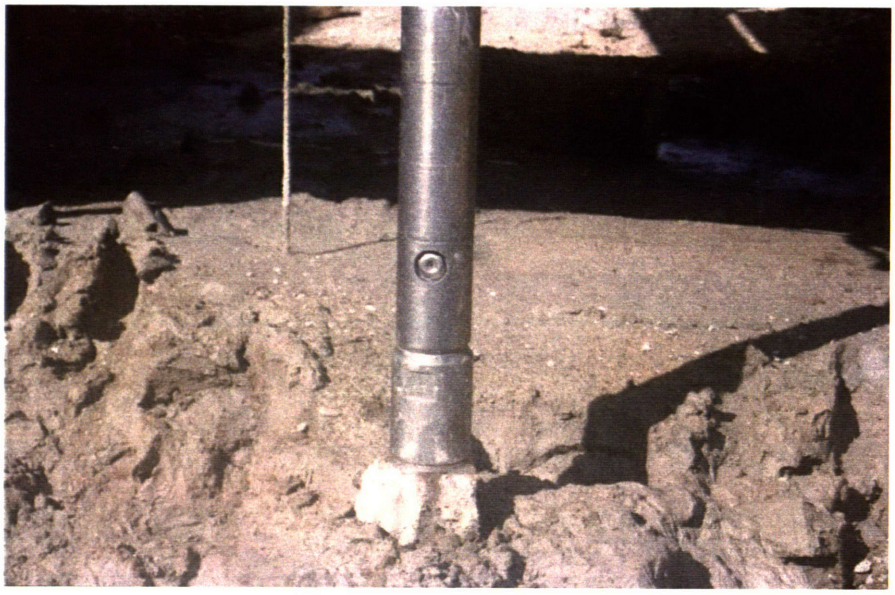

Figure 2-1. Jet grouting monitor with side nozzle and cutting bit at toe

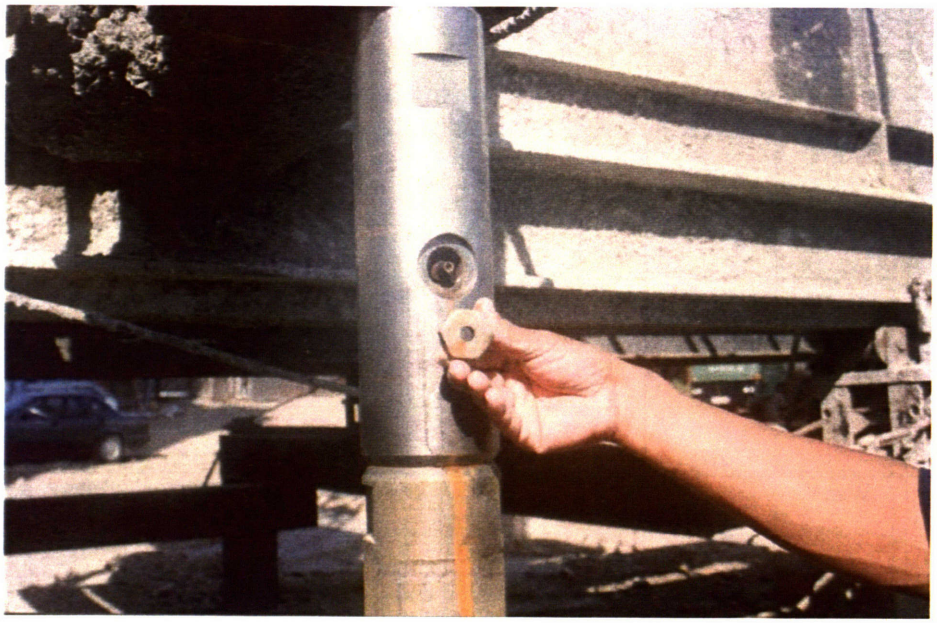

Figure 2-2. Detail of nozzle with annular hole for compressed air

Figure 2-3. Jet grout columns in uniform sand (from Pacchiosi brochure)

Figure 2-4. Jet grout columns in gravelly soil with cobbles and boulders (from Trevi brochure)

Figure 2-5. Jet grout columns in silty sand (from Pacchiosi brocure)

Figure 2-6. Jet grout columns in silty clay

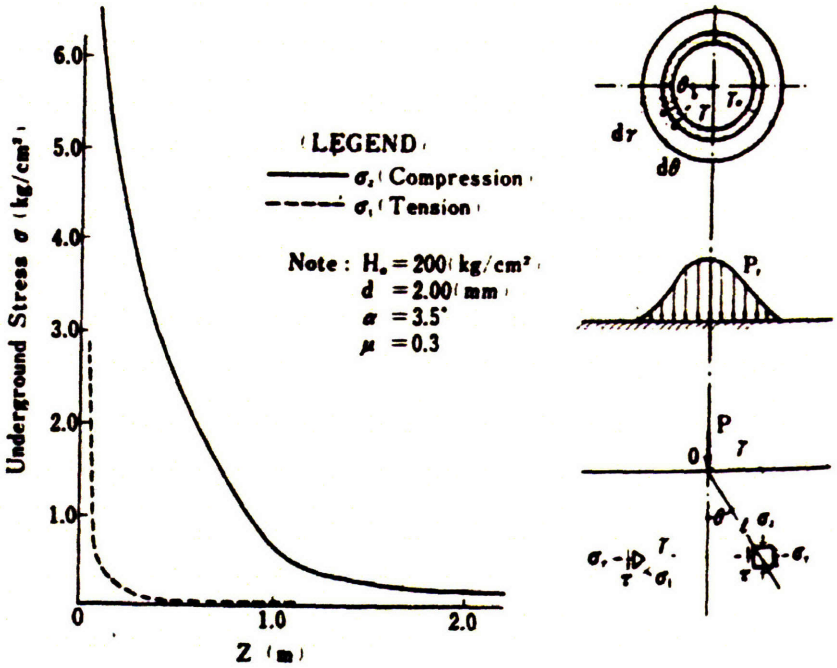

Figure 2-7. Stress distribution in soil and rock induced by jetting pressure (after Yahiro and Yoshida, 1973)

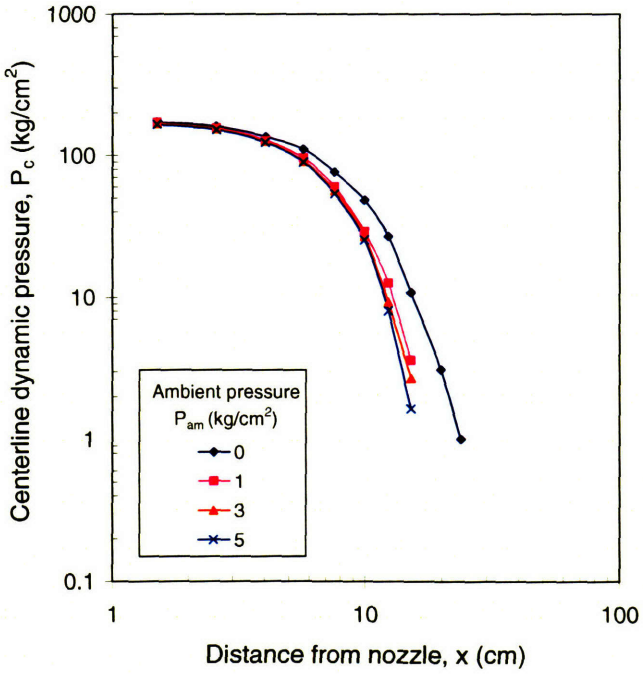

Figure 2-8. Effect of ambient pressure on centerline pressure decay for jetting in water medium (after Yahiro and Yoshida, 1974)

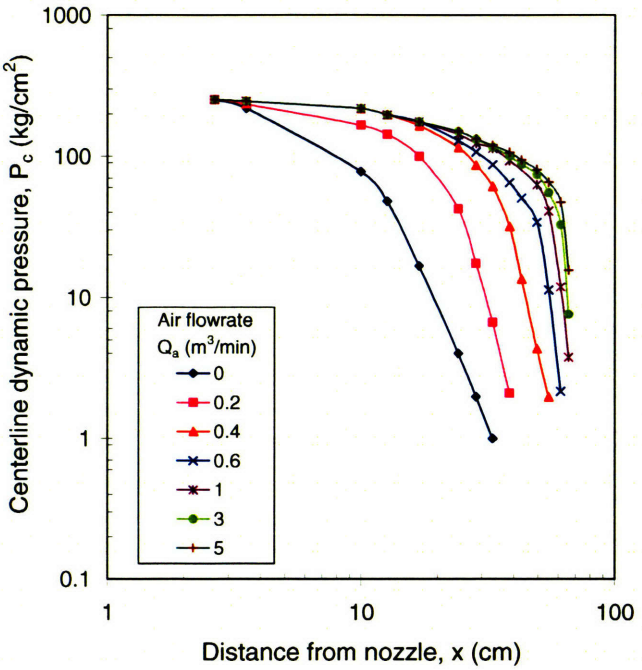

Figure 2-9. Effect of compressed air flowrate on centerline pressure decay for jetting in water medium (after Yahiro and Yoshida, 1974)

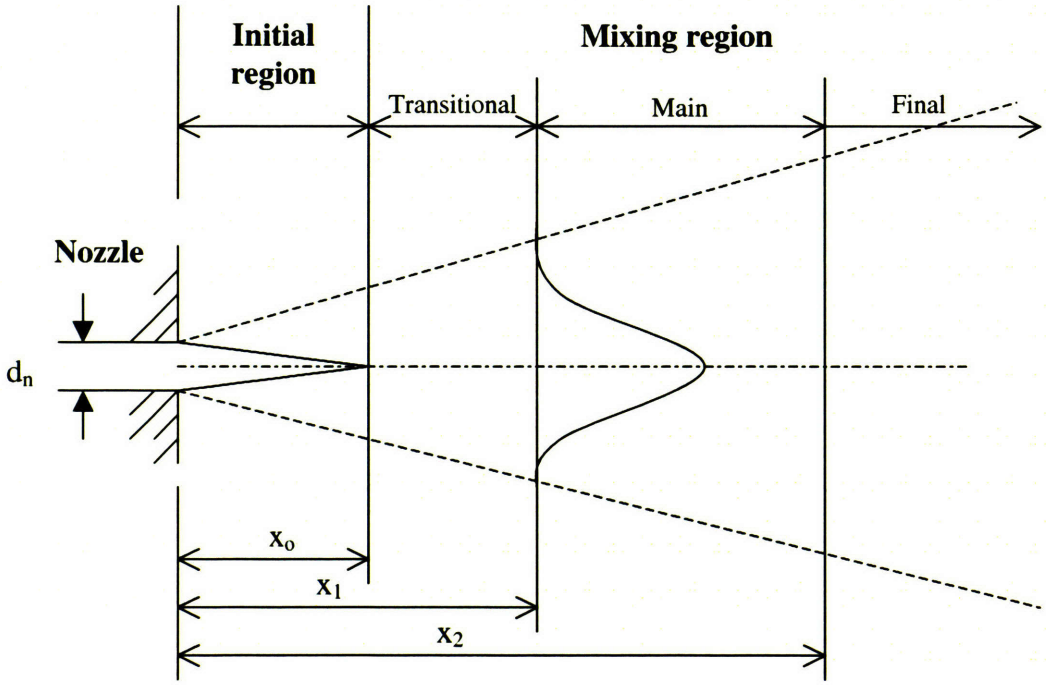

Figure 2-10. Boundary of diffusion regions in a jet

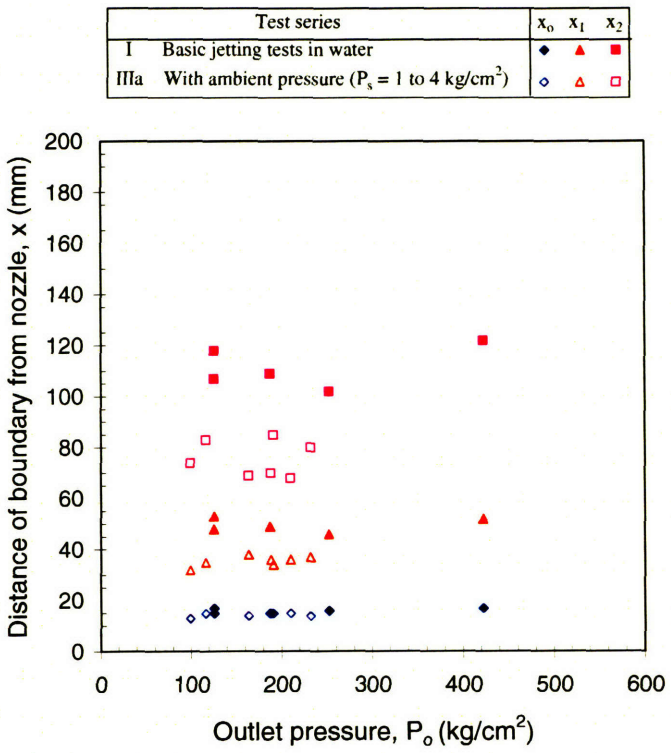

Figure 2-11. Effect of ambient pressure on jet diffusion boundaries

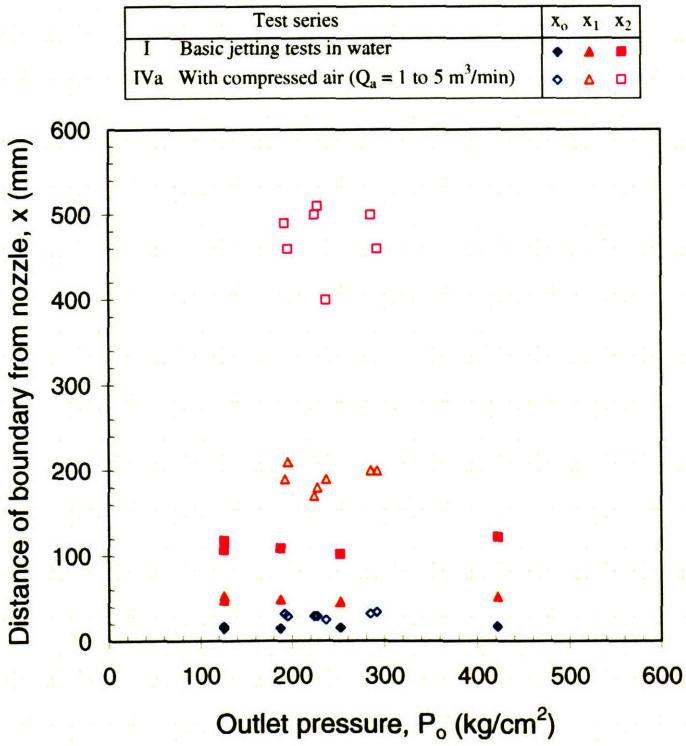

Figure 2-12. Effect of compressed air on jet diffusion boundaries

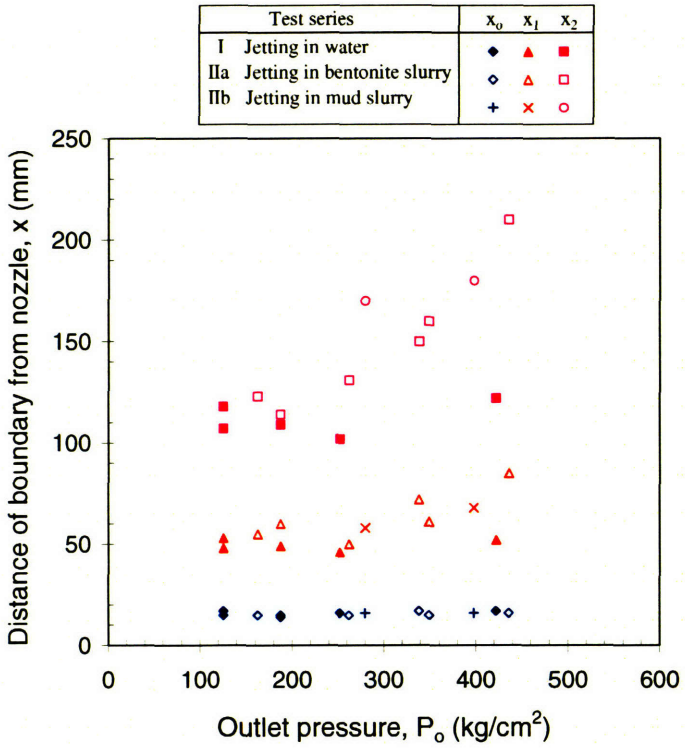

Figure 2-13. Effect of jetting in bentonite and mud slurry

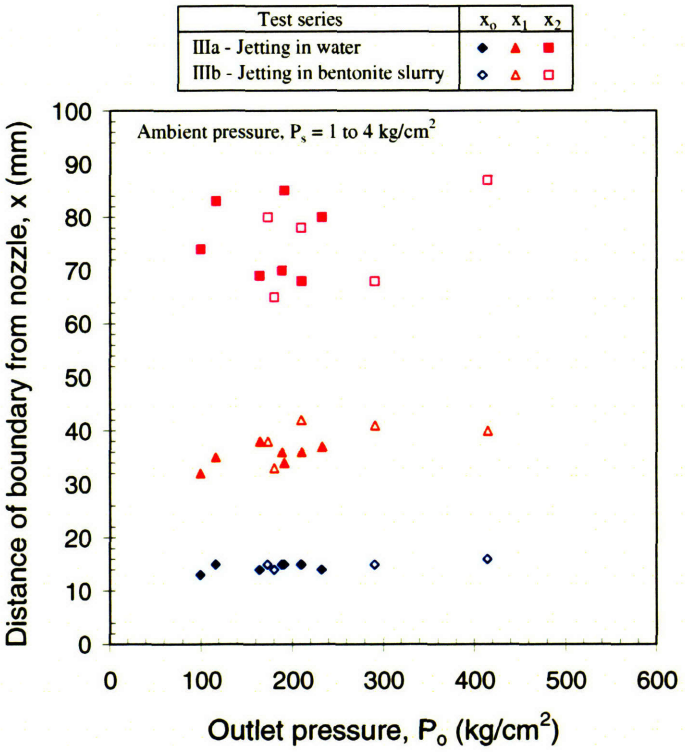

Figure 2-14. Effect of jetting in bentonite slurry under an ambient pressure

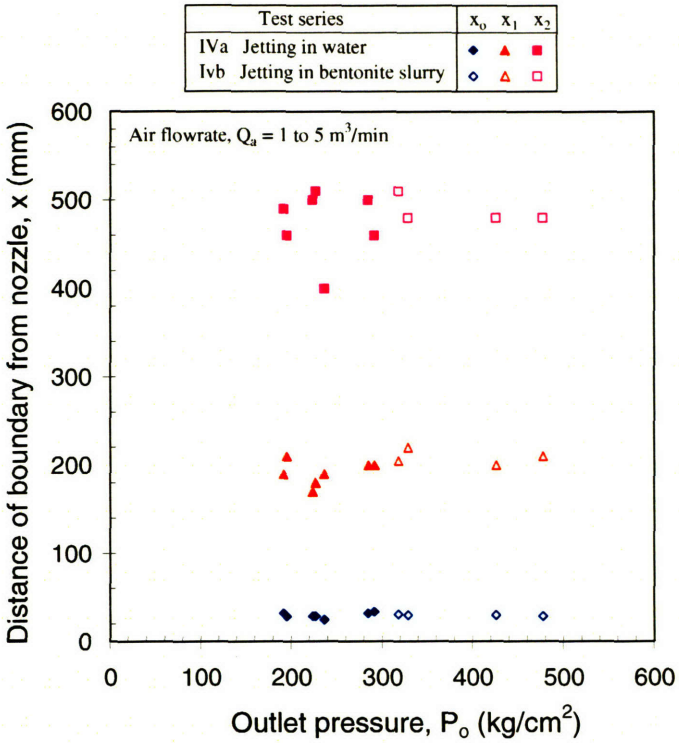

Figure 2-15. Effect of jetting in bentonite slurry under compressed air

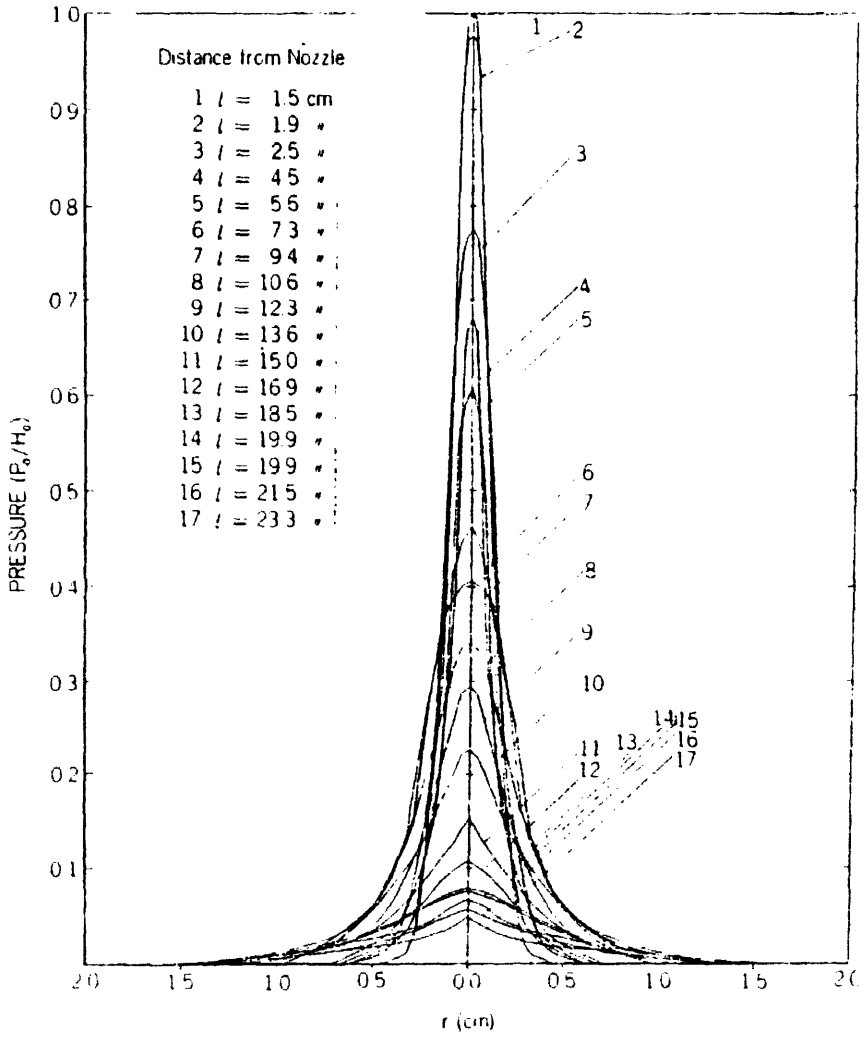

Figure 2-16. Radial pressure distribution at various distances from nozzle (after Yahiro and Yoshida, 1974)

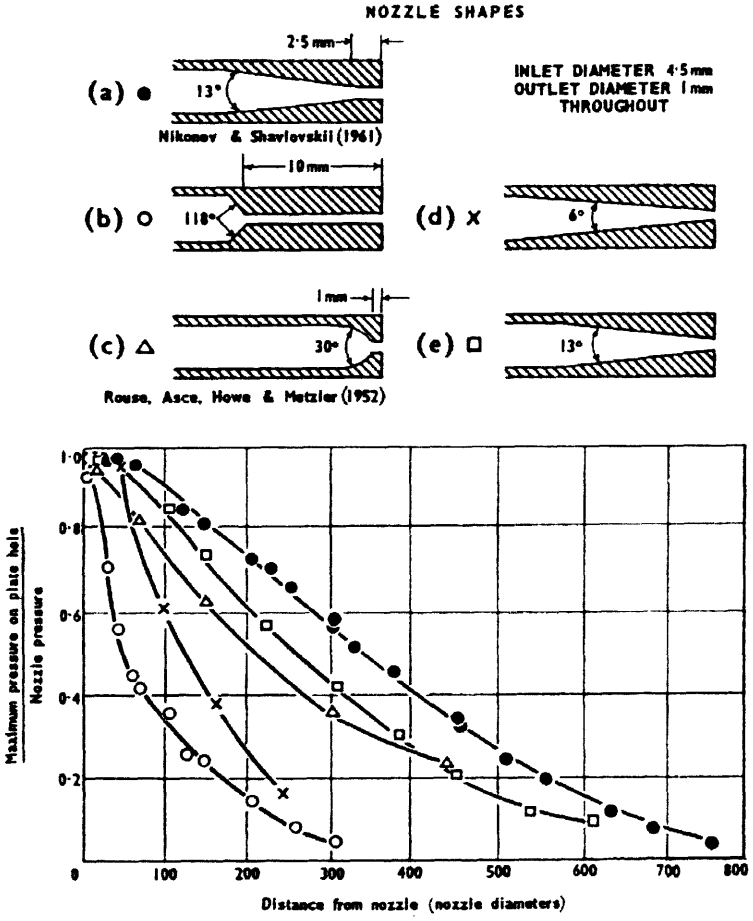

(a) Nozzle taper

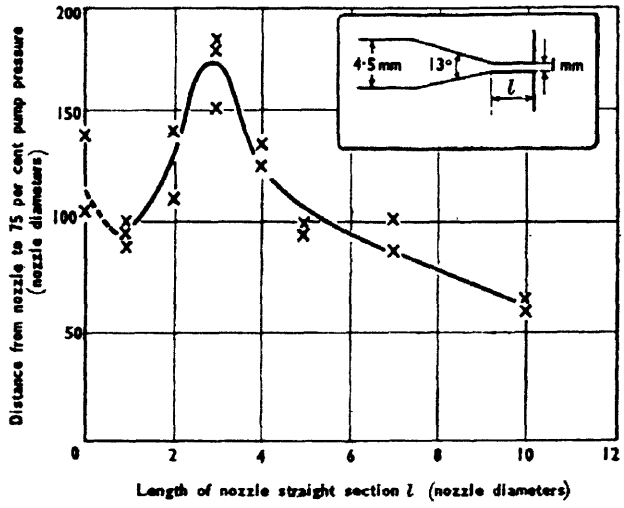

(b) Length of straight portion

Figure 2-17. Effect of nozzle shape on jet performance (after Leach and Walker, 1966)

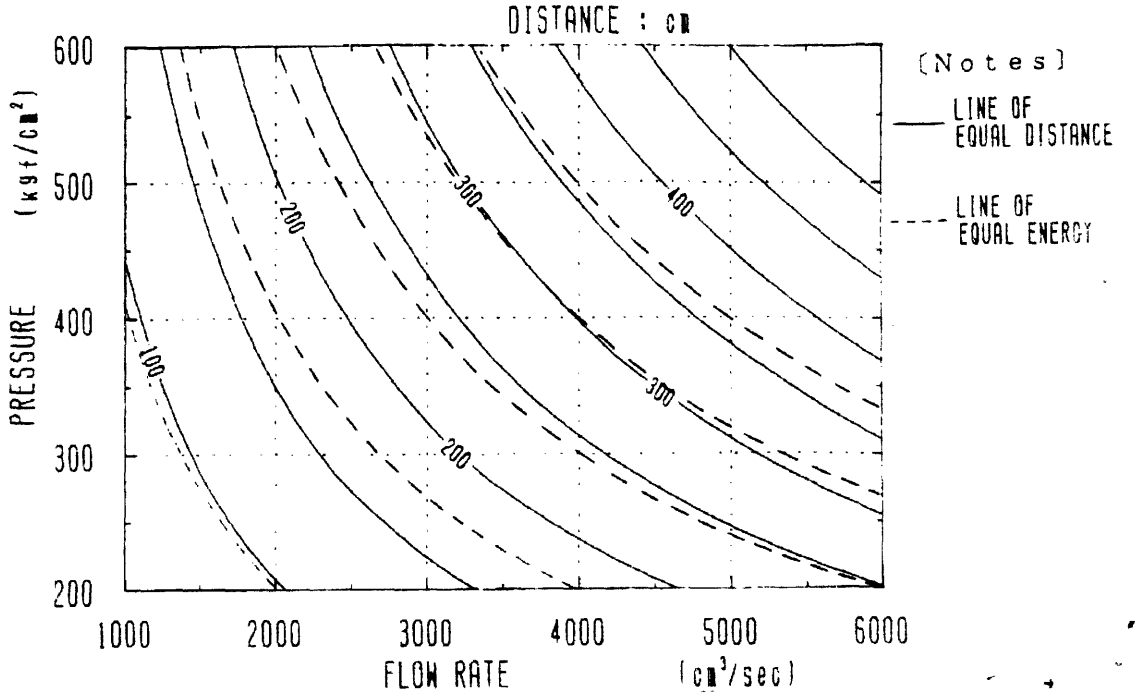

Figure 2-18. Contours of equal energy (PQ) and cutting distance in sand (after Yoshida et al., 1989)

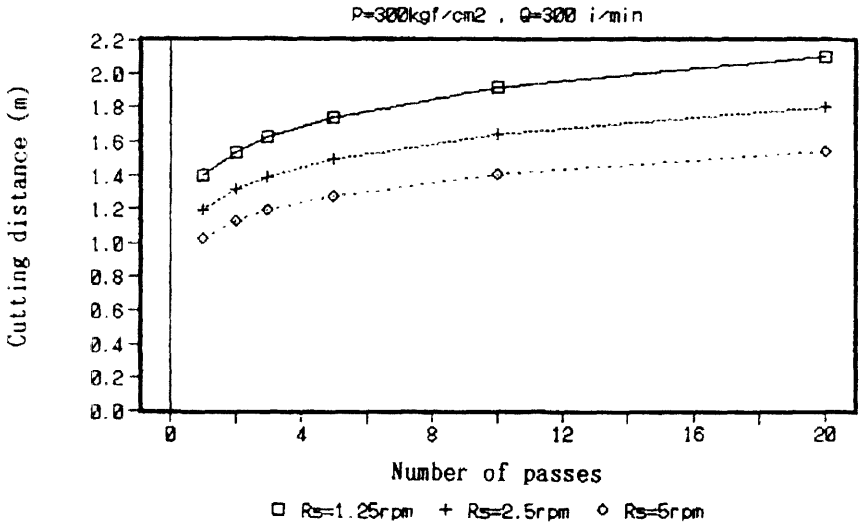

Figure 2-19. Relationship between cutting distance in sand and number of passes (after Yoshida et al., 1991)

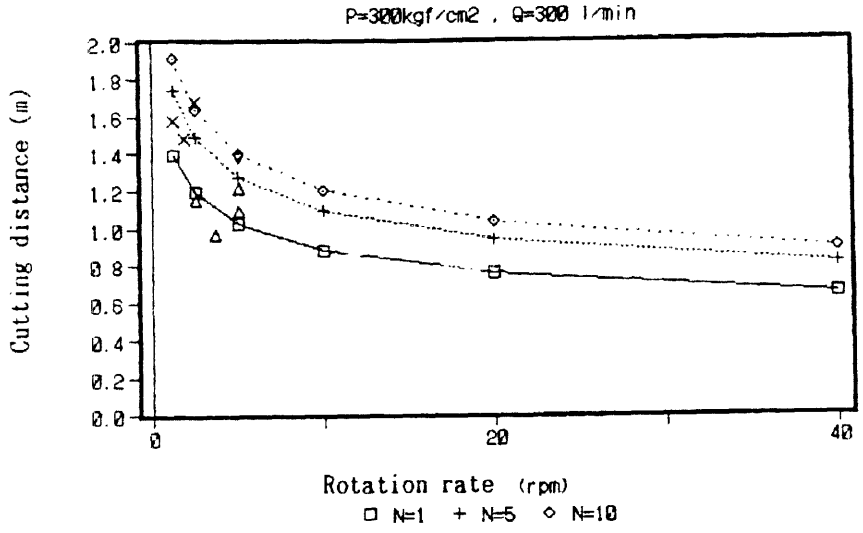

Figure 2-20. Relationship between cutting distance in sand and rotation rate (after Yoshida et al., 1991)

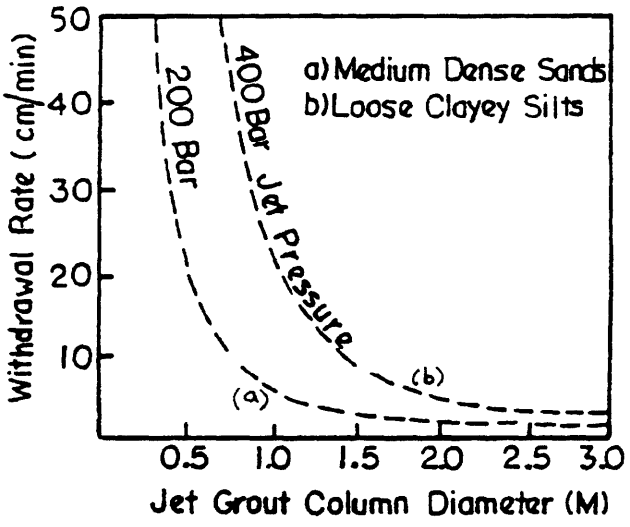

Figure 2-21. Relationship between jet grout column diameter and withdrawal rate (after Coomber, 1985)

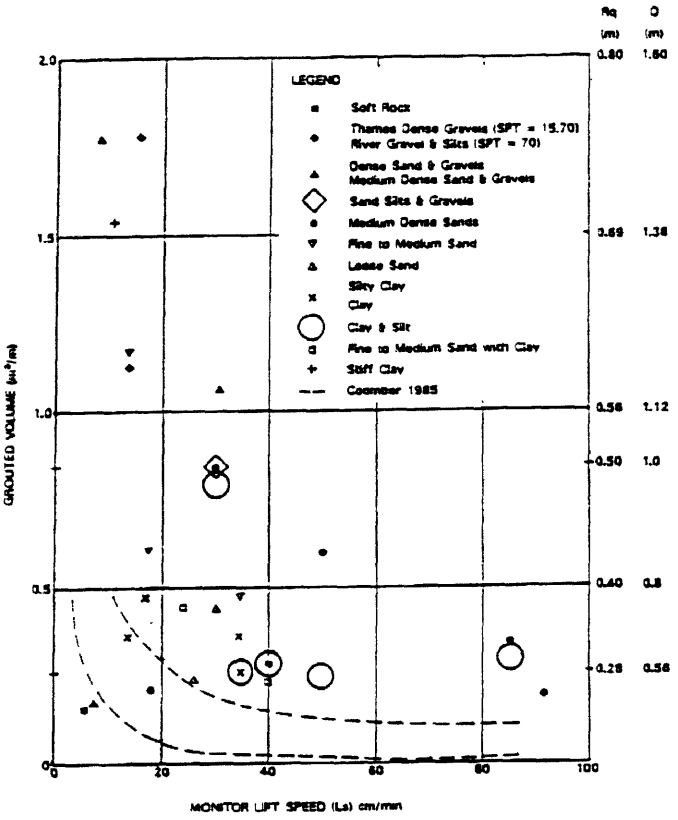

Figure 2-22. Relationship between grouted volume and withdrawal rate (lift speed) (after Covil and Skinner, 1994)

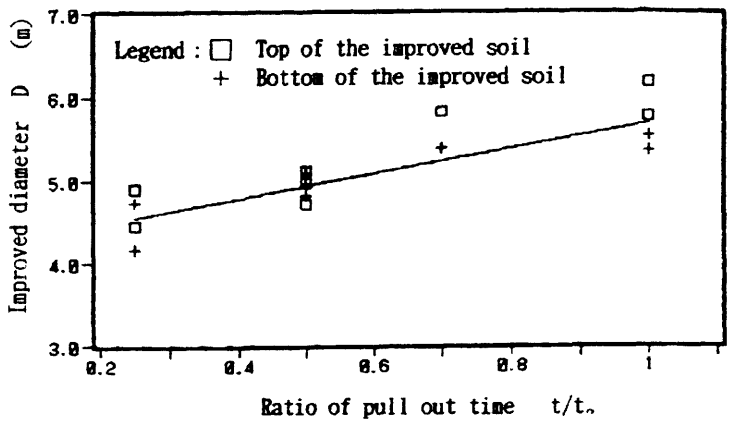

Soil is silty sand with SPT, N= 10 to 15 blows/300mm
P = 300 bar, Q = 300 l/min
t_0 = Longest duration of jetting adopted in the trials
t = Reduced duration of jetting ($t < t_0$)

Figure 2-23. Relationship between column diameter and duration of jetting (pullout time) (after Yoshida et al., 1996)

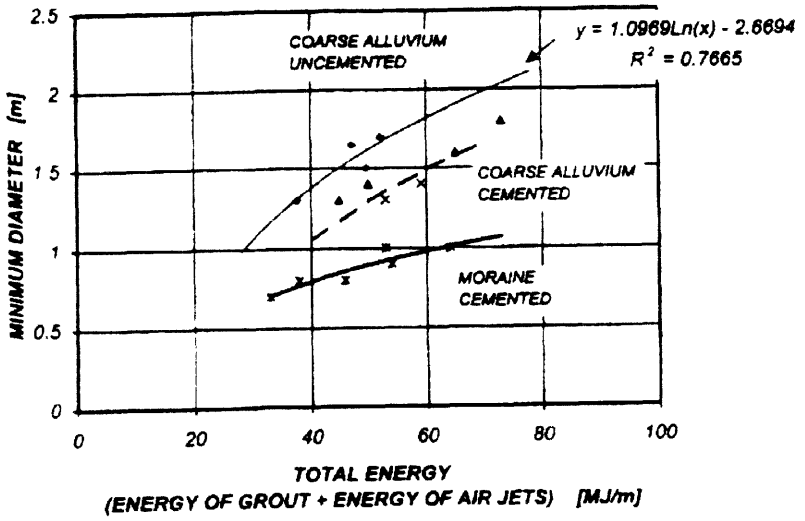

Figure 2-24. Relationship between column diameter and total energy (after Sembenelli and Sembenelli, 1999)

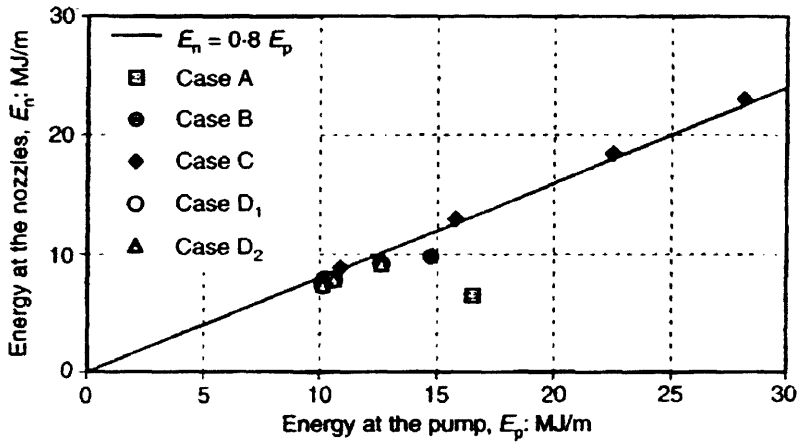

Figure 2-25. Comparison of energy at the nozzle and at the pump
(after Croce and Flora, 2000)

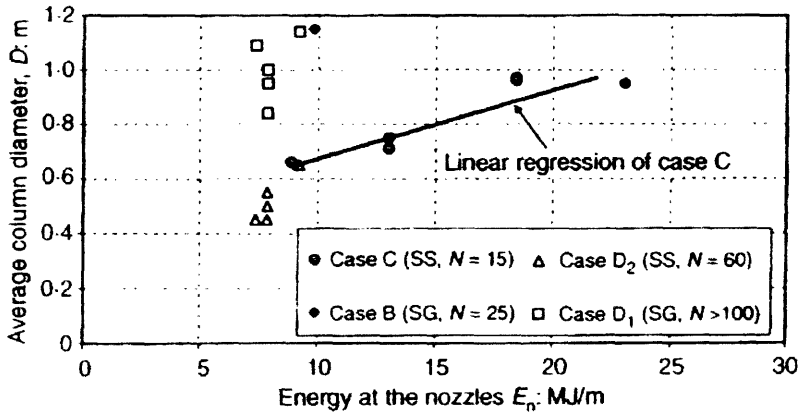

Figure 2-26. Relationship between column diameter and energy at the nozzle
(after Croce and Flora, 2000)

CHAPTER THREE

PROPOSED MODEL FOR JET EXCAVATION

3.1 General

The process of jet grouting is generally carried out below the ground water table. Therefore in all cases, the jet can be considered to be submerged. The hydrodynamic properties of a submerged fluid jet are therefore directly relevant to the study of the jet grouting process. Section 3.2 describes the characteristic properties of submerged jets and how they can be applied to the jet grouting process, while Section 3.3 proposes an analytical model for single fluid jet excavation in cohesive soils.

3.2 Hydrodynamics of Turbulent Jets

3.2.1 Basic submerged free jet

The submerged free jet corresponds to the situation where a fluid jet issues into an external medium with the same fluid properties. The jet is unconfined and is free to expand to its full limit without restriction. Figure 3-1 shows the basic structure of a submerged free jet. Two main zones can be identified, a zone of flow establishment followed by a zone of established flow. In the zone of flow establishment, there is a conical potential core where the velocity of the fluid is the same as the initial exit velocity of the jet, v_o. Immediately surrounding the potential core, there is a region of diffusion where, eddies are generated and mixing progresses inward and outward around the core region. As the jet is decelerated, the fluid from the surrounding (i.e., host) medium is gradually accelerated and entrained. The limit of the initial zone of flow establishment is

reached when the mixing region has penetrated to the centerline of the jet and the potential core is consumed. Beyond this point, the flow is fully established and the eddy region continues to expand steadily, with a reduction in the velocity throughout the zone. The boundaries between the various zones are not precisely defined due to the stochastic nature of the mixing process and transition zones that necessarily exist between two flow regimes. Experimental results from Albertson et al. (1950) suggest that the nominal outer boundaries, where the flow velocities are a small percentage of the centerline velocity, will have a slope of 1:5 (Figure 3-1).

For a submerged free jet, the static pressure distribution is assumed to be essentially constant throughout the zone of motion. It has been shown that the pressure differences arising from the flow in the transverse direction are negligibly small (less than 1% of the longitudinal velocity head, Holdhusen, 1950). Therefore the sole force producing the deceleration of the jet and the acceleration of the surrounding fluid is the longitudinal shear within the mixing region. As the process of mixing is internal, the momentum flux is constant for all normal sections of the flow.

The intensity of longitudinal shear (τ) at any point in a turbulent fluid may be expressed as the sum of two components, the mean viscous shear stress ($\mu \partial v_x / \partial r$) and an apparent turbulent shear stress ($\rho v_x' v_r'$):

$$\tau = \mu \frac{\partial v_x}{\partial r} - \rho v_x' v_{r_r}' \tag{3.1}$$

where μ is the dynamic molecular (laminar) viscosity, ρ is the fluid density, $\partial v_x / \partial r$ is the velocity gradient perpendicular to the nozzle axis, and $v_x' v_r'$ is the mean product of the turbulent velocity components in the axial and radial directions.

For flows with high Reynolds number ($R_e > 5 \times 10^5$), which generate conditions of pronounced mixing in the eddy region of a spreading jet, the component for mean viscous shear will be relatively small and turbulent shear stresses will dominate (i.e. $\tau \approx -\rho v_x' v_r'$). As a result, the viscous shear stress will not have any significant influence on the mixing process or diffusion characteristics of the jet. The characteristics of the mean flow will therefore be dynamically similar and the velocity distribution will have the same form in all sections within the diffused region.

Holdhusen (1950) demonstrated analytically that, for a circular jet under conditions of dynamic similarity and momentum conservation, the centerline axial velocity, v_{xc} decays inversely with the distance, x from the nozzle, regardless of the velocity distribution within the zone of established flow:

$$\frac{v_{xc}}{v_o} = \frac{x_o}{x} \tag{3.2}$$

where x_o is the length of the potential core.

This relationship is corroborated by the experimental results of various researchers, such as Albertson et al. (1950) using submerged air jets (Figure 3-2), and Forstall and Gaylord (1955) for submerged water jets (Figure 3-3).

Albertson et al. (1950) determined that $v_{xc}/v_o = 6.2\ d_n/x$ in air, whilst Forstall and Gaylord (1955) obtained $v_{xc}/v_o = 6.4\ d_n/x$ in water. These observations confirm that the characteristics of a submerged free jet determined in the above experiments can be extended to both gases or liquids. An alternative equation in the empirical form $v_{xc}/v_o = 6.6 d_n/x - 0.49$ was proposed by Citrini (1950).

Daily and Harleman (1966) suggest that $v_{xc}/v_o = 6.4\ d_n/x'$, where x' is measured from the geometric origin of the spread angle of the jet, located at $x = 0.6 d_n$ in front of the

nozzle. For all practical purposes, Rajaratnam (1976) recommends that it is sufficient to adopt $v_{xc}/v_o = 6.3(d_n/x)$, with the distance, x measured from the nozzle face, due to the imprecise location of the geometric origin. All the above equations suggest that the potential core length of a submerged free jet is of the order of $x_o/d_n = 6.1$ to 7.0.

Baines (1950) demonstrated that dynamic similarity (i.e. all cross-sections having the same velocity distribution profile) is satisfied in any normal section within the zone of established flow for a constant Reynold's number (Figure 3-4a), defined as $R_e = \rho v_o d_n/\mu$ and plots of v_{xc}/v_o versus x/d_n will be parallel lines with the same negative slope in a log-log plot (Figure 3-4b). This implies that the length of the potential core (determined by the intersection of the sloping line and the horizontal line representing $v_{xc}/v_o = 1$) will increase with increasing R_e. Figure 3-5 shows that, at high values of R_e, the effects of the viscous shear becomes progressively smaller compared to the turbulent shear, and the corresponding potential core length approaches an asymptotic value of around $x_o/d_n = 6.3$ to 6.4.

Various researchers have proposed different functions to describe the velocity distribution in the diffusion zone of a jet:

$$\frac{v_{xr}}{v_{xc}} = f(\eta) \tag{3.3}$$

where v_{xr} is the local velocity at a radial distance r from the centerline axis, v_{xc} is the centerline velocity and $\eta = r/x$ is the obliquity angle. Experimental results have shown that the velocity distribution can be reasonably described by a normal probability function of the form:

$$\frac{v_{xr}}{v_{xc}} = \exp\left[-\tfrac{1}{2}\left(\frac{r^2}{r_i^2}\right)\right] \tag{3.4}$$

where r_i is the radial distance corresponding to the point of inflexion of the exponential curve (Figure 3-6).

For dynamic similarity, the growth of the jet width must be linear, i.e. $r_i/x = C$, where C is a constant defining the rate of spread of the jet width. Albertson et. al. (1950) obtained $C = 0.081$ based on experimental data.

The use of the normal velocity distribution is very attractive due to its simplicity in comparison with other forms of equations. However, it is recognized that, this unbounded function will over-predict the actual volume of the entrained fluid mass. It is nevertheless an extremely useful tool for developing analytical expressions for complex turbulent flow problems (Forstall and Gaylord 1955, Daily and Harleman 1966).

3.2.2. Submerged deflected jet

The characteristics of a submerged stationary jet issuing perpendicular into a cross flow are of interest in the study of jet grouting, since this behavior is analogous to a jet issuing from a nozzle which is traversing parallel to a stationary fluid medium (Figure 3-7). Experimental observations indicate that a stationary jet issuing into a cross flow is deflected as a result of the interaction between the jet and flowing stream. Studies conducted on cross flows mainly involve smoking jets emanating from a fixed orifice, at 90^o to the cross flow generated by a wind tunnel (Keffer and Baines, 1963; Smith and Mungal, 1998). Air is normally used together with a tracer in the experiments for convenience. The jet characteristics however, are equally applicable to any other fluid medium for conditions where buoyancy effects are negligible.

Figure 3-8 shows the basic structure of a submerged deflected jet in a cross-flow. There is an initial zone of flow establishment, followed by a zone of established flow (Keffer and Baines, 1963) similar to the structure observed previously for a submerged free jet. Immediately upon entering the cross flow, the edges of the jet are subjected to intense shear stresses resulting from the velocity gradient between the jet and cross-flow. The entrained fluid in the surrounding is accelerated as the jet spreads, the jet fluid being correspondingly decelerated. As the flow at the upstream surface of the jet is decelerated, a positive (compressive) pressure region is created. The sides of the jet are subjected to lateral shearing stresses directed toward the rear of the jet. Flow separation occurs at the rear and gives rise to a negative (suction) pressure region, creating wakes. Within this zone of flow establishment, there is a potential core that exists with a constant velocity equal to the initial jet velocity, v_o. At the end of the zone of flow establishment, eddies in the diffusion region around the potential core merges completely. In the zone of established flow, the whole jet cross section becomes turbulent and the continued lateral diffusion of the jet momentum causes a decrease in the centerline velocity of the flow.

Pratte and Baines (1967) suggest that eddies in the zone of established flow just beyond the potential core, consist of two vortices rotating opposite each other with approximately constant vortical intensity (Figure 3-8b). The vortices expand and occupy a larger and larger part of the jet cross section further downstream. This transition region is called the zone of maximum deflection. In the final region, the two turbulent vortices are carried along at the cross flow velocity. The vortices continue to grow at a decreasing rate and reduction in angular velocity. The turbulent and vortex motions are diffused and dissipated by viscosity and the jet approaches the condition of the surroundings. This

final region is called the vortex zone. It was observed that the presence of the vortices remained about 1000 nozzle diameters downstream.

Figure 3-9 depicts the typical shapes of a deflected air jet in a cross flow as indicated by concentration profiles of acetone vapor used as a tracer (Smith and Mungal, 1998). The cross-section of the jet appears as a kidney shape, i.e. the two vortices are attached to the sides of the jet. The cross-sectional shape remains approximately the same as that established at the end of the potential core, suggesting that dynamic similarity is conserved in the zone of flow establishment.

The flow field of the jet depends primarily on the ratio of the jet momentum to the cross flow momentum (Smith and Mungal, 1998). The effective velocity ratio, R is defined as the square root of the momentum flux ratio:

$$R = \sqrt{\frac{\rho v_o^2}{\rho_{cf} u_o^2}} \tag{3.5}$$

where ρ is the mass density of fluid jet in the nozzle, v_o is the initial exit velocity of the jet, ρ_{cf} is the mass density of fluid in cross-flow and u_o the cross flow velocity. For equal density of the two fluids, $R = v_o/u_o$.

A convenient system of axes for analyzing the characteristics of a deflected jet is shown in Figure 3-10, where x axis is in the direction of the initial jet exit direction, z axis is in the direction of the cross flow, and y axis is perpendicular to the x and z axes. The curvilinear axis ξ defines the central axis (streamline) of the jet flow, while η and ζ define the minimum and maximum dimensions of a plane with ξ = constant.

Figure 3-11 depicts the trajectory of the jet centerline in the x-z plane. It can be seen that jet penetration in the x direction is increased with increasing values of the

velocity ratio, R (for R = 2 to 10). The jet centerline excess velocity decay along the ξ - axis is shown in Figure 3-12. It is obvious that the centerline velocity decay of a cross-flow is much more rapid in comparison with a submerged free jet, the difference being larger for decreasing R values. The length of the potential core (x_o) is increased as a result of an increase in velocity ratio (Figure 3-13). At large values of R (> 30 to 40), the length of the potential core approaches that of a free jet (i.e. $x_o/d_n = 6.2$).

The jet centerline profile is plotted with respect to the ξ – axis in Figure 3-14. Two straight lines can be observed. The initial line represents the potential core region where $x = \xi$, indicating that the jet is essentially straight and undeflected (up to $\xi/(d_nR) =$ 2). The second line represents the vortex zone, where $x/(d_nR)$ varies with the one third power of $\xi/(d_nR)$. The end of the zone of maximum deflection (or starting of the vortex zone) can be identified at about $\xi/(d_nR) = 5$. Figure 3-15 depicts the width of the jet cross section in the ζ - axis as a function of $\xi/(d_nR)$. The ends of the potential core region and the zone of maximum deflection are similarly identifiable at about $\xi/(d_nR)$ = 2 and 5 respectively.

The lateral spread of a deflected jet is described by the velocity excess ($v - u_o$) and the half-width of the cross-sectional profile in the η direction. Keffer and Baines (1963) indicate that dynamic similarity is observed in the zone of established flow as shown in Figure 3-16.

Pratte and Baines (1967) suggest that the trajectory of a deflected jet in a cross flow can be described by an empirical equation in the form, $x/(d_nR) = a[z/(d_nR)]^b$, where a and b are experimental constants, and d_n is the nozzle diameter. Figure 3-17 shows that the profiles for the centerline, top and bottom jet boundaries plot parallel to one another

in a logarithmic plot, with a slope given by $b = 0.28$, while $a = 2.63$, 2.05 and 1.35 for the top, middle and bottom profiles respectively.

Table 3-1 shows the typical range of operational parameters used in jet grouting operations. Based on these parameters, the traverse velocity of the nozzle (v_t) can be calculated using the expression $v_t = \pi d_m R_s$, where d_m is the diameter of the rotating monitor and R_s is the rotation speed. The jet velocities at the nozzle exit are computed using $v_o = \sqrt{(2P_o/\rho)}$. For simplicity, the calculation does not include additional enhancements of the jet velocity by the adoption of a compressed air shroud in double and triple fluid systems. The results in Figure 3-18 show that the velocity ratios are very high (R > 2000), even at the upper range of rotation speeds (close to 30 rpm). Therefore, it is highly likely that the jet condition is equivalent to a submerged free jet (i.e. cross-flow effects are negligible).

Typical jet trajectories calculated using the expressions of Pratte and Baines (1967) are shown in Figure 3-19 for two sets of nozzle sizes and pressures typically adopted for jet grouting. In both cases, it is observed that the jets can extend to very large distances if unconfined, up to several meters, the jet deflection being greater at larger distances from the nozzle. The diameters of jet grout columns achieved in the ground are generally within about 5 m, hence the penetration of the jet can be estimated to be within about 2.5 m. At these distances, the jet would be expected to remain straight and be uninfluenced by the rotation speed of the nozzle. The corresponding jet cross section should also remain circular, rather than kidney-shaped (as seen for the deflected jet in Figure 3-9). The η - axis would become less curved, while still preserving the dynamic similarity within the cross sections in the zone of establishment. From the above

evaluation of deflected jet characteristics, it may be concluded that at normal jet grouting operational conditions, the jet characteristics will tend toward that of a basic submerged free jet, and are not likely to be influenced by the rotation speed to any significant extent. Hence the jetting process can be modeled by a quasi-stationary submerged free jet.

3.2.3 Jetting into medium of different fluid density

In the jet grouting process, the fluid in the cutting jet is either water or cement grout. The jet issues into a fluidized environment, as it exits from the nozzle, consisting of the return slurry in the annular space between the rod and borehole wall. As a result of mixing with the soil, the density of the return slurry is bounded by the density of the jetting fluid and that of the surrounding soil. Hence, the jet issues into a medium of different density. This section discusses how the characteristics of a submerged free jet can be adjusted to account for the effect of this density contrast in the jetting process.

Ricou and Spalding (1961) performed direct measurements of mass entrainment, using gas jets of differing density to that of the surrounding air. They proposed that there is a universal relationship in the form:

$$\frac{m_j}{m_o} = 0.32\left(\frac{x}{d_n}\right)\sqrt{\frac{\rho_{am}}{\rho}} \tag{3.6}$$

where m_j is the rate of mass flow in the jet cross-section at a given distance, x from the nozzle, m_o is the rate of mass flow at the nozzle exit, ρ_{am} is the density of the ambient fluid medium, and ρ = density of the injected fluid. The authors suggest that the relationship is equally applicable to all fluid jets, where buoyancy effects are absent.

By substituting $m_j = \rho_j Q_j$ and $m_o = \rho_o Q_o$ respectively in Eqn 3.6, where Q_j is the flowrate in the jet cross-section at distance x from the nozzle, and Q_o the flowrate at the nozzle exit, Eqn 3.6 can be expressed in the form:

$$\frac{\rho_j Q_j}{\rho_o Q_o} = 0.32\left(\frac{x}{d_n}\right)\sqrt{\frac{\rho_{am}}{\rho}} \tag{3.6a}$$

If the density of the injection fluid and host medium are the same (i.e. $\rho_j = \rho_{am} = \rho$), then Eqn 3.6a reduces to:

$$\frac{Q_j}{Q_o} = 0.32\left(\frac{x}{d_n}\right) \tag{3.6b}$$

which was corroborated by the experimental results of Albertson et al. (1950) for submerged air jets issuing into a medium of the same density. Eqn 3.6 is therefore a more general expression for mass entrainment for fluids of different densities.

Using the results of Ricou and Spalding (1961), the mass flux at distance, x from the nozzle is given by $m_j = 0.32\ (x/d_n)\ m_o\sqrt{(\rho_{am}/\rho)}$. The corresponding flowrate, Q_j can be found from:

$$Q_j = \int_0^\infty v_{xr}\, dA \tag{3.7}$$

where $v_{xr} = v_{xc}\ exp\ [-\frac{1}{2}(r^2/r_j^2)]$ and $dA = 2\pi r dr$. The mass flux at the nozzle, $m_o = \frac{1}{4}\pi d_n^2 \rho v_o$.

Hence, it can be shown that the density within the body of the jet is:

$$\rho_j = \frac{0.08}{C}\sqrt{\rho_{am}\rho} \tag{3.8}$$

where $C = r_j/x$.

For jetting in a medium of equal density (i.e. $\rho_j = \rho_{am} = \rho$), we obtain $C = 0.08$. This is consistent with the experimental value of $C = 0.081$ given by Albertson et al. (1950). Hence, Eqn 3.8 reduces to:

$$\rho_j = \sqrt{\rho_{am}\rho} \tag{3.9}$$

indicating that the density in all cross sections of the jet is the same and independent of the distance from the nozzle.

The momentum in any cross section of the jet can be expressed as

$$M = \int_0^\infty \rho_j v_{xr} dQ \tag{3.10}$$

where $dQ = v_{xr}(2\pi r dr)$.

The momentum at the nozzle exit, $M_o = \rho v_o^2 A_o$, where $A_o = \frac{1}{4}\pi d_n^2$. For conservation of momentum in all cross sections, $M = M_o$ leading to the general result,

$$\frac{v_{xc}}{v_o} = \frac{x_o}{x} \tag{3.11}$$

where the length of potential core, x_o is now given by:

$$x_o = \frac{d_n}{\sqrt{8Y_m}}\sqrt{\frac{\rho}{\rho_j}} \tag{3.12}$$

with $Y_m = \int_0^\infty f^2(\eta)\eta d\eta$ and $f(\eta) = \exp\left\{-\frac{1}{2}\left(r^2/r_i^2\right)\right\}$.

Solving for Y_m gives, $Y_m = \frac{1}{2}C^2$, where $C = r_i/x$ as before, leading to the expression:

$$x_o = \frac{d_n}{2C}\sqrt{\frac{\rho}{\rho_j}} \tag{3.12a}$$

or alternatively, since $\rho_j = \sqrt{(\rho_{am}\rho)}$,

$$x_o = \frac{d_n}{2C}\left(\frac{\rho}{\rho_{am}}\right)^{\frac{1}{4}} \tag{3.12b}$$

Substituting for $C = 0.08$,

$$x_o = 6.25 d_n \left(\frac{\rho}{\rho_{am}}\right)^{\frac{1}{4}} \tag{3.13}$$

This means that the potential core length is reduced when the jet issues into a fluid with higher density, as is the case in most jet grouting situations.

Figure 3-20 summarizes the core length, x_o as a function of the density ratio, ρ/ρ_{am} based on Eqn 3.13. The potential core length can be normalized by the nozzle diameters, to produce a unique function of the density ratio as shown in Figure 3-21. This result shows clearly how the density contrast causes changes in the core length compared to the submerged free jet condition.

3.3. Proposed Model for Jet Excavation

3.3.1 Application of free jet characteristics to partially confined jets

Abramovich (1963) stated that experimental investigations established an interesting analogy between the velocity fields at the lateral cross sections in the mixing chamber of an ejector and at the cross sections of a free jet (Figure 3-22). It was observed that the process of equalization of the flow parameters in a mixing chamber occurs in such a manner that the velocity field at each of its cross sections appears as if it were the central part of the velocity distribution function at the corresponding cross section of a free jet, up to the radial distance bounded by the walls of the chamber as illustrated in Figure 3-23. However, in contrast with a free jet, in which the pressure can be regarded

as constant along the radius and along the length, a pressure increase occurs in the chamber of an ejector according to the degree of mixing of flows. The constancy of the static pressure exists only in the radial direction.

By extension of this analogy to the jet grouting process, we may hypothesize that the velocity distribution in the cutting jet is likened to that of a free jet with boundaries corresponding to the size of the cavity excavated in the ground (Figure 3-24). The shape of the cavity formed depends on the erosion properties of the soil and the expansion of the jet is limited by the resistance of the soil at the jet-soil interface. The difference in the kinematic component of the energy, as a result of the curtailment of the outer regions of the velocity distribution of an equivalent free jet, will be reflected as an increase in the static pressure in the longitudinal direction of the jet flow. The following sections present a theoretical model based on this concept.

3.3.2 Proposed formulations for jet expansion in soil

In the jet grouting process, the monitor is submerged in the return slurry (in the borehole) during jetting. We assume that the slurry fills the full depth of the borehole and friction losses in the discharge flow in the annular space between the drill rod and borehole wall are negligible. On this basis, the ambient pressure at the level of the nozzle is dependent only on the depth of the nozzle, and is given by

$$P_s = \rho_s g z_n \tag{3.14}$$

where ρ_s is the density of return slurry and z_n is the depth of nozzle below ground.

For a given fluid density, ρ and dynamic viscosity, μ and assuming that losses in the nozzle are small, the nozzle exit velocity, v_o can be calculated using the expression

$$v_o = \sqrt{\frac{(P_i - P_s)}{\rho}} \tag{3.15}$$

where P_i is the nozzle pressure and P_s is the ambient pressure at nozzle exit.

The length of the potential core of the jet, x_o is a function of the nozzle diameter, d_n and the density ratio of the jetting and ambient fluids, based on Eqn 3.13, giving $x_o = 6.25\ d_n\ (\rho/\rho_{am})^{0.25}$. At a distance x from the nozzle, the centerline velocity (v_{xc}) characteristics along the longitudinal axis of the jet can be represented by the following expressions:-

For $x < x_o$, $$v_{xc} = v_o \tag{3.16}$$

For $x > x_o$, $$v_{xc} = \frac{v_o xo}{x} \tag{3.17}$$

In the mixing region ($x > x_o$), the velocity distribution in any plane perpendicular to the jet axis can be represented by a normal distribution function (Figure 3-25),

$$\frac{v_{xr}}{v_{xc}} = \exp\left[-\tfrac{1}{2}\left(\frac{r^2}{r_i^2}\right)\right] \tag{3.18}$$

where r is the radius from centerline axis of the jet and r_i is the radius at the inflexion point.

The turbulent shear stress in the fluid ($\tau = -\rho v_x' v_r'$) is commonly expressed in the form $\tau = -\eta\, \partial v_x / \partial r$, where η is the dynamic eddy viscosity of the fluid. The kinematic eddy viscosity ($\varepsilon = \eta/\rho$), in turn, is related to the nozzle velocity and nozzle diameter by the equation (Daily and Harleman 1966):

$$\varepsilon = 0.013 v_o d_n \tag{3.19}$$

Alternatively, the dynamic eddy viscosity can be related to the Reynold's number, R_e:

$$\eta = 0.013 \mu R_e \tag{3.20}$$

where $R_e = \rho v_o d_n/\mu$, indicating that the dynamic eddy viscosity, η is a direct function of the dynamic molecular viscosity, μ and the Reynold's number of the jet, R_e.

The point of inflexion in the normal distribution velocity function corresponds to the location of maximum shear stress in the cross-section of the jet at $r = r_i$:

$$\tau_{\max} = -\eta \frac{dv_{xr}}{dr} \tag{3.21}$$

The annular shear stress, τ within the jet body (Figure 3-26) is given by

$$\tau = \eta v_{xc} \exp\left[-\tfrac{1}{2}\left(\frac{r^2}{r_i^2}\right)\right]\left\{\frac{r}{r_i^2}\right\} \tag{3.22}$$

Excavation by a turbulent fluid jet in soil is a function of the hydrodynamic characteristics of the jet and the resistance of the soil to disintegration. For a cohesive soil, failure conditions can be assumed to be undrained due to the rapid rate of loading applied by a fluid jet (Shibazaki 2003).

It is recognized that real fluids adhere to a solid surface and a "no-slip" condition always exist at the interface between a flowing fluid and a solid boundary, where the velocity is zero (Dailey and Harleman 1966). As a result, the velocity gradient and shear stress at any given cross-section of the flow will have maximum values at the solid boundary, with decreasing magnitude towards the main body of the flow. The velocity gradient immediately next to the wall is very large and viscous shear forces dominate within a very thin layer next to the wall. Outside this boundary layer, the velocity gradient tapers off very rapidly towards that of the main flow and effects of viscous shear become small. The streamlines of the main flow beyond the boundary layer conform essentially to the flow regime of the bulk fluid. The thickness of the boundary layer increases with distance from the leading edge of the wall.

The characteristics of the boundary layer is directly influenced by the Reynold's number R_l defined as $R_l = \rho U_o l/\mu$, where U_o is the velocity of the main flow immediately outside the boundary layer and l is the distance from the leading edge of the solid boundary. The wall shear stress is commonly expressed as $\tau_w = \frac{1}{2} c_f \rho U_o^2$, where c_f is the local wall shear stress coefficient which varies with R_x. The boundary layer may be classified as laminar when $R_x < 5 \times 10^5$, and turbulent when $R_x > 5 \times 10^5$ (Schlichting 1987).

For a laminar boundary layer, the value of c_f is given by the Blasius solution developed for laminar flow over a flat plate (Dailey and Harleman 1966):

$$c_f = \frac{0.664}{\sqrt{R_l}} \tag{3.23}$$

When the flow becomes turbulent, the boundary layer consists of a very thin viscous sublayer immediately next to the wall where the flow remains laminar, followed by an outer region of turbulent flow. When the wall surface is very rough, the laminar sublayer may be disrupted and turbulence fully extends to the wall. A wall is described as smooth when the protrusions in the wall surface are less than the viscous sublayer.

In the case of flow over a clayey soil, the wall can be regarded as be reasonably smooth since the grain size is very small (less than 0.002mm). We may then adopt the empirical expression for c_f developed by Schultz-Grunow (1940) for turbulent boundary layer flow over smooth walls:

$$c_f = \frac{0.37}{(\log R_l)^{2.58}} \tag{3.24}$$

In applying the above concepts to the present case involving a jet, we assume that the velocity (U_o) immediately outside the boundary layer is equal to the velocity in the jet

at radius, r from the jet axis given by, $v_{xr} = v_{xc}\, exp(-½\, r^2/r_i^2)$. By setting $U_o = v_{xr}$ in the above equations, we obtain $\tau_w = ½\, c_f\, \rho_j v_{xr}^2$. It is hypothesized that the spread of the jet will be limited to the radius (r) at which the wall shear stress, τ_w becomes equal to the peak undrained shearing resistance of the soil, τ_u (Figure 3-27). The shape of the cavity excavated therefore follows the locus of r satisfying the equation

$$r = r_i \sqrt{2\left(\frac{v_{xc}}{v_{xr}}\right)} \tag{3.25}$$

where, $v_{xr} = \sqrt{(2\tau_u/c_f \rho_j)}$.

As r_i gets larger at further distances from the nozzle, the radius of the jet will be limited to $r_s = r_i$ at some distance $x = x_s$. It can be shown that under this condition, the jet velocity is given by $v_{xr} = v_{xc}\, e^{-½}$ and the soil shearing resistance can be estimated as

$$\tau_u = \tfrac{1}{2} c_f \rho_j v_{xc}^2 e^{-1} \tag{3.26}$$

Figure 3-28 depicts the predicted shape of cut based on the concept developed above.

3.3.3 Estimation of ultimate cutting distance

In any given plane perpendicular to the jet axis in the mixing region, the stagnation pressure (p_{xr}) at radius (r) from the centerline axis is given by:

$$p_{xr} = \tfrac{1}{2} \rho v_{xr}^2 \tag{3.27}$$

Substituting for v_{xr},

$$p_{xr} = \tfrac{1}{2} \rho_j v_{xc}^2 \exp\left[-\frac{r^2}{r_i^2}\right] \tag{3.28}$$

Figure 3-29 shows the dynamic pressure distribution at different distances from the nozzle.

At some distance, $x = x_s$ downstream of the nozzle, the total force (F_b) acting at the jet tip bearing over a circular area of radius r is given by

$$F_b = \int_0^r p_{xr}(2\pi r dr) \tag{3.29}$$

Hence, the average bearing pressure (p_{xa}) close to the jet tip is then given by

$$p_{xa} = \frac{F_b}{\pi r^2} \tag{3.30}$$

$$p_{xa} = \frac{\frac{1}{2}\rho_j v_{xc}^2}{\left(\frac{r^2}{r_i^2}\right)}\left\{1-\exp\left[-\frac{r^2}{r_i^2}\right]\right\} \tag{3.31}$$

At large distances downstream of the nozzle, $r_i > r_s$, (i.e. r^2/r_i^2 is small) and the average bearing pressure (p_{xa}) approaches the stagnation pressure (p_{xc}) at the centerline axis, i.e.

$$p_{xa} = \tfrac{1}{2}\rho_j v_{xc}^2 \tag{3.32}$$

The above analysis demonstrates that at large distances from the nozzle, the average bearing pressure acting at the jet tip becomes independent of the jet radius and it is then possible to calculate the average bearing pressure by simply considering the centerline velocity characteristics. Substituting for v_{xc}

$$p_{xa} = \tfrac{1}{2}\rho_j \frac{(v_o x_o)^2}{x^2} \tag{3.33}$$

Therefore, the average bearing pressure at the jet tip varies inversely with the square of the distance from the nozzle. At the limit of jet penetration (at $x = l_j$), the average bearing pressure (p_{xa}) diminishes to the ultimate bearing resistance of the soil ($q_{bu} = N_c\, s_u$) where

N_c is a bearing capacity coefficient which depends on the plastic failure mechanism in the soil mass. By equating p_{xd} to q_{bu}, it can be shown that :

$$\frac{l_j}{d_n} = 6.25\sqrt{\frac{(P_i - P_s)}{q_{bu}}} \tag{3.34}$$

Hence, a simple normalized equation is obtained relating ultimate jet penetration distance (l_j), nozzle diameter (d_n), nozzle pressure difference ($P_i - P_s$) and soil bearing resistance (q_{bu}). It is noted that d_n and (P_i-P_s) are properties of the jet, while q_{bu} describes the condition governing soil failure, thus the proposed excavation model links the effects of the fluid and soil media explicitly. It is noted that the resulting expression for jet penetration distance is independent of the jet fluid density or the density of the ambient medium. Figure 3-31 shows the normalized relationship developed for the cutting distance.

3.4 Advantage of new model over current predictive methods

The proposed analytical model for jet excavation has been developed based on a detailed review of prior knowledge of submerged free and partially confined fluid jets. The model predicts the profile of the excavated soil and the ultimate cutting distance of the jet. The model takes into account both the hydrodynamic characteristics of the jet, as well as the undrained resistance of low permeability cohesive soil. The new model has significant advantages over the current practice, which attempts to establish empirical correlations between jet grout column diameter and the specific energy consumed (E_s), such as methods proposed by Tornarghi (1989) and Croce and Flora (2000) discussed in Chapter 2. Tornaghi's approach considers only the operational parameters of the jetting

system (i.e. pump pressure, flowrate and rod withdrawal speed) using the parameter, specific energy, $E_s = PQ/v_t$. Croce and Flora's approach determines the energy consumed at the nozzle per unit length of column formed, determining $E_s = \frac{1}{2}mv_o^2/H$ from the mass flowrate (m), and jet exit velocity (v_o). As shown earlier in Chapter 2, these approaches are empirical and do not take into account the properties of the soil or the actual mechanisms of the jet grouting process. The new model is an improvement to these methods, as it describes the excavation process using fundamental theories in fluid dynamics and soil mechanics to develop a rational framework for analysis. In addition, the ability to predict the profile of the excavation, allows the lift step for jetting operations to be determined directly.

Table 3-1. Typical jet grouting operational parameters

Jet grouting system	Monitor diameter, d_m (mm)	Fluid density, ρ (kg/m^2)	Nozzle pressure, P_o (bar)	Rotation speed, R_s (rpm)
Single fluid	60	1500	200	5 to 30
Double fluid	90	1500	400	5 to 30
Triple fluid	90	1000	400	5 to 30

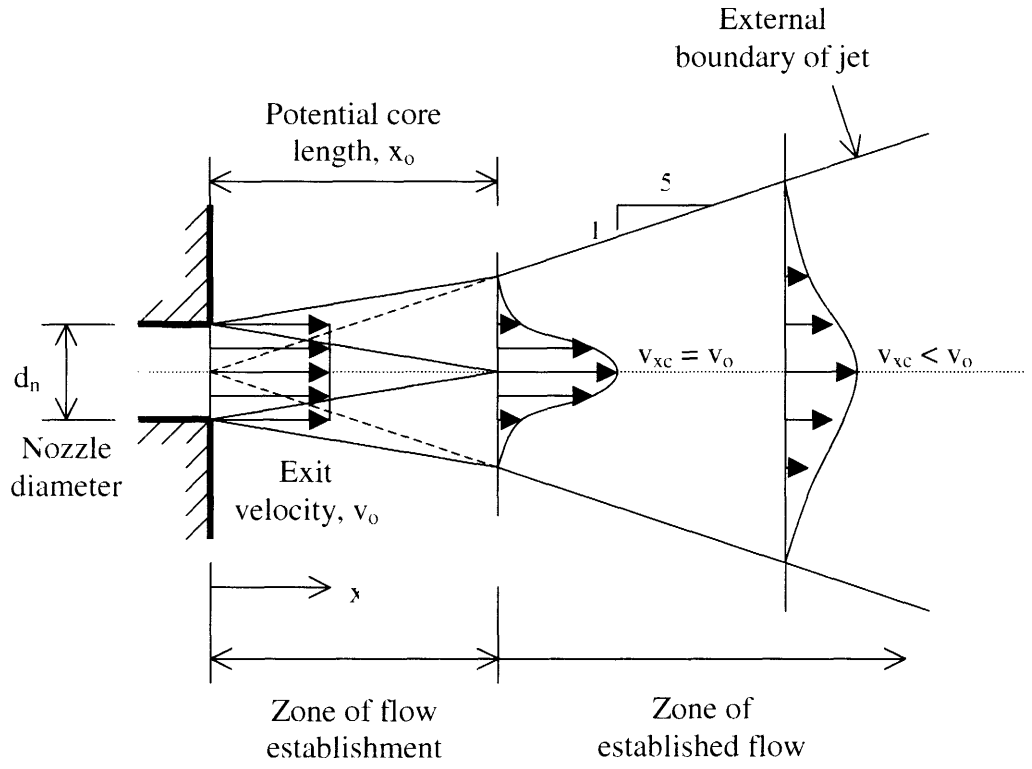

Figure 3-1. Schematic representation of jet diffusion (after Albertson et al., 1950)

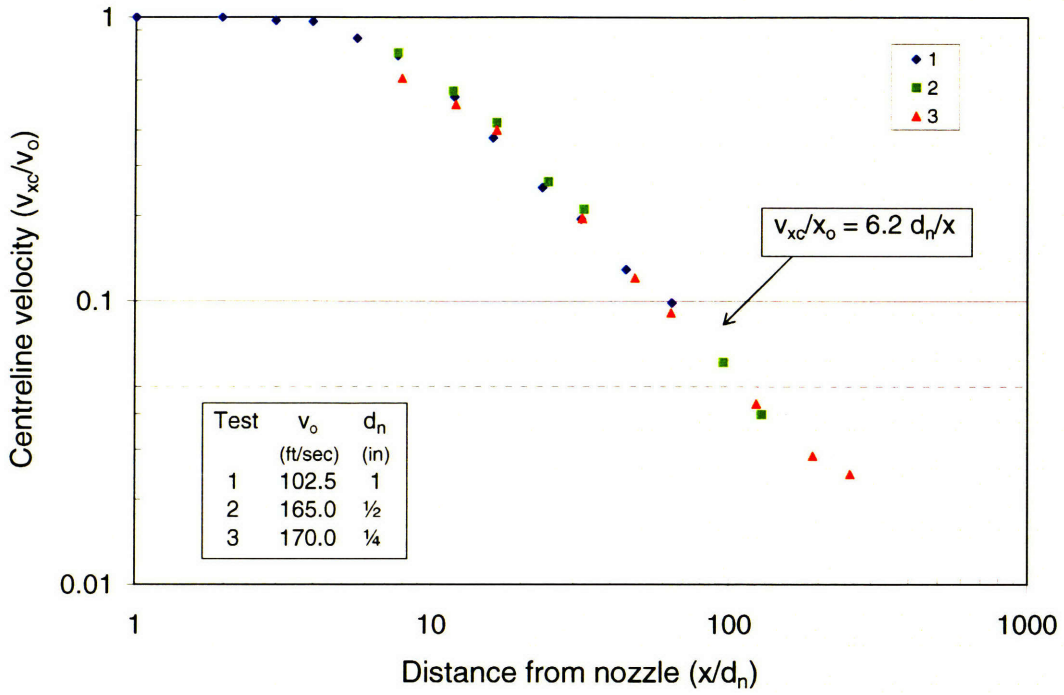

Figure 3-2. Centerline velocity decay in submerged free air jet
(after Albertson et al.,1950)

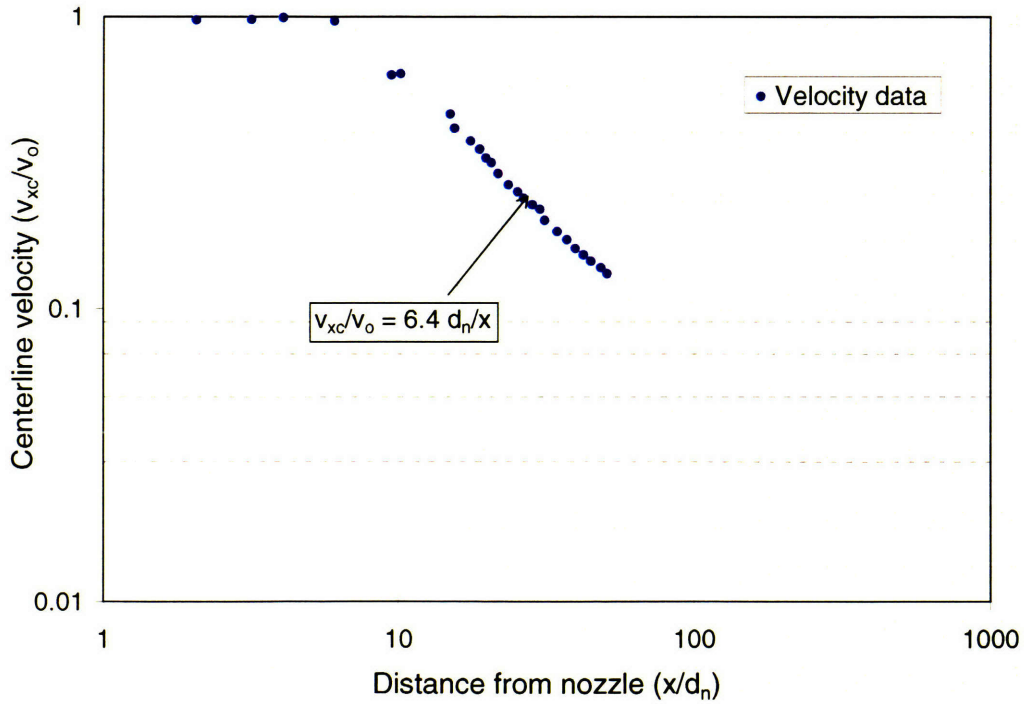

Figure 3-3. Centerline velocity decay in submerged free water jet
(after Forstall and Gaylord, 1955)

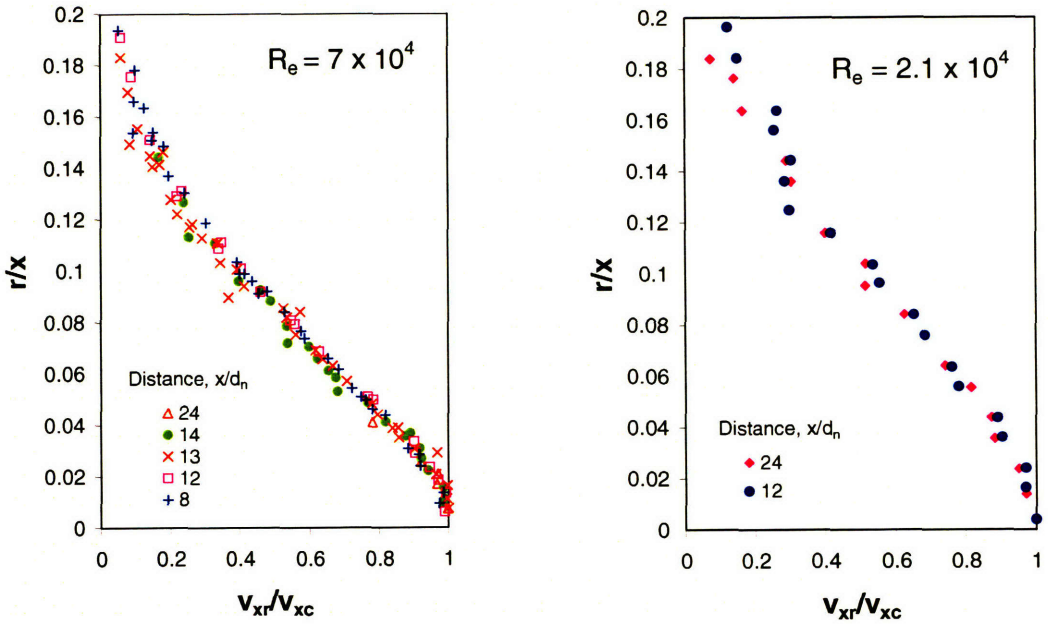

(a) Velocity distribution in jet cross-sections

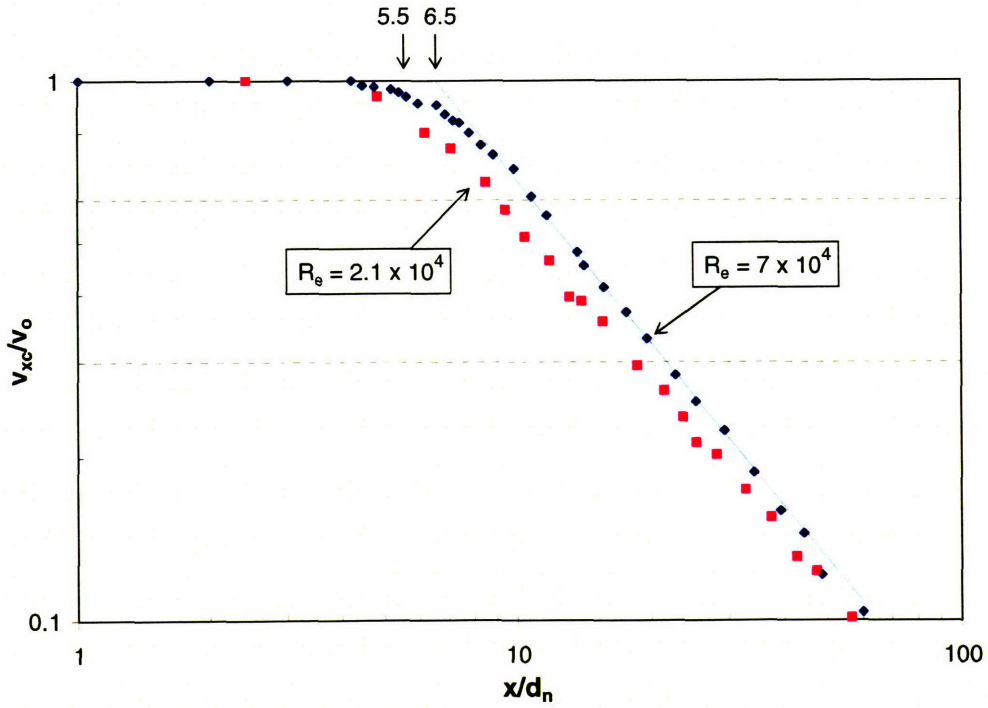

(a) Centerline velocity decay

Figure 3-4. Dynamic similarity for constant Reynold's number (after Baines, 1950)

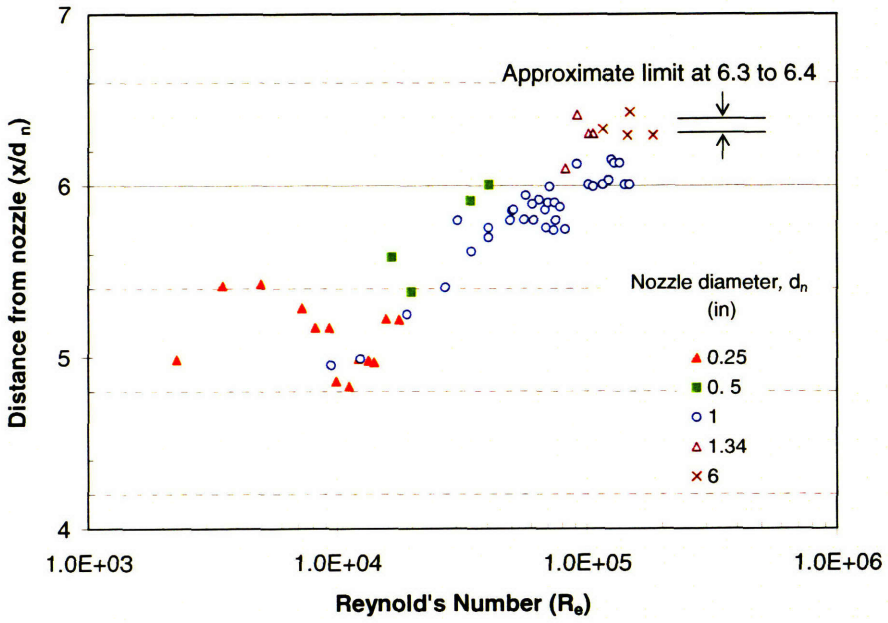

Figure 3-5. Effect of Reynold's number on length of potential core (after Baines, 1950)

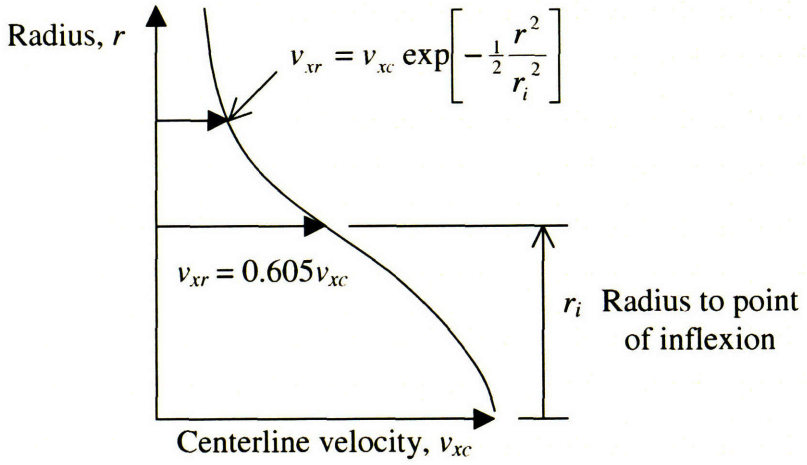

Figure 3-6. Radial distribution of axial velocity components in a diffused jet

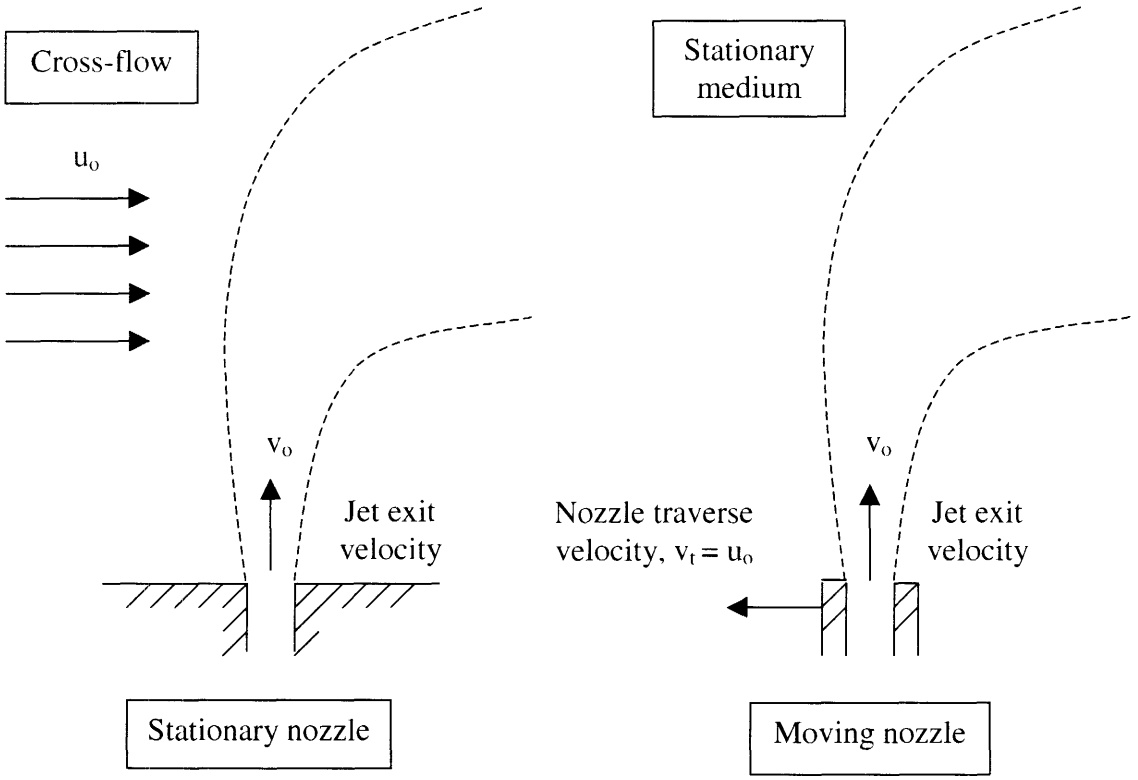

Figure 3-7. Equivalence between a stationary fluid jet issuing into a cross flow and a traversing jet issuing into stationary medium

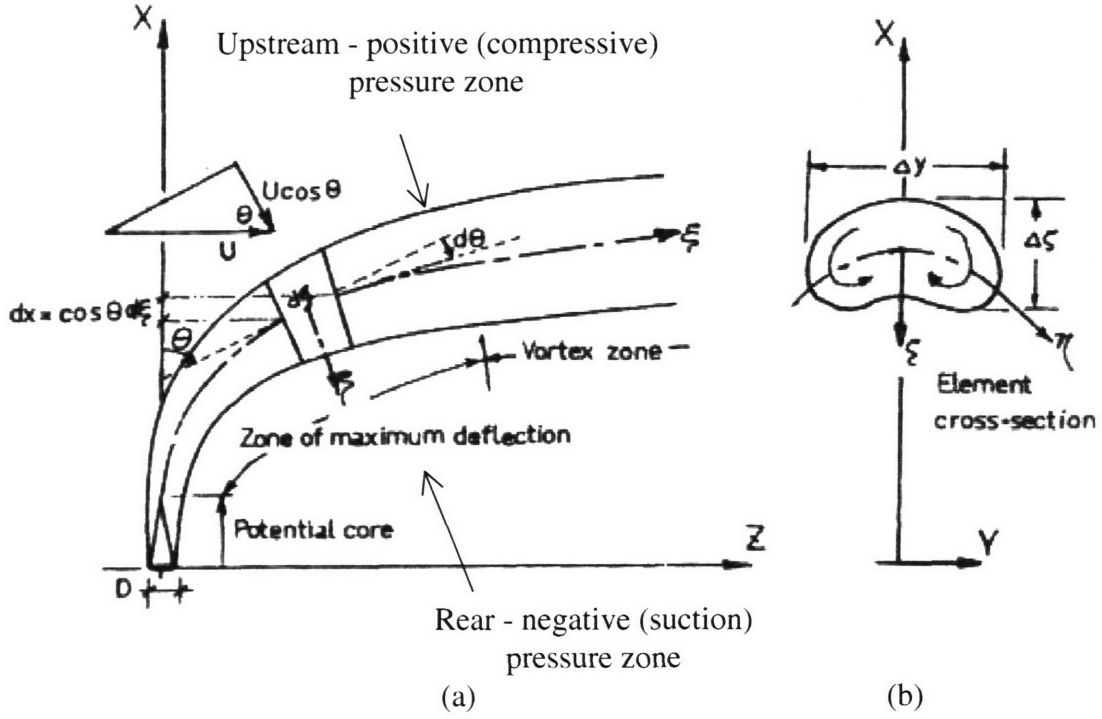

Figure 3-8. Characteristics of a submerged deflected jet (after Pratte and Baines, 1967)

(a) Distance $z = Rd_n$ (b) Distance $z = 2Rd_n$

Reynold's number, $R_e = 3.3 \times 10^4$
Nozzle diameter, $d_n = 5$ mm
Velocity ratio, $R = 10$

Figure 3-9. Measured concentration profiles showing kidney-shaped cross-sections of deflected air jet (after Smith and Mungal, 1998)

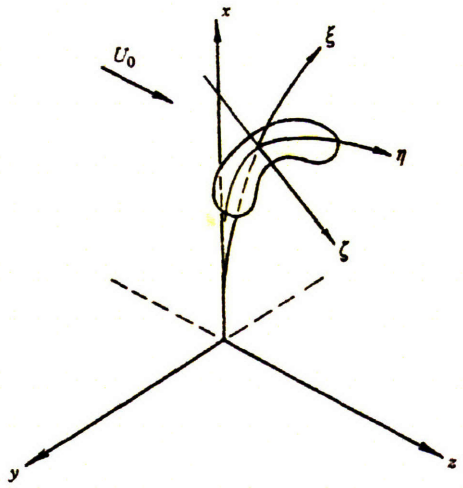

Figure 3-10. Natural system of axes for deflected jet (Keffer and Baines, 1963)

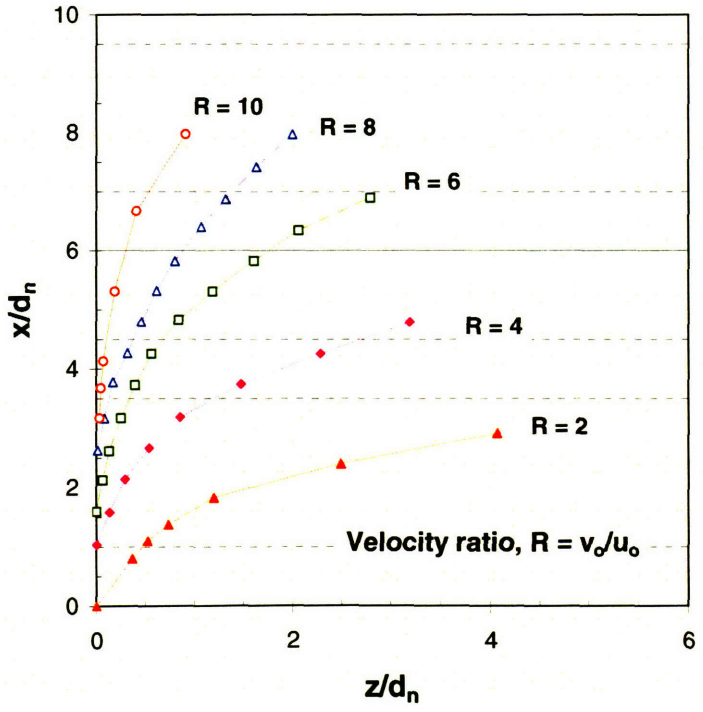

Figure 3-11. Variation of jet centerline trajectory with velocity ratio (after Keffer and Baines, 1963)

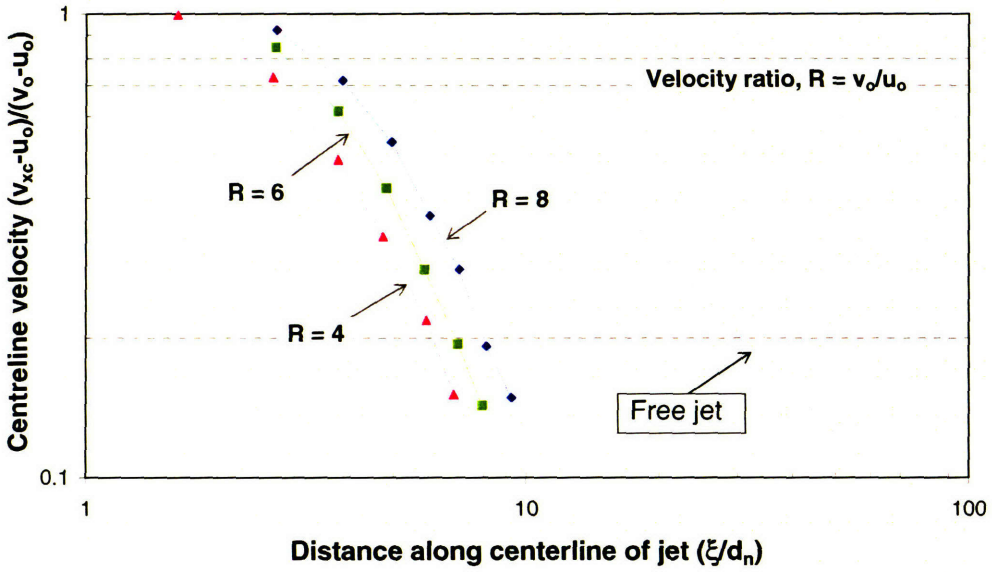

Figure 3-12. Centerline velocity decay in the ξ – axis, hatched line represents the characteristics of a free jet (after Keffer and Baines, 1963).

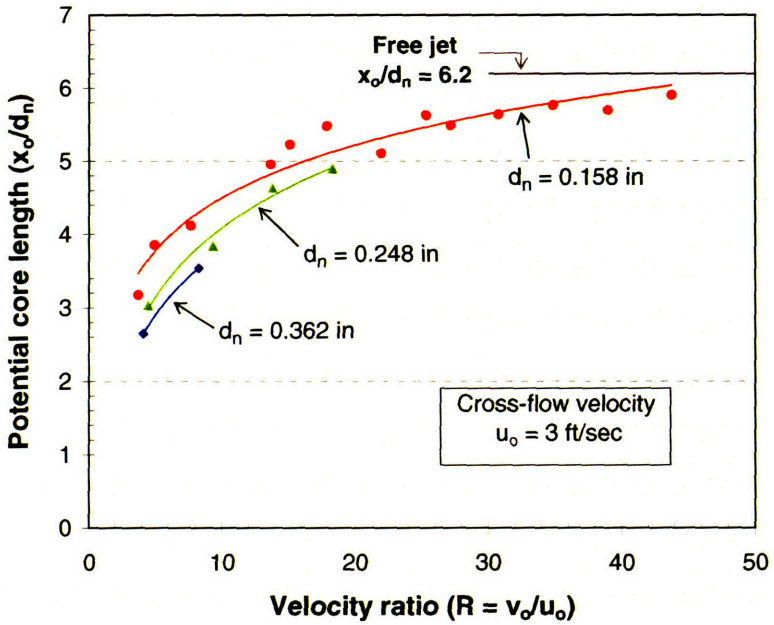

Figure 3-13 Effect velocity ratio, R on length of potential core (after Pratte and Baines, 1967)

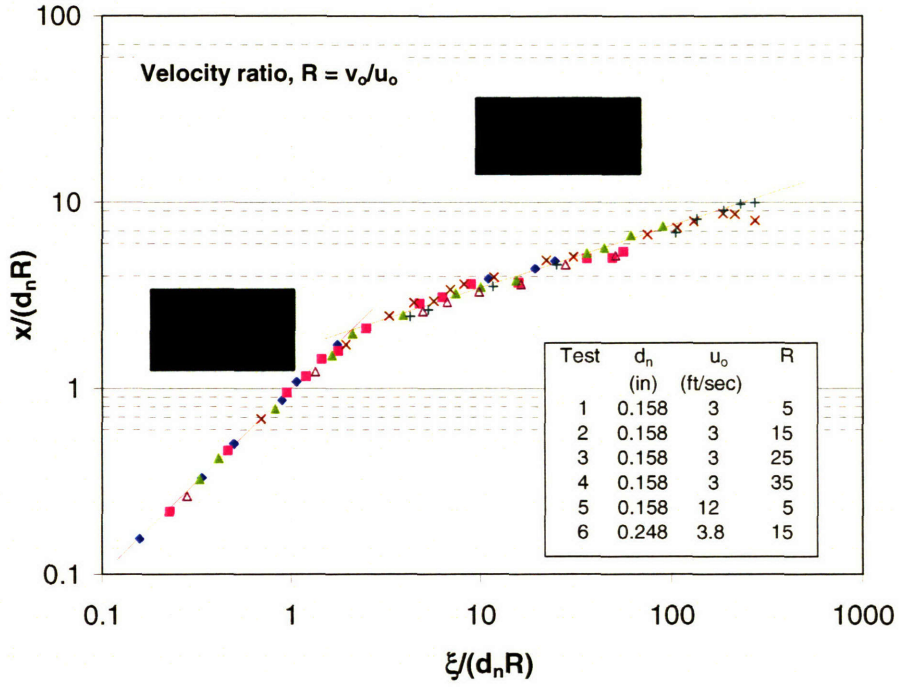

Figure 3-14. Centerline jet penetration along ξ – axis (after Pratte and Baines, 1967)

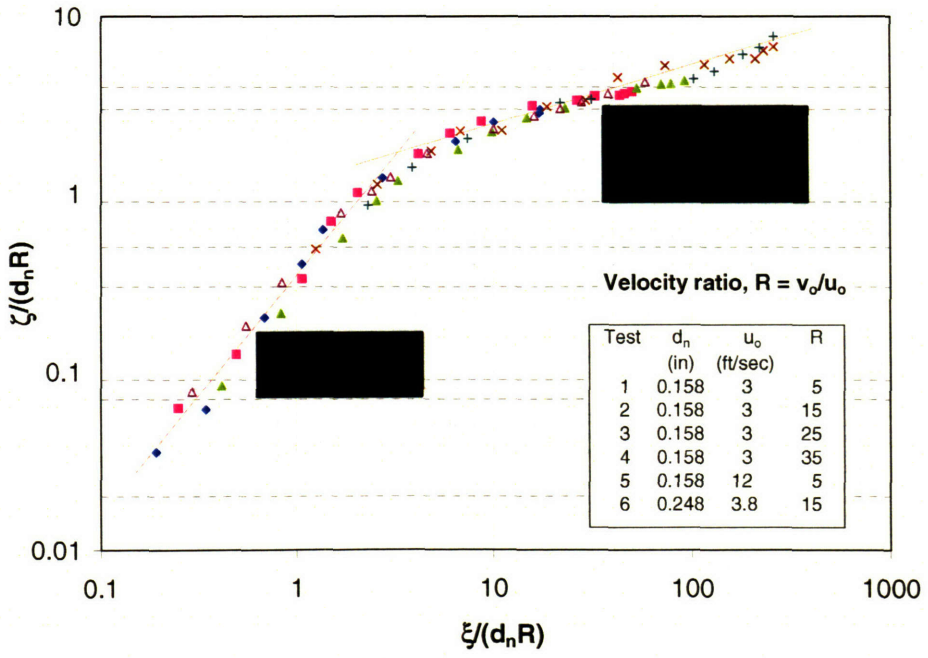

Figure 3-15. Lateral jet spread in ζ direction (after Pratte and Baines, 1967)

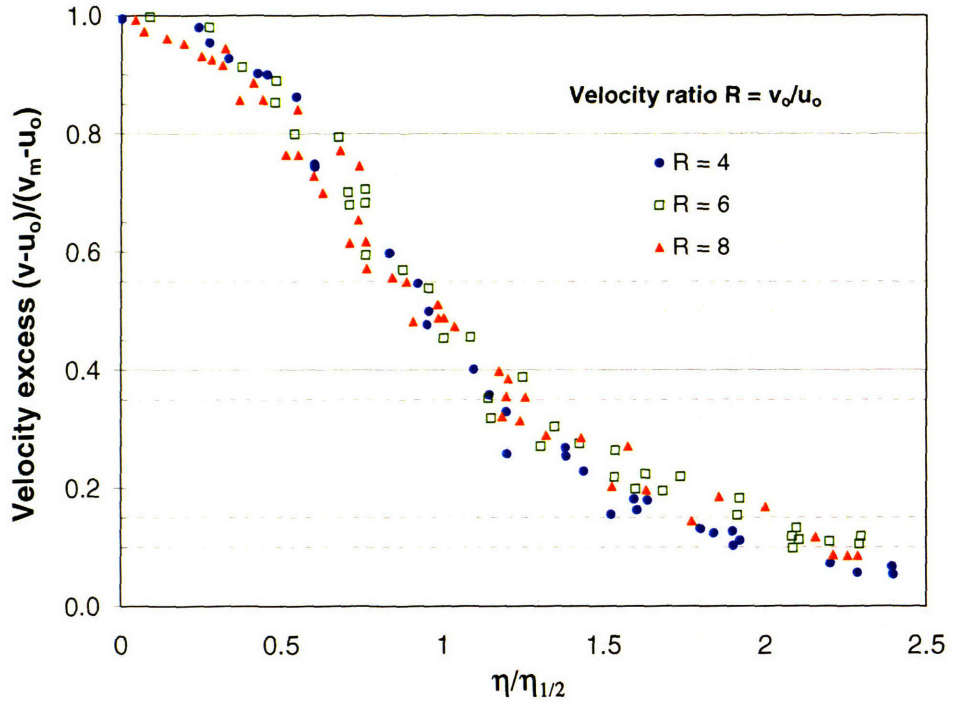

Figure 3-16. Similarity of lateral distribution of jet velocity along η axis (after Keffer and Baines, 1963)

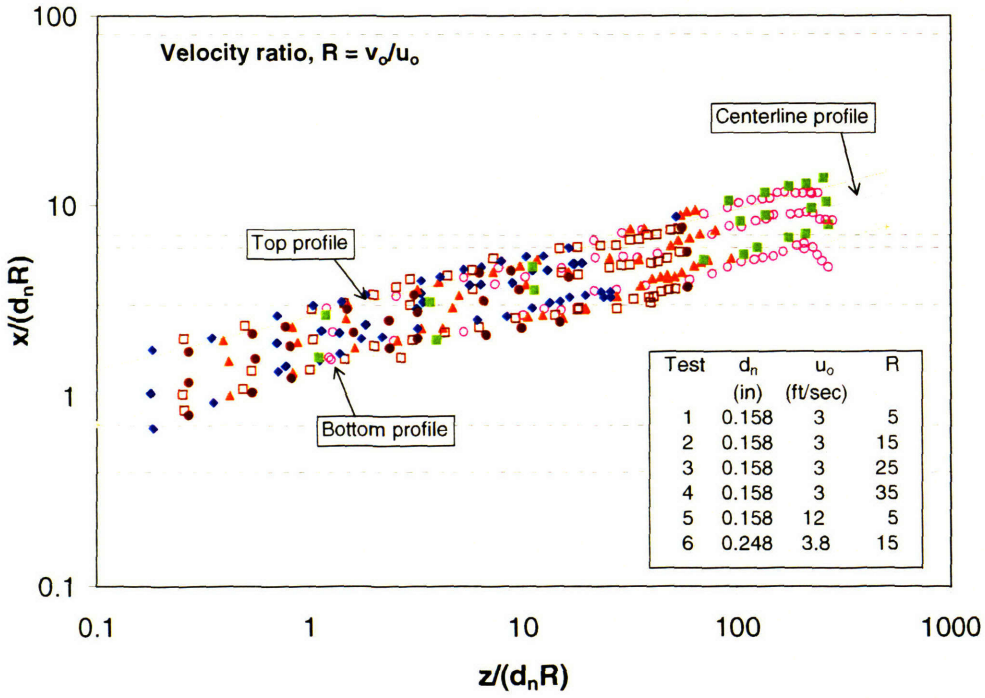

Figure 3-17. Normalized jet trajectory (after Pratte and Baines, 1967)

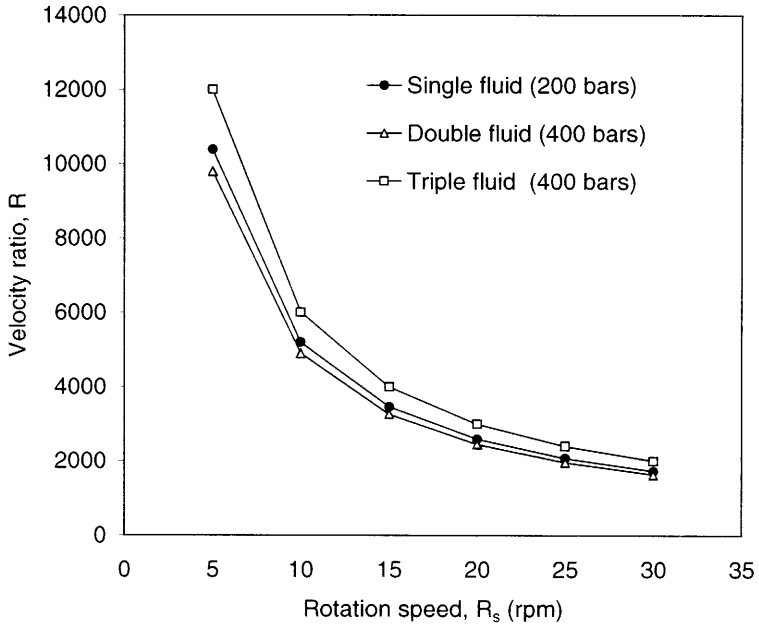

Figure 3-18. Typical velocity ratios in jet grouting operations

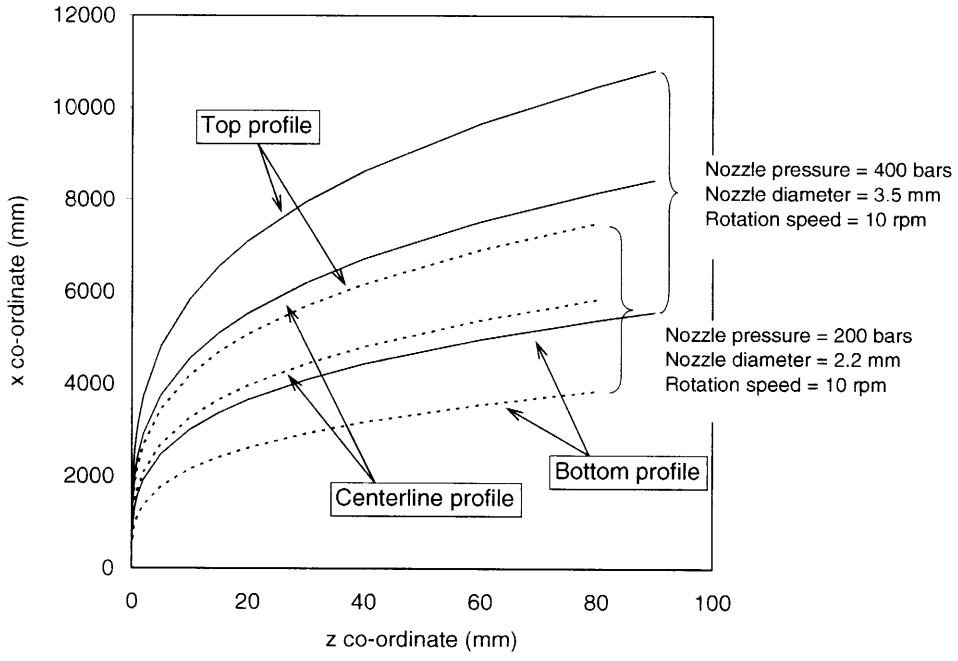

Figure 3-19. Typical jet trajectory for jet grouting without compressed air

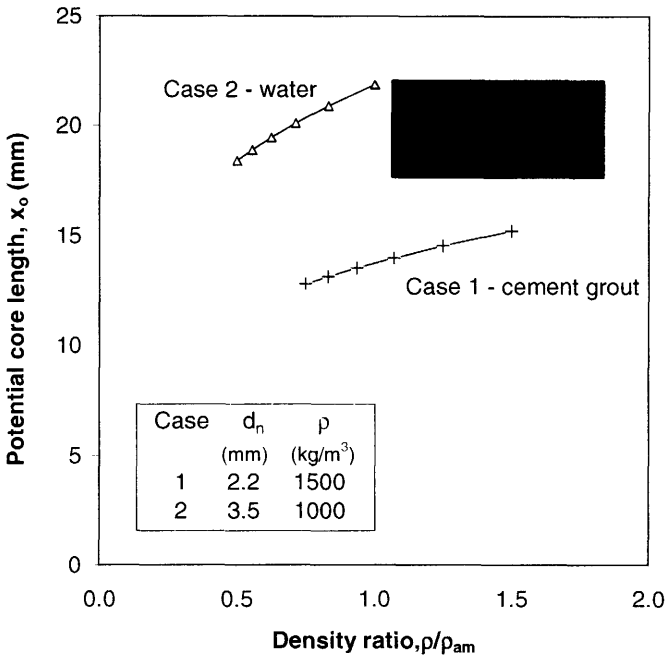

Figure 3-20. Variation of potential core length with fluid density ratio based on Eqn.3.13

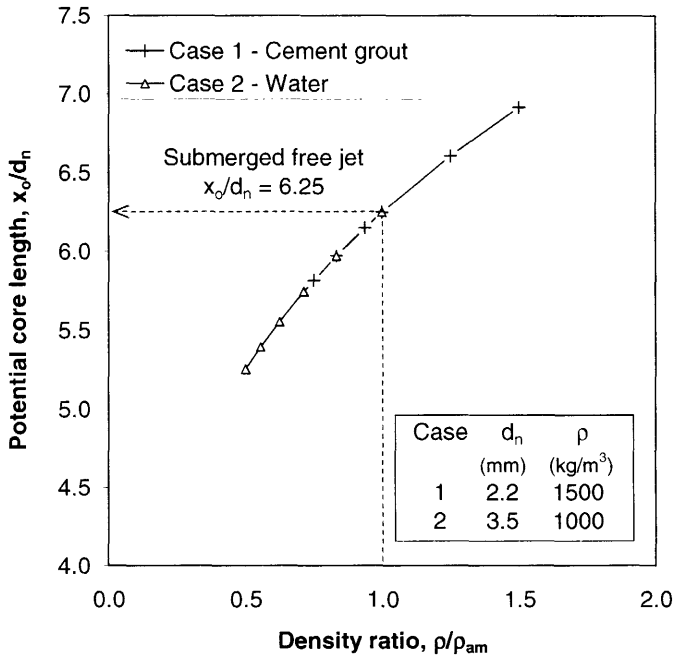

Figure 3-21. Variation of normalized core length with fluid density ratio

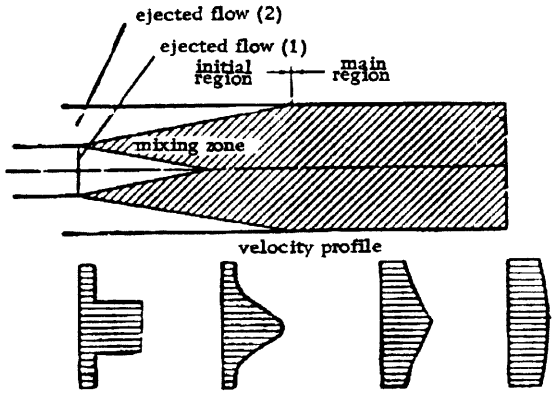

Figure 3-22. Flow pattern in the mixing chamber of an ejector (after Abramovich, 1963)

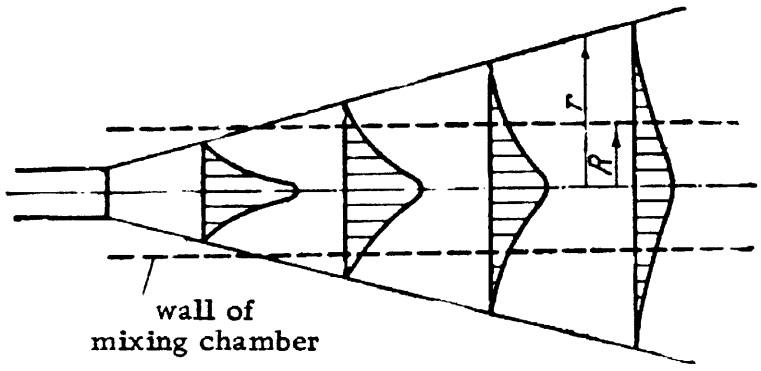

Figure 3-23. Analogy between fluid flow in a free jet and in the mixing chamber of an ejector (after Abramovich, 1963)

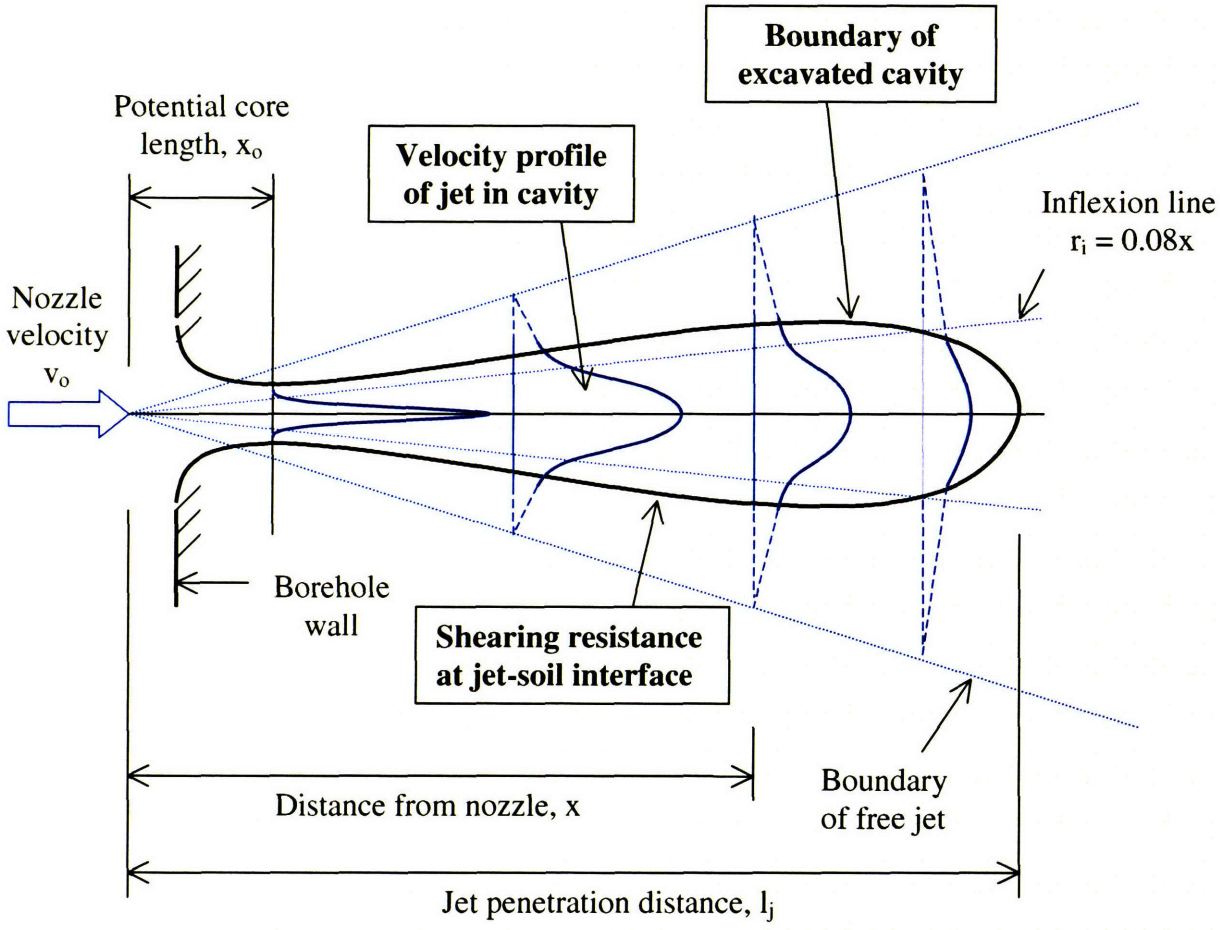

Figure 3-24. Application of free jet characteristics to proposed excavation model

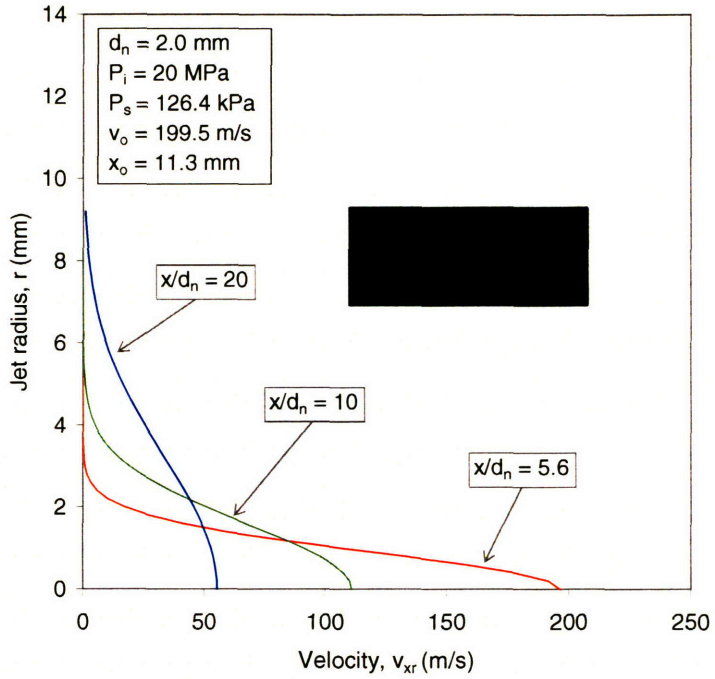

Figure 3-25. Assumed velocity distribution in jetting process based on Eqn. 3.18

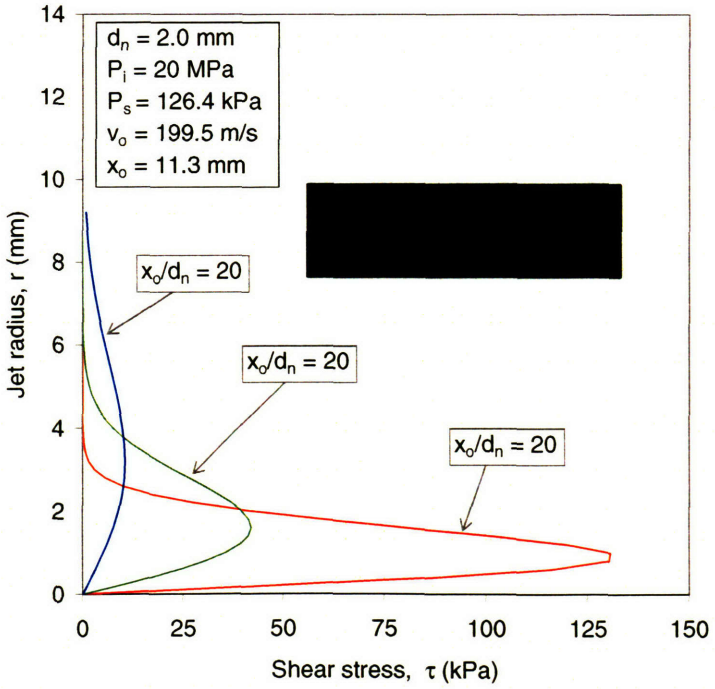

Figure 3-26. Typical turbulent shear stress distribution in a jet based on Eqn. 3.22

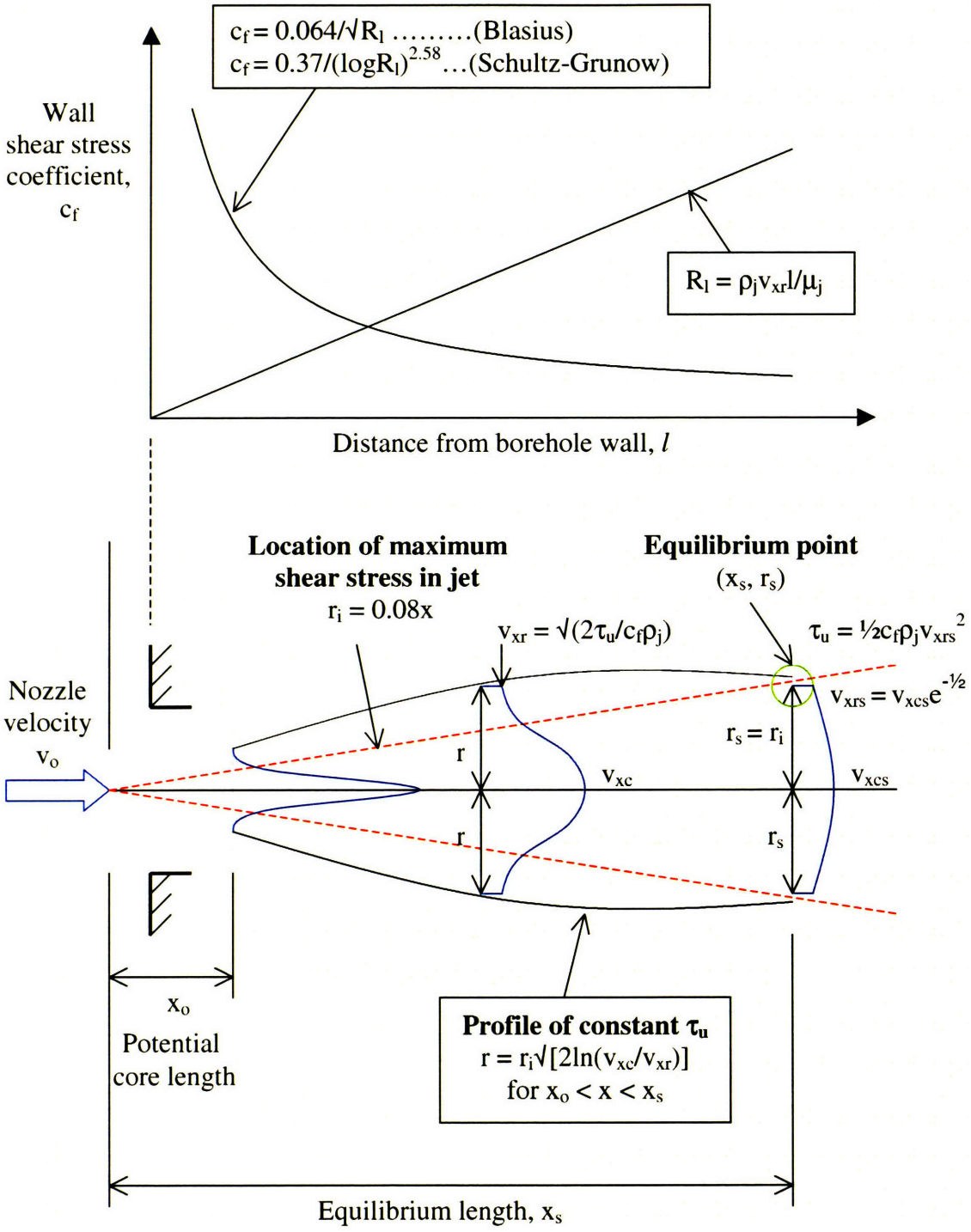

Figure 3-27. Computation of jet width based on Eqn.3.25

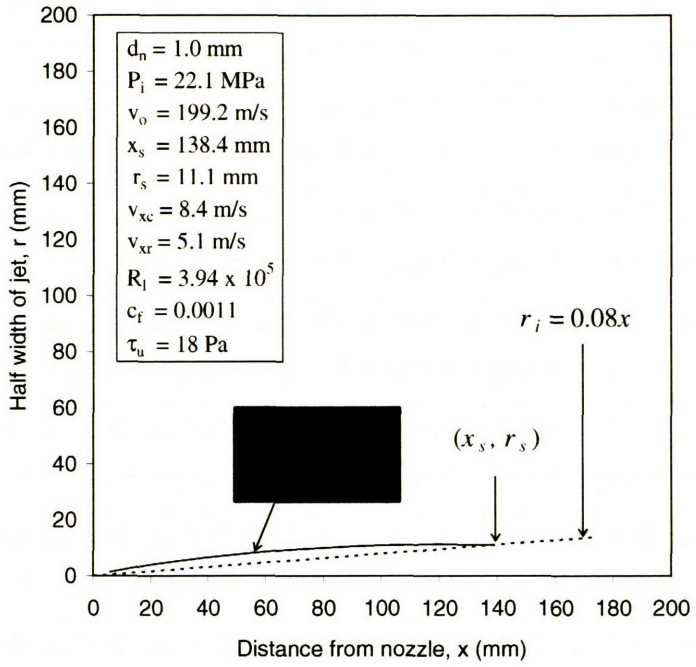

Figure 3-28. Predicted shape of cut based on Eqn. 3.25

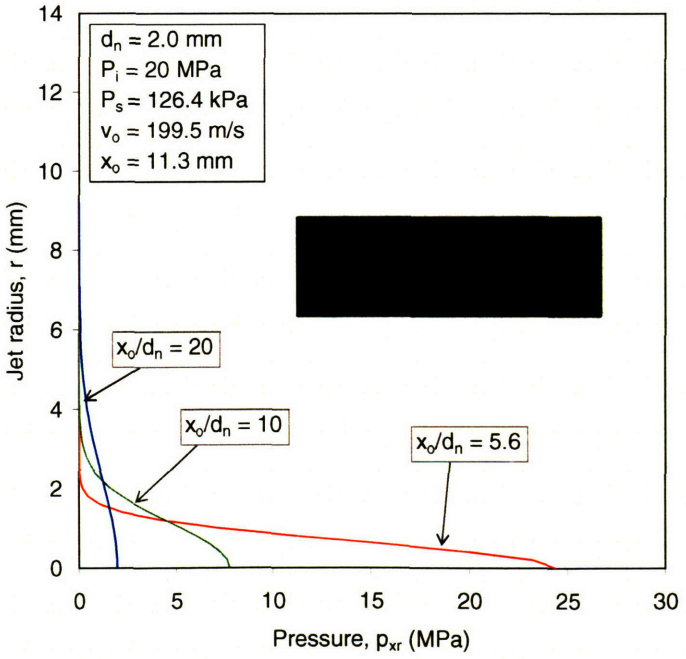

Figure 3-29. Typical dynamic pressure distribution in a jet based on Eqn 3.28

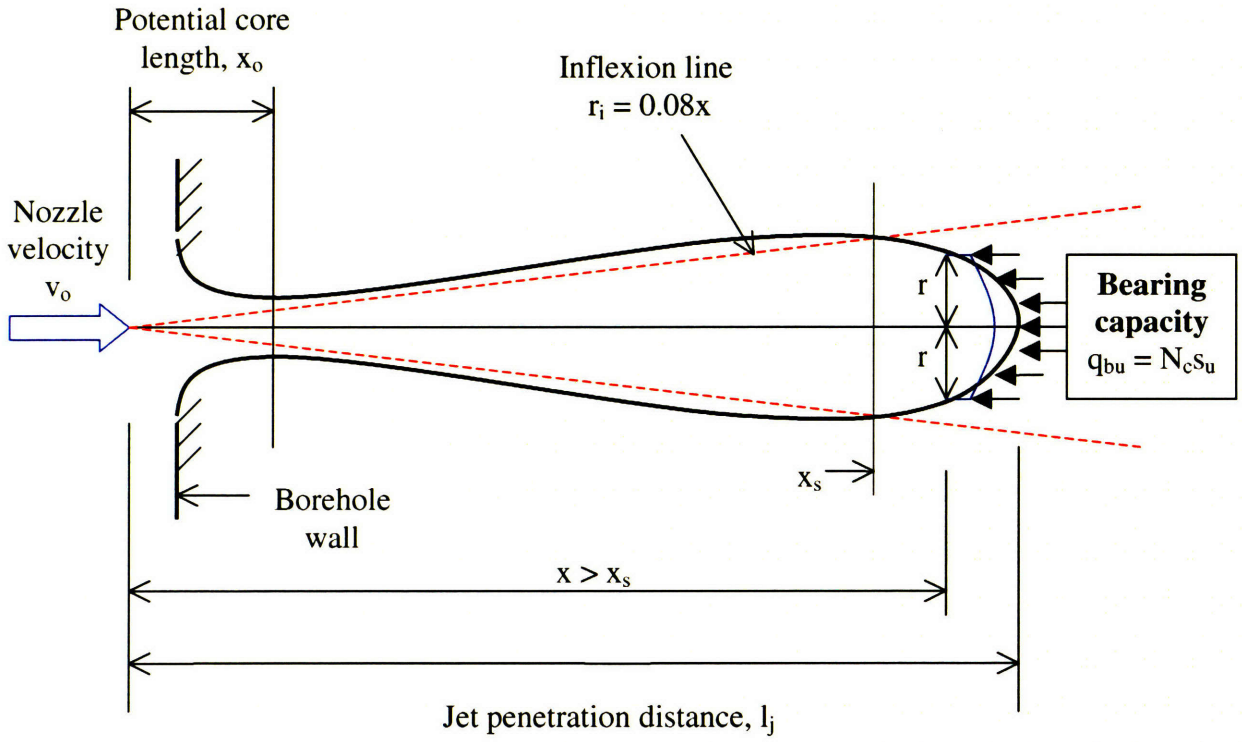

Figure 3-30. Soil bearing resistance at tip of jet

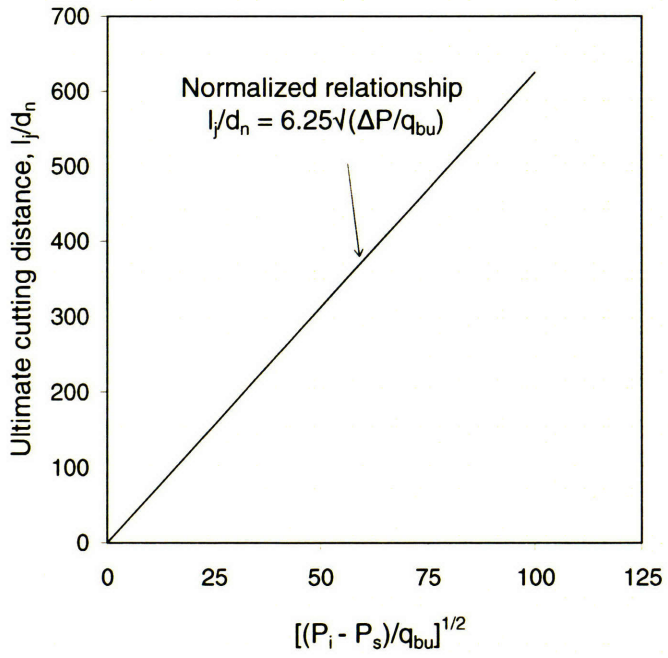

Figure 3-31. Normalized relationship for ultimate cutting distance based on Eqn. 3.34

CHAPTER FOUR
DESIGN OF LABORATORY EXPERIMENTS

4.1 Introduction

The primary goals of this research are to investigate the achievable jet penetration and excavation dimensions for forming a jet grout column in clay. This chapter describes laboratory jet excavations that were conducted using a model cohesive soil. One practical advantage of choosing a cohesive material is its low hydraulic conductivity, which ensures that the boundary conditions at the jet-soil interface are well defined, as there is no permeation/bleeding of the jet fluid into the surrounding soil during jetting and the soil is effectively sheared under undrained conditions. The research focuses on the single fluid jetting system, as this will establish the fundamental framework for understanding the jet-soil interaction behavior.

The objectives of the laboratory measurements were to observe the physical form (geometry, mixing) of the excavation to clarify the mechanisms of jet excavation, and to validate the analytical relationships linking operational parameters of the fluid jet and shear strength properties of the cohesive soil described in Chapter 3. The experiments were designed to enable physical measurements of the actual cut excavated by a fluid jet with controlled jetting parameters. The following sections present the design of the laboratory equipment, the method of preparation of the model soil and jetting fluid, and the procedures adopted in the jetting tests. A detailed evaluation of the properties of the model soil is also included. Figure 4-1 shows the layout of the testing equipment. A view of the test set up in the laboratory is shown in Figure 4-2.

4.2 Design of Laboratory Single Fluid Jetting System

4.2.1 Design of jetting equipment

Jet grouting involves the use of high velocity jets with fluid velocities in the order of 200 to 350 m/s. In field operations, very high capacity pumps operating at pressures of 2900 to 8700 psi (200 to 600 bars) are used to produce the high flow rates of 70 to 180 l/min. It is not practical to produce such high flow rates in the laboratory, mainly due to problems with containment and disposal of the resulting sludge produced by such an operation. The current test set up was scaled down to provide maximum flowrate of 4.3 gal/min (Figure 4-1), producing a sludge discharge up to about 52 gal for a maximum test duration of 12 min. This volume can be stored in a standard 55 gal drum.

To meet the above flow criterion, a high pressure triple-plunger electric pump, with a 1 ins diameter Type 416 stainless steel shaft was selected. The maximum rated capacity of this pump is limited to 3600 psi (Figure 4-3). The pump is driven by a 208-230/460 VAC 60Hz 3-phase AC motor producing 10 hp output power at a rotor speed of 1760 rpm (Figure 4-4). The pump and motor shafts were linked using a Buna-N spider coupling with a capacity of 7000 rpm and 417 in-lbs torque. For safety control, the outlet of the pump was fitted with a high pressure Type 316 stainless steel liquid relief valve set at 3500 psi pressure. A re-circulating line, consisting of a ¾ in. diameter high pressure hose rated at 1000 psi working pressure, was used to connect the discharge from the relief valve back to the inlet of the pump. The pressure in the outlet of the pump was monitored using a 2½ in diameter Type 304 stainless steel – case Grade B pressure gauge with maximum measurements up to 5000 psi and 2% accuracy.

The jetting system was contained within a three-sided wooden enclosure to achieve sufficient rigidity against the reaction forces and vibration generated during jetting (Figure 4-5). The jetting monitor was formed from a 3 ft long Type 304 stainless steel seamless pipe (Schedule 80 with 1.05 in outer diameter and 0.742 in inner diameter) fixed to a 90 degree elbow with maximum pressure rating of 3000 psi, to which the nozzle is attached (Figure 4-6). The pipe was secured to the testing platform by two cast iron flange-mounted steel ball bearings, with 7400 lb load capacity and 1800 rpm maximum rotation speed (Figure 4-7). To allow rotation of the monitor pipe, a swivel was introduced at the top of the pipe, consisting of a high pressure rotary joint with a maximum pressure rating of 3675 psi (Figure 4-8). Rotation of the pipe was achieved using a V-belt system (Figure 4-9) driven by a variable speed DC motor attached to the side of the enclosure wall (Figure 4-10). A control dial allows the speed of the motor to be selected (Figure 4-11). Figure 4-12 shows the calibration curve obtained for the rotation speed of the monitor pipe.

A series of nozzles were designed such that the smallest diameter would give test pressures as close as possible to the maximum pumping pressure of 3600 psi, whilst the largest would ensure that test pressures were sufficient to enable cutting of the soil. Two nozzle diameters were used in the experimental tests with nozzle diameters of 1.0mm and 2.5mm, corresponding to the highest and lowest possible operating pressures of the pump during each test. The nozzles were made from pre-manufactured ½ in diameter steel high pressure threaded hexagonal head solid plugs rated at 6000 psi (Figure 4-13). Each nozzle was formed by drilling a conical hole from the inlet side of the plugs using a cone angle of 14 degrees, followed by a straight section equal to 3 times the nozzle diameter on the

exit side (Figure 4-14). Typical views of the nozzle inlet and exit are shown in Figures 4-15 and 4-16, respectively.

The hydraulic lines between (a) the pump and the swivel, and (b) the bypass discharge line from the pump, consisted of ½ in diameter high pressure hoses rated for a working pressure of 4000 psi and 16,000 psi bursting pressure (Figure 4-17). The applied pressure in the line leading to the nozzle was measured by a 6 in diameter Grade 3A aluminum-case pressure test gauge, with measurements up to 5000 psi and an accuracy of 0.25% (Figure 4-18). It was assumed that the head loss in the line between the pressure gauge and the nozzle is small due to the short distance between the two points (10 ft). A brass flowmeter, with a scale reading of 0.5 to 5 gal/min (2 to 19 l/min) and rated at 3500 psi, was inserted in the line to measure the flowrate through the nozzle. Regulation of flow in the network was achieved using ½ in diameter zinc coated carbon steel hydraulic ball valves with 7250 psi pressure rating. Nominal 1 in diameter low pressure plastic hose was used as suction hose at the inlet of the pump.

Other accessories of the system included a 50 gal polyethylene drum for containing fresh water, a 55 gal steel drum for discharge collection, a 30 gal polyethylene drum for mixing and containing grout and a 16 gal steel drum for containing discharge during flushing of the jetting system after completion of each test (Figure 4-1). A 115 VAC 60 Hz clamp-mounted direct-drive electric agitator was used for mixing the grout (Figure 4-19). The agitator includes a triple-blade 3 in diameter propeller attached to a 30 in long shaft with $^{5}/_{16}$ in diameter, all formed from Type 316 stainless steel. Figure 4-20 shows a view of the jet impacting a solid surface at a pressure of about 100 psi and

flowate of 10 l/min. The specifications for the laboratory experimental setup are given in Appendix A.

4.2.2 Preparation of model soil

The size of the soil specimens was based on an estimated range of jet penetration (for selected soil strength and operational parameters) allowing for a clearance of at least 4ins from the side walls for even the largest excavation. In the final design, a specimen diameter of 30ins was considered the most appropriate for the range of test pressures to be executed. Considering the effort in manufacturing such large specimens, it was considered prudent to have multiple tests carried out within each specimen. In order to avoid potential interference between each excavation, a minimum vertical separation of 4 in was allowed between the levels of jetting. On this basis, a maximum of three cuts could be made in a soil specimen about 16ins thick. A test tank with depth of 27 in was used to ensure that there was sufficient freeboard to contain the slurry discharged during the tests.

Due to the large volume of the soil specimens (approximately 7.8 cubic ft), it is impractical to prepare clay specimens by consolidation from a slurry condition, due to the long drainage path (and resulting consolidation time). Assuming that the cohesive (i.e. peak undrained shear) strength of the clay is the main governing parameter controlling jet excavation, the model soil is instead manufactured by mixing kaolin with cement to produce specimens with controlled cohesion/undrained shear styrength. In a mixture of cement, kaolin and water, hydration occurs during curing, with adsorption of free water by the cement particles. Cementation bonding develops between particles of soil due to

presence of the cement particles, developing a cohesive strength component in the model soil.

The raw materials used in the present experiments consisted of Edgar Plastic Kaolin (EPK) clay and fast set Portland Cement Type III. Initial trial mixes were carried out using small samples 50 mm in diameter and 50 mm in height to determine the time required for curing. The water to soil ratio by mass was kept the same, while the cement to soil ratio by mass (CSR) was varied from 5 to 15 %.

Laboratory vane shear tests and fall cone tests were used to measure the shear strengths at different curing times. Figure 4-21 shows that the undrained shear strength of the samples with CSR = 10 and 15 % were well in excess of the target value, s_u = 50 kPa, indicating that model soils produced using these mix ratios would be too strong for the jets to cut effectively using even the highest test pressure of 3500 psi. In comparison measurements at CSR of 5% produced a cohesive strength in the range, s_u = 19 to 32 kPa which is more appropriate for the cutting experiments. For this mix ratio, at least 3 days of curing was required for the moisture content and shear strength to reach a reasonably stable value (Figures 4-21 and 4-22). The actual jetting experiments used model soils with CSR = 2.5 %, 5 % and 7.5 %, keeping the water to soil ratio the same. This gave a target shear strength ranging approximately from 5 to 45 kPa, for a curing time of at least 3 days.

Table 4-1 summarizes the design mix and theoretical properties for each test specimen, assuming the soil to be fully saturated. For each specimen, the model soil (cemented kaolin) was cast in two or three batches depending on the height of specimen required. In each batch, powdered kaolin was first placed in the mixer. Cement powder

was then added and thoroughly mixed with the clay in the dry. Water of equal mass to the clay was then added to obtain a blended paste. The resulting paste was very fluid and highly workable.

The test tank consisted of a 30 in diameter plastic tank 27 in deep. The weight of a typical soil specimen was about 280 kg. Therefore, a lifting system had to be designed for extracting the specimen from the tank after completion of the experiments. The final design was a wooden platform, placed at the base of the tank, with four steel rods attached to its bottom for lifting. The diameter of the platform was slightly smaller than the internal dimension of the test tank, in order for proper insertion and subsequent lifting. Lifting was achieved by attaching the top of each steel rod to two steel cross-beams, each secured with a nut (Figure 4-23). An overhead gantry crane suspended from the ceiling of the laboratory provided the lifting force. A hole was drilled in the side of the test tank close to its bottom, for insertion of a small tube for injection of compressed air supplied by a pneumatic compressor. The compressed air expands in the void beneath the platform and assists in the lifting action by pushing upwards against the weight of the specimen. Required air pressures ranged from 40 to 100 psi.

During preparation for casting of the soil, the lifting platform was first placed in the bottom of the test tank (Figure 4-24). A smooth plastic lining was then laid against the sides to reduce friction on the internal surface of the test tank. In some cases, flexible steel sheets were added between the plastic lining and the tank wall to ensure minimal contact with the wall, which will improve the ease of extraction of the specimen. A PVC pipe (24 in long with 4.5 in outer diameter and 0.25 in wall thickness), was placed at the center of the test tank. The position of the PVC pipe was securely fixed at the center of

the platform by four steel studs driven into the wooden surface. The blended soil paste was transferred from the mixer into the test tank and filled around the PVC pipe (Figure 4-25). After preparation of each specimen (2 to 3 batches each), the test tank containing the model soil was left to cure for 3 to 5 days prior to the jetting tests.

Samples of the model soil were collected during casting and covered in a plastic sheet to simulate curing under the same conditions as that in the test tank. The samples were tested to evaluate the strength, density and moisture content of the model soil at the time of jetting. The strength of the samples was measured mainly using the laboratory vane shear test. The strength data will be discussed in Section 4.2.

4.2.3 Preparation of jetting fluid

An important aspect of the experiments is to obtain a mold of the excavated cavity formed by the jet, so that the dimensions of the cavity can be measured. The experiments required a fluid that would flow freely during jetting, and then gel to form a stiff mass within the excavated cavity without collapsing. It was anticipated that the jetting experiments would involve the following sequence of activities:

(a) mixing of jetting fluid, 5 min

(b) jetting at first level, 1 min

(c) lowering test tank to second jetting level, 5 min

(d) jetting at second level, 1 min

(e) lowering test tank to third jetting level, 5 min

(f) jetting at third level, 1 min

(g) removing test tank from test enclosure, 5 min

(h) dismantling nozzle, 2 min

(i) flushing through monitor pipe, 10 min

(j) flushing through discharge lines, 10 min

The total time required to complete the above activities was 45 min. Another 15 min was allowed to cater for any contingency that may arise. Hence, the jetting fluid used for the experiments must have an initial setting time of at least 60 min in order to complete all the activities and prevent clogging of the equipment.

In order to achieve the above requirements, a sodium silicate based grout was selected for the experiments. The jetting fluid was produced from commercially available sodium silicate solution (Terraset Type A) using an ester hardener (Terraset Type B) as the reacting agent. The proportion of water, sodium silicate and hardener was fixed at 70%:27%:3% by volume based on the manufacturer's recommendations. Table 4-2 summarizes the densities obtained for the different components. The average density of the jetting fluid was 1.112 g/cm^3.

A Brookfield digital viscometer model LVDV-I+ was used to measure the viscosity of the jetting fluid (Figure 4-26). A UL adapter had to be used for measuring ultra low viscosities. The viscometer has a full-scale accuracy of 1 % for viscosity measurements. Figure 4-27 shows the viscosity-time relationship for tests on two samples of the jetting fluid. It can be seen that a significant increase in viscosity occurs at t = 70 to 80 mins.

The jetting fluid was mixed immediately prior to the jet cutting experiments, using the following procedure: (a) the required amount of water was first placed in the grout tank and fitted with an agitator, (b) the hardener was then added to the water and

stirred continuously for at least 5 minutes before adding the sodium silicate solution. This procedure ensures that the hardener is sufficiently diluted in order to avoid flash setting from taking place.

4.2.4 Procedures for cutting of model soil

The jet cutting experiments were carried out on model soil specimens with a range of undrained shear strengths (based on mix designs with CSR = 2.7 to 7.5 %). The test tank containing the cured soil was placed with the PVC pipe directly beneath the nozzle position. The platform was initially raised to the maximum height using a hydraulic lift and seated on wooden supports such that the nozzle is located at the lowest jetting level in the test tank (Figure 4-28). The PVC pipe was raised manually above the nozzle position and secured in position by hooks fixed to the ceiling of the test chamber (Figure 4-29).

Once the grout was mixed and ready, and the pump primed, the PVC pipe was first filled with grout solution at low pressure until it overflowed from the top. The jetting monitor was then set to the predetermined rotation speed, before the pressure was raised to the target level within about 5 seconds. The flowrate was read from the flowmeter and jetting was continued to the specified number of revolutions. The test tank was then lowered by approximately 4 ins for jetting at the next higher level. The procedure was repeated for two or three jetting levels. During jetting, a mixture of soil and grout is discharged up the PVC pipe and overflows into the test tank, filling the upper surface of the specimen. The discharged sludge was left to set at the top of the specimen and inside the PVC pipe (Figures 4-30 and 4-31).

After completion of the jetting experiments, the test tank was immediately removed from the test chamber and the jetting system thoroughly flushed with water to remove all the grout from the pump and hydraulic lines. This operation had to be completed within about 45 mins to avoid the grout setting and clogging the pumping system.

After a waiting period of approximately 24 hr, the model soil was lifted out of the test tank, with the assistance of compressed air pumped below the base of the soil specimen (Figures 4-32 to 4-33). The plastic lining was then unwrapped from the specimen (Figure 4-34). The specimen was divided into eight equal segments and alternate segments were excavated to expose the vertical soil faces. Figures 4-35 to 4-38 demonstrate the typical staged excavation of a soil segment. Wherever possible, the surface of the grouted "disc" was carefully located and exposed for measurement and inspection (Figures 4-39 and 4-40). The cuts in the vertical soil face (Figures 4-41) were mapped by tracing over their profiles using a permanent marker on clear transparency. The maximum cutting distance and shape of the cuts were measured off the marked transparencies for each soil face.

4.2.5 Scope of test program

Table 4-3 lists the various jetting parameters and model soil mixtures (CSR) used for the jetting experiments. A total of 9 specimens (T1 to T9) were prepared and tested. Tests on Specimen T1 were designed to study the effect of the number of revolutions (i.e. the number of passes of the nozzle) on cutting distance. Tests on Specimen T6 were carried out to verify the influence of rotation speed on cutting distance. A repeatability

check on the test results for the same jetting parameters and soil shear strength was carried out using Specimen T9. The majority of tests were conducted on model soils with CSR = 5% (T1, T2, T3, T6 and T9). Specimens T4, T5 and T7 involve a low strength mix with CSR = 2.5 %, while only one specimen (T8) was prepared using a stronger soil mix (CSR = 7.5 %). Due to the capacity of the safety valve used, all tests were conducted using pressures below 3500 psi, with a minimum pressure of 100 psi (used in tests T3, T5 and T7; Table 4.3).

Some difficulties were initially encountered when handling soils of very soft consistency manufactured using a low strength mix with CSR = 2.5 %. A low strength specimen T4, cast to the full height of 17¼ in, partially collapsed about 15mins after removal from the test tank. Fortunately, only the upper cut and part of the middle cut was lost; the complete lower cut remained intact. Another low strength specimen T5, cast in two batches to a height of 9 in was also unstable, collapsing under its self-weight upon removal from the test tank. No measurements were possible in this case. Subsequently, specimen T7 (CSR = 2.5 %) was manufactured with two rather than three batches of soil to reduce the height of the specimen and the waiting period prior to exhumation was extended from 24 hr to about 3 days from the completion of cutting tests. All other tests on model soils with CSR = 5 % and 7.5 % were stable and complete measurements obtained.

4.3 Properties of Model soil

4.3.1 Characterization of test specimens

The properties of the model soil were determined from measurements of bulk mass density (γ_t), moisture content (w) and laboratory vane shear strength (s_{uv}). Soil samples were obtained by manually pressing thin-walled containers into the excavated horizontal soil face during exhumation of the specimen (Figures 4-42 to 4-45). Samples were taken at two to three different depths. A hole was drilled into the bottom of the container to ensure no air was trapped during sampling. The volume of the container was obtained by filling the container with water and measuring the mass of water. The mass of the sample was measured immediately after sampling was completed. Laboratory vane shear tests were conducted on the samples to evaluate the shear strength and sensitivity of the soil. Moisture contents were obtained for all samples. Block samples were collected wherever possible for additional density measurements. These were trimmed into a cylindrical shape and several measurements of the diameter and height were made using a vernier caliper to obtain the average diameter and height.

The degree of saturation (S) and void ratio (e) of the model soil were determined from the density and moisture content measurements, assuming the specific gravity of kaolin, G_s = 2.64 and cement, G_c = 3.15. These were calculated for each strength category (CSR = 2.5%, 5% and 7.5%) using the following expressions:-

$$S = \frac{[wG_s(1+CSR)]}{\left\{\frac{[G_s\gamma_w(1+CSR)(1+w)]}{\gamma}\right\} - CSR\left(\frac{G_s}{G_c}\right) - 1} \tag{4.1}$$

$$e = \frac{wG_s(1+CSR)}{S} \tag{4.2}$$

where w is the moisture content.

Figures 4-46 to 4-51 illustrate the variation of bulk density, moisture content, void ratio and degree of saturation with specimen depth for T7, T9 and T8 respectively (i.e. mixes with CSR = 2.5 %, 5 % and 7.5 %). As can be seen, there was no significant variation in these properties between batches within each specimen, hence the mixing of the batches can be regarded as reasonably uniform. Accordingly, it can be assumed that the same quality of mixing was achieved for all other test specimens. The theoretical values of the above properties calculated for the design mix in Table 4-1 (assumed to be fully saturated) are indicated for comparison. The moisture contents were slightly higher for T9 and about the same for T8 in comparison with the design mix values. The moisture contents for T7, however, were lower than the design mix value. Some kaolin was observed to stick to the sides of the mixer during blending, which may have resulted in a reduction of the actual mass of kaolin in the model soil. This would produce a wetter mixture and is reflected in a moisture content that is higher than the design mix. The low moisture content is likely to be due to the effect of drying out over the several days required for making the measurements when the specimens were exhumed. The bulk densities for all three specimens are lower than the theoretical value calculated for the design mix. This suggests that some air may have been entrained during mixing and transferring of the blended soil paste into the test tank, when the specimens were prepared. This would increase the total volume of the model soil. The void ratios were observed to be very high (ranging from of 2.5 to 3.0). This is consistent with the method of casting the soil, where no load was applied to consolidate it and curing took place under constant volume. The void ratios were higher than the design mix due to the likely

entrapment of air as indicated previously. The degree of saturation generally ranged from 90 to 100%.

The statistical spread of the measurements obtained for the above four properties are shown in Figures 4-52 to 4-55, where the mean value is plotted with +/- one standard deviation bounds indicated. The difference in the results between specimens may be attributed to the mixing conditions.

4.3.2 Shear strength

The shear strength of the model soil was measured using torvane shear tests and laboratory vane shear tests[1]. Torvane tests are conducted directly on flat soil surfaces with the vanes penetrating ¼ in into the soil. A torque is applied to cause a direct shear failure around the periphery of the vane. The time for shearing is rather short, of the order of 5 to 10 seconds. For laboratory vane shear tests, the vane is inserted into the body of the sample and the soil is sheared by applying a torque at a constant rate of 0.1 °/sec. The time to reach failure for the present experiments ranged from 2 to 12 min. Since the vane is surrounded by soil on its sides, top and bottom, the shearing resistance is a combination of direct shear along its perimeter and tangential shear along its top and bottom surfaces. The shear strength is assumed to be uniform on all the surfaces. However, when slippage occurs at the cylindrical periphery, the strains in the top and

---

[1]Initially, hand-held penetrometer tests were also carried out to obtain the unconfined compressive strength of the model soil. However, there were inconsistent measurements between the ¼ in diameter standard point and a 1 in diameter footing. The penetrometer readings were therefore excluded from the current presentation.

bottom surfaces are still within the yield limit and plastic strains have not yet been fully developed. Hence, the values of shear strength computed in the laboratory vane shear tests would be smaller than that induced by a pure shear mechanism. Since the torvane test provides a measurement of direct shear and is conducted at a higher shearing rate, the soil strength given by a torvane test is expected to be higher than that obtained from a laboratory vane shear test.

In the present experiments, the shear strength of the model soil was measured using a torvane of standard dimension (1 in diameter) or with an enlarged vane (2 in diameter). The standard vane was used mainly for the stiffer specimens with cement-soil ratios of 5 % and 7.5 %. The majority of the measurements for the low strength specimens (CSR = 2.5 %) were carried out using the large torvane (with a smaller number of standard torvane tests). Measurements were made on horizontal soil surfaces as the "pies" within each segment were removed in layers, and on vertical soil faces of the sections. For each torvane test, three samples of the soil immediately adjacent to the test location were placed in tares for moisture content measurement.

Figure 4-56 summarizes the relationship between the moisture content and shear strength for all of the torvane measurements. For each model soil (CSR = 2.5 %, 5 % and 7.5 %), there was a slight trend of decreasing shear strength with moisture content. However, as noted in Section 4.2.1, the void ratios were very high, suggesting that the shear strength of the model soil was controlled mainly by cementation between soil particles. The scatter of the data is indicative of the degree of uniformity that is achieved by the mixing technique adopted for manufacturing the model soil specimens at the scale needed for the jetting experiments. It should be noted that there is no significant

difference between the torvane tests carried out on a horizontal soil face and those carried out on a vertical soil face in any of the specimens. This suggests that the model soil has an isotropic shear strength. It was also observed that there was no significant difference between the strengths obtained using a standard vane and a large vane for the low strength specimens.

Figures 4-57 to 4-59 compare the laboratory vane shear strengths obtained from insitu samples and those obtained from torvane tests for different CSR. It can be seen that the torvane strengths were consistent with the peak laboratory vane shear strengths. Hence, the torvane strengths represent peak shear strengths of the soil.

As the shear strengths of the soil were obtained at the time when the soil faces were exposed, there was a time delay between measurements for the same test specimen. Figure 4-60 to 4-62 summarize the torvane strength data as functions of the curing time from casting. The earliest time at which the shear strengths were measured was at least 112 hr (4.7 days) after casting of the specimen. Table 4-4 lists the general trend of strength gain with time as shown by the data. It was observed that the average rate of shear strength increase for CSR = 2.5 % and CSR = 7.5 % were similar, i.e. $\Delta s_u/\Delta t$ = 0.028 kPa/hr (T4), 0.020 kPa/hr (T7) and 0.027 kPa/hr (T8). For CSR = 5 %, the rate of strength increase for measurements at times less than about 200 hr (8.3 days) were also in a similar range, i.e. $\Delta s_u/\Delta t$ = 0.033 kPa/hr (T1) and 0.036 kPa/hr (T9). However, T2 appear to indicate an anomaly with a slight decreasing trend with time ($\Delta s_u/\Delta t$ = -0.015 kPa/hr), which suggests that, for all practical purposes, the ultimate strength has been reached within a short curing period for this specimen. Beyond 200 hr after casting, the rate of strength increase for CSR = 5 % appeared to be higher, $\Delta s_u/\Delta t$ = 0.11 kPa/hr (T3)

and 0.096 kPa/hr (T6). This observed higher rate of strength gain at the later stages could be due to some other phenomenon other than hydration of the cement, and may suggest that the soil has dried out when the torvane measurements were made.

The relationship between the peak and residual shear strengths obtained from laboratory vane shear tests is shown in Figures 4-63 to 65. The sensitivity (i.e. ratio of peak to residual vane shear strength) varied between, s_{up}/s_{ur} = 2 to 3 in general. The sensitivity is higher for the soil with the higher cement content, i.e. closer to 2 for CSR = 2.5 % and 3 for CSR = 7.5 %, with CSR = 5 % falling in between.

Table 4-1. Summary of design mix and theoretical properties of model soil

Specimen	CSR [%]	No. of batches	Mass of Cement [kg]	Mass of Kaolin [kg]	Volume of Water [l]	Moisture content [%]	Bulk * density [kg/m^3]	Void* ratio
T1	5.0	3	6.804	136.08	136.08	95.24	1469.9	2.53
T2	5.0	3	6.804	136.08	136.08	95.24	1469.9	2.53
T3	5.0	3	6.804	136.08	136.08	95.24	1469.9	2.53
T4	2.5	3	3.402	136.08	136.08	97.56	1460.3	2.59
T5	2.5	2	2.268	90.72	90.72	97.56	1460.3	2.59
T6	5.0	3	6.804	136.08	136.08	95.24	1469.9	2.53
T7	2.5	2	2.268	90.72	90.72	97.56	1460.3	2.59
T8	7.5	3	10.206	136.08	136.08	93.02	1479.4	2.48
T9	5.0	3	5.561	111.22	111.22	95.24	1469.9	2.53

*Note: Bulk density and void ratio are calculated assuming full saturation

Table 4-2 Density measurements for sodium silicate grout

	Mass density, ρ (g/cm^3)				
Sample #	1	2	3	4	Average
Sodium silicate	1.396	1.395	1.402	-	1.398
Ester hardener	1.145	1.169	1.172	1.159	1.161
Grout	1.113	1.111	1.111	-	1.112

Table 4-3. Summary of test program

Specimen No.	Test No.	Cement to soil mass ratio	Nozzle Diameter	Pressure	Flowrate	Rotational Speed	Number of Revolution	Elapsed Time	Time of jetting
		CSR [%]	d_n [mm]	P_i [psi]	Q_m [l/min]	R_s [rpm]	N_r [rev]	t_r [sec]	t_j [hr]
T1	Upper	5	1.0	3200	6.2	10	10	60	
	Middle			2000	5.1	10	10	60	88.3
	Lower			1000	3.8	10	10	60	
T2	Upper	5	1.0	3200	8.0	10	20	120	73.8
	Middle			3200	7.8	10	5	30	
	Lower			3200	7.6	10	1	6	
T3	Upper	5	2.5	100	9.0	10	10	60	123.4
	Middle			200	14.0	10	10	60	
	Lower			300	17.2	10	10	60	
T4	Upper*	2.5	1.0	3200	7.8	10	10	60	95.1
	Middle			2000	5.9	10	10	60	
	Lower			1000	4.1	10	10	60	
T5	Upper*	2.5	1.0	300	17.2	10	10	60	301.0
	Lower*			100	8.0	10	10	60	
T6	Upper	5	1.0	3200	7.5	20	10	30	121.6
	Middle			3200	7.5	10	10	60	
	Lower			3200	7.5	5	10	120	
T7	Middle	2.5	2.5	100	10.0	10	10	60	118.3
	Lower			300	15.5	10	10	60	
T8	Upper	7.5	1.0	1000	4.5	10	10	60	95.4
	Middle			2100	6.1	10	10	60	
	Lower			3250	8.0	10	10	60	
T9	Upper	5	1	3400	8.2	10	10	60	74.9
	Middle			3350	8.2	10	10	60	
	Lower			3350	8.2	10	10	60	

*No data due to specimen collapse

Table 4-4. Effect of time on observed shear strength of model soil

Cement to soil mass ratio	Specimen No.	Time of strength measurements from casting	Average rate of strength increase
CSR [%]		t [hr]	$\Delta s_u/\Delta t$ [kPa/hr]
2.5	T4	119 to 211	0.028
	T7	143 to 265	0.020
5.0	T2	112 to 168	-0.015
	T9	127 to 221	0.036
	T1	166 to 214	0.033
	T3	192 to 243	0.110
	T6	193 to 360	0.096
7.5	T8	140 to 284	0.027

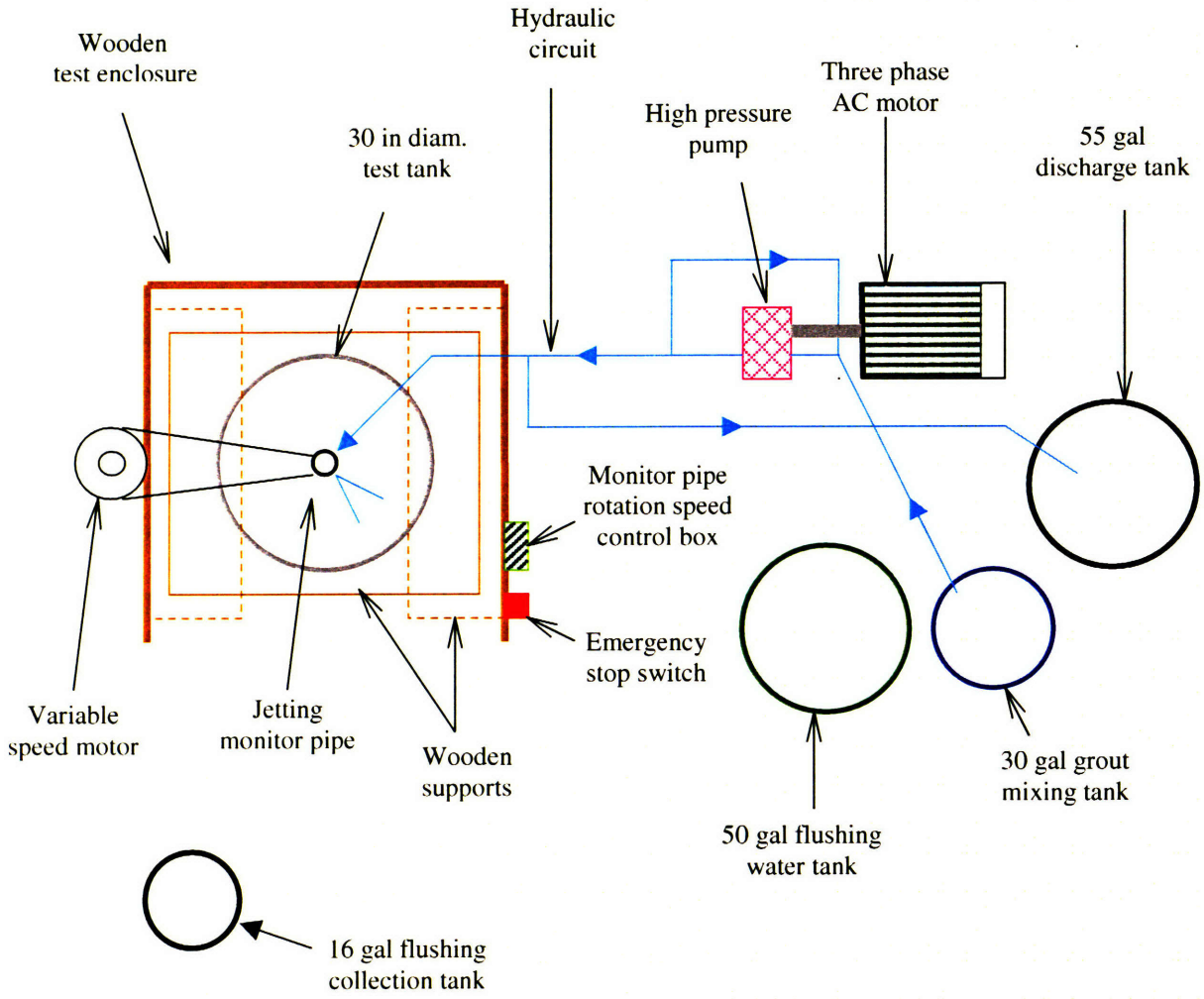

Figure 4-1. Plan layout for laboratory jetting experiments

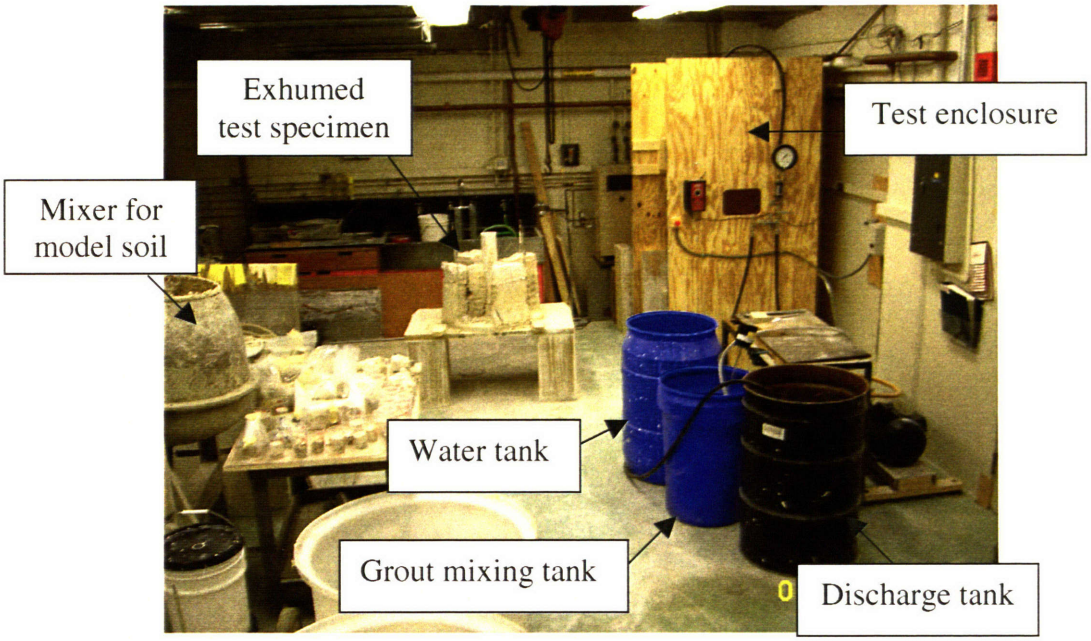

Figure 4-2. View of laboratory test set up

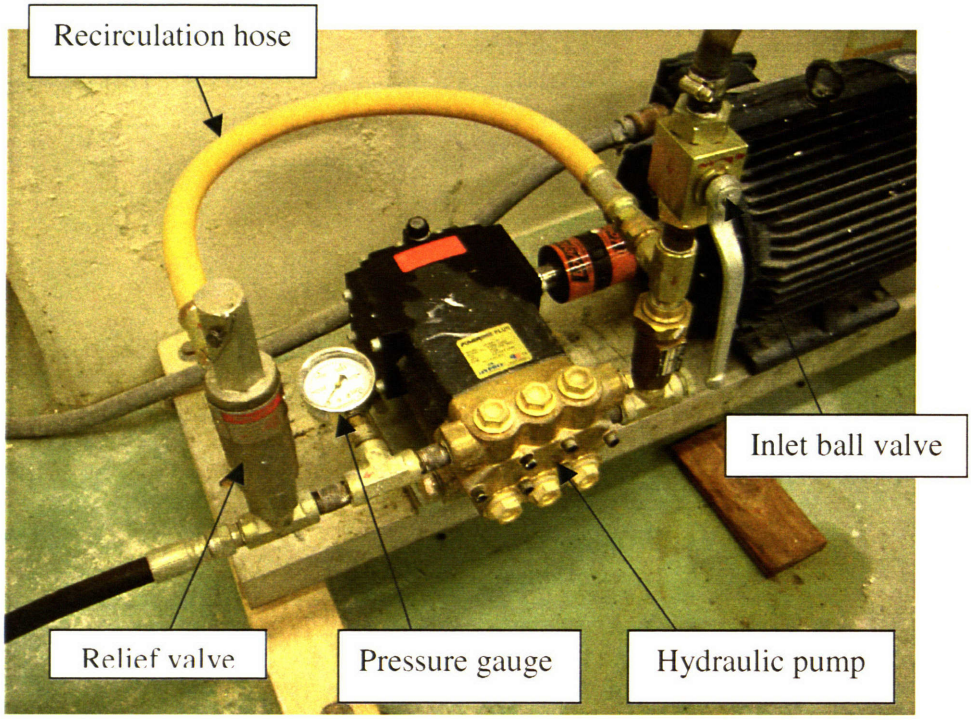

Figure 4-3. Electric triple-plunger hydraulic pump and accessories

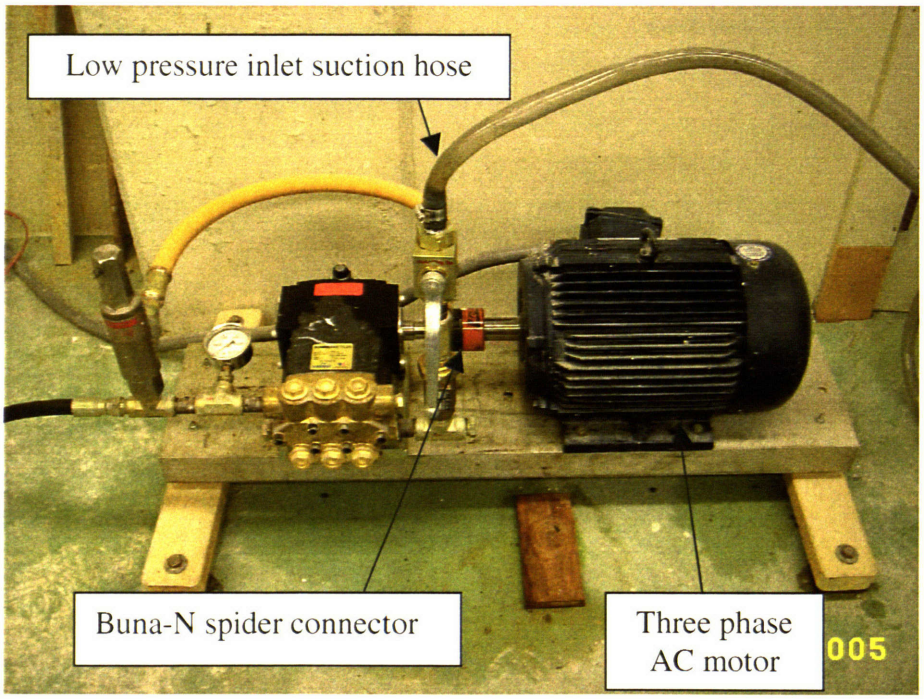

Figure 4-4. Three phase AC motor for driving pump

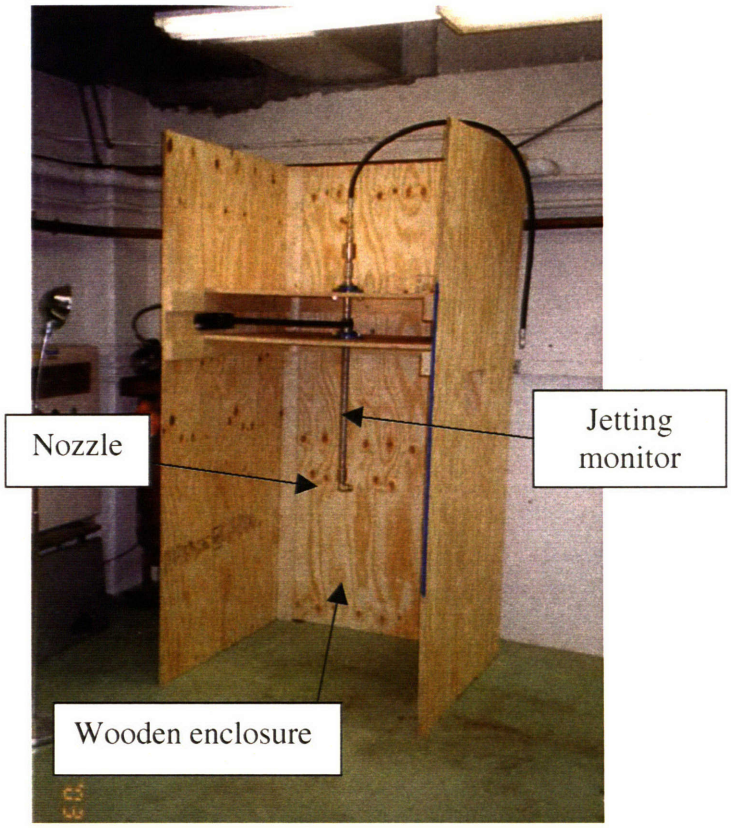

Figure 4-5. Test enclosure containing jetting equipment

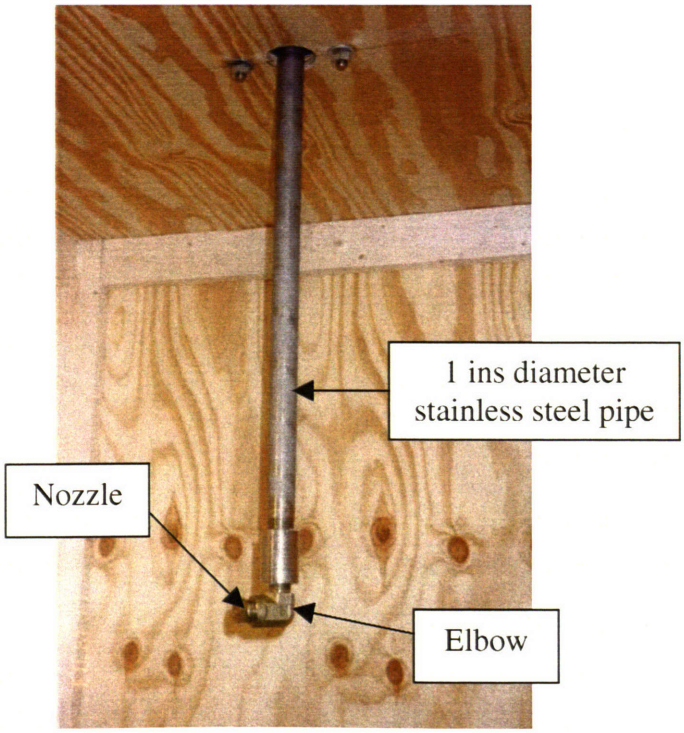

Figure 4-6. Monitor pipe with elbow for attachment of nozzle

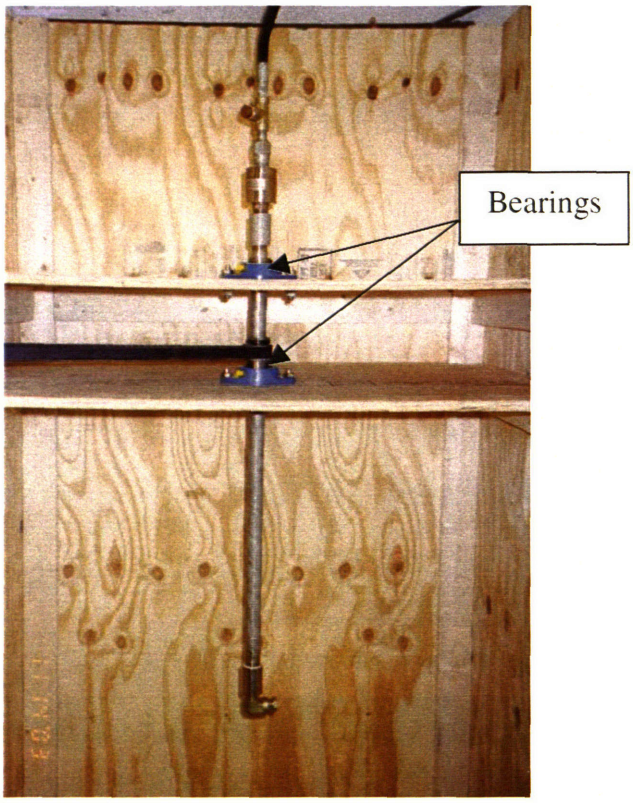

Figure 4-7. Securing of monitor pipe to test platform using flange-mounted bearings

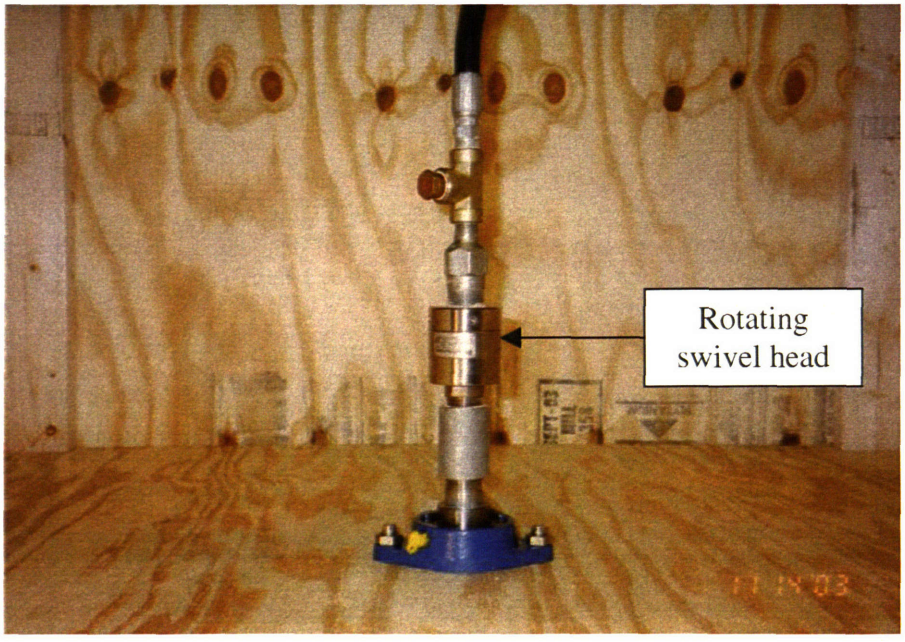

Figure 4-8. Swivel head

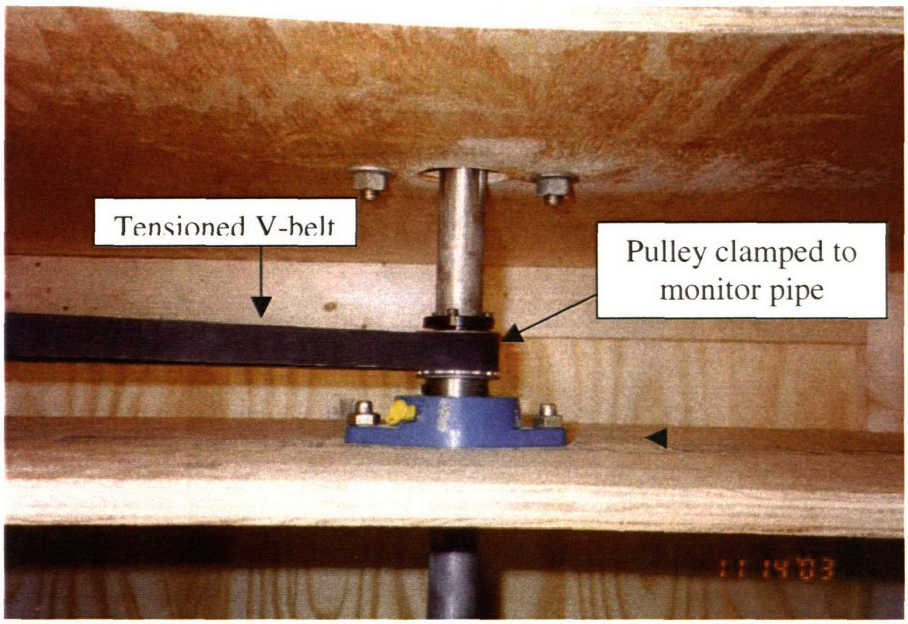

Figure 4-9. V-belt for rotary motion

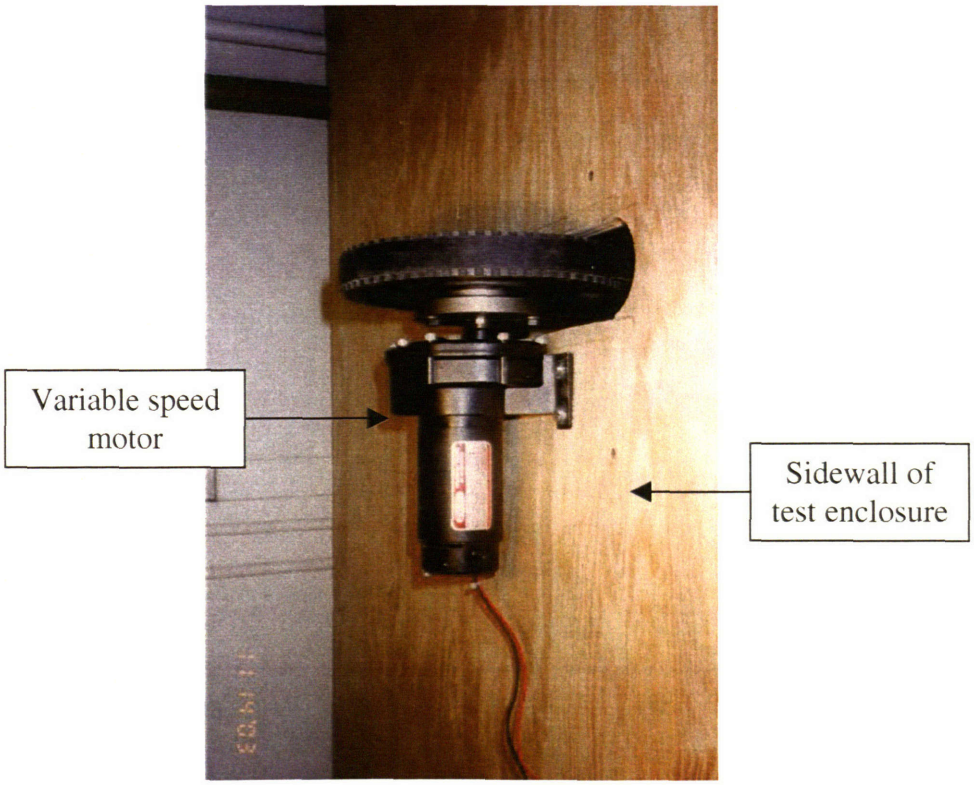

Figure 4-10. Variable speed DC motor for driving V-belt

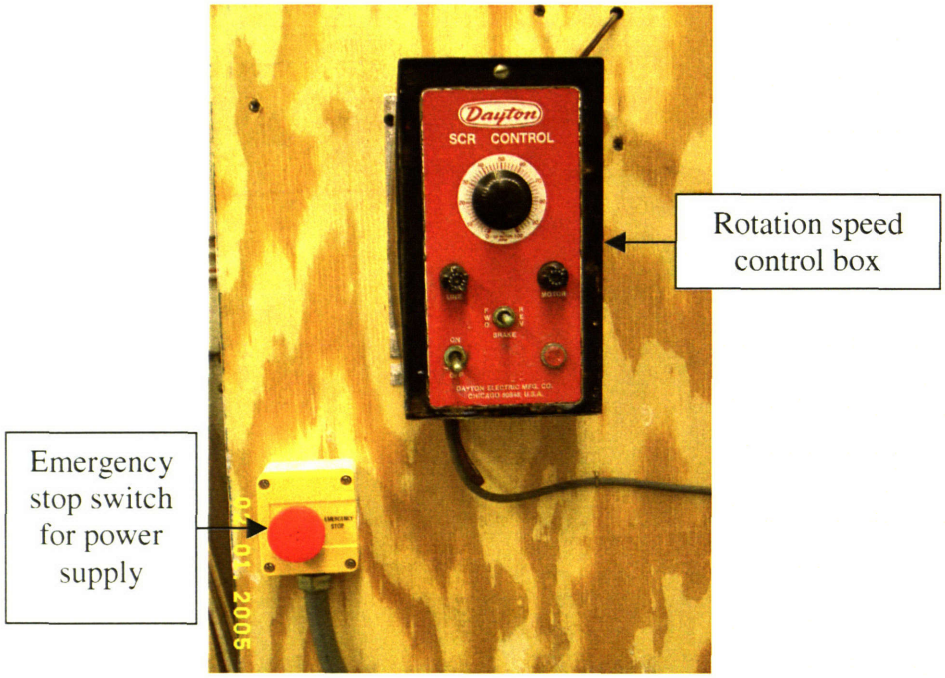

Figure 4-11. Speed control box for variable speed motor

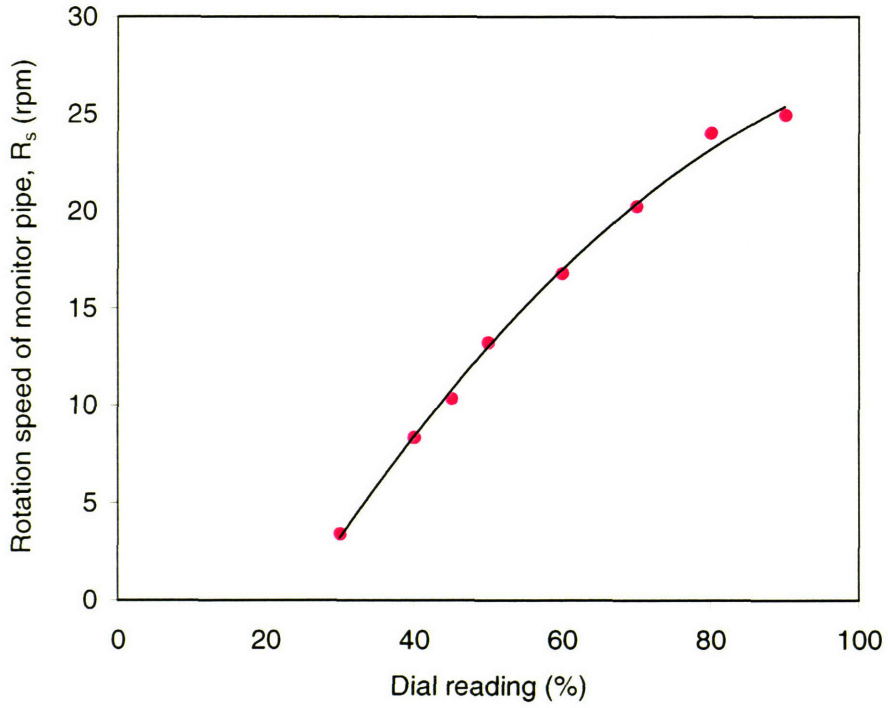

Figure 4-12. Calibration curve for variable speed motor switch system

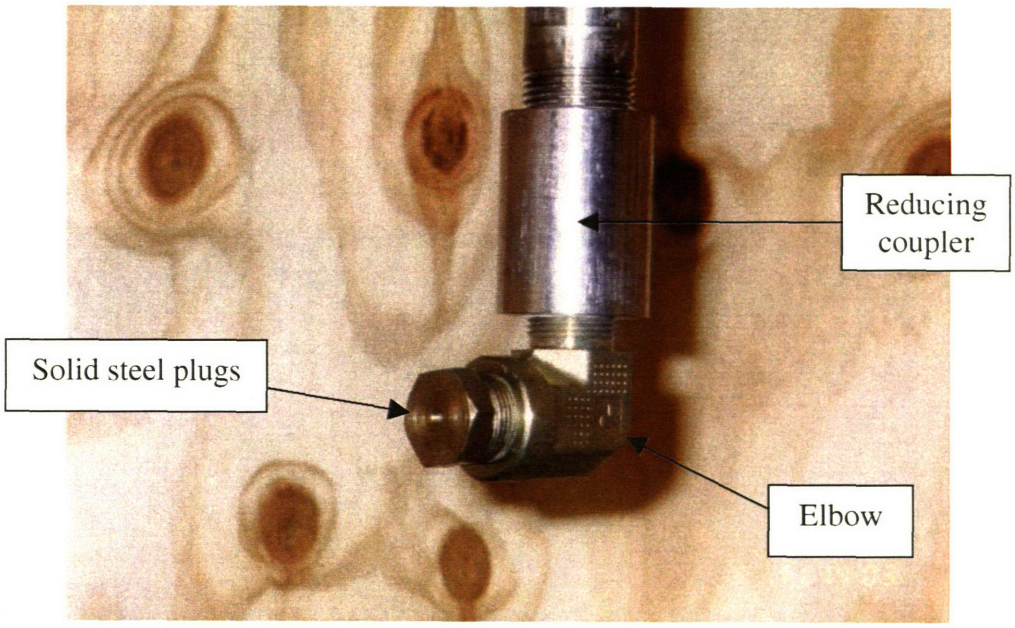

Figure 4-13. High pressure stainless steel hexagonal solid plugs forming nozzle

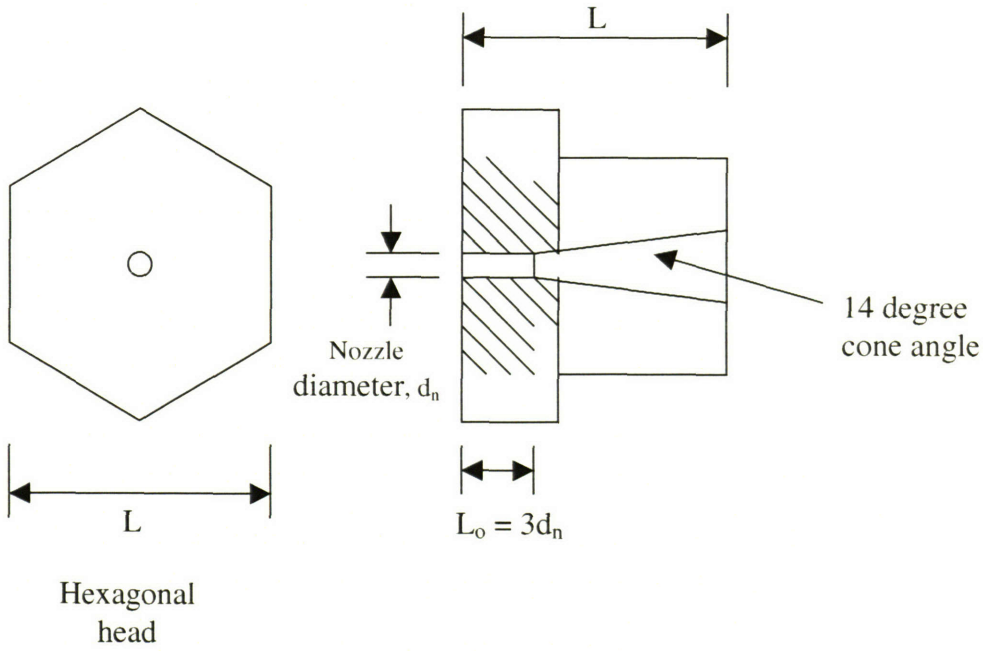

Figure 4-14. Nozzle dimensions

Figure 4-15. View of inlet of nozzle

Figure 4-16. View of exit of nozzle

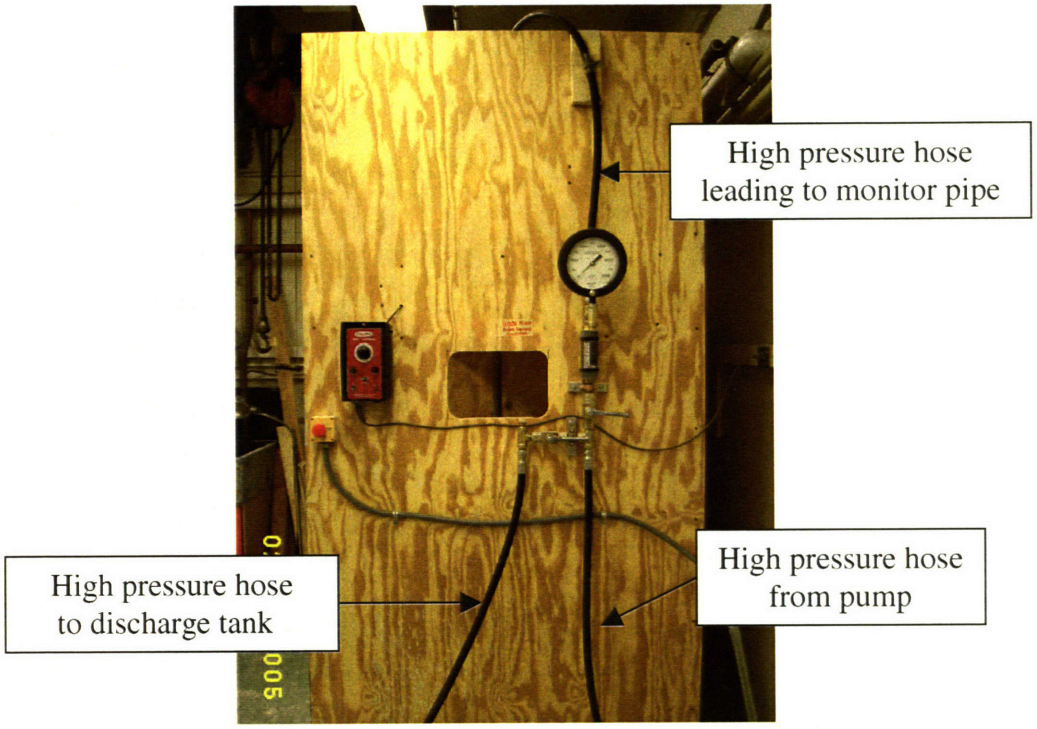

Figure 4-17. High pressure hydraulic lines for pressurized flow

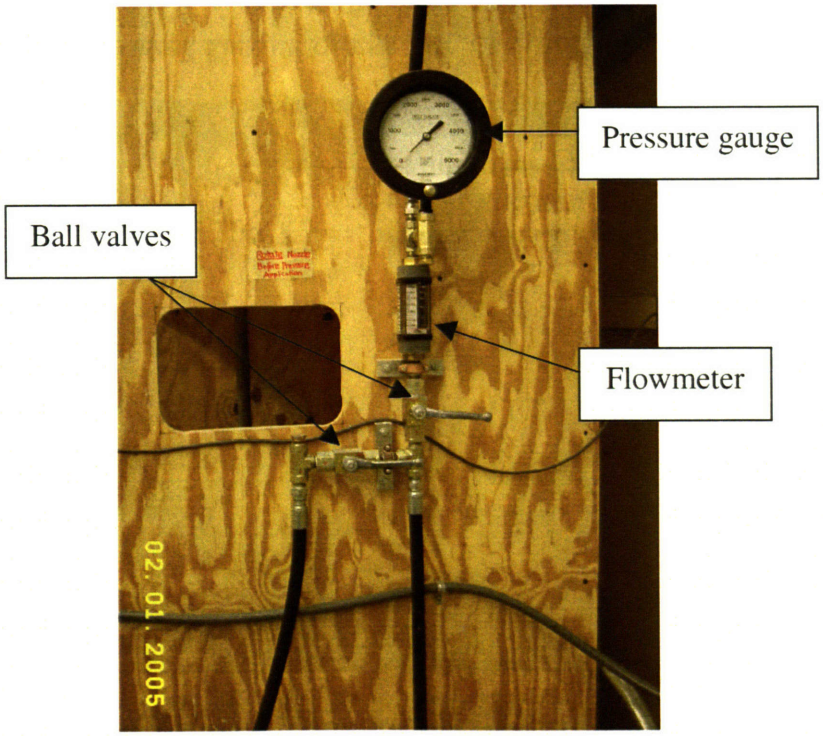

Figure 4-18. Pressure gauge and flowmeter arrangement

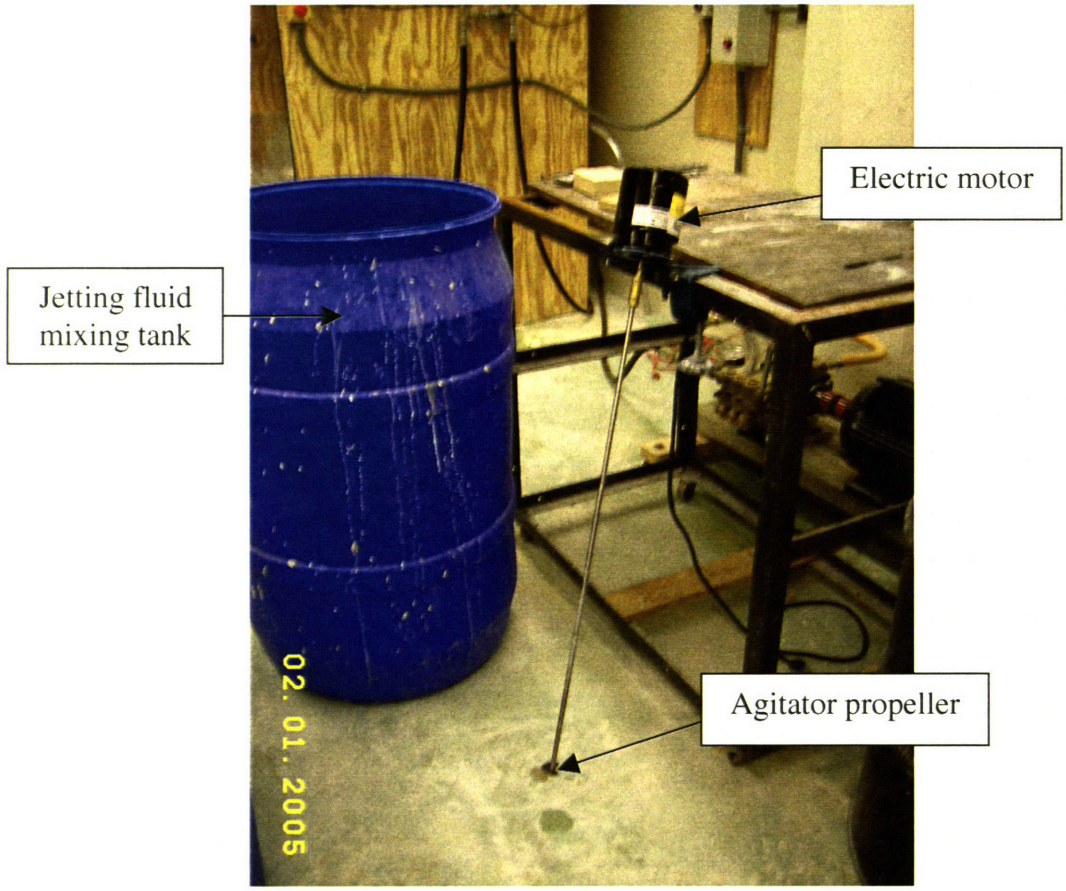

Figure 4-19. Agitator for mixing grout

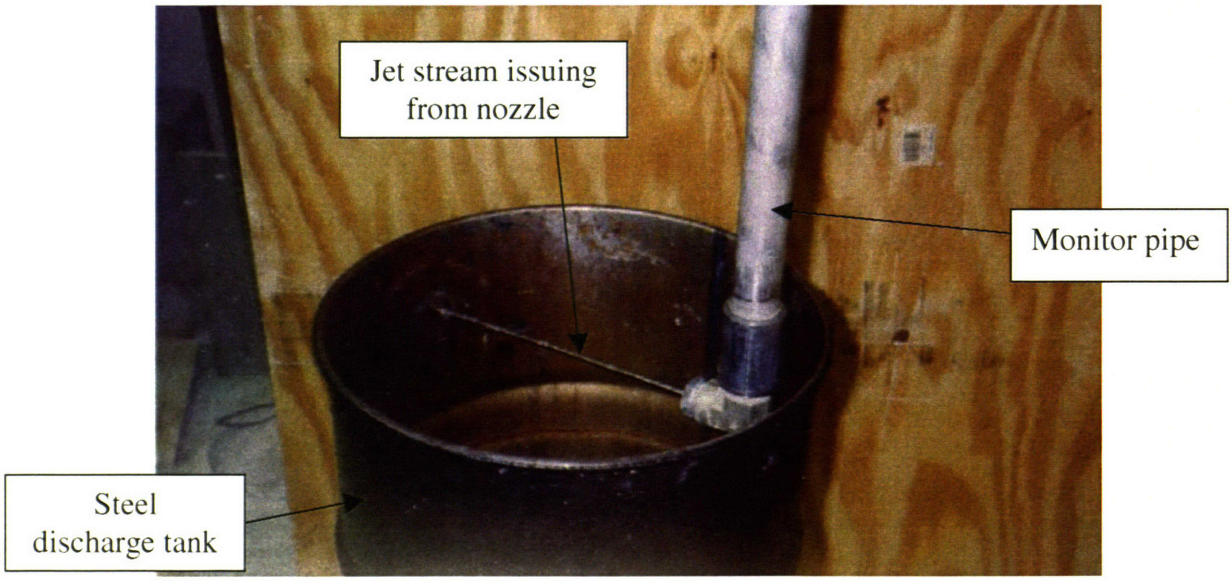

Figure 4-20. Illustration of jet impacting a steel surface at a pressure of 100 psi

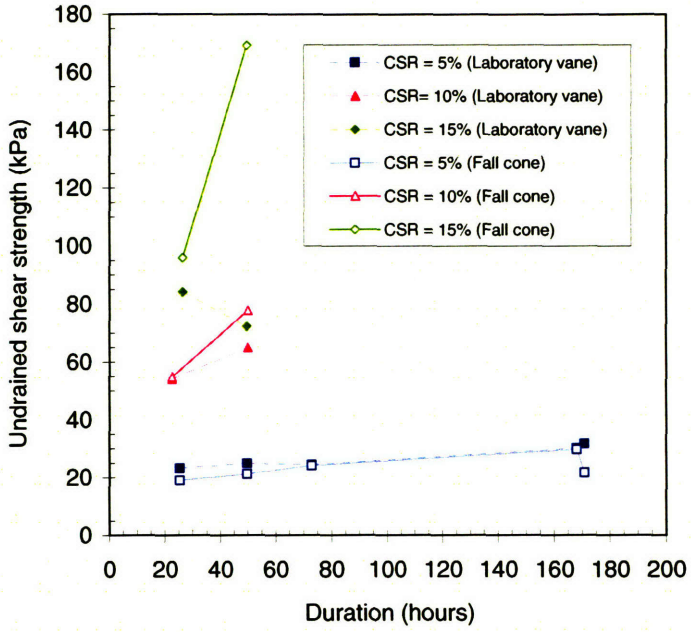

Figure 4-21. Variation of undrained shear strength with curing time for trial mixes

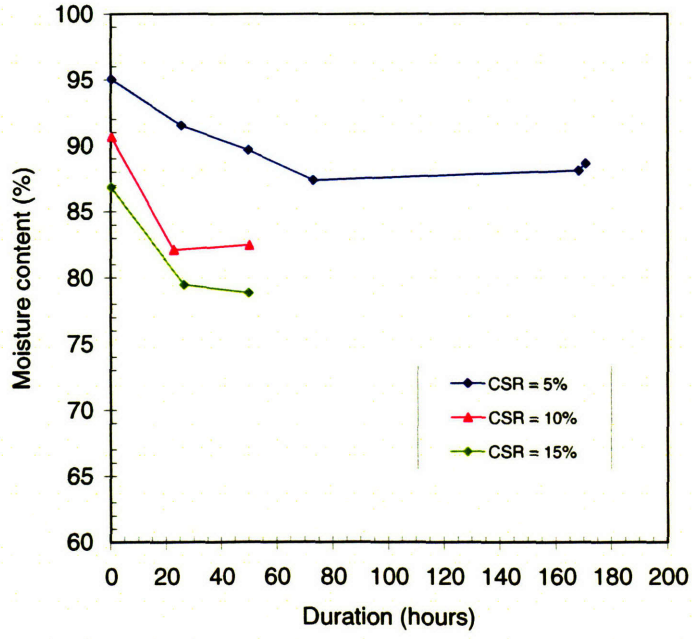

Figure 4-22. Variation of moisture content with curing time for trial mixes

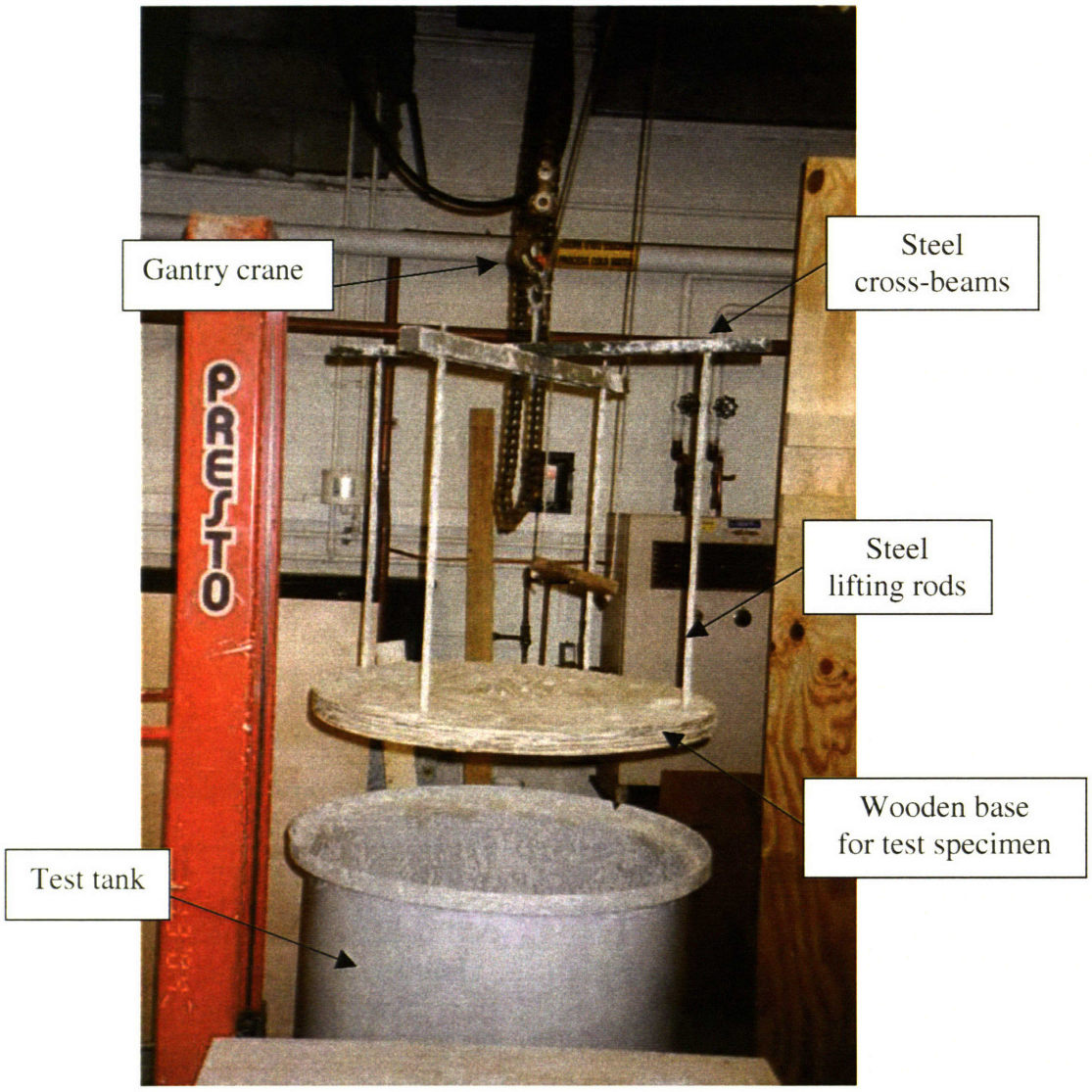

Figure 4-23. Wooden lifting platform for removal of specimen from test tank

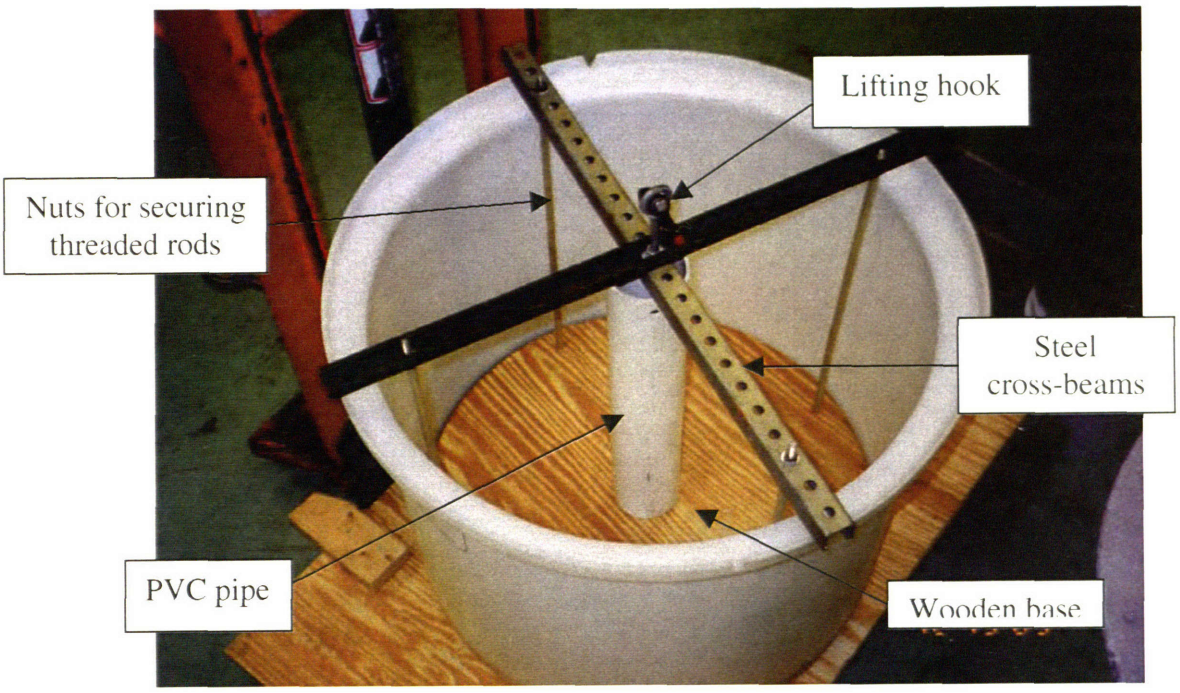

Figure 4-24. Placement of lifting platform in test tank

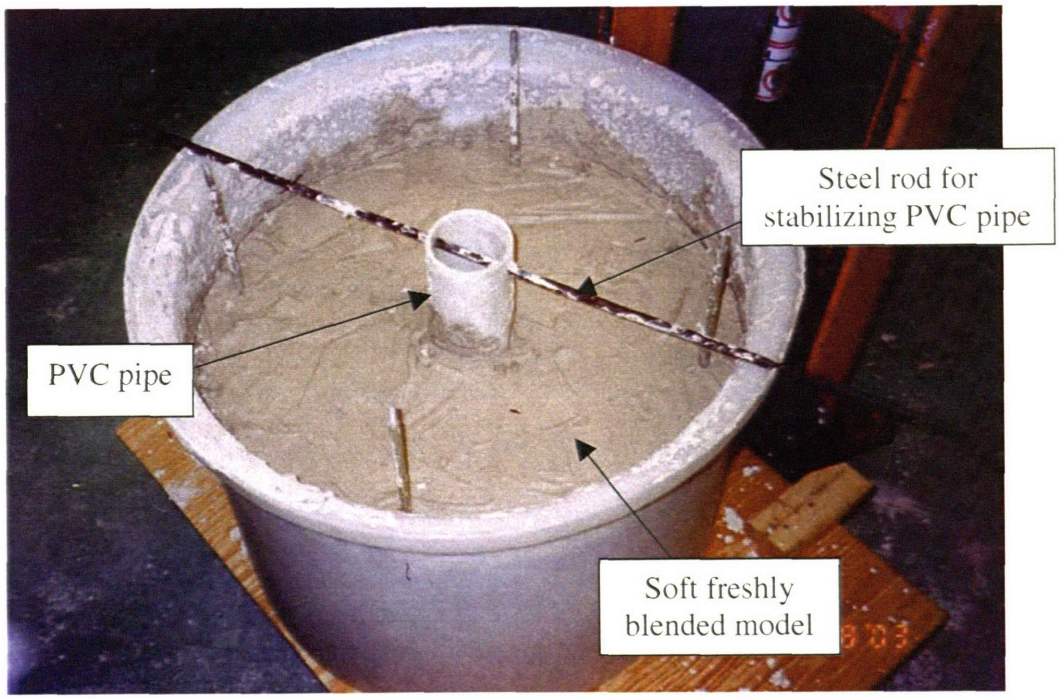

Figure 4-25. Filling test tank with blended soil paste

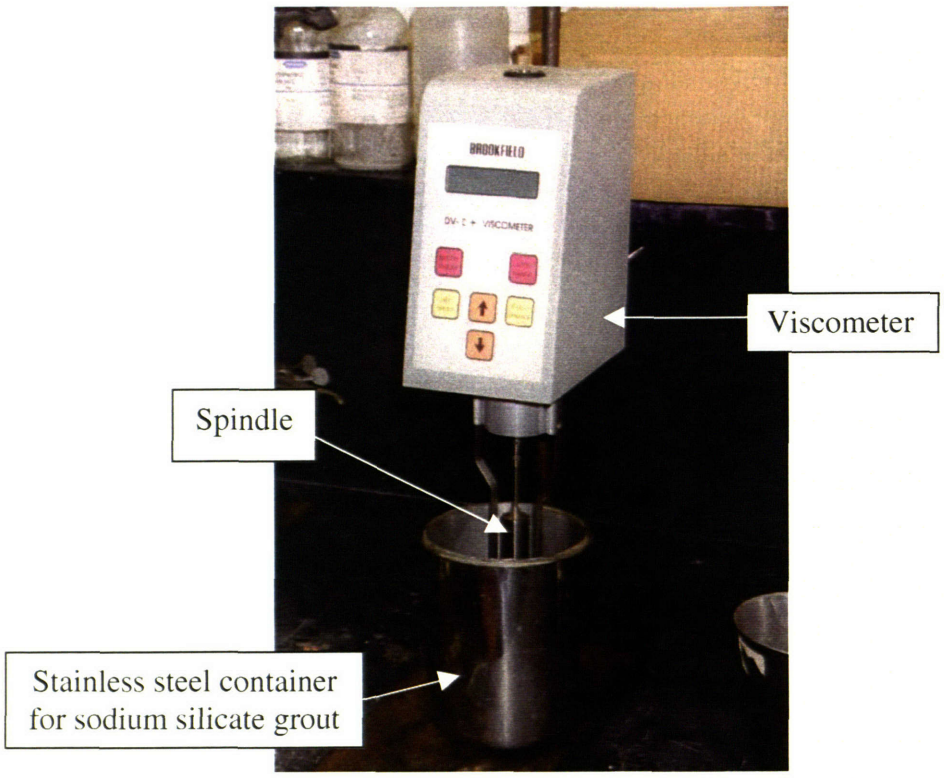

Figure 4-26. Brookfield LVDV-I+ Viscometer

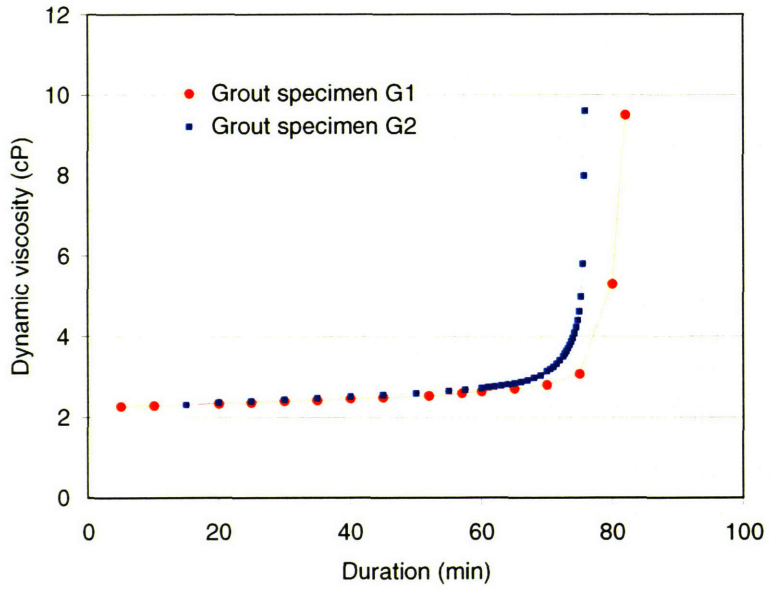

Figure 4-27. Viscosity-time relationship for sodium silicate grout

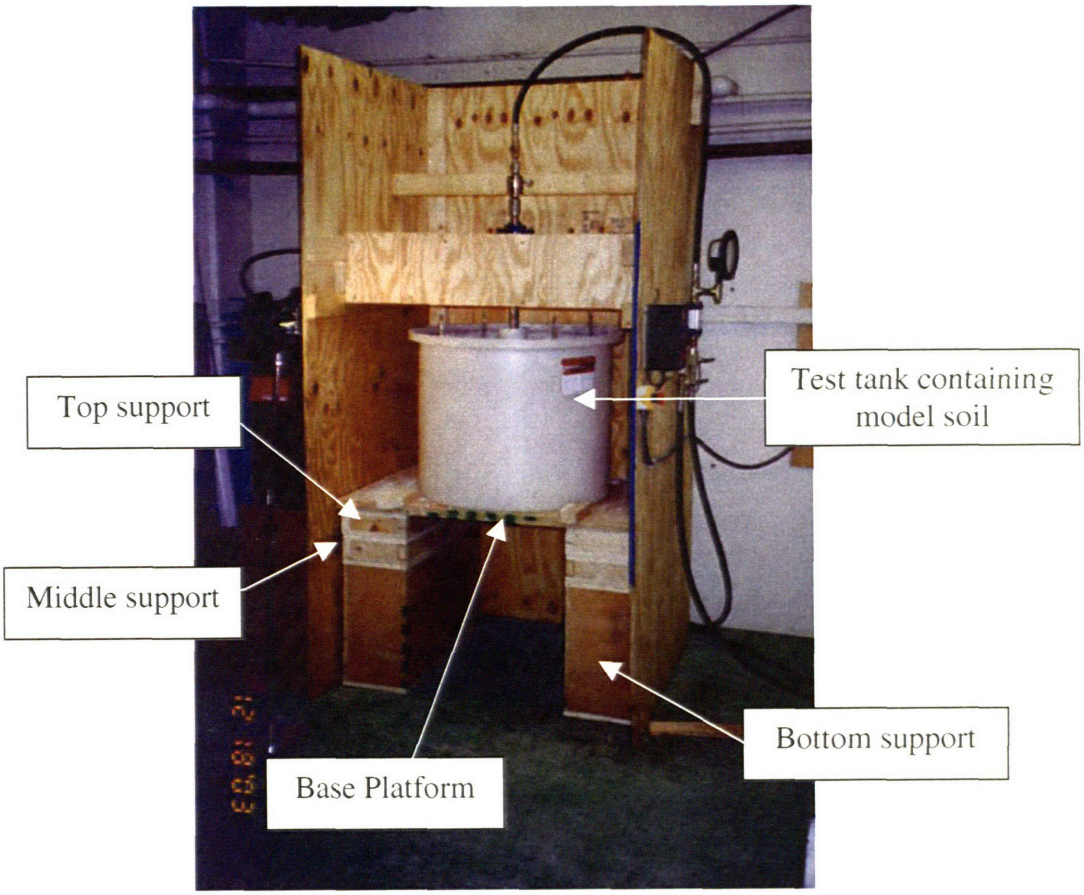

Figure 4-28. Test in progress

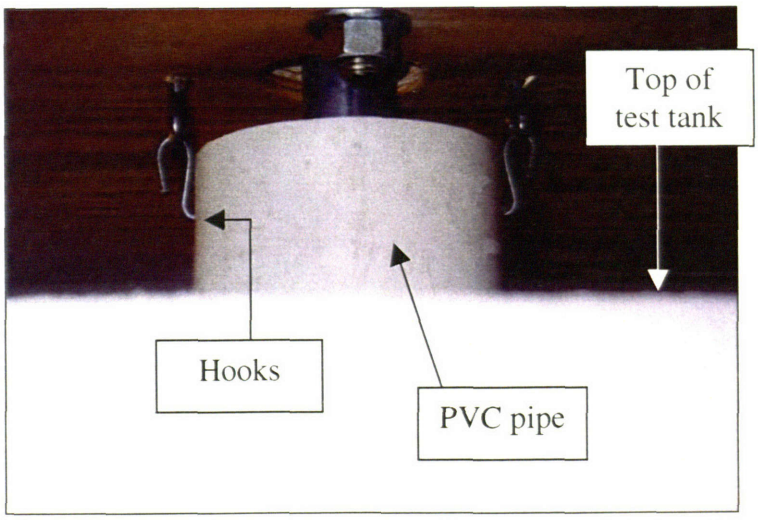

Figure 4-29. Securing hooks to maintain PVC pipe in position during jetting

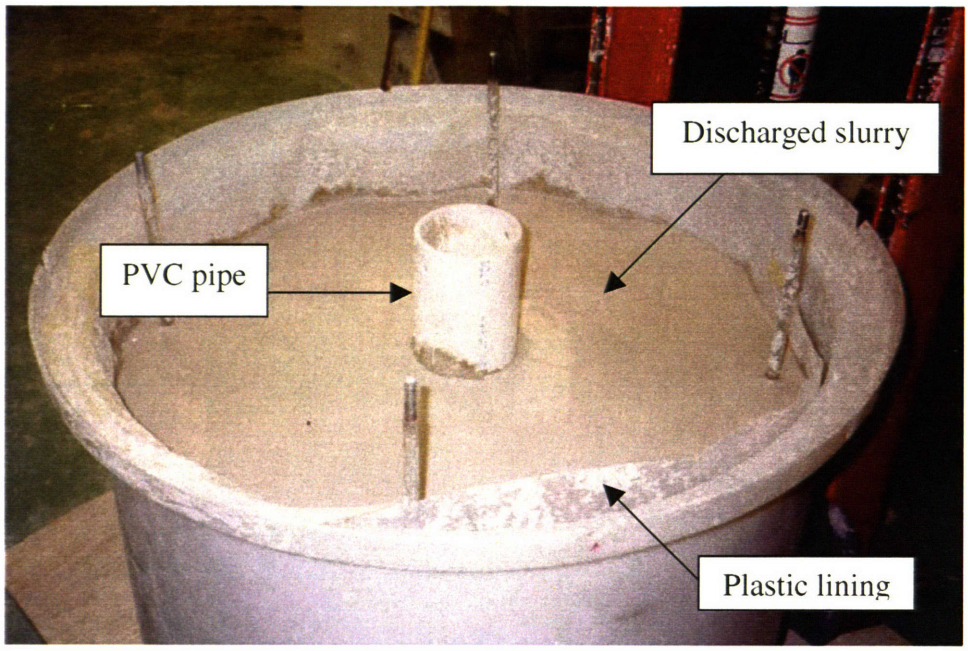

Figure 4-30. Discharged slurry fills upper surface of specimen after completion of jetting

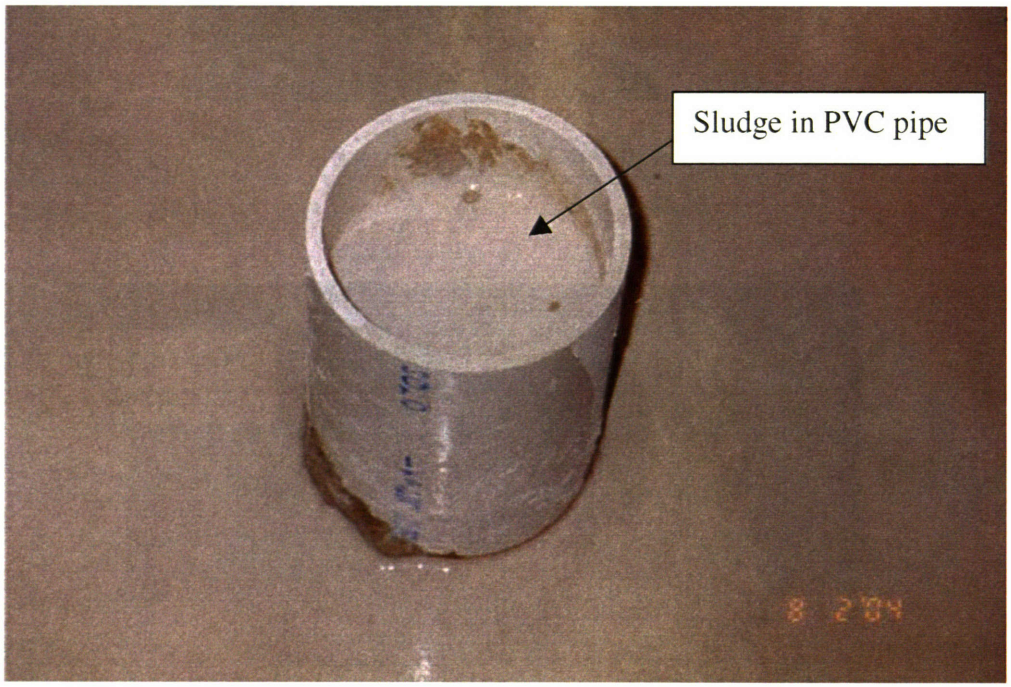

Figure 4-31. PVC pipe filled with discharged slurry

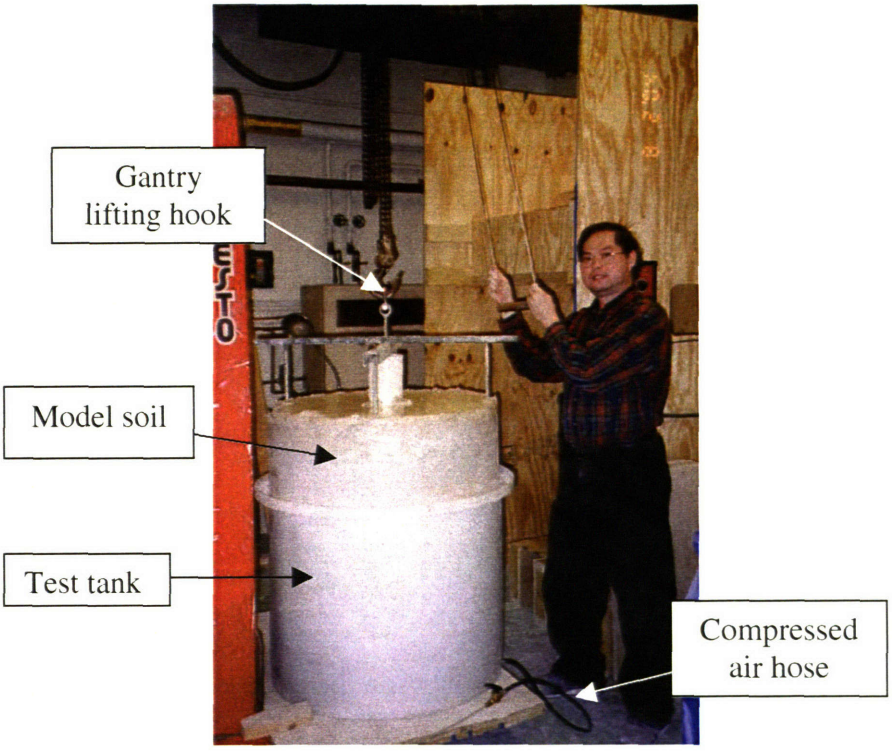

Figure 4-32. Lifting specimen from test tank, assisted by compressed air

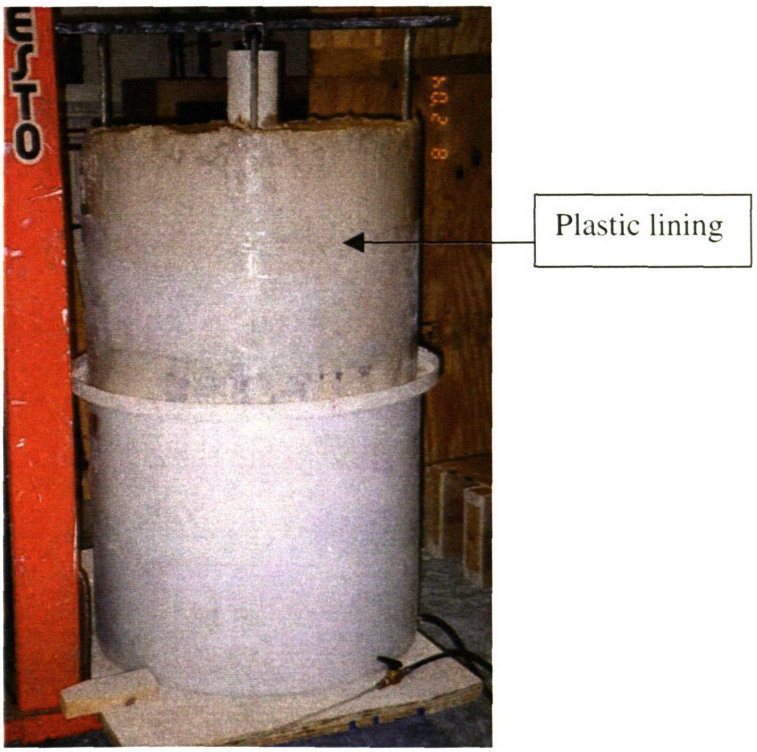

Figure 4-33. Specimen fully removed

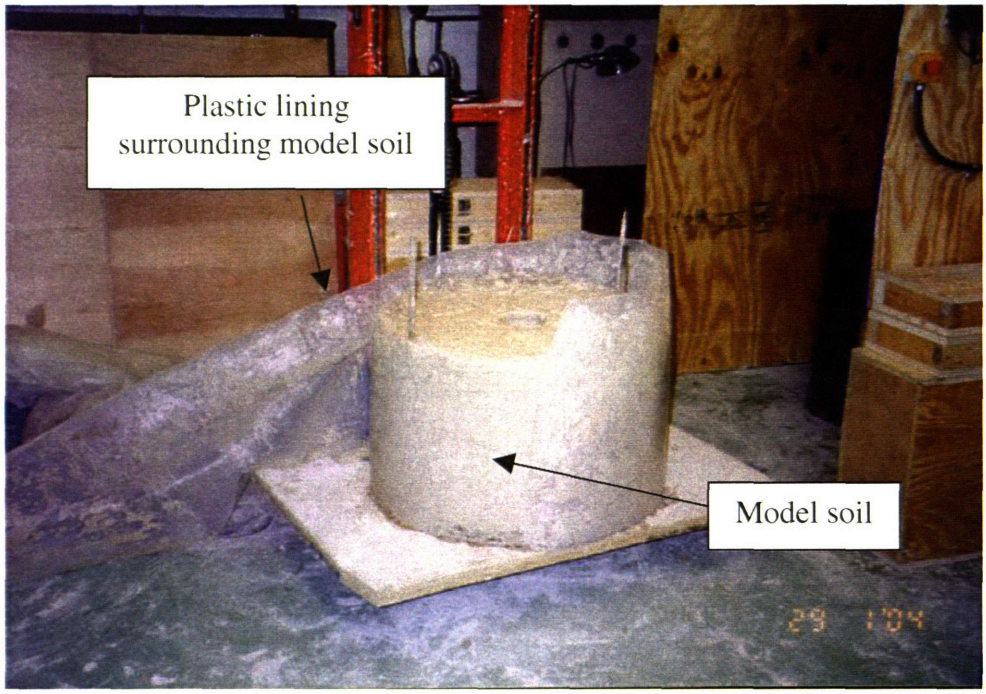

Figure 4-34. Unwrapping of plastic lining around test specimen

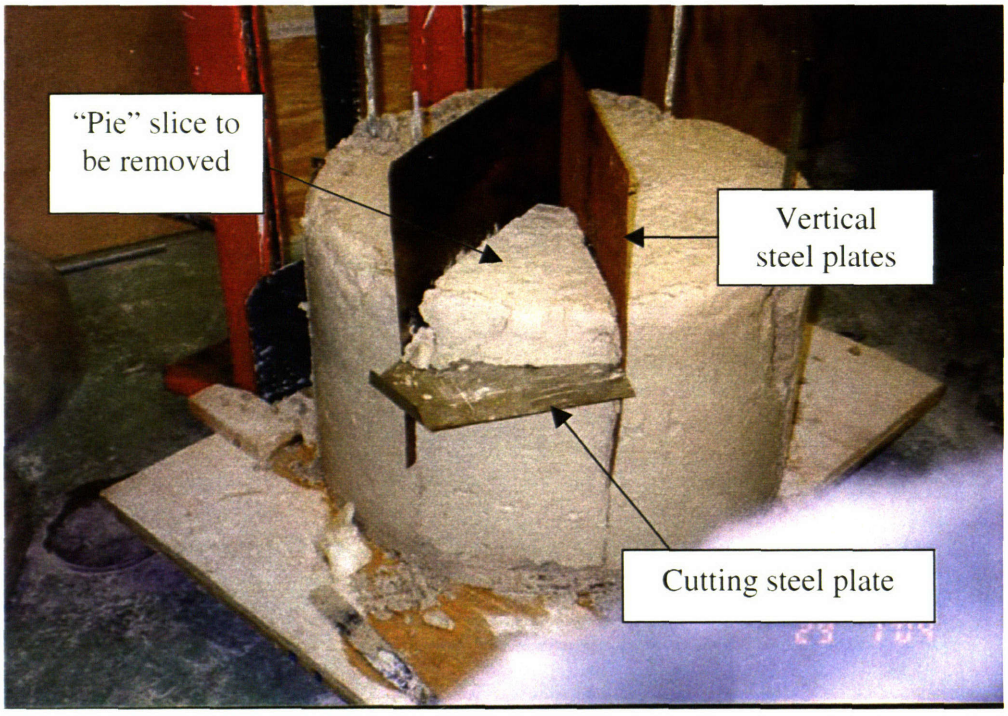

Figure 4-35. First stage of excavation of soil segment

Figure 4-36. Second stage of excavation of soil segment

Figure 4-37. Third stage of excavation of soil segment

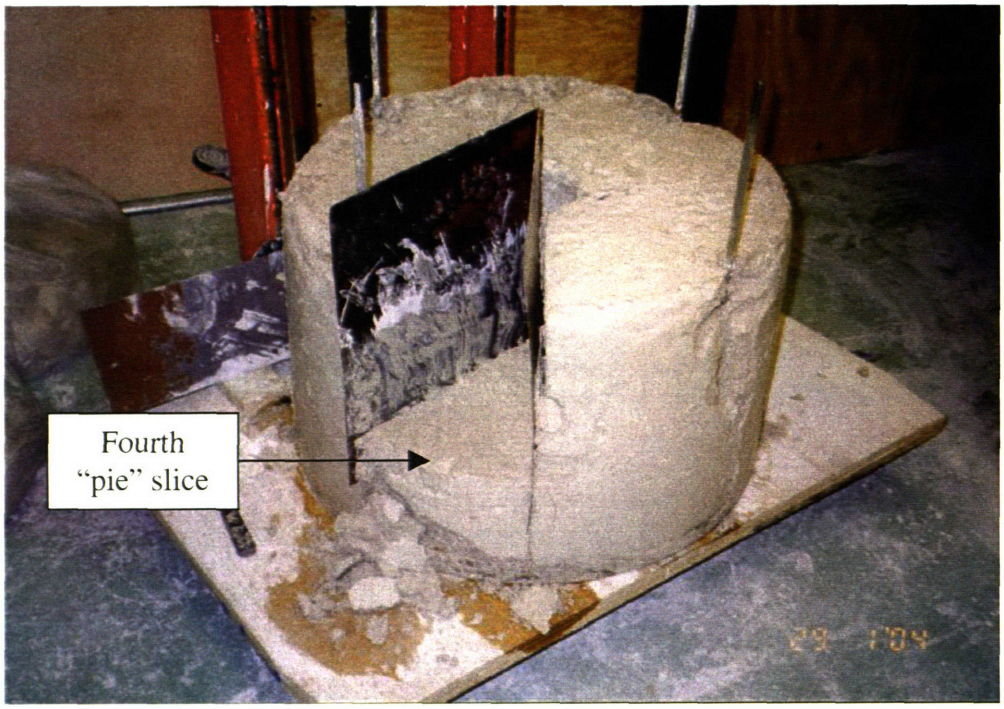

Figure 4-38. Final stage of excavation of soil segment

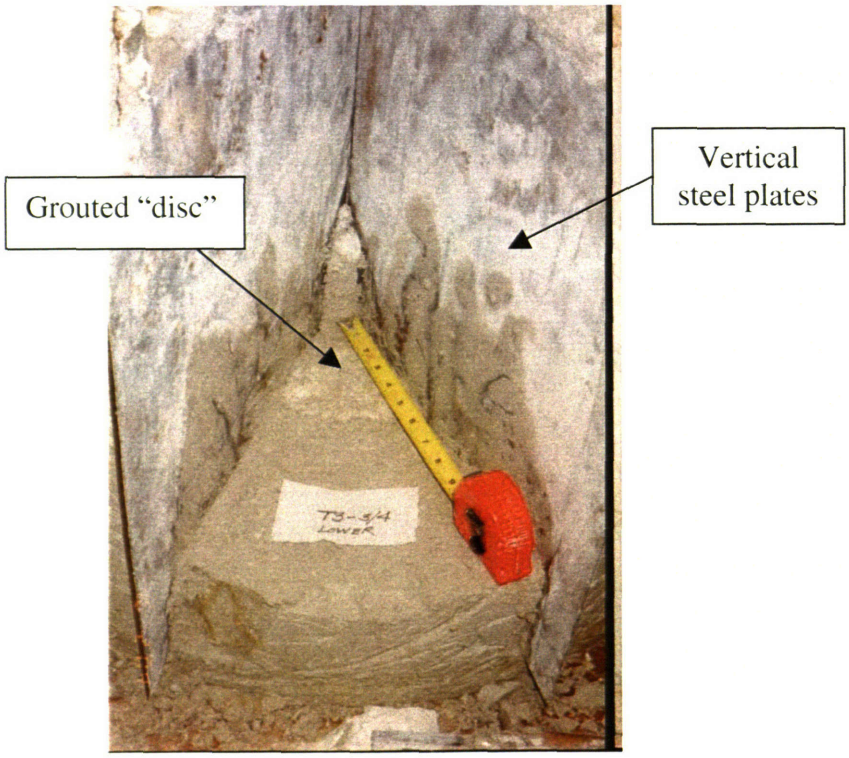

Figure 4-39. Measuring cutting distance in horizontal surface

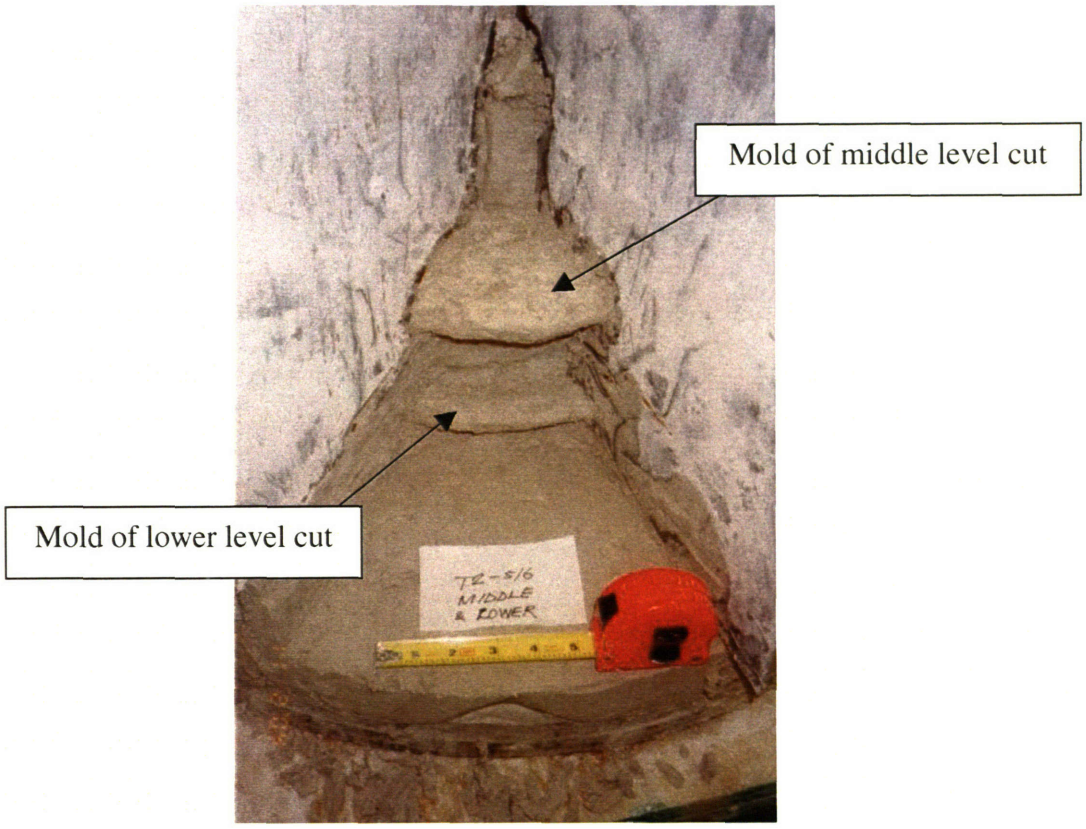

Figure 4-40. Exhumation of model soil to expose grouted molds of jet excavated cavity

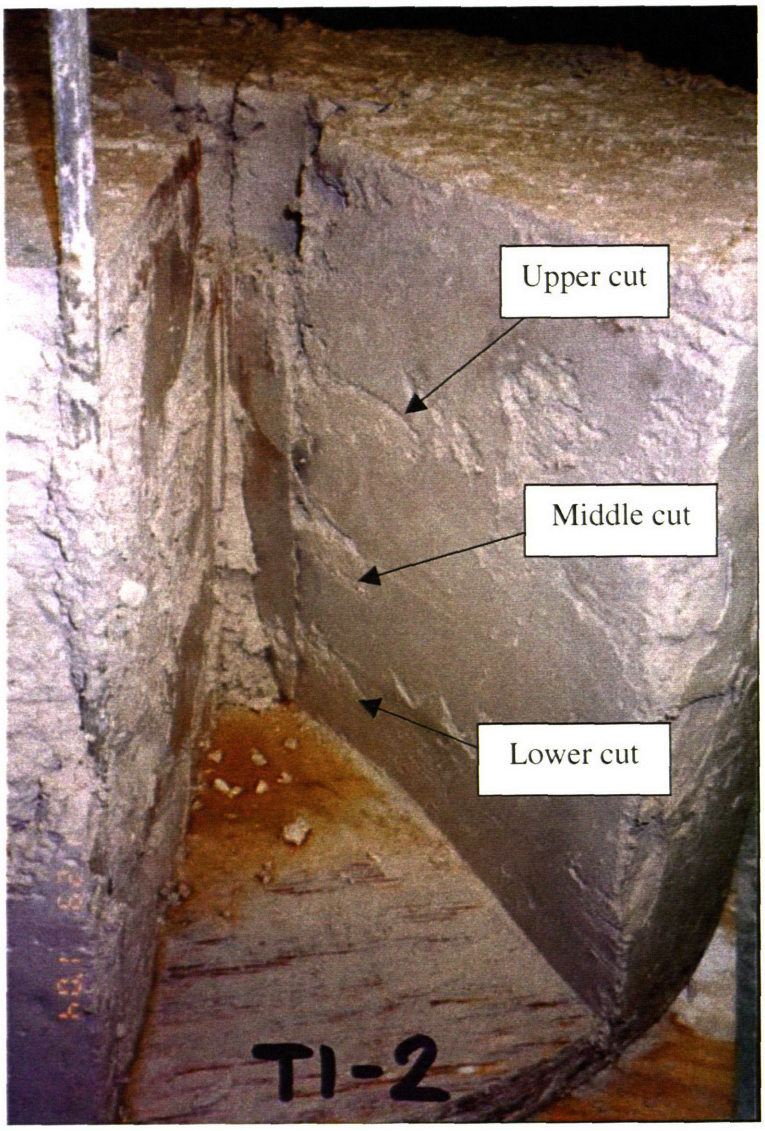

Figure 4-41. Cuts exposed in vertical soil face

Figure 4-42. Placing thin walled sampler on horizontal soil surface

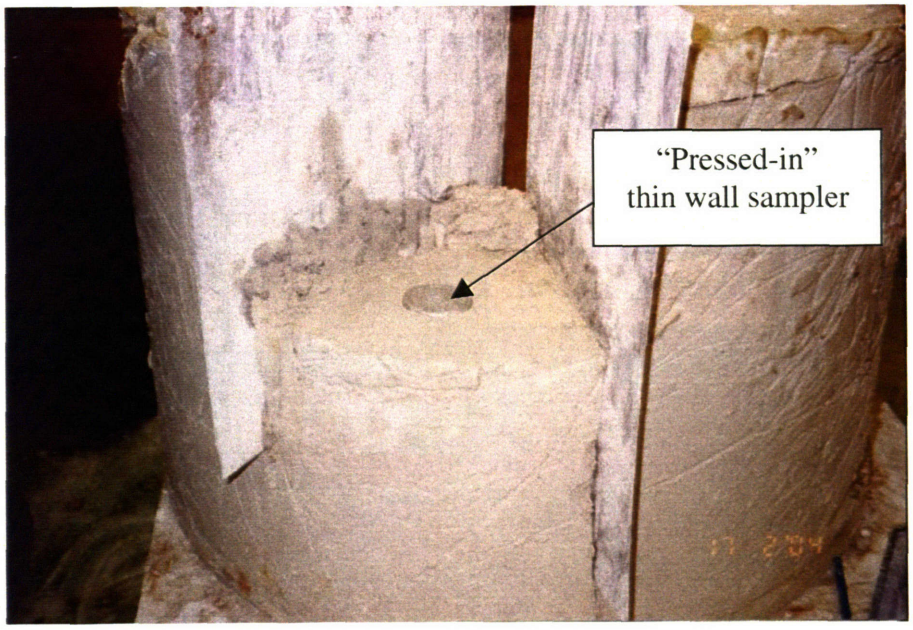

Figure 4-43. Pressing sampler into soil surface

Figure 4-44. Excavating around sampler

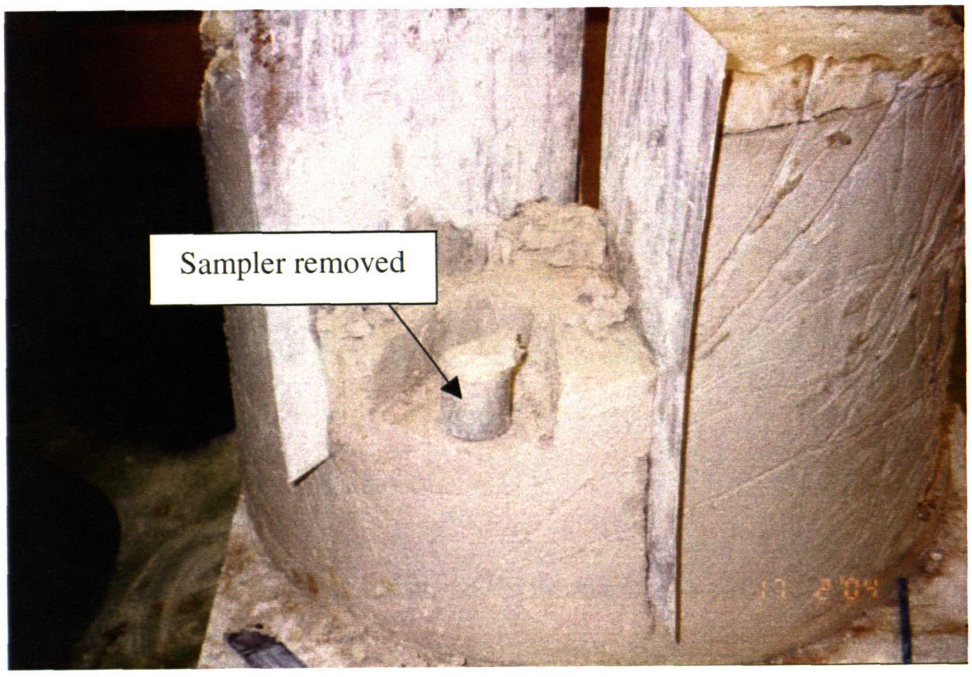

Figure 4-45. Trimming of sampler

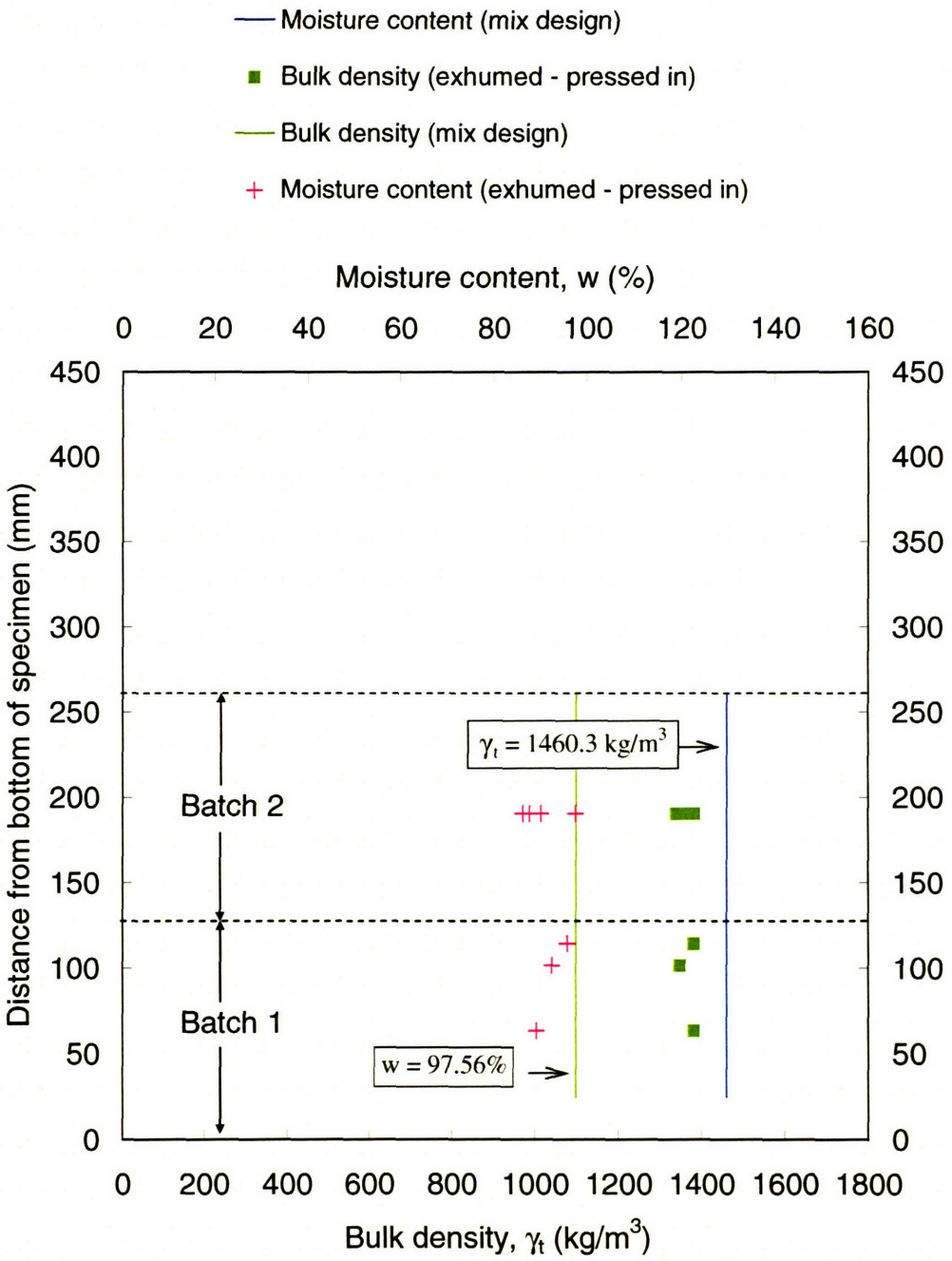

Figure 4-46. Variation of bulk density and moisture content with specimen depth (Specimen T7, CSR = 2.5%)

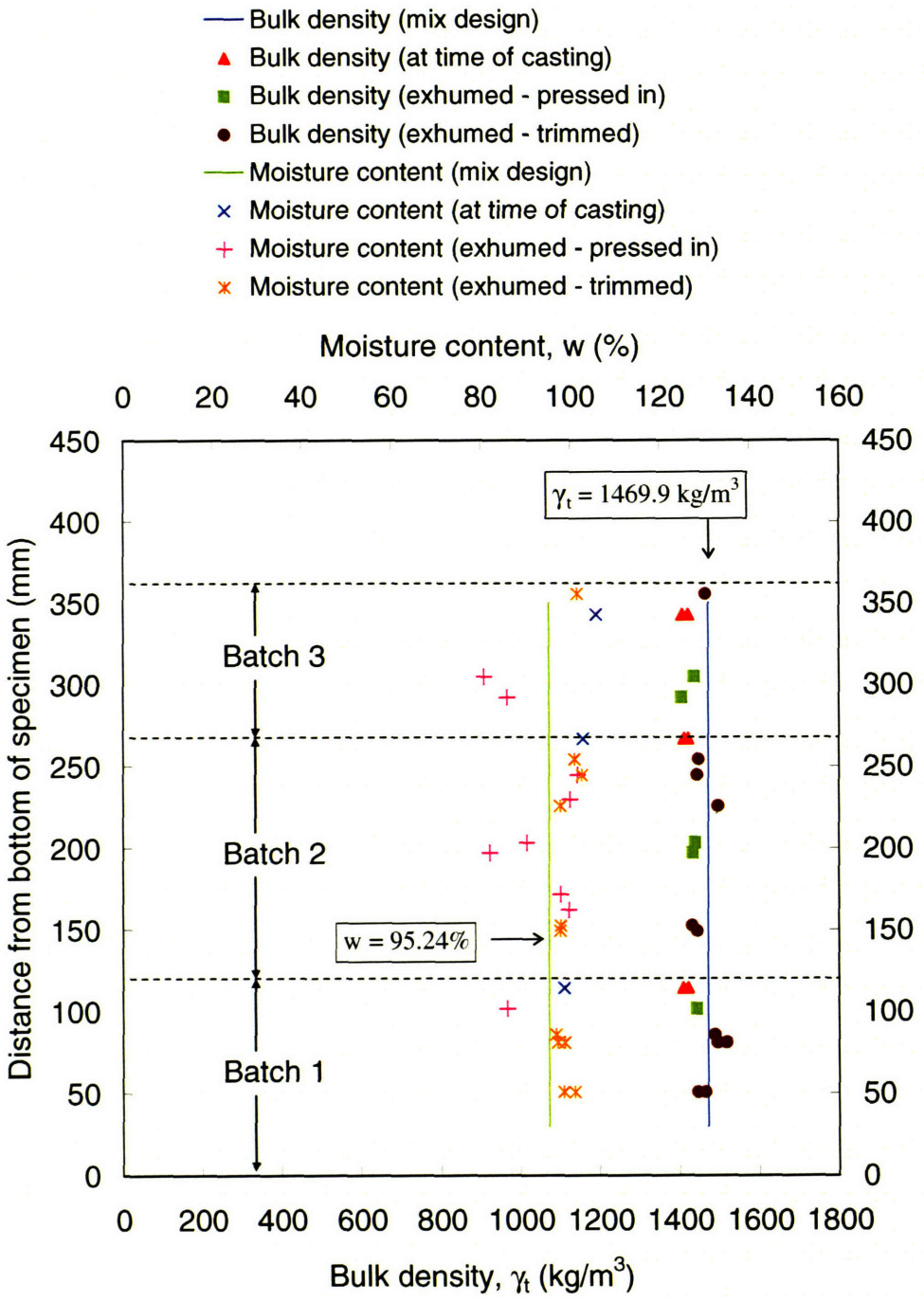

Figure 4-47. Variation of bulk density and moisture content with specimen depth (Specimen T9, CSR = 5%)

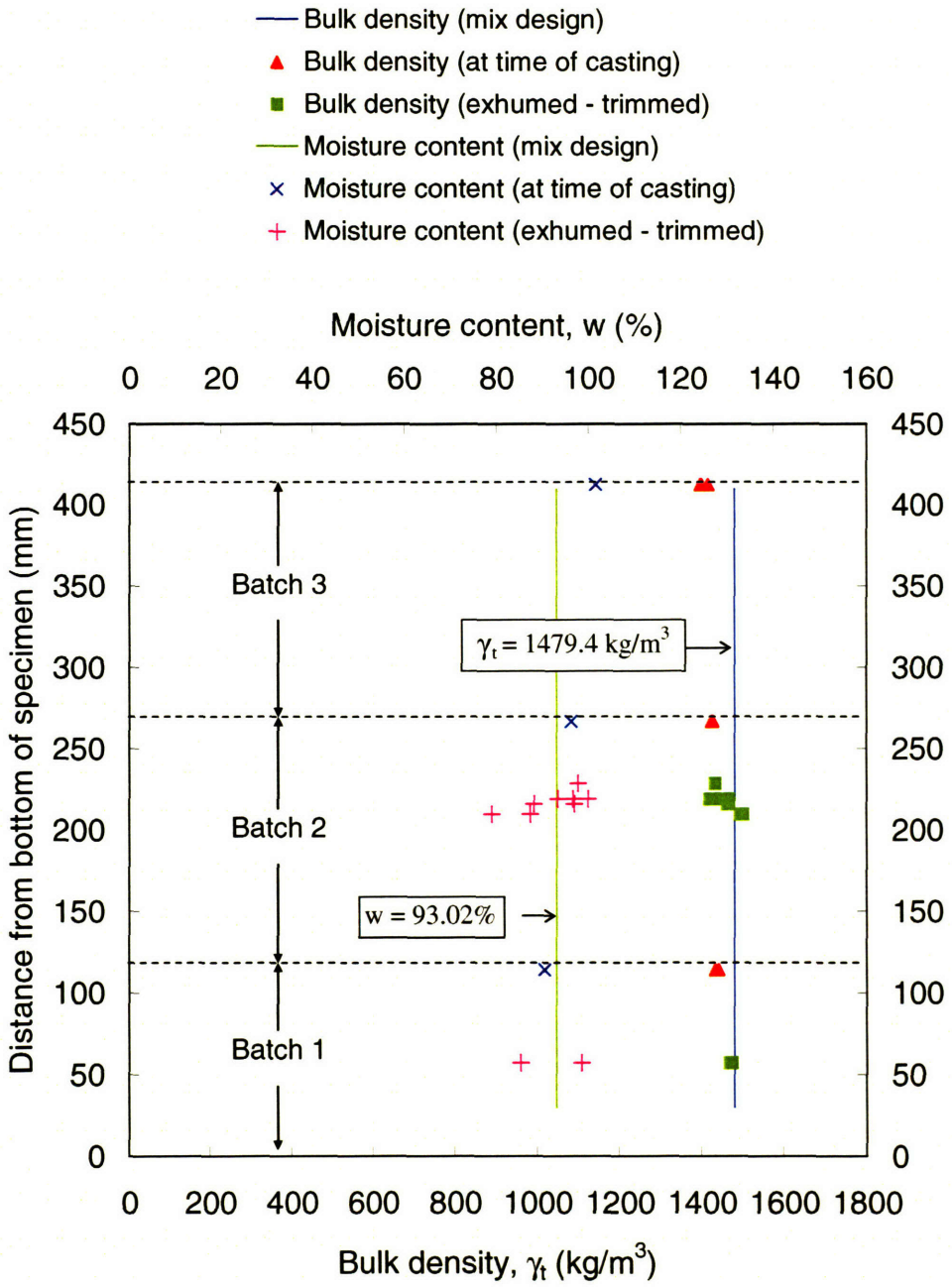

Figure 4-48. Variation of bulk density and moisture content with specimen depth (Specimen T8, CSR = 7.5%)

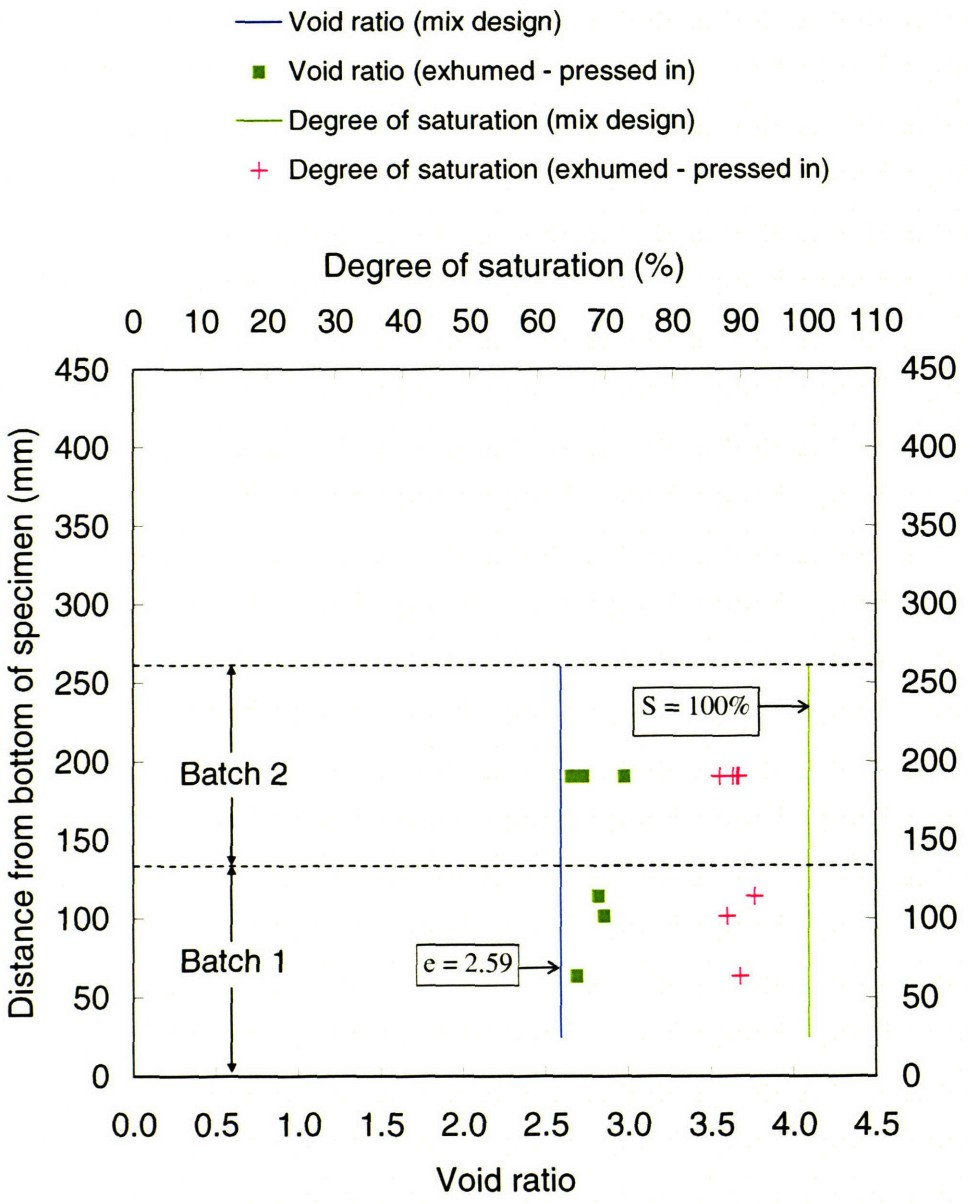

Figure 4-49. Variation of void ratio and degree of saturation with specimen depth (Specimen T7, CSR = 2.5%)

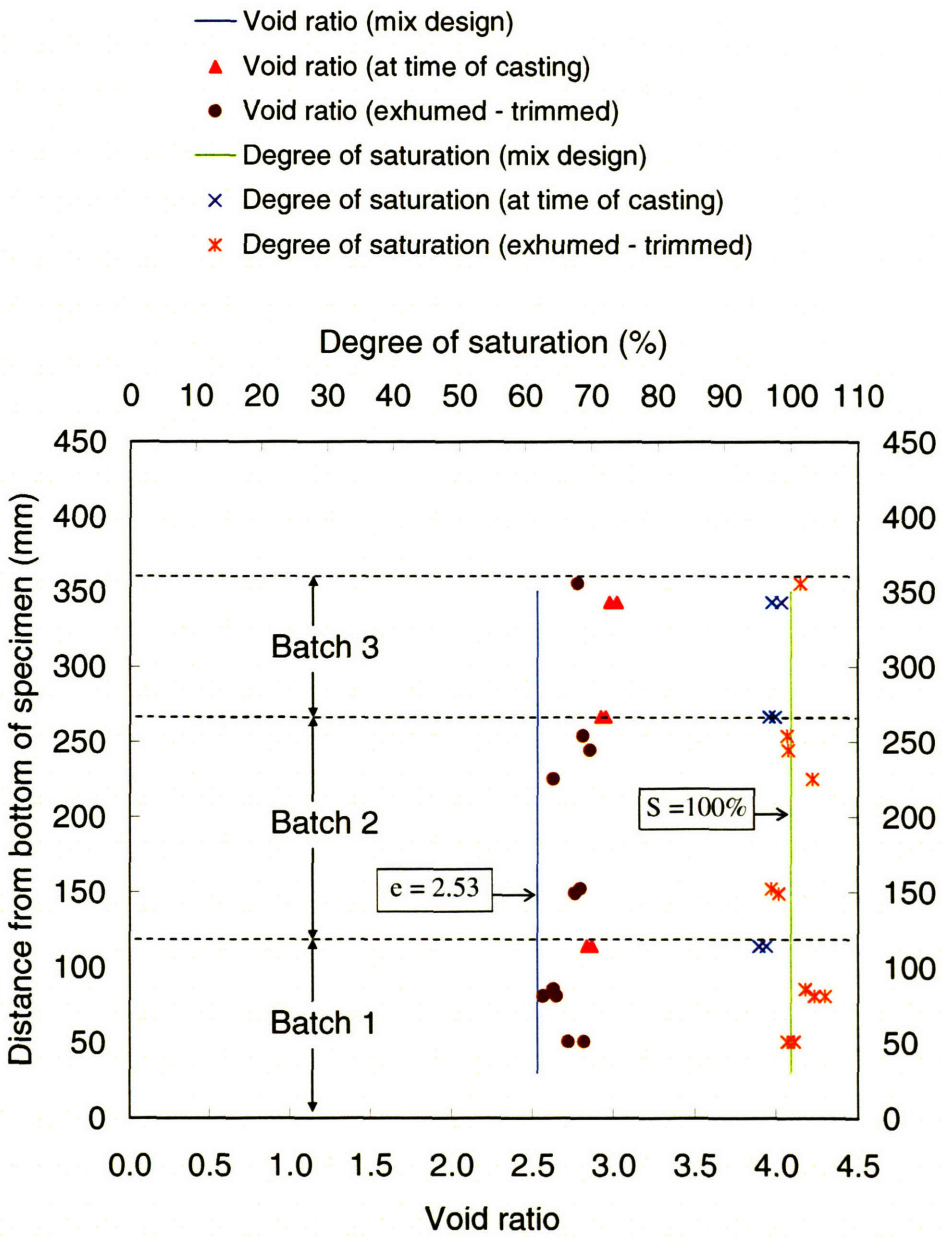

Figure 4-50. Variation of void ratio and degree of saturation with specimen depth (Specimen T9, CSR = 5%)

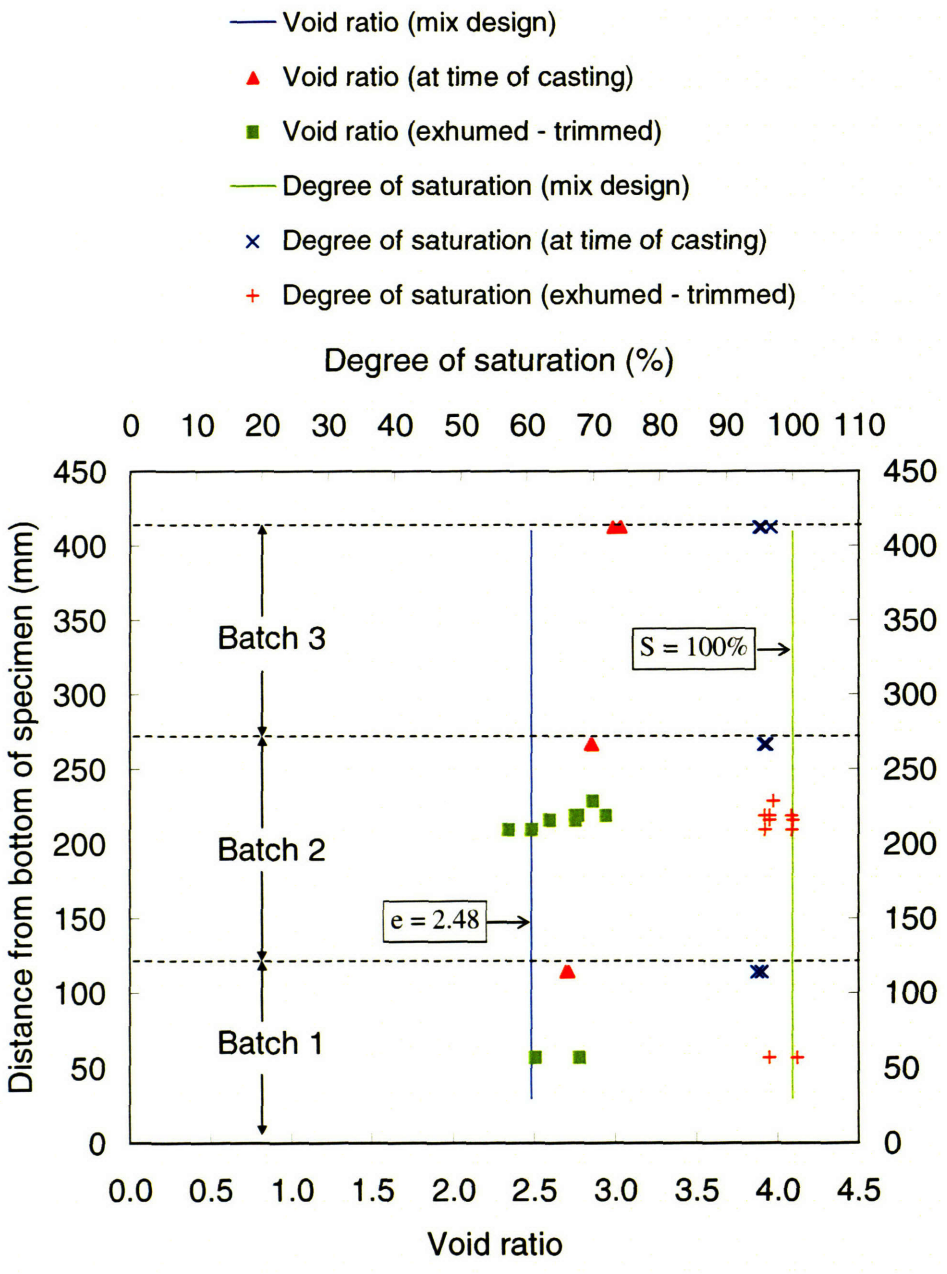

Figure 4-51. Variation of void ratio and degree of saturation with specimen depth (Specimen T8, CSR = 7.5%)

Specimen	Method	Bulk density (kg/m^3)	
		Mean	Std dev
◆ T7	Pressed-in	1366	18
■ T9	Casting	1414	7
▲ T9	Pressed-in	1429	15
○ T9	Trimming	1465	28
◆ T8	Casting	1419	16
● T8	Trimming	1474	70

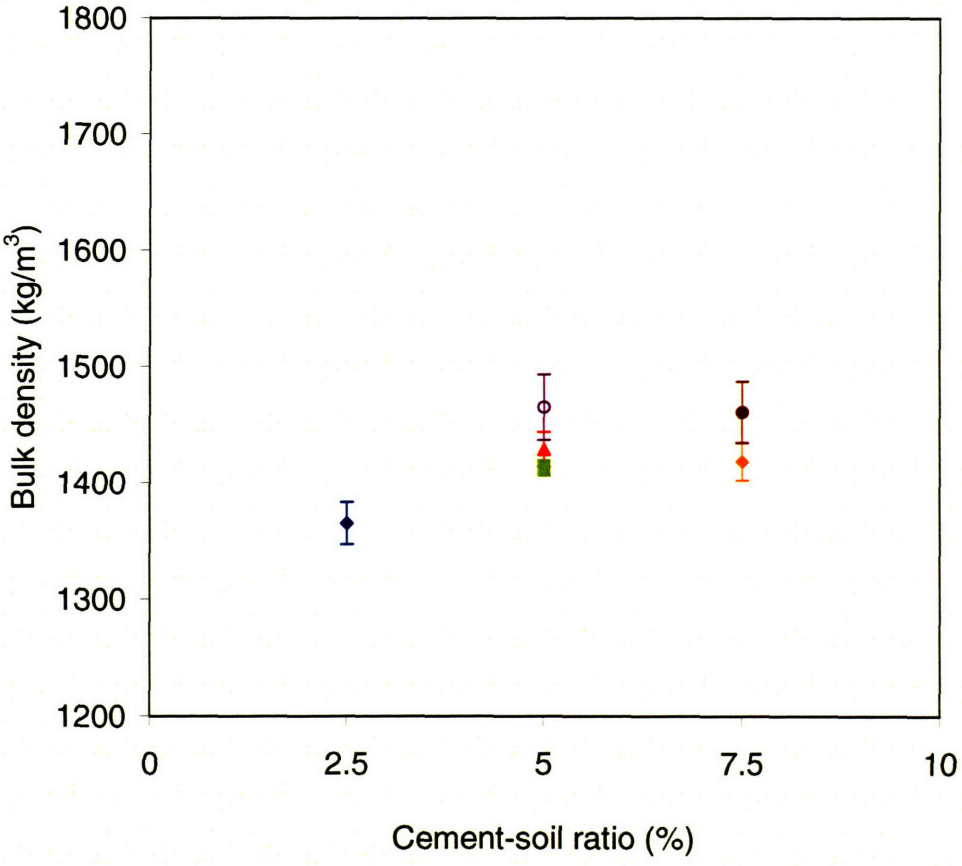

Figure 4-52. Variation of bulk density with cement-soil ratio

Specimen	Method	Moisture content (%)	
		Mean	Std dev
◆ T7	Pressed-in	91.3	4.2
■ T9	Casting	102.4	3.3
▲ T9	Pressed-in	90.2	7.9
○ T9	Trimming	99.1	2.0
◆ T8	Casting	96.8	5.0
● T8	Trimming	92.2	6.9

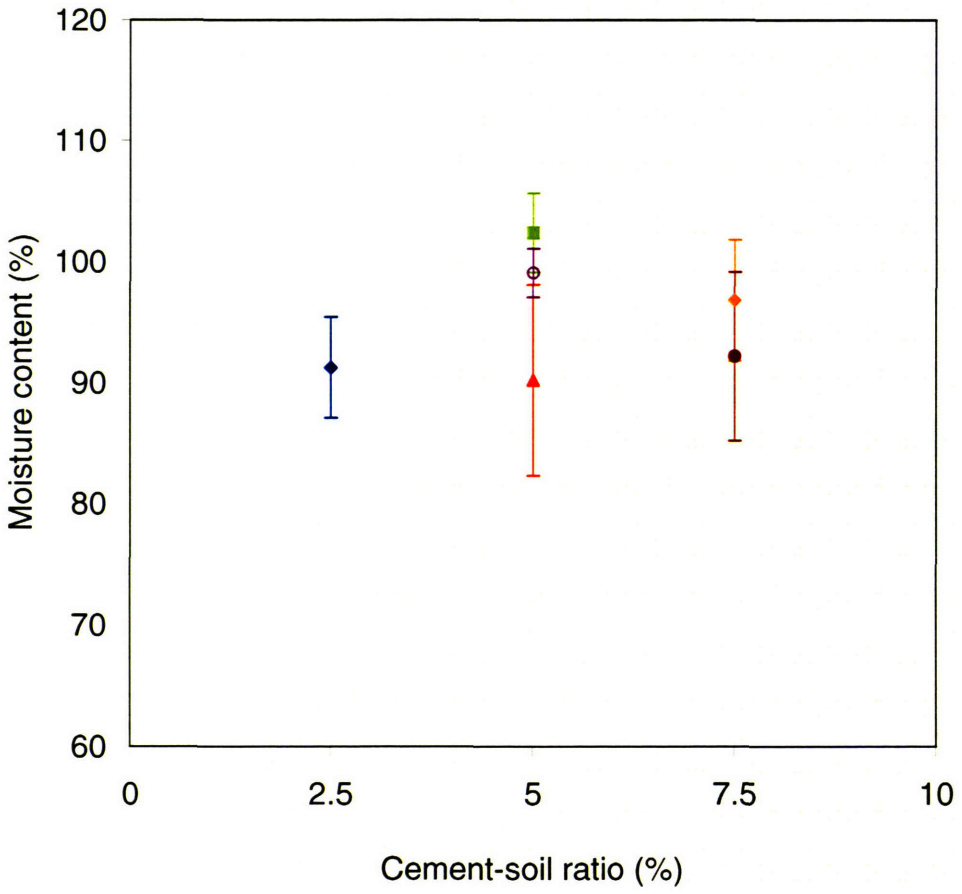

Figure 4-53. Variation of moisture content with cement-soil ratio

Specimen	Method	Void ratio	
		Mean	Std dev
◆ T7	Pressed-in	2.7	0.11
■ T9	Casting	2.9	0.07
▲ T9	Pressed-in	2.5	0.08
○ T9	Trimming	2.8	0.05
◆ T8	Casting	2.9	0.14
● T8	Trimming	2.7	0.19

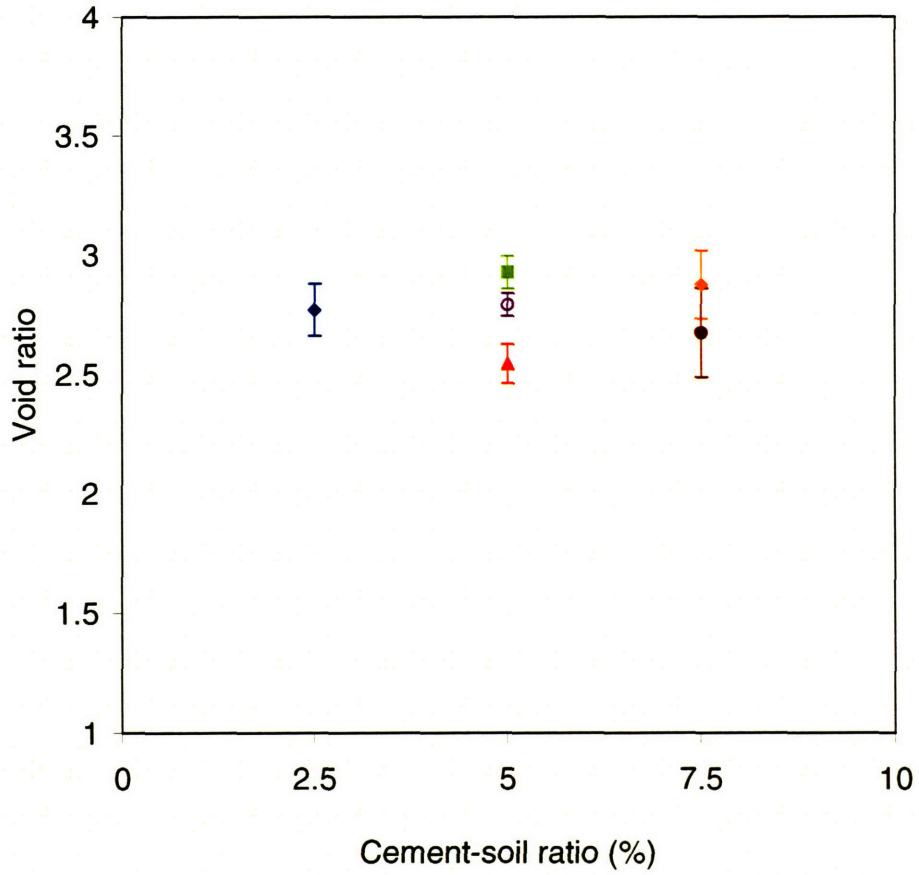

Figure 4-54. Variation of void ratio with cement-soil ratio

Specimen	Method	Degree of Saturation (%)	
		Mean	Std dev
◆ T7	Pressed-in	89.2	1.6
■ T9	Casting	96.9	1.2
▲ T9	Pressed-in	92.5	2.0
○ T9	Trimming	100.8	2.4
◆ T8	Casting	95.5	0.7
● T8	Trimming	97.9	2.0

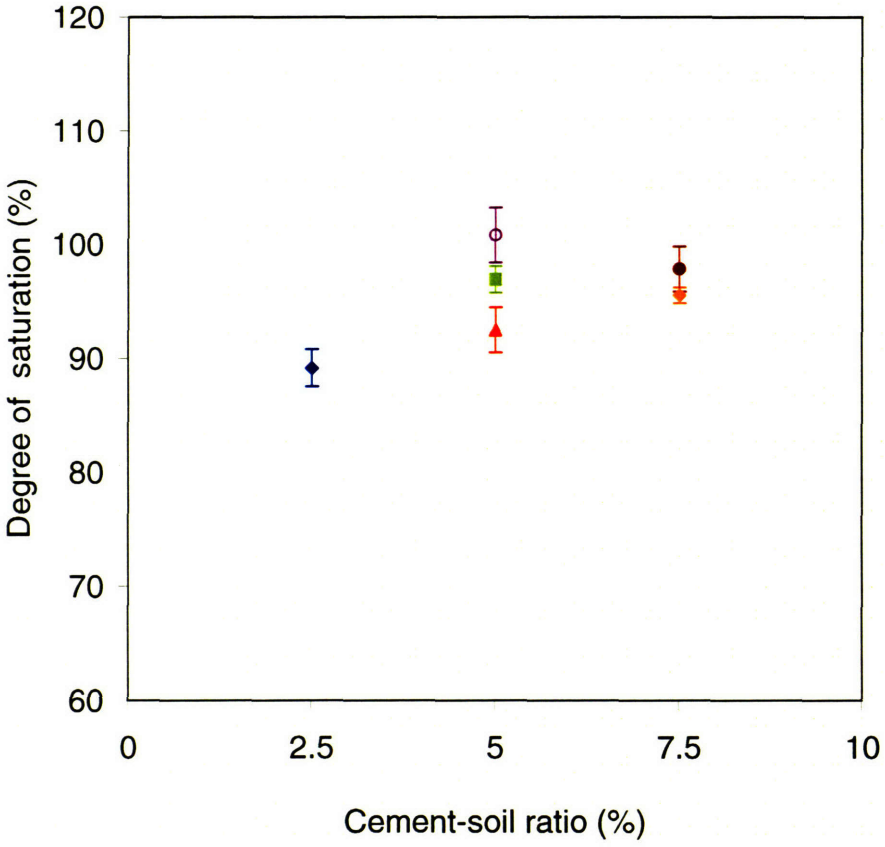

Figure 4-55. Variation of degree of saturation with cement-soil ratio

CSR (%)	Symbol	Orientation	Vane size
2.5	○	V	standard
	●	H	
	○	V	large
	●	H	
5.0	+	V	standard
	□	H	
7.5	○	V	standard
	△	H	

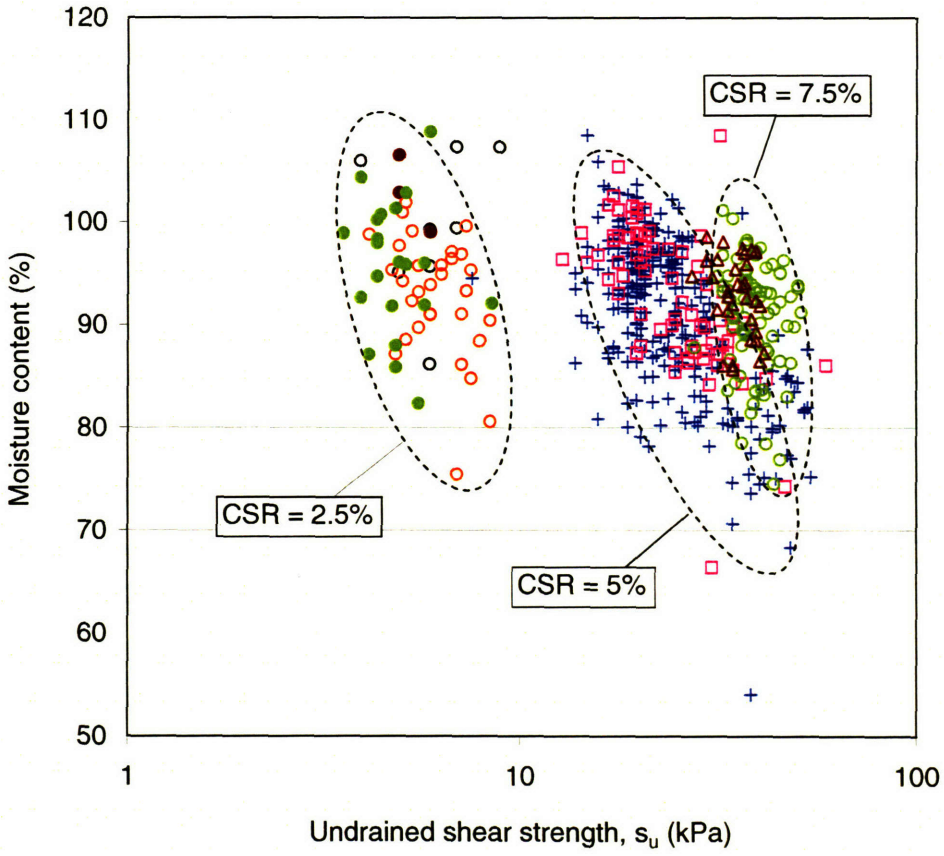

Figure 4-56. Comparison of torvane shear strengths measured on vertical and horizontal soil faces (for all specimens)

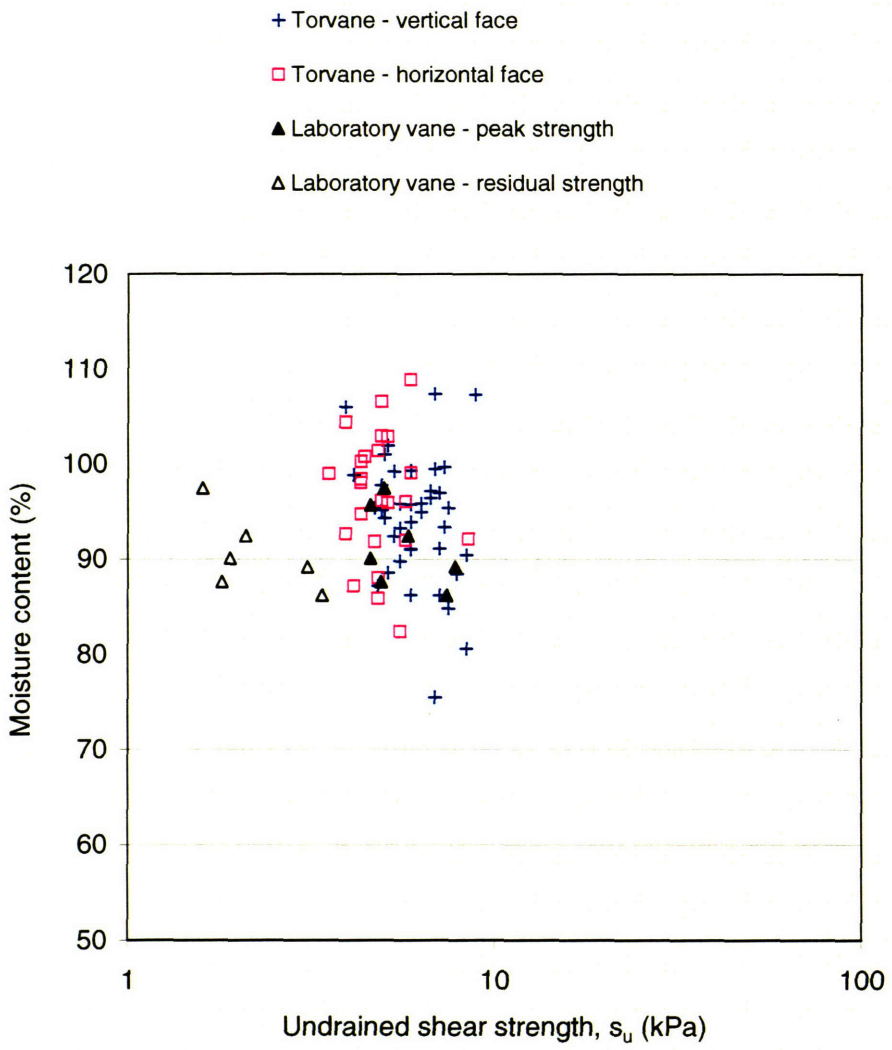

Figure 4-57. Comparison of torvane shear strengths and laboratory vane shear strengths (Specimens T4 and T7, CSR = 2.5%)

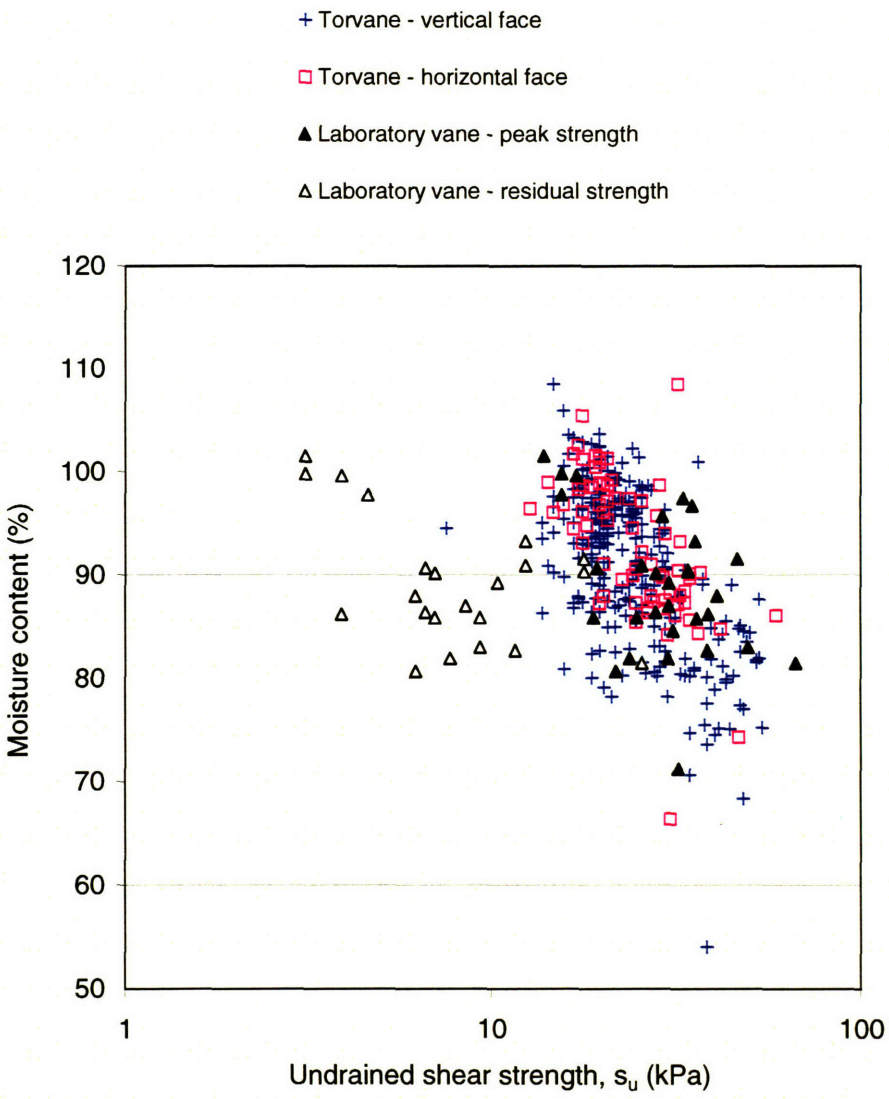

Figure 4-58. Comparison of torvane shear strengths with laboratory vane shear strengths (Specimens T1, T2, T3, T6 and T9, CSR = 5%)

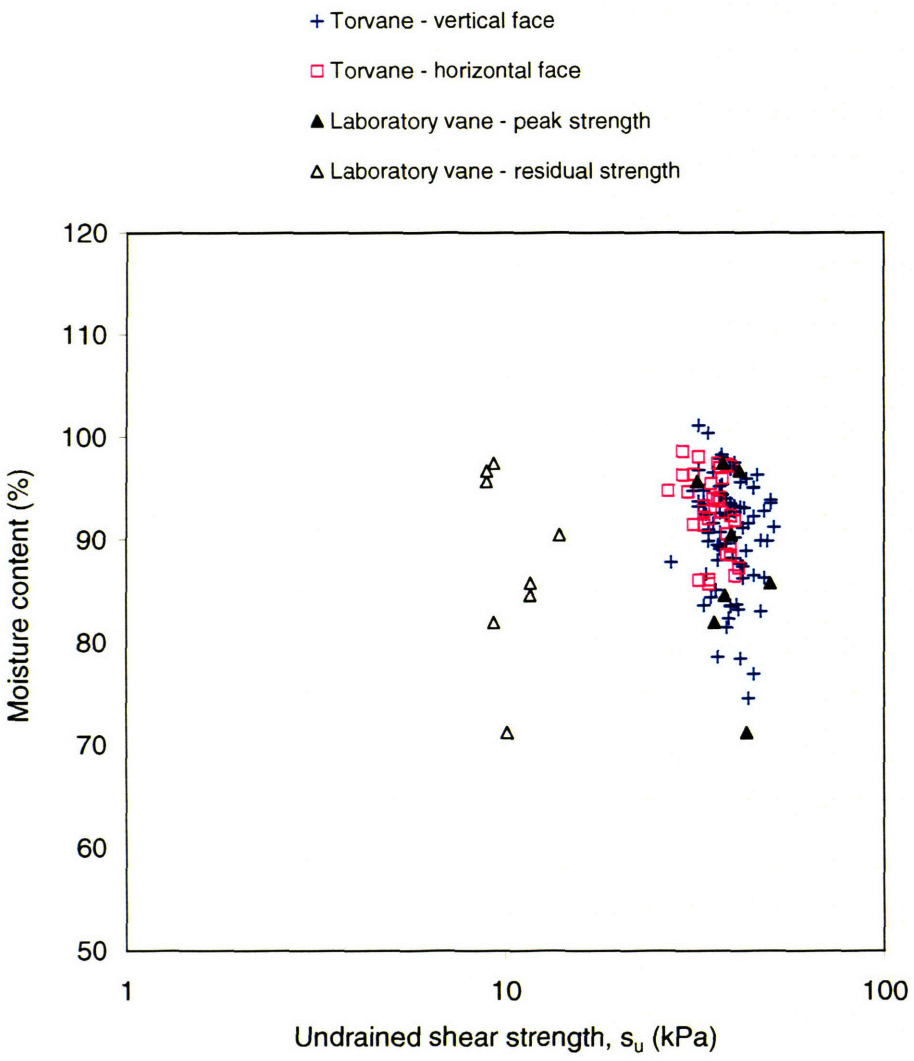

Figure 4-59. Comparison of torvane shear strengths and laboratory vane shear strengths (Specimen T8, CSR = 7.5%)

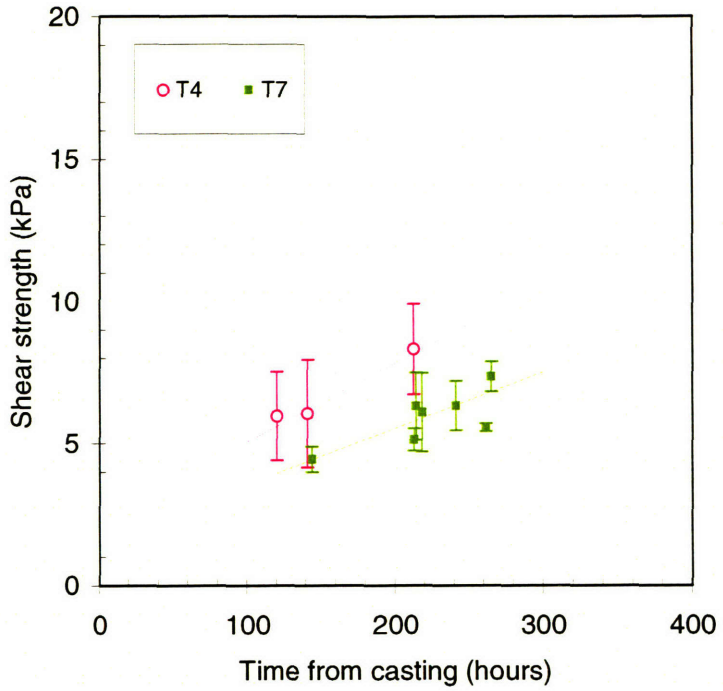

Figure 4-60. Effect of curing time on shear strength (CSR = 2.5%)

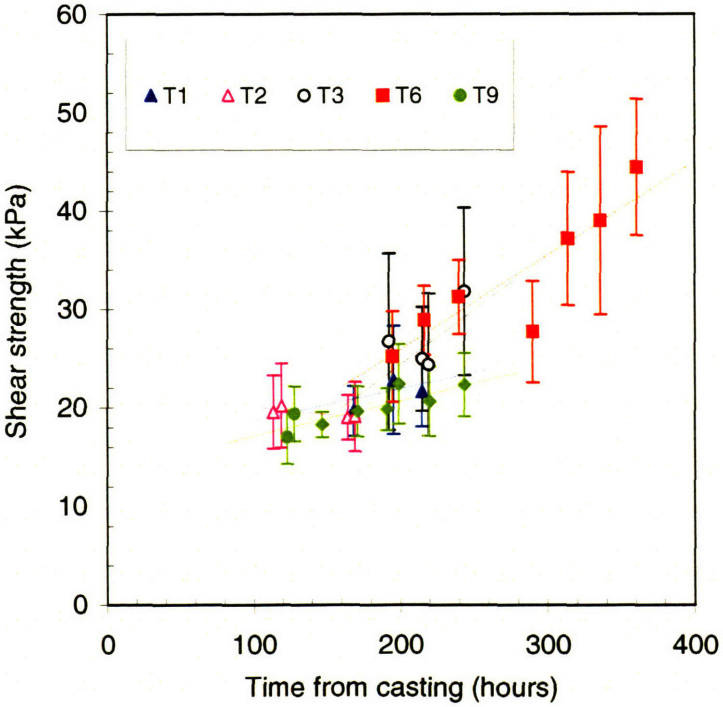

Figure 4-61. Effect of curing time on shear strength (CSR = 5%)

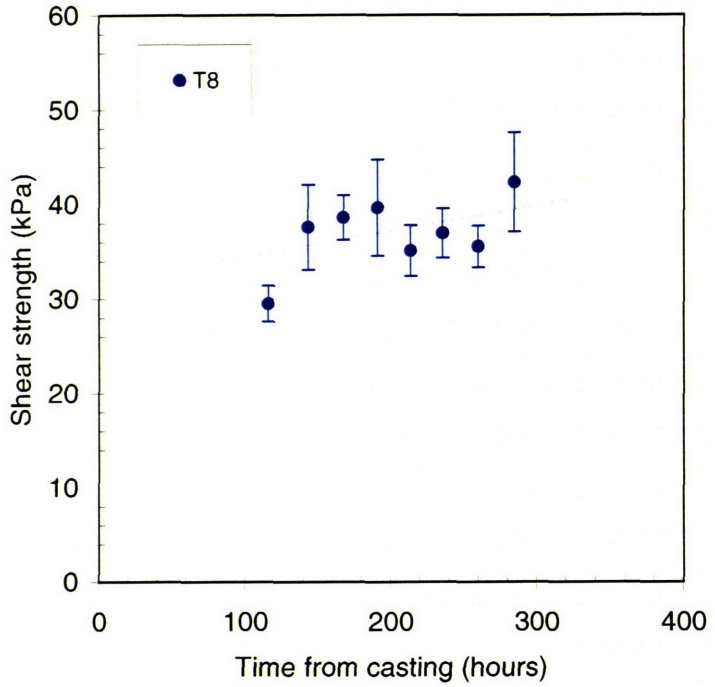

Figure 4-62. Effect of curing time on shear strength (CSR = 7.5%)

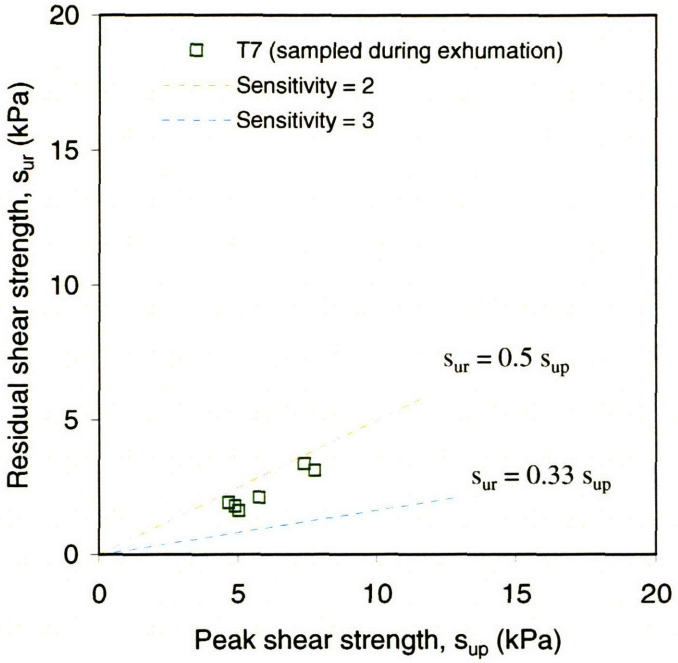

Figure 4-63. Laboratory vane shear strength (CSR = 2.5%)

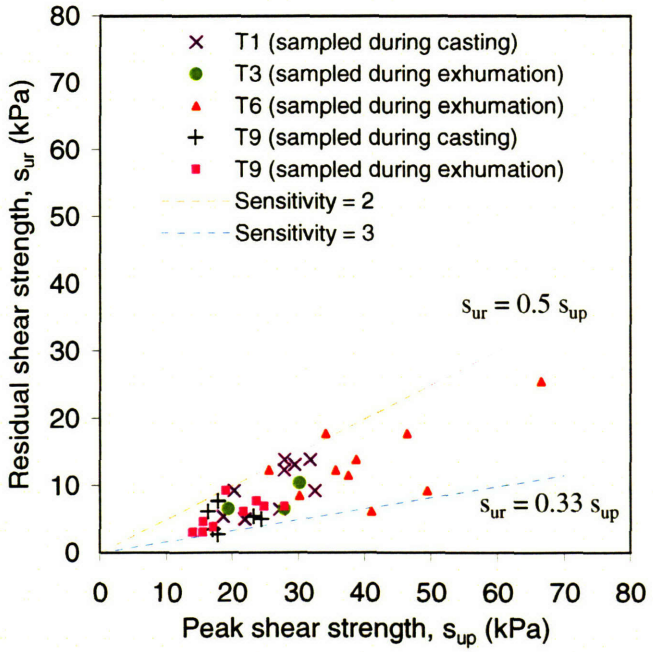

Figure 4-64. Laboratory vane shear strength (CSR = 5%)

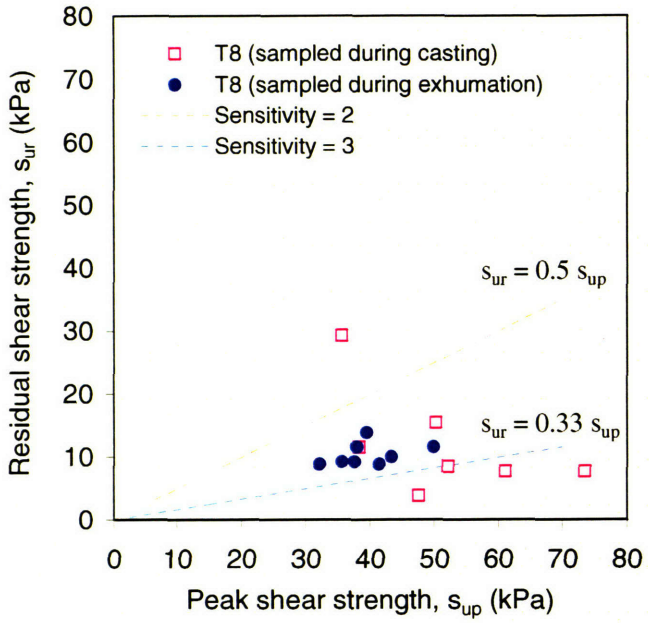

Figure 4-65. Laboratory vane shear strength (CSR = 7.5%)

CHAPTER FIVE

RESULTS AND INTERPRETATION OF JET EXCAVATION EXPERIMENTS

5.1 Introduction

This Chapter presents the results from all of the jetting experiments, including observations made on the physical form of the excavated cavity during exhumation of the specimens and the method of interpretation of the data. The reduced data are compared with the analytical model for ultimate jet penetration and excavated geometry developed in Chapter 3.

5.2 Experimental Observations

5.2.1 Radial sections through grouted discs

The vertical cross-sectional geometry of the jet excavated model soil was observed directly from the vertical soil faces during exhumation of the specimens. The boundary between the grouted soil and the undisturbed soil could be consistently identified in a freshly exposed soil face, due to the distinct, softer consistency of the grouted soil in comparison with the undisturbed soil. The demarcation was particularly clear for the stronger specimens with CSR = 5% and 7.5%. However, identification of the boundary was less distinct for the lower strength specimens with CSR = 2.5%, where the strength of the undisturbed soil was also very soft. In this case, the exposed vertical soil face was allowed to dry out so that the grout would harden quickly. This alternative procedure allows the boundary between the hardened grout and the softer undisturbed soil to be distinguished.

The following compares the shapes of cuts observed in jetting tests with the same rotation speed (R_s = 10 rpm) and number of revolutions (N_r = 10 rev). The tests can be divided into two categories: (a) tests associated with high pressures, P_i = 1000 to 3400 psi (using 1.0 mm diameter nozzle) and, (b) tests associated with low pressures, P_i = 100 to 300 psi, (using 2.5 mm diameter nozzle).

The majority of jetting tests were conducted on model soils with CSR = 5 %. For these specimens, high jetting pressures appeared to produce cuts that were longer and wider (Figure 5-1), while low jetting pressures tended to produce cuts that were shorter and thinner (Figure 5-2). The shape was more well-developed and consistent for the longer cuts in comparison with the shorter cuts. For low strength specimens (CSR = 2.5 %), Figure 5-3 and 5-4 show that the cuts were deep and the shapes were well developed, even for the lowest pressure (P_i = 100 psi). For CSR = 7.5 %, the jet penetrations were significantly limited, even at the highest jetting pressure, P_i = 3250 psi (Figure 5-5). The shapes of the cuts were less well defined and cut boundaries were more irregular. Figure 5-6 shows a radial cross-section through a grouted disc obtained from specimen T9 (P_i = 3350 psi), indicating an initial region of jet expansion up to some maximum width before reducing towards the tip of the cut. The tip of the cut was observed to be approximately rounded. Based on the above observations, the characteristic shape of the cut formed by the jet can be conceptualized as shown in Figure 5-7.

Further photographic records of the cuts observed on the vertical soil faces for each specimen are cataloged in Appendix B.

5.2.2 Vertical profile of grouted discs

The shapes of the cuts were mapped to obtain a quantitative record of their dimensions for further evaluation. This was done by placing a clear transparency on the vertical soil face and carefully tracing the boundaries using a permanent marker. The measurements were made with reference to the outer edge of the PVC pipe (which defines the borehole face) and the bottom of the specimen. The shapes on the transparencies were transposed into a rectangular co-ordinate system with the origin at the intersection between the edge of the borehole wall and the bottom of the specimen.

Figures 5-8a to 5-8h show selected examples of the results of mapping for all the specimens to demonstrate the typical shapes obtained. The torvane data obtained during exhumation of the specimens is also indicated (discussed in Section 4.2.2). In general, it was observed that the shapes of the cuts were not regular, being sensitive to local soil conditions and the turbulent behavior of the jet. The longitudinal axes of the jet were not always straight, but were sometimes curvilinear (Figure 5-8c), indicating that jet flow follows the path of weakest resistance. Figures 5-8(e) and 5-8(h) show that the excavation is not always horizontal with respect to the specimen base. This could be attributed to the practical accuracy of positioning the test tank and the leveling of the supporting platform, which may result in relative displacement of the specimen to the nozzle position. Figure 5-8(a) shows a typical example where occasional scouring of the soil at the entrance of the cut prevented the full dimensions of the jet close to the nozzle from being obtained.

A complete record of the shapes of the cuts as observed during exhumation is given in Appendix C. The distances of the extreme tip of the cut measured from the borehole face (l_b) in each section are summarized in Appendix D.

5.2.3 Plan profile of grouted discs

It is common in jet grouting practice to compare the diameters of grout columns formed for different operational parameters. Following a similar approach, plan profiles of the grouted discs observed in the jetting experiments were constructed for comparison, as shown in Figure 5-9. For each test specimen, the extreme edge of the grouted discs with respect to the origin of the specimen (x = 0, y = 0) is first determined. The radial distance of the tip of cut from the origin was calculated by adding the distance of cut from the borehole wall (l_b), obtained in the vertical profiles in Section 5.2.2, to the radius of the PVC pipe (4½ in OD). The co-ordinates of the tip in each of the eight vertical sections were computed assuming that the segments are equally spaced at 45° apart. As discussed in the earlier section, the actual position of the jetting monitor pipe may be displaced from the origin of the specimen due to inaccuracies in setting up the test tank. The centroidal axis of the jetting monitor pipe (x', y') relative to the origin was determined using the co-ordinates of the cut tips. The mean radius of the grouted disc (R') was then computed as the average distance between the actual tip positions and the monitor pipe axis.

Table 5-1 lists the calculated offset position of the monitor pipe and the statistical spread of the data for R'. The maximum off-set of the monitor pipe position from the theoretical center of the specimen was estimated to be about 9 mm in the x direction and 5 mm in the y direction. Overall, the mean deviation was only about 1.5 mm in the x direction and 0.4 mm in the y direction. Hence, the positioning of the test specimen with respect to the jetting monitor was within reasonable practical tolerance. The spatial

variability of R' can be evaluated using the coefficient of variation (COV) of the mean radius for each cut. The COV ranged from: (a) 1.8 to 9.0 % (mean value 6.4 %) for CSR = 2.5 %, (b) 3.3 to 9.9 % (mean value 5.9 %) for CSR = 5 % and, (c) 4.1 to 8.2 % (mean value 6.2 %) for CSR = 7.5 %. This indicates that the degree of variability was approximately the same for model soils of different mixes and that the mixing process was reasonably consistent.

5.2.4 Test repeatability

Cutting experiments in Specimen T9 (CSR = 5 %) were carried out specifically to evaluate the repeatability of the jetting test results when using the same set of operational parameters. These experiments used default values of rotation speed, R_s = 10 rpm and number of revolutions, N_r = 10 rev, with a 1 mm diameter nozzle to produce the maximum cutting distance using the highest available test pressures (in this case, a test pressure of between 3350 psi and 3400 psi was attained).

Figure 5-10 shows a view of the exhumed cuts, which suggests that the cuts were visually almost identical. From Figure 5-11, it was observed that the mean radius for the upper and middle cuts were very similar (R'_u = 215.2 ± 7.2 mm for P_i = 3400 psi compared with R'_M = 210.4 ± 12.6 mm for P_i = 3350 psi), whereas the lower cut was approximately 10% smaller (R'_L = 192.9 ± 10.1 mm for P_i = 3350 psi). Figure 5-12 shows the eight vertical profiles in T9 superimposed on the same plot, together with the respective torvane strengths. An examination of the shear strength profile suggests that the lower region of the specimen was stronger than the upper region, which could explain the reduced extent of the lower cut. The upper region was also more uniform and hence,

the upper and middle cuts were more consistent with each other. The mean shear strength in the proximity of each cut was determined for comparison in Figure 5-13. As can be seen, the data indicate that the results were consistent and repeatability was very good.

5.2.5 Effect of rotation speed

A trial was carried out in Specimen T6 (CSR = 5 %) to determine the rotation speed that would give the ultimate cutting distance achievable in the model soil. The smallest nozzle diameter (d_n = 1.0 mm) was used in order to attain the maximum pressures possible and the jetting pressure (P_j) was held constant at 3200 psi for all three tests. The same number of revolutions (N_r = 10 rev) was used in all cases, while the rotation speed was varied (R_s = 5, 10 and 20 rpm). Figure 5-14 shows the resulting dimensions of the grouted discs in plan.

Figure 5-15 summarizes the mean radius (R') of the grouted disc as a function of the rotation speed for jetting tests. The trial results indicated that a rotation speed of R_s = 10 rpm was sufficient to achieve the ultimate cutting distance (R' = 184.9 ± 11.3 mm). The mean radius for R_s = 5 rpm (R' = 177.0 ± 7.1 mm) and R_s = 20 rpm (R' = 175.8 ± 8.1 mm) were 4.3 % and 4.9 % smaller respectively. This result is consistent with the observation of Lunardi (1997), discussed in Section 2.1.2.1, that there is a lower limit for the rotation speed below which jet reflection will occur, resulting in a smaller penetration (as is the case for R_s = 5 rpm). On the other hand, at a higher rotation speed, the time of action of the jet on the soil surface is limited and penetration of the jet is also reduced (Yoshida et al. 1991). Again this is consistent with data for R_s = 20 rpm. In between,

there exists an optimum rotation speed that produces the maximum excavation radius (R_s = 10 rpm).

5.2.6 Effect of number of revolutions

Data from Specimens T1 and T2 (CSR = 5 %) were used to investigate the effect of the number of revolutions on the ultimate cutting distance (Figure 5-16). The number of revolutions of the nozzle (or the number of passes of the jet) was varied (N_r = 1, 5 and 10 revolutions) while keeping the other operational parameters constant (P_i = 3200 psi, R_s = 10 rpm). Again the smallest diameter (d_n = 1.0mm) was used to attain the maximum pressures possible.

Figure 5-17 indicates that the maximum cutting distance was effectively achieved with a single pass of the jet (R' = 183.1 ± 14.3 mm for N_r = 1 rev). No obvious increase of the cutting distance was demonstrated with additional passes of the jet (R' = 188.2 ± 12.9 mm for N_r = 5 and R' = 176.9 ± 8.7 mm for N_r = 10 rev). This is consistent with the observations of Guatterri et al. (1988) in field trials, that the full jet grout column diameter was achieved within the first two revolutions of the nozzle. Figure 5-18 compares the vertical profiles of the three cuts, which suggests that the width of the cut is not significantly increased when N_r is increased. Figure 5-19 shows a typical view of the middle and lower cuts in specimen T2 (for N_r = 5 and 1 rev respectively), which indicates that the cutting distance achieved is virtually the same.

For the present experiments, N_r = 10 was selected as a default parameter to ensure that the ultimate cutting distance was attained in each test and to eliminate errors associated with initiation and curtailment of the jetting process.

5.2.7 Effect of jetting pressure

To study the effects of jetting pressures on cutting distance, two sets of tests were performed; (a) high pressure tests (P_i = 1000 to 3250 psi) using a 1.0 mm diameter nozzle and, (b) low pressure tests (P_i = 100 to 300 psi) using a 2.5 mm diameter nozzle. Specimens T1 (CSR = 5%), T4 (CSR = 2.5 %) and T8 (CSR = 7.5 %) were subjected to high pressure tests, with all other operational parameters kept constant (R_s = 10 rpm, N_r = 10 rev). Figures 5-20 to 5-22 show that there is a clear trend of increasing cutting distance with increase in jetting pressure for each soil strength category (CSR) for tests in the high pressure range. Specimens T3 (CSR = 5 %) and T7 (2.5 %) were tested in the low pressure range. Figures 5-23 and 5-24 also show a similar trend of increasing cutting distance with pressure. The anomaly observed for P_i = 200 psi in Figure 5-23 was due to a localized zone of stronger soil which has an average shear strength (25.3 ± 8.8 kPa) about 18 % higher than the upper and lower cuts (21.4 ± 2.5 kPa and 22.2 ± 6.6 kPa respectively).

Figure 5-25 compares the efficiency of cutting when the jetting pressures were raised. The relative increase in cutting distance was expressed as a ratio of R' to the minimum R' associated with the lowest jetting pressure in each specimen (P_i = 1000 psi for high pressure tests and P_i = 100 psi for low pressure tests). It can be seen that for high pressure tests, the relative increase was of a similar order for model soils with CSR = 5

and 7.5 % (Figure 5-25a). When the jetting pressure was raised by about 2 times from P_i = 1000 psi, the relative increase in cutting distance was only 19 to 24 %. Similarly, when the jetting pressures were raised by about 3 times, the relative increase in cutting distance was only 41 to 52 %. For the lower strength soil specimens (CSR = 2.5 %, Figure 5-25a) the relative increase in excavation radius is much larger (about 44 %) when the jetting pressure was doubled. Figure 5-25b shows that the cutting performance for both CSR = 2.5 and 5 % was approximately the same (46 to 51 %) when the jetting pressures were increased three times from 100 psi.

5.2.8 Effect of cement-soil mass ratio

Figures 5-26 and 5-27 show the effect of CSR on cutting distance when operational parameters are held constant. It can be seen that the cutting distance varies inversely with CSR, the relationship being highly non-linear. There is relatively small difference in the measured cutting distance for tests with CSR = 5 and 7.5 %, but much larger effects when comparing tests with CSR = 5 % and 2.5 %. Figure 5-28 compares the relative changes of the mean radius of cut for these tests, using CSR = 5 % as the reference bench mark. For P_i = 1000 psi, the change in cutting distance was +50 % for CSR = 2.5 and -14 % for CSR = 7.5 %. For P_i = 2000 psi, the change in cutting distance was +81 % for CSR = 2.5 and -11 % for CSR = 7.5 %.

5.2.9 Effect of nozzle diameter

The effect of nozzle diameter can be assessed by comparing the conditions that produce the same cutting distance in model soil of given CSR. Figure 5-29 shows that for CSR = 2.5 %, cutting distance of a similar order can be achieved using low jetting pressures of 100 to 300 psi with a 2.5 mm nozzle (T7, R' = 164.5 to 249.2 mm) compared with that using high jetting pressures of 1000 to 3200 psi with a 1.0 mm diameter nozzle with (T4, R' = 187.2 to 270.2 mm). Similarly, for CSR = 5 %, the cutting distance achieved using low pressures with a large nozzle (T3, R' = 107.2 to 157.4 mm) was comparable to that achieved using high pressures with a small nozzle (T1, R' = 125.1 to 176.9 mm). This implies that cutting distance is not only a function of pressure, but also the diameter of the nozzle. As discussed in Chapter 3, the nozzle size determines the length of the potential core (x_o) of the jet, over which the jetting energy is preserved. Hence the longer the potential core length, the larger the expected cutting distance. In the present experiments, x_o was about 5.8 to 5.9 mm for T4 and T7, and 14.6 to 14.8 mm for T1 and T3. The potential core length of a jet produced using a 2.5 mm diameter nozzle is therefore approximately 2.5 times longer than that for a jet produced using a 1.0 mm diameter nozzle, which is significant.

5.2.10 Anatomy of grouted discs

During the exhumation of specimens, cross-sectional incisions were made through the grouted lobes to examine their physical anatomy. It was observed that there was a thin zone of soil immediately surrounding the cut, about 10mm thick, that consisted of much harder material, even in comparison with the undisturbed soil. Figure 5-30 depicts a view

of a typical exposed section through the grouted disc in a specimen with CSR = 5%, which clearly shows the boundaries of the different zones.

Figure 5-31 shows that the features were less distinct for a softer specimen (T7) with CSR = 2.5%. Moisture contents were obtained for samples taken from the surfaces of the different zones in the lower cut of specimen T7. It can be seen from Figure 5-32 that the moisture content in the central grouted zone was extremely high, ranging from 168 to 177% (samples GS1 to GS3). Just outside the central core, the moisture content decreased to about 82 to 87% (samples S1 to S5), which was on average about 8 % drier than the undisturbed soil where the moisture content varied between 88 to 96% (samples S6 to S8). It is clear that the zone of high moisture content represents the body of the fluid jet in the soil. It was plausible that the lower moisture content in the interface zone was caused by drying of the adjacent soil due to curing of the silicate grout in the body of the grouted soil.

In order to further study the characteristics of the jet body, samples were taken from the material in each cut in specimen T9, as well as the sludge discharged to the surface, for moisture content and density measurements (Table 5-2). The jetting parameters for all three cuts in T9 were the same, so a direct comparison with regards to the uniformity of the mixing process in the jet body was possible. It can be seen that the moisture content of the material in the jet body was very high, ranging from 153% to 304% (Figure 5-33). This was consistent with the observation above, that the zone of jetted soil exhibited very high moisture contents that were as much as twice that of the surrounding soil. The densities of the grouted soil (ρ_j) generally fall within a range between 1120 and 1318 kg/m^3. These values lie between the density of the grout (1112

kg/m^3) and the undisturbed soil (ranging from 1403 to 1515 kg/m^3 as shown in Figure 4-47). The mean moisture content and density of the middle and lower cuts were very similar (w = 262 to 269 %, ρ_j = 1197 to 1204 kg/m^3), although they were 26 % lower and 4.5 % higher respectively than the upper cut (w = 197 %, ρ_j = 1254 kg/m^3). Figure 5-33 shows that the density of the discharged sludge ranged from 1224 to 1281 kg/m^3, which was similar to the values obtained for the grouted soil. The properties of the sludge are therefore reasonably representative of the properties within the grouted soil zone.

Chapter 3 presented a theoretical relationship for the density in an expanding jet (ρ_j) with simultaneous entrainment of the surrounding ambient medium of density ρ_{am} is given by $\rho_j = \sqrt{(\rho_{am}\rho)}$ where ρ is the density of the jetting fluid. Assuming that the equation equally applies to the present condition, and using the average density of grout measured earlier (ρ = 1112 kg/m^3), the density of the ambient medium was calculated for each corresponding density measurement of the grouted zone and discharged sludge. From Table 5-2, it can be seen that the calculated mean density of the ambient medium ranged from ρ_{am} = 1294 to 1433 kg/m^3. These values were consistent with the measured densities for the undisturbed soil (ρ_s = 1403 to 1515 kg/m^3). Hence, it would appear that an entrainment process has taken place during the jetting operation, with soil particles in the surrounding specimen being dislodged and drawn into the body of the jet. Although the medium surrounding the jet was a soil and not a fluid, the theory appears to be equally applicable. The argument for the entrainment process was corroborated by the observation of an initial zone of expanding width in the shape of the cuts discussed in Section 5.2.1.

5.2.11 Determination of jet penetration distance

In the presentation of the theoretical jet excavation model in Chapter 3, the ultimate jet penetration distance (l_j) is defined as the maximum distance of the jet tip relative to the nozzle exit. For the present experiments, the distance of the nozzle from the vertical axis of the monitor pipe (x_n) was obtained using a vernier caliper (Figure 5-34). The jet penetration distance (l_j) is then determined by subtracting x_n from the radius (R') of the cut tip positions derived in Section 5.2.3. Measurements showed that x_n was 47.80 ± 0.12 mm for the 1.0 mm diameter nozzle and 47.67 ± 0.18 mm for the 2.5 mm diameter nozzle. Hence the variation in x_n is very small. The data derived for l_j is listed in Table 5-3 and summarized in Figure 5-35. A comparison of the observed jet penetration distance with that predicted by the theoretical model is discussed in Section 5.4.2. The reader is referred to Appendix D for a detailed breakdown of the data.

5.2.12 Determination of jet width

The shape of the cut obtained from the grouted mold in the vertical soil faces is representative of the form of the fluid jet body during excavation of the soil. The shape of the cut was observed to be highly variable, and the surfaces are uneven, mainly due to the random nature of the interaction between the jet and soil in a highly turbulent environment. As for most turbulent fluid problems, the mean flow parameters rather than the instantaneous time-dependent components are used in analytical descriptions of fluid behavior. Using a similar approach, an averaged shape of the jet body assuming symmetrical expansion of the jet can be used to improve the data presentation for interpretation of the jet-soil interaction behavior in the present experiments. In order to

compensate for random localized variations of the cut boundaries, the half width of the cuts was used to describe the jet dimensions. The half width (b) at any given distance (x) from the nozzle is defined as $b = w_j/2$, where w_j is the vertical distance between the actual upper and bottom boundaries of the cut (Figure 5-36). The vertical profile for each cut was sub-divided into several vertical slices at equal intervals of 5 or 10 mm along the horizontal x-axis, and the width of the cut in each slice was measured. The cut tip was assumed to be located on the central axis of the jet with zero width. Figure 5-37 depicts examples of the graphical plots of half width of selected cuts. Comparison of the experimental data with the jet width predicted by the theoretical model is relegated to Section 5.3.4. Graphical plots of the half width derived for all the cuts are presented in Appendix E.

5.3. Comparison of Jet Excavation Model with Experimental Observations

5.3.1 Interpretation of soil shear strength at time of jetting

Undrained shear strength is an important parameter affecting the interpretation of the jetting experiments. This section presents a more detailed interpretation of the time-dependent shear strength properties of the model soil and provides a best estimate of the shear strength parameters prevailing at the time of the jetting experiments. Chapter 4 has reported significant variations in the shear strength of the model soils as functions of the time period after casting (Figures 4-60 to 4-62). In order to interpret the jetting data, the shear strength at the time of jetting has to be determined from torvane data measured during specimen exhumation.

The main challenge in the interpretation of the torvane data for such large specimens is that the measurements were obtained, (a) from different parts of the specimen, (b) at different times after casting and jetting and (c) in both vertical and horizontal directions. The scatter in the data is large and no simple correlation is possible. Laboratory vane shear tests conducted on samples obtained during exhumation were too few and insufficient to provide a clear trend in the data for regression analysis, and were only useful in providing an independent verification of the torvane data. However, more controlled strength properties obtained during initial trials for the design mix are available, where very small specimens were made under ideal mixing conditions and measured using laboratory vane shear tests. A linear regression through these data found s_u [kPa] = 0.0539t [hrs] + 21.70 (with r^2 = 0.95), where t is the time from casting (Figure 5-38). At the time of jetting tests, laboratory vane data on batch samples in test T1 is available. These data show problems of non-uniform mixing and confirm that the scatter in the data was largely due to imperfect mixing at the scale of such large test specimens. As a result of the above, one logical way to estimate the shear strength at the time of jetting is to assume that, (a) mass strength in the test specimen is lower than the design mix due to imperfect mixing, but (b) strength gain over time is less than or at best equal to the mix design. Therefore, a simple linear fit to the torvane data can be used to estimate the conditions at the time of jetting.

For each specimen, an initial assessment of the global trend was made based on all the available torvane data taken together to obtain the global rate of strength gain over time. The torvane data was subsequently separated into horizontal zones in accordance with the proximity of the measurements to the upper, middle and lower cuts to refine the

analysis. Using the slope of the global trend line, a best-fit line was found for each zone. The reference strength used a direct arithmetic mean of the shear strengths in each zone at the time of exhumation. The regression equations obtained for each zone were then used to extrapolate to the respective shear strengths at the time of jetting.

The majority of test specimens (T1, T2, T3, T6 and T9) were manufactured with CSR = 5% (Figures 5-39a, 39b, 39c, 39e and 39h). For these specimens, data from the initial design mix for CSR = 5 % (s_u [kPa] = 0.0539t [hrs] + 27.1) was used directly to provide a reference baseline for determining the strength-time relationships. In the evaluation of the best-fit trend lines for the full size specimens, the slope of the assumed regression (i.e. rate of strength gain) is always constrained to be less than or equal to the design mix. In the case of T6, torvane shear strengths were excessively high for tests carried out beyond about 250 hours. It was reasoned that significantly high strength values above the design mix line represent a different phenomena from that of a hydration process (probably due to drying out), and were excluded from the analyses.

For specimens with CSR = 2.5 % (T4 and T7) and CSR = 7.5 % (T8), it is assumed that the upper limit for rate of strength gain over time will not be significantly different from that for the design mix (for CSR = 5 %). The strength-time relationship was similarly found from regression analysis of the torvane data. The rates of strength gain for these specimens were all within that for the design mix, hence the regression equations were considered reasonable (Figures 5-39d and 5-39f).

The time of jetting and interpreted shear strengths for each test specimen are summarized in Figure 5-40.

5.3.2 Comparison of theoretical and measured jet penetration distance

In Chapter 3, the theoretical formulation relates the jet penetration distance (l_j) to nozzle diameter (d_n), nozzle pressure difference ($P_i - P_s$) and ultimate soil bearing capacity (q_{bu}) of the soil as follows:-

$$\frac{l_j}{d_n} = 6.25\sqrt{\frac{(P_i - P_s)}{q_{bu}}} \tag{3.34}$$

In the present experiments, the level of the return slurry within the PVC pipe determines the pressure at the nozzle exit, P_s. As the position of the PVC pipe was secured to the ceiling of the test chamber during the tests, the nozzle was always maintained at a fixed distance just below the bottom of the PVC pipe. It was observed that the return slurry overflowed through two drilled holes located about 1 in below the top of the PVC pipe during jetting. Based on the length of the PVC pipe of 24 in, the pressure at the nozzle exit ($P_s = \rho_s g \Delta z_n$) was calculated assuming that ρ_s = 1250 kg/m^3 and Δz_n = 23ins (584mm), giving P_s = 1.06 psi (7.3 kPa). This pressure is very small in comparison with the range of test pressures used in the experiments (P_i = 100 to 3400 psi). Hence, the pressure difference term ($P_i - P_s$) was dominated by the applied pressure, P_i.

The bearing capacity term in Eqn 3.34 is defined by $q_{bu} = N_c s_u$, where N_c is a bearing capacity factor and s_u is the undrained shear strength of the model soil at the time of jetting (Figure 5-40). The bearing capacity factor N_c is assumed to be a constant related to the failure mode of the soil at the jet tip, and must be back-figured from the experimental data.

Figure 5-41 shows a normalized plot of the jetted length l_j/d_n versus $\sqrt{(P_i/s_u)}$ for data obtained from the eight laboratory jetting tests (Table 5-3). The mean values in each

cut, as well as the one standard deviation bounds are shown to indicate the statistical spread of the results. As can be seen, there is a very clear linear correlation between the parameters, as expected from the theoretical formulation. This confirms that, for a given nozzle diameter, jet penetration is governed by the relative magnitude of applied pressure to the undrained shear strength of the soil. A linear regression analysis through the data gives

$$\frac{l_j}{d_n} = 4.033\sqrt{\frac{P_i}{s_u}} \tag{5.1}$$

with a coefficient of correlation, $r^2 = 0.95$.

By substituting $q_{bu} = N_c\, s_u$ in Eqn.5.1, we obtain

$$\frac{l_j}{d_n} = \frac{6.25}{\sqrt{N_c}}\sqrt{\frac{P_i}{s_u}} \tag{5.2}$$

A direct comparison of the terms in the two equations leads to the conclusion that $N_c = 2.4$. The low value of N_c suggests that the failure at the tip if the jet is not a pure compressive bearing mode as defined in classical soil mechanics for undrained loading of a surface punch (where $N_c = 5.1$ to 5.7, depending on the shape of the punch). If we consider that the jet is not stationary but is continuously traversing, and soil on one side is continuously being removed, resistance at the jet front would be reduced due to lack of confinement on one side of the soil mass (Figure 5-42). Further more, the complex interaction between the tip of a traversing jet stream and the soil, with return flow being discharged to one side of the excavated slot, would lead to a non-uniform stress distribution at the base of the slot, with higher pressures skewed towards the upstream side of the slot, possibly resulting in a condition of eccentric loading and elevation of the

local shear intensity. The uneven loading condition promotes failure of the soil and is reflected as a lower N_c value.

5.3.3 Comparison with field trial data

Many jet grouting data from full scale field trials have been published in the literature. However in many cases, the data is incomplete and are not useful for the purpose of verifying the excavation model presented in this research. Four case histories on jet grouting in cohesive soils have been identified (Davie et al. 2003, Durgunoglu et al. 2003, Dazceer and Golkap 2003 and Samano et al. 1999), which contain sufficient information with regards to operational parameters, nozzle sizes, soil strength and the achieved jet grout column diameters to allow a reasonably accurate interpretation of the data. These trials involve cohesive soils with a wide range of shear strengths, and are representative of the typical range of soil strengths encountered in jet grouting practice.

The data gathered included 40 trial columns in stiff slightly gravelly and sandy clay (I_p = 40 to 65 %) with s_u = 65 kPa (Davie et al. 2003), three trial columns in alluvial deposits consisting predominantly of slightly cemented micaceous silt with interbedded sandy gravels and clays (I_p = 10 to 20 %), with s_u = 50 kPa (Durgunoglu et al. 2003), four trial columns in soft silty clay and stiff clay with s_u at least 25 kPa (Duzceer and Golkap 2003) and six trial columns in very soft highly plastic clay (w_n = 200 to 400 %) with s_u = 8 to 12 kPa (Samano et al. 1999). In all the cases, the top 2.5 to 6m of the columns was exhumed to measure the diameters achieved. The diameters reported are the average values for each column. In the trials, either two or three nozzles were used, with diameters ranging from 1.8 to 2.2 mm. The trials reported by Davie et al. (2003) include

either one or two stages of pre-cutting with water, prior to the jet grouting pass. Column 8/P of Durgunoglu et al. (2003) involves a single stage of pre-cutting. All other trials were conducted without pre-cutting. Appendix G provides a detailed tabulation of the trial data given in the papers.

The diameters of the jetting monitors used (d_m) were not reported in the papers and is assumed to be 90 mm, which is the nominal size used in the industry (Lunardi 1997). The jet penetration distance, l_j is calculated by subtracting the assumed monitor diameter from the measured jet grout column diameter, D, i.e. $l_j = (D - d_m)/2$. Table 5-4 summarizes the key data for the field trials. Figure 5-43 compares the measured and computed jet penetration distance. As can be seen, the jet penetration distance using the theoretical formulation (Eqn 3.34) with $N_c = 2.4$ is in good agreement with the full-scale field trial measurements. The margin of error is within ±15 %. It was noted that the field trials which included precutting (Davie et al. 2003, Durgunoglu et al. 2003) produced larger column sizes than that computed from theory. This can be explained by the fact that precutting causes churning and remolding of the soil and has a tendency to reduce its strength prior to the jet grouting pass. An improved prediction would be expected if a lower shear strength is adopted. The predicted l_j for the trial data of Duzceer and Golkap (2003) is lower than the measured values. This is consistent with the fact that the shear strength assumed in the calculation (s_u = 25 kPa) is a lower bound as the upper stiff clay layer is stronger (SPT N = 10 blows/0.3m) and the strength would be higher on average. Overall, the computed jet penetration distance based on the proposed theory is reasonable.

5.3.4 Jet width

Section 3.3 presented a hypothesis that the spread of the fluid jet will be limited to a radius, r at which the wall shear stress, τ_w becomes equal to the soil shearing resistance, τ_u. The shape of the cavity excavated therefore follows the locus of r satisfying the equation:

$$r = r_i \sqrt{2\left(\frac{v_{xc}}{v_{xr}}\right)} \tag{3.25}$$

where,

$$v_{xc} = \frac{v_o x_o}{x}$$

$$v_{xr} = \sqrt{\frac{2\tau_u}{c_f \rho_f}}$$

c_f is the wall shear stress coefficient and ρ_j is the jet density.

In order to validate the above hypothesis, the predicted widths of the jet body can be compared with the actual cut dimensions obtained from the experiments. The line passing through the inflexion points of the velocity profiles in each jet cross-section, given by $r_i = 0.08x$, is a universal characteristic of the jet. This line also represents the locus of maximum shear stress in the jet and can be used as a reference baseline for interpretation of the measured data (Figure 5-44). The matching point (x_s, r_s) at which the inflexion line intersects the measured cut boundary determines the conditions governing the theoretical limit of jet expansion.

The velocity, v_{xrs} at radius, r_s from the jet axis is known from the expressions:

$$v_{xcs} = \frac{v_o x_o}{x_s} \tag{5.3}$$

$$v_{xrs} = v_{xcs} \exp\left[-\tfrac{1}{2}\left(\frac{r_s^2}{r_i^2}\right)\right] \tag{5.4}$$

The Reynold's number in the jetting experiments, $R_l = \rho_j v_{xrs} l/\mu_j < 5 \times 10^5$ (where l is the distance from the leading edge of the solid boundary, i.e. the borehole wall), indicating that the flow condition in the boundary layer is laminar (Schlichting, 1987). Hence, the Blasius formula can be used to determine the wall shear stress coefficient, i.e. $c_f = 0.664/\sqrt{R_l}$. Figure 5-45 shows the typical variation of R_l and c_f with distance, l. The corresponding shearing resistance, τ_u at the jet-soil boundary can then be calculated using the equation:

$$\tau_u = \tfrac{1}{2} c_f \rho_j v_{xcs}^2 e^{-1} \tag{5.5}$$

Table 5-5 summarizes the parameters obtained at the matching points for the jetting tests. Figures 5-46a through 5-46j show typical plots for the predicted and measured vertical jet sections. In general, the form of the theoretical shapes is in good agreement with the dimensions of the actual cut, suggesting that the theoretical assumptions regarding the excavation mechanism were reasonable (Figures 5-46a to 5-46e). Where the theoretical shapes were different, the theory tends to under-predict the jet width in the majority of cases (Figures 5-46f to 5-46i). In all the above cases, the boundary of the cuts extends above the inflexion line, indicating that jet expansion is curtailed at a distance beyond the location of maximum shear stress in the jet, when $x < x_s$. Only in a small number of cases, does the theory give an over-prediction (Figure 5-46j). These situations occur when the measured cut boundaries plot close to the inflexion line.

The plots of measured and predicted shapes for all the cuts are summarized in Appendix E. The parameters at the equilibrium points derived for each cut are summarized in Appendix F.

5.3.5 Jet-soil interface shearing resistance

Figure 5-47 summarizes the ratio of the back-calculated shearing resistance at the jet-soil interface, τ_u to the best estimate of undrained shear strength, s_u of the model soil at each level of excavation. It was observed that the shearing resistances were all very low, with the majority falling in the range τ_u/s_u = 0.001 to 0.002, with an upper bound $\tau_u/s_u < 0.004$. Chapter 4 established from laboratory vane shear tests that the sensitivity of the model soil is in the range s_t = 2 to 3. This means that the mobilized shearing resistances at the jet-soil interface, τ_u were much smaller than the residual shear strengths of the soil. This can be explained by the fact that the interaction between a fast flowing fluid over a soil surface involves the plucking of particles from the surface as a result of random turbulent bursts which occur at the protrusions in the surface. The mechanism is therefore not one of pure shear within a soil mass where shearing takes place mainly through solid-solid particle interaction.

Kamphuis and Hall (1983) reported correlations between the critical shear stress, τ_c for initiation of soil erosion and soil strength for test specimens with greater than 60% clay content. They propose that $\tau_c = 3.8 + 0.55\ (s_v/1000)$ for shear strengths in the range 5 kPa $< s_v <$ 25 kPa, where s_v is the laboratory vane shear strength. As can be seen, the proposed correlation represents a lower bound on the shearing resistance, τ_u at the jet-soil interface measured in the current jetting experiments.

The experiments of Kamphuis and Hall (1983) were conducted on specimens (150 mm by 600 mm and 100 mm deep) which were consolidated from a clay slurry, in a unidirectional flow flume-tunnel with the flow parallel to the plane of the specimens (i.e. parallel to the orientation of the clay particles). The authors noted that in the majority of tests, the appearance of small pit marks on the soil surface indicates the initiation of erosion. The critical shear stress, τ_c for each specimen increased with the consolidating pressure under which the specimens were made. Based on this observation, the authors suggest that inter-particle bonding forces play an important role in the onset of erosion.

In the present jetting tests, the model soil was prepared without a consolidating pressure, the strength being derived mainly from pure cohesion due to cementation bonding between particles. As a result, the shearing resistance τ_u at the jet-soil interface is expected to be higher than the critical shear stress, τ_c associated with a normally consolidated cohesive soil.

5.3.6 Jet tip region

The jet extends beyond the equilibrium length, x_s to the ultimate jet penetration, l_j. The behavior in this region cannot be explained by the entrainment theory and some other mechanism is involved. It was likely that this second region is associated with deflection of the jet due to sideway discharge close to its tip. It was observed that, in the majority of cases, the equilibrium point is located close to the jet tip. Figures 5-48a to 5-48c compare the ratio $\Delta l/r_s$ (where $\Delta l = l_j - x_s$, is the jet extension length) as a function of the equilibrium length ratio (x_s/x_o). In all cases, there was a trend of decreasing $\Delta l/r_s$ with

increasing nozzle pressure and jet penetration (as indicated by larger values of x_s/x_o). At the limit it appears that $\Delta l/r_s \rightarrow 1.0$, occurring approximately at x_s/x_o between 15 and 20.

It can be seen that the length difference, Δl was consistently longer with respect to r_s for the low pressure tests (T7 and T3) conducted at 100 to 300 psi (Figures 5-48a and 5-48b). For the high pressure tests (P_i = 1000 to 3400 psi), it is observed that $\Delta l/r_s = 1.0$ occurs for cases when $P_i > 3200$ psi. This is clearly demonstrated in T4 for CSR = 2.5 % and T8 for CSR = 7.5 % (Figures 5-48a and 5-48c). However, for specimens with CSR = 5 % (Figure 5-48b), $\Delta l/r_s = 1.0$ is observed only for T2 and T9, but not for T6 (even though P_i = 3200 psi). On further analysis, it appears that the ratio of pressure to soil strength, P_i/s_u is also an important factor for achieving $\Delta l/r_s = 1.0$, i.e. $P_i/s_u > 1203$ (T2 and T9) compared with T6 (P_i/s_u = 947 to 1050). The corresponding ratios for T4 and T8 are P_i/s_u = 1468 and P_i/s_u = 578 respectively. The above observations suggest that higher P_i/s_u ratios are required for softer soils in comparison with stiffer soils.

In actual practice, jet grouting in the field typically uses jetting pressures in the order of 2900 to 8700 psi (200 to 600 bars). For all practical intentions, it is reasonable to expect $\Delta l/r_s \approx 1.0$. Hence, the jet penetration distance, l_j can be related to the equilibrium length, x_s and equilibrium radius, r_s as $l_j = x_s + r_s$. Since $r_s = 0.08x_s$, we can express the equilibrium radius as

$$r_s = \frac{l_j}{13.5} \tag{5.6}$$

The width of the jet in the ground, w_j can be conservatively estimated assuming $w_j = 2r_s$. The computed jet width would determine the upper bound distance for the required lift step, Δz for jetting monitor displacement, so that overlapping cuts can be ensured and

continuous columns can be formed. The jet penetration distance, l_j, jet width, w_j and the lift step, Δz are therefore directly related.

Table 5-6 summarizes the width of cut estimated using Eqn 5.6 for selected case history data referenced in Section 5.4.3. It is noted that the computed widths, w_j ranged from 36 to 75 mm, and are comparable to the typical lift step, Δz = 40 mm commonly adopted in practice (Lunardi 1991). Hence, Eqn 5.6 can be used to provide a reasonable estimate of the lift step required for jet grouting operations.

Table 5-1. Co-ordinates of centroid and radius of cut

Specimen	CSR (%)	Cut level	Centroid of measurements		Radius of cut from centroid, R'		
			x' (mm)	y' (mm)	Mean (mm)	Std dev (mm)	COV (%)
T1	5.0	Upper	-6.56	-2.92	176.9	8.7	4.9
		Middle	-4.24	-4.48	149.7	8.9	5.9
		Lower	-2.99	-1.31	125.2	8.7	6.9
T2	5.0	Middle	8.90	1.69	188.2	12.9	6.9
		Lower	-6.51	-2.94	183.1	14.3	7.8
T3	5.0	Upper	2.19	2.89	107.2	9.7	9.0
		Middle	6.75	0.87	119.9	8.7	7.3
		Lower	-1.85	1.37	157.4	8.2	5.2
T4	2.5	Middle	-0.19*	5.04*	270.2	4.9	1.8
		Lower	-0.19	5.04	187.2	14.3	7.6
T6	5.0	Upper	-4.80	1.73	175.8	8.1	4.6
		Middle	-6.03	0.98	184.9	11.3	6.1
		Lower	-1.55	3.40	177.1	7.1	4.0
T7	2.5	Middle	3.87	-0.88	107.2	9.7	9.0
		Lower	-2.88	-2.79	119.9	8.7	7.3
T8	7.5	Upper	-8.94	-1.16	107.1	8.8	8.2
		Middle	-6.99	2.81	132.5	8.5	6.4
		Lower	-6.28	4.35	162.5	6.7	4.1
T9	5.0	Upper	1.91	-4.39	215.2	7.2	3.3
		Middle	4.35	0.27	210.4	12.6	6.0
		Lower	0.52	-0.57	192.9	10.1	5.2

*Assumed to be the same as T4 Lower cut

Table 5-2. Moisture content and density of grouted soil (Specimen T9)

Location	Sample	Moisture content of grouted soil (%)	Bulk density of grouted soil ρ_j (kg/m^3)	Density of jetting fluid ρ (kg/m^3)	Calculated ambient density $\rho_{am}=\rho_j^3/\rho$ (kg/m^3)
Upper cut					
T9-1/2U	U1	247.1	1231	1112	1363
	927	227.4	1274	1112	1460
	T3	237.7	1171	1112	1234
T9-3/4U	V4	162.6	1258	1112	1423
	24	156.5	1318	1112	1563
	L93	153.6	1271	1112	1454
T9-5/6U	-		1221	1112	1341
	Average =	197.5	1254		1405
	Std dev =	44.2	46		104
Middle cut					
T9-1/2M	19	304.1	1169	1112	1231
	15	250.8	1259	1112	1425
	A69	254.4	1182	1112	1258
	Average =	269.7	1204		1305
	Std dev =	29.8	48		105
Lower cut					
T9-3/4L	22	285.4	1120	1112	1129
	11	294.3	1133	1112	1156
	E20	250.4	1317	1112	1560
T9-5/6L	19	238.7	1198	1112	1291
	20	234.9	1184	1112	1261
	15	269.0	1168	1112	1226
T9-5/6L	-		1260	1112	1429
	Average =	262.1	1197		1293
	Std dev =	24.7	69		153
Fresh sludge	15		1224	1112	1348
	G3		1281	1112	1477
	T5		1280	1112	1474
	Average =		1262		1433
	Std dev =		32		73

Table 5-3. Jet penetration distance and undrained shear strength at time of jetting

Specimen	Cut level	Nozzle diameter d_n (mm)	Pressure P_i (psi)	Shear strength s_u (kPa)	Jet penetration, l_j		
					Mean (mm)	Std dev (mm)	COV (%)
T1	Upper	1.0	3200	16.9	129.2	8.7	6.7
	Middle		2000	17.1	101.9	9.0	8.8
	Lower		1000	15.9	77.4	8.7	11.2
T2	Upper	1.0	3200	13.7	184.3	14.7	8.0
	Middle		3200	16.3	140.5	12.9	9.2
	Lower		3200	16.0	135.4	14.3	10.6
T3	Upper	2.5	100	18.3	59.5	9.7	16.3
	Middle		200	20.2	72.2	8.7	12.0
	Lower		300	20.7	109.7	8.2	7.5
T4	Middle	1.0	2000	5.6	225.9	5.2	2.3
	Lower		1000	4.7	139.4	14.3	10.3
T6	Upper	1.0	3200	22.9	127.9	8.1	6.3
	Middle		3200	23.3	137.1	11.3	8.2
	Lower		3200	21.0	129.2	7.1	5.5
T7	Middle	2.5	100	4.1	116.8	5.3	4.5
	Lower		300	4.2	180.9	15.4	8.5
T8	Upper	1.0	1000	34.2	59.5	8.8	14.8
	Middle		2100	35.8	84.9	8.5	10.0
	Lower		3250	38.8	114.9	6.7	5.8
T9	Upper	1.0	3400	14.4	167.5	7.2	4.3
	Middle		3350	16.4	162.6	12.6	7.7
	Lower		3350	19.2	145.2	10.1	7.0

Table 5-4. Summary of key parameters for jet grout trials in case histories

Reference	Col. No.	Nozzle diameter	Pump Pressure	Undrained shear strength	Column diameter	Jet penetration distance	Ultimate bearing capacity
		d_n (mm)	P_i (MPa)	s_u (kPa)	D (mm)	l_j (mm)	$q_{bu} = 2.4s_u$ (kPa)
Davie et al. (2003)	I	1.8	47.5 to 55	65	582.0±59.4	246.0±29.7	156
	II		50		534.2±56.3	222.1±28.1	
	IIa		50		524.8±40.0	217.4±20.0	
	III		55		632.1±14.9	271.1±7.5	
Durgunoglu et al. (2003)	3/F	2.0	50	50	575	242.5	120
	4/G	2.2			575	242.5	
	8/P	2.0			705	307.5	
Duzceer and Golkap (2003)	TT1	2.4	45	25	793	351.5	60
	TT2		47.5		823	366.5	
	TT4		47.5		918	414.0	
	TT6		47.5		787	348.5	
Samano et al. (1999)	G2	2.0	46	10	1030	470	24
	G3		24		840	375	
	G4		12		630	270	
	G5		46		1110	510	
	G6		24		920	415	
	G7		12		710	310	

Table 5-5. Interpreted parameters at equilibrium point for laboratory jetting tests

Specimen	Cement-soil CSR (%)	Soil strength at time of jetting s_u (kPa)	Cut level	Equilibrium length x_s (mm)		Equilibrium radius r_s (mm)		Jet-soil interface shear resistance τ_u (Pa)	
				Mean	Std dev	Mean	Std dev	Mean	Std dev
T2	5.0	16.3	Middle	130.8	14.5	10.5	1.2	20.3	4.5
		16.0	Lower	129.6	20.6	10.4	1.6	21.5	7.8
T3	5.0	18.3	Upper	47.7	8.7	3.8	0.7	47.0	17.0
		20.2	Middle	61.0	11.5	4.9	0.9	49.1	20.7
		20.7	Lower	75.1	24.6	6.0	2.0	53.1	36.9
T4	2.5	5.6	Middle	191.2	4.4	15.3	0.4	6.5	0.7
		4.7	Lower	131.2	12.5	10.5	1.0	8.4	2.0
T6	5.0	22.9	Upper	93.6	8.9	7.5	0.7	37.6	7.5
		23.3	Middle	107.1	13.3	8.6	1.1	28.9	5.9
		21.0	Lower	108.8	19.5	8.7	1.6	31.4	13.9
T7	2.5	4.1	Upper	91.1	16.0	7.2	1.5	13.9	9.0
		4.2	Lower	167.5	15.4	13.4	1.2	7.9	1.6
T8	7.5	34.2	Upper	53.4	13.3	4.3	1.1	45.3	14.9
		35.8	Middle	76.1	9.2	6.1	0.7	42.9	11.7
		38.8	Lower	106.6	11.2	8.5	0.9	29.4	6.4
T9	5.0	14.4	Upper	151.1	13.0	12.1	1.0	12.9	2.6
		16.4	Middle	145.1	17.7	11.6	1.4	20.3	4.5
		19.2	Lower	133.4	7.0	10.7	0.6	21.5	7.8

Table 5-6. Computed equilibrium point co-ordinates and jet width for field trials

Reference	Col. No.	Undrained shear strength	Pump Pressure		Jet penetration distance	P_i/s_u ratio	Equilibrium point		Jet width
		s_u (kPa)	P_i (MPa)	P_i (psi)	l_j (mm)		x_s (mm)	r_s (mm)	w_j (mm)
Davie et al. (2003)	III	65	55	7977	271.1±7.5	846	250.9	20.1	40.2
Durgunoglu et al. (2003)	3/F	50	50	7252	242.5	1000	224.5	18.0	36.0
	4/G				242.5	1000	224.5	18.0	36.0
	8/P				307.5	1000	284.7	22.8	45.6
Duzceer and Golkap (2003)	TT1	25	45	6526	351.5	1800	325.5	26.0	52
	TT2		47.5	6889	366.5	1900	339.4	27.2	54.4
	TT4		47.5	6889	414.0	1900	383.3	30.7	61.4
	TT6		47.5	6889	348.5	1900	322.7	25.8	51.6
Samano et al. (1999)	G2	10	46	6671	470	4600	435.2	34.8	69.6
	G3		24	3480	375	2400	347.2	27.8	55.6
	G4		12	1740	270	1200	250.0	20.0	40.0
	G5		46	6671	510	4600	472.2	37.8	75.6
	G6		24	3480	415	2400	384.3	30.7	61.4
	G7		12	1740	310	1200	287.0	23.0	46

Specimen	Cut level	d_n (mm)	P_i (psi)	R_s (rpm)	N_r (rev)	CSR (%)	l_i (mm)	
							Mean	Std dev
T1	Upper	1.0	3200	10	10	5.0	129.2	8.7
	Middle		2000				101.9	9.0
	Lower		1000				77.4	8.7
T9	Upper	1.0	3400	10	10	5.0	167.5	7.2
	Middle		3350				162.6	12.6
	Lower		3350				145.2	10.1

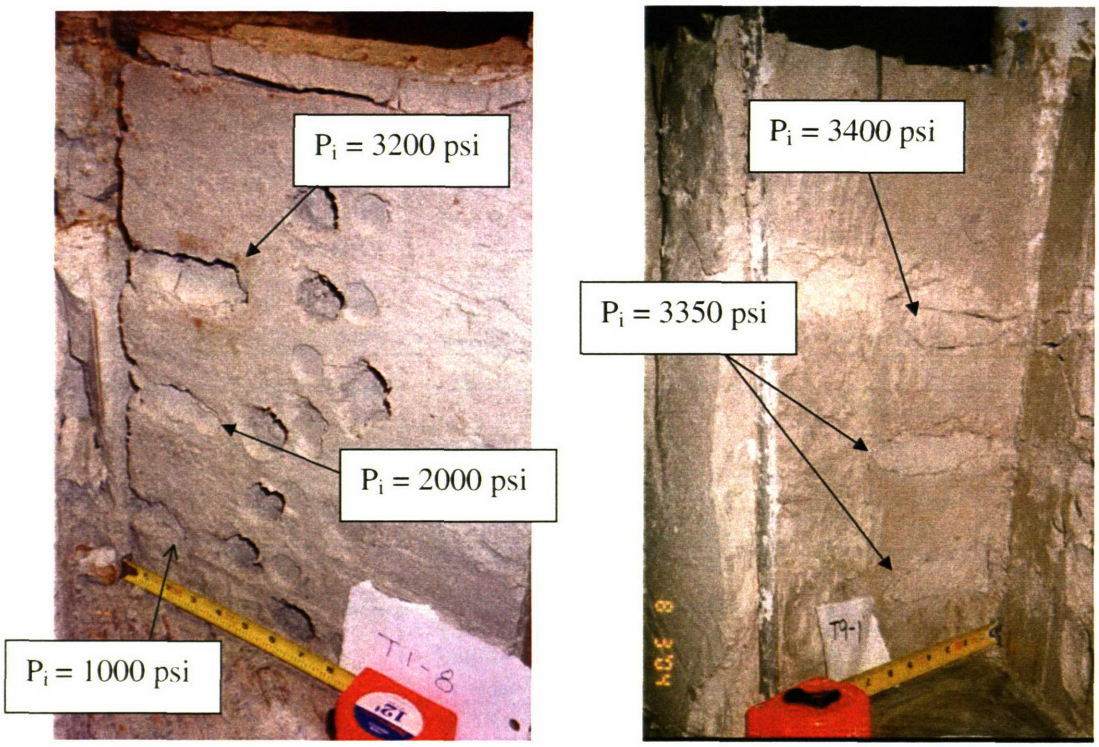

(a) Section T1-8 (b) Section T9-1

Figure 5-1. High pressure tests in specimens with CSR = 5 %
- cuts are deep and well developed

Specimen	Cut level	d_n (mm)	P_i (psi)	R_s (rpm)	N_r	CSR (%)	l_i (mm)	
							Mean	Std dev
T3	Upper	1.0	100	10	10	5.0	59.5	9.7
	Middle		200				72.2	8.7
	Lower		300				109.7	8.2

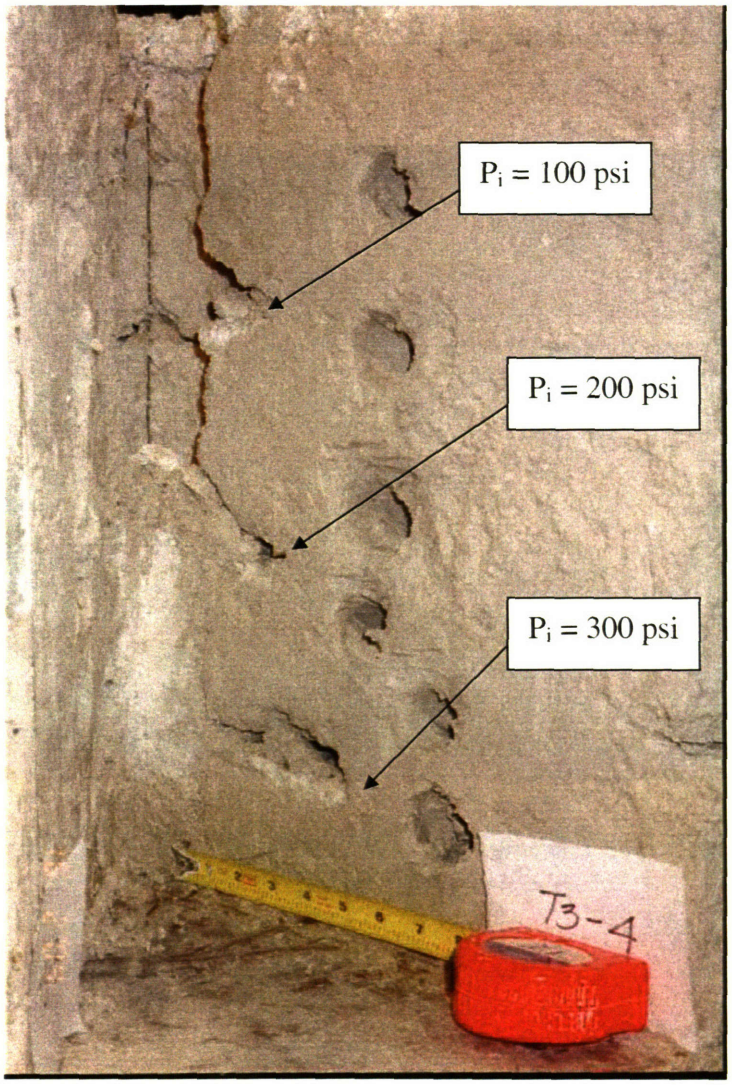

Figure 5-2. Low pressure test in specimen with CSR = 5 %
- cuts are shallow and thin

Specimen	Cut level	d_n (mm)	P_i (psi)	R_s (rpm)	N_r	CSR (%)	l_j (mm)	
							Mean	Std dev
T4	Middle Lower	1.0	2000 1000	10	10	2.5	225.9 139.4	5.2 14.3

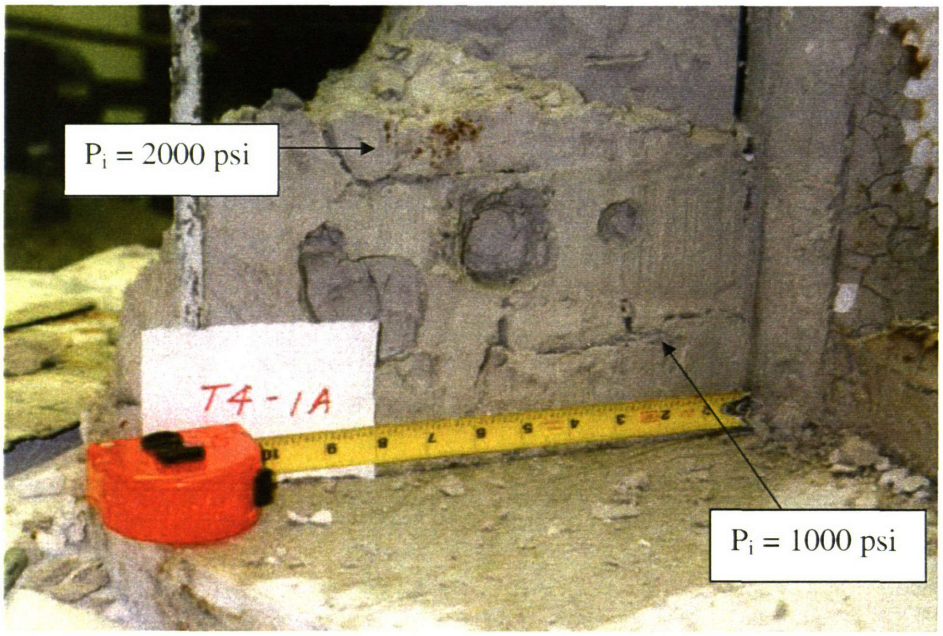

Figure 5-3. High pressure test in specimen with CSR = 2.5 %
- cuts are deep and well developed

Specimen	Cut level	d_n (mm)	P_i (psi)	R_s (rpm)	N_r	CSR (%)	l_j (mm)	
							Mean	Std dev
T7	Upper	1.0	100	10	10	2.5	116.8	5.3
	Lower		300				180.9	15.4

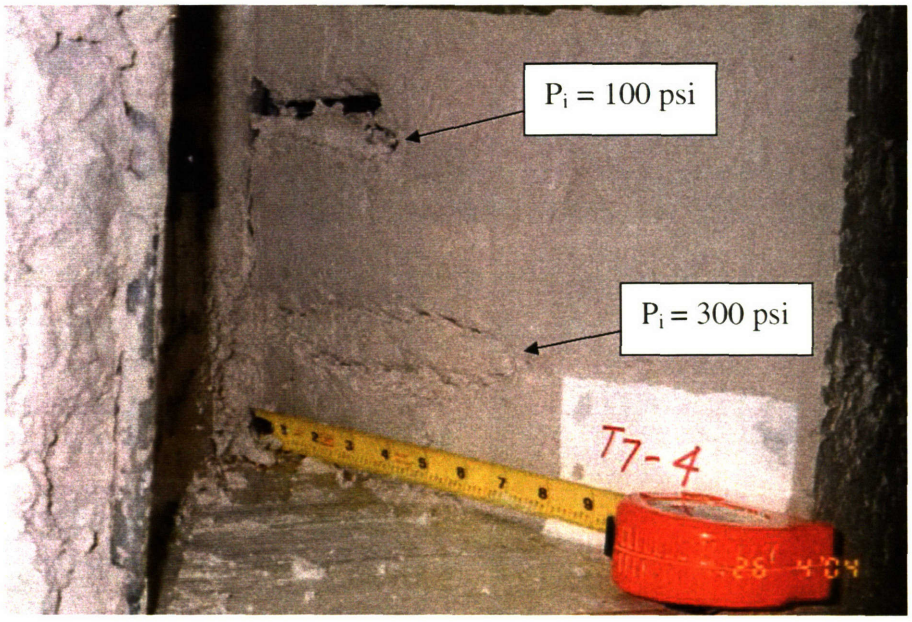

Figure 5-4. Low pressure test in specimen with CSR = 2.5 %
- cut is deep and well developed

Specimen	Cut level	d_n (mm)	P_i (psi)	R_s (rpm)	N_r	CSR (%)	l_j (mm)	
							Mean	Std dev
T8	Upper	1.0	1000	10	10	7.5	59.5	8.8
	Middle		2100				84.9	8.5
	Lower		3250				114.9	6.8

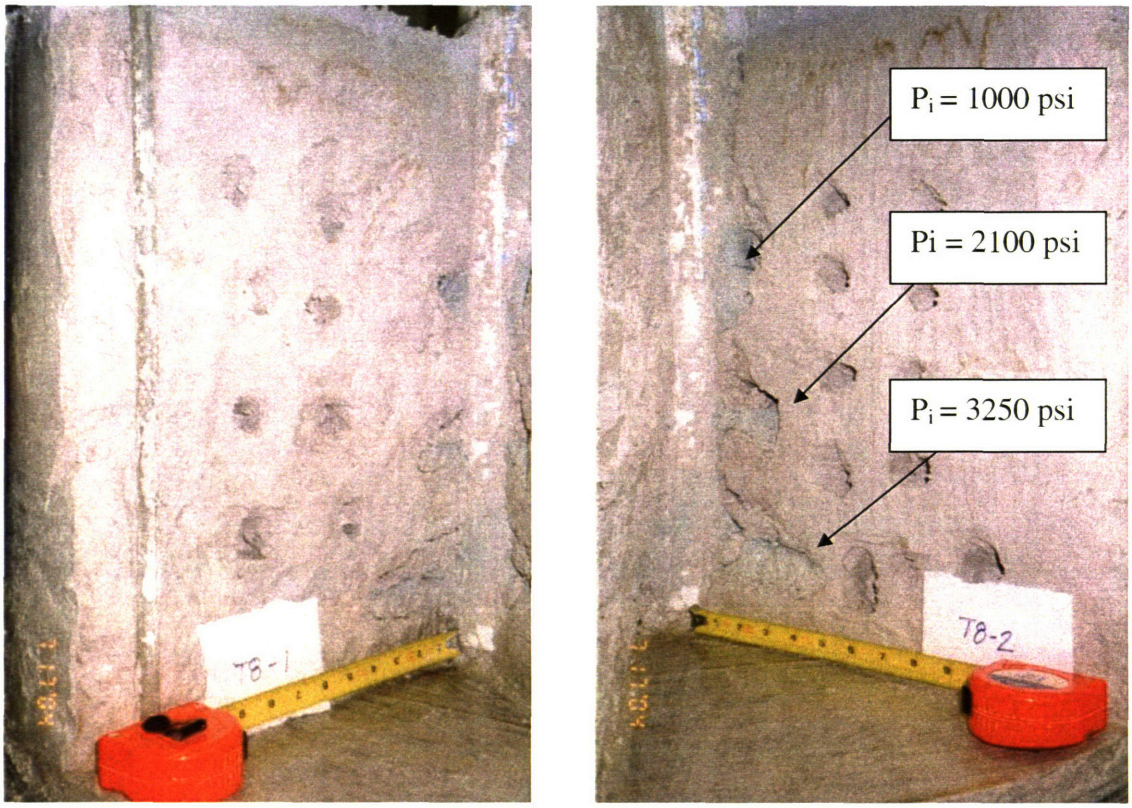

Figure 5-5. High pressure test in specimen with CSR = 7.5 %
- significant attenuation of jet penetration

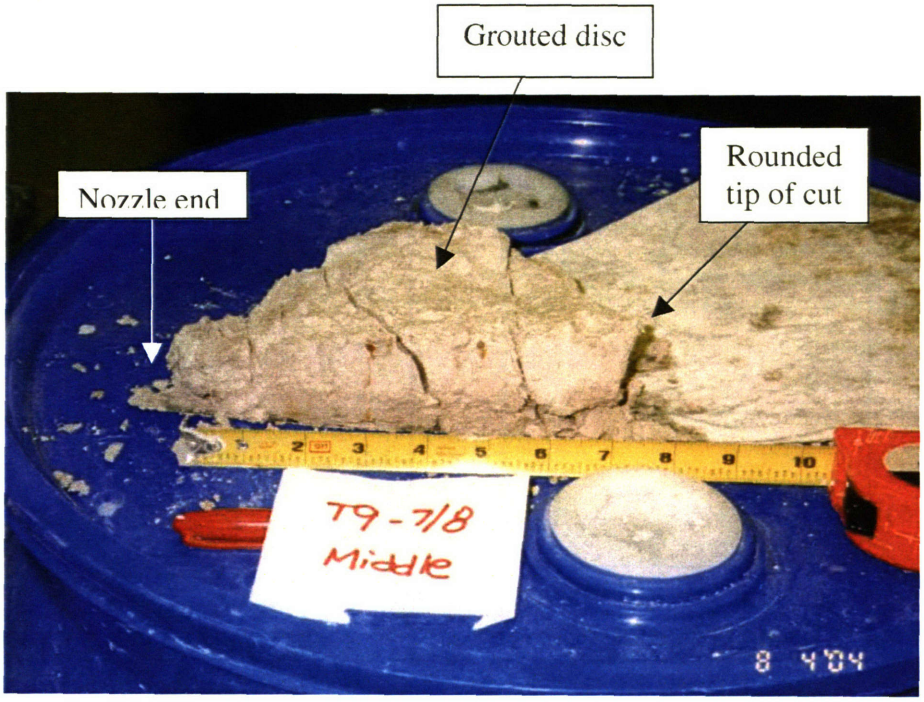

Figure 5-6. Radial section through grouted disc

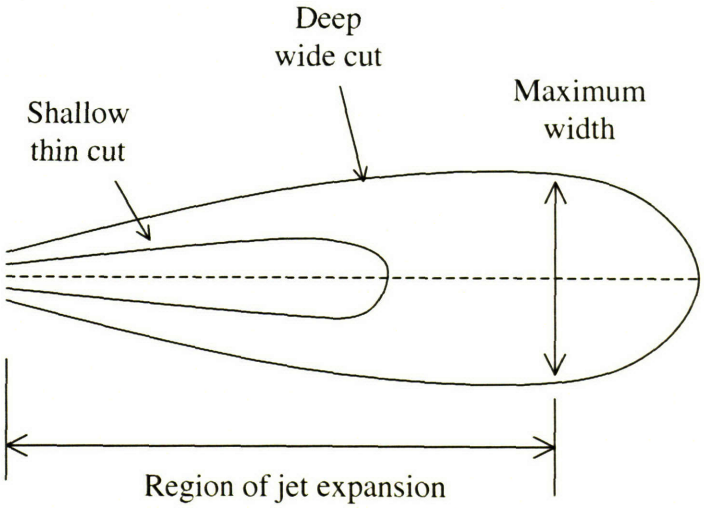

Figure 5-7. Characteristic shape of cut

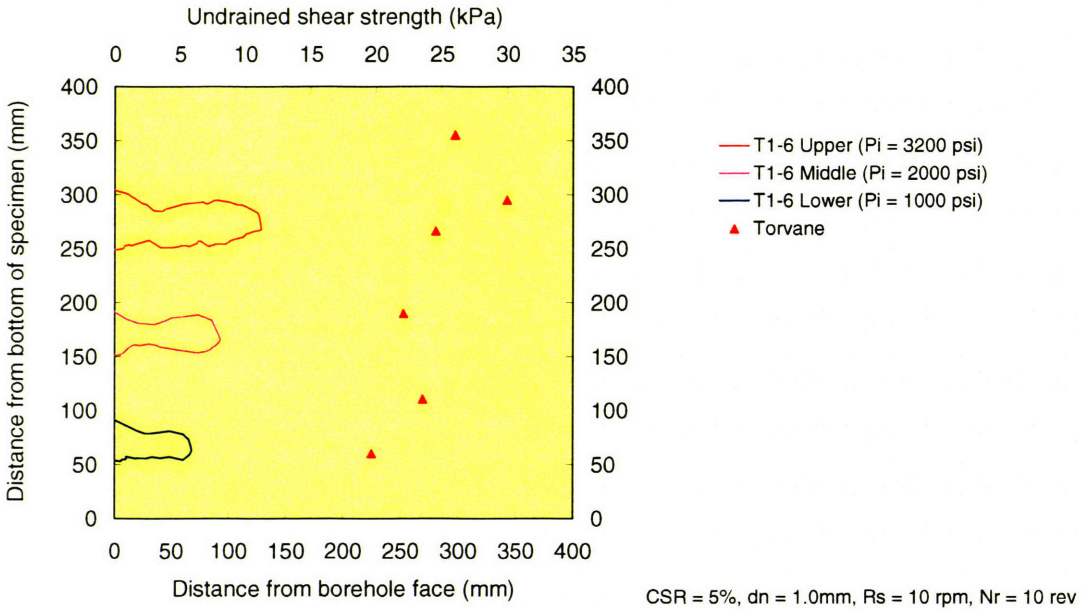

Figure 5-8(a) Vertical profile for Specimen T1, Section 6

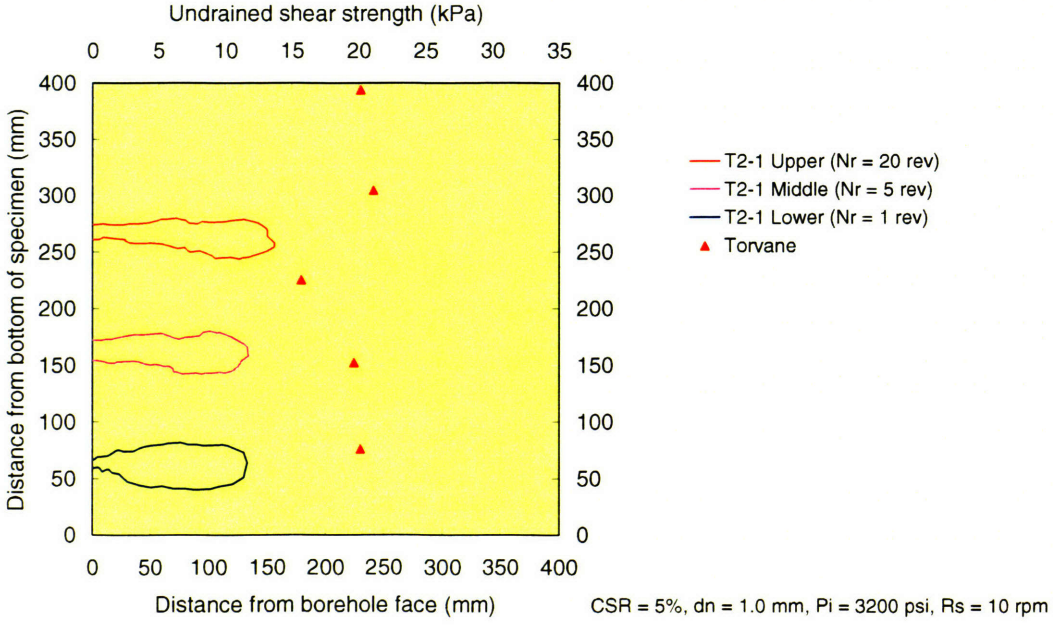

Figure 5-8(b). Vertical profile for Specimen T2, Section 1

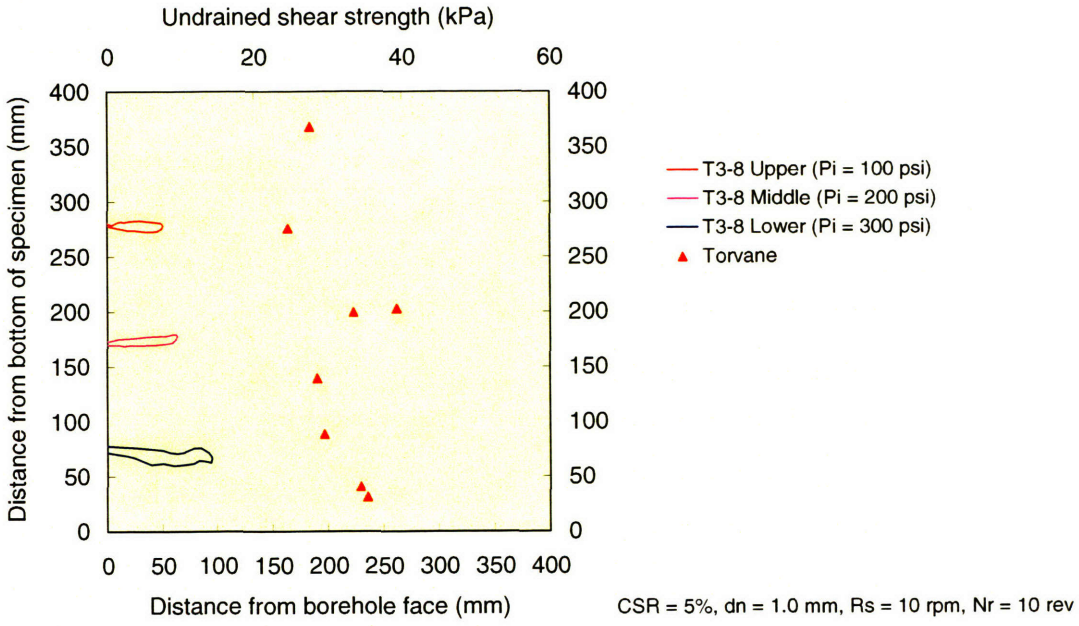

Figure 5-8(c). Vertical profile for Specimen T3, Section 3

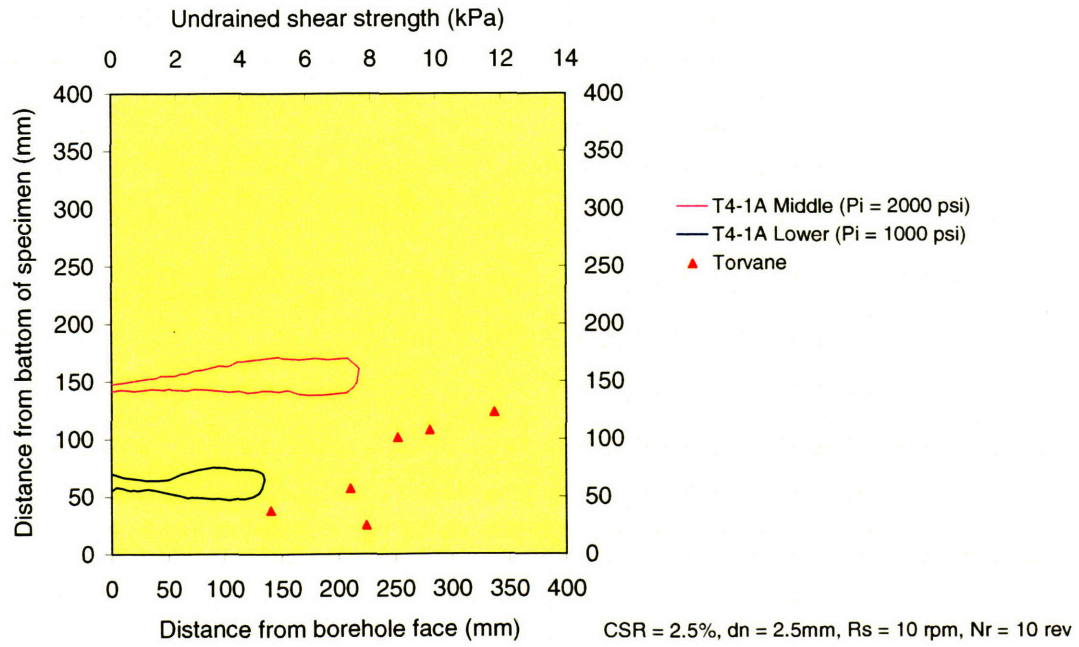

Figure 5-8(d). Vertical profile for Specimen T4, Section 1A

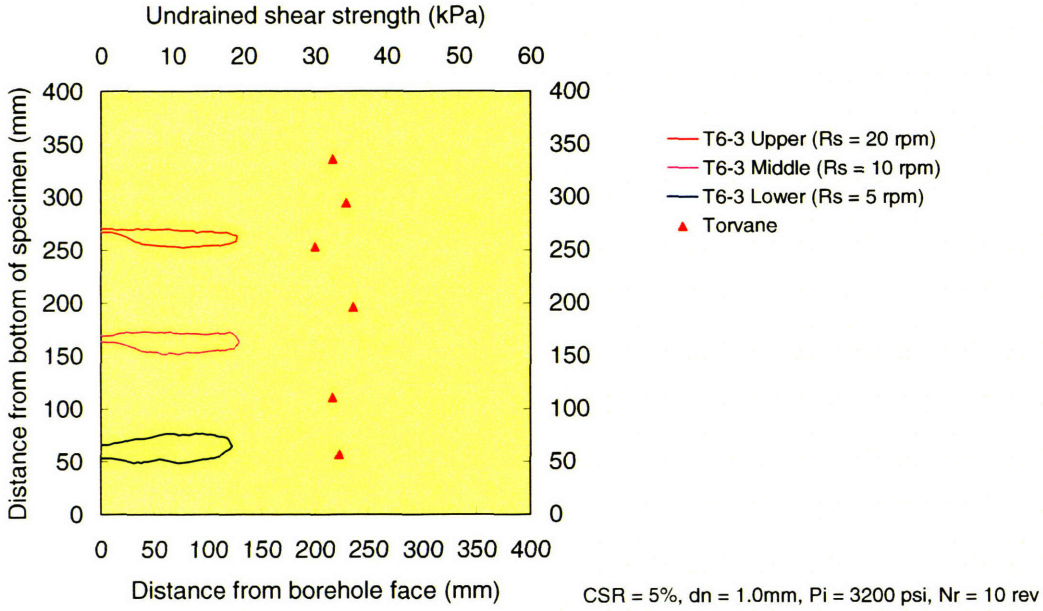

Figure 5-8(e). Vertical profile for Specimen T6, Section 3

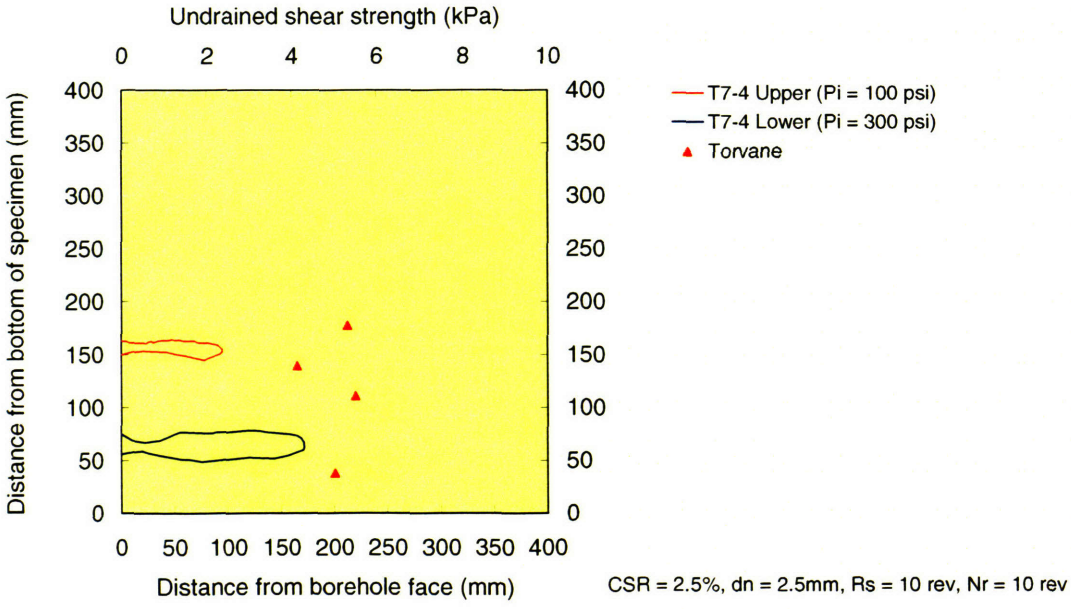

Figure 5-8(f). Vertical profile for Specimen T7, Section 4

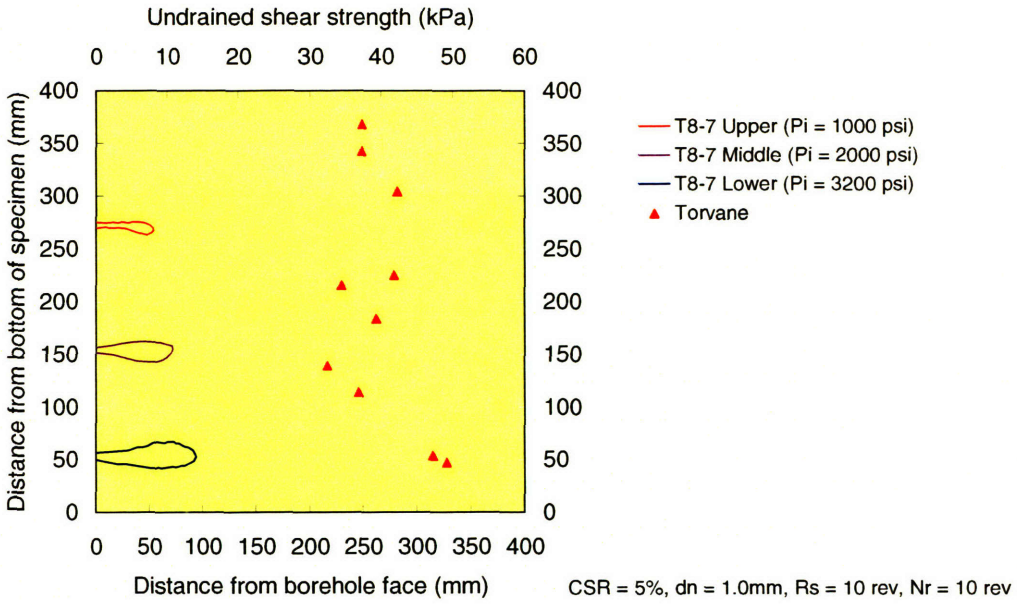

Figure 5-8(g). Vertical profile for Specimen T8, Section 7

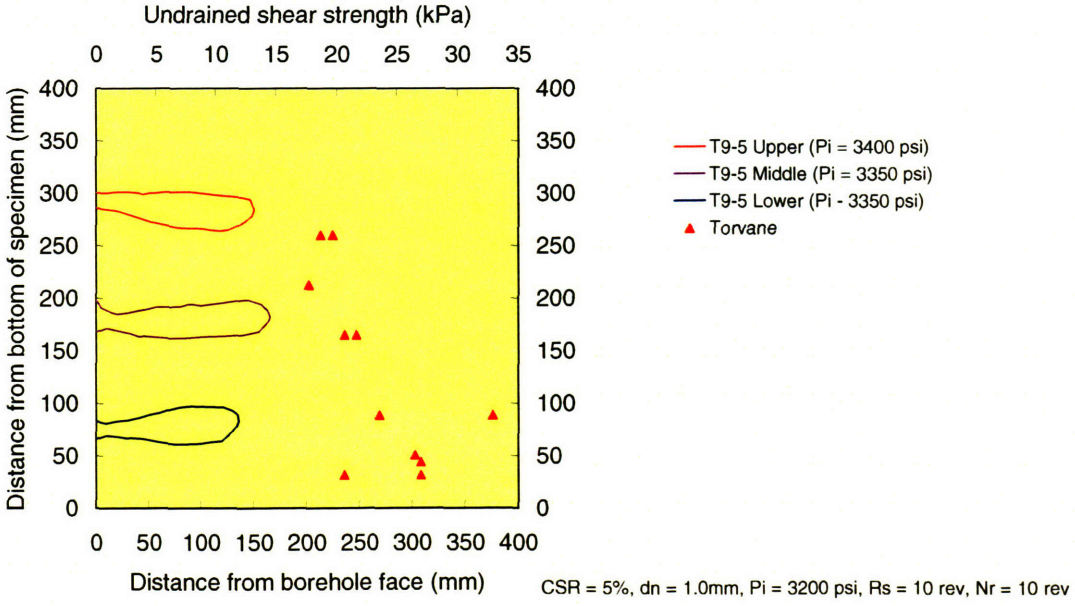

Figure 5-8(h). Vertical profile for Specimen T9, Section 5

Specimen/ Cut level	CSR (%)	d_n (mm)	R_s (rpm)	N_r (rev)	P_i (psi)
T4 Lower	2.5	1.0	10	10	1000
T1 Lower	5.0				
T8 Upper	7.5				

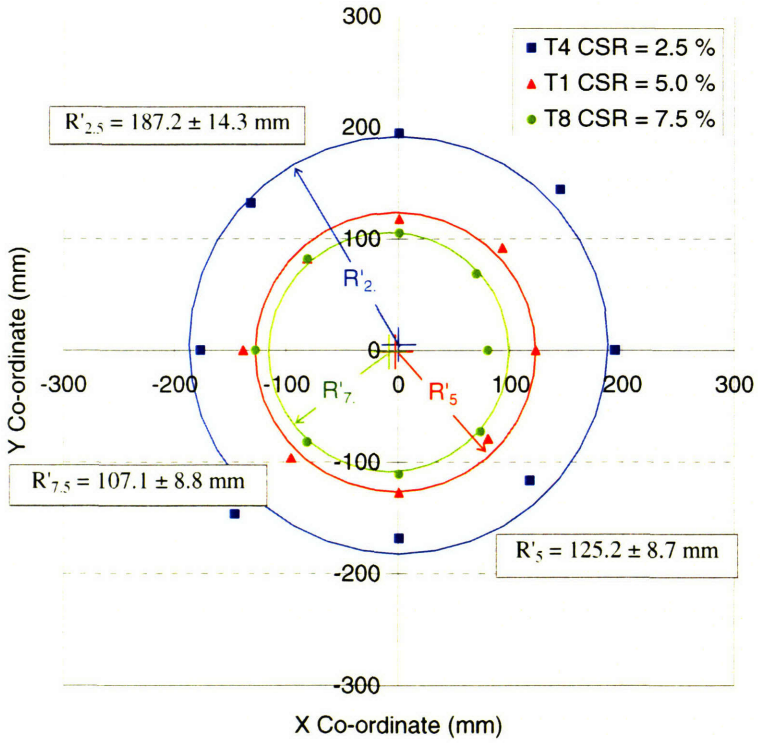

Figure 5-9. Typical plan profile showing the mean radii of grouted discs

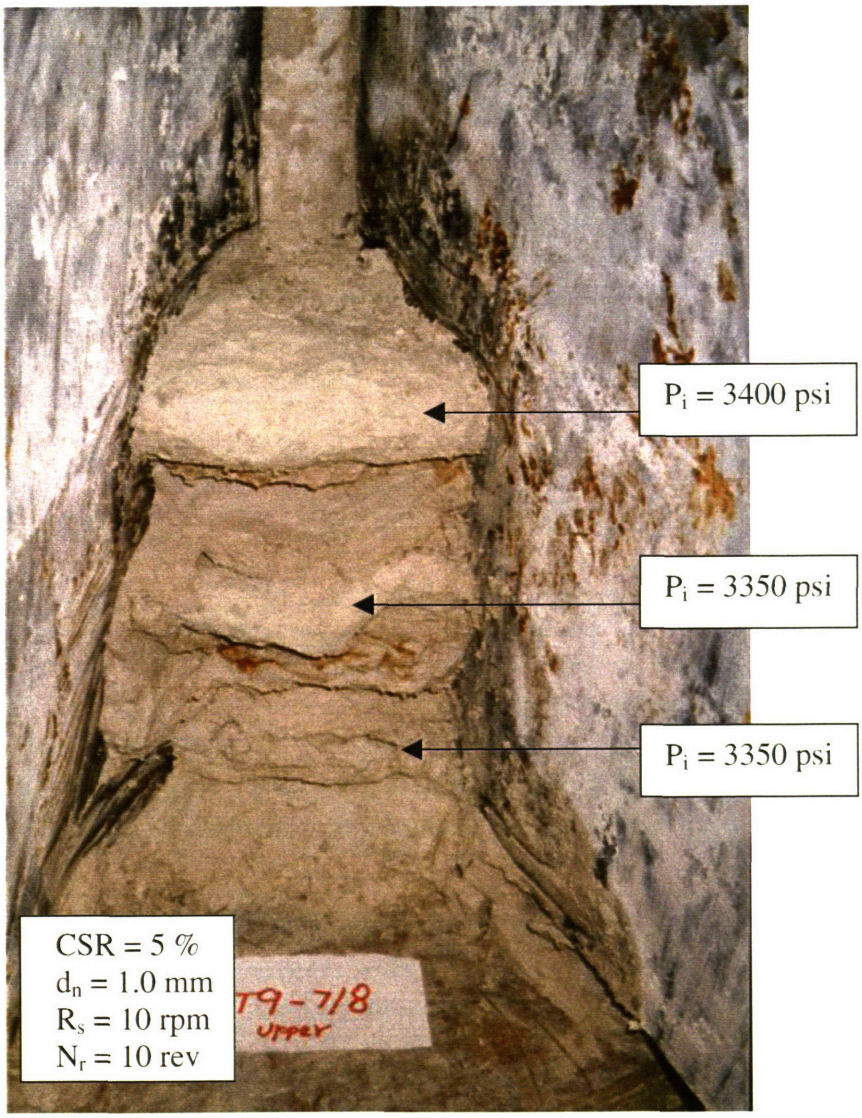

Figure 5-10. Exhumed grouted discs in Specimen T9 (Segment 7/8) showing three virtually identical cuts

Specimen/ Cut level	P_i (psi)	d_n (mm)	R_s (rpm)	N_r (rev)	CSR (%)
T9 Upper	3400	1.0	10	10	5.0 %
T9 Middle	3350				
T9 Lower	3350				

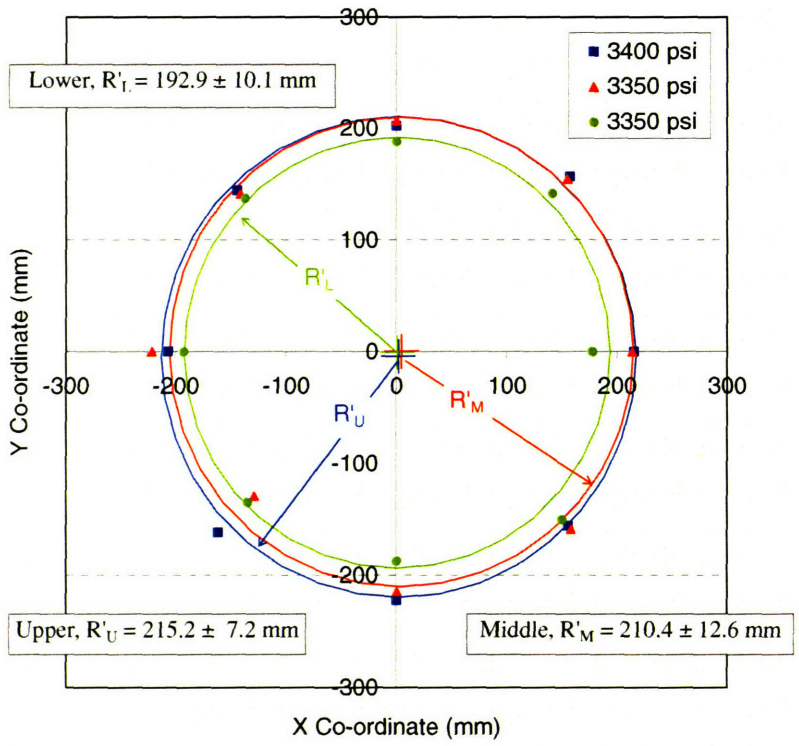

Figure 5-11. Plan profile of grouted discs exhumed in Specimen T9 (CSR = 5.0 %)

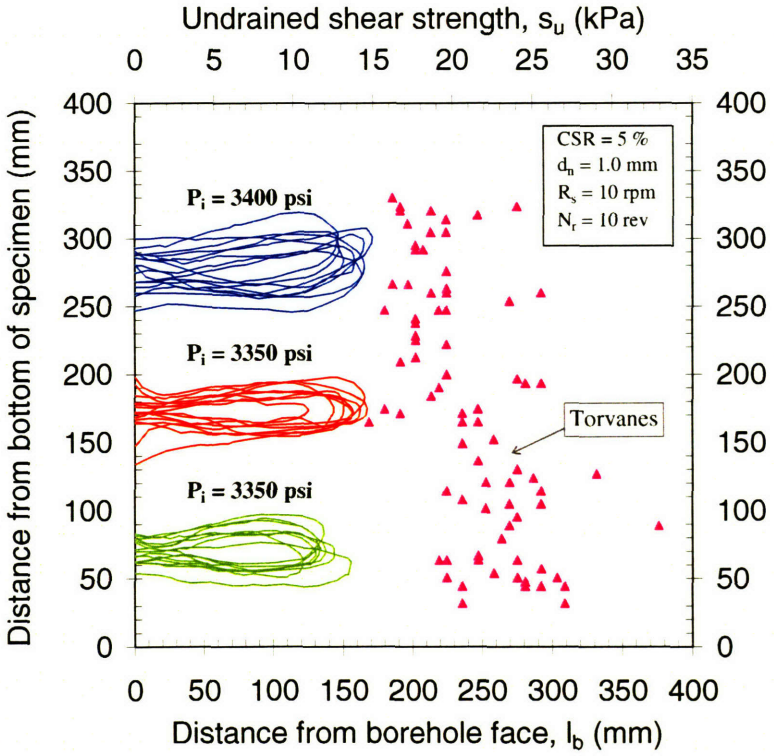

Figure 5-12. Vertical profile of cuts and torvane shear strength in Specimen T9

Test	s_u (kPa)		R' (mm)	
	Mean	Std dev	Mean	Std dev
▲ T9 Upper	19.2	2.4	215.2	7.2
■ T9 Middle	20.4	3.1	210.4	12.6
● T9 Lower	23.8	2.9	192.9	10.1

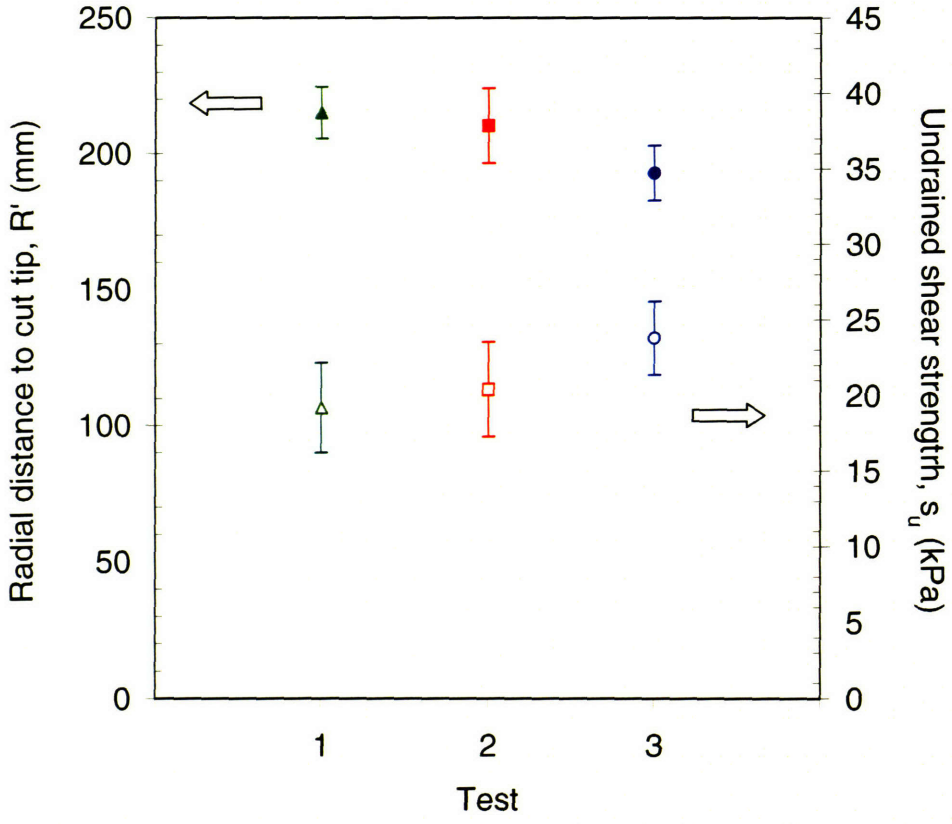

τ_cFigure 5-13. Comparison of test results in relation to shear strength of soil (Specimen T9)

Specimen/ Cut level	R_s (rpm)	d_n (mm)	P_i (psi)	N_r (rev)	CSR (%)
T6 Upper	20	1.0	3200	10	5.0 %
T6 Middle	10				
T6 Lower	5				

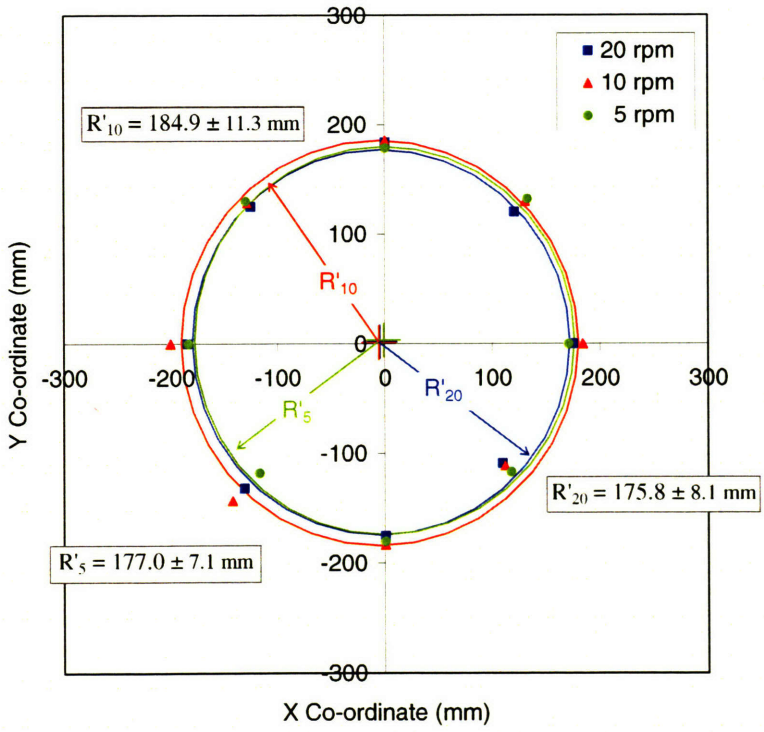

Figure 5-14. Variation of mean radius of cut with rotation speed (T6, CSR = 5 %)

Test	R_s (rpm)	R' (mm)	
		Mean	Std dev
◆ T6 Upper	20	175.8	8.1
■ T6 Middle	10	184.9	11.3
▲ T6 Lower	5	177.1	7.1

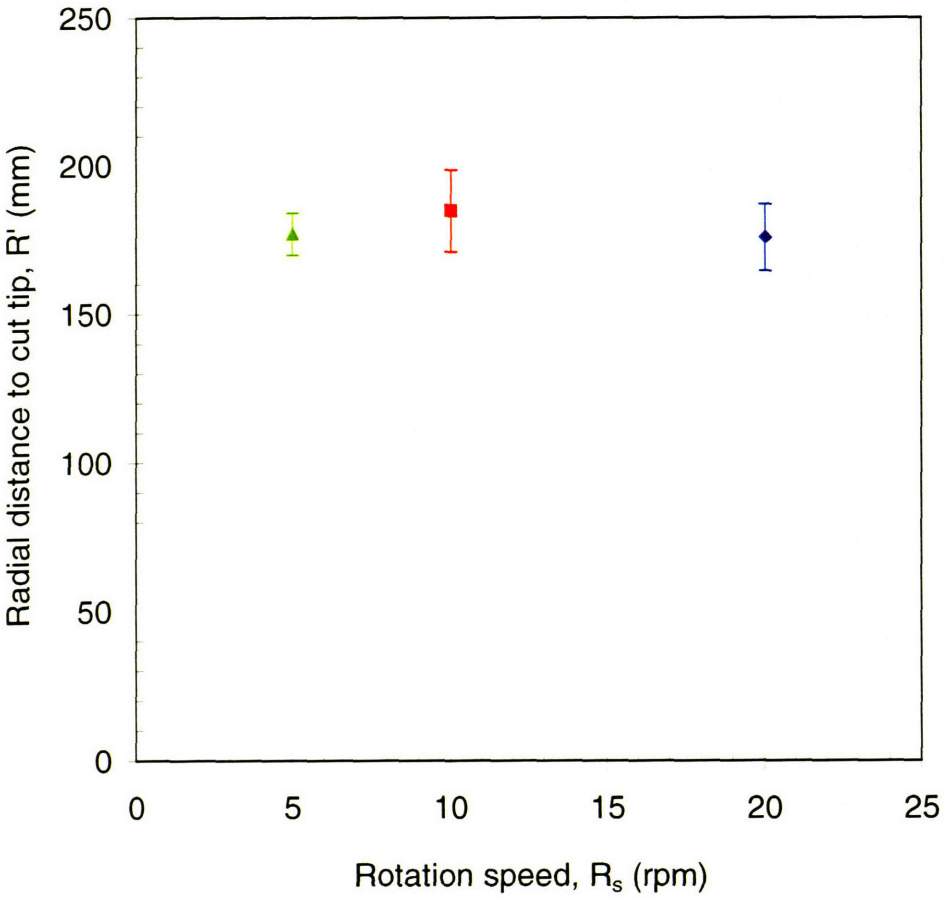

Figure 5-15. Effect of rotation speed on mean radius of cut
(CSR = 5%, d_n = 1.0mm, P_i = 3200 psi, N_r =10 rev)

Specimen/Cut level	N_r (rev)	d_n (mm)	P_i (psi)	R_s (rpm)	CSR (%)
T1 Upper	10	1.0	3200	10	5.0
T2 Middle	5				
T2 Lower	1				

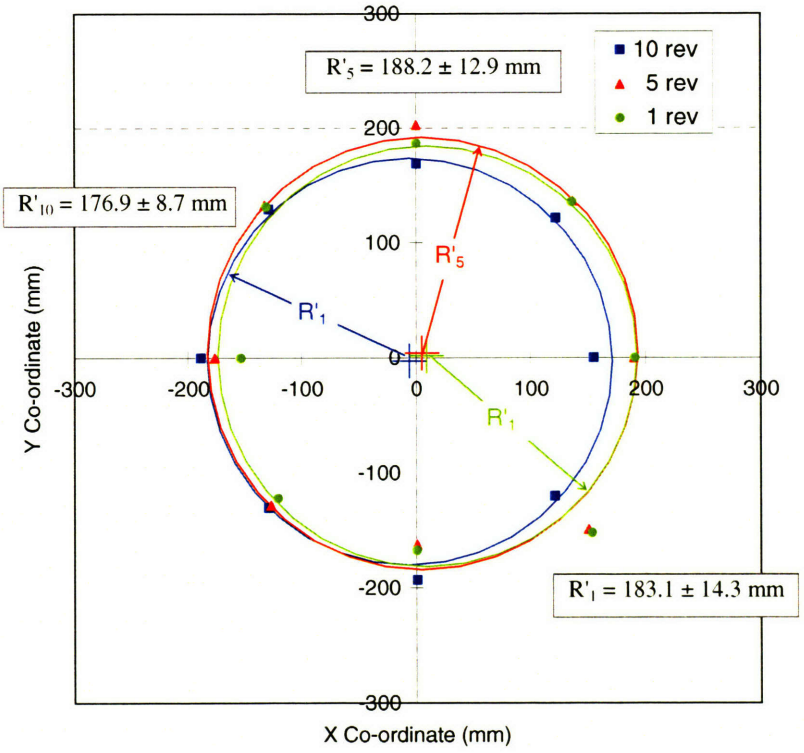

Figure 5-16. Variation of mean radius of cut with number of revolutions of nozzle (T1 and T2, CSR = 5.0 %)

Test	N_r (rev)	R' (mm)	
		Mean	Std dev
● T1 Upper	10	176.9	8.78
■ T2 Middle	5	188.2	12.9
▲ T2 Lower	1	183.1	14.3

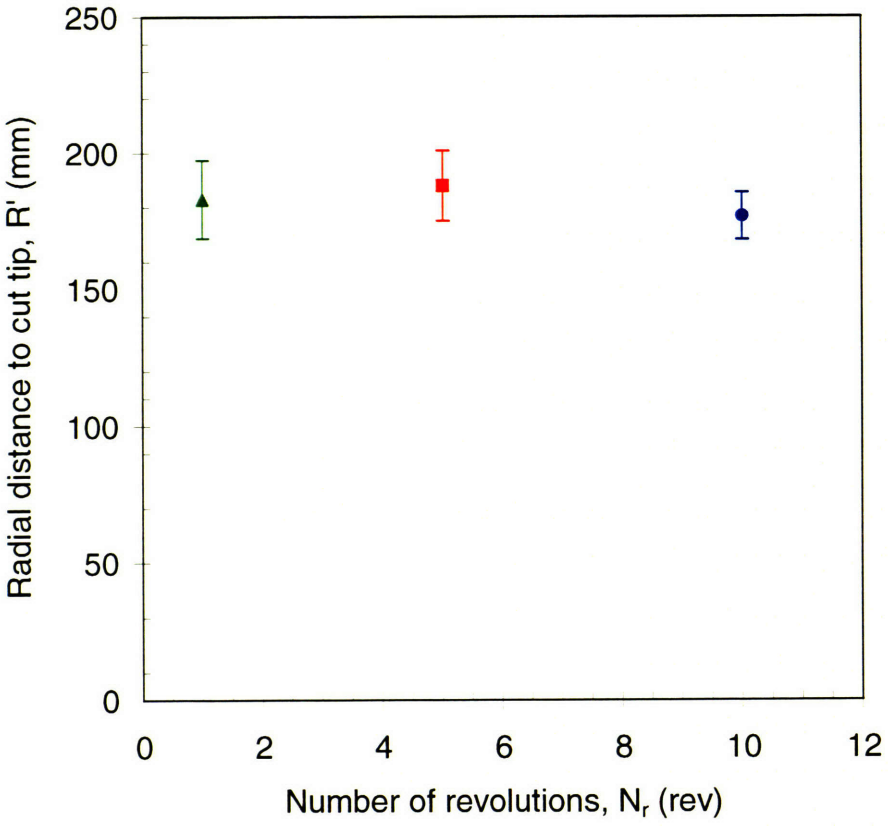

Figure 5-17. Effect of number of revolutions on mean radius of cut
(CSR = 5%, d_n = 1.0mm, P_i = 3200 psi, R_s = 10 rpm)

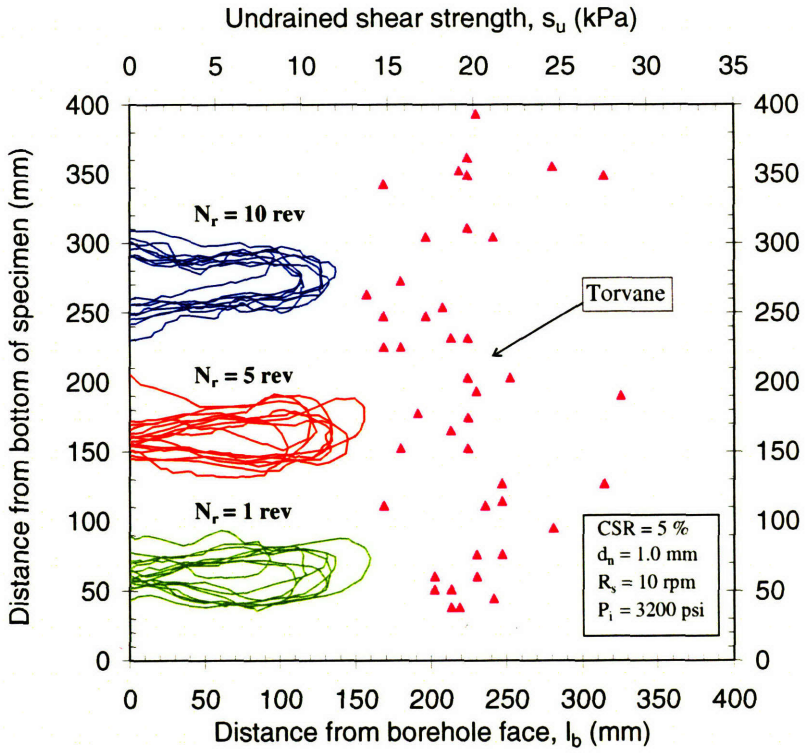

Figure 5-18. Vertical profile of cuts and torvane shear strength (Specimen T1 Upper, T2 Middle and T2 Lower)

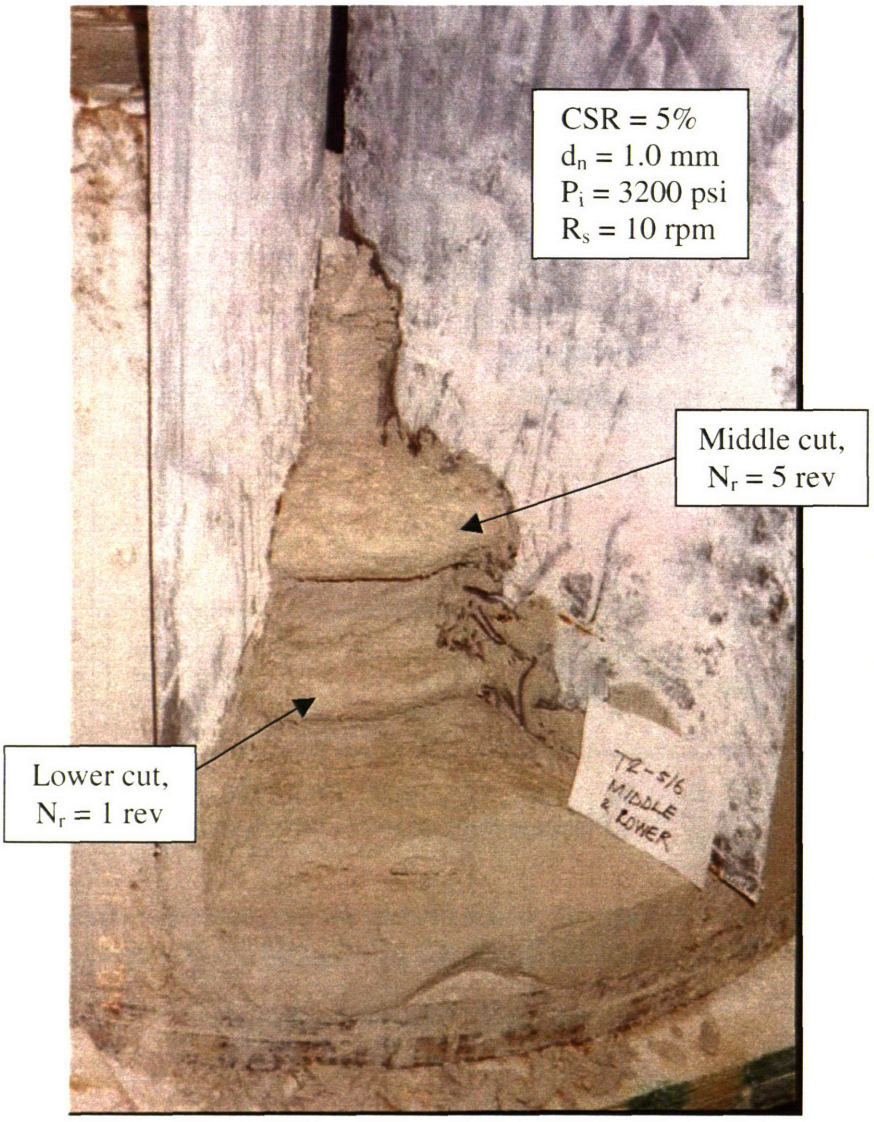

Figure 5-19. Exhumed grouted disc in Specimen T2 (Segment 5/6, Middle and Lower) showing very similar cuts for different number of revolutions of the nozzle

Specimen/ Cut level	P_i (psi)	d_n (mm)	R_s (rpm)	N_r (rev)	CSR (%)
T1 Upper	3200	1.0	10	10	5.0
T1 Middle	2000				
T1 Lower	1000				

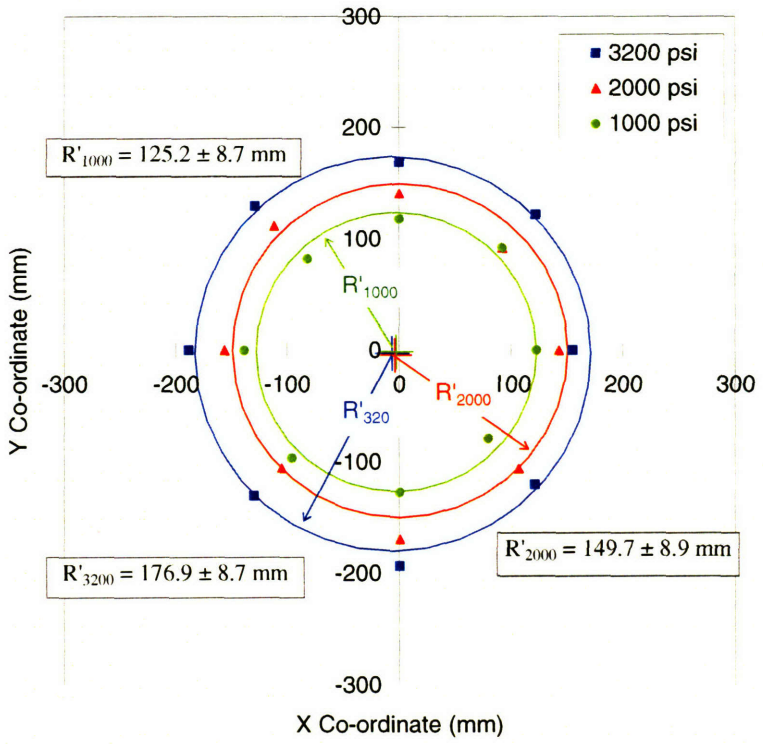

Figure 5-20. Variation of mean radius of cut with jetting pressure (T1, CSR = 5.0 %)

Specimen/Cut level	P_i (psi)	d_n (mm)	R_s (rpm)	N_r (rev)	CSR(%)
T4 Middle	2000	1.0	10	10	2.5
T4 Lower	1000				

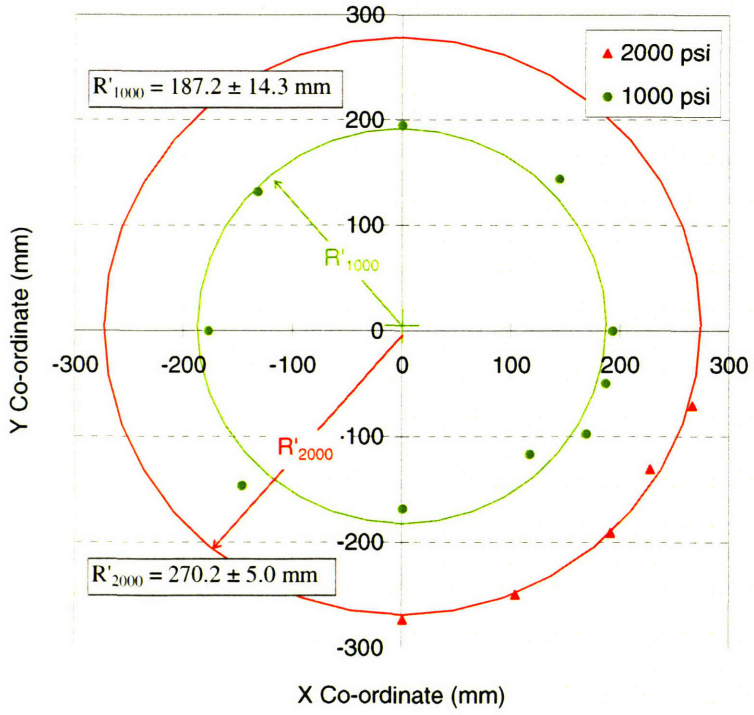

Figure 5-21. Variation of mean radius of cut with jetting pressure (T4, CSR = 2.5 %)

Specimen/ Cut level	P_i (psi)	d_n (mm)	R_s (rpm)	N_r (rev)	CSR (%)
T8 Upper	1000	1.0	10	10	7.5 %
T8 Middle	2100				
T8 Lower	3250				

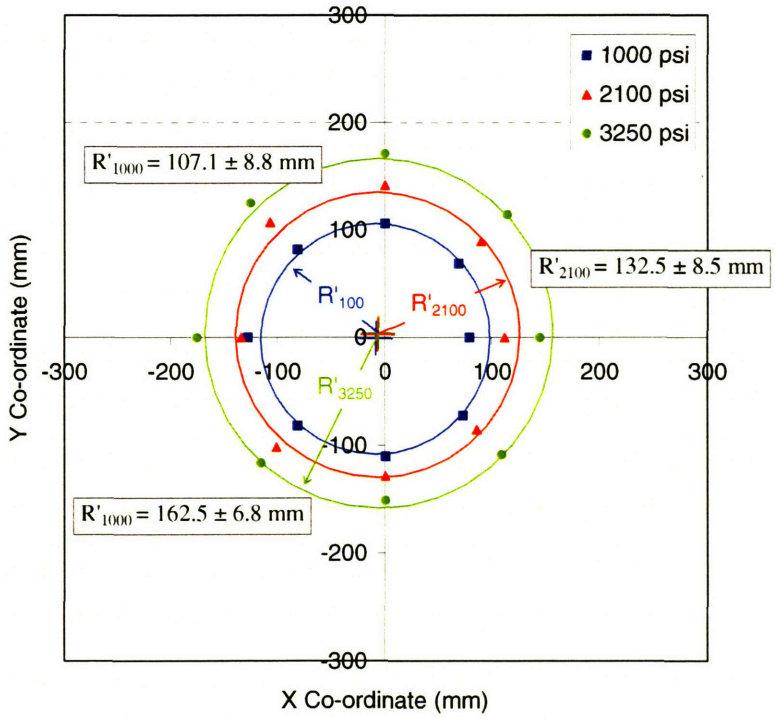

Figure 5-22. Variation of mean radius of cut with jetting pressure (T8, CSR = 7.5 %)

Specimen/ Cut level	P_i (psi)	d_n (mm)	R_s (rpm)	N_r (rev)	CSR (%)
T3 Upper	100	2.5	10	10	5.0 %
T3 Middle	200				
T3 Lower	300				

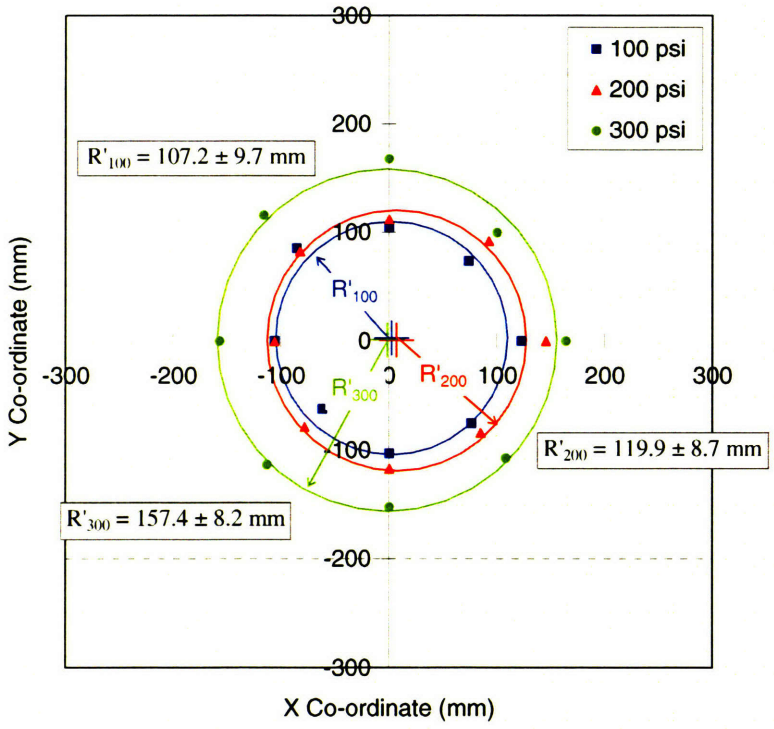

Figure 5-23. Variation of mean radius of cut with jetting pressure (T3, CSR 5.0 %)

Specimen/Cut level	P_i (psi)	d_n (mm)	R_s (rpm)	N_r (rev)	CSR(%)
T7 Upper	100	2.5	10	10	2.5
T7 Lower	300				

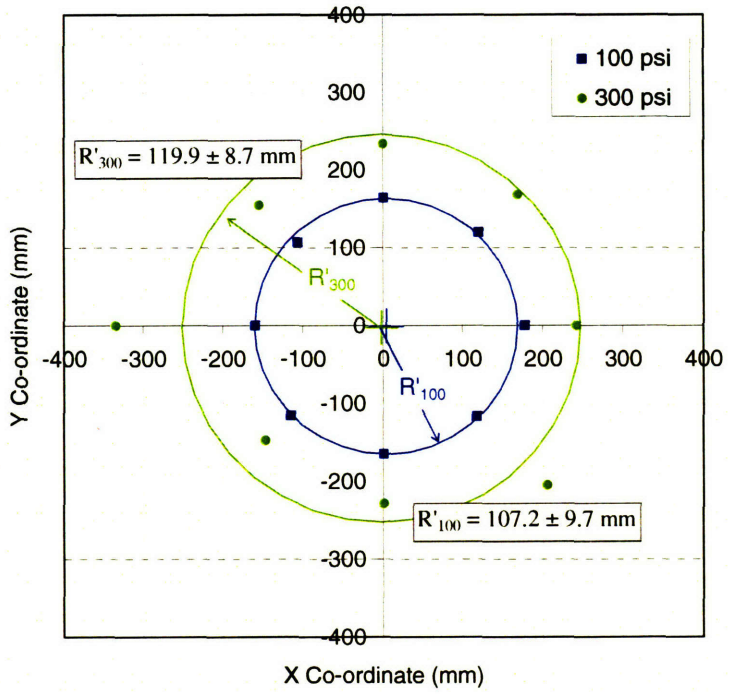

Figure 5-24. Variation of mean radius of cut with jetting pressure (T7, CSR = 2.5 %)

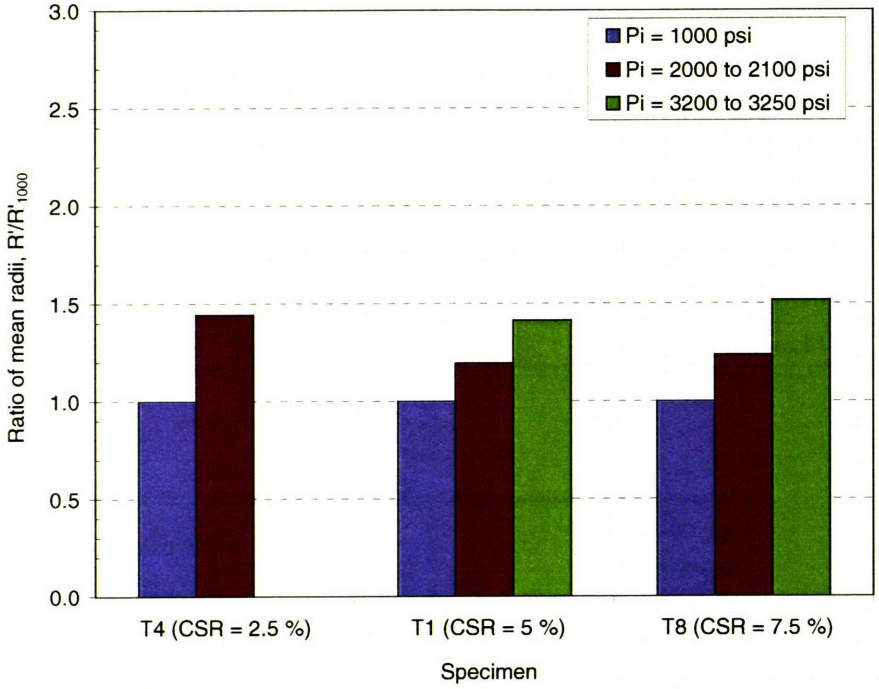

(a) High pressure tests (d_n = 1.0 mm)

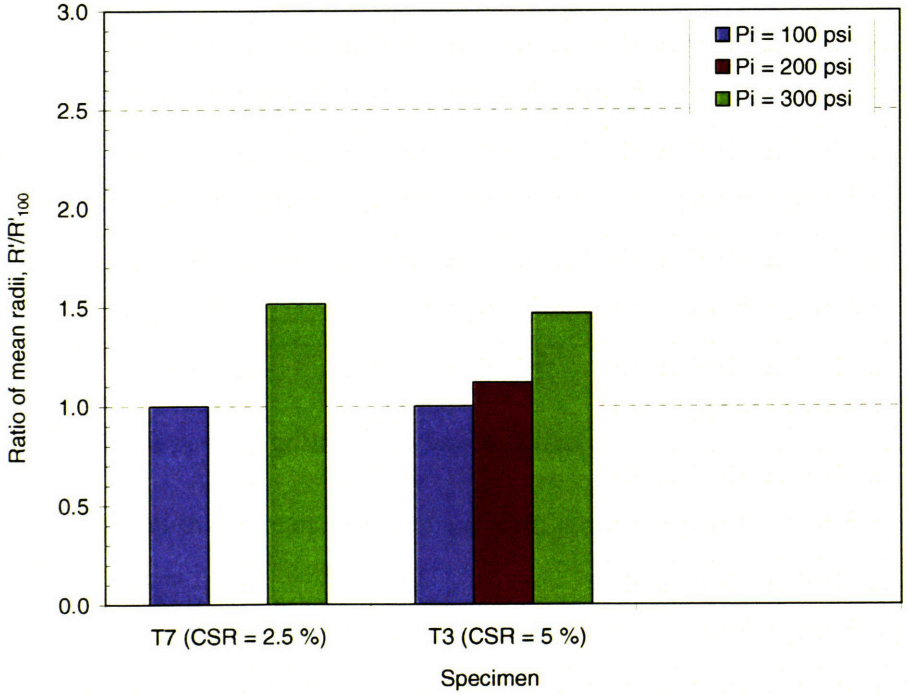

(b) Low pressure tests (d_n = 2.5 mm)

Figure 5-25. Relative increase in mean radius of cut with increasing jetting pressures

Specimen/ Cut level	CSR (%)	d_n (mm)	R_s (rpm)	N_r (rev)	P_i (psi)
T4 Lower	2.5	1.0	10	10	1000
T1 Lower	5.0				
T8 Upper	7.5				

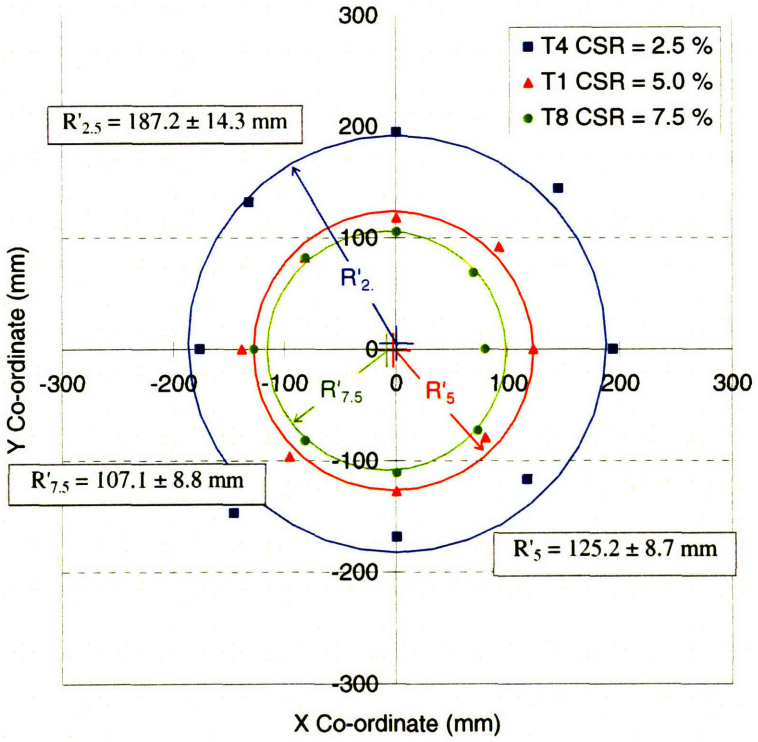

Figure 5-26. Variation of mean radius of cut with cement-soil ratio (constant P_i = 1000 psi)

Specimen/ Cut level	CSR (%)	d_n (mm)	R_s (rpm)	N_r (rev)	Pi (psi)
T4 Middle	2.5	1.0	10	10	2000
T1 Middle	5.0				
T8 Middle	7.5				

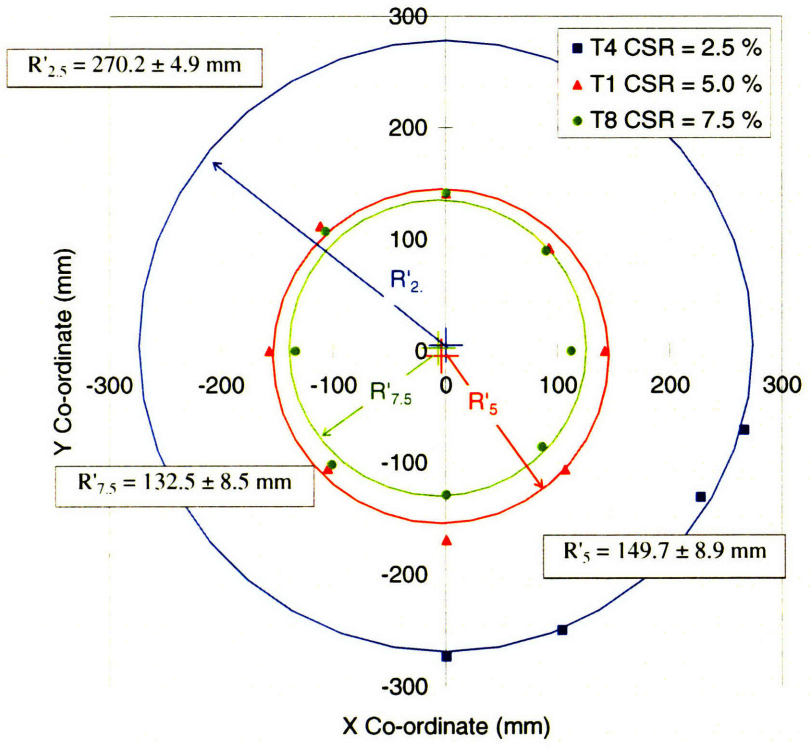

Figure 5-27. Variation of mean radius of cut with cement-soil ratio (constant P_i = 2000 psi)

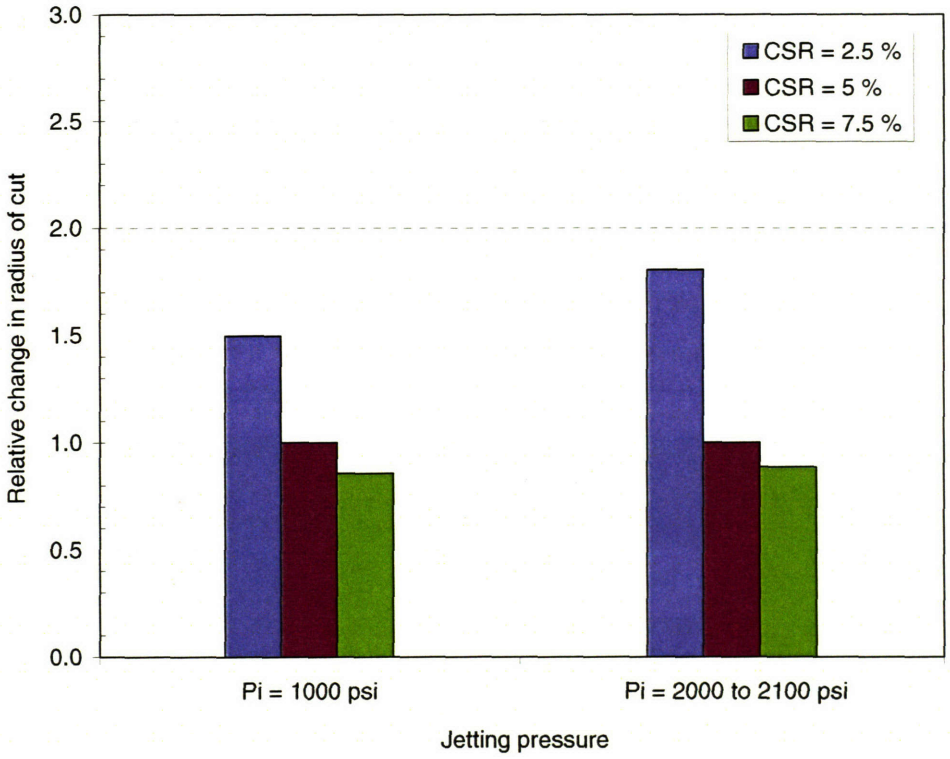

Figure 5-28. Relative change in cutting distance with CSR

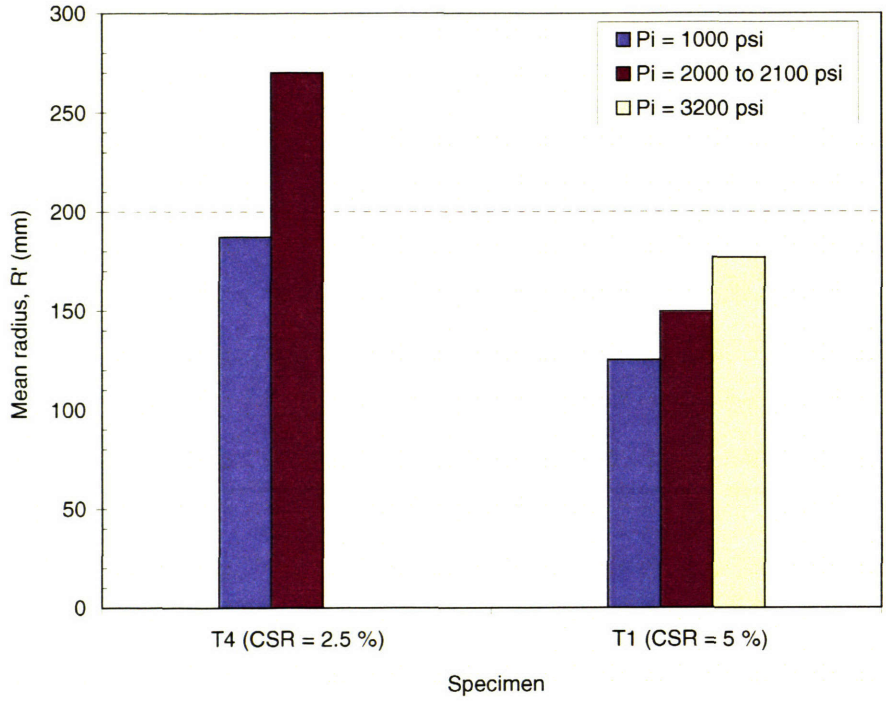

(a) d_n = 1.0 mm

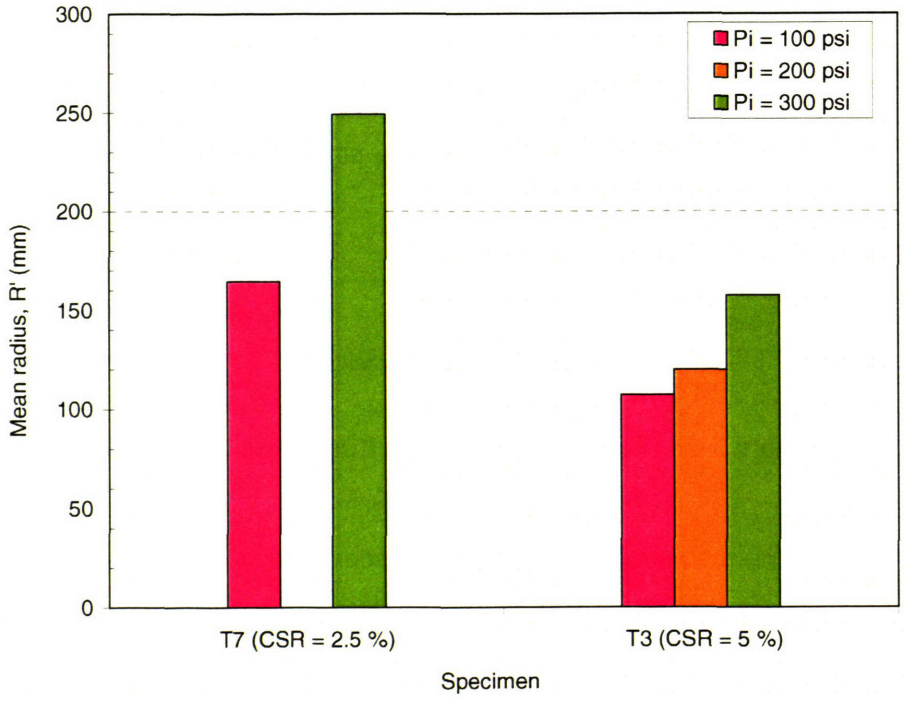

(b) d_n = 2.5 mm

Figure 5-29. Comparison of mean radius of cut for different nozzle sizes

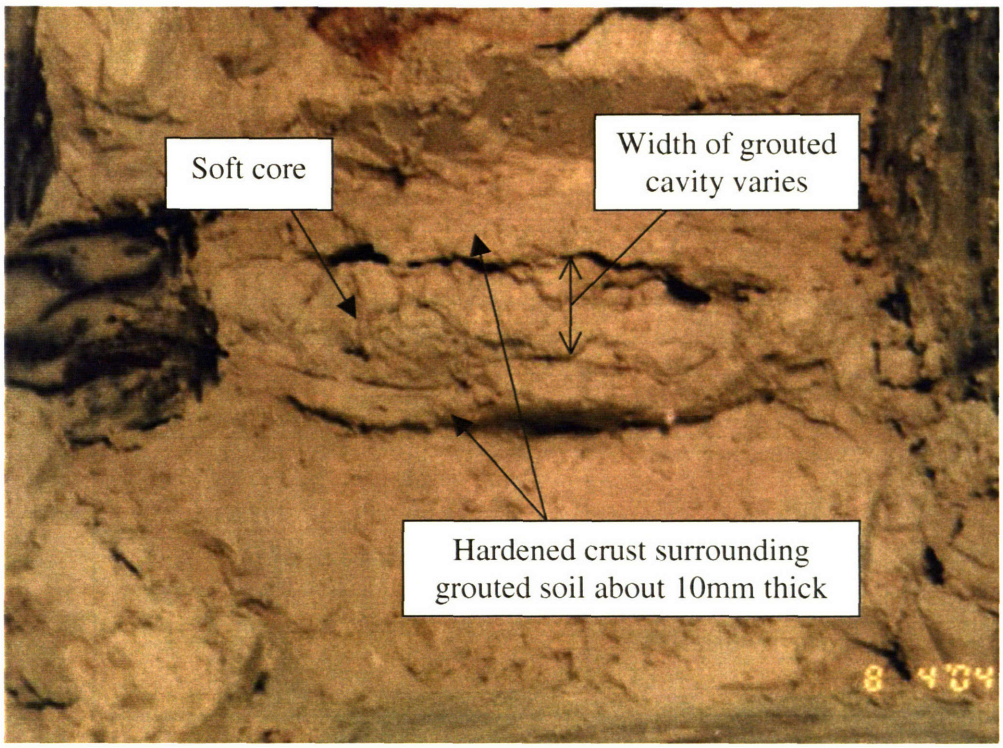

Figure 5-30. Cross-section of grouted excavation cavity (T9-7/8 Lower, CSR = 5 %)

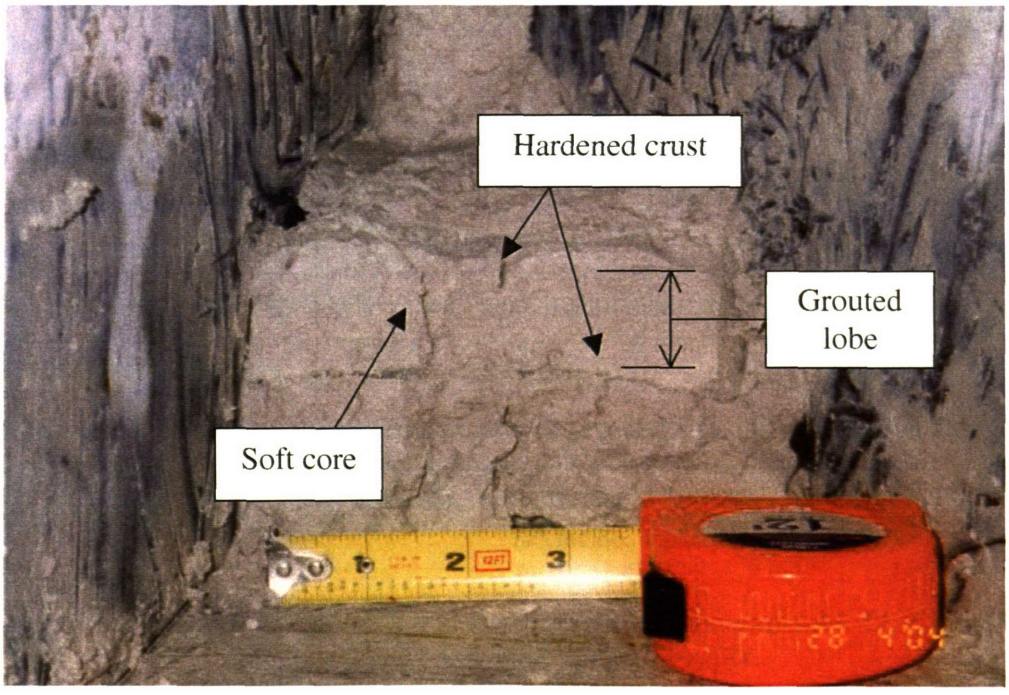

Figure 5-31. Grouted lobe in a low strength specimen (T7-7/8 Lower, CSR = 2.5 %)

CSR (%)	d_n (mm)	P_i (psi)	R_s (rpm)	N_r (rev)
2.5	2.5	300	10	10

Location of sample	Sample no.	Moisture content (%)
Immediately above grouted soil zone	S1	87.61
	S2	84.21
Grouted soil zone	GS1	168.10
	GS2	177.22
	GS3	177.63
Immediately below grouted soil zone	S3	82.79
	S4	85.54
	S5	86.06
Undisturbed soil	S6	94.80
	S7	88.36
	S8	96.55

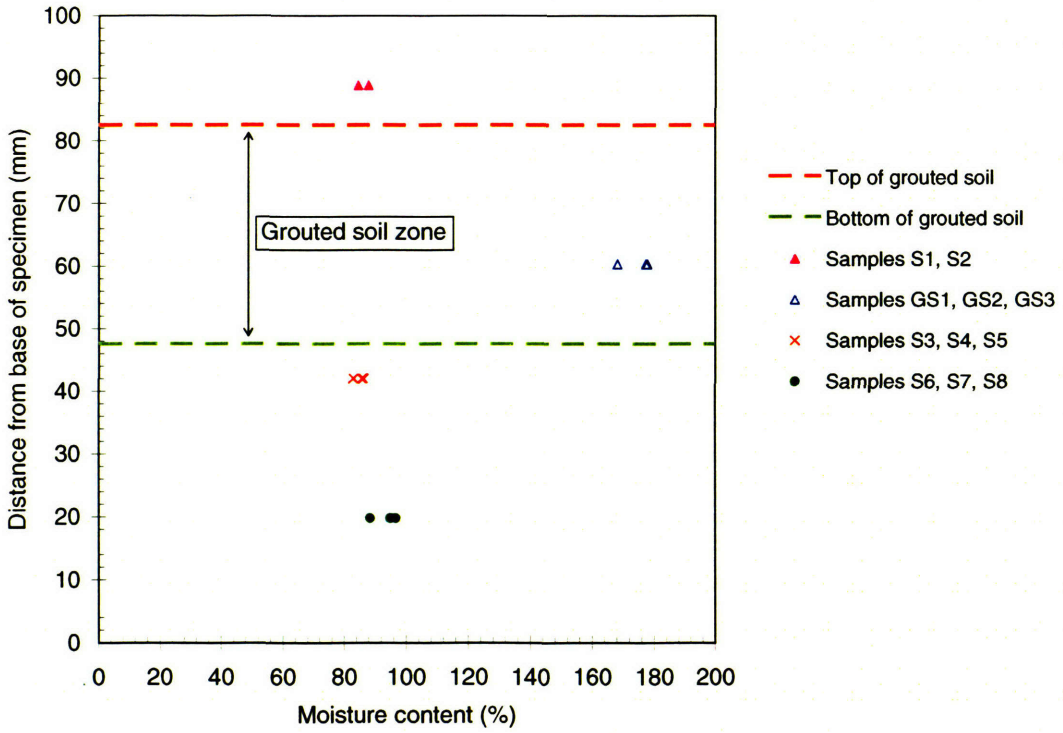

Figure 5-32. Moisture content measurements within and around grouted soil zone (Specimen T7, Segment 7/8, Lower cut)

Cut level	Pi (psi)	d_n (mm)	R_s (rpm)	N_r (rev)	CSR (%)
Upper	3400	1.0	10	10	5.0
Middle	3350				
Lower	3350				

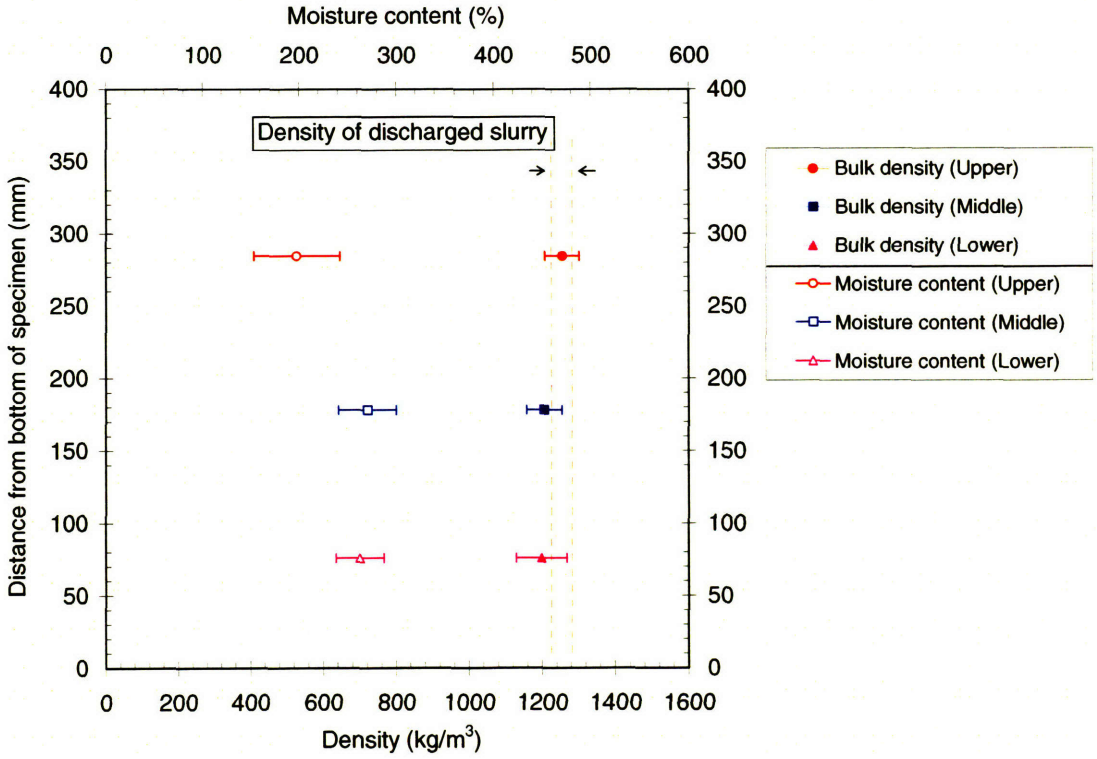

Figure 5-33. Moisture content and density of grouted soil and discharged sludge (Specimen T9)

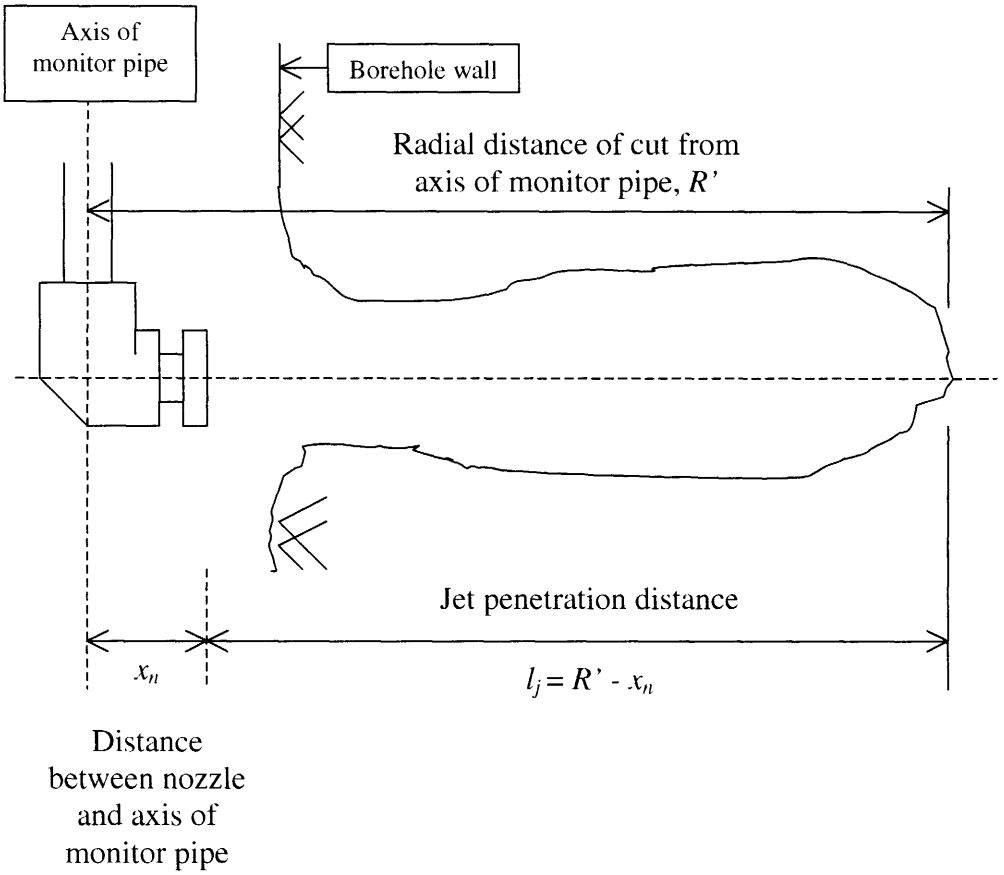

Figure 5-34. Determination of jet penetration distance

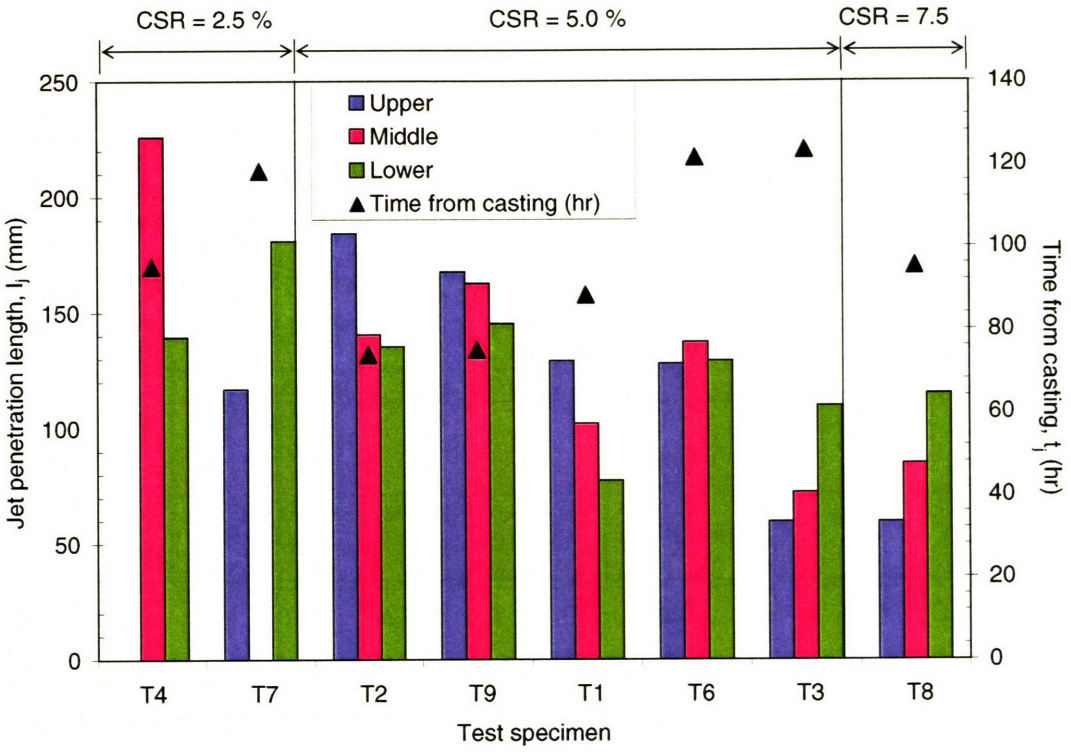

Figure 5-35. Summary of observed jet penetration distance in jetting tests

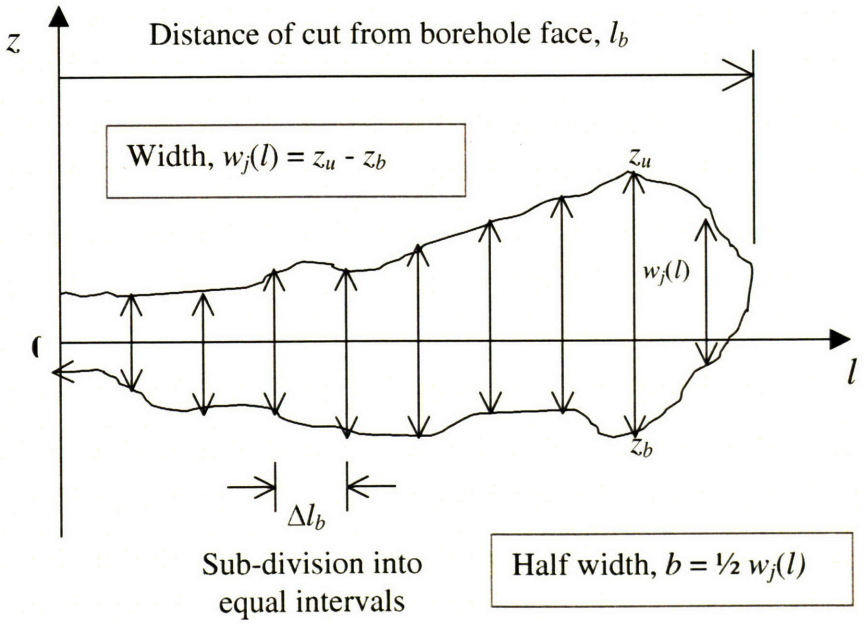

Figure 5-36. Sub-division of vertical profile into slices for measuring jet width

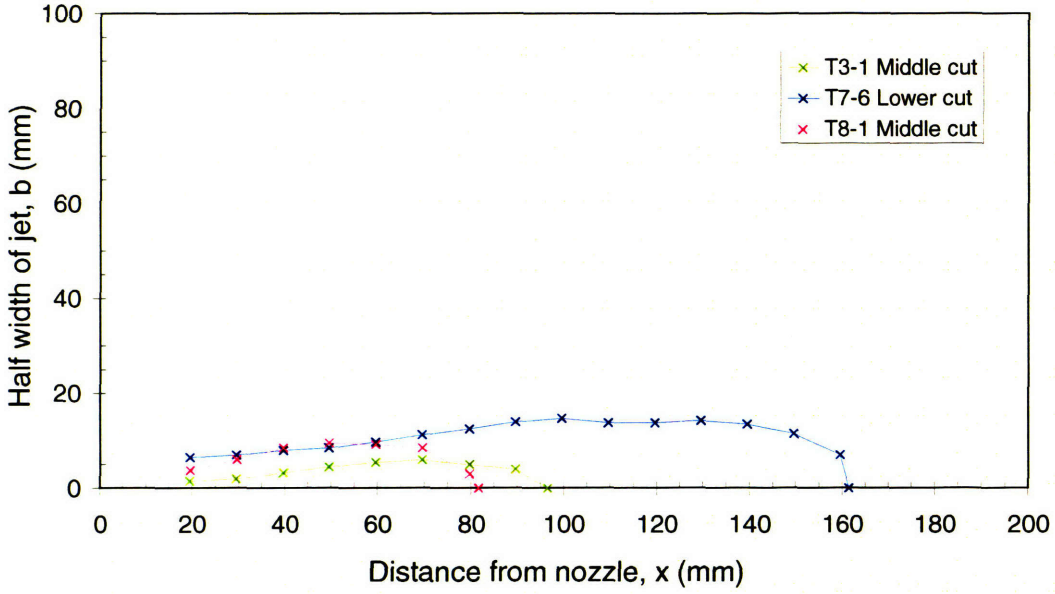

Figure 5-37. Typical profiles of half widths of jet

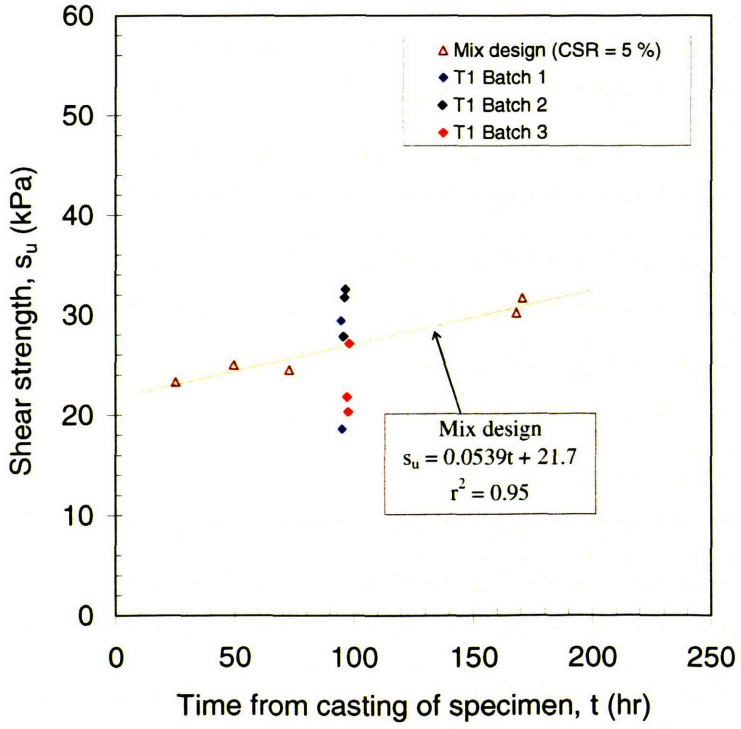

Figure 5-38. Comparison of shear strength data for design mix and batching of test specimen T1 (CSR = 5 %)

Test	Sample/ Cut level	Regression equation for shear strength s_u (kPa)	Time of jetting t_j (hr)	Shear strength at time of jetting s_u (kPa)
Laboratory vane	Mix design	$s_u = 0.0539t + 21.7$		
	Batch 1 Batch 2 Batch 3			
Torvane	TV Upper	$s_u = 0.0446t + 13.0$	88.3	16.9
	TV Middle	$s_u = 0.0446t + 13.2$		17.1
	TV Lower	$s_u = 0.0446t + 12.0$		15.9

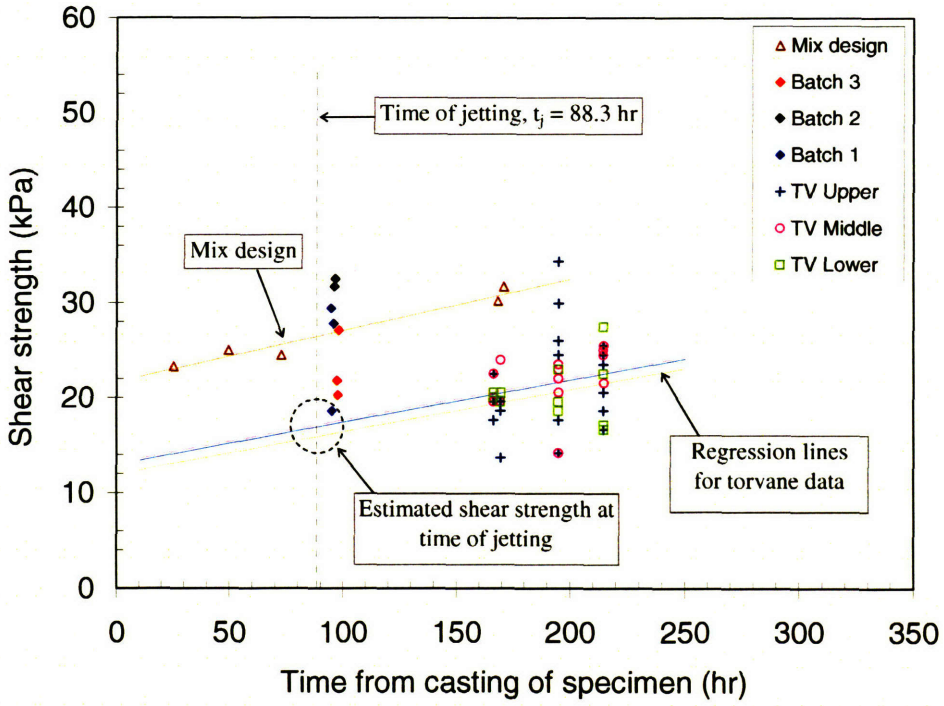

Figure 5-39(a). Assessment of shear strength at time of jetting (T1)

Test	Sample/ Cut level	Regression equation for shear strength s_u (kPa)	Time of jetting t_j (hr)	Shear strength at time of jetting s_u (kPa)
Laboratory vane	Mix design	$s_u = 0.0539t + 21.7$		
Torvane	TV Upper	$s_u = 0.0539t + 9.7$	73.8	13.7
	TV Middle	$s_u = 0.0539t + 12.4$		16.3
	TV Lower	$s_u = 0.0539t + 12.0$		16.0

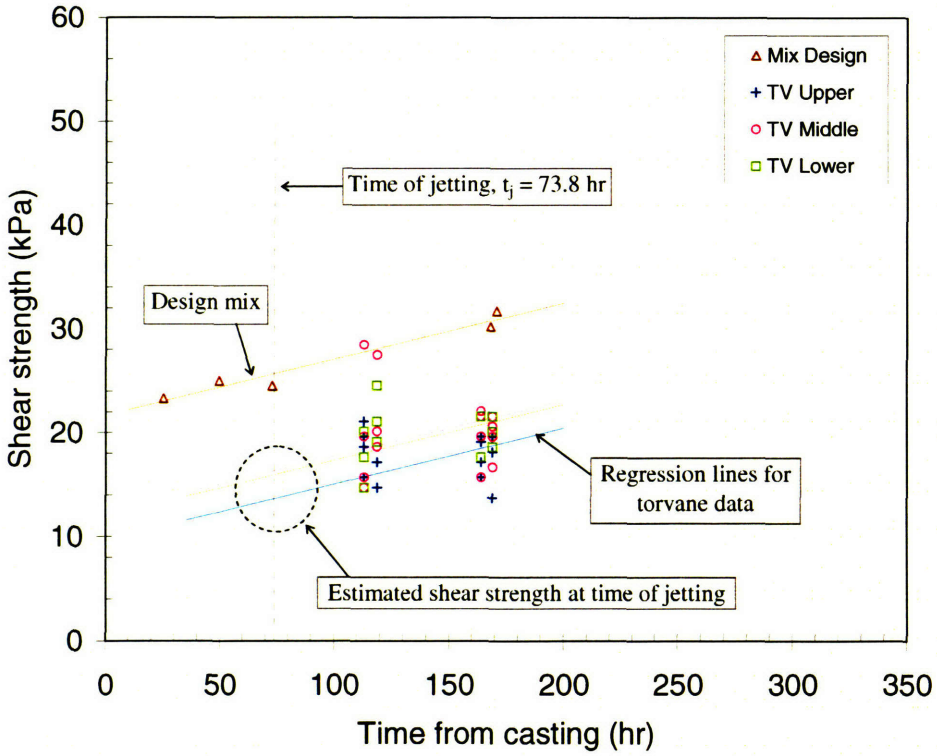

Figure 5-39(b). Assessment of shear strength at time of jetting (T2)

Test	Sample/ Cut level	Regression equation for shear strength s_u (kPa)	Time of jetting t_j (hr)	Shear strength at time of jetting s_u (kPa)
Laboratory vane	Mix design	$s_u = 0.0539t + 21.7$		
	PS Upper PS Middle PS Lower			
Torvane	TV Upper	$s_u = 0.0539t + 11.7$	123.4	18.3
	TV Middle	$s_u = 0.0539t + 13.6$		20.2
	TV Lower	$s_u = 0.0539t + 14.0$		20.7

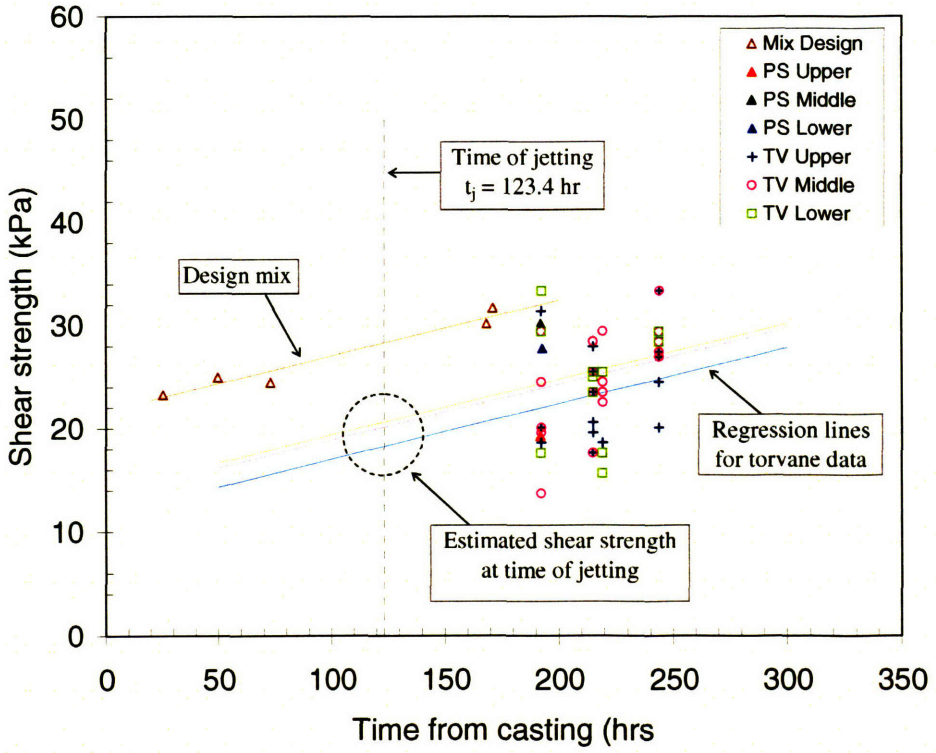

Figure 5-39(c). Assessment of shear strength at time of jetting (T3)

Test	Sample/ cut level	Regression equation for shear strength s_u (kPa)	Time of jetting t_j (hr)	Shear strength at time of jetting s_u (kPa)
Torvane	TV Upper	$s_u = 0.0283t + 3.1$	95.1	5.8
	TV Middle	$s_u = 0.0283t + 2.9$		5.6
	TV Lower	$s_u = 0.0283t + 2.0$		4.7

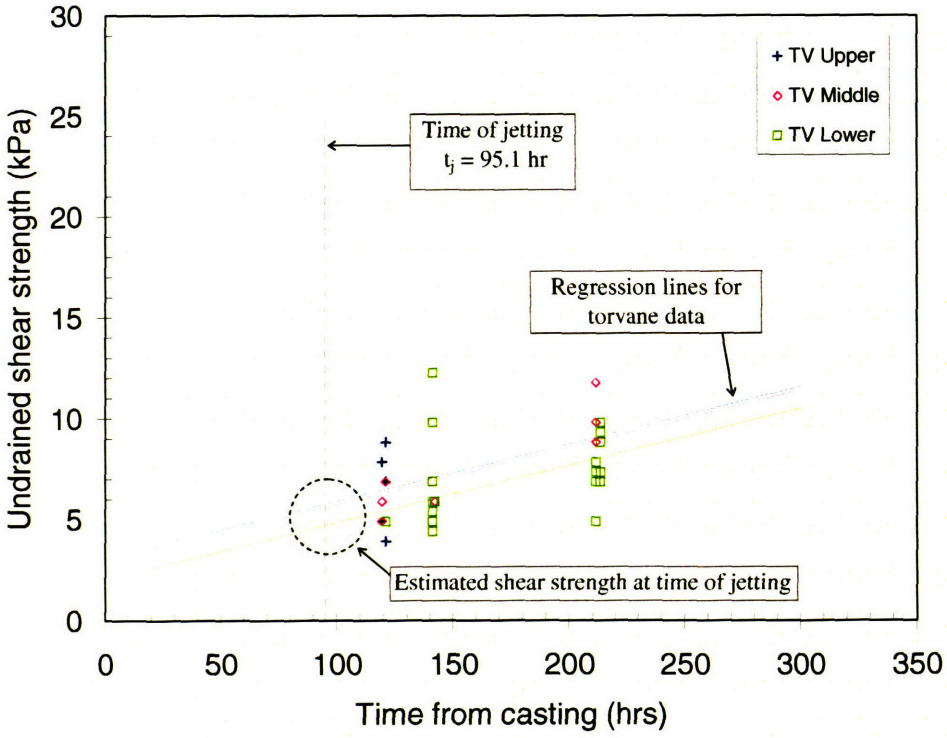

Figure 5-39(d). Assessment of shear strength at time of jetting (T4)

Test	Sample/ Cut level	Regression equation for shear strength s_u (kPa)	Time of jetting t_j (hr)	Shear strength at time of jetting s_u (kPa)
Laboratory vane	Mix design	$s_u = 0.0539t + 21.7$		
	PS Upper PS Middle			
Torvane	TV Upper	$s_u = 0.0539t + 16.4$	121.6	22.9
	TV Middle	$s_u = 0.0539t + 16.8$		23.3
	TV Lower	$s_u = 0.0539t + 14.5$		21.0

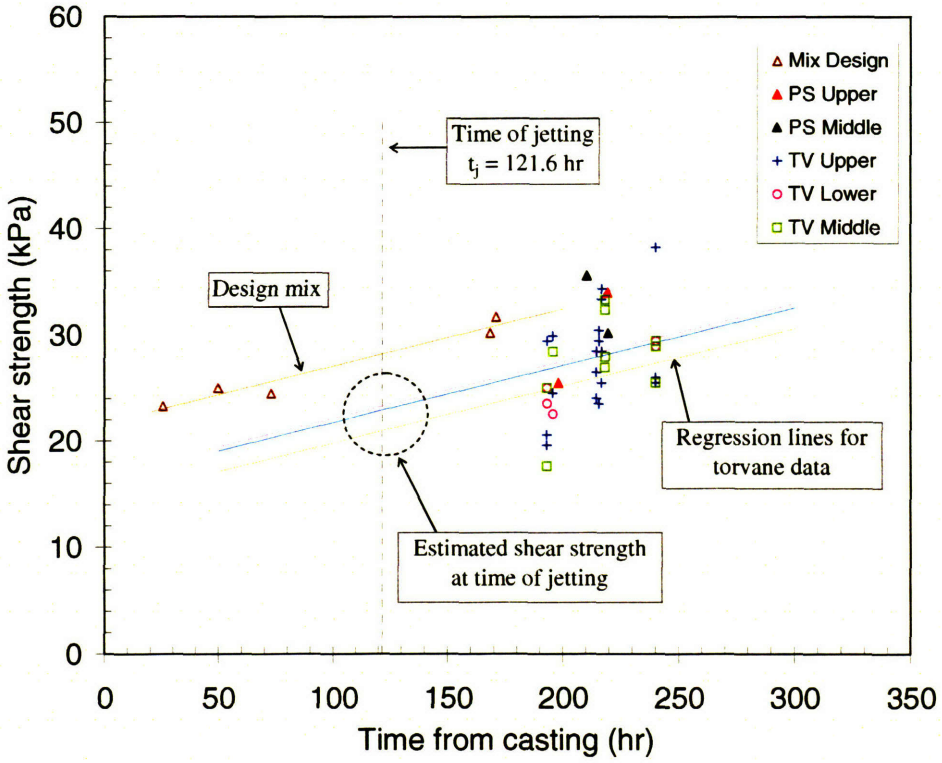

Figure 5-39(e). Assessment of shear strength at time of jetting (T6)

Test	Sample/ Cut level	Regression equation for shear strength s_u (kPa)	Time of jetting t_j (hr)	Shear strength at time of jetting s_u (kPa)
Laboratory vane	PS Upper PS Lower			
Torvane	TV Upper TV Lower	$s_u = 0.0175t + 2.10$ $s_u = 0.0175t + 2.13$	118.3	4.17 4.20

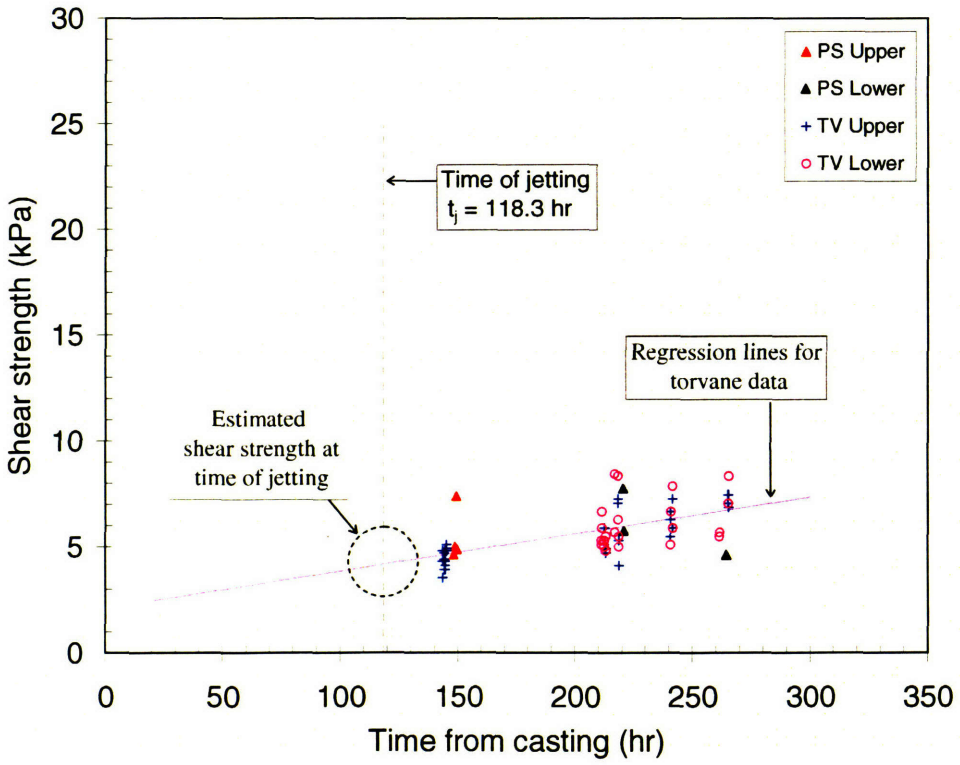

Figure 5-39(f). Assessment of shear strength at time of jetting (T7)

Test	Sample/ Cut level	Regression equation for shear strength s_u (kPa)	Time of jetting t_j (hr)	Shear strength at time of jetting s_u (kPa)
Laboratory vane	PS Upper PS Middle			
Torvane	TV Upper TV Middle TV Lower	$s_u = 0.0273t + 31.6$ $s_u = 0.0273t + 36.2$ $s_u = 0.0273t + 33.2$	95.4	34.2 35.8 38.8

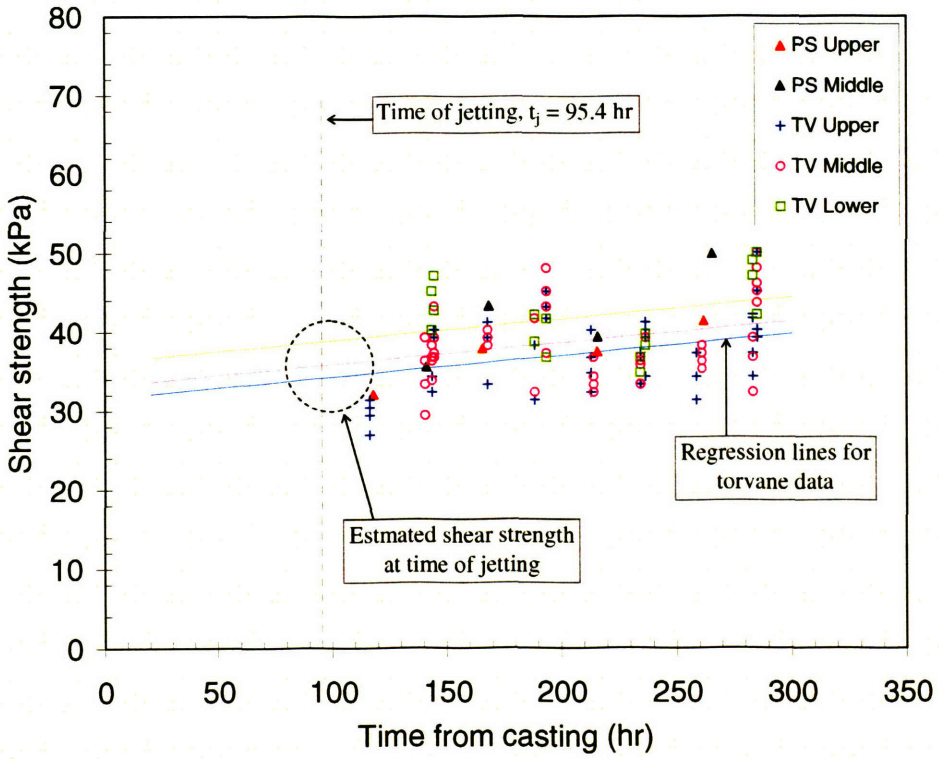

Figure 5-39(g). Assessment of shear strength at time of jetting (T8)

Test	Sample/ Cut level	Regression equation for shear strength s_u (kPa)	Time of jetting t_j (hr)	Shear strength at time of jetting s_u (kPa)
Laboratory vane	Mix design	$s_u = 0.0539t + 21.7$		
	PS Upper PS Middle PS Lower			
	Batch 1 Batch 2 Batch 3			
Torvane	TV Upper TV Middle TV Lower	$s_u = 0.0375t + 11.6$ $s_u = 0.0375t + 13.6$ $s_u = 0.0375t + 16.4$	74.9	14.5 16.5 19.2

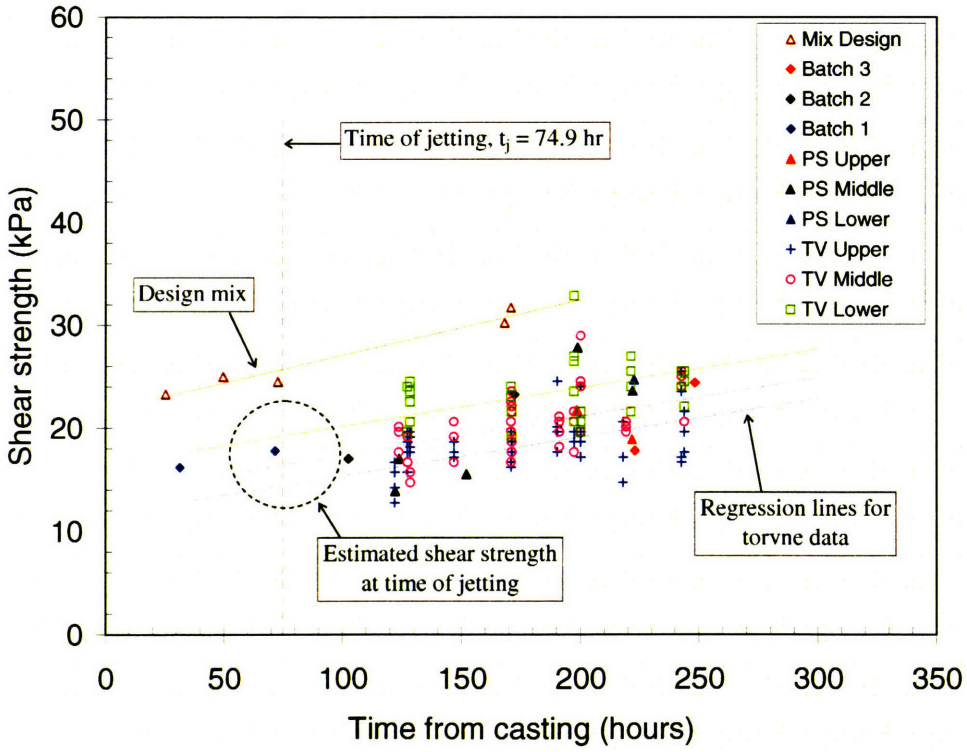

Figure 5-39(h). Assessment of shear strength at time of jetting (T9)

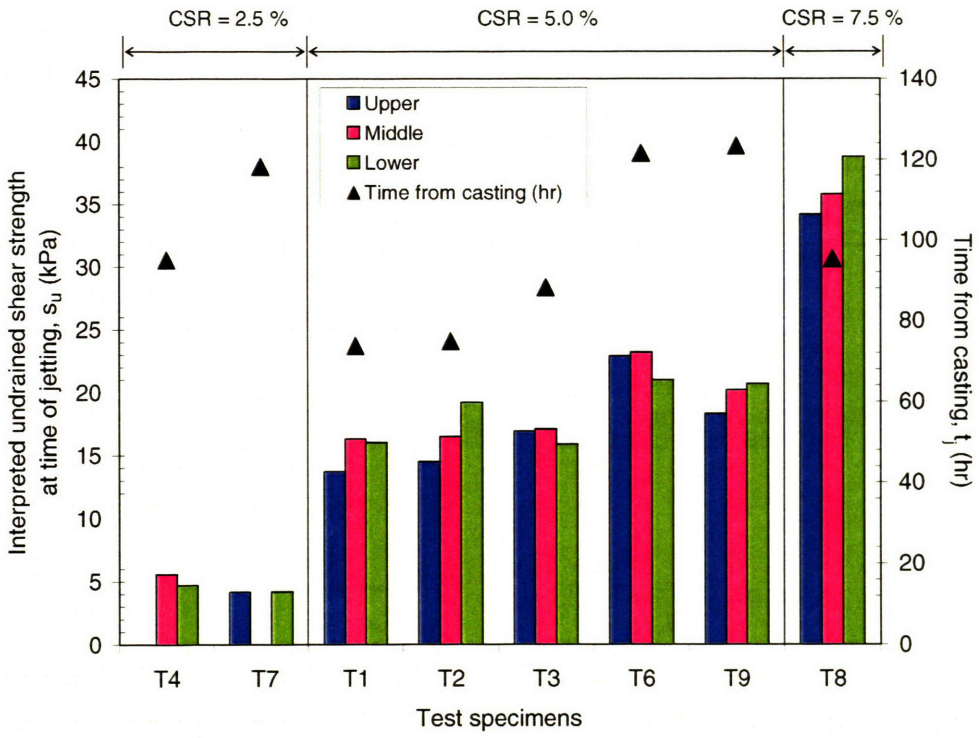

Figure 5-40. Summary of interpreted shear strength at time of jetting

Specimen	Cut level	Cement to soil mass ratio	Nozzle diameter	Pressure	Shear strength at time of jetting
		CSR (%)	d_n (mm)	P_i (psi)	s_u (kPa)
T4	Middle Lower	2.5	1.0	2000 1000	5.6 4.7
T7	Upper Lower		2.5	100 300	4.17 4.20
T1	Upper Middle Lower	5.0	10	3200 2000 1000	16.9 17.1 15.9
T2	Middle Lower		1.0	3200	16.3 16.0
T3	Upper Middle Lower		2.5	100 200 300	18.3 20.2 20.7
T6	Upper Middle Lower		1.0	3200	22.9 23.2 21.0
T9	Upper Middle Lower		1.0	3400 3350 3350	14.5 16.5 19.2
T8	Upper Middle Lower	7.5	1.0	1000 2100 3250	34.2 35.8 38.8

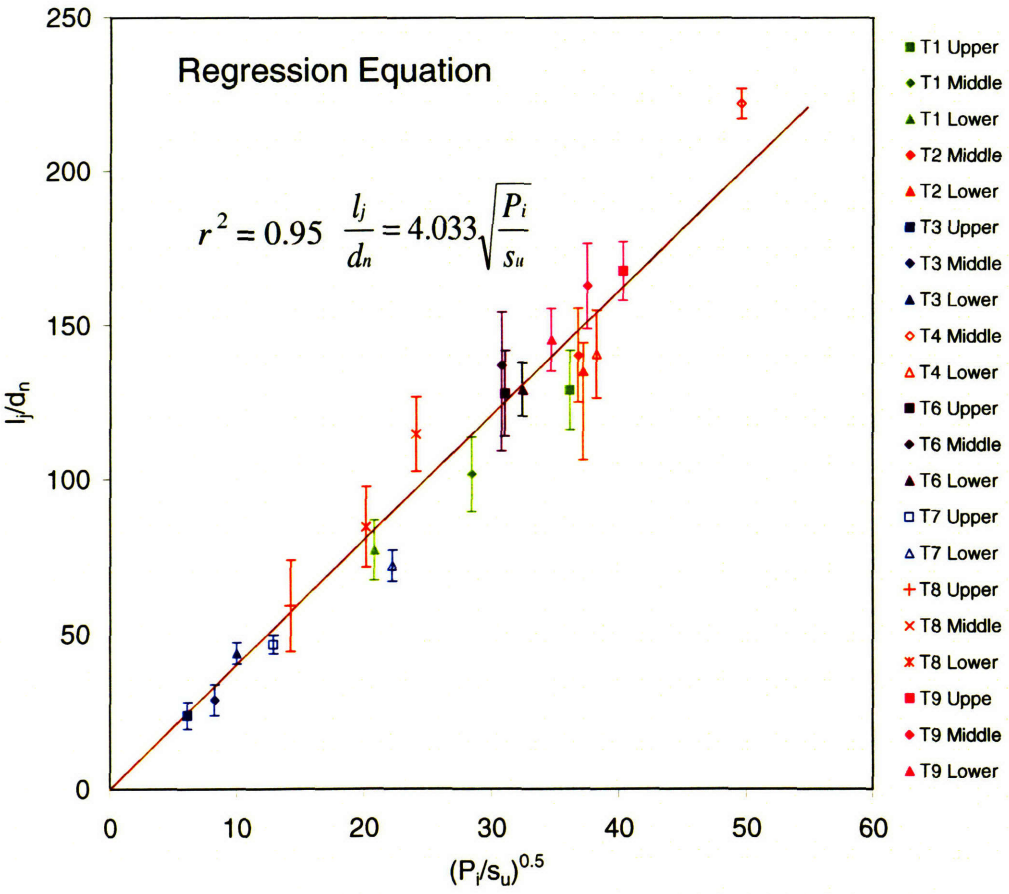

Figure 5-41. Normalized relationship between cutting distance and pressure-strength ratio

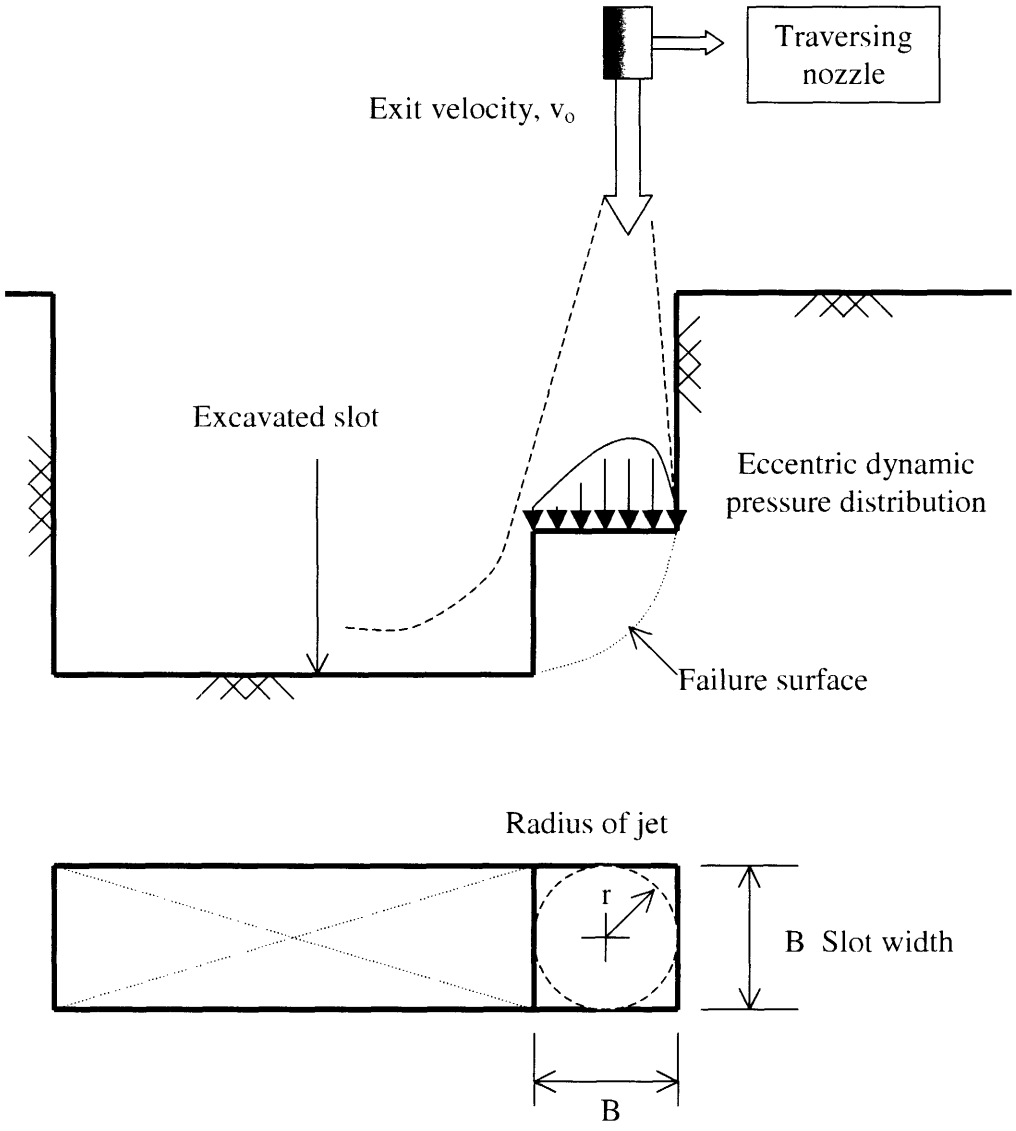

Figure 5-42. Probable mechanism of failure at tip of jet

Case history	Reference	Shear strength s_u (kPa)	Pre-cutting		
			None	Single-stage	Two-stage
1	Davie et al. (2003)	65		I, II, III	IIa
2	Durgunoglu et al. (2003)	50	3/F, 4/G	8/P	
3	Duzceer and Gokalp (2003)	25	TT1, TT2, TT4, TT6		
4	Samano et al. (1999)	10	G2 to G7		

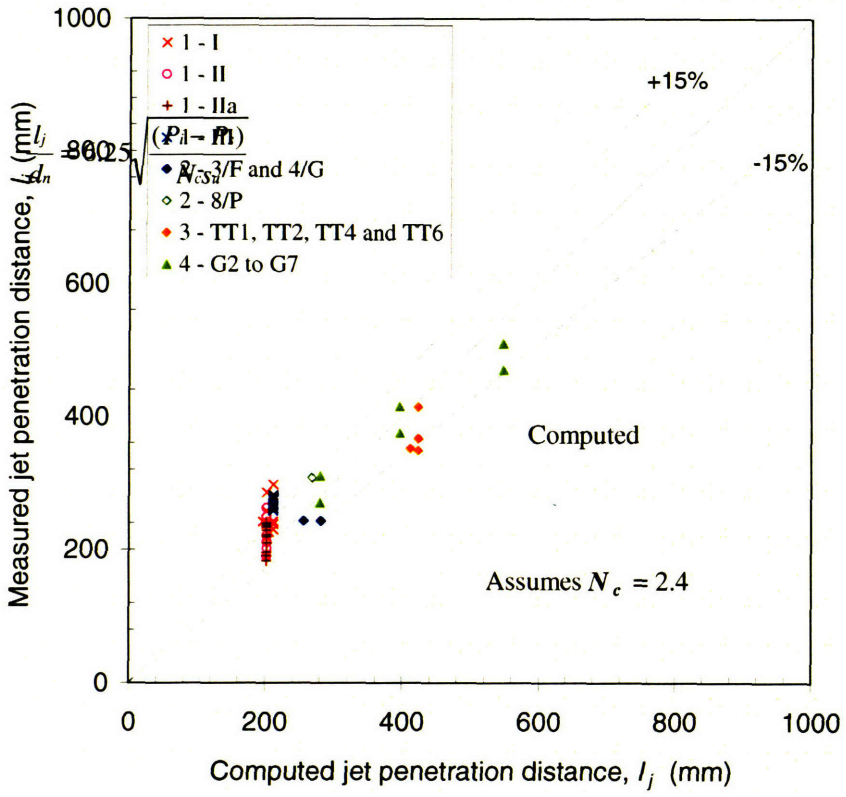

Figure 5-43. Comparison between computed jet penetration and results of field trials reported in literature

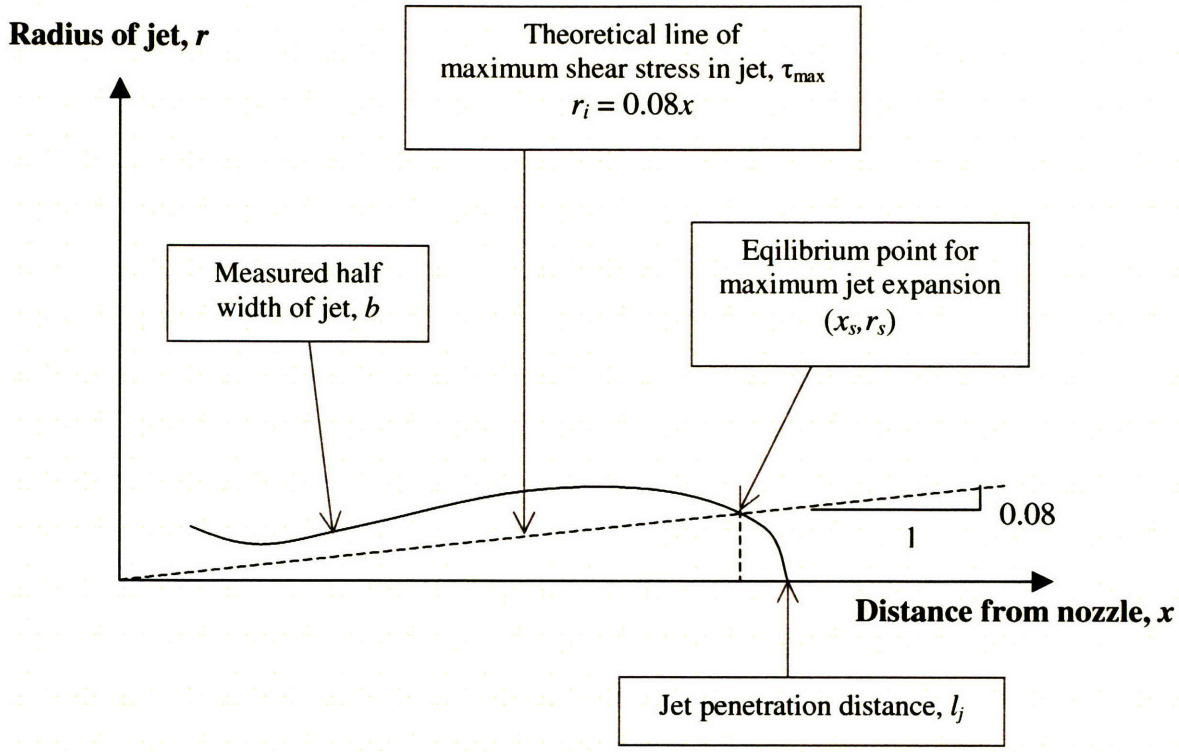

Figure 5-44. Interpretation of parameters at the equilibrium point

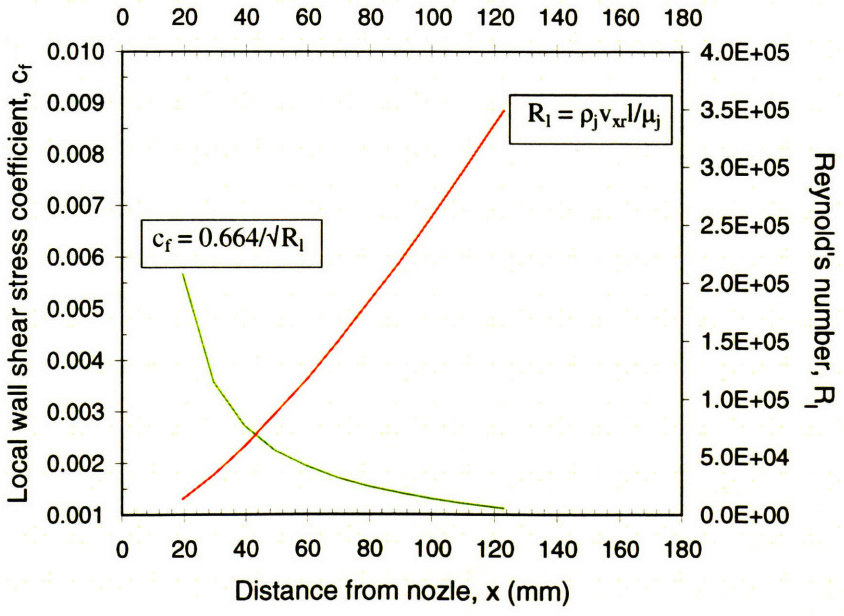

Figure 5-45. Typical variation of Reynold's number and wall shear coefficient

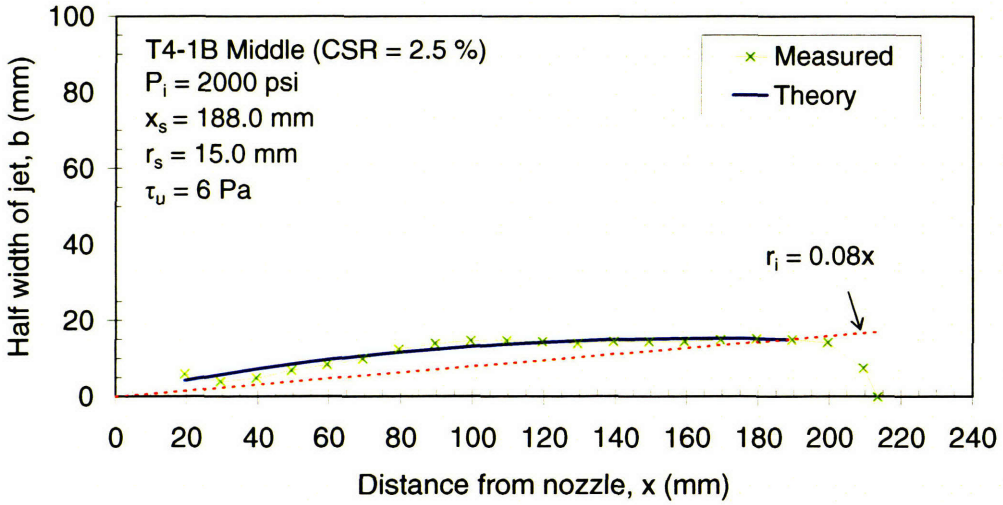

Figure 5-46(a) Specimen T4, Section 1B, Middle cut

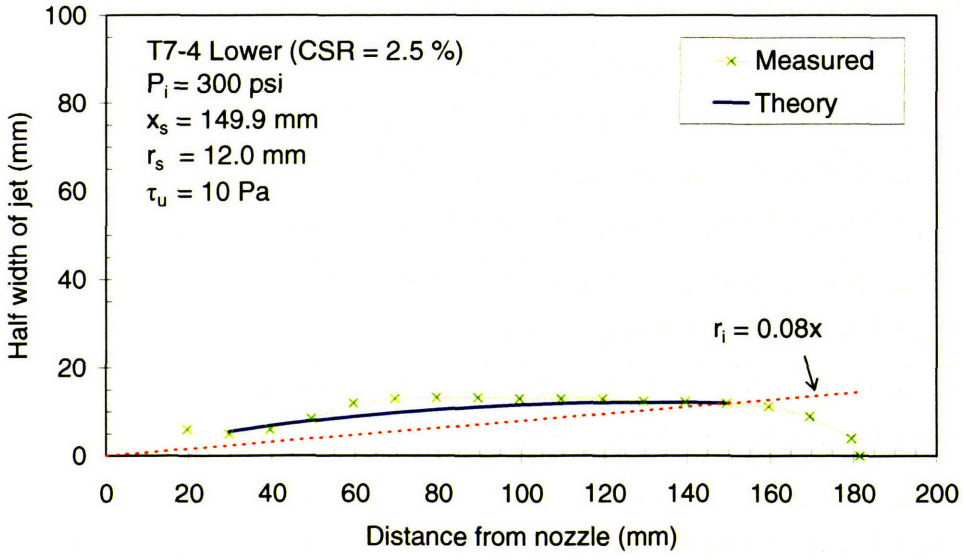

Figure 5-46(b) Specimen T7, Section 4, Lower cut

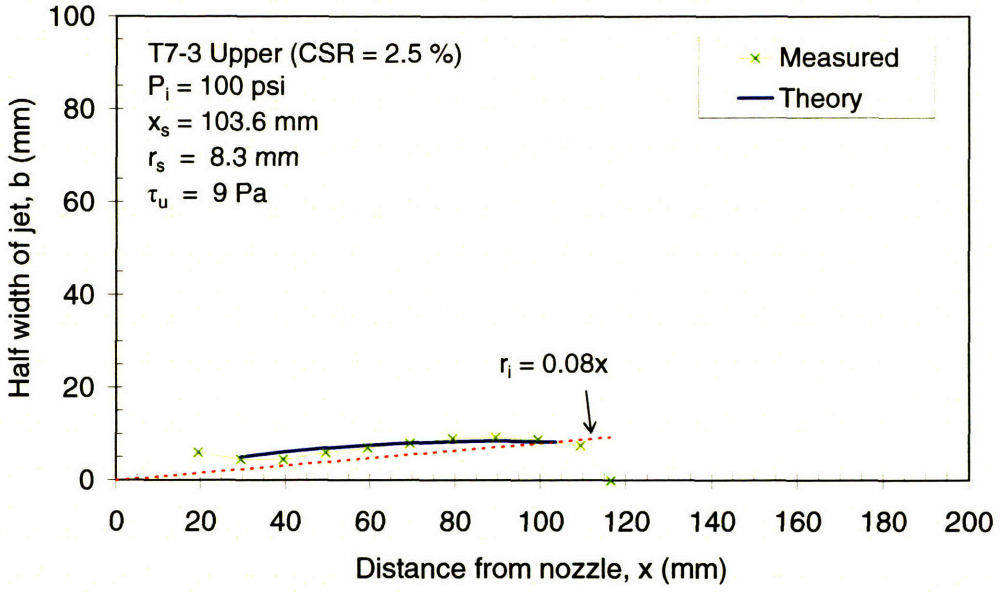

Figure 5-46(c). Specimen T7, Section 3, Upper cut

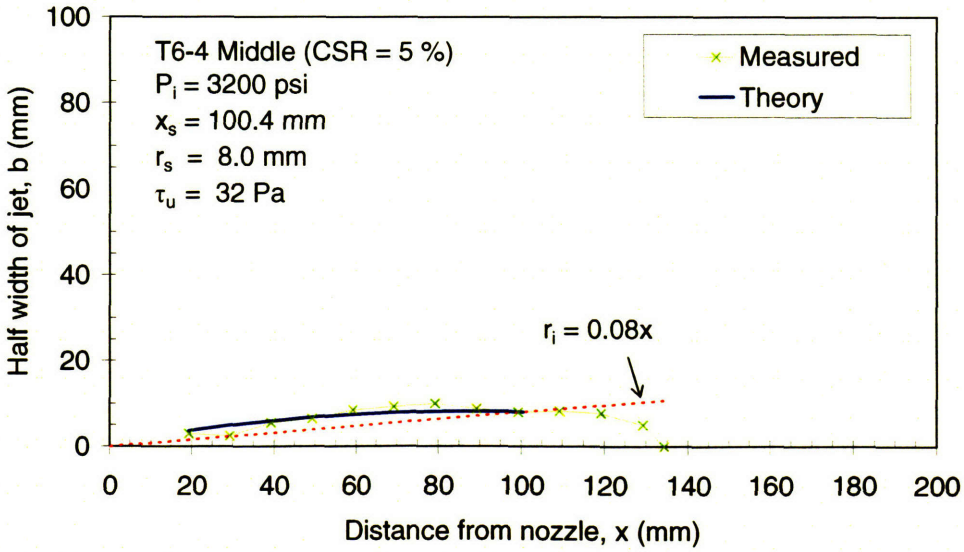

Figure 5-46(d). Specimen T6, Section 4, Middle cut

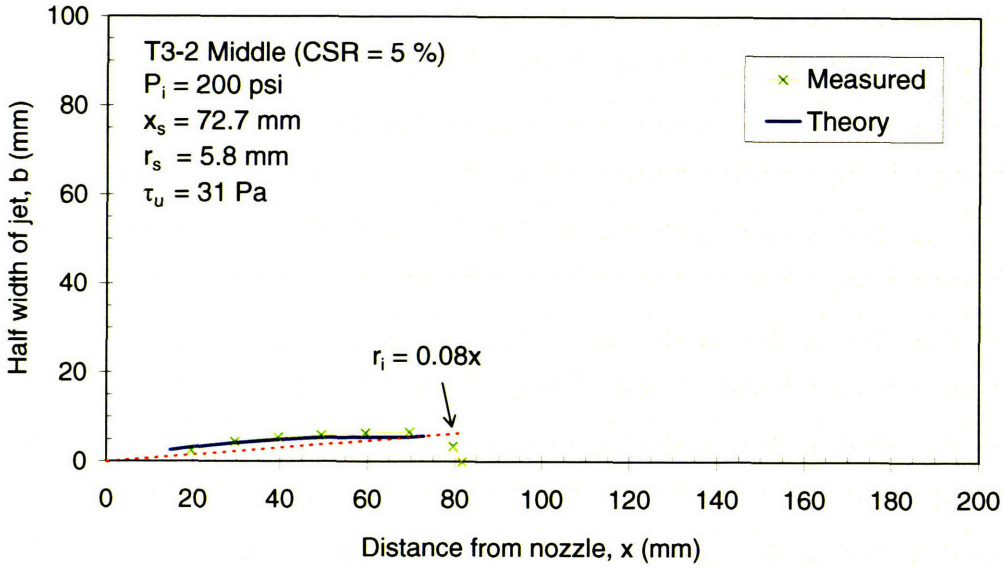

Figure 5-46 (e). Specimen T3, Section 2, Middle cut

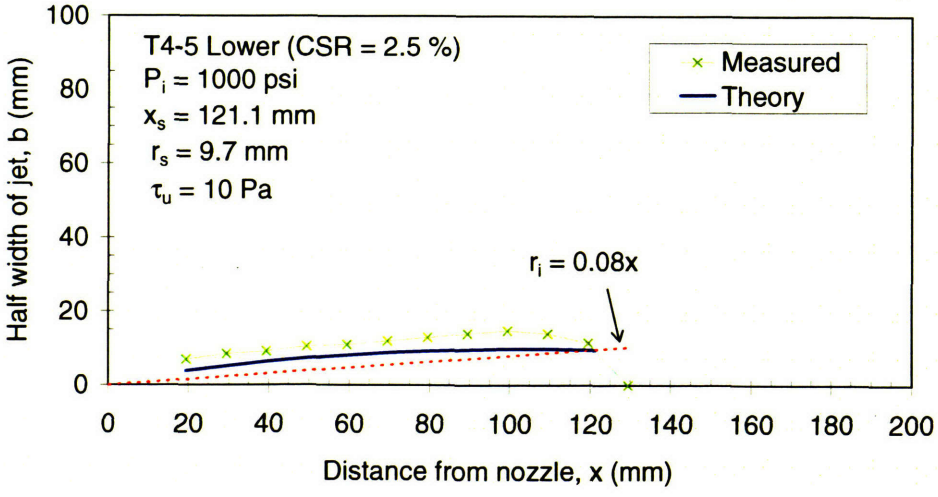

Figure 5-46 (f). Specimen T4, Section 5, Lower cut

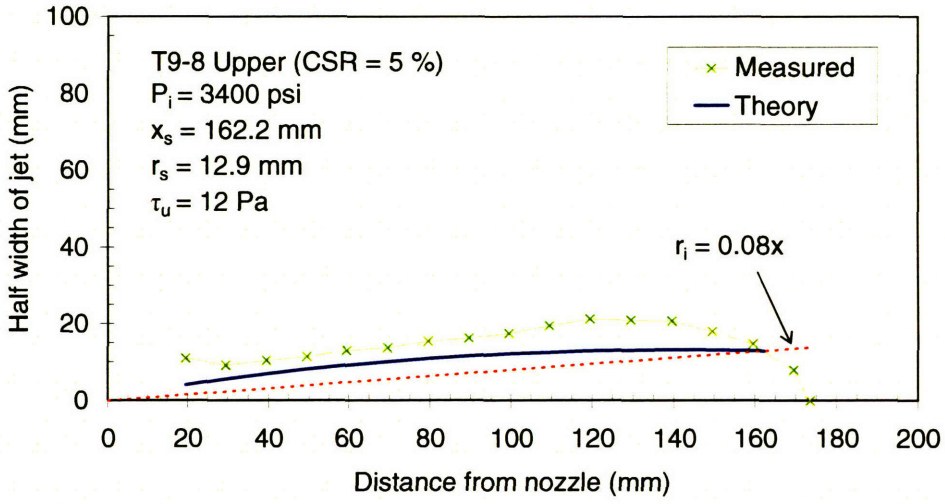

Figure 5-46(g). Specimen T9, Section 8, Upper cut

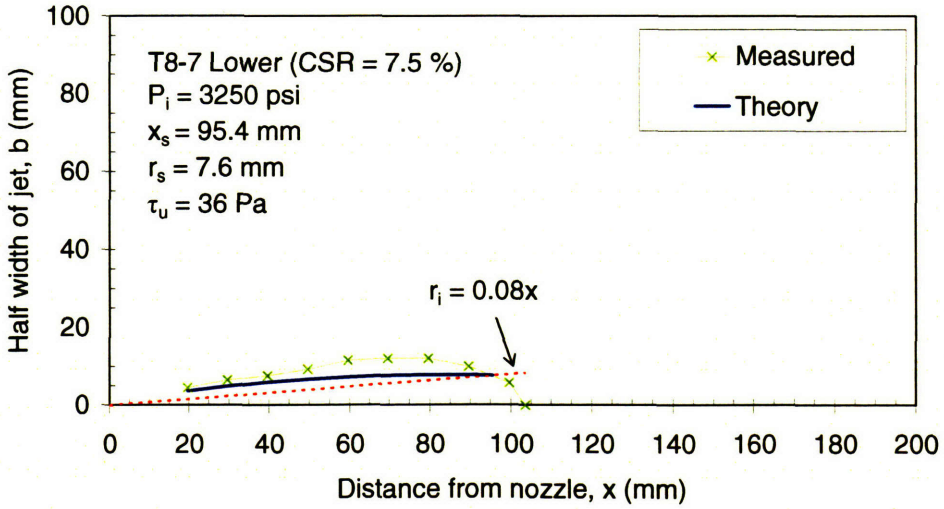

Figure 5-46(h). Specimen T8, Section 7, Lower cut

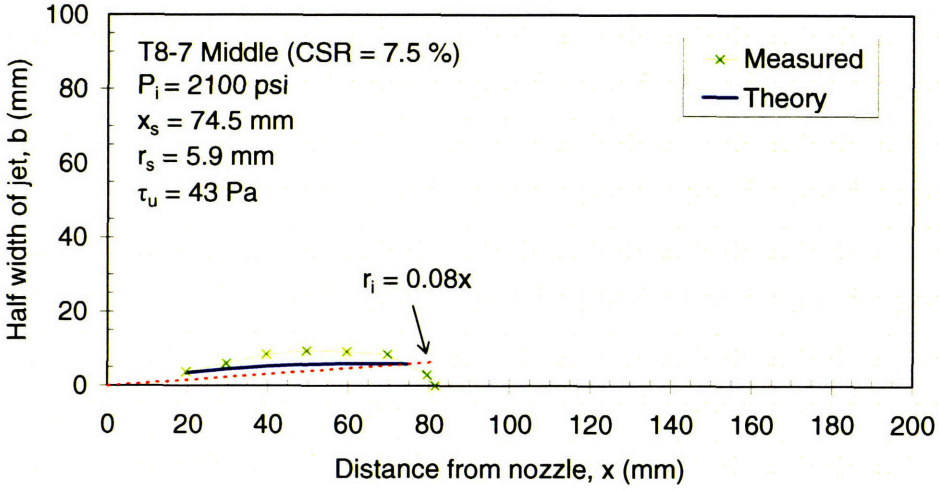

Figure 5-46(i). Specimen T8, Section 7, Middle cut

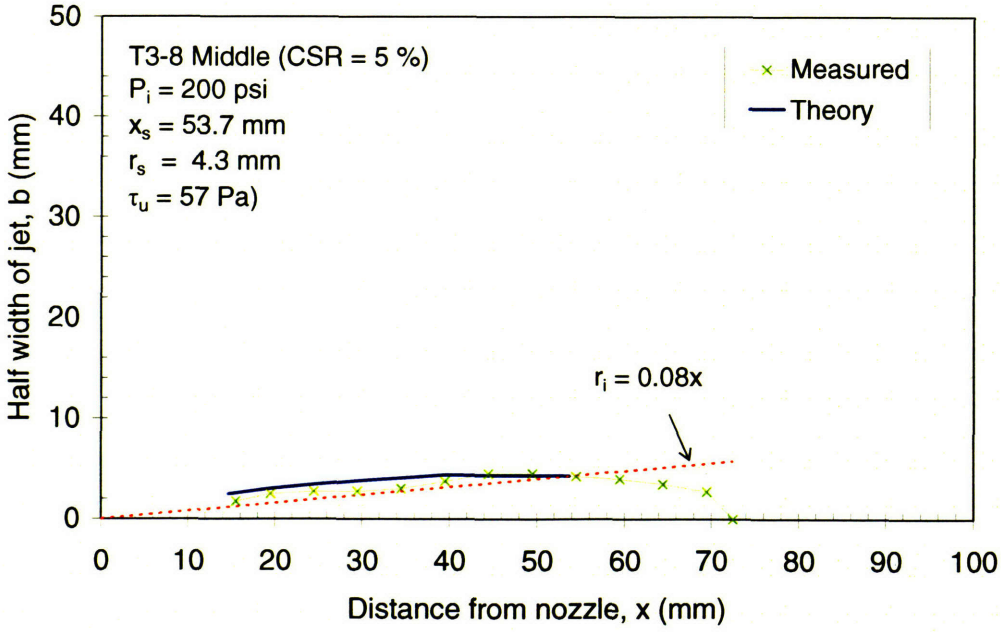

Figure 5-46(j). Specimen T3, Section 8, Middle cut

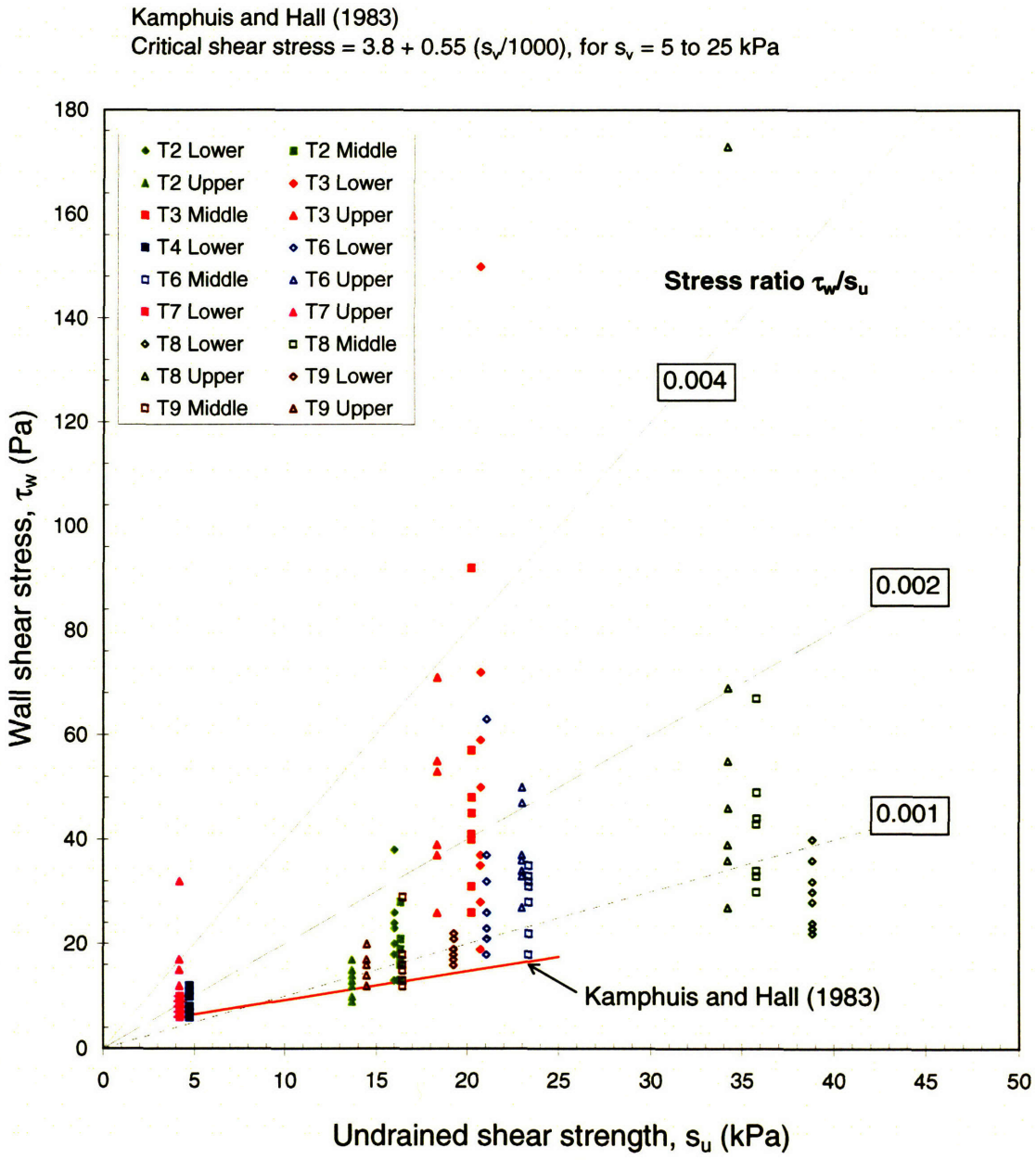

Figure 5-47. Comparison of back-figured jet-soil interface shear resistance and reference undrained shear strengths of models soil specimens

Specimen	Cut level	Cement-soil mass ratio	Pressure		Shear strength at time of jetting	P_i/s_u
		CSR (%)	P_i (psi)	P_i (MPa)	s_u (kPa)	
T4	Lower	2.5	1000	6.90	4.7	1468
T7	Middle		100	0.69	4.1	168
	Lower		300	2.07	4.2	493

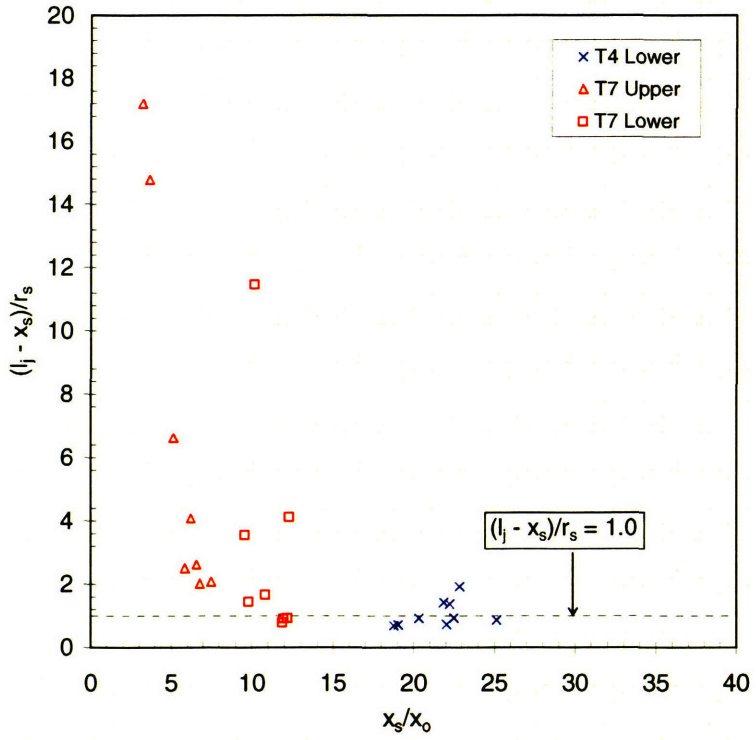

Figure 5-48(a). Jet extension length for specimens with CSR = 2.5 %

Specimen	Cut level	Cement-soil mass ratio	Pressure		Shear strength at time of jetting	P_i/s_u
		CSR (%)	P_i (psi)	P_i (MPa)	s_u (kPa)	
T2	Upper	5.0	3200	22.06	13.7	1610
	Middle		3200	22.06	16.3	1353
	Lower		3200	22.06	16.0	1379
T3	Upper		100	0.69	18.3	38
	Middle		200	1.38	20.2	68
	Lower		300	2.07	20.7	100
T6	Upper		3200	22.06	22.9	963
	Middle		3200	22.06	23.3	947
	Lower		3200	22.06	21.0	1050
T9	Upper		3400	23.44	14.4	1628
	Middle		3350	23.10	16.4	1408
	Lower		3350	23.10	19.2	1203

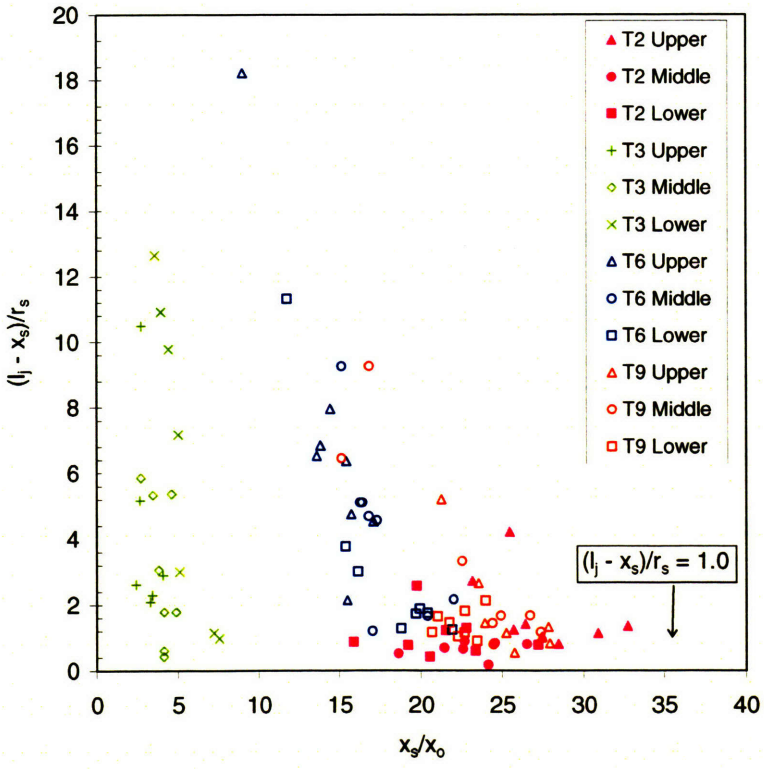

Figure 5-48(b). Jet extension length for specimens with CSR = 5.0 %

Specimen	Cut level	Cement-soil mass ratio	Pressure		Shear strength at time of jetting	P_i/s_u
		CSR (%)	P_i (psi)	P_i (MPa)	s_u (kPa)	
T8	Upper	7.5	1000	6.90	34.2	201
	Middle		2100	14.48	35.8	404
	Lower		3250	22.41	38.8	578

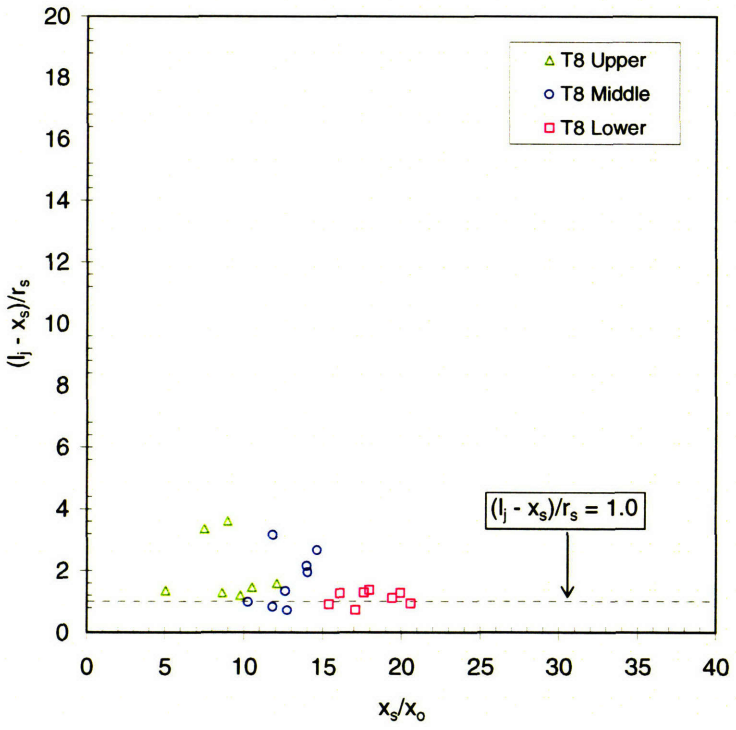

Figure 5-48(c). Jet extension length for specimens with CSR = 7.5 %

CHAPTER SIX
SUMMARY, CONCLUSIONS AND RECOMMENDATIONS

6.1 Summary

Jet grouting can be performed in a wide range of soils, but has limited effectiveness in cohesive soils with s_u > 50 kPa. The successful performance is highly dependent on the excavation process and how the operational jetting parameters (pressure, flowrate, rotation speed and withdrawal rate) relate to the achievable column diameters. A review of the current state of practice and research (Chapter 2) shows that the methods of predicting jet grout column diameter are highly empirical and rely heavily on a limited database of (relatively shallow) field trials to select the operational parameters.

The interaction between the fluid jet and soil is complex, and different excavation mechanisms are expected for granular and cohesive soils. Research on jet cutting performance has been limited to laboratory experiments on sand (where columns up to 5m can be grouted). To date, there has been no specific investigation directed at cohesive soils, even though these are commonly encountered in practice. This thesis is therefore aimed at clarifying the excavation mechanism associated with jet cutting in a cohesive soil, based on both theoretical and experimental approaches.

Chapter 3 proposed an analytical model for jet excavation based on a detailed review of prior knowledge of submerged free and partially confined fluid jets. The model predicts the profile of the excavated soil and the ultimate cutting distance of the jet. The

model takes into account both the hydrodynamic characteristics of the jet, as well as the undrained shearing resistance of low permeability cohesive soil.

The new model has significant advantages over the current practice, which attempts to establish empirical correlations between jet grout column diameter and the specific energy consumed (E_s), such as methods proposed by Tornarghi (1989) and Croce and Flora (2000). These approaches do not consider the properties of the soil or the actual mechanisms of the jet grouting process. The new model is an improvement to these methods, as it describes the excavation process using fundamental theories in fluid dynamics and soil mechanics to develop a rational framework for analysis. In addition, the ability to predict the profile of the excavation, allows the lift step for jetting operations to be determined directly.

6.1.1 Laboratory experiments

This research demonstrated that model soils can be successfully prepared by mixing powdered kaolin and cement to produce a material possessing true cohesion. Specimens with shear strengths ranging from 5 to 45 kPa were obtained using cement-soil mass ratios of 2.5 to 7.5 % and curing times of approximately three days. The strength of the soil is derived from the hydration of cement, resulting in cementation bonding between soil particles. This preparation technique has proved a practical alternative to the conventional method of consolidating test specimens from a clay slurry (which would take several months for the large specimens used in these experiments). The model soil prepared using this technique has a high initial void ratio (ranging from 2.5 to 3.0) and a degree of saturation of 90 to 100 %.

Jetting was carried out using a single nozzle with a diameter of 1.0 or 2.5 mm, and pressures ranging from 100 to 3400 psi. The shape of the cut in the model soil was captured by forming a mold of the excavated cavity. This was achieved using a sodium silicate grout as the jetting fluid, together with an ester hardener that set-up approximately one hour after mixing. The hardened mold was exhumed for observation and measurement of the dimensions of the cut surfaces. The boundary of the jet-soil interface can be identified by the contrasting consistency of the soft grouted soil, compared to the surrounding undisturbed soil. The cut boundaries were mapped in detail for subsequent analysis.

Vertical sections through the grouted discs show that there is an initial region of jet expansion up to some maximum width with reducing thickness towards the tip. The tip of the cut was observed to be approximately rounded. The initial expansion of the jet suggests that soil was entrained during jetting. The region close to the jet tip is associated with the deflection of the jet due to sideway discharge of the fluid when the pressure in the jet is insufficient to penetrate the soil. Test measurements show that it was possible to estimate the density of the jet body, ρ_j from entrainment theory using $\rho_j = \sqrt{(\rho\rho_{am})}$, where ρ is the density of the jetting fluid and ρ_{am} is the density of the surrounding medium (i.e. the soil).

The shear strength of the model soil was measured locally using a torvane during specimen exhumation. These data show little spatial variation within each specimen. However, there is a consistent increase in shear strength with time from casting of the model soil. The actual strength at the time of jetting has been estimated by linear extrapolation of data from the exhumation phase.

6.1.2 Interpretation of jetting test results

The analysis of jet excavation (Section 3.3) is based on an adaptation of the theoretical model proposed by Abramovich (1963) for a partially confined jet. The model predicts that the cutting distance of a jet, l_j is limited by the ultimate bearing capacity, q_{bu} of the soil at the jet tip. From theoretical considerations, a simple normalized equation is found as follows:

$$\frac{l_j}{d_n} = 6.25\sqrt{\frac{(P_i - P_s)}{q_{bu}}} \tag{3.34}$$

where, d_n is the nozzle diameter and $(P_i - P_s)$ is the pressure difference across the nozzle.

The soil bearing capacity is given by $q_{bu} = N_c \cdot s_u$ where N_c is the bearing capacity coefficient of the soil. The actual geometry of the bearing mechanism is unknown and hence, N_c must be back-figured from the laboratory experiments. There is excellent agreement between the theoretical cutting distance and the laboratory tests with $N_c = 2.4$. The relationship has also been corroborated by field trial data, which indicated that the prediction was within ±15%.

The analytical model also provides a means of predicting the shape of the excavation in the soil, assuming that the spread of the jet will be limited to the radius, r, at which the wall shear stress, τ_w becomes equal to the shearing resistance at the jet-soil boundary, τ_u. The model is applicable within the zone of established flow ($x > x_o$) up to the equilibrium length, x_s. The shape of the cavity excavated follows the locus of r satisfying the equation:

$$r = r_i\sqrt{2\left(\frac{v_{xo}}{v_{xr}}\right)} \tag{3.25}$$

where, $r_i = 0.08x$, $v_{xc} = v_o x_o / x$ and $v_{xr} = \sqrt{(2\tau_u / c_f \rho_j)}$.

The line passing through the inflexion points of the velocity profiles in each jet cross-section, given by $r_i = 0.08x$ is a universal characteristic of the jet. This line also represents the location of maximum shear stress in the jet. The theoretical limit of jet expansion is reached when $r_s = r_i$, at the equilibrium length, x_s.

In general, the form of the theoretical shapes is in good agreement with the dimensions of the actual cuts observed in the experiments, suggesting that the theoretical assumptions regarding the excavation mechanism were reasonable. In most cases, the theory tends to under-predict the jet width.

The back-figured shear stresses at the jet-soil boundary, τ_u, were much smaller than the residual soil strengths of the model soil and correspond more closely to the erosional strength of clays reported in the literature. This result is attributed to the fact that fluid action at the soil interface involves plucking of soil particles from protrusions in the surface, and does not correspond to a shear mechanism where soil-soil particle interaction is involved. However, the estimated shear stresses at the jet-soil interface were higher than the critical shear stress normally associated with initiation of soil erosion in clays in low velocity flows.

The region beyond the equilibrium length, x_s is associated with deflection of the jet due to sideway discharge close to its tip. It was found from the experiments that $l_j = (x_s + r_s)$ for the range of pressures commonly adopted in jet grouting practice. The equilibrium radius, r_s can be predicted using the expression:

$$r_s = \frac{l_j}{13.5} \tag{5.6}$$

The width of the jet in the ground, w can be conservatively estimated assuming $w/r_s = 2$. The computed jet width would determine the upper bound distance for the required lift step for jetting monitor displacement, so that overlapping cuts can be ensured and continuous columns can be formed.

6.2 Conclusions

The main conclusions of this work are as follows:

a. Model soils can be prepared by mixing powdered kaolin and cement to produce a material possessing true cohesion. Undrained shear strengths ranging from s_u = 5 to 45 kPa can be obtained using cement-soil mass ratios of 2.5 to 7.5 %, for curing times of approximately three days.

b. It is possible to perform controlled laboratory tests of jet excavation in a model cohesive soil. The shape of the cut in the model soil can be captured by forming a mold of the excavated cavity, using sodium silicate grout and ester hardener as the jetting fluid.

c. The analogy observed by Abramovich (1963) between the velocity distribution of a free jet and the behavior of a partially confined jet, can be applied to the jet excavation problem in soil.

d. The extent of jet excavation can be predicted using a bearing capacity failure mechanism at the tip of the jet, using N_c = 2.4. The accuracy of predicted cutting distance using this model is within 15%.

e. The expansion of the jet is limited by the shearing resistance at the jet-soil interface. The shearing resistance can be lower than the residual strength of the soil, but is higher than the critical shear stress associated with initiation of erosion of clays.

f. The computed width of the jet using the analytical model can be used to give an estimation of the required lift step for jetting monitor displacement.

6.3 Recommendations

This thesis represents a first step in defining the jet excavation mechanism in soils based on fundamental theories in hydrodynamics and soil mechanics. Much experience has been gained from carrying out the high velocity jetting experiments within the constraints of a laboratory environment. The scope of the present research has been necessarily confined in order to focus on the fundamental issues and achieve the goals within a reasonable time frame.

The following recommendations are offered for further study:-

a. The laboratory experiments carried out in the present study were limited by the pumping pressures available and control of discharge volumes. The range of test pressures should be increased to extend the measurements above 3500 psi to verify the validity of the model for longer jet penetrations. However, larger specimen sizes would be required and improved methods of handling the heavier specimens would be necessary. In addition, jetting tests on model soils with higher shear strengths should be carried out to determine if there is any limiting condition for cutting of a cohesive soil.

b. The anatomy of the grouted discs should be characterized in greater detail in order to obtain an improved appreciation of the effect of jetting operation on the interface at the soil-fluid boundary. This will greatly assist with interpretation of the physical processes acting at the soil boundary and clarify the significance of the low shear stresses observed in the present study.

c. The present study is limited to a rotating jet in a fixed horizontal plane, without vertical displacement. Columns of grouted soil mass can be formed by displacing a rotating jet in the vertical direction. Experiments can be carried out to study the effect of the withdrawal rate of the nozzle on the cutting distance and uniformity of mixing in the resulting column of grouted soil mass.

d. The strength and deformation properties of the grouted soil mass are important with respect to the behavior of a jet grout column under load. Research should be carried out to study the effect of different jetting parameters on the engineering properties of the grouted soil mass. Samples can be taken from the grouted model soil and subjected to laboratory triaxial compression and tensile tests to obtain the stress-deformation and strength characteristics. In particular, an investigation of the effect of the brittle nature of a grouted soil would be of interest.

REFERENCES

List of abbreviations:
ASCE – American Society of Civil Engineers
BHRA – British Hydraulic Research Association
DFI – Deep Foundation Institute
IMM – Institute of Mining and Metallurgy
ISSMGE – International Society of Soil Mechanics and Geotechnical Engineering

Abramovich, G. N. (1963). *The theory of turbulent jets*. MIT Press, Massachusetts, 671pp.

Albertson, M. L., Dai, Y. B., Jensen, R. A., and Rouse, H. (1950). "Diffusion of submerged jets." *Trans. ASCE*, 115, 639-664.

Baines, W. D. (1950). "Discussion. Diffusion of submerged jets." *Trans. ASCE*, 115, 677-684.

Bell, A. L. (1983). "Control of geometry; jet grouting in sands." *GKN Keller Technical Report*, 77p (unpublished).

Bell, A. L. (1993). "Jet grouting" in *Ground Improvement*, Moseley, M. P. ed., Chapman and Hall, Glasgow, 149-174.

Chambosse, G., and Kirsch, K. (1995). "State of the art of the jet grouting method in Germany." *Proc. 4th Pacific Rim Int. Conf. on Water Jet Technology*, Shimizu, Japan, Tech. Paper 67-53E.

Citrini, D. (1950). "Discussion. Diffusion of submerged jets." *Trans. ASCE*, 115, 671-675.

Coomber, D. B. (1985). "Tunnelling and soil stabilization by jet grouting". *Proc. Symp. on Tunnelling*, Brighton, England, IMM, Paper 22.

Covil, C. S., and Skinner, A. E. (1994). "Jet grouting – a review of some of the operating parameters that form the basis of the jet grouting process." *Grouting in the Ground*, Thomas Telford, London, 605 –632.

Croce, P., and Flora, A. (2000). "Analysis of single-fluid jet grouting." *Geotechnique* 50 (6), Thomas Telford, 739-748.

Daily, J. W. and Harleman, D. R. F. (1966). *Fluid Dynamics*, Addison-Wesley Publ. Co., Inc, Reading, MA, 454p.

Davie, J., Piyal, M, Sanver, A., and Tekinturhan, B. (2003). "Jet grout partially support natural draft cooling tower." *Grouting and Ground Treatment*, Geotechnical Special Publication No.120, Johnson, L. F., Bruce, D. A., and Byle, M.J. eds, ASCE, 365-376.

Durgunoglu, H. T., Kulac, H. F., Yilmaz, S., and Kocak, D. (2003). "Case history for soil improvement of SETAT 2002 high rise residential by jet grouting in Istanbul." *Grouting and Ground Treatment*, Geotechnical Special Publication No.120, Johnson, L. F., Bruce, D. A., and Byle, M.J. eds, ASCE, 377-388.

Duzceer, R., and Gokalp, A. (2003). "Construction and quality control of jet grouting applications in Turkey". *Grouting and Ground Treatment*, Geotechnical Special Publication No.120, ASCE, 281-293.

Essler, R. D. (1995). "Applications of jet grouting in civil engineering." *Engineering Geology of Construction*, Special Publication No.10, Geological Soc. of Engineering Geology, 85-93.

Forstall, W. and Gaylord, E. W. (1955). "Momentum and mass transfer in a submerged water jet." *J. Applied Mechanics Div.*, ASME, 161-164.

Guatteri, G., Kauschinger, J. L., Doria, A. C., and Perry, E. B. (1988). "Advances in the construction and design of jet grouting methods in South America". *2nd Int. Conf. on Case Histories in Geotechnical Engineering*, St. Louis, University of Missouri, Rolla, 1037-1046.

Holdhusen, J. S. (1950). "Discussion. Diffusion of submerged jets." *Trans. ASCE*, 115, 665-671.

Japanese Jet Grouting Association (1994). *Jet Grout Design Manual.* 6th Edition, 79p. (in Japanese).

Japanese Superjet Research Association (1995). *Superjet Technical Manual.* 1st Edition, 41p. (in Japanese).

Kamphuis , J. W. and Hall, K. R. (1983). "Cohesive material erosion by unidirectional current". *J. Hydraulic Engineering*, ASCE, 109(1), 49-61.

Kanematsu, H. (1980). "High pressure jet grouting method." *Doboku Sekoh (Civil Construction)*, 21(13).

Kauschinger, J. L., Perry, E. B., and Hankour, R. (1992). "Jet grouting: state of the practice." *Grouting, Soil Improvement and Geosynthetics*, Geotechnical Special Publication, 30(1), ASCE, 169-181.

Keffer, J. F. and Baines, W. D. (1963). "The round turbulent jet in a cross-wind." *J. Fluid Mechanics*, 15, Part 4, 481-496.

Leach, S. J. and Walker, G. L. (1966). "Some aspects of rock cutting by high speed water jets." *Phil. Trans.*, Royal Society of London, 260-A, 295-308.

Lunardi, P. (1997). "Ground improvement by means of jet grouting." *Ground Improvement*, 1, ISSMGE, 65-85.

Luo, S. Q., Khoo, B. T., and Ho, C. E. (1997). "Application of the triple tube jet grouting technique for underpass excavation." *Proc. 3rd Young Geotechnical Engineers Conf., Singapore*, 181-188.

Miki, G. (1985). "Soil improvement by jet grouting." *Proc. 3rd Int. Geot. Sem. on Soil Improvement*, Singapore, Nanyang Technological Institute, 45-52.

Miki, G., and Nakanishi W (1984). "Technical progress of the jet grouting method and its newest type." *Proc. Int. Conf. on Insitu Soil and Rock Reinforcement*, 1, Paris, 195-200.

Pagliacci, F., Trevisani, S., and Chong, L. "Recent development in jet grouting techniques – Singapore Pulau Seraya power station, a case history." Proc. *3rd Int. Conf. on Deep Foundation Practice*, Singapore, CI-Premier, 219-225.

Pratte, B. D., and Baines, W. D. (1967). "Profiles of the round turbulent jet in a cross flow."*J. Hydraulics Division*, ASCE, 92, HY6, 53-64.

Rajaratnam, N. (1976). *Turbulent Jets*. Elsevier Scientific Publishing Co., Amsterdam, 304p.

Ricou, F. P. and Spalding, D. B. (1961). "Measurements of entrainment by axisymmetrical turbulent jets." *J. Fluid Mechanics*, 11, ASME, 21-32.

Samano, A. A., Schmitter, J. M., and Ayala, R. M. (1999). "Mejoramiento de suelos blandos mediante jet grouting". *Proc. 11th Panamerican Conf. on Soil Mechanics and Foundation Engineering*, Iguassu, 83-90.

Shavlovsky, D. S. (1972). "Hydrodynamics of high pressure fine continuous jets." *Proc. 1st Int. Sym. on Jet Cutting Technology*, Coventry, BHRA, A6/81-A6/92.

Schlichting, H. (1987). *Boundary Layer Theory*, 7th Edn, McGraw-Hill Book Co., 817p.

Schlosser F (1997). "Soil improvement and reinforcement." *Proc. 14th Int. Conf. on Soil Mechanics and Foundation Engineering*, Hamburg, ISSMGE, 2445-2466.

Schultz-Grunow, F. (1940). "Neues widerstandsgesetz fur glatte Platten" *Luftfahrt-forschung*, 17 (239).

Smith, S. H. and Mungal, M. G. (1998). "Mixing, structure and scaling of the jet in crossflow." *J. Fluid Mechanics*, 357, 83-122.

Sembenelli, P. G. and Sembenelli, G. (1999). "Deep jet-grouted cut-offs in riverine alluvia for Ertan cofferdams." *J. Geotechnical and Geoenvironmental Engineering*, 125 (2), ASCE, 142-153.

Shibazaki, M. (1997). "State of the art grouting in Japan." *Proc. 2nd Int. Conf. on Ground Improvement Geosystems : Grouting and Deep Mixing*, Tokyo, 2, Balkema, 851 - 867.

Shibazaki, M. (2003). "State of practice of jet grouting." *Grouting and Ground Treatment*, Geotechnical Special Publication No.120, 1, ASCE, 198-217.

Shibazaki, M., Yokoo, M., and Yoshida, H. (2003). "Development of oversized jet grouting." *Grouting and Ground Treatment*, Geotechnical Special Publication No.120, 1, ASCE, 294-302.

Tornaghi, R. (1989). "Trattamento colonnare dei terreni mediante gettiniezione (jet grouting)." *Proc. XVII Convegno Nazionale di Geotecnica,* Taormona, AGS, (in Italian), 193-203.

Welsh, J. P. (1998). "State of the art of grouting in North America." *Ground Improvement*, 2, 11–15.

Welsh J P, Rubright R M and Coomber D B (1986). "Jet grouting for support of structures." *Proc. ASCE Convention*, Seattle, 17p.

Yahiro T and Yoshida H (1973). "Induction method utilizing high speed water jet." *Proc. 8th Int. Conf. on Soil Mechanics and Foundation Engineering, Moscow*, pp 402 – 404.

Yahiro, T. and Yoshida, H. (1974). "On the characteristics of high speed water jet in the liquid and its utilization on induction grouting method." *Proc. 2nd Int. Sym. on Jet Cutting Technology*, Cambridge, BHRA, G4/41-G4/63.

Yahiro T, Yoshida H and Nishi K (1982). "Soil improvement method utilizing a high speed water jet and air jet on the development and application of columnar solidified construction method (column jet method)." *Proc 6th Int. Sym. on Jet Cutting Technology, Surrey*, pp 397 - 427.

Yanaida, K. (1974). "Flow characteristics of water jets." *Proc. 2nd Int. Sym. on Jet Cutting Technology*, Cambridge, BHRA, A2/19-A2/32.

Yoshida, H., Shimazaki, M., Kubo, H., Jimbo, S., and Sakakibara, M. (1989). "The effect of pressure and flow rate on cutting soil utilizing water jet for wider application." *Proc. 5th American Water Jet Conference*, Toronto, WJTA, 297-305.

Yoshida, H., Asano, R., Kubo, H., Jinbo, S. and Uesawa, S. (1991). "Effect of nozzle traverse rate and number of passes on soft ground cutting by water jet." *Proc. 6th American Water Jet Conference*, Houston, WJTA, 381-392.

Yoshida, H., Jimbo, S., and Uesawa, S. (1996). "Development and practical applications of large diameter soil improvement method." *Proc. 2nd Int. Conf. on Ground Improvement Geosystems : Grouting and Deep Mixing*, Tokyo, 2, Balkema, 721-726.

APPENDIX A

SPECIFICATIONS FOR LABORATORY TEST SET UP

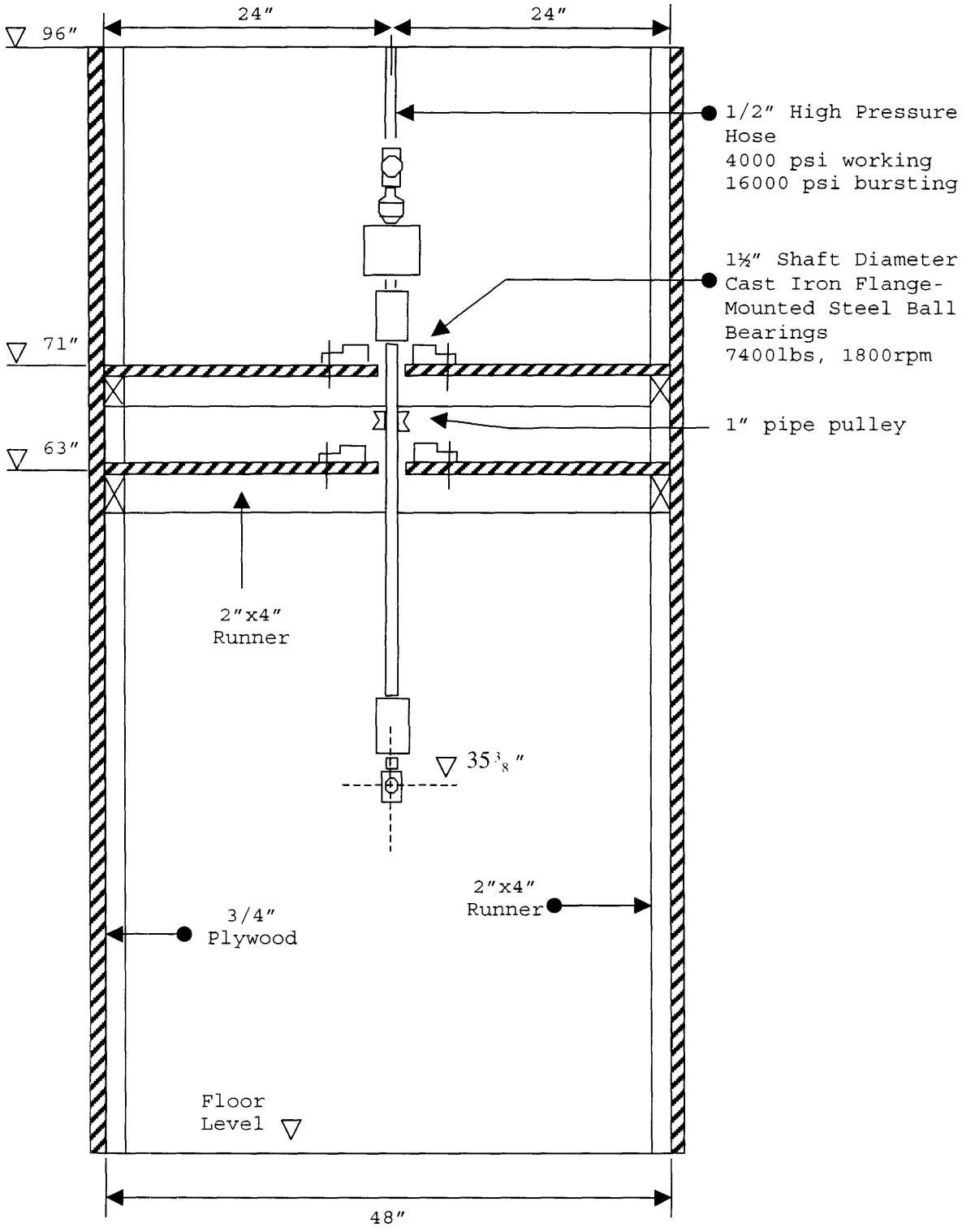

Figure A-1 (a) Test Enclosure – Front View

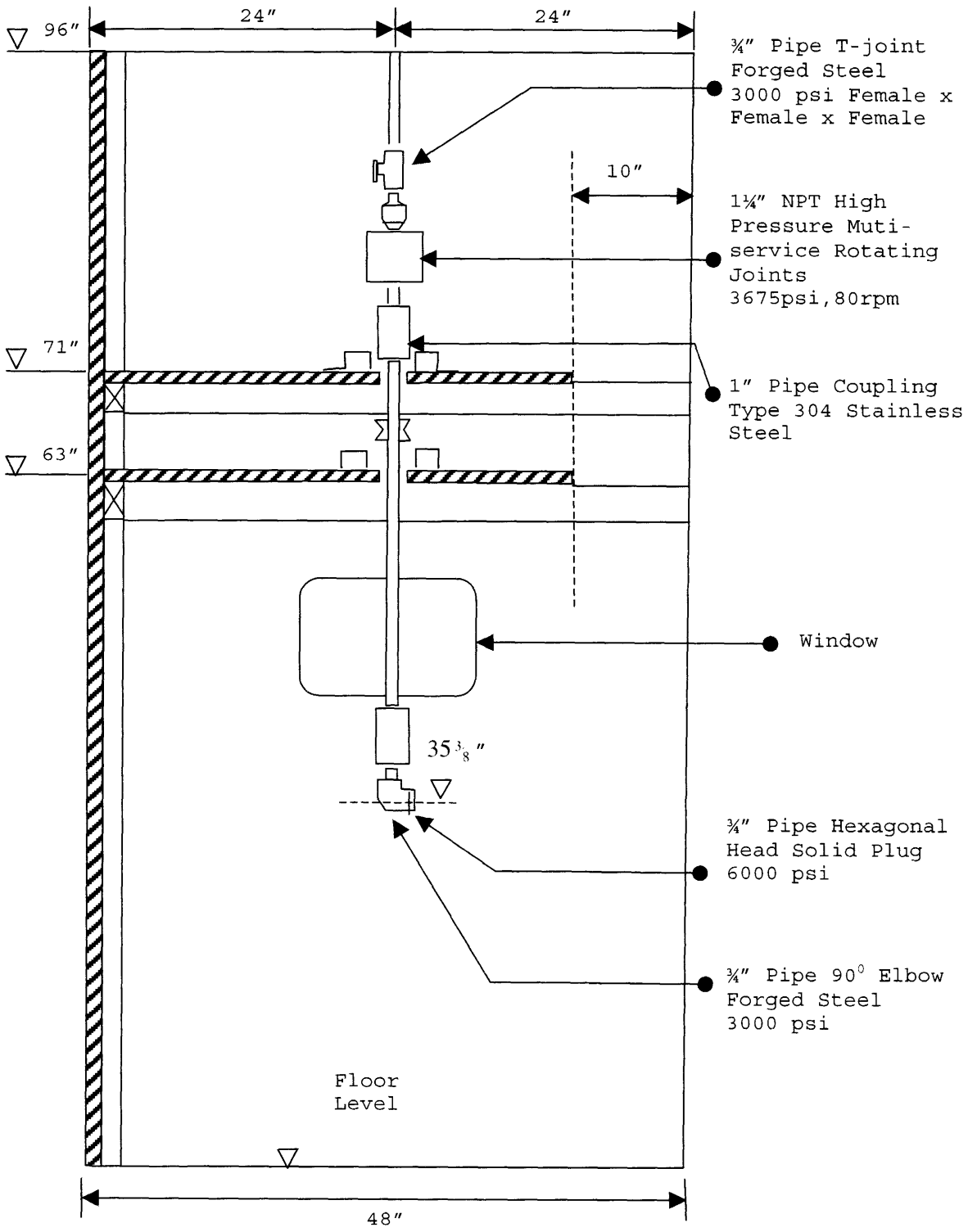

Figure A-1 (b) Test Enclosure – Side View

APPENDIX B

PHOTOGRAPHIC RECORDS OF GROUTED DISCS

Figure B-1(a). View of exposed vertical soil face (Specimen T1, Section 4)

Figure B-1(b). View of exposed vertical soil face (Specimen T1, Section 6)

Figure B-1(c). View of exposed vertical soil face (Specimen T1, Section 7)

Figure B-1(d). View of exposed vertical soil face (Specimen T1, Section 8)

Figure B-1(e). View of exposed vertical soil face (Specimen T1, Section 7:left and Section 2:right)

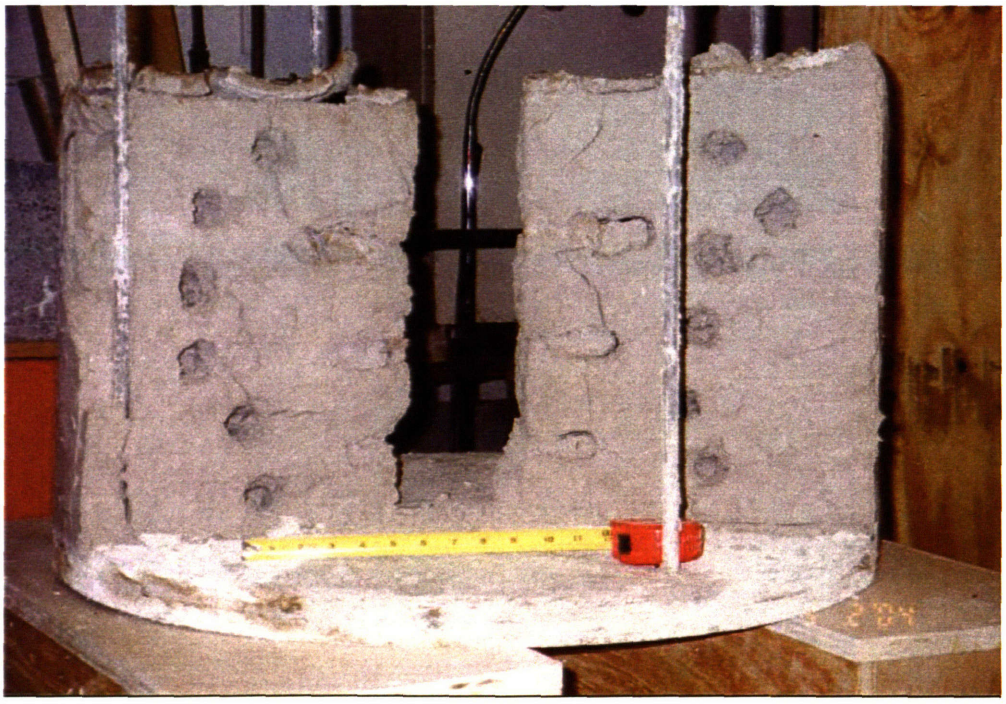

Figure B-1(f). View of exposed vertical soil face (Specimen T1, Section 3:left and Section 6:right)

Figure B-2(a). View of exposed vertical soil face (Specimen T2, Section 5)

Figure B-2(b). View of exposed vertical soil face (Specimen T2, Section 6)

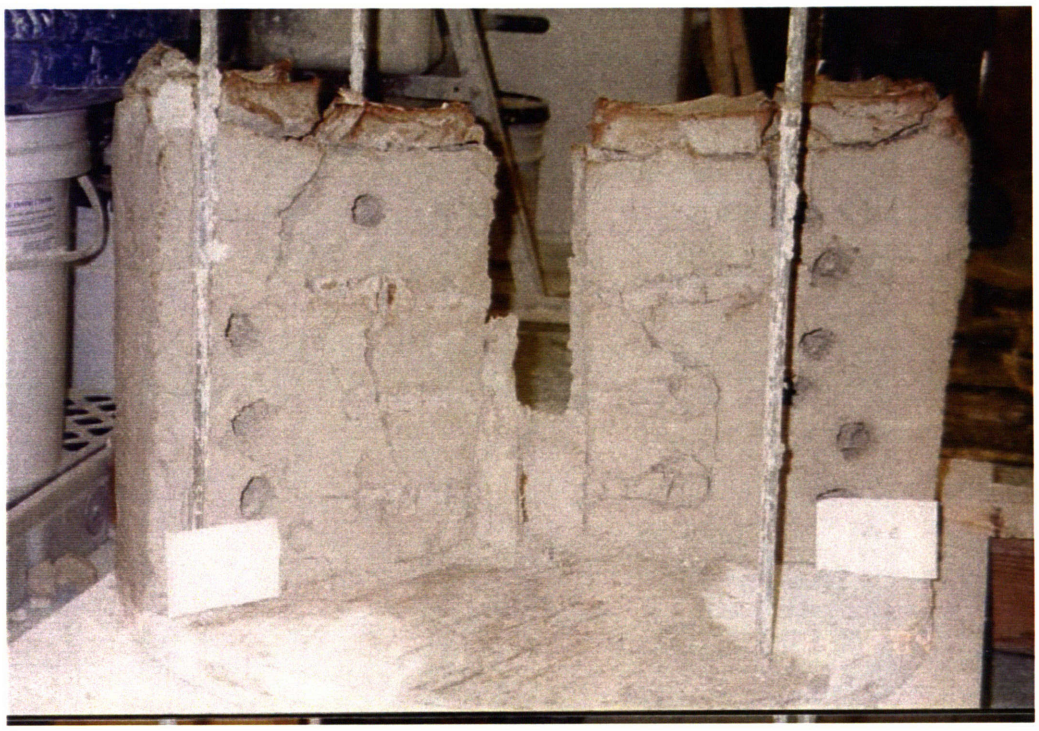

Figure B-2(c). View of exposed vertical soil face (Specimen T2, Section 3:left and Section 6:right)

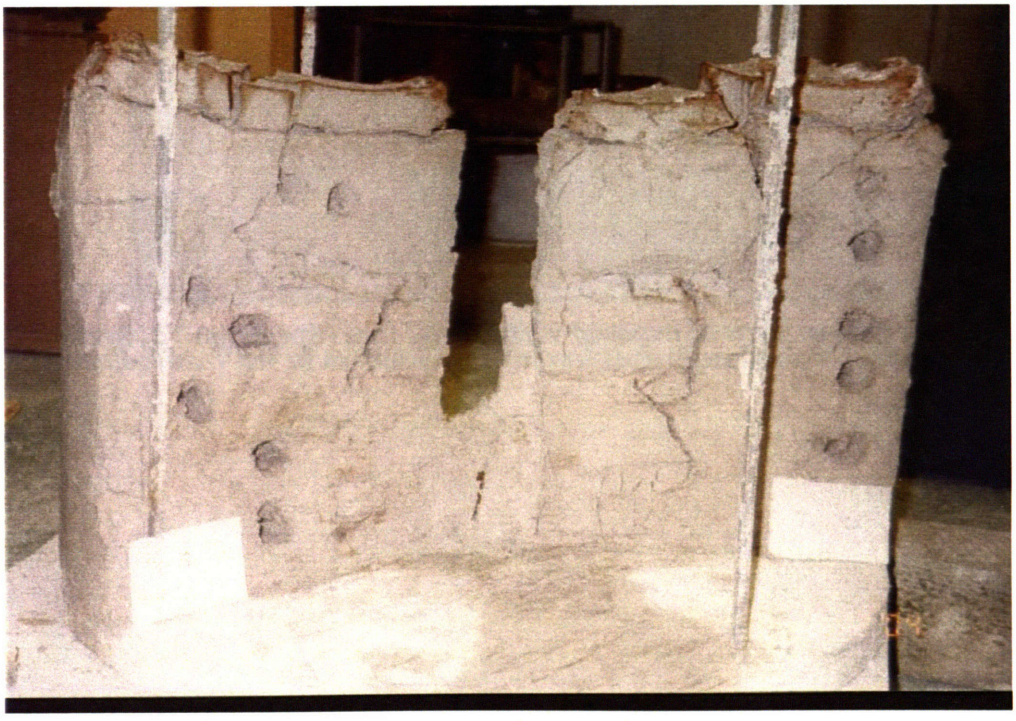

Figure B-2(d). View of exposed vertical soil face (Specimen T2, Section 7:left and Section 2:right)

Figure B-3(a). View of exposed vertical soil face (Specimen T3, Section 2)

Figure B-3(b). View of exposed vertical soil face (Specimen T3, Section 3)

Figure B-3(c). View of exposed vertical soil face (Specimen T3, Section 4)

Figure B-3(d). View of exposed vertical soil face (Specimen T3, Section 6)

Figure B-3(e). View of exposed vertical soil face (Specimen T3, Section 8)

Figure B-3(f). View of exposed vertical soil face (Specimen T3, Section 3:left and Section 6:right)

Figure B-3(g). View of exposed vertical soil face (Specimen T3, Section 7:left and Section 2:right)

Figure B-3(h). View of exhumed grouted disc in Specimen T3 (Segment 7/8, Lower cut)

Figure B-4(a). View of exposed vertical soil face (Specimen T4, Section 1)

Figure B-4(b). View of exposed vertical soil face (Specimen T4, Section 2)

Figure B-4(c). View of exposed vertical soil face (Specimen T4, Section 3)

Figure B-4(d). View of exposed vertical soil face (Specimen T4, Section 4)

Figure B-4(e). View of exposed vertical soil face (Specimen T4, Section 5)

Figure B-4(f). View of exposed vertical soil face (Specimen T4, Section 6)

Figure B-4(g). View of exposed vertical soil face (Specimen T4, Section 7)

Figure B-4(h). View of exposed vertical soil face (Specimen T4, Section 7A)

Figure B-4(i). View of exposed vertical soil face (Specimen T4, Section 8)

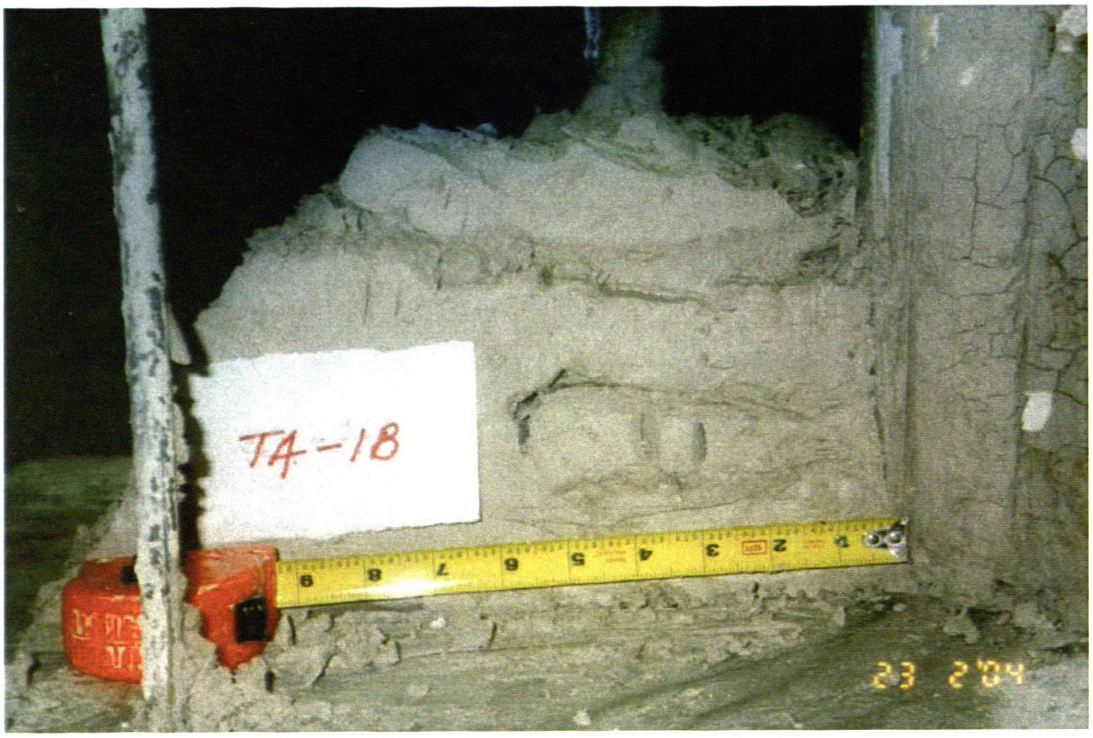

Figure B-4(j). View of exposed vertical soil face (Specimen T4, Section 1B)

Figure B-4(k). View of exposed vertical soil face (Specimen T4, Section 1A)

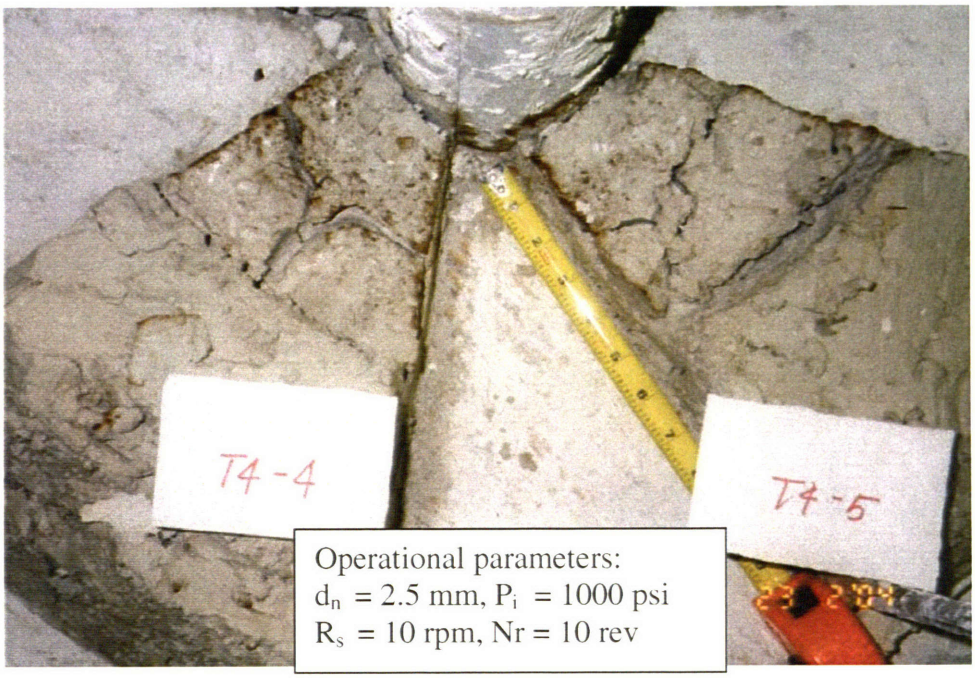

Figure B-4(l). View of exhumed grouted disc in Specimen T4 Lower cut (Segment 3/4:left and Segment 5/6:right)

Figure B-5(a). View of exposed vertical soil face (Specimen T6, Section 1)

Figure B-5(b). View of exposed vertical soil face (Specimen T6, Section 3)

Figure B-5(c). View of exposed vertical soil face (Specimen T6, Section 4)

Figure B-5(d). View of exposed vertical soil face (Specimen T6, Section 5)

Figure B-5(e). View of exposed vertical soil face (Specimen T6, Section 6)

Figure B-5(f). View of exposed vertical soil face (Specimen T6, Section 7)

Figure B-5(g). View of exposed vertical soil face (Specimen T6, Section 8)

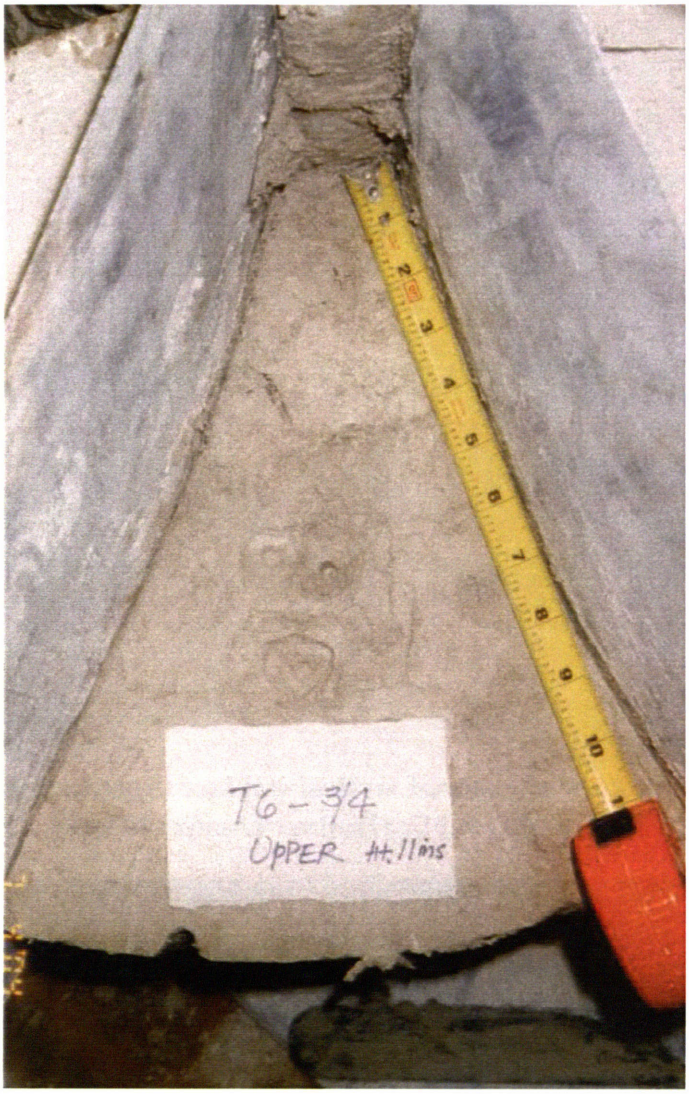

Figure B-5(h). View of exhumed grouted disc in Specimen T6 (Segment 3/4, Upper cut)

Figure B-6(a). View of exposed vertical soil face (Specimen T7, Section 1)

Figure B-6(b). View of exposed vertical soil face (Specimen T7, Section3; left and Section 4; right)

Figure B-6(c). View of exposed vertical soil face (Specimen T7, Section 3)

Figure B-6(d). View of exposed vertical soil face (Specimen T7, Section 4)

Figure B-6(e). View of exposed vertical soil face (Specimen T7, Section 5)

Figure B-6(f). View of exposed vertical soil face (Specimen T7, Section 6)

Figure B-6(g). View of exposed vertical soil face (Specimen T7, Section 7)

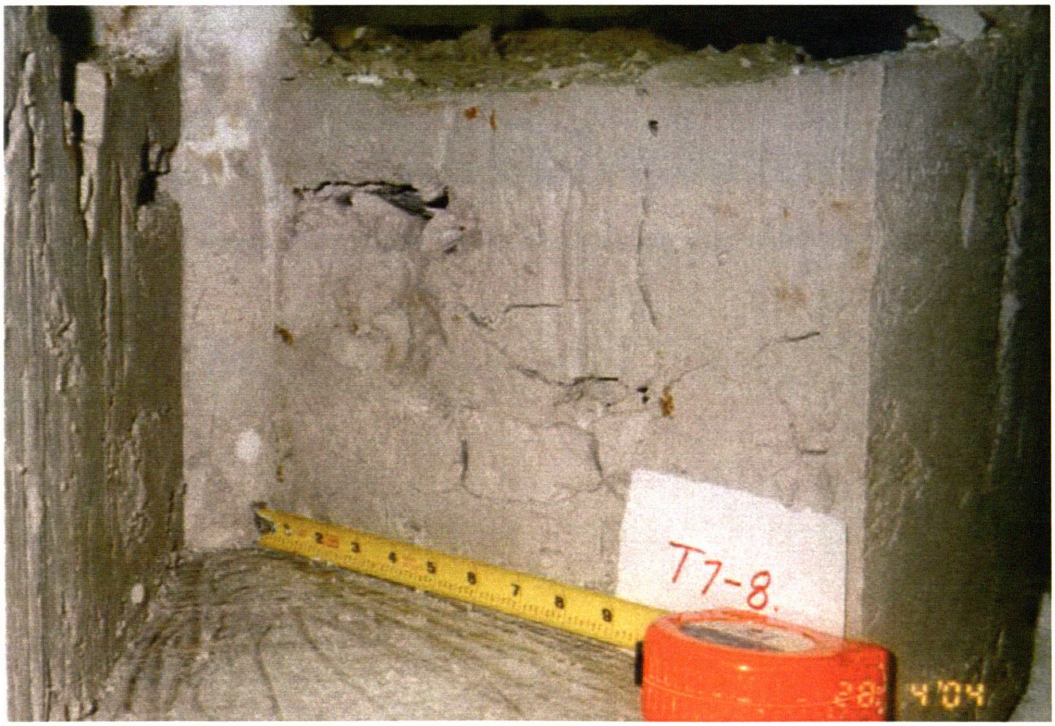

Figure B-6(h). View of exposed vertical soil face (Specimen T7, Section 8)

Figure B-7(a). View of exposed vertical soil face (Specimen T8, Section 1)

Figure B-7(b). View of exposed vertical soil face (Specimen T8, Section 2)

Figure B-7(c). View of exposed vertical soil face (Specimen T8, Section 3)

Figure B-7(d). View of exposed vertical soil face (Specimen T8, Section 4)

Figure B-7(e). View of exposed vertical soil face (Specimen T8, Section 5)

Figure B-7(f). View of exposed vertical soil face (Specimen T8, Section 6)

Figure B-7(g). View of exposed vertical soil face (Specimen T8, Section 7)

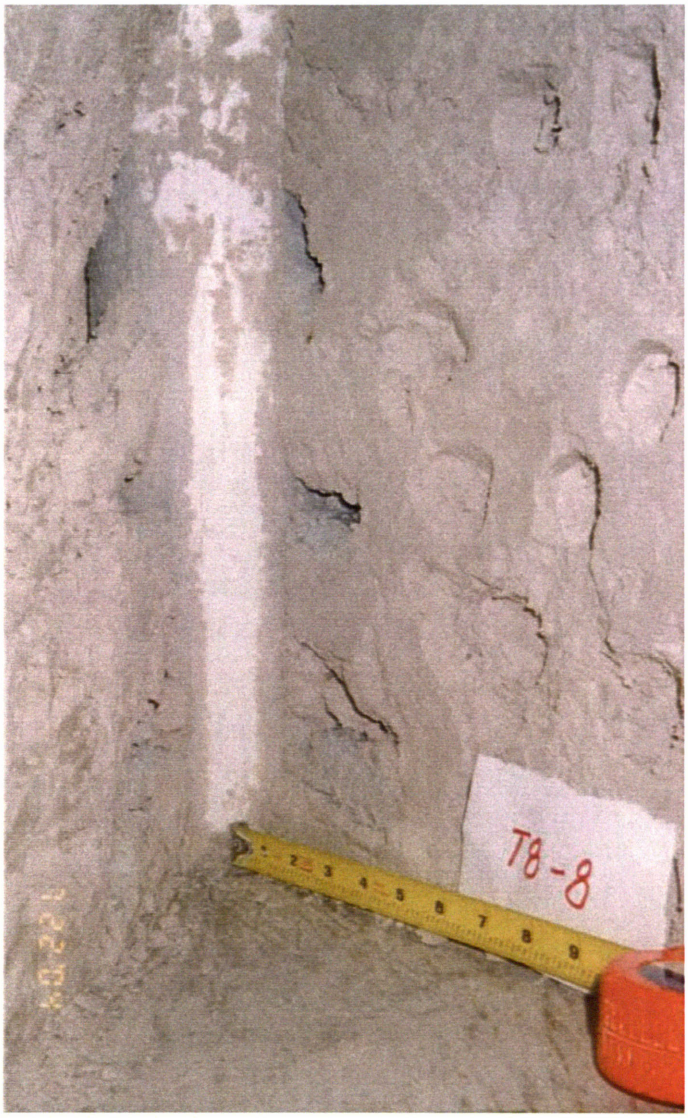

Figure B-7(h). View of exposed vertical soil face (Specimen T8, Section 8)

Figure B-8(a). View of exposed vertical soil face (Specimen T9, Section 1)

Figure B-8(b). View of exposed vertical soil face (Specimen T9, Section 2)

Figure B-8(c). View of exposed vertical soil face (Specimen T9, Section 3)

Figure B-8(d). View of exposed vertical soil face (Specimen T9, Section 4)

Figure B-8(e). View of exposed vertical soil face (Specimen T9, Section 5)

Figure B-8(f). View of exposed vertical soil face (Specimen T9, Section 6)

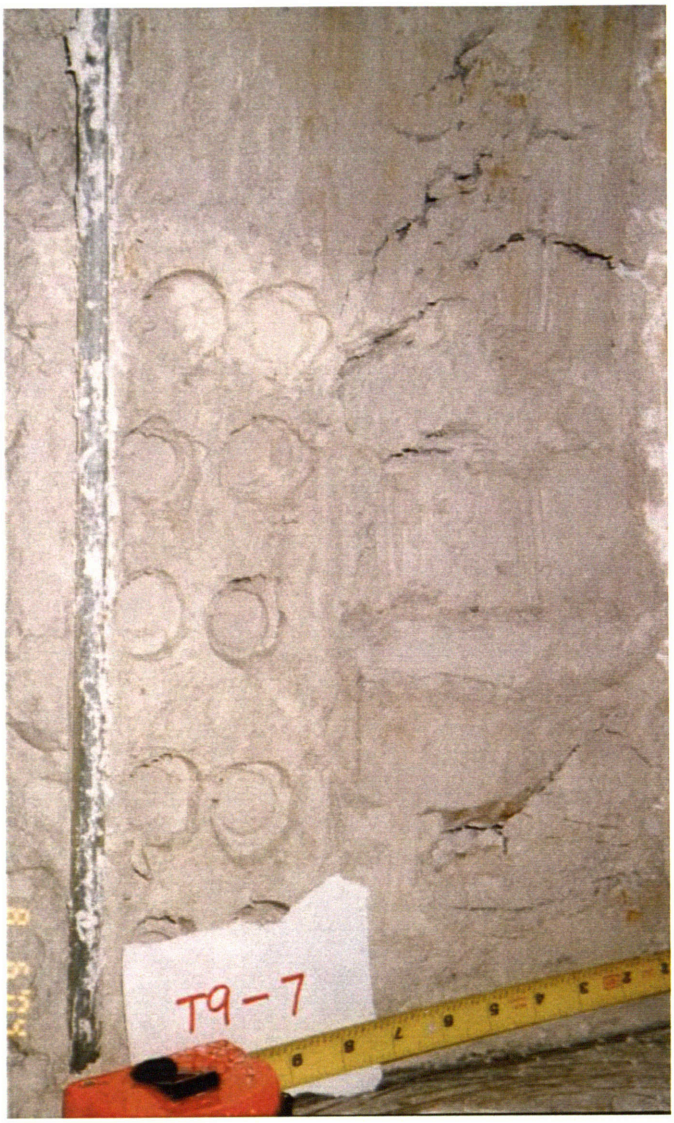

Figure B-8(g). View of exposed vertical soil face (Specimen T9, Section 7)

Figure B-8(h). View of exposed vertical soil face (Specimen T9, Section 8)

Figure B-8(i). View of exhumed grouted disc in Specimen T9 (Segment 3/4, Middle cut)

Figure B-8(j). View of exhumed grouted disc in Specimen T9 (Segment 7/8, Middle cut)

APPENDIX C

CUT SECTIONS IN VERTICAL SOIL FACE
&
TORVANE SHEAR STRENGTH PROFILES

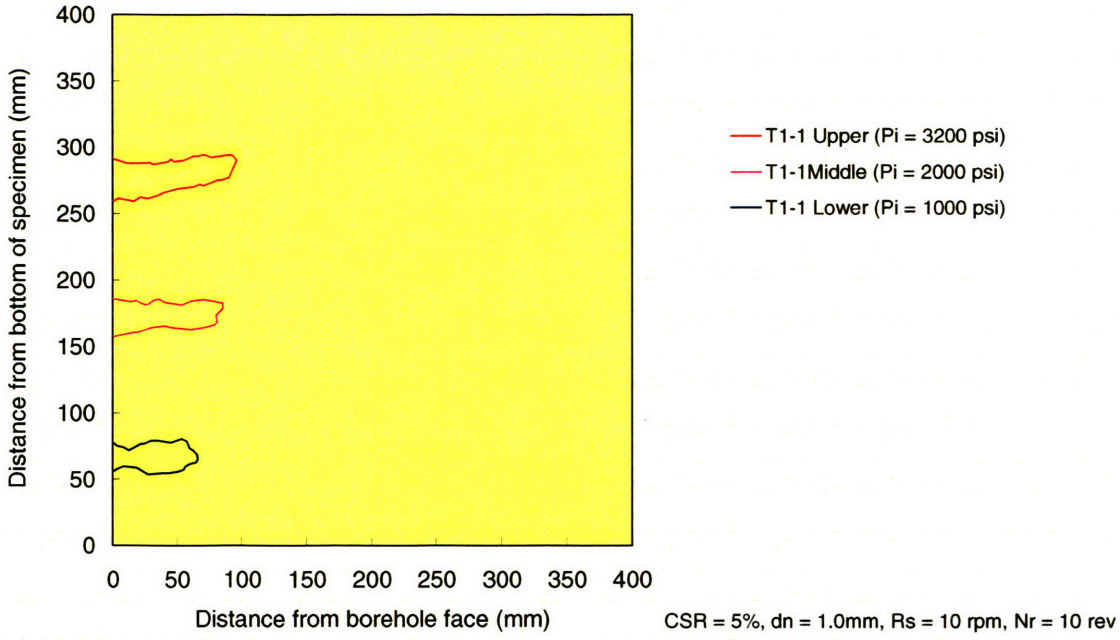

Figure C-1(a). Shape of cut for specimen T1 (Section1)

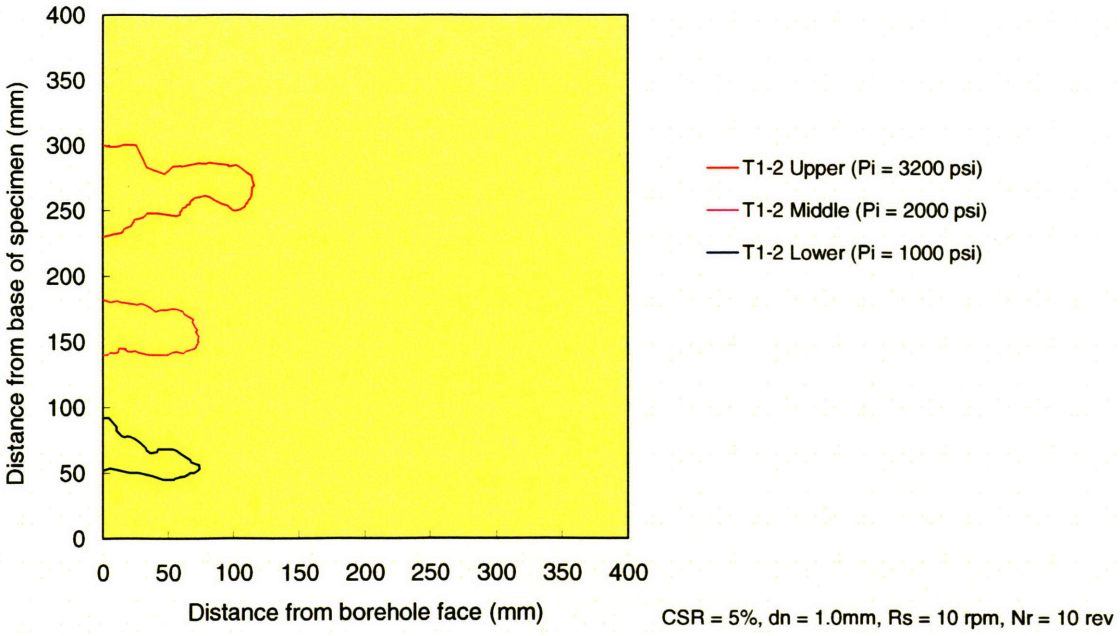

Figure C-1(b). Shape of cut for specimen T1 (Section 2)

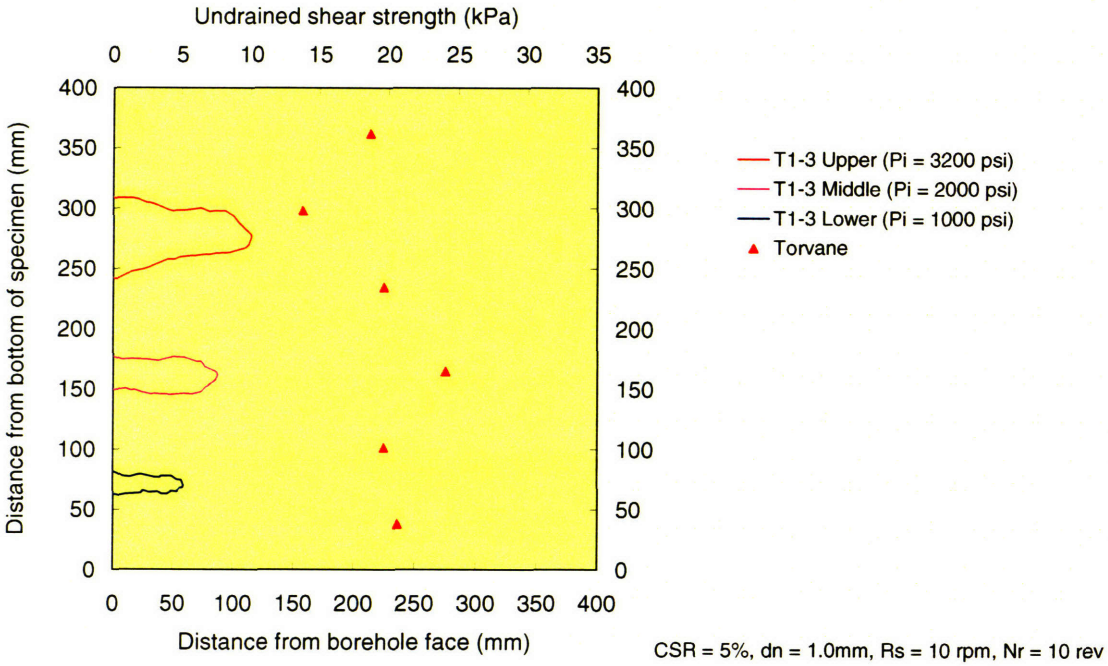

Figure C-1(c). Shape of cut for specimen T1 (Section 3)

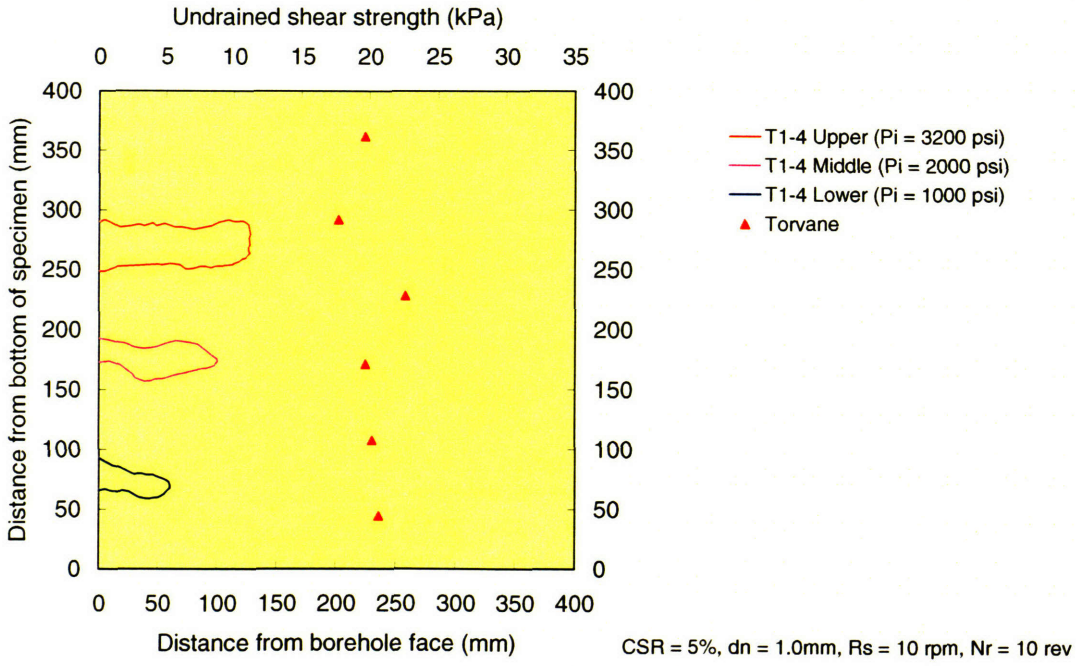

Figure C-1(d). Shape of cut for specimen T1 (Section 4)

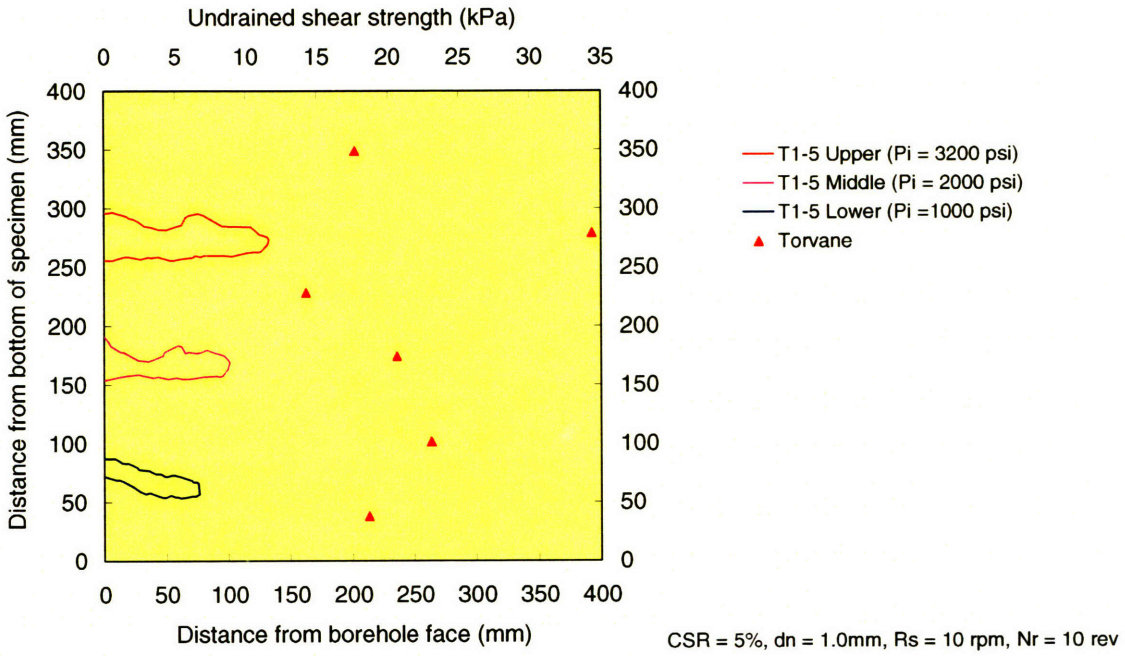

Figure C-1(e). Shape of cut for specimen T1 (Section 5)

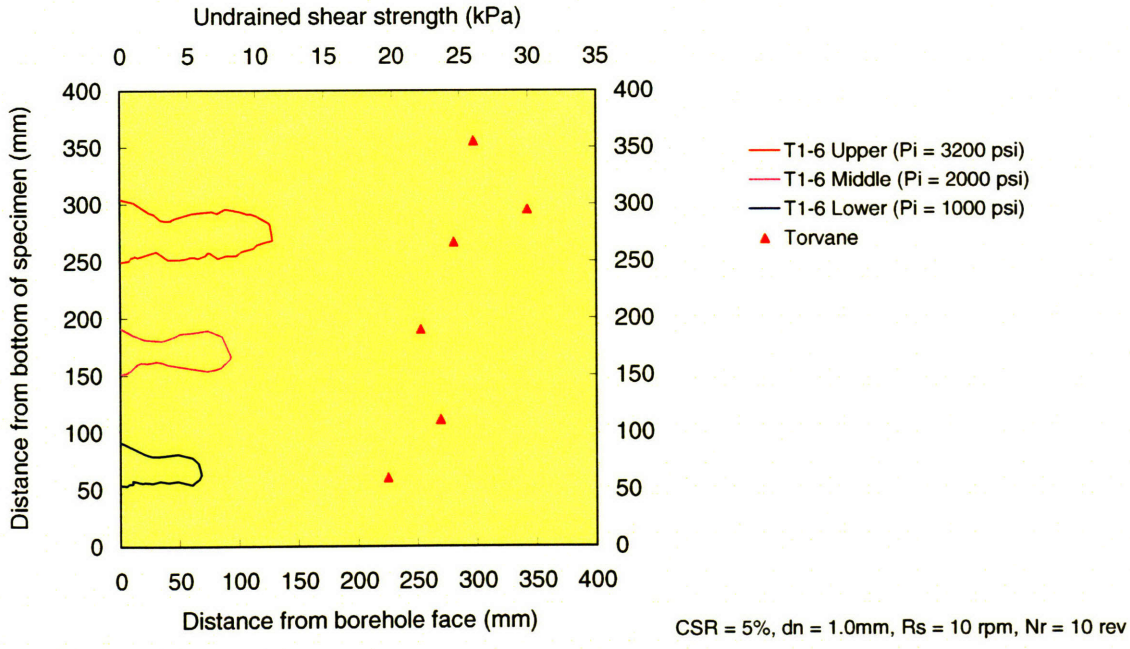

Figure C-1(f). Shape of cut for specimen T1 (Section 6)

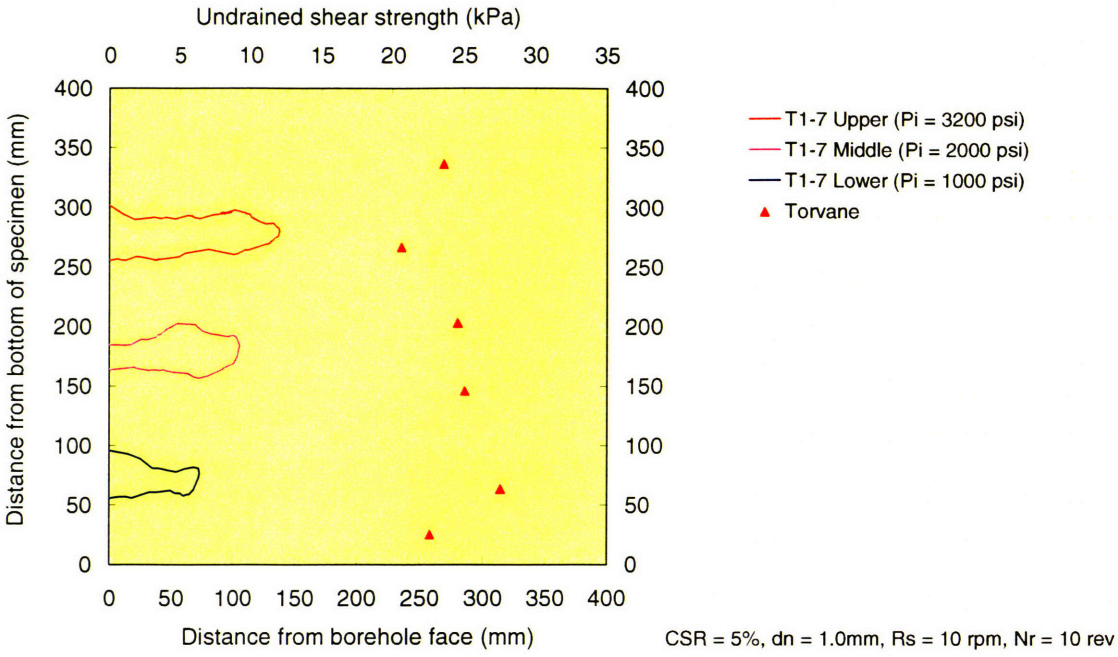

Figure C-1(g). Shape of cut for specimen T1 (Section 7)

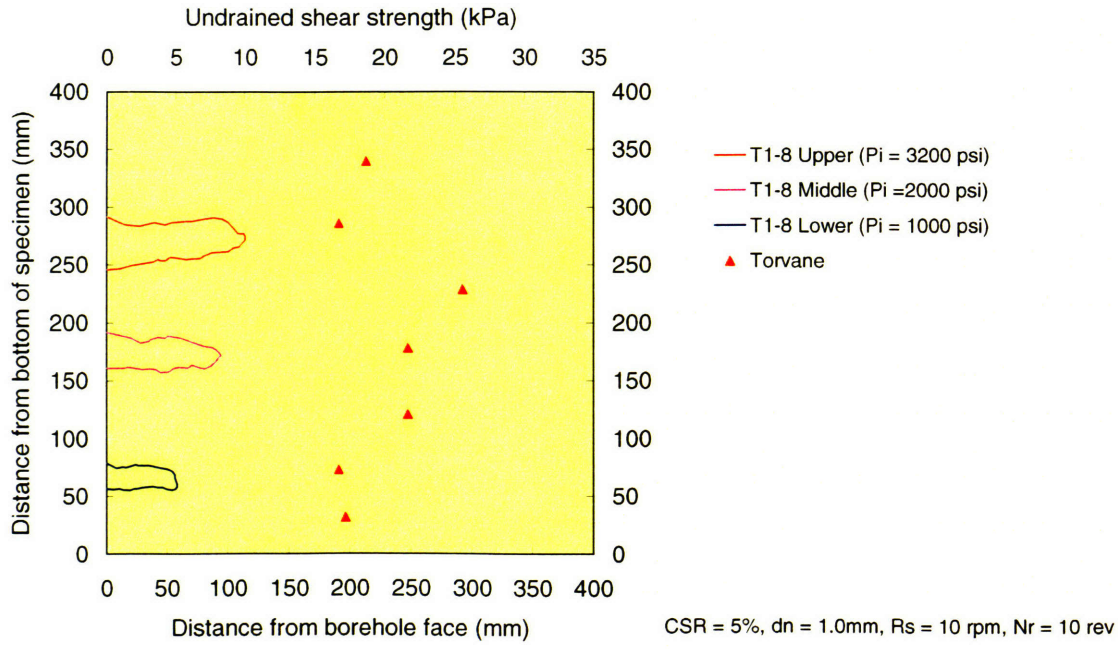

Figure C-1(h). Shape of cut for specimen T1 (Section 8)

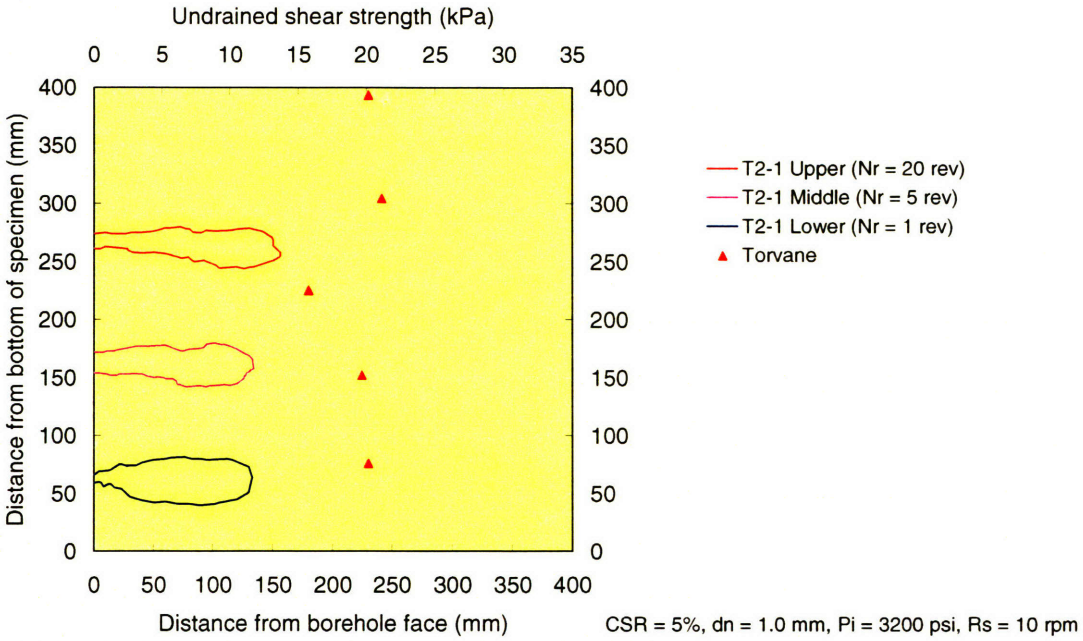

Figure C-2(a). Shape of cut for specimen T2 (Section 1)

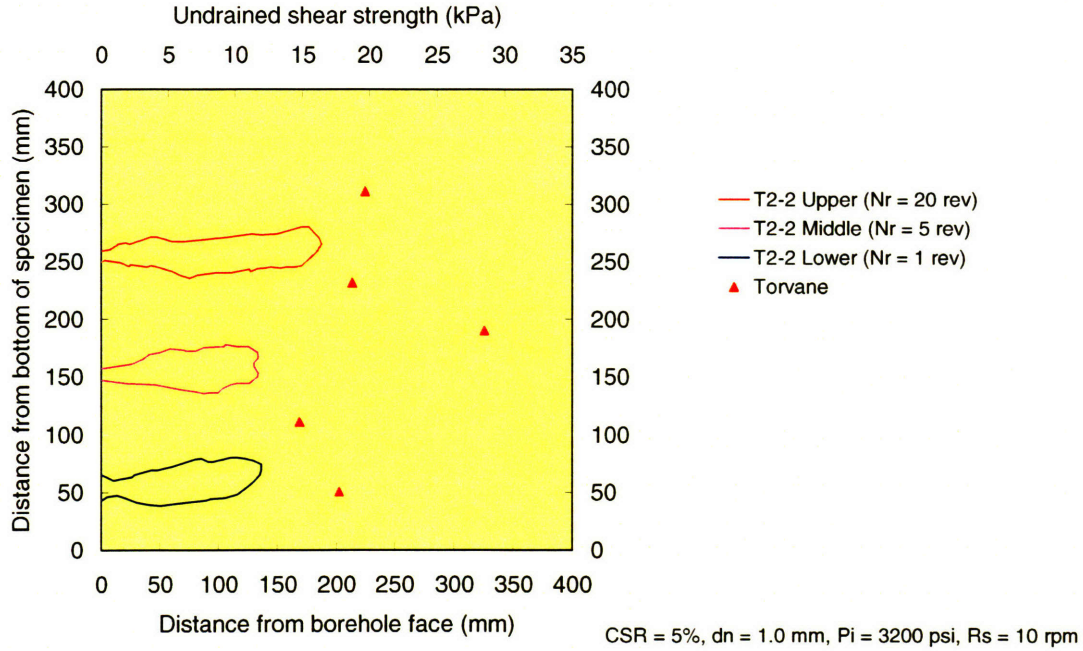

Figure C-2(b). Shape of cut for specimen T2 (Section 2)

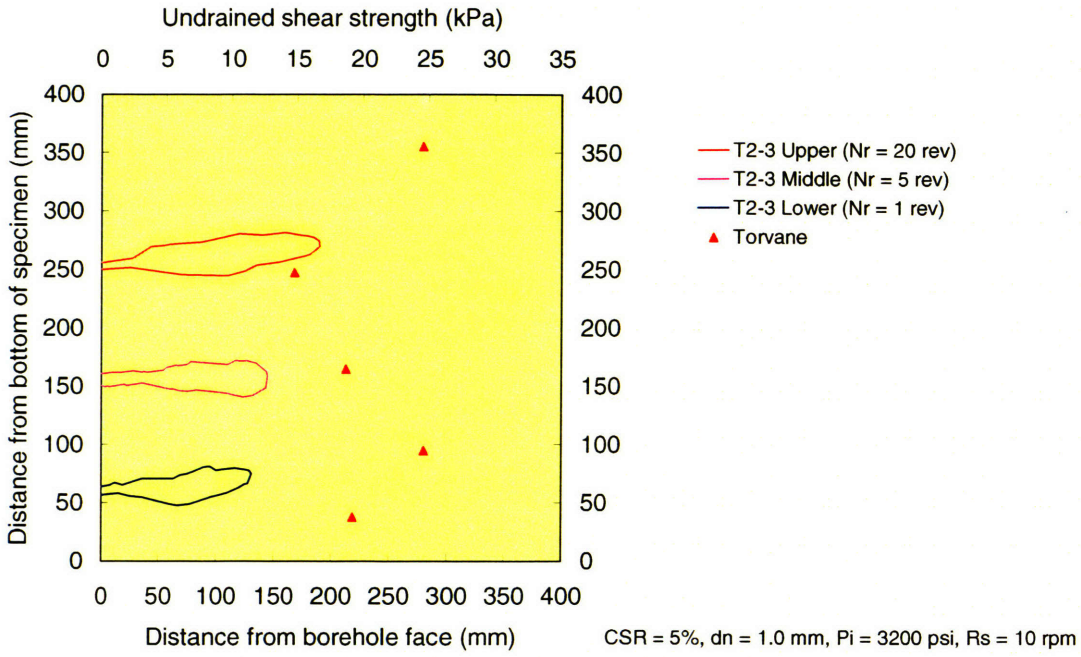

Figure C-2(c). Shape of cut for specimen T2 (Section 3)

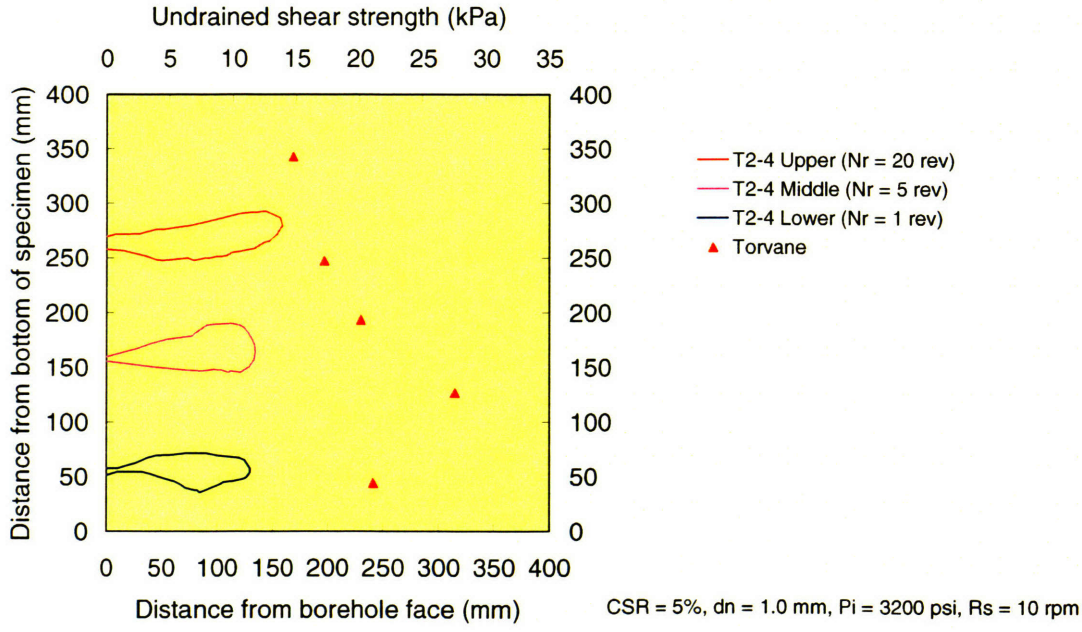

Figure C-2(d). Shape of cut for specimen T2 (Section 4)

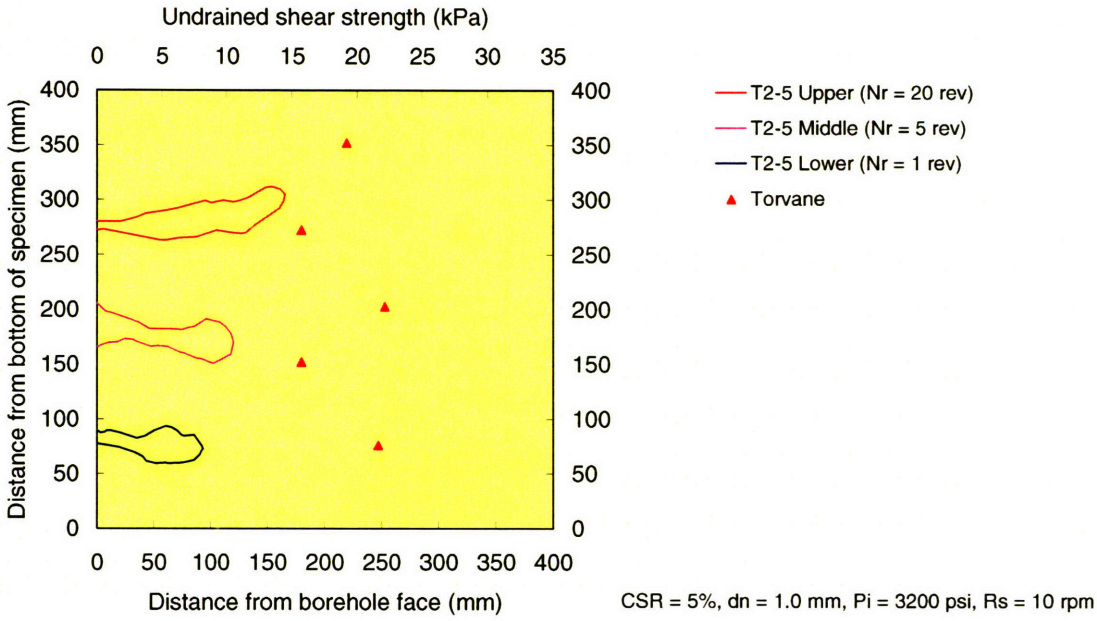

Figure C-2(e). Shape of cut for specimen T2 (Section 5)

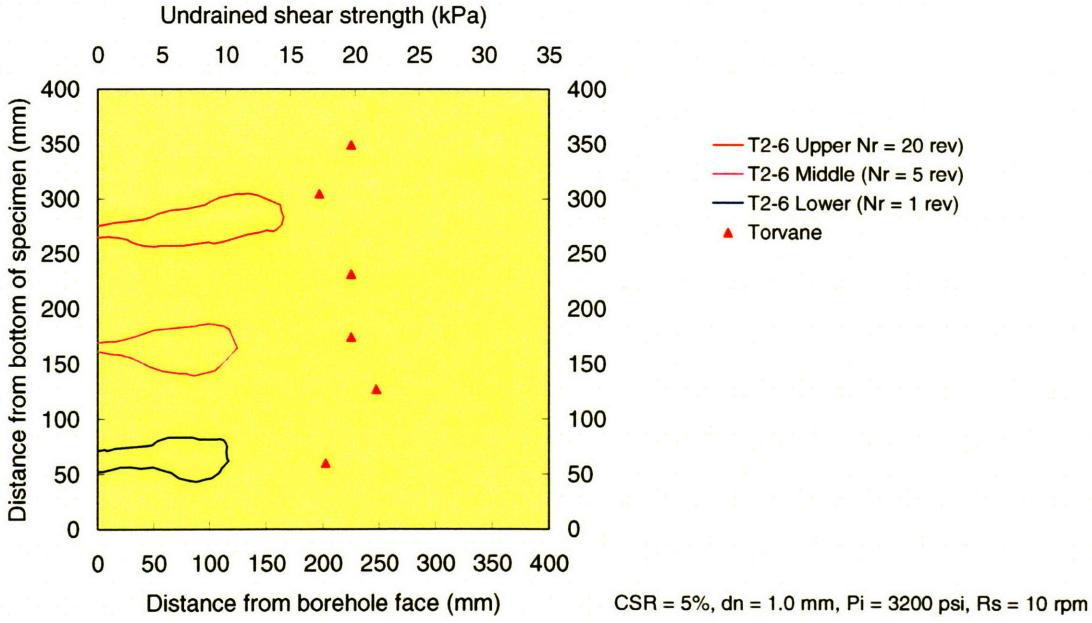

Figure C-2(f). Shape of cut for specimen T2 (Section 6)

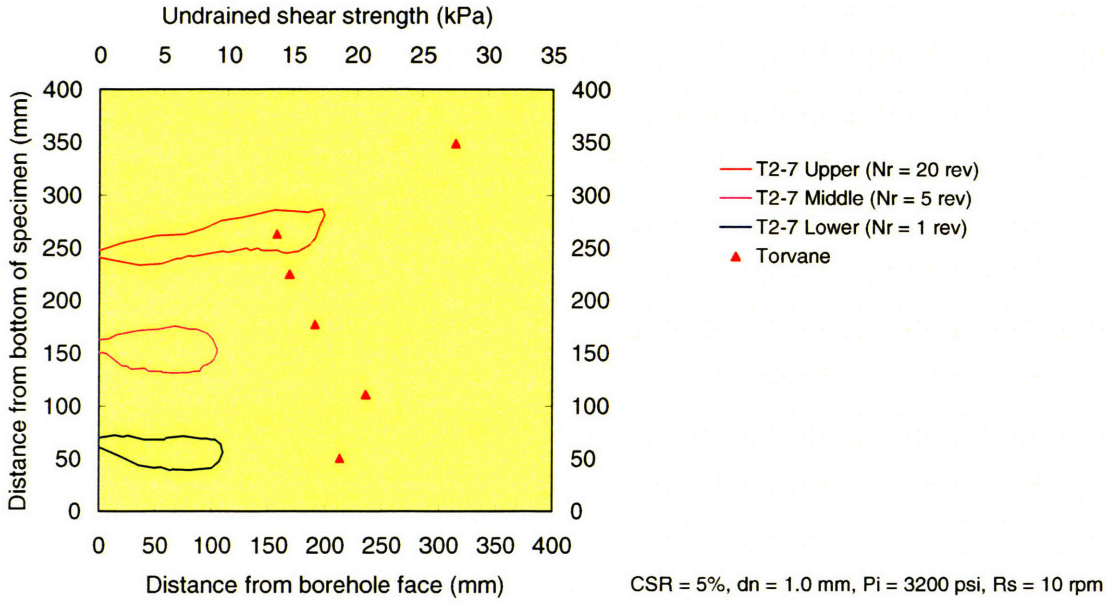

Figure C-2(g). Shape of cut for specimen T2 (Section 7)

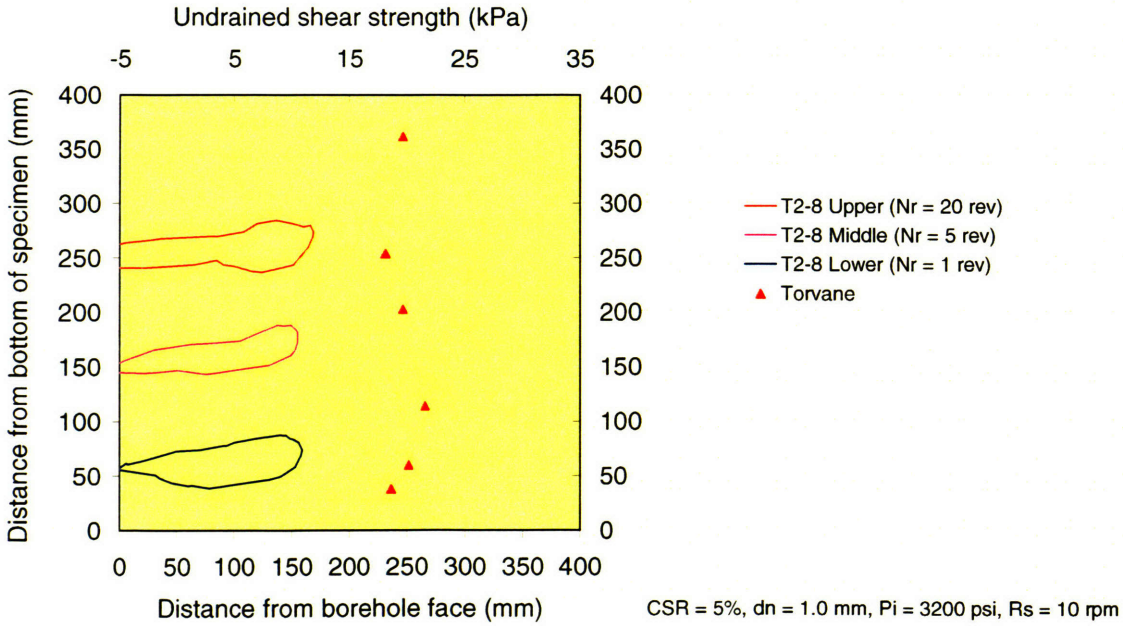

Figure C-2(h). Shape of cut for specimen T2 (Section 8)

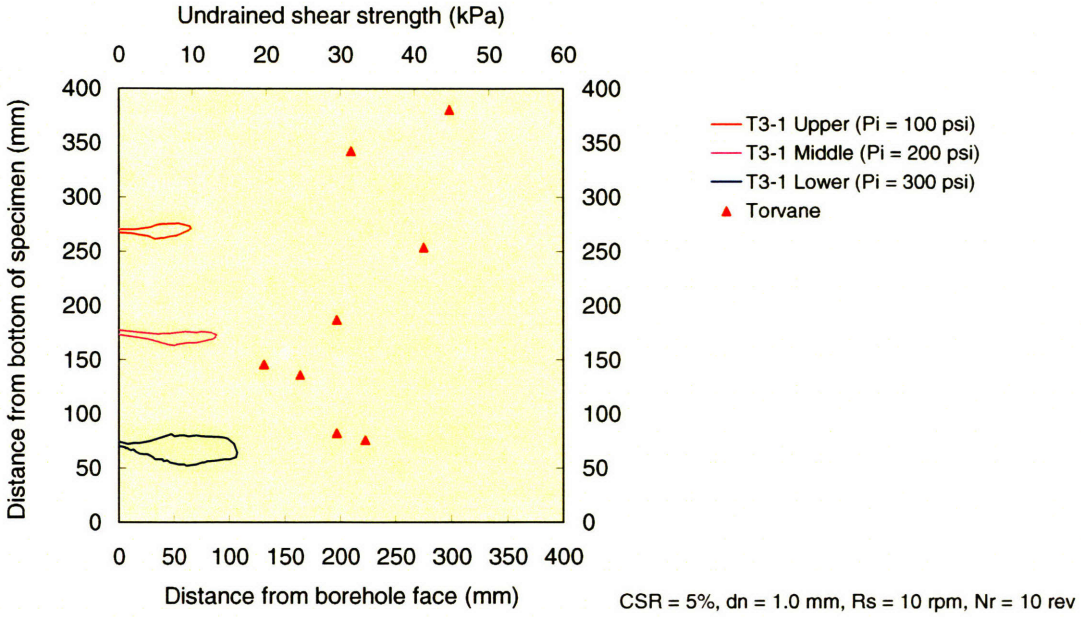

Figure C-3(a). Shape of cut for specimen T3 (Section 1)

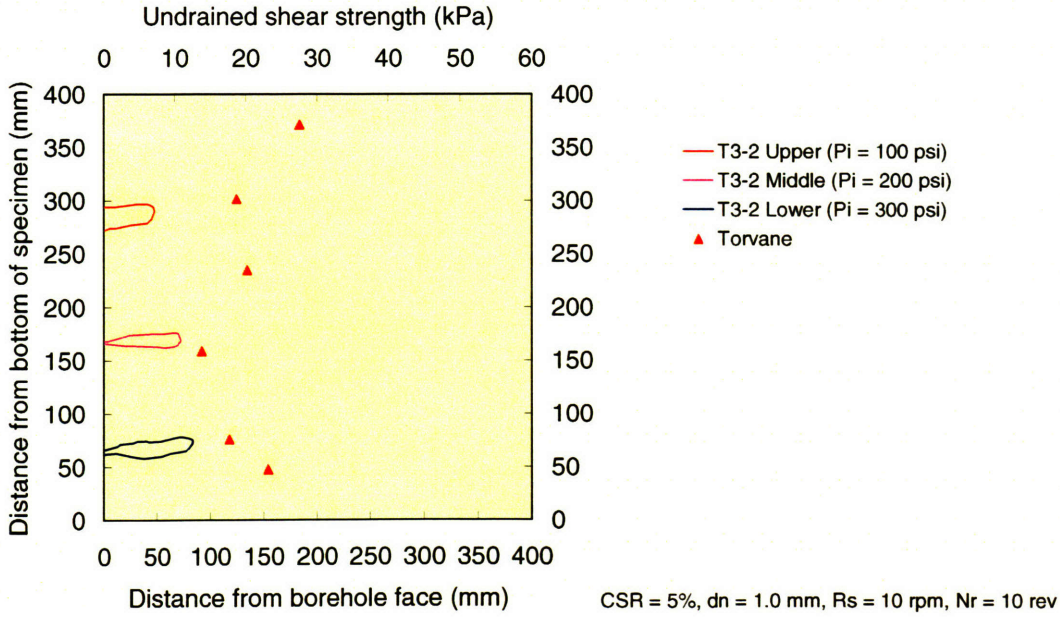

Figure C-3(b). Shape of cut for specimen T3 (Section 2)

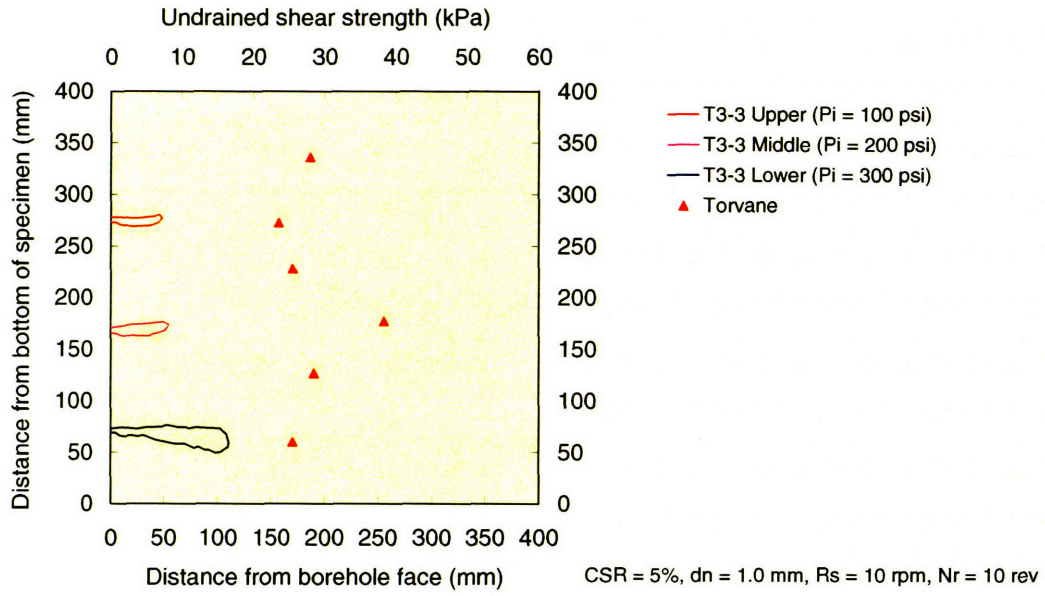

Figure C-3(c). Shape of cut for specimen T3 (Section 3)

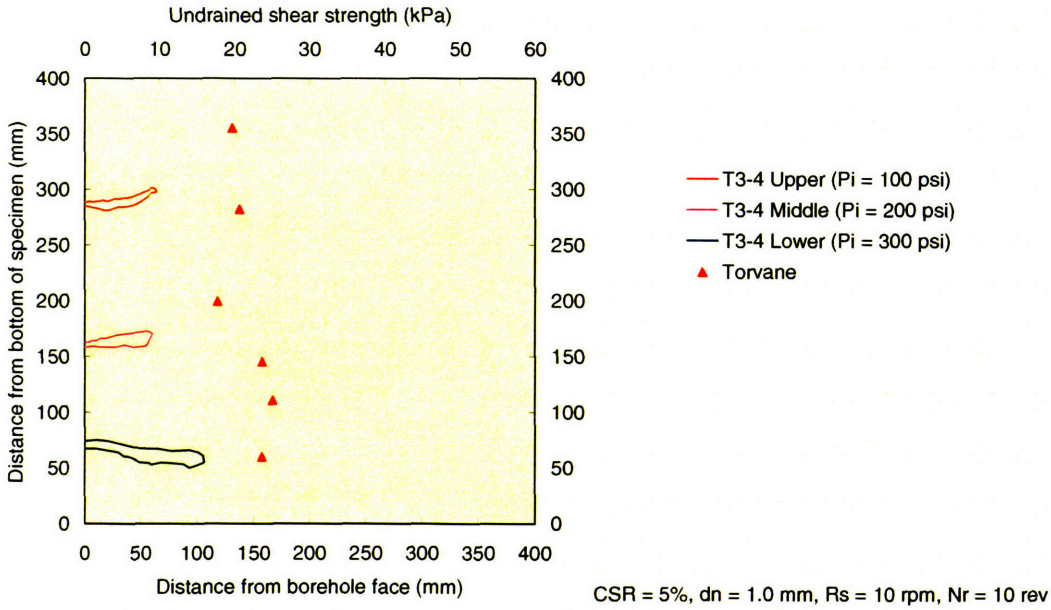

Figure C-3(d). Shape of cut for specimen T3 (Section 4)

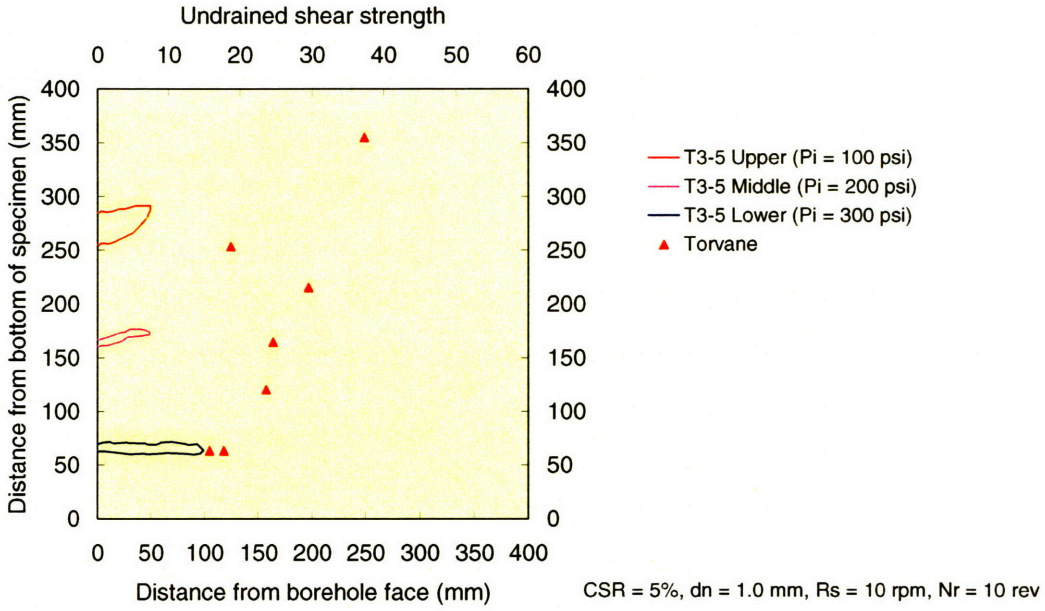

Figure C3(e). Shape of cut for specimen T3 (Section 5)

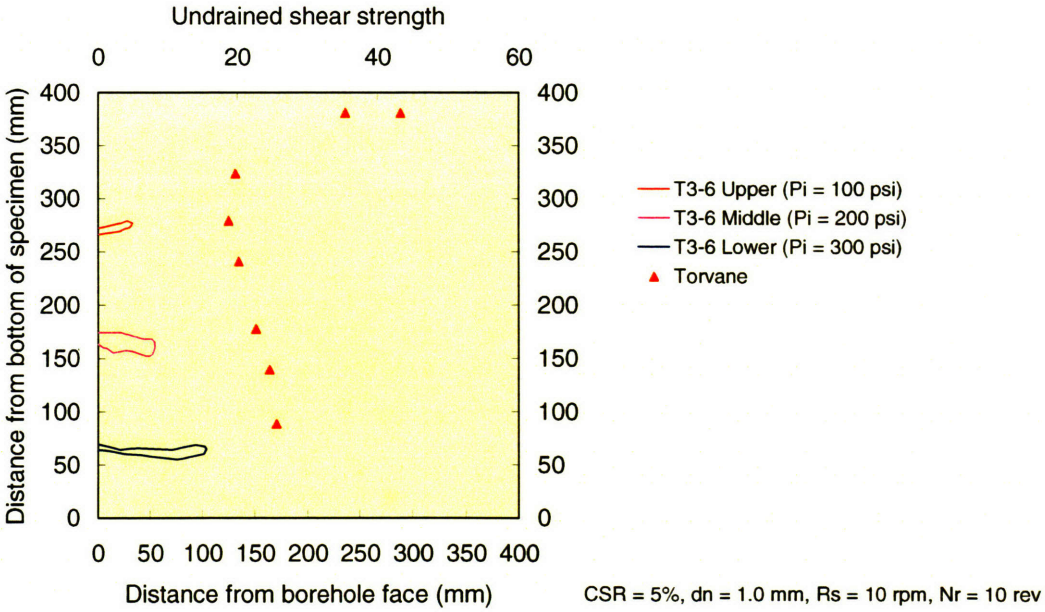

Figure C-3(f). Shape of cut for specimen T3 (Section 6)

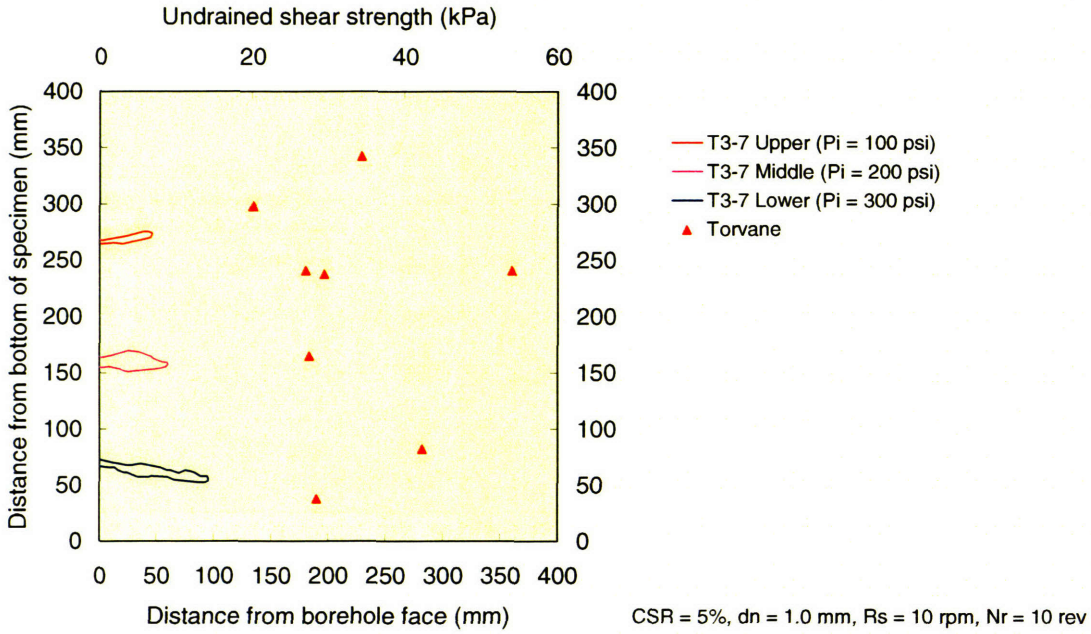

Figure C-3(g). Shape of cut for specimen T3 (Section 7)

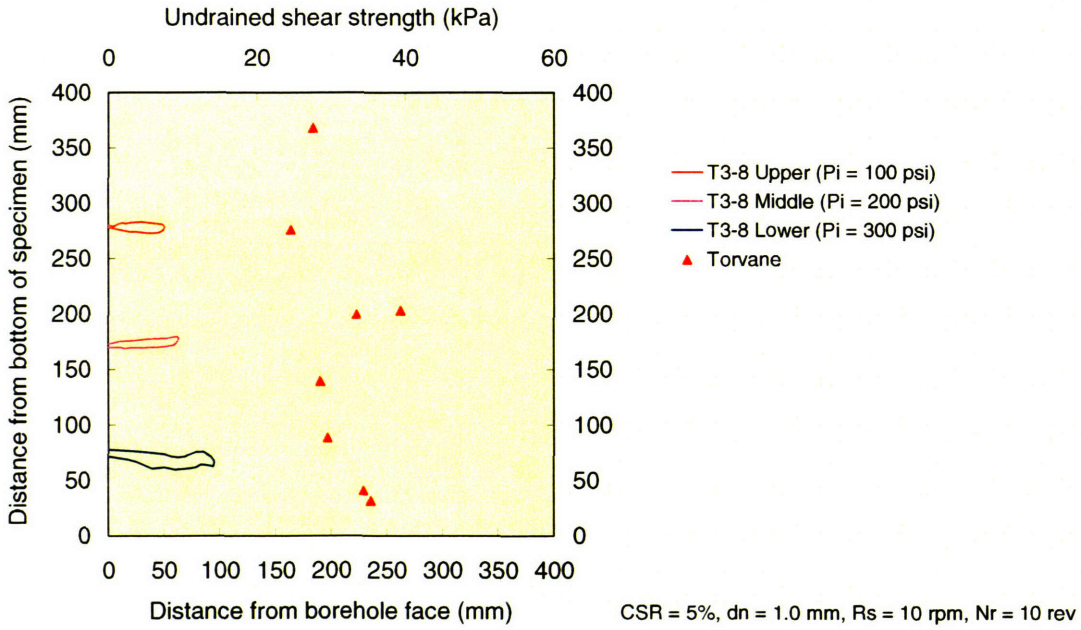

Figure C-3(h). Shape of cut for specimen T3 (Section 8)

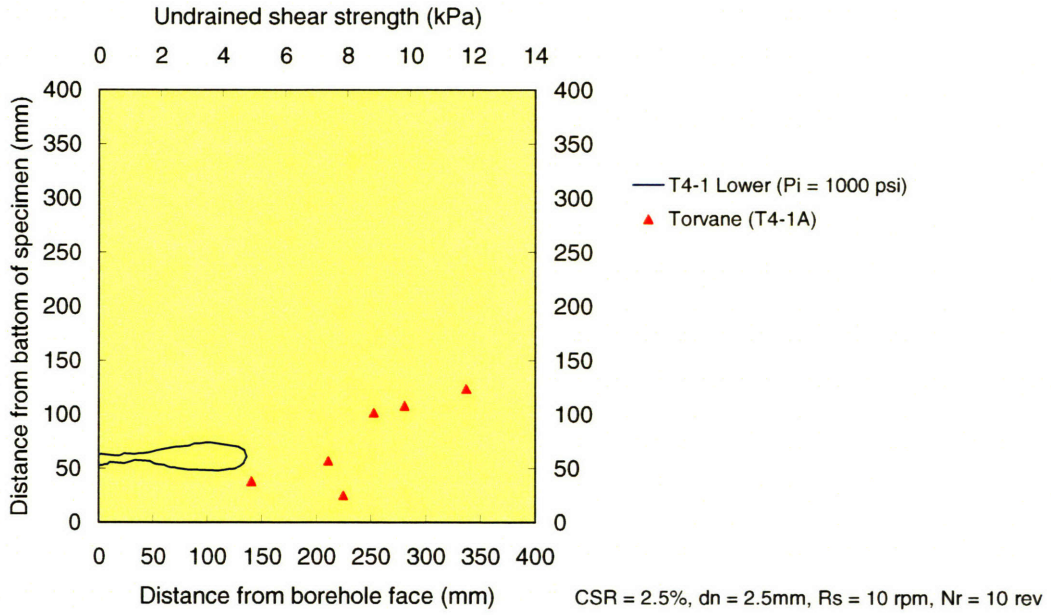

Figure C-4(a). Shape of cut for specimen T4 (Section 1)

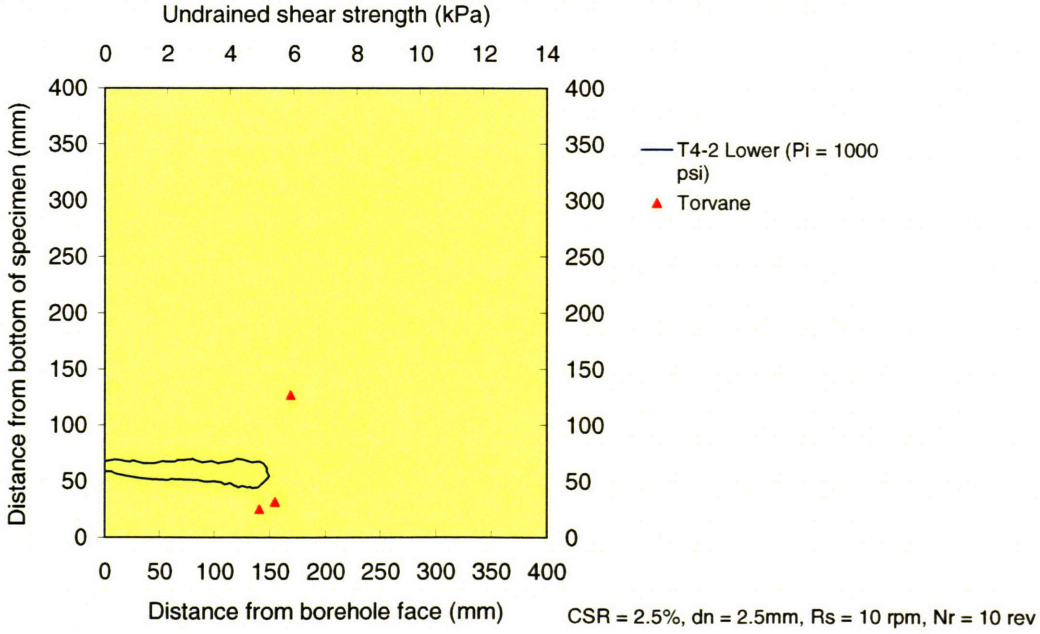

Figure C-4(b). Shape of cut for specimen T4 (Section 2)

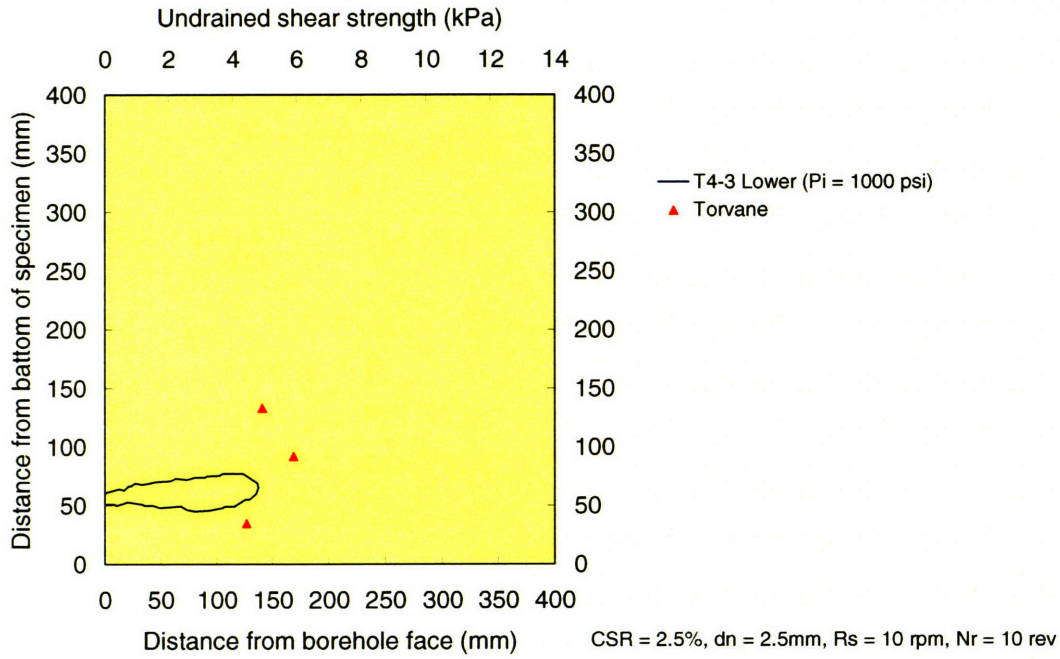

Figure C-4(c). Shape of cut for specimen T4 (Section 3)

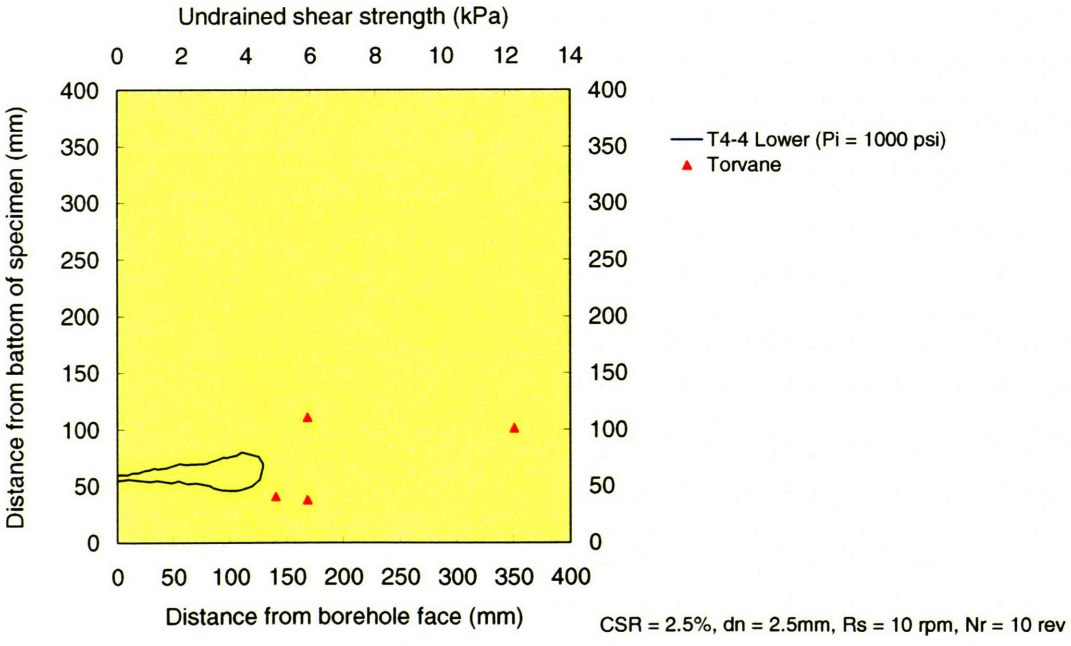

Figure C-4(d). Shape of cut for specimen T4 (Section 4)

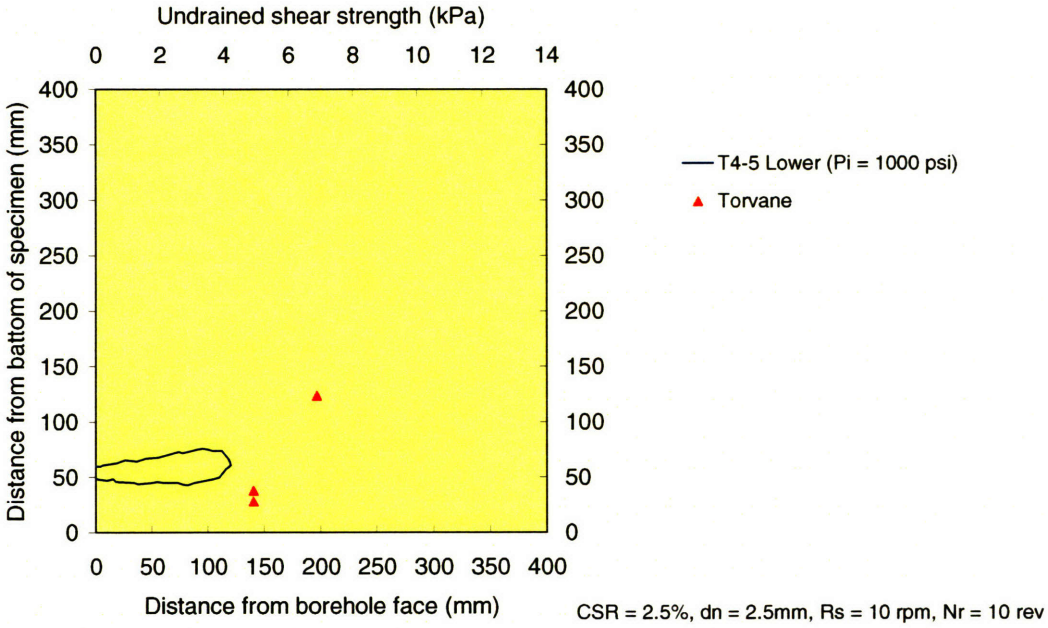

Figure C-4(e). Shape of cut for specimen T4 (Section 5)

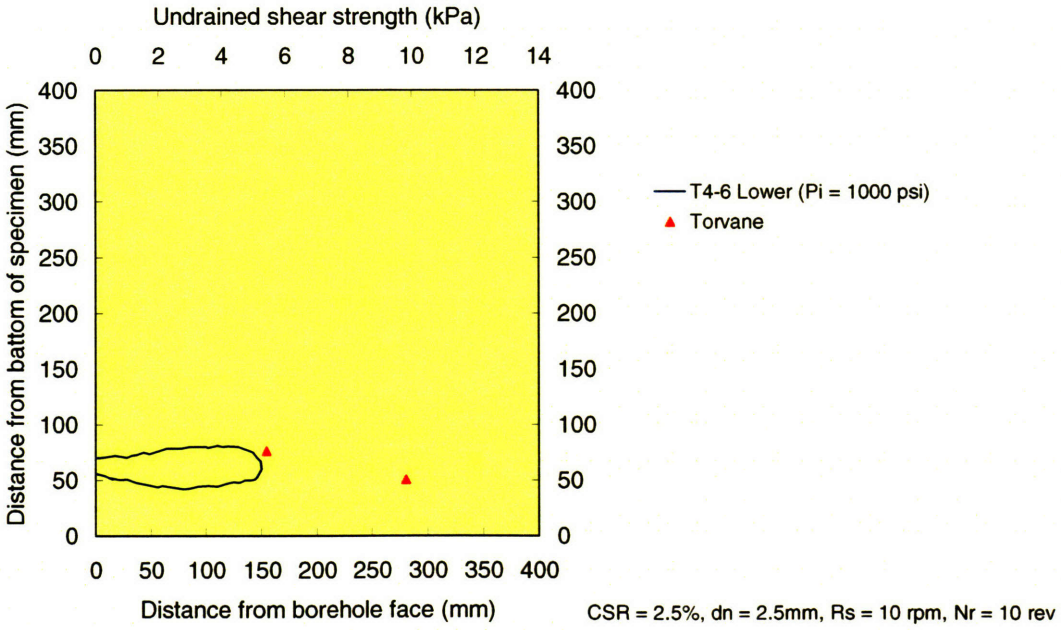

Figure C-4(f). Shape of cut for specimen T4 (Section 6)

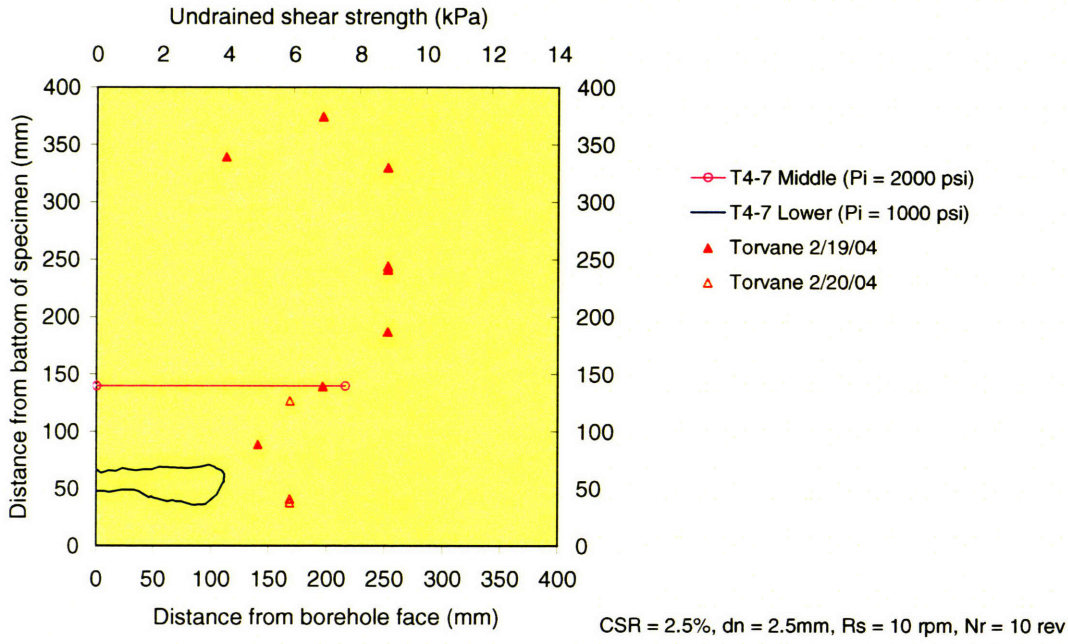

Figure C-4(g). Shape of cut for specimen T4 (Section 7)

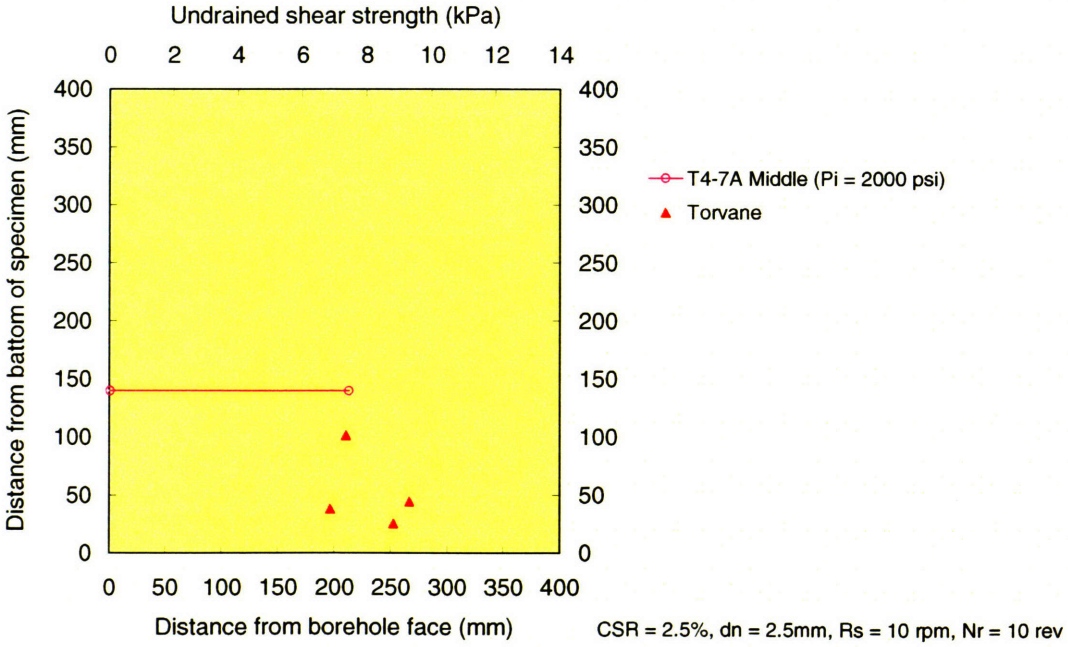

Figure C-4(h). Shape of cut for specimen T4 (Section 7A)

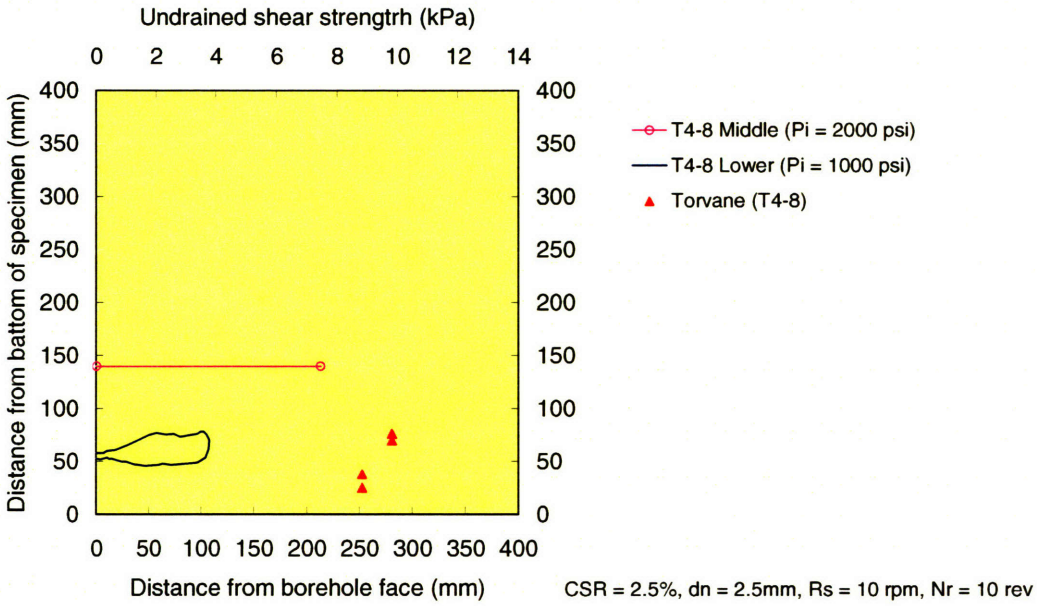

Figure BC-4(i). Shape of cut for specimen T4 (Section 8)

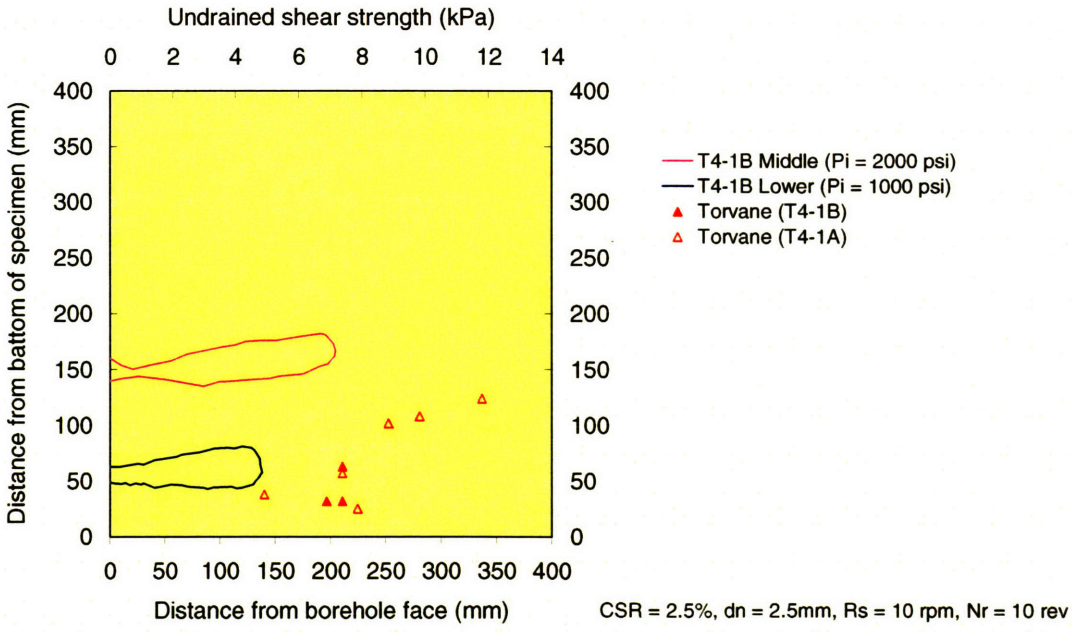

Figure C-4(j). Shape of cut for specimen T4 (Section 4-1A)

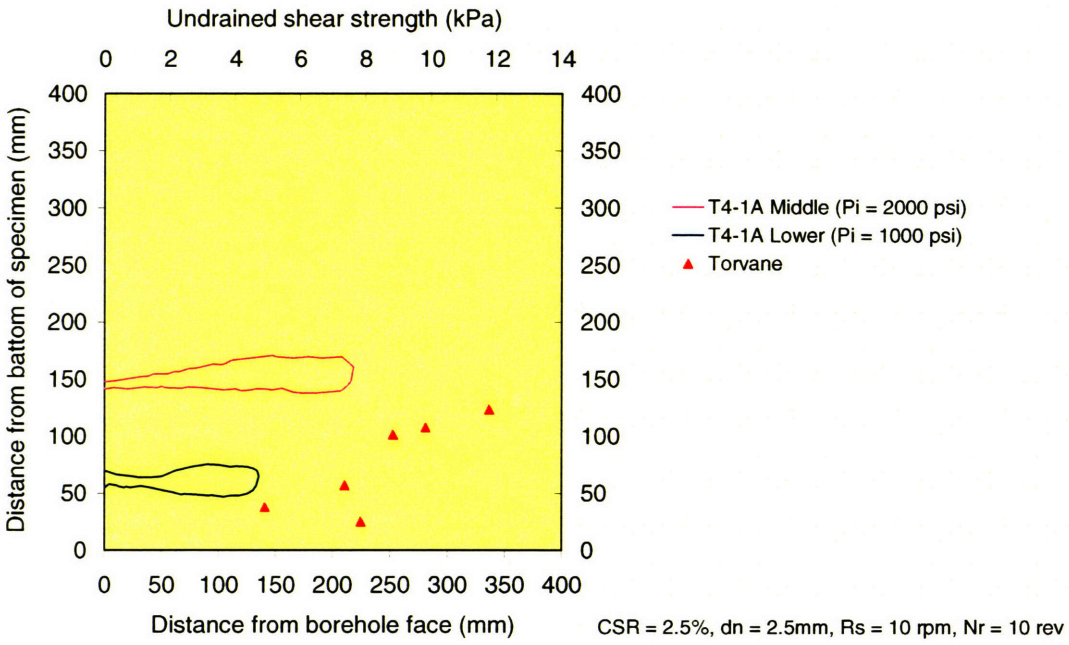

Figure C-4(k). Shape of cut for specimen T4 (Section 4-1B)

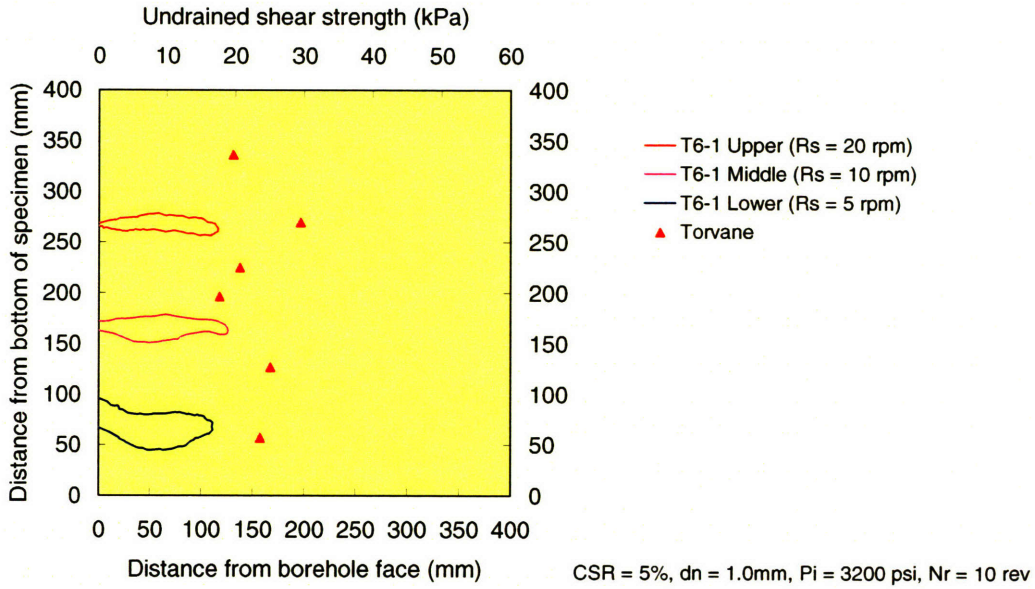

Figure C-5(a). Shape of cut for specimen T6 (Section 1)

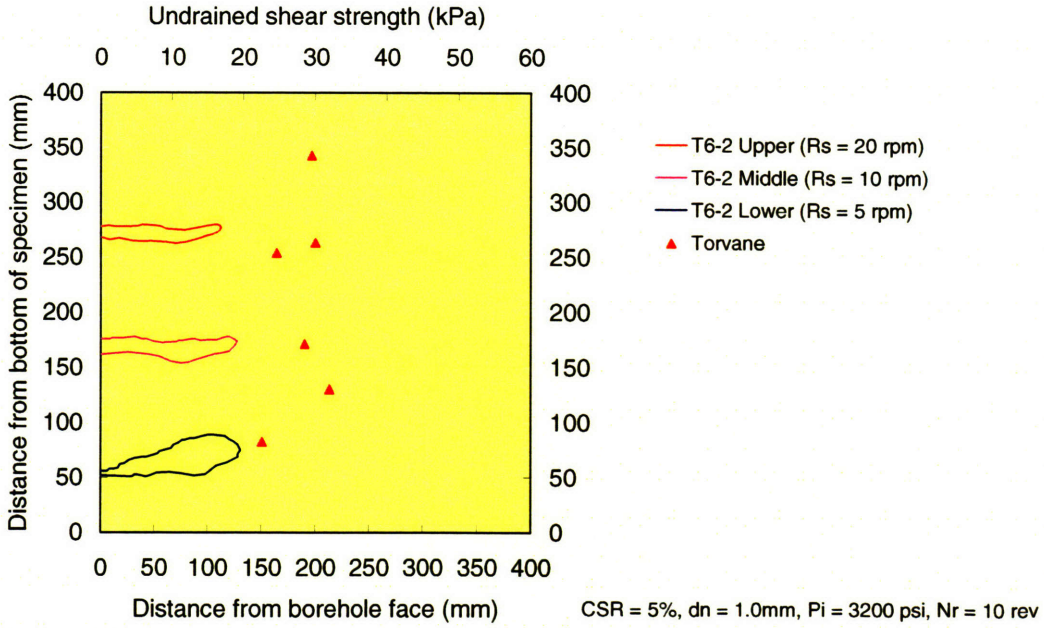

Figure C-5(b). Shape of cut for specimen T6 (Section 2)

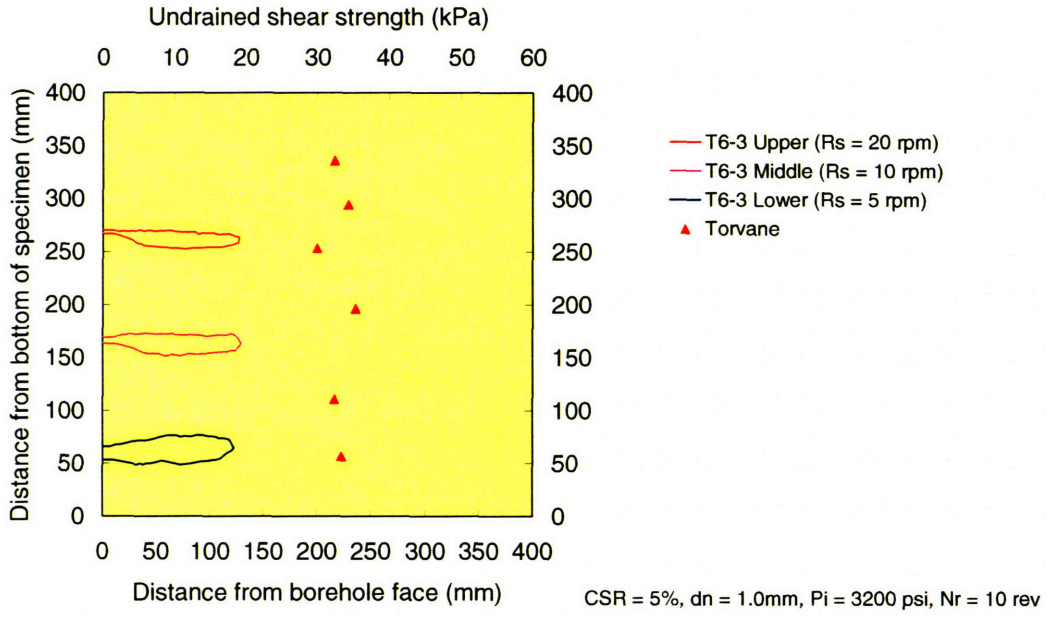

Figure C-5(c). Shape of cut for specimen T6 (Section 3)

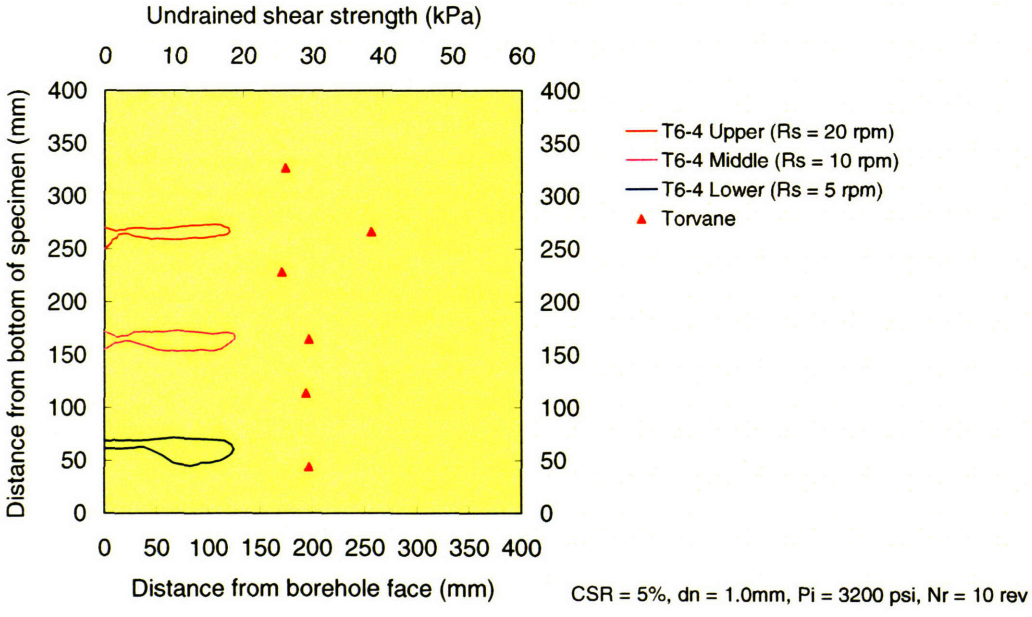

Figure C-5(d). Shape of cut for specimen T6 (Section 4)

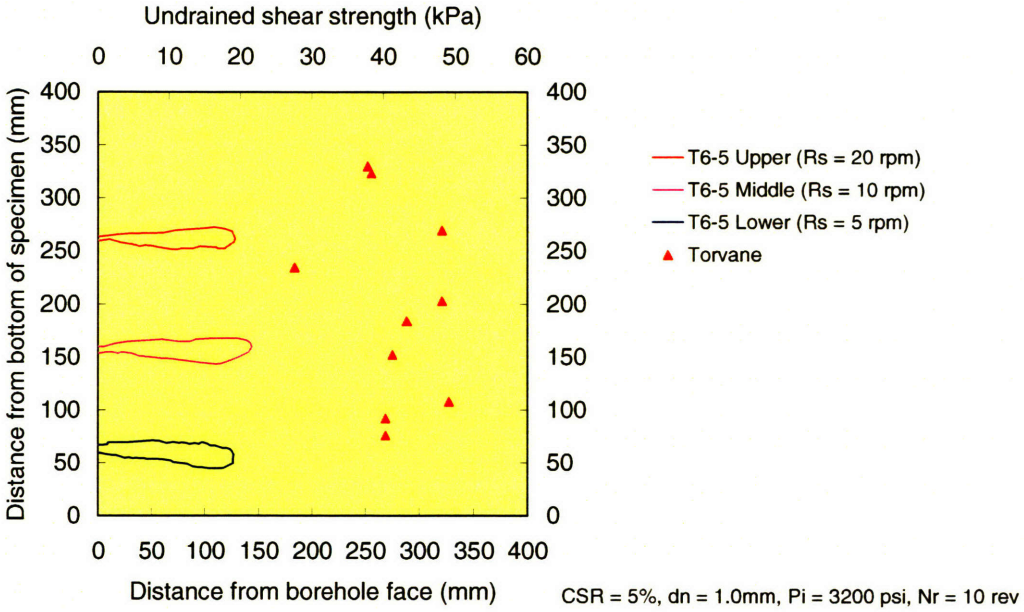

Figure C-5(e). Shape of cut for specimen T6 (Section 5)

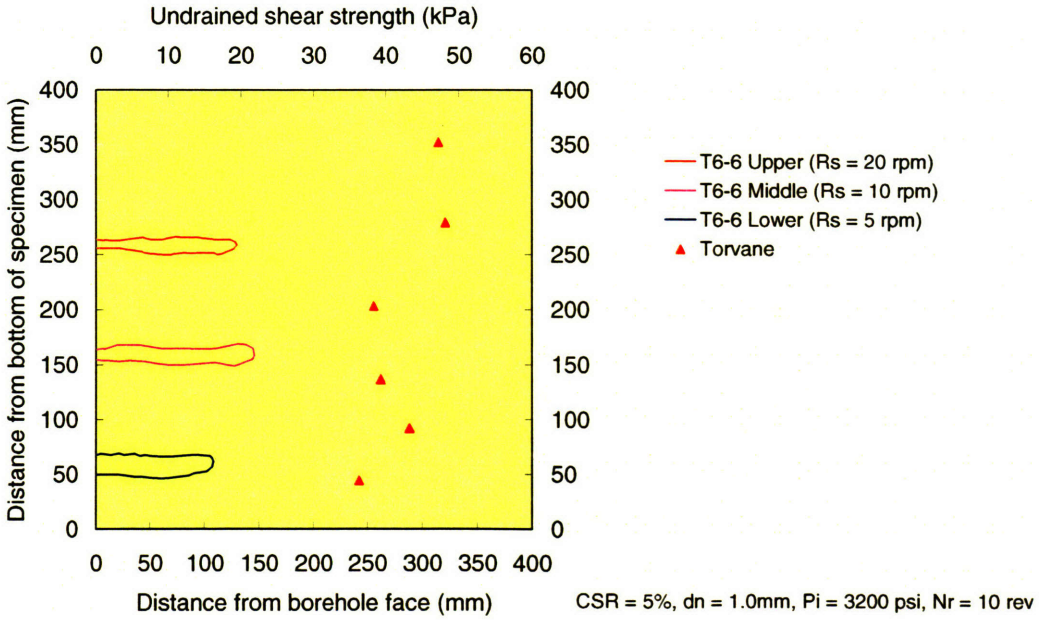

Figure C-5(f). Shape of cut for specimen T6 (Section 6)

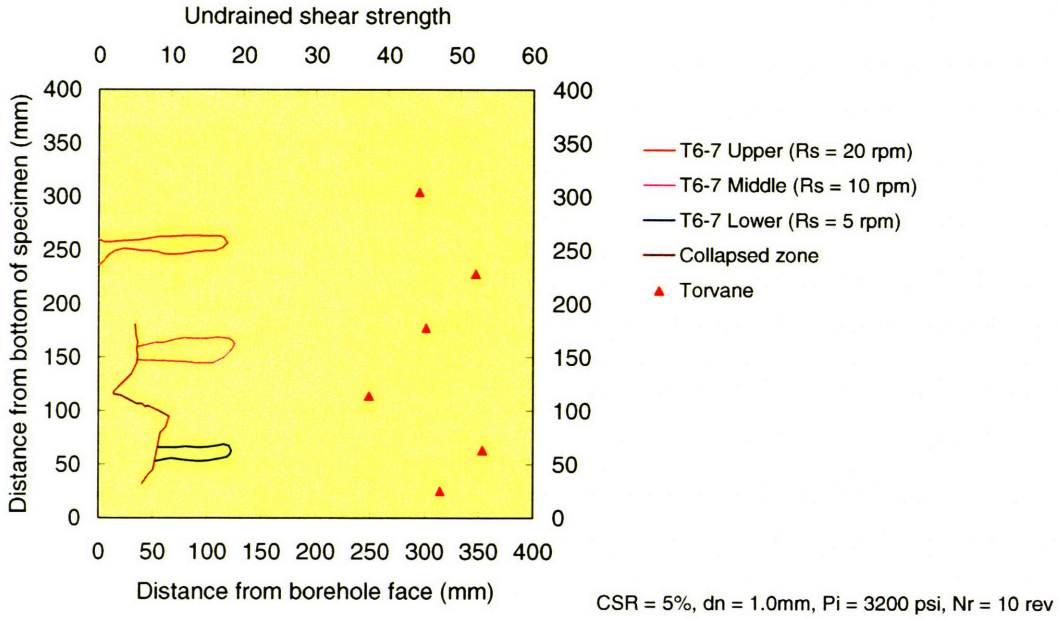

Figure C-5(g). Shape of cut for specimen T6 (Section 7)

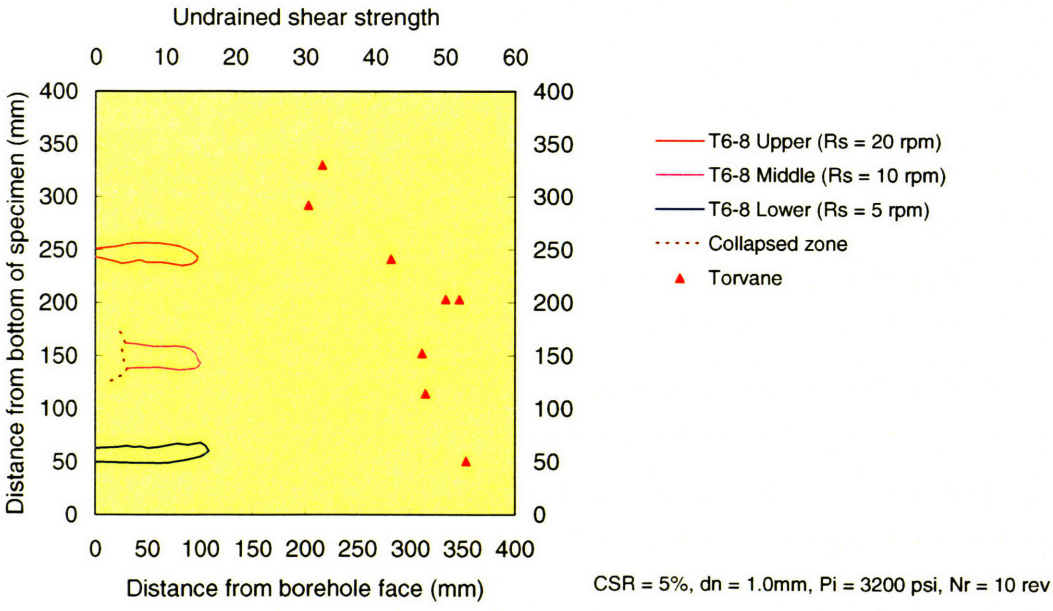

Figure C-5(h). Shape of cut for specimen T6 (Section 8)

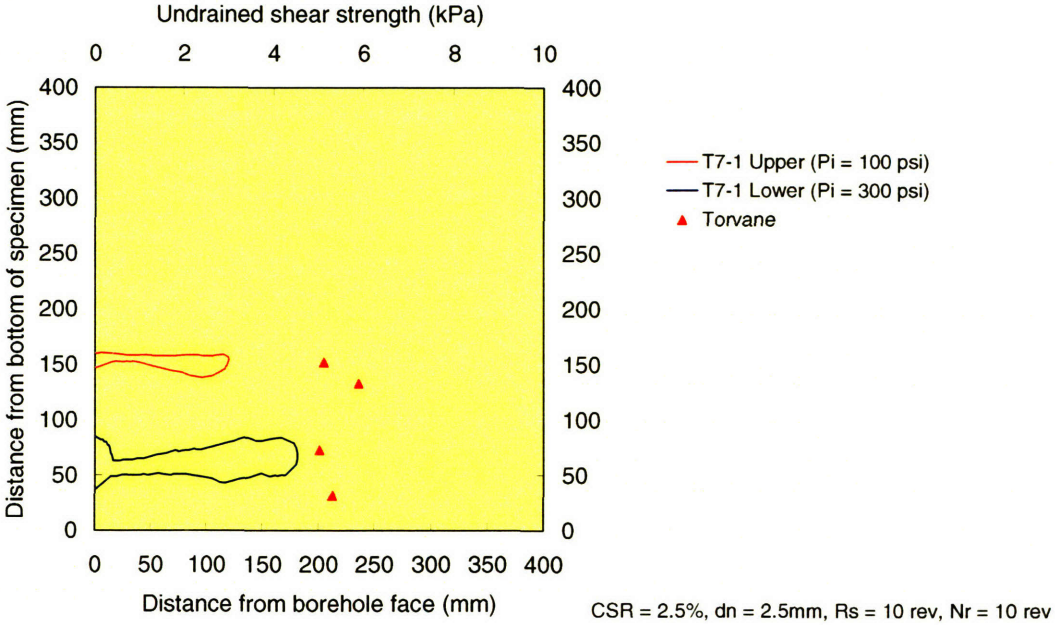

Figure C-6(a). Shape of cut for specimen T7 (Section 1)

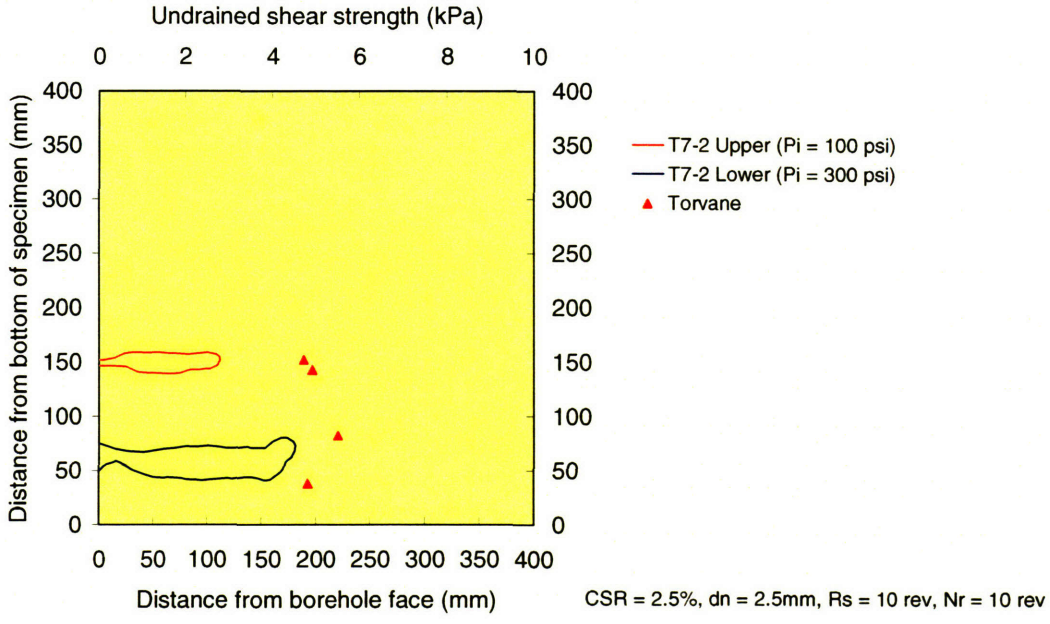

Figure C-6(b). Shape of cut for specimen T7 (Section 2)

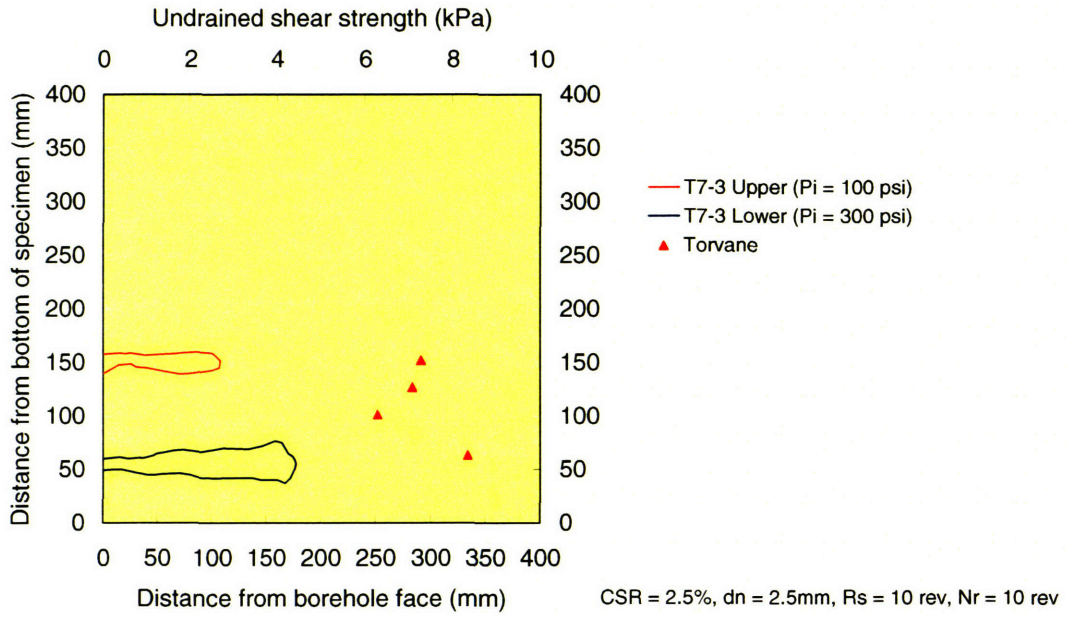

Figure C-6(c). Shape of cut for specimen T7 (Section 3)

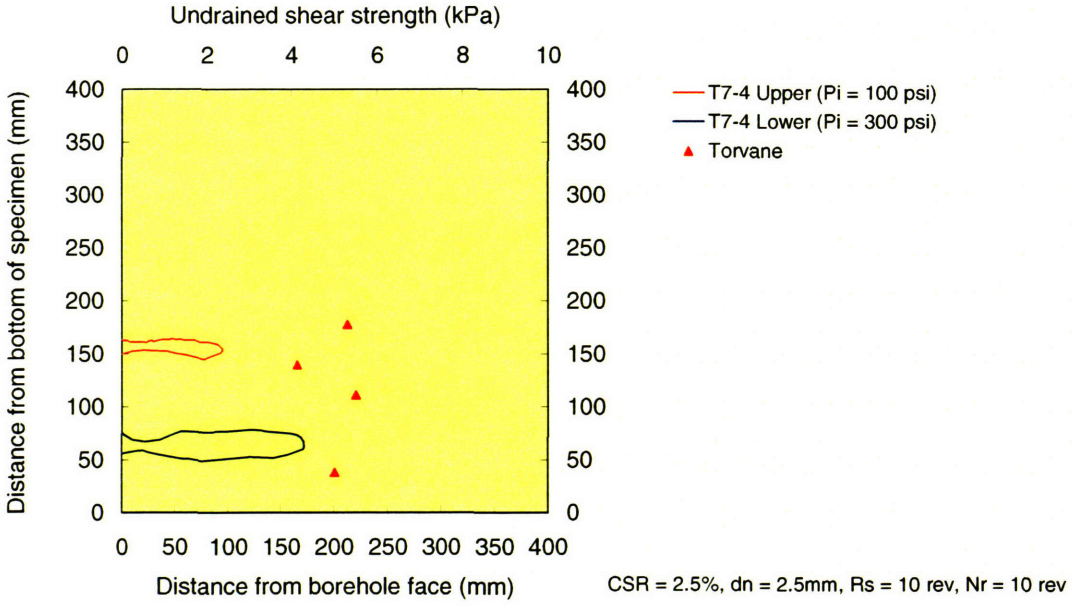

Figure C-6(d). Shape of cut for specimen T7 (Section 4)

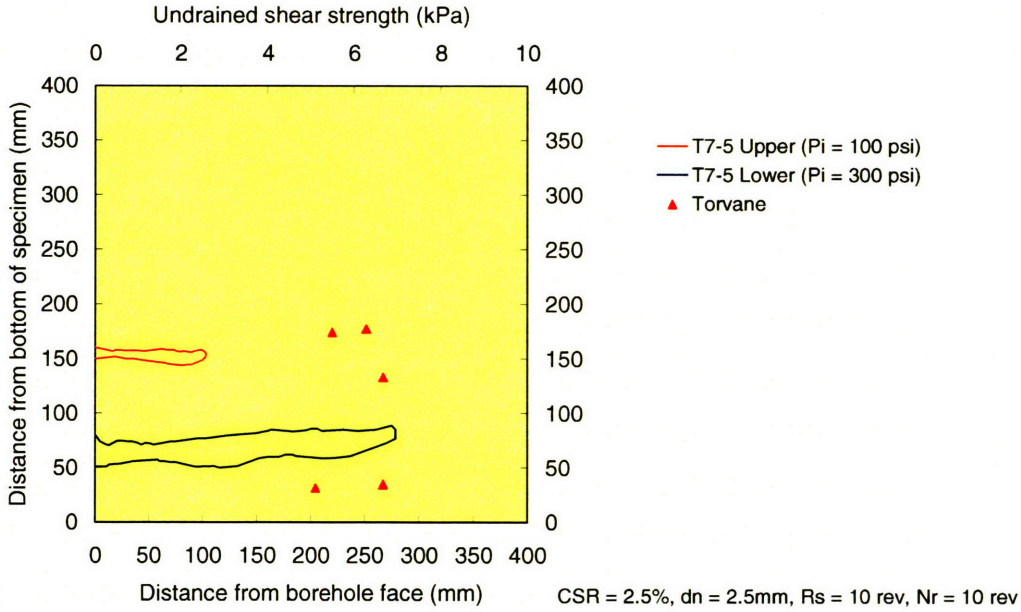

Figure C-6(e). Shape of cut for specimen T7 (Section 5)

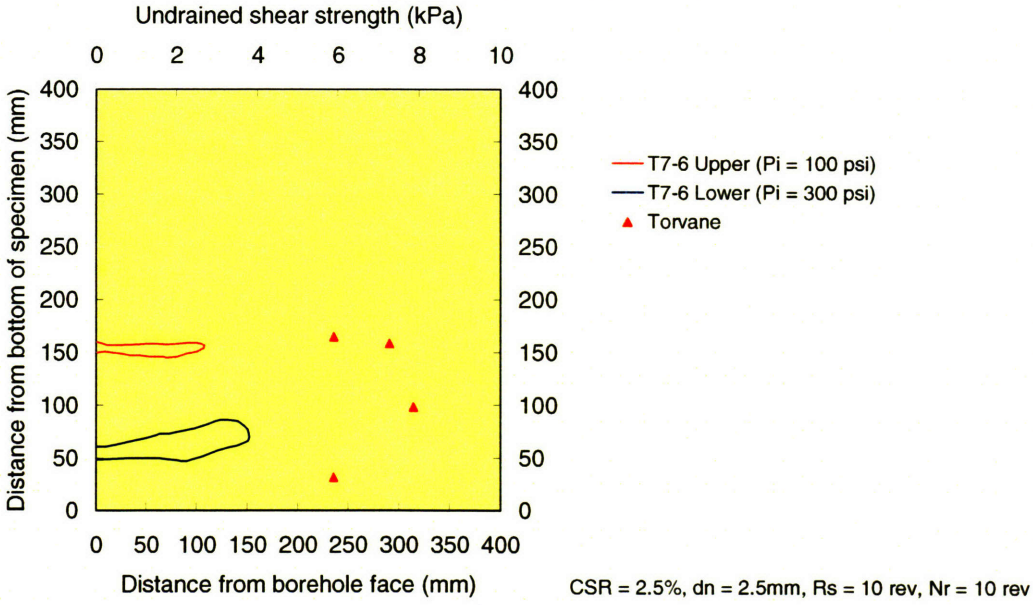

Figure C-6(f). Shape of cut for specimen T7 (Section 6)

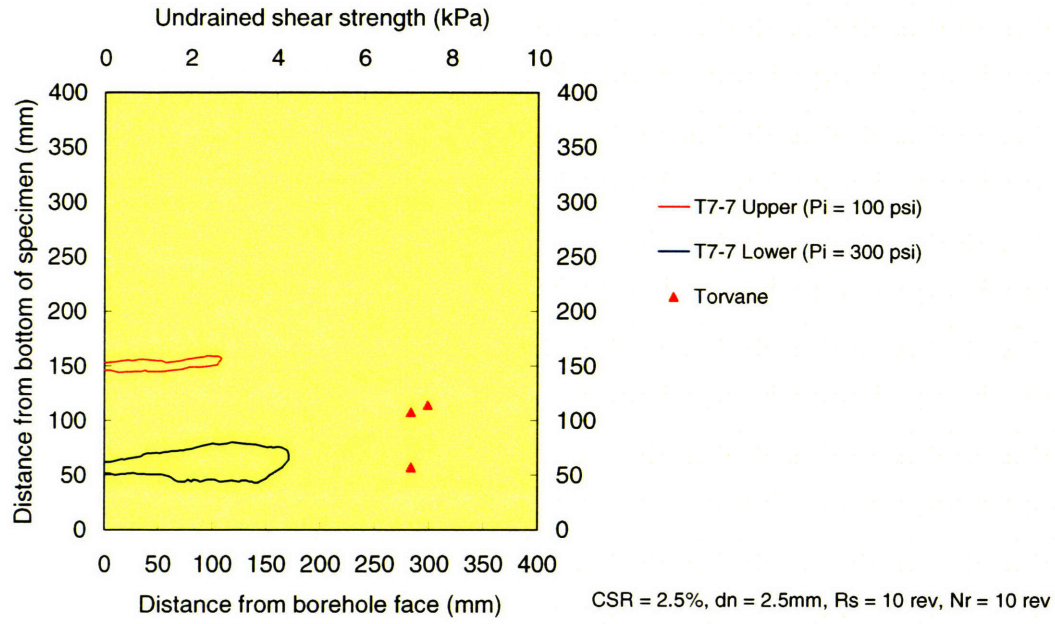

Figure C-6(g). Shape of cut for specimen T7 (Section 7)

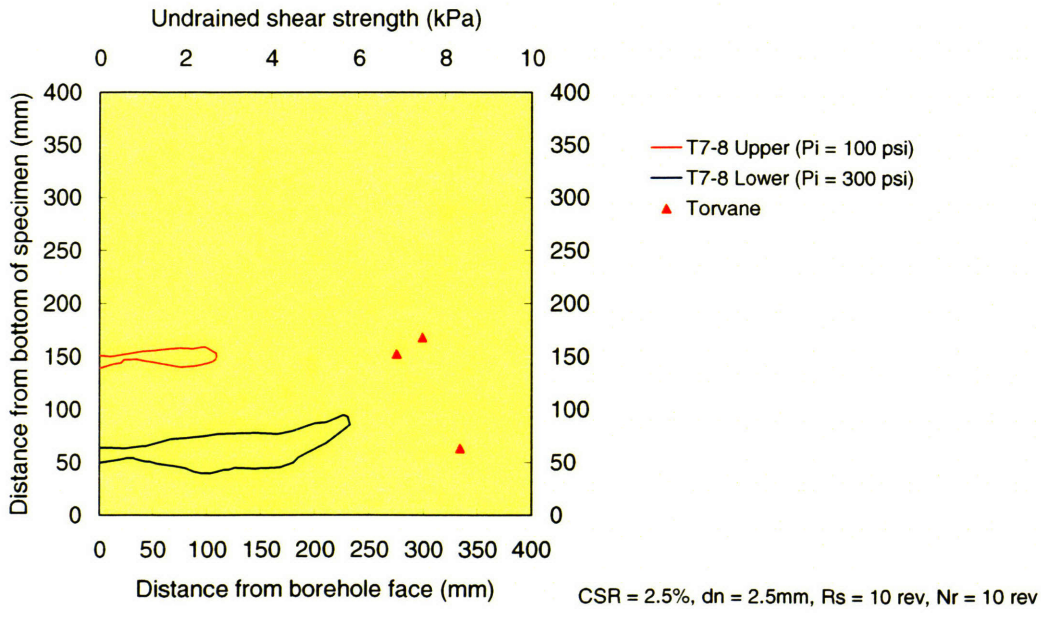

Figure C-6(h). Shape of cut for specimen T7 (Section 8)

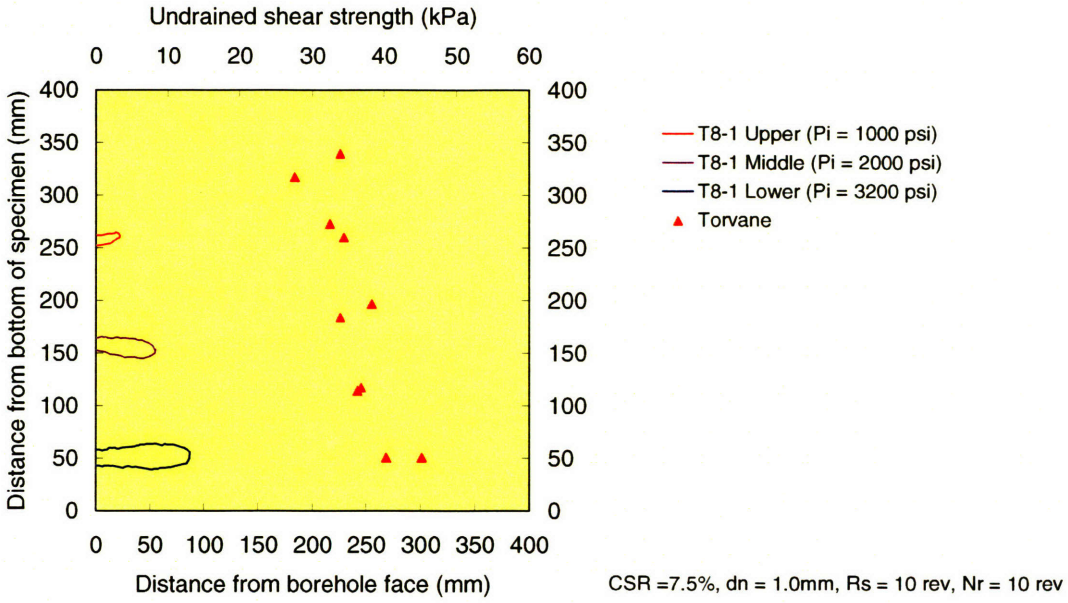

Figure C-7(a). Shape of cut for specimen T8 (Section 1)

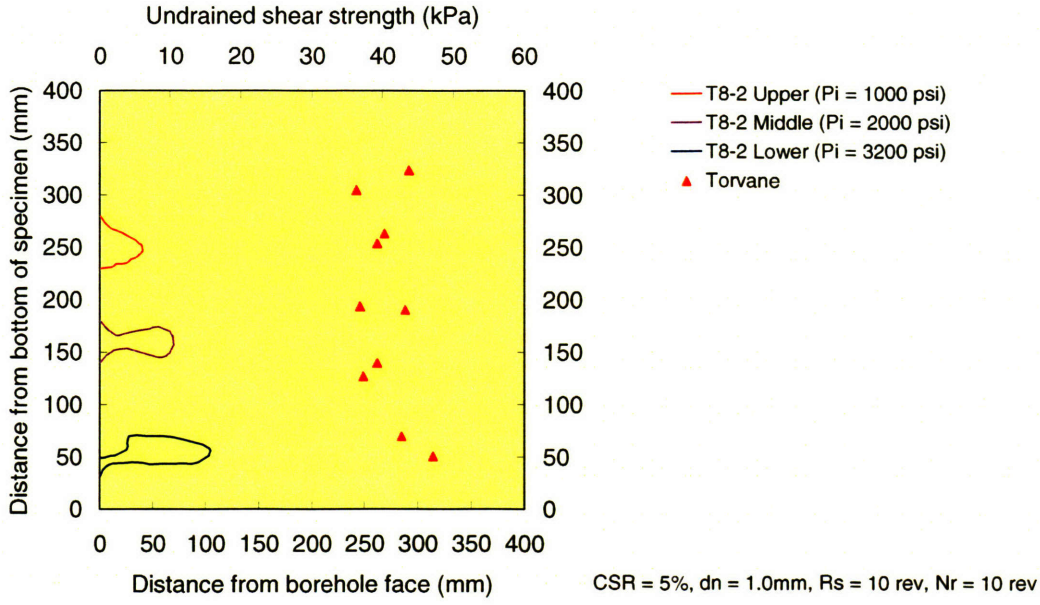

Figure C-7(b). Shape of cut for specimen T8 (Section 2)

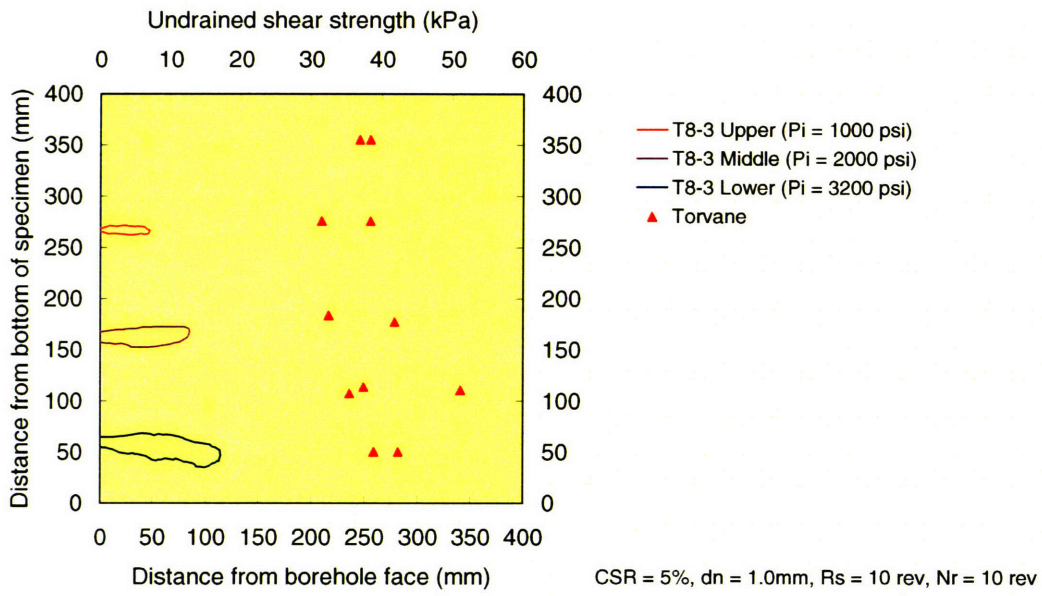

Figure C-7(c). Shape of cut for specimen T8 (Section 3)

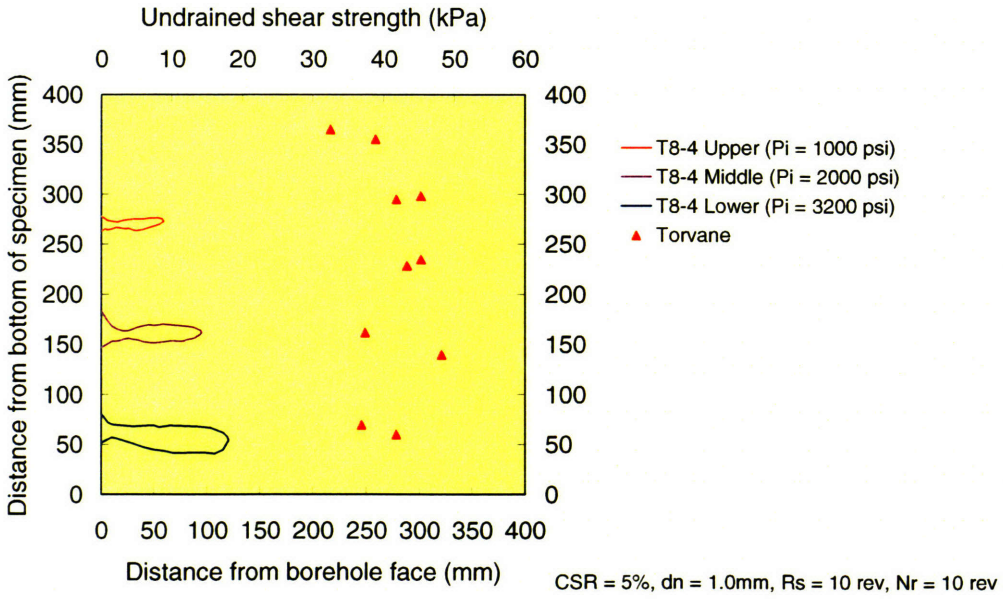

Figure C-7(d). Shape of cut for specimen T8 (Section 4)

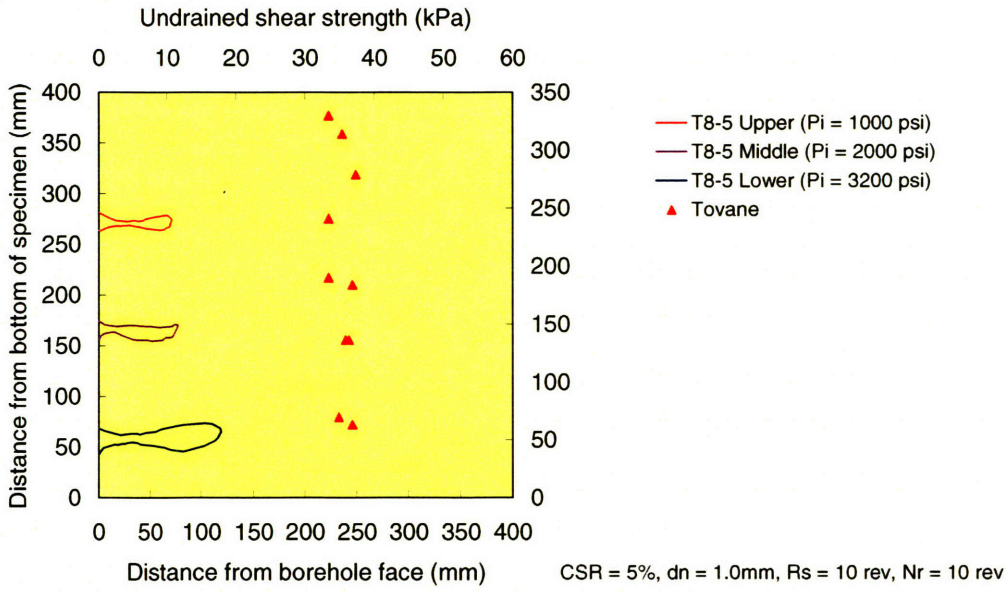

Figure C-7(e). Shape of cut for specimen T8 (Section 5)

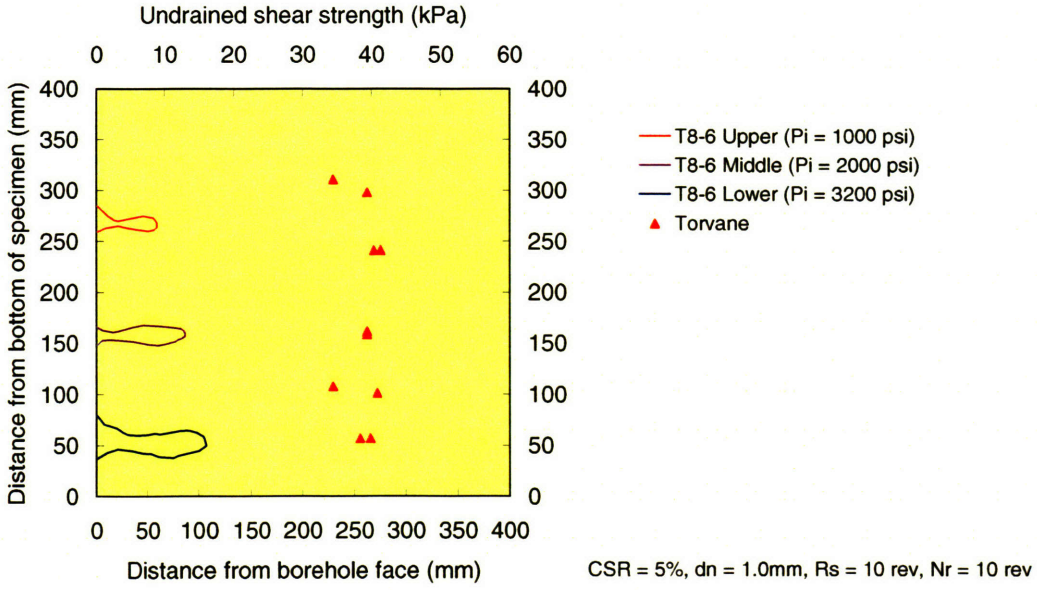

Figure C-7(f). Shape of cut for specimen T8 (Section 6)

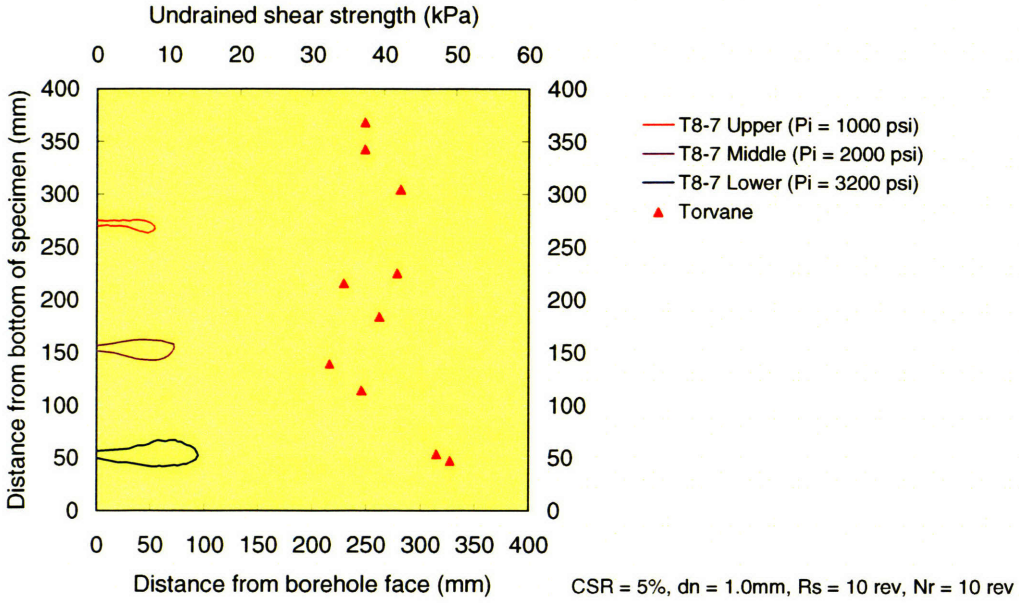

Figure C-7(g). Shape of cut for specimen T8 (Section 7)

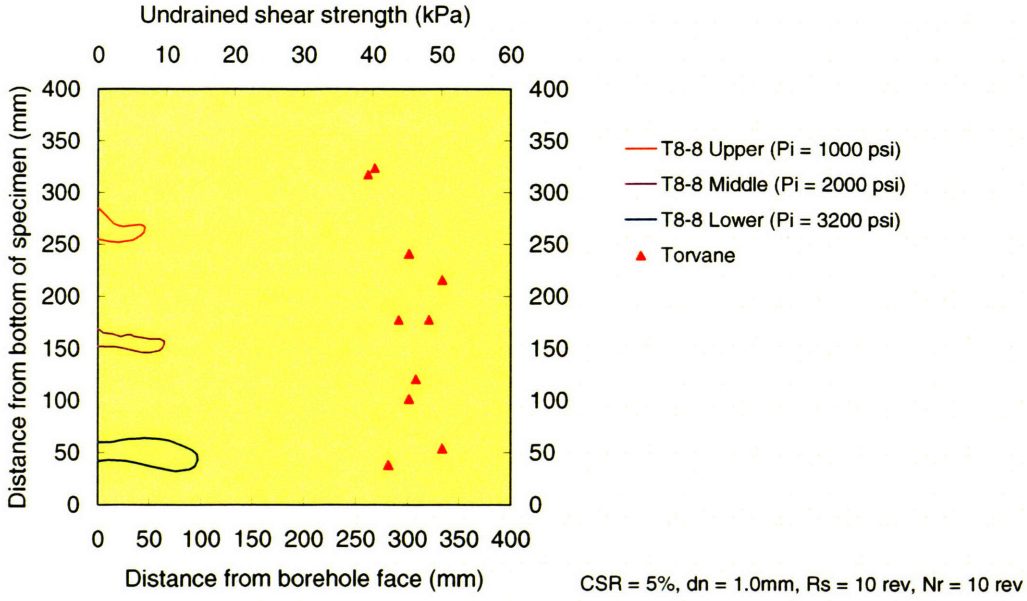

Figure C-7(h). Shape of cut for specimen T8 (Section 8)

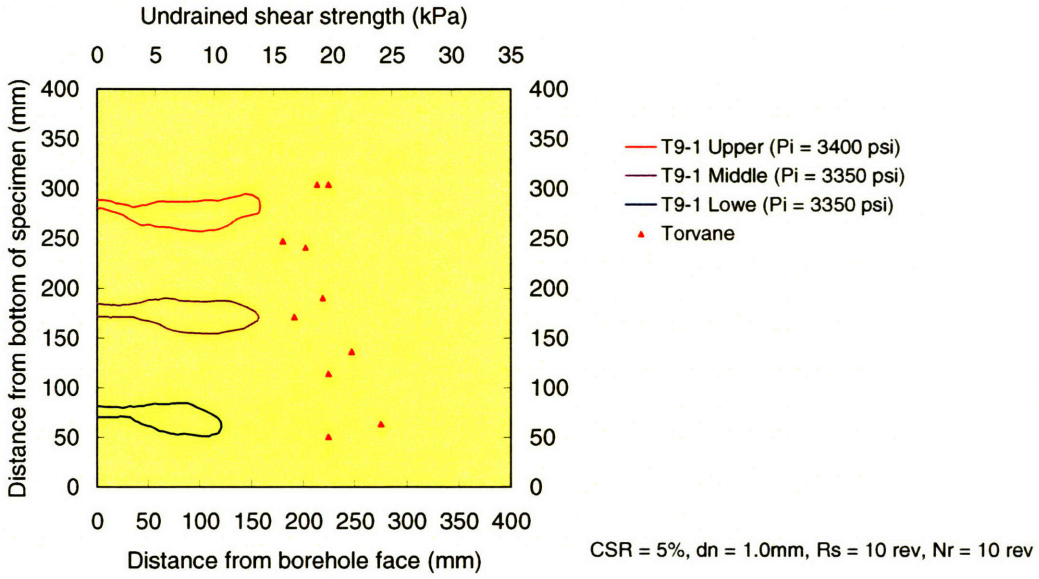

Figure C-8(a). Shape of cut for specimen T9 (Section 1)

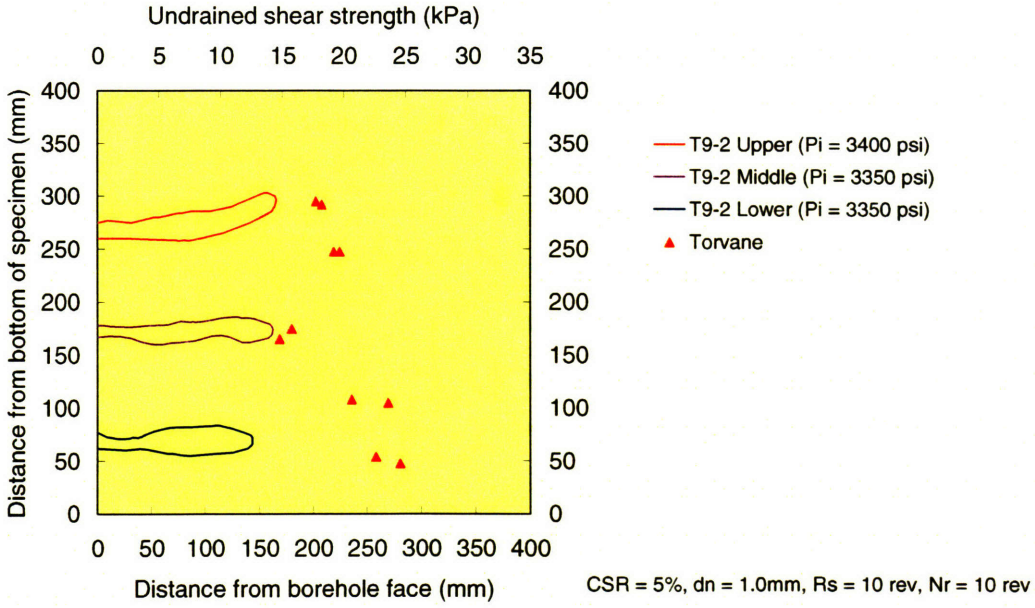

Figure C-8(b). Shape of cut for specimen T9 (Section 2)

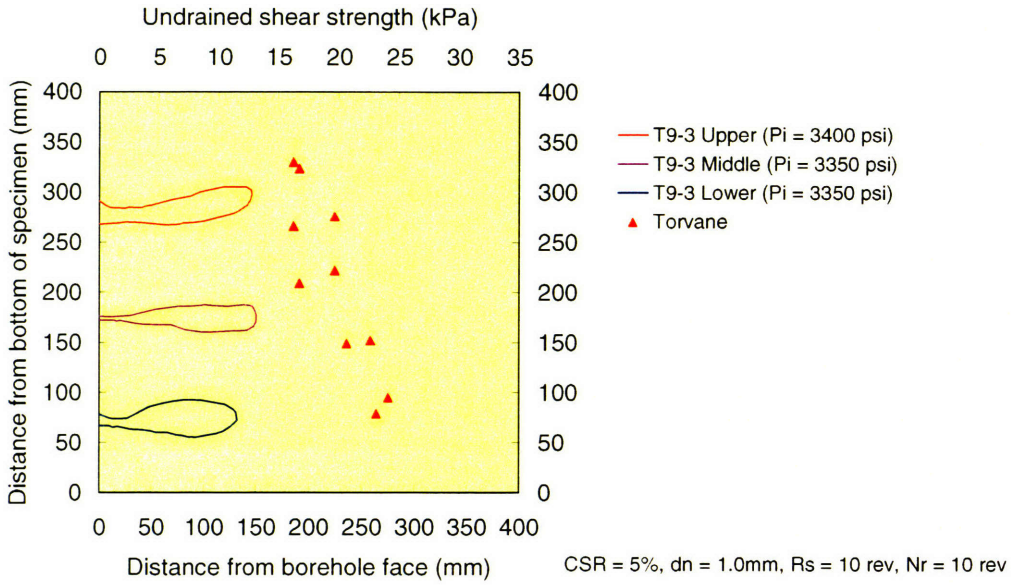

Figure C-8(c). Shape of cut for specimen T9 (Section 3)

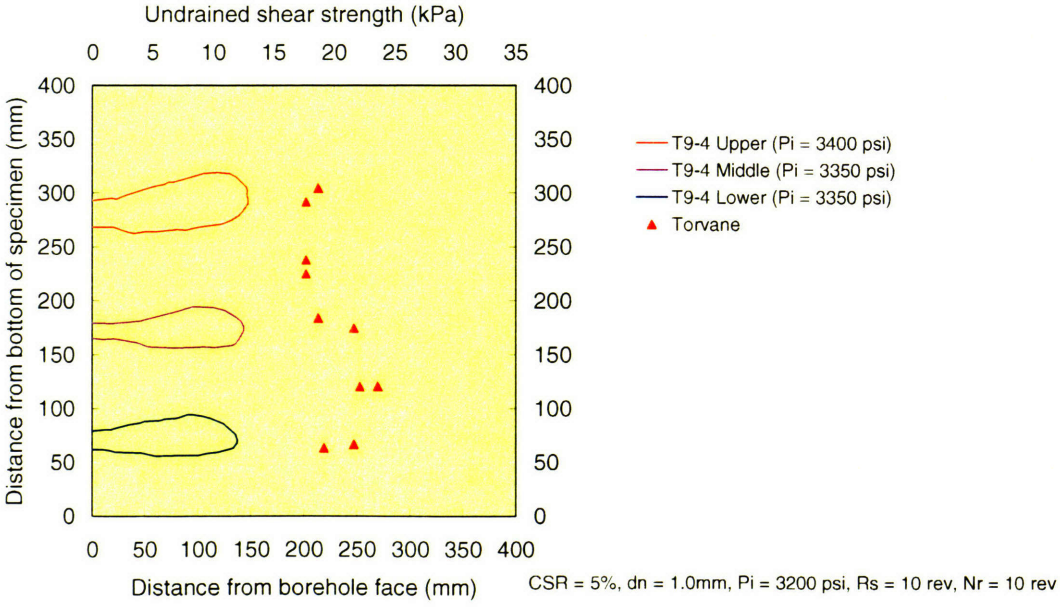

Figure C-8(d). Shape of cut for specimen T9 (Section 4)

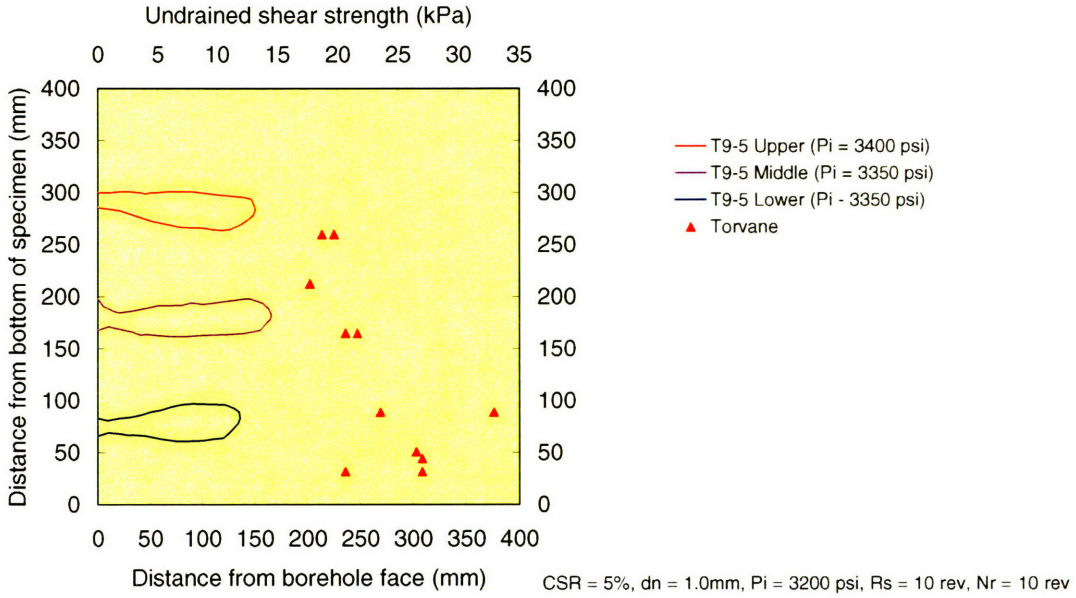

Figure C-8(e). Shape of cut for specimen T9 (Section 5)

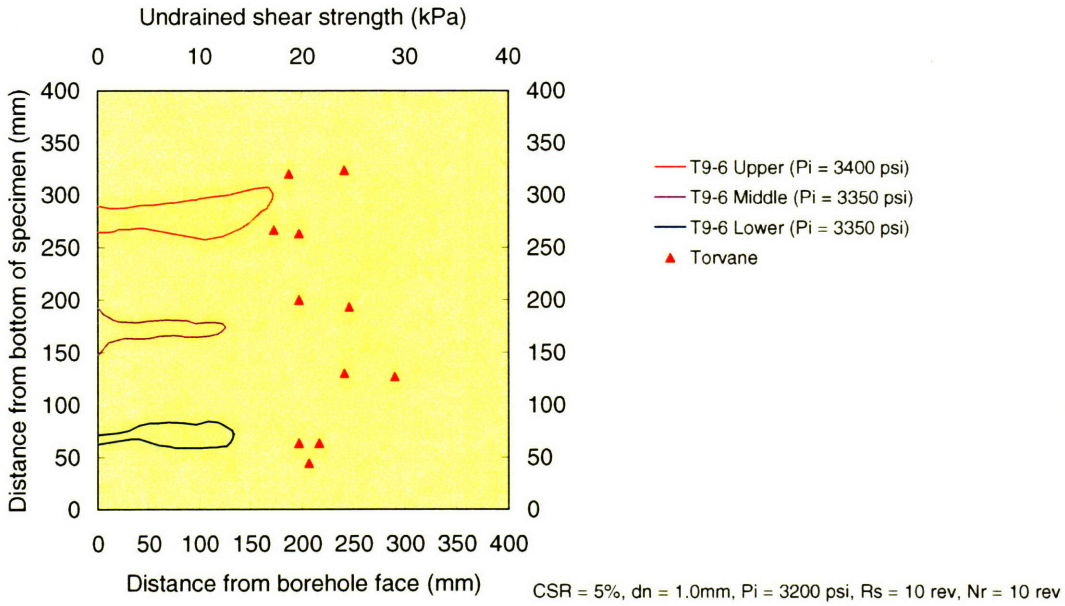

Figure C-8(f). Shape of cut for specimen T9 (Section 6)

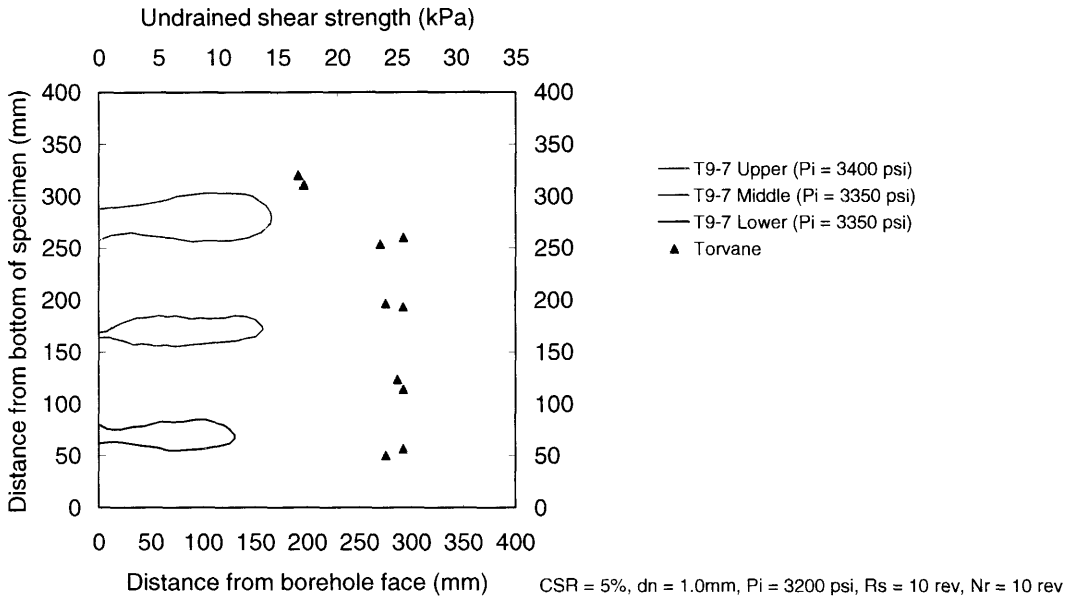

Figure C-8(g). Shape of cut for specimen T9 (Section 7)

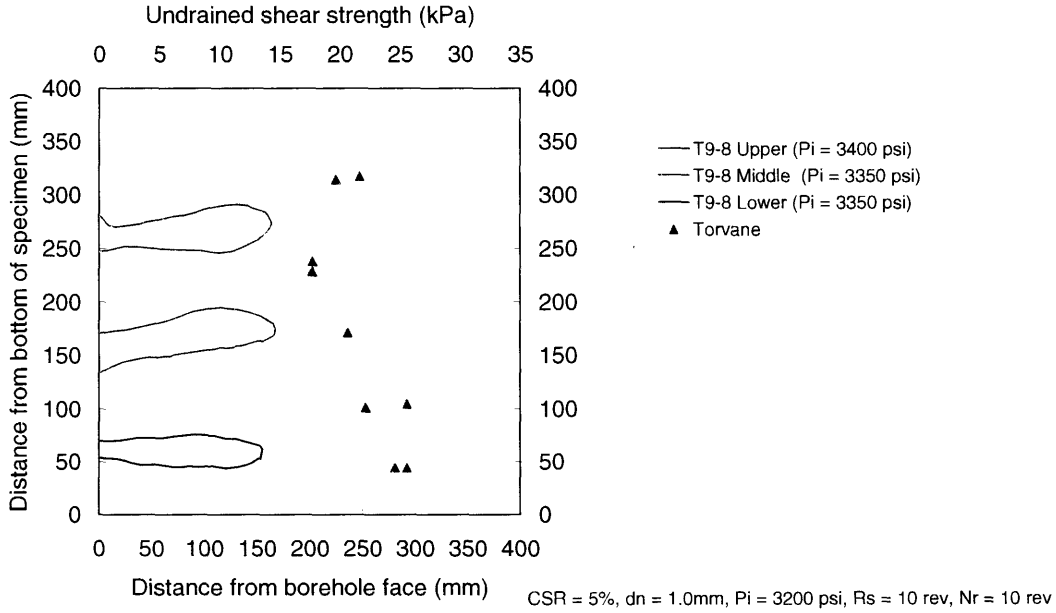

Figure C-8(h). Shape of cut for specimen T9 (Section 8)

APPENDIX D

SUMMARY OF MEASURED CUTTING DISTANCE

Table D-1. Measured cutting distance (Specimen T1)

Cut level	Section	Measured distance, l_b (mm)	Radius from specimen center, R_o (mm)	Centroid		Radius from centroid, R' (mm)	Jet penetration length, l_j (mm)
				X' (mm)	Y' (mm)		
Upper	T1-1	97	154.2	-6.56	-2.92	160.7	113.0
	T1-2	115	172.2			178.9	131.1
	T1-3	112	169.2			172.2	124.4
	T1-4	126	183.2			180.7	132.9
	T1-5	132	189.2			182.6	134.9
	T1-6	127	184.2			177.5	129.7
	T1-7	136	193.2			190.3	142.6
	T1-8	113	170.2			172.9	125.1
Middle	T1-1	85	142.2	-4.24	-4.13	146.5	98.7
	T1-2	73	130.2			136.3	88.6
	T1-3	84	141.2			145.7	97.9
	T1-4	101	158.2			158.4	110.7
	T1-5	100	157.2			153.0	105.2
	T1-6	92	149.2			143.0	95.2
	T1-7	112	169.2			164.7	117.0
	T1-8	93	150.2			150.1	102.4
Lower	T1-1	65	122.2	-2.99	-1.31	125.2	77.4
	T1-2	73	130.2			133.2	85.5
	T1-3	61	118.2			119.5	71.8
	T1-4	59	116.2			115.0	67.3
	T1-5	82	139.2			136.2	88.4
	T1-6	79	136.2			133.1	85.4
	T1-7	70	127.2			125.9	78.1
	T1-8	55	112.2			113.4	65.6

Table D-2. Measured cutting distance (Specimen T2)

Cut level	Section	Measured distance, l_b (mm)	Radius from specimen center, R_o (mm)	Centroid		Radius from centroid, R' (mm)	Jet penetration length, l_j (mm)
				X' (mm)	Y' (mm)		
Upper	T2-1	168	225.2	4.66	4.13	221.3	173.6
	T2-2	187	244.2			241.9	194.1
	T2-3	190	247.2			247.8	200.0
	T2-4	155	212.2			215.3	167.5
	T2-5	165	222.2			226.0	178.2
	T2-6	164	221.2			223.5	175.7
	T2-7	200	257.2			256.6	208.9
	T2-8	170	227.2			224.0	176.3
Middle	T2-1	132	189.2	8.90	1.69	184.5	136.8
	T2-2	136	193.2			186.9	139.2
	T2-3	146	203.2			199.1	151.3
	T2-4	131	188.2			188.6	140.9
	T2-5	120	177.2			181.9	134.1
	T2-6	124	181.2			187.4	139.6
	T2-7	105	162.2			166.3	118.6
	T2-8	154	211.2			210.9	163.1
Lower	T2-1	133	145.2	-6.51	-2.94	181.3	133.5
	T2-2	135	130.2			184.7	137.0
	T2-3	130	112.2			185.7	137.9
	T2-4	129	117.2			191.4	143.7
	T2-5	97	106.2			163.1	115.3
	T2-6	115	111.2			179.7	131.9
	T2-7	110	117.2			169.0	121.3
	T2-8	158	119.2			210.2	162.4

Table D-3. Measured cutting distance (Specimen T3)

Cut level	Section	Measured distance, l_b (mm)	Radius from specimen center, R_o (mm)	Centroid X' (mm)	Centroid Y' (mm)	Radius from centroid, R' (mm)	Jet penetration length, l_j (mm)
Upper	T3-1	65	122.2	2.19	2.89	120.0	72.3
	T3-2	47	104.2			100.6	52.9
	T3-3	48	105.2			102.3	54.6
	T3-4	64	121.2			120.7	73.0
	T3-5	49	106.2			108.4	60.7
	T3-6	31	88.2			91.7	44.1
	T3-7	46	103.2			106.1	58.4
	T3-8	50	107.2			107.7	60.0
Middle	T3-1	88	145.2	6.75	0.87	138.4	90.7
	T3-2	73	130.2			124.8	77.2
	T3-3	55	112.2			111.5	63.8
	T3-4	60	117.2			121.4	73.7
	T3-5	49	106.2			112.9	65.2
	T3-6	54	111.2			116.6	68.9
	T3-7	60	117.2			118.2	70.5
	T3-8	62	119.2			115.1	67.5
Lower	T3-1	107	164.2	-1.85	1.37	166.0	118.3
	T3-2	84	141.2			141.5	93.8
	T3-3	111	168.2			166.8	119.1
	T3-4	107	164.2			161.9	114.2
	T3-5	100	157.2			155.3	107.6
	T3-6	103	160.2			159.8	112.2
	T3-7	95	152.2			153.5	105.9
	T3-8	95	152.2			154.4	106.8
	T3-3/4	114	171.2				
		114	171.2				
		111	168.2				
	T3-7/8	111	168.2				
		114	171.2				
		98	155.2				

Table D-4. Measured cutting distance (Specimen T4)

Cut level	Section	Measured distance, l_b (mm)	Radius from specimen center, R_o (mm)	Centroid		Radius from centroid, R` (mm)	Jet penetration length, l_j (mm)
				X` (mm)	Y` (mm)		
Middle	T4-7	216	273.2	-0.19	5.04	278.2	230.4
	T4-7A	213	270.2			274.9	227.1
	T4-8	213	270.2			273.9	226.1
	T4-1B	205	262.2			264.9	217.1
	T4-1A	218	275.2			276.7	228.9
Lower	T4-1	136	193.2	-0.19	5.04	193.4	145.7
	T4-2	147	204.2			200.8	153.0
	T4-3	138	195.2			190.1	142.4
	T4-4	130	187.2			183.4	135.7
	T4-5	120	177.2			177.0	129.2
	T4-6	150	207.2			210.6	162.9
	T4-7	111	168.2			173.2	125.4
	T4-8	108	165.2			168.9	121.1
	T4-1B	138	195.2				
	T4-1A	136	193.2				

Table D-5. Measured cutting distance (Specimen T6)

Cut level	Section	Measured distance, l_b (mm)	Radius from specimen center, R_o (mm)	Centroid		Radius from centroid, R' (mm)	Jet penetration length, l_j (mm)
				X' (mm)	Y' (mm)		
Upper	T6-1	117	174.2	-4.80	1.73	179.0	131.1
	T6-2	113	170.2			172.4	124.5
	T6-3	127	184.2			182.5	134.6
	T6-4	120	177.2			172.5	123.7
	T6-5	128	185.2			180.4	132.5
	T6-6	129	186.2			184.0	136.2
	T6-7	118	175.2			176.9	129.1
	T6-8	97	154.2			158.8	110.9
	T6-3/4	127	184.2				
		114	171.2				
		111	168.2				
Middle	T6-1	126	183.2	-6.03	0.98	189.2	141.3
	T6-2	127	184.2			187.8	139.9
	T6-3	129	186.2			185.3	137.0
	T6-4	125	182.2			177.2	129.4
	T6-5	144	201.2			195.1	147.3
	T6-6	145	202.2			198.6	150.8
	T6-7	126	183.2			184.2	136.4
	T6-8	100	157.2			162.1	114.3
Lower	T6-1	113	170.2	-1.55	3.40	171.7	123.9
	T6-2	130	187.2			185.9	138.0
	T6-3	122	179.2			175.8	127.9
	T6-4	127	184.2			180.7	132.8
	T6-5	127	184.2			182.6	134.8
	T6-6	109	166.2			167.5	119.6
	T6-7	123	180.2			183.6	135.7
	T6-8	108	165.2			168.7	120.8

Table D-6. Measured cutting distance (Specimen T7)

Cut level	Section	Measured distance, l_b (mm)	Radius from specimen center, R_o (mm)	Centroid		Radius from centroid, R` (mm)	Jet penetration length, l_j (mm)
				X` (mm)	Y` (mm)		
Upper	T7-1	120	117.2	3.87	-0.88	173.3	125.6
	T7-2	112	169.2			167.1	119.4
	T7-3	107	164.2			165.1	117.4
	T7-4	94	151.2			154.5	106.9
	T7-5	103	160.2			164.0	116.4
	T7-6	106.5	163.7			165.8	118.1
	T7-7	108	165.2			164.3	116.6
	T7-8	108	165.2			161.8	114.1
	T7-1/2	120.7	177.9				
		119.1	176.3				
		114.3	171.5				
Lower	T7-1	184	241.2	-2.88	-2.79	244.0	196.4
	T7-2	181	238.2			242.2	194.5
	T7-3	177	234.2			237.0	189.3
	T7-4	162	219.2			219.1	171.5
	T7-5	278	335.2			332.3	284.6
	T7-6	151	208.2			204.1	156.5
	T7-7	171	228.2			225.4	177.7
	T7-8	232	289.2			289.2	241.6

*T7-5 and T7-8 excluded

Table D-7. Measured cutting distance (Specimen T8)

Cut level	Section	Measured distance, l_b (mm)	Radius from specimen center, R_o (mm)	Centroid		Radius from centroid, R' (mm)	Jet penetration length, l_j (mm)
				X' (mm)	Y' (mm)		
Upper	T8-1	22	79.2	-8.94	-1.16	88.1	40.5
	T8-2	40	97.2			104.4	56.8
	T8-3	48.5	105.7			107.2	59.8
	T8-4	58.5	115.7			110.4	62.8
	T8-5	71	128.2			119.2	71.6
	T8-6	59	116.2			109.1	61.5
	T8-7	53.5	110.7			109.9	62.2
	T8-8	45.5	102.7			108.4	60.8
Middle	T8-1	54.5	111.7	-6.99	2.81	118.7	71.0
	T8-2	69.5	126.7			129.8	82.2
	T8-3	84.5	141.7			139.0	91.4
	T8-4	94.5	151.7			144.7	97.1
	T8-5	77	134.7			127.2	79.6
	T8-6	86.5	143.7			140.9	93.2
	T8-7	71.5	128.7			131.6	84.0
	T8-8	64	121.2			128.1	80.5
Lower	T8-1	87	144.2	-6.28	4.35	150.5	102.9
	T8-2	104.5	161.7			163.2	115.6
	T8-3	114	171.2			166.9	119.3
	T8-4	120	177.2			169.6	122.0
	T8-5	119	176.2			169.9	122.3
	T8-6	107	164.2			162.9	115.3
	T8-7	94	151.2			155.6	108.0
	T8-8	96.5	153.7			161.2	113.5

Table D-8. Measured cutting distance (Specimen T9)

Cut level	Section	Measured distance, l_b (mm)	Radius from specimen center, R_o (mm)	Centroid		Radius from centroid, R` (mm)	Jet penetration length, l_j (mm)
				X` (mm)	Y` (mm)		
Upper	T9-1	158	215.2	1.91	-4.39	213.3	165.5
	T9-2	165	222.2			223.9	176.2
	T9-3	145.5	202.7			207.1	159.3
	T9-4	147	204.2			208.6	160.9
	T9-5	150	207.2			209.1	161.4
	T9-6	171	228.2			226.4	178.7
	T9-7	165	222.2			217.8	170.0
	T9-8	163	220.2			215.7	167.9
Middle	T9-1	156.5	213.7	4.35	0.27	209.3	161.6
	T9-2	162	219.2			215.9	168.2
	T9-3	150	207.2			206.9	159.2
	T9-4	143	200.2			203.0	155.3
	T9-5	165	222.2			226.5	178.8
	T9-6	125	182.2			185.4	137.7
	T9-7	157	214.2			214.4	166.7
	T9-8	167	224.2			221.3	173.5
Lower	T9-1	120.5	177.7	0.52	-0.57	172.1	129.4
	T9-2	143	200.2			200.2	152.4
	T9-3	131.5	188.7			189.2	141.5
	T9-4	137	194.2			194.9	147.2
	T9-5	136	193.2			193.7	145.9
	T9-6	133.5	190.7			190.6	142.9
	T9-7	130	187.2			186.6	138.8
	T9-8	155	212.2			211.4	163.6

APPENDIX E

PREDICTED SHAPE OF CUTS

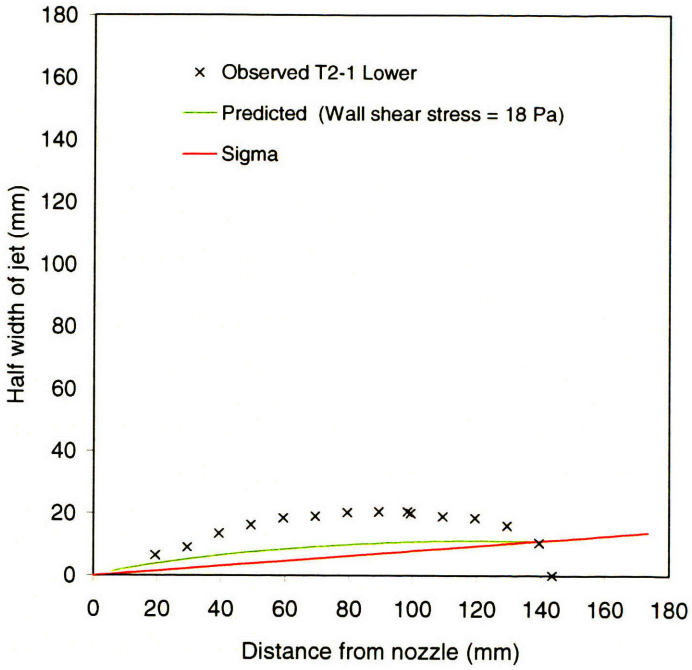

Figure E-1(a). Shape of cut (Specimen T2, Section 1, Lower cut)

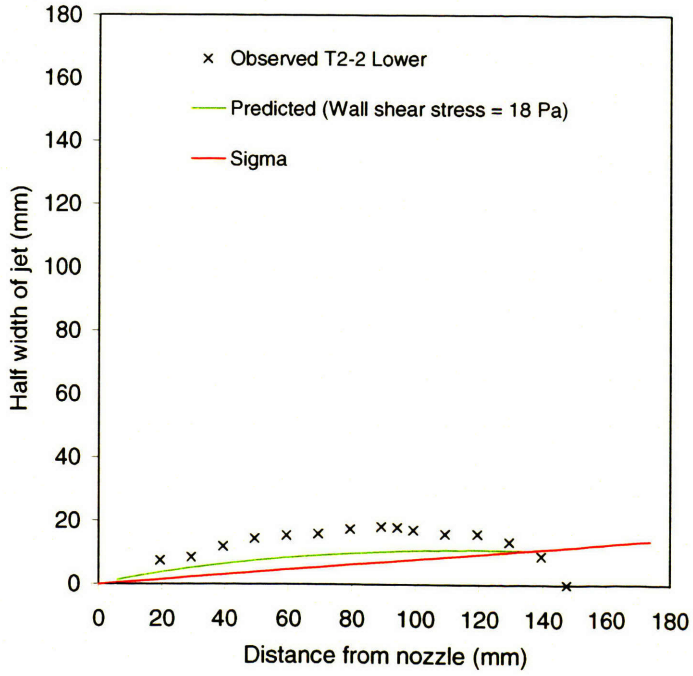

Figure E-1(b). Shape of cut (Specimen T2, Section 2, Lower cut)

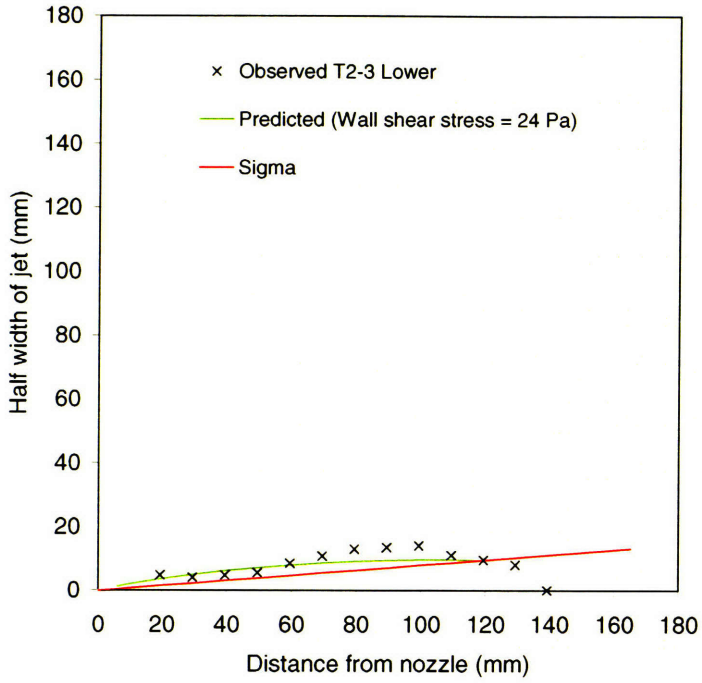

Figure E-1(c). Shape of cut (Specimen T2, Section 3, Lower cut)

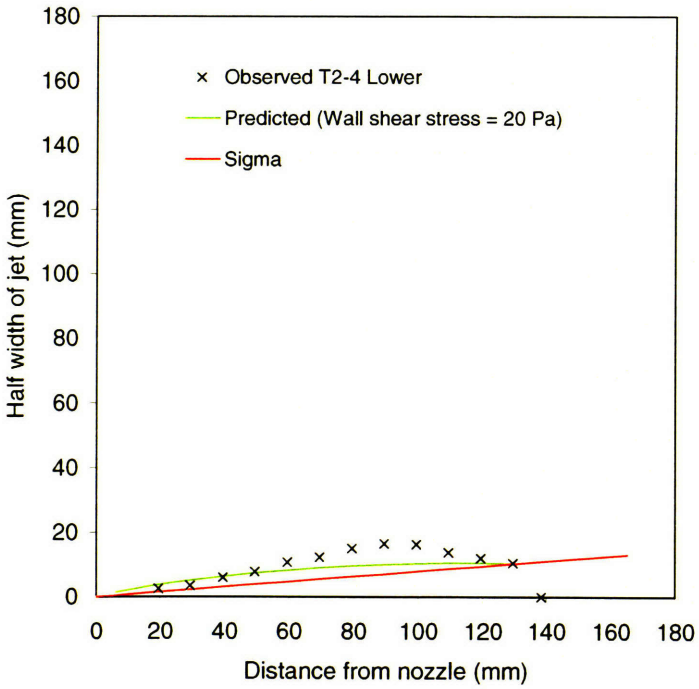

Figure E-1(d). Shape of cut (Specimen T2, Section 4, Lower cut)

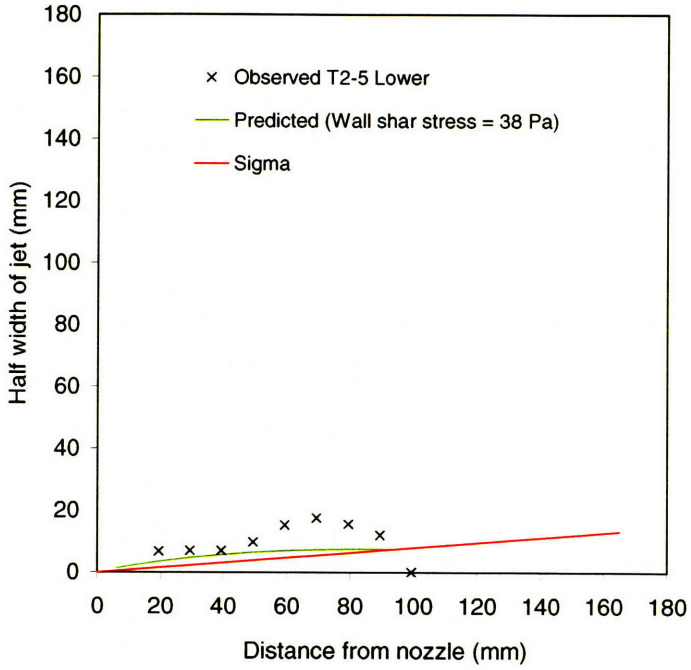

Figure E-1(e). Shape of cut (Specimen T2, Section 5, Lower cut)

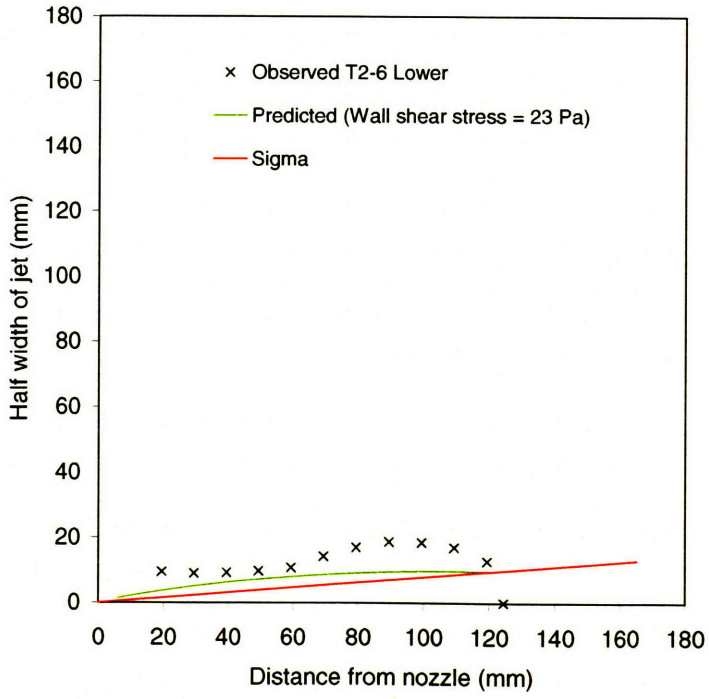

Figure E-1(f). Shape of cut (Specimen T2, Section 6, Lower cut)

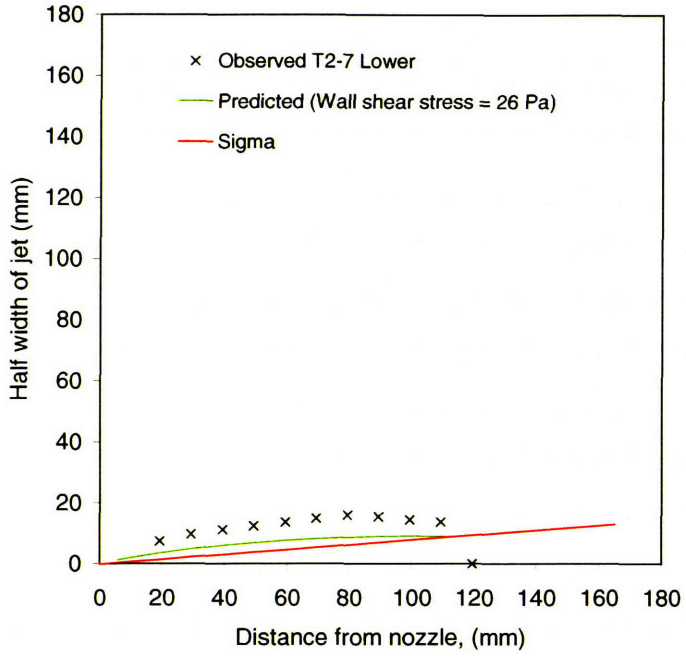

Figure E-1(g). Shape of cut (Specimen T2, Section 7, Lower cut)

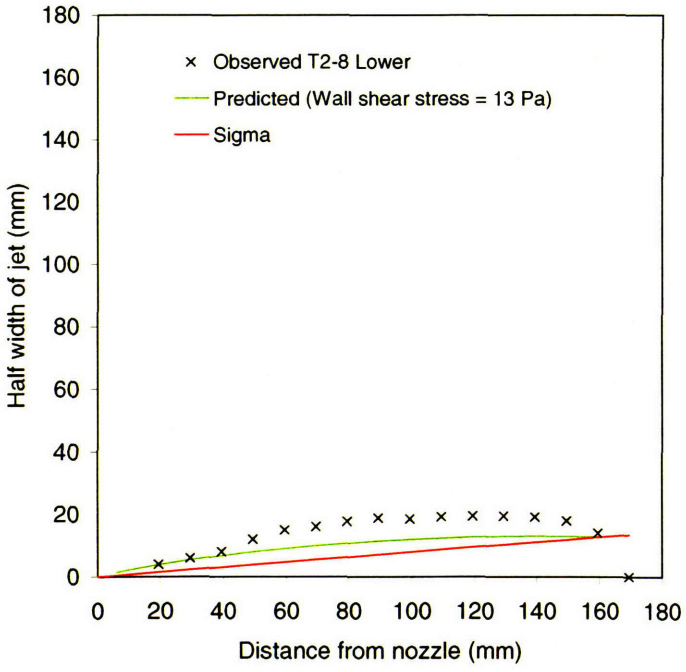

Figure E-1(h). Shape of cut (Specimen T2, Section 8, Lower cut)

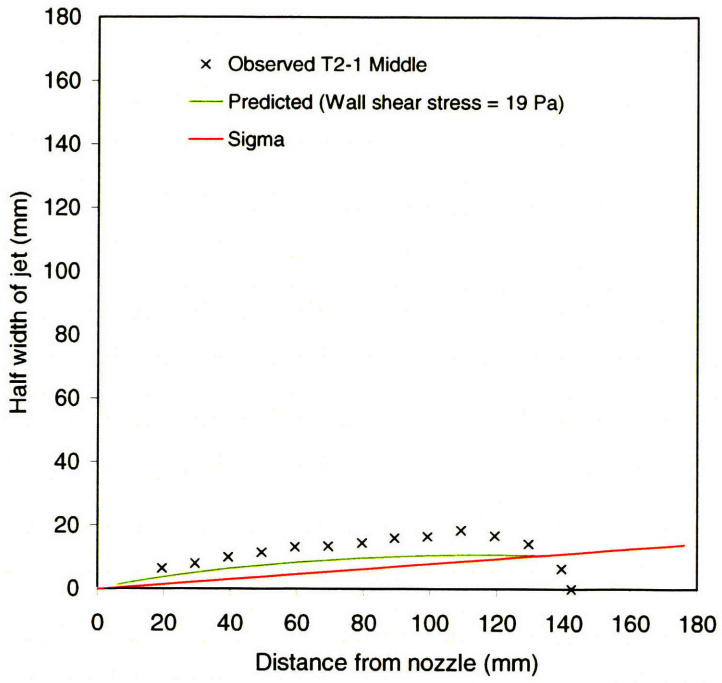

Figure E-2(a). Shape of cut (Specimen T2, Section 1, Middle cut)

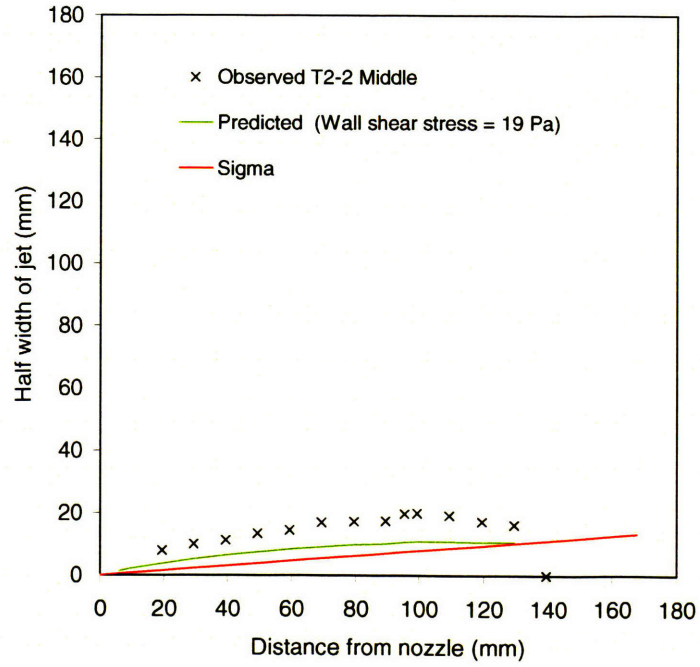

Figure E-2(b). Shape of cut (Specimen T2, Section 2, Middle cut)

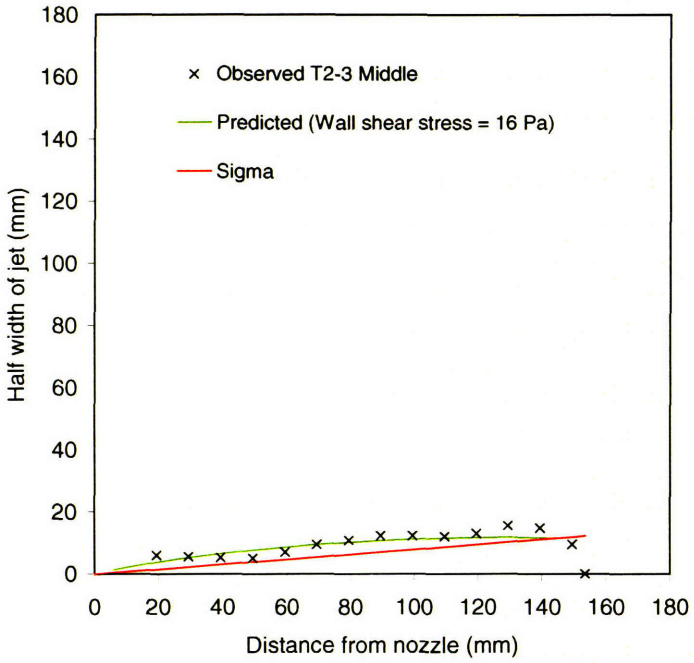

Figure E-2(c). Shape of cut (Specimen T2, Section 3, Middle cut)

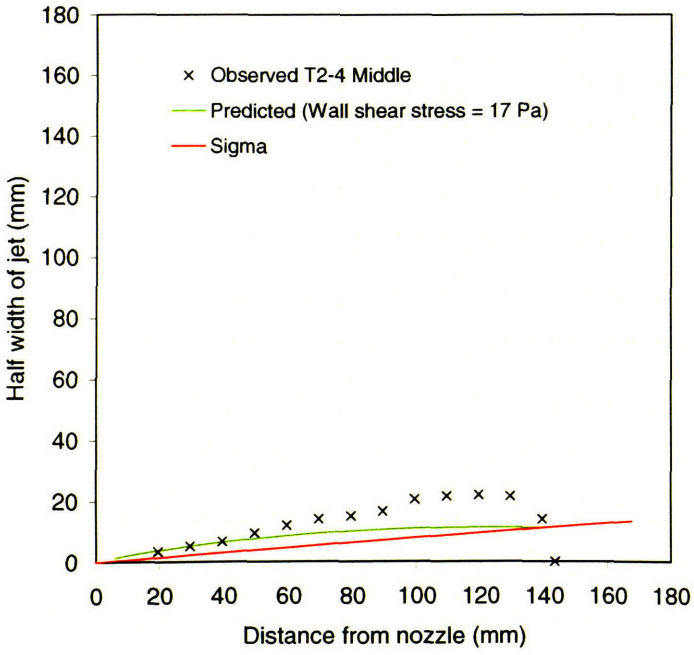

Figure E-2(d). Shape of cut (Specimen T2, Section 4, Middle cut)

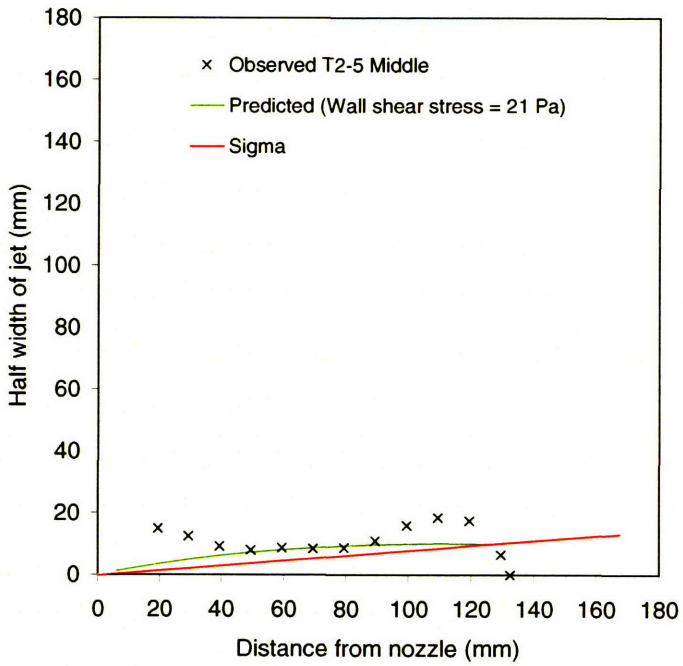

Figure E-2(e). Shape of cut (Specimen T2, Section 5, Middle cut)

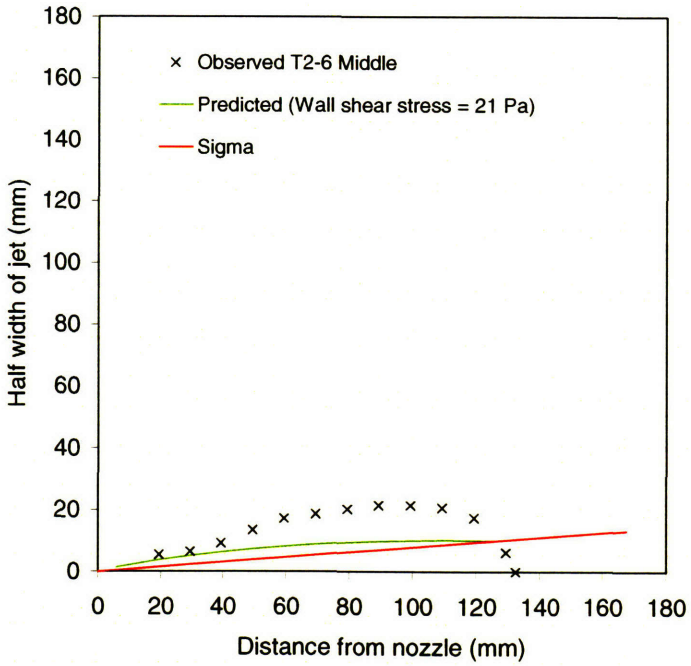

Figure E-2(f). Shape of cut (Specimen T2, Section 6, Middle cut)

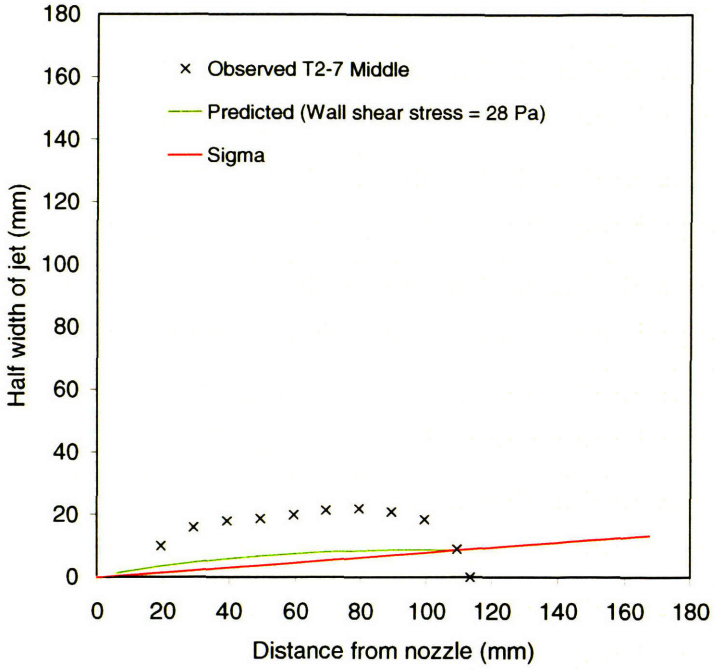

Figure E-2(g). Shape of cut (Specimen T2, Section 7, Middle cut)

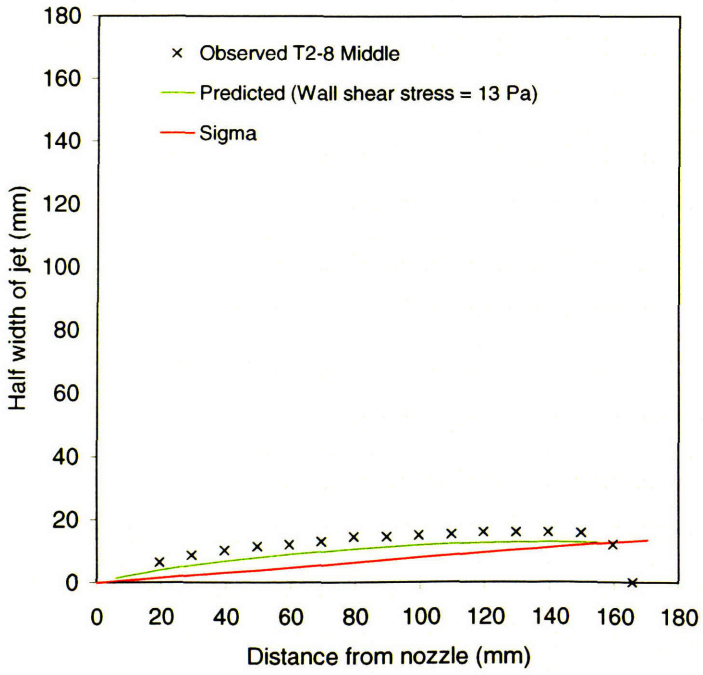

Figure E-2(h). Shape of cut (Specimen T2, Section 8, Middle cut)

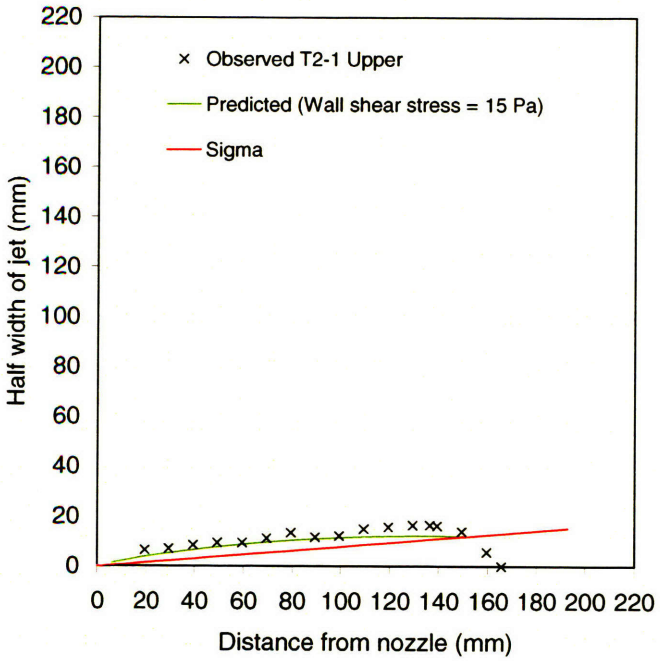

Figure E-3(a). Shape of cut (Specimen T2, Section 1, Upper cut)

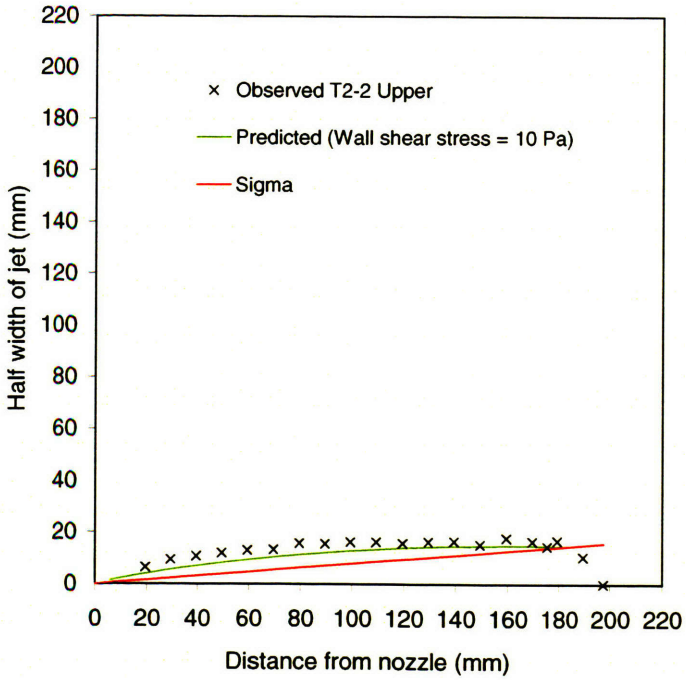

Figure E-3(b). Shape of cut (Specimen T2, Section 2, Upper cut)

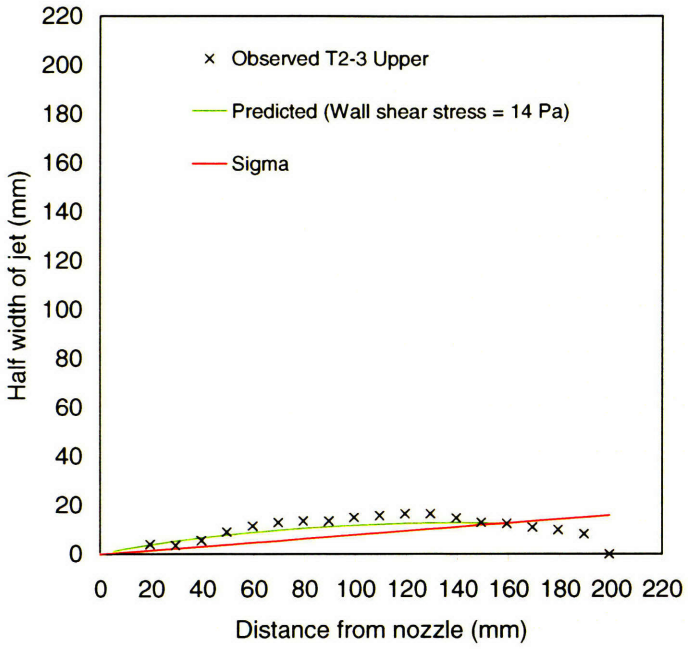

Figure E-3(c). Shape of cut (Specimen T2, Section 3, Upper cut)

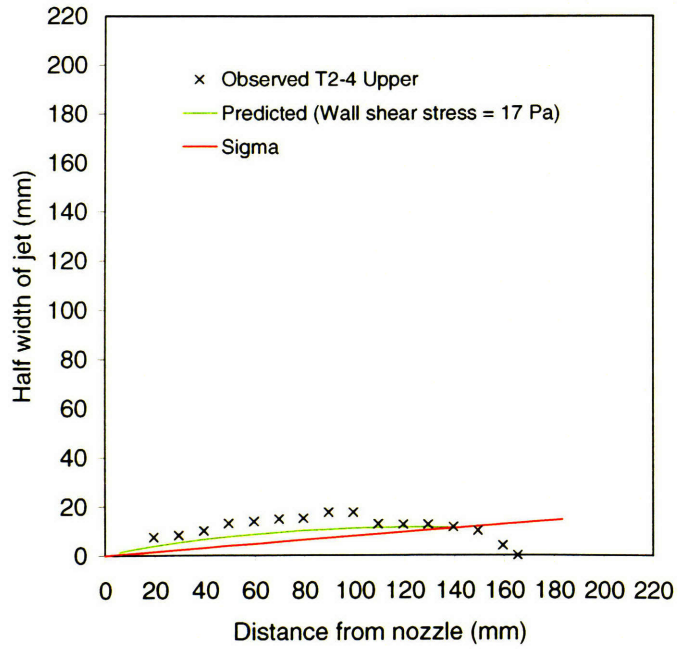

Figure E-3(d). Shape of cut (Specimen T2, Section 2, Upper cut)

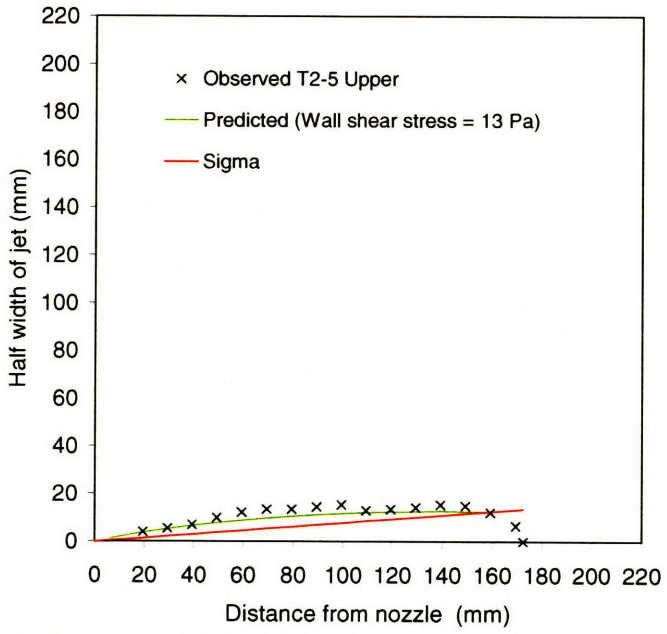

Figure E-3(e). Shape of cut (Specimen T2, Section 5, Upper cut)

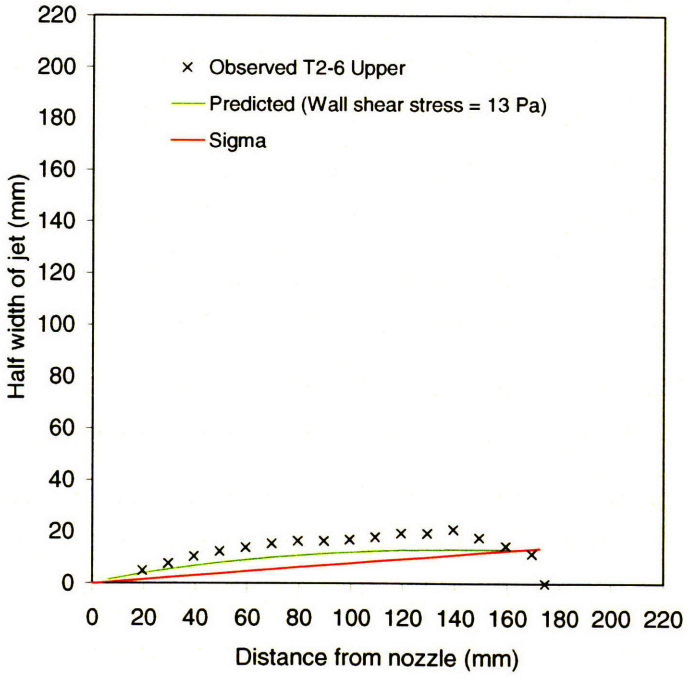

Figure E-3(f). Shape of cut (Specimen T2, Section 6, Upper cut)

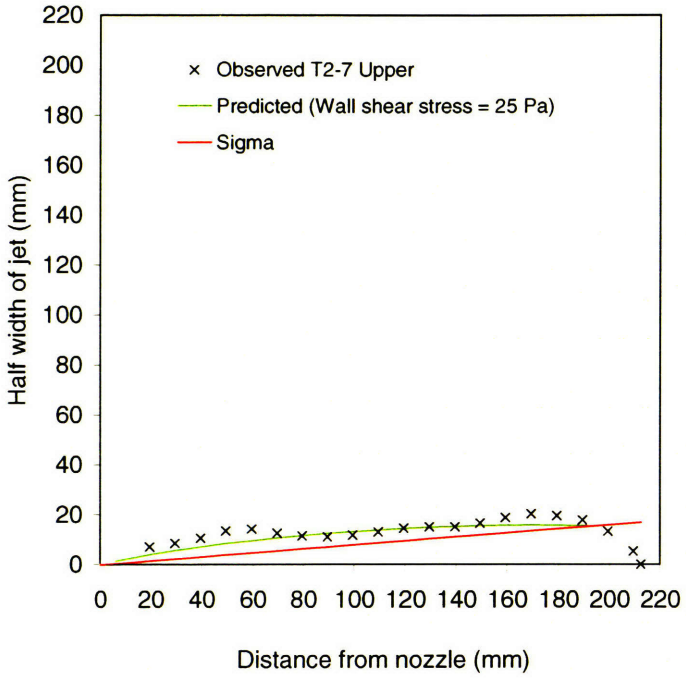

Figure E-3(g). Shape of cut (Specimen T2, Section 7, Upper cut)

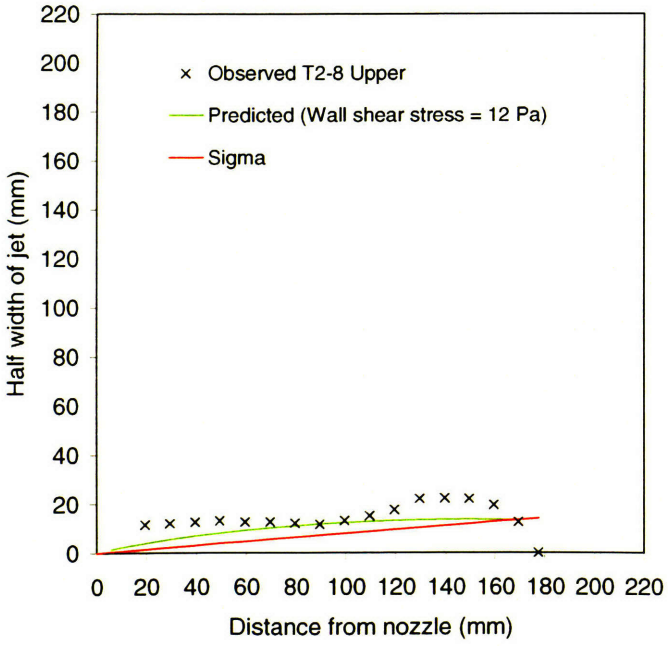

Figure E-3(h). Shape of cut (Specimen T2, Section 8, Upper cut)

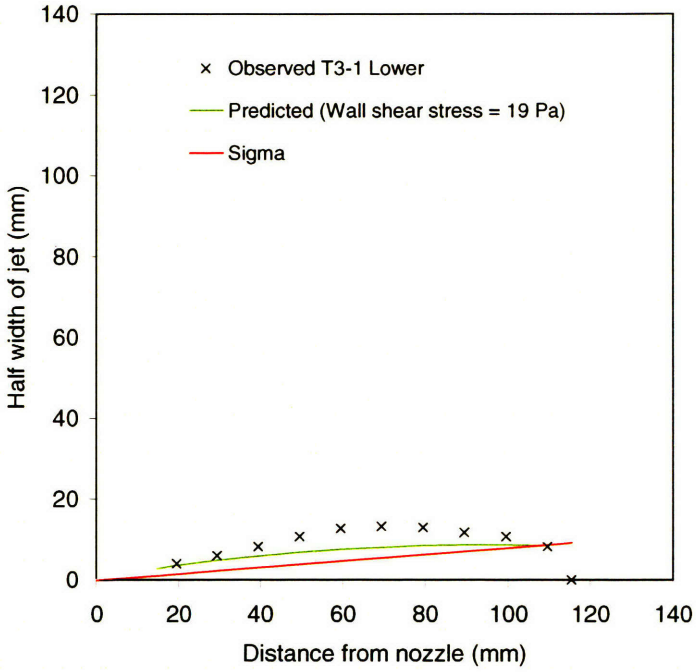

Figure E-4(a). Shape of cut (Specimen T3, Section 1, Lower cut)

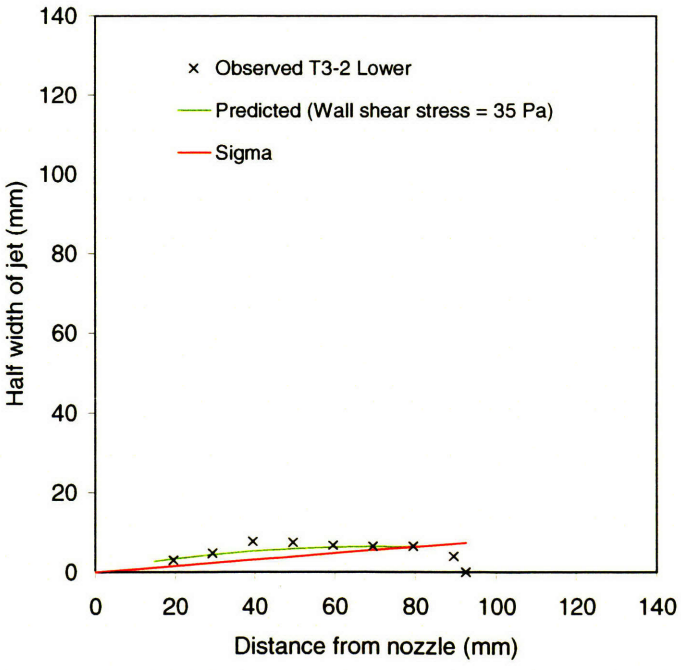

Figure E-4(b). Shape of cut (Specimen T3, Section 2, Lower cut)

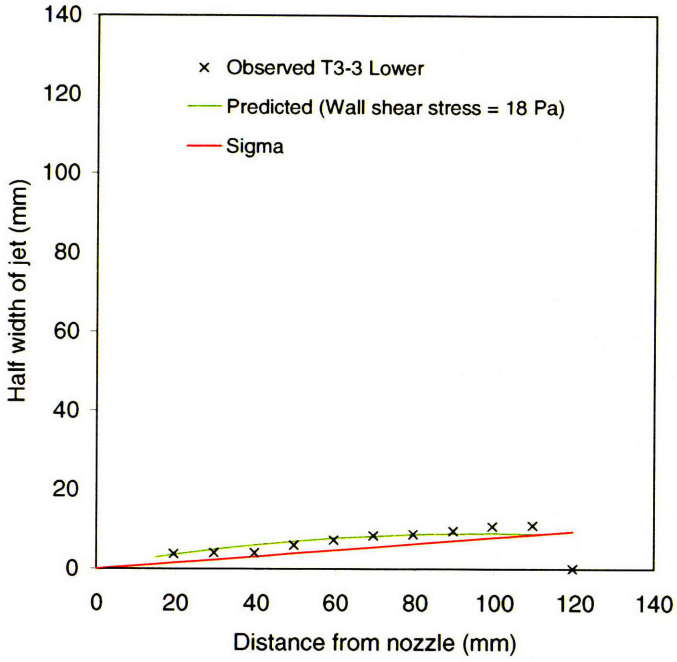

Figure E-4(c). Shape of cut (Specimen T3, Section 3, Lower cut)

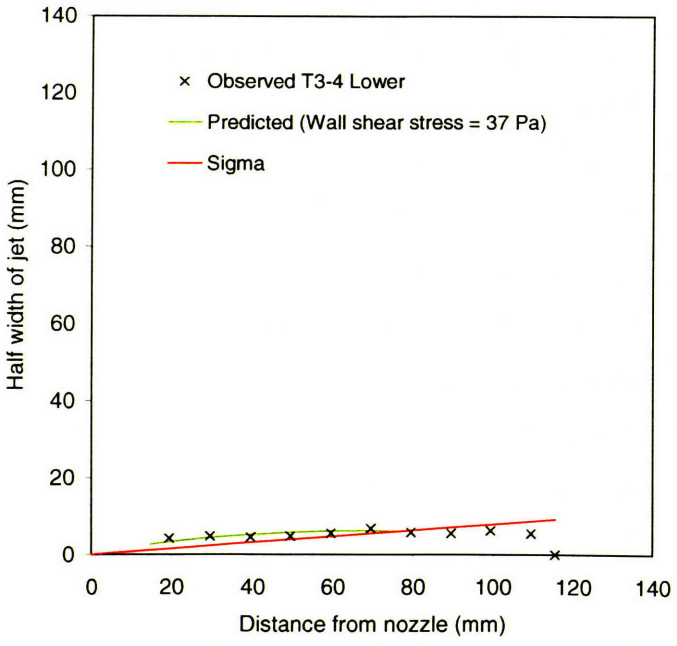

Figure E-4(d). Shape of cut (Specimen T3, Section 4, Lower cut)

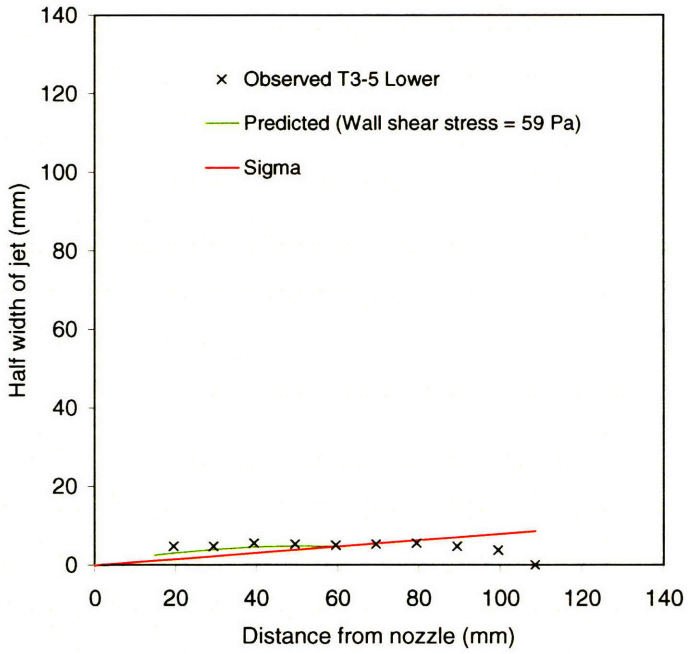

Figure E-4(e). Shape of cut (Specimen T3, Section 5, Lower cut)

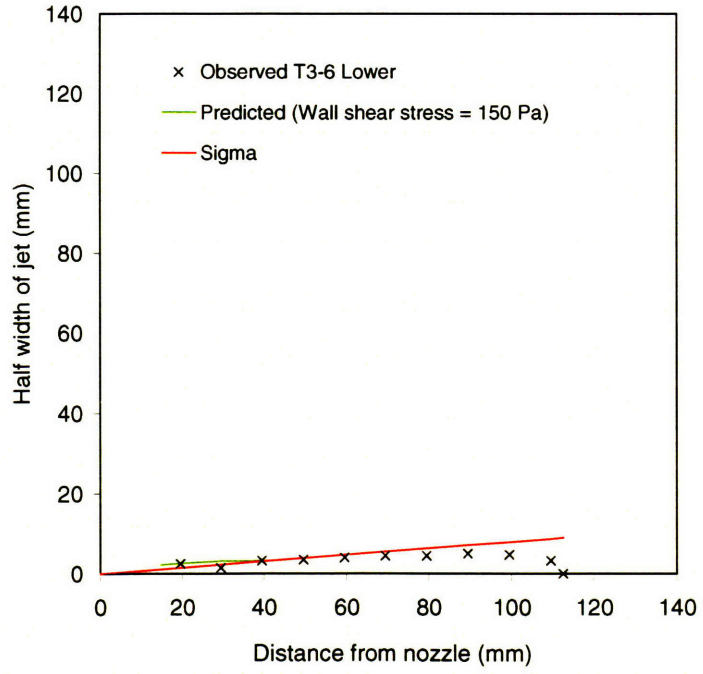

Figure E-4(f). Shape of cut (Specimen T3, Section 6, Lower cut)

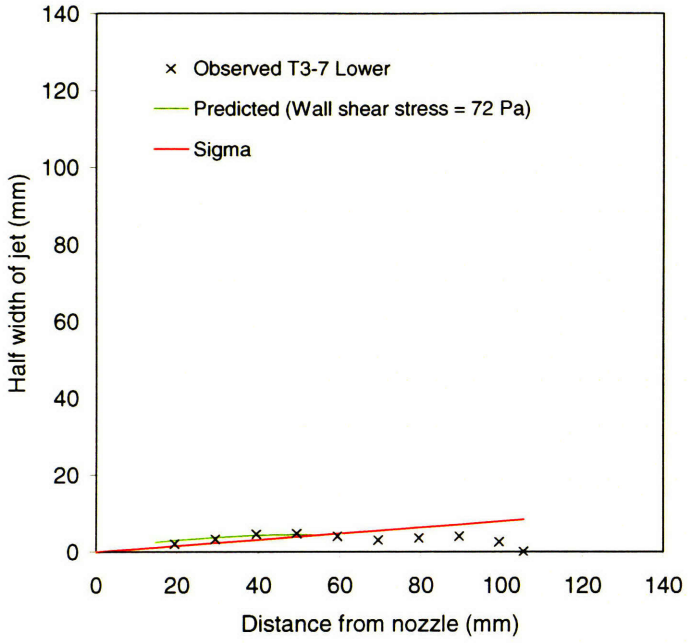

Figure E-4(g). Shape of cut (Specimen T3, Section 7, Lower cut)

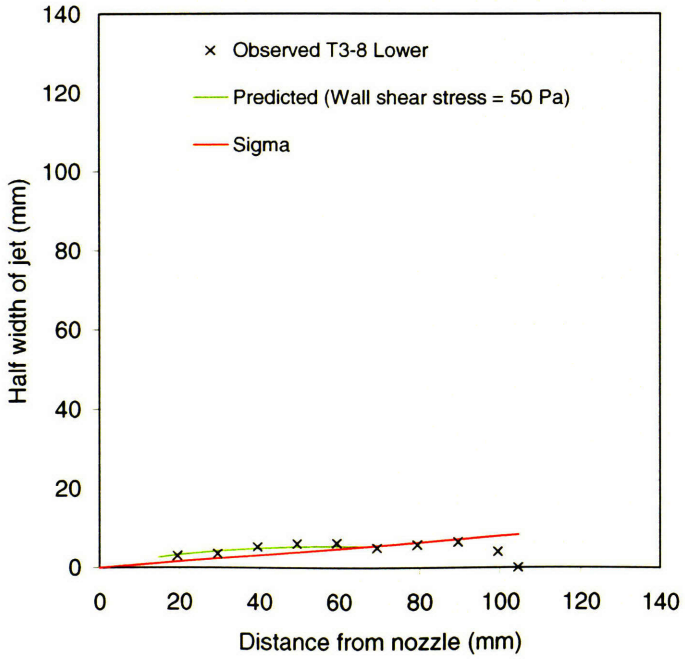

Figure E-4(h). Shape of cut (Specimen T3, Section 8, Lower cut)

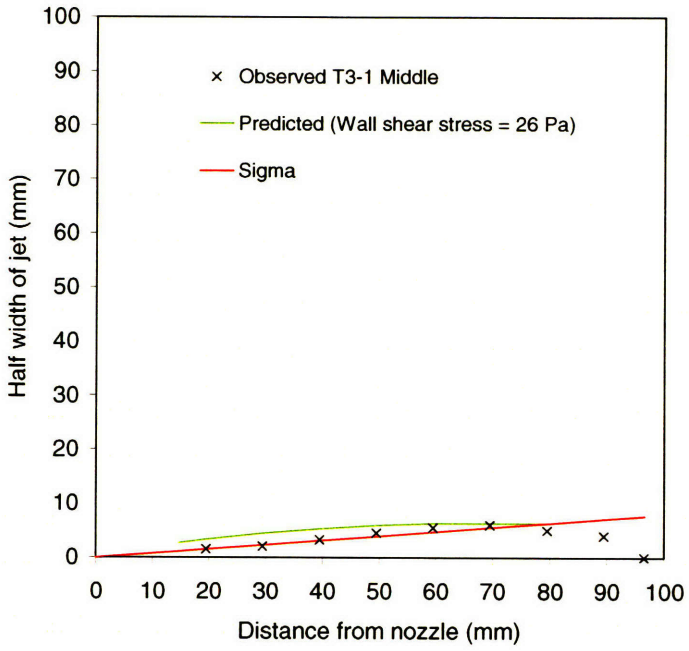

Figure E-5(a). Shape of cut (Specimen T3, Section 1, Middle cut)

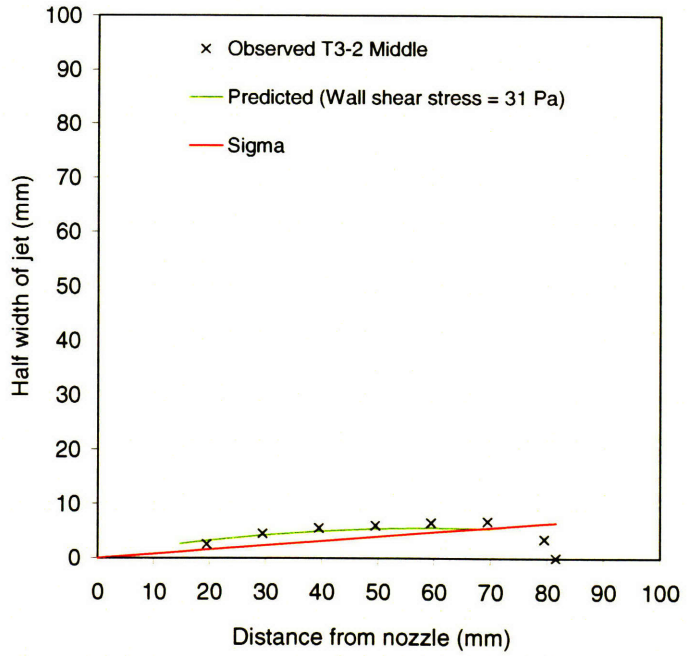

Figure E-5(b). Shape of cut (Specimen T3, Section 2, Middle cut)

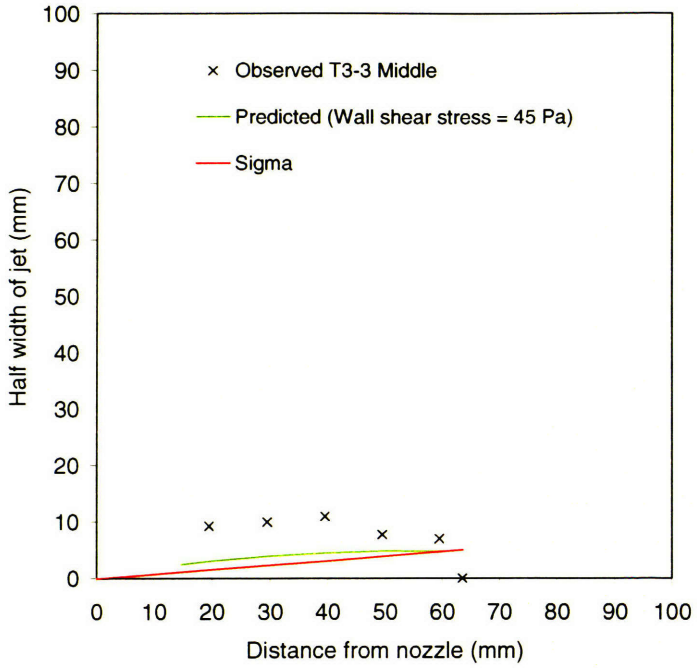

Figure E-5(c). Shape of cut (Specimen T3, Section 3, Middle cut)

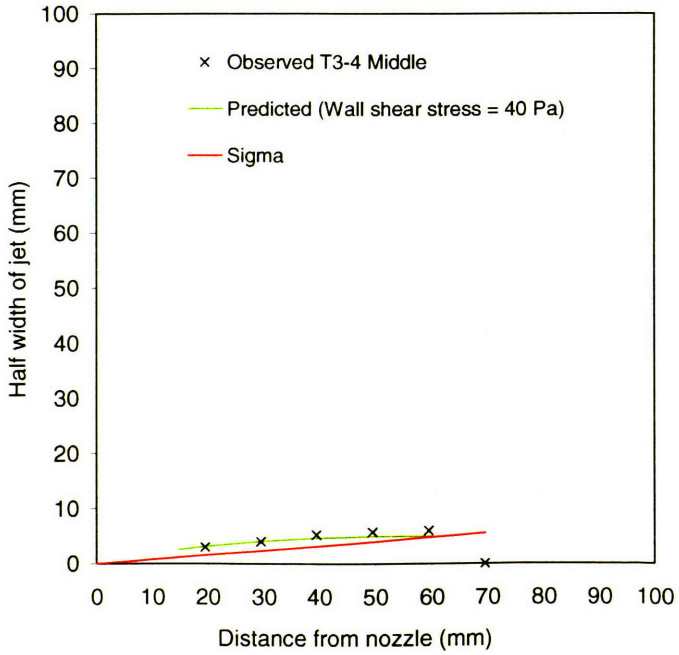

Figure E-5(d). Shape of cut (Specimen T3, Section 4, Middle cut)

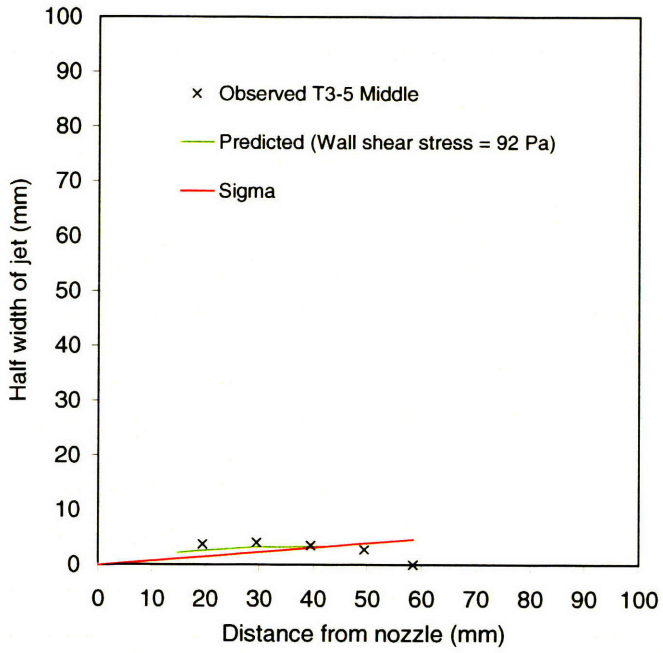

Figure E-5(e). Shape of cut (Specimen T3, Section 5, Middle cut)

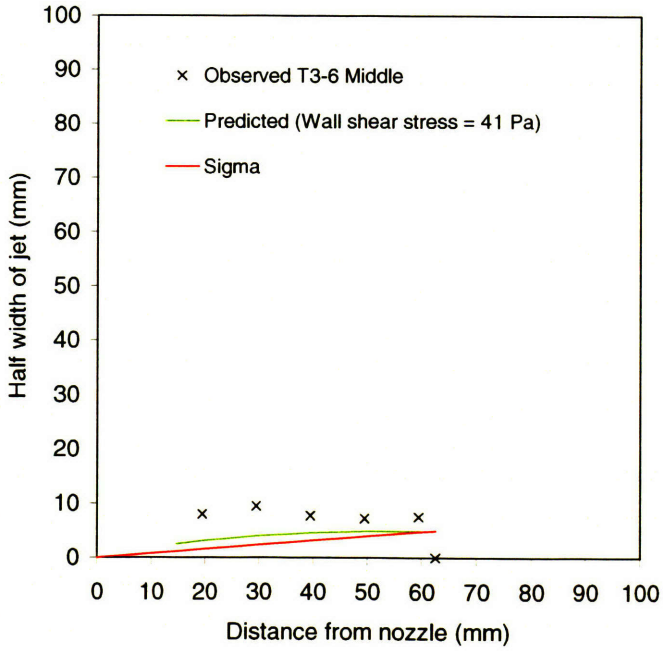

Figure E-5(f). Shape of cut (Specimen T3, Section 6, Middle cut)

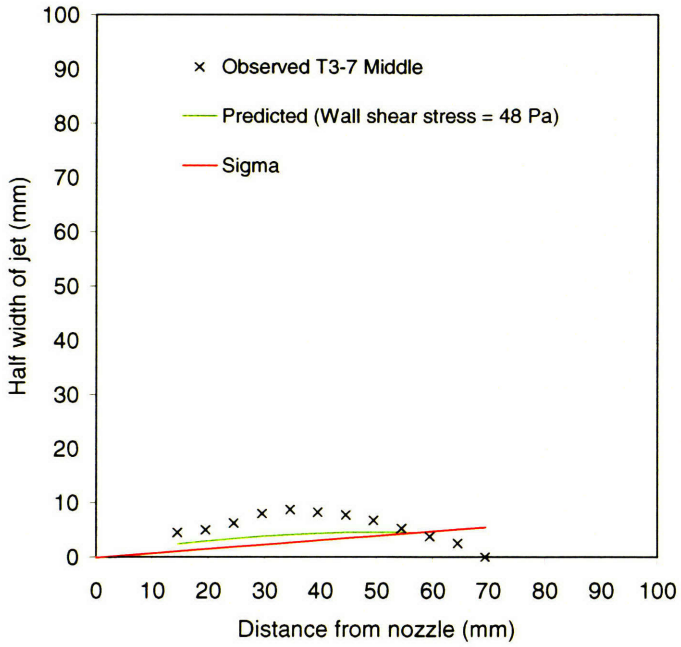

Figure E-5(g). Shape of cut (Specimen T3, Section 7, Middle cut)

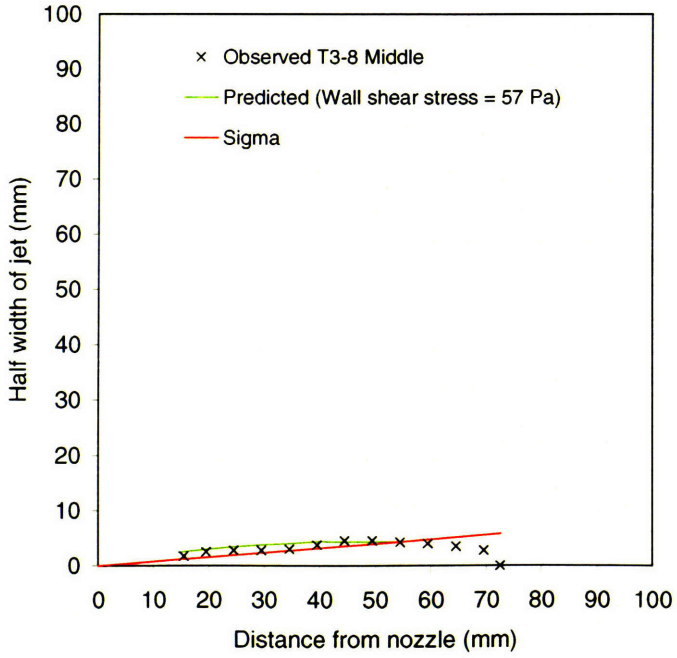

Figure E-5(h). Shape of cut (Specimen T3, Section 8, Middle cut)

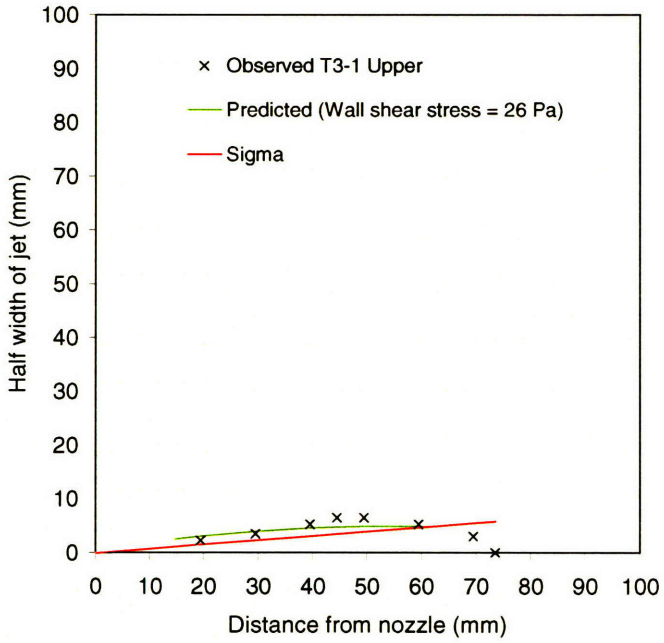

Figure E-6(a). Shape of cut (Specimen T3, Section 1, Upper cut)

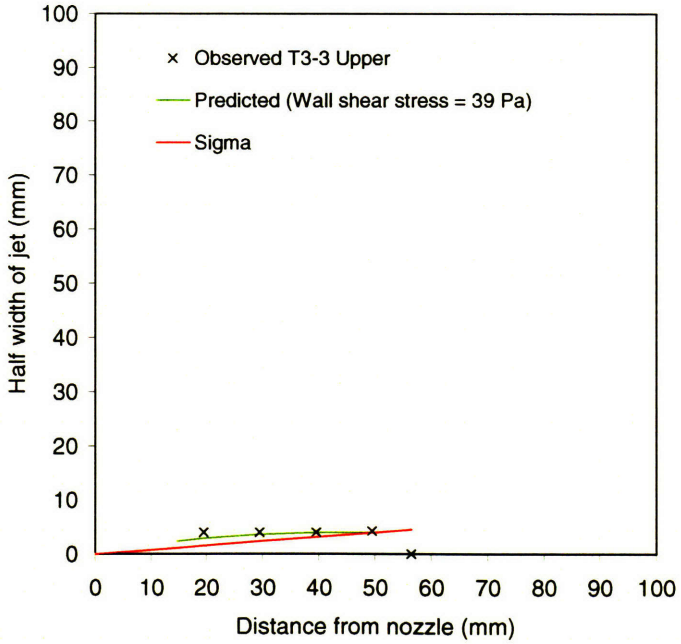

Figure E-6(b). Shape of cut (Specimen T3, Section 3, Upper cut)

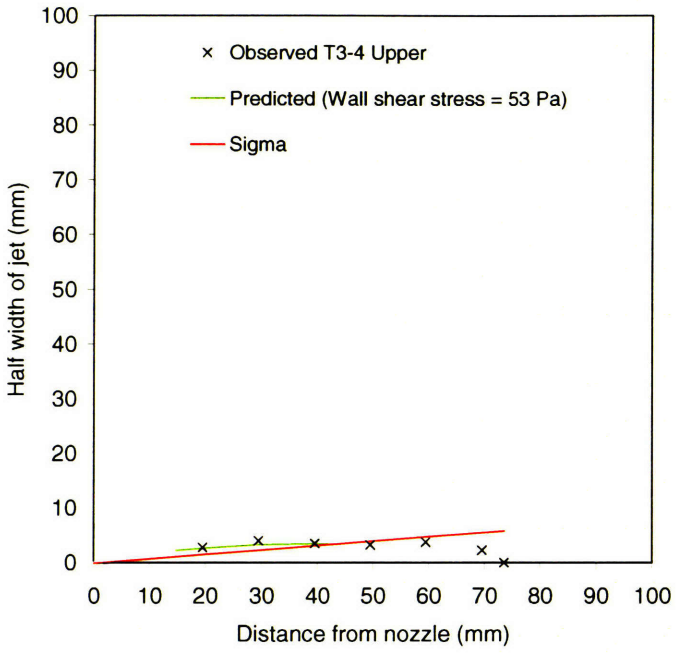

Figure E-6(c). Shape of cut (Specimen T3, Section 4, Upper cut)

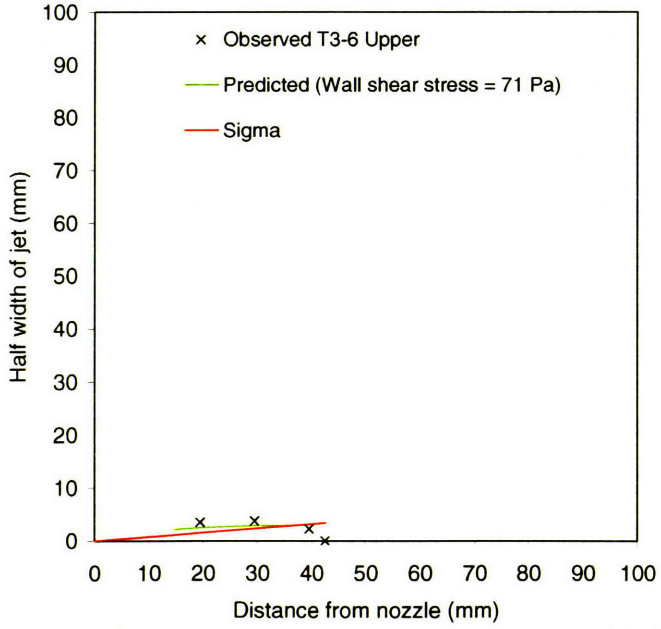

Figure E-6(d). Shape of cut (Specimen T3, Section 6, Upper cut)

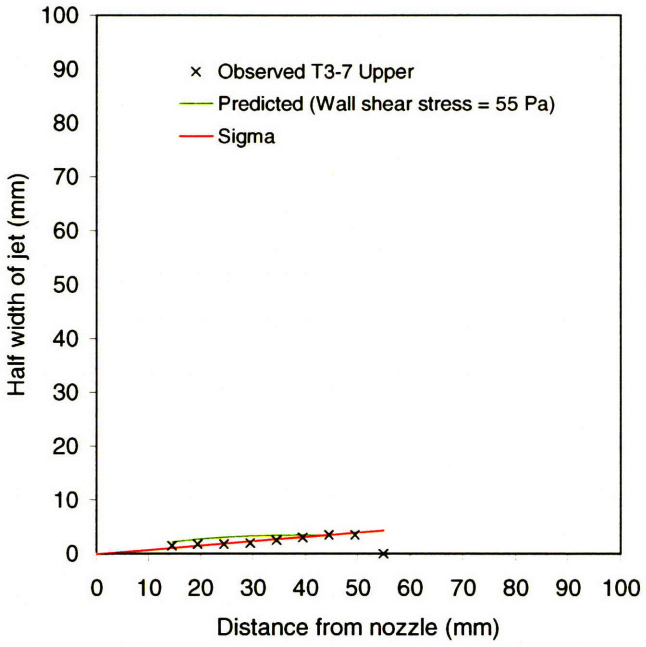

Figure E-6(e). Shape of cut (Specimen T3, Section 7, Upper cut)

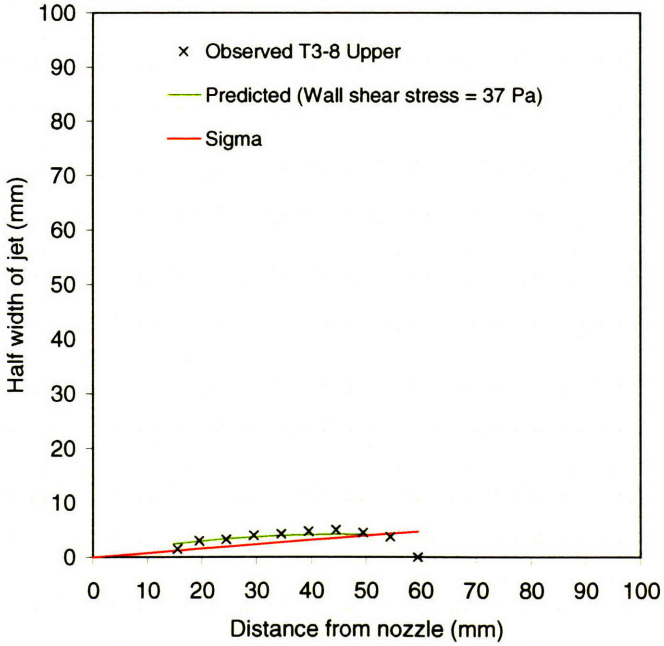

Figure E-6(f). Shape of cut (Specimen T3, Section 8, Upper cut)

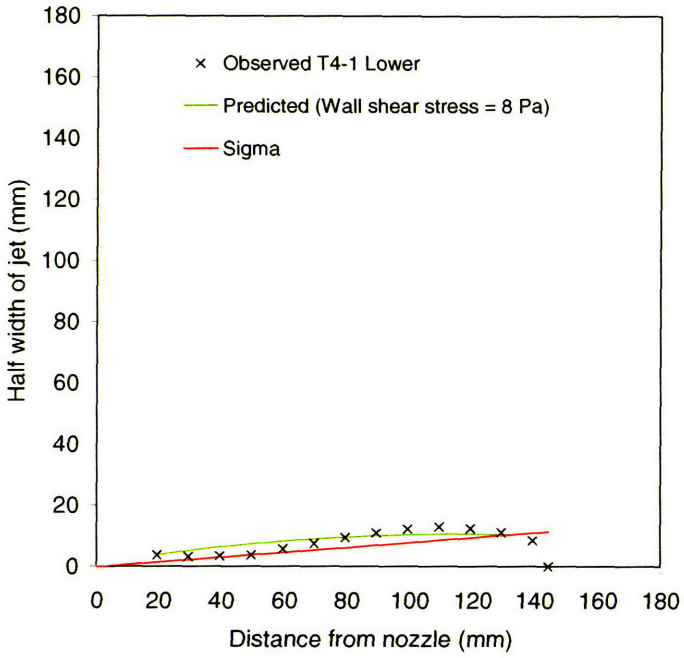

Figure E-7(a). Shape of cut (Specimen T4, Section 1, Lower cut)

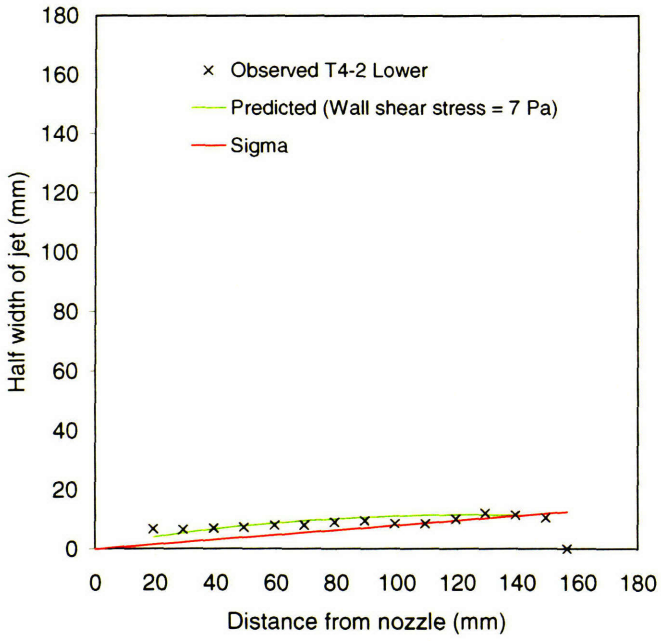

Figure E-7(b). Shape of cut (Specimen T4, Section 1, Lower cut)

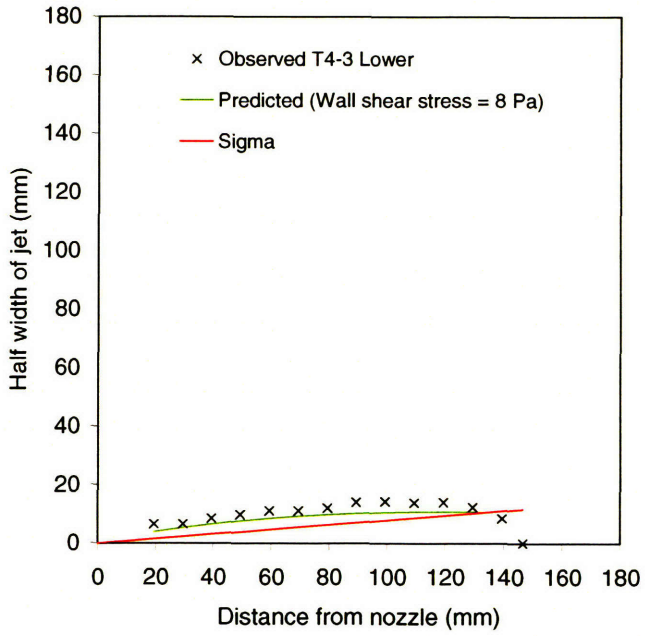

Figure E-7(c). Shape of cut (Specimen T4, Section 3, Lower cut)

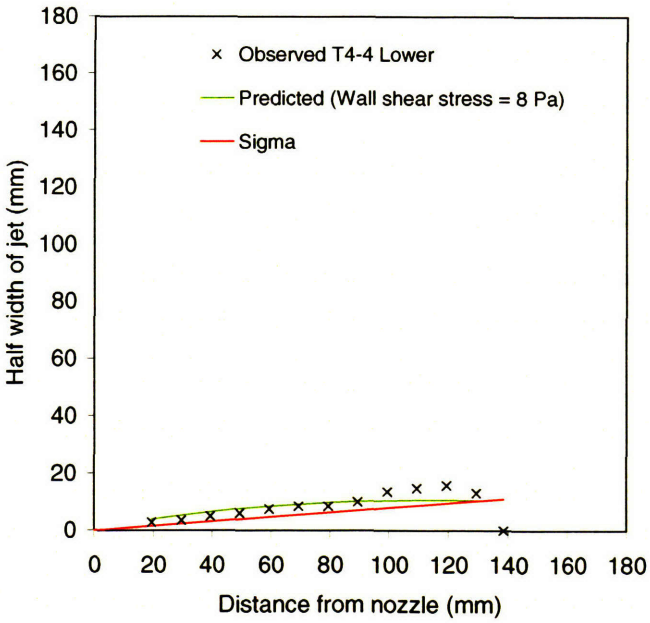

Figure E-7(d). Shape of cut (Specimen T4, Section 4, Lower cut)

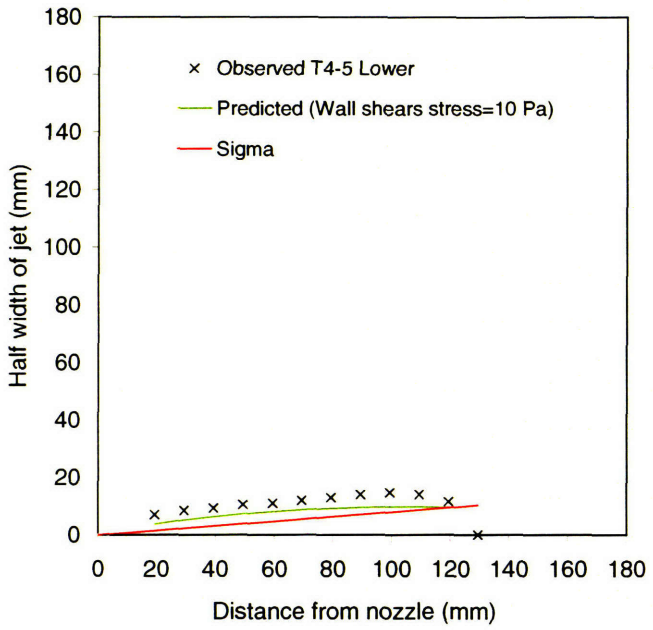

Figure E-7(e). Shape of cut (Specimen T4, Section 5, Lower cut)

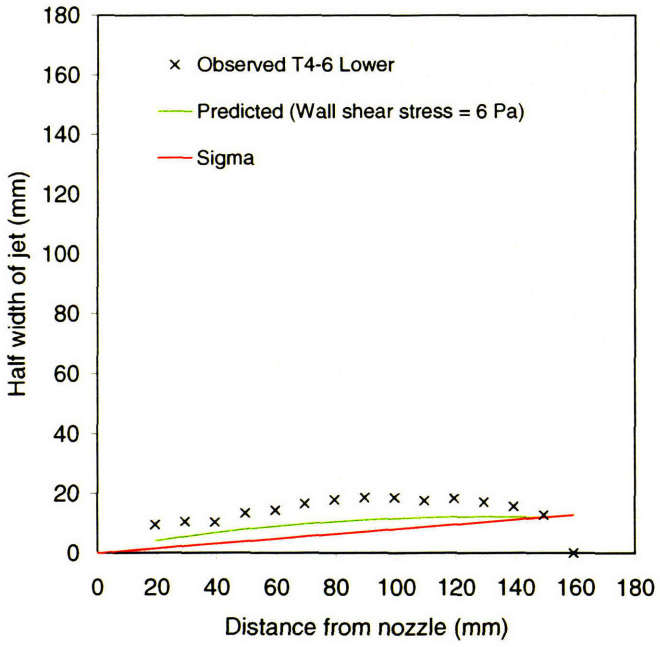

Figure E-7(f). Shape of cut (Specimen T4, Section 6, Lower cut)

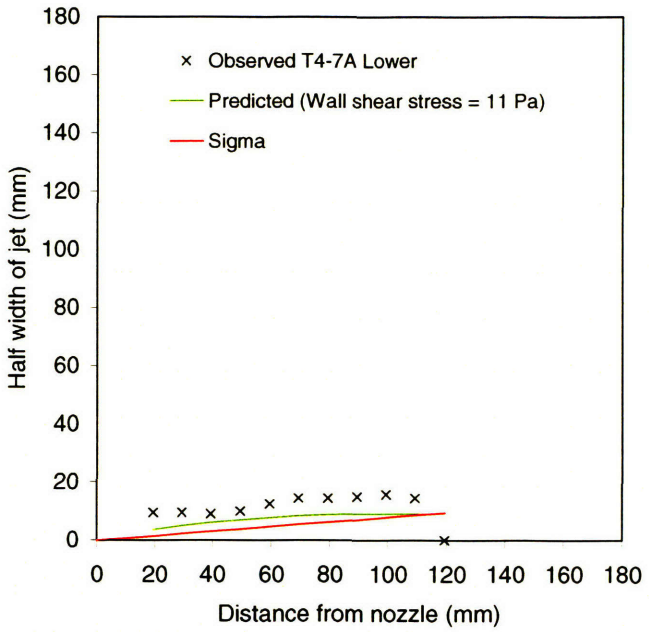

Figure E-7(g). Shape of cut (Specimen T4, Section 7A, Lower cut)

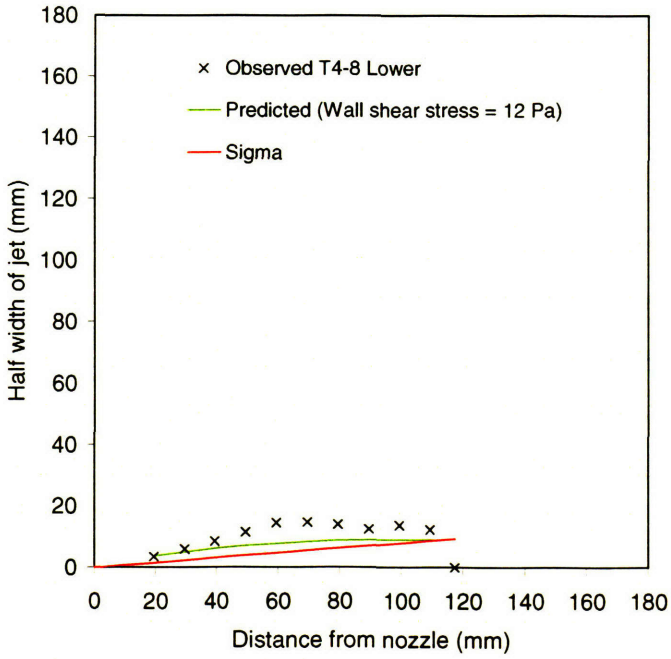

Figure E-7(h). Shape of cut (Specimen T4, Section 8, Lower cut)

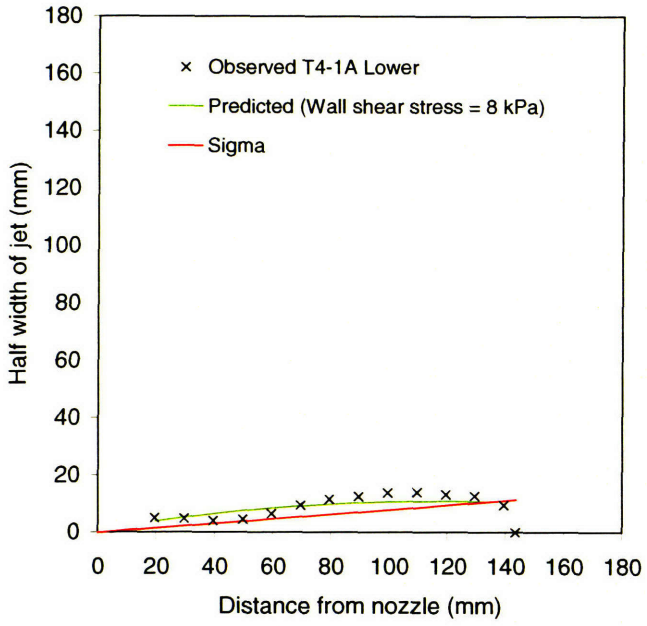

Figure E-7(i). Shape of cut (Specimen T4, Section 1A, Lower cut)

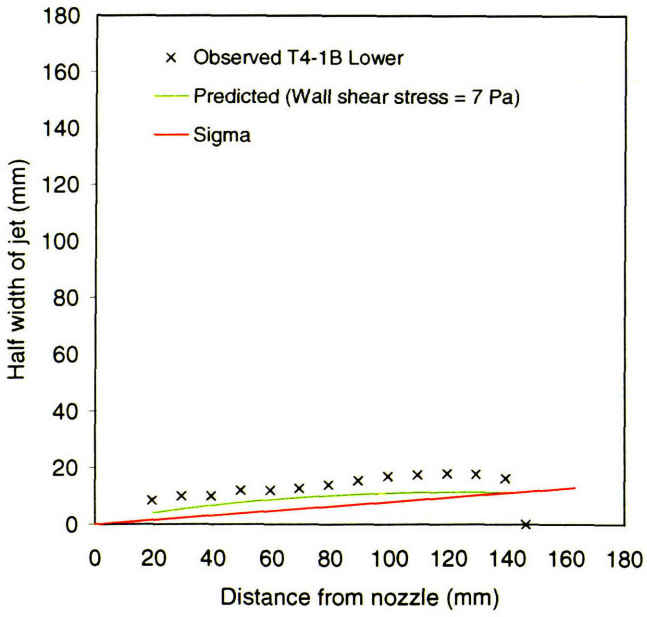

Figure E-7(j). Shape of cut (Specimen T4, Section 1B, Lower cut)

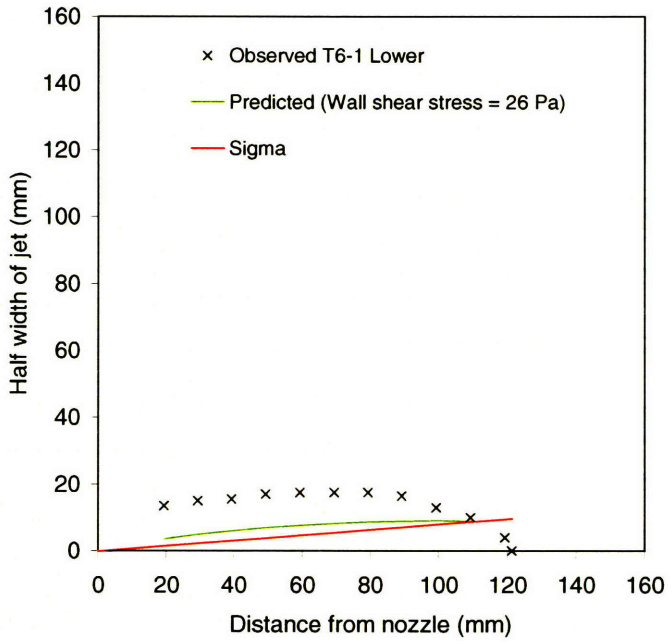

Figure E-8(a). Shape of cut (Specimen T6, Section 1, Lower cut)

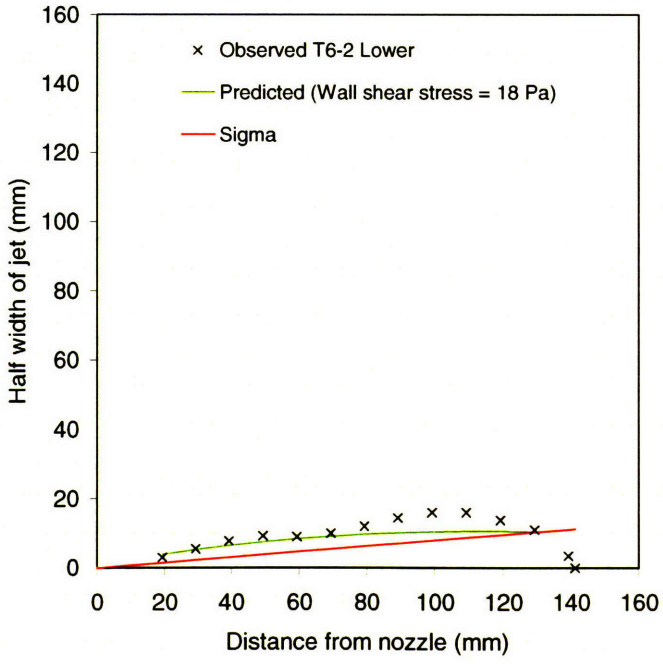

Figure E-8(b). Shape of cut (Specimen T6, Section 2, Lower cut)

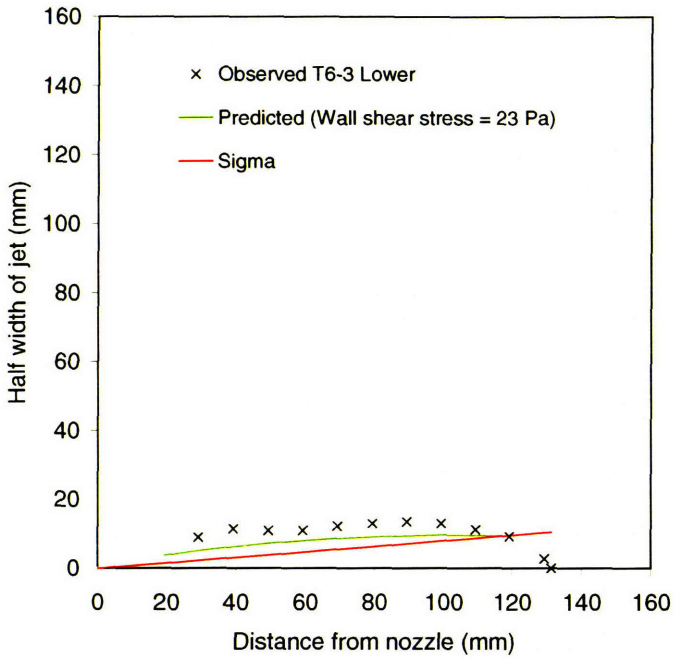

Figure E-8(c). Shape of cut (Specimen T6, Section 3, Lower cut)

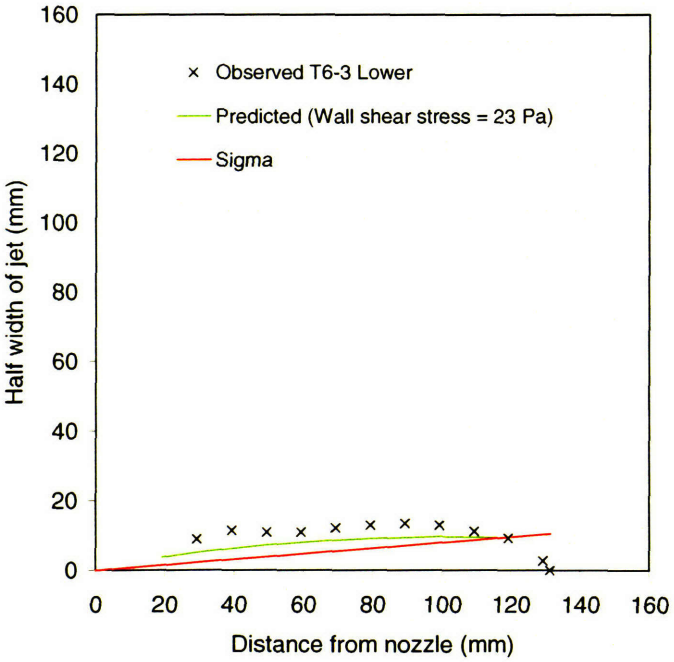

Figure E-8(d). Shape of cut (Specimen T6, Section 4, Lower cut)

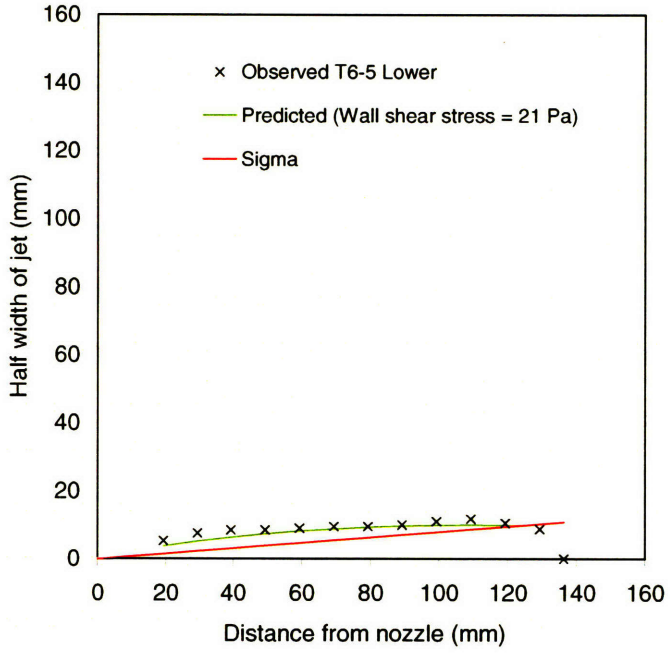

Figure E-8(e). Shape of cut (Specimen T6, Section 5, Lower cut)

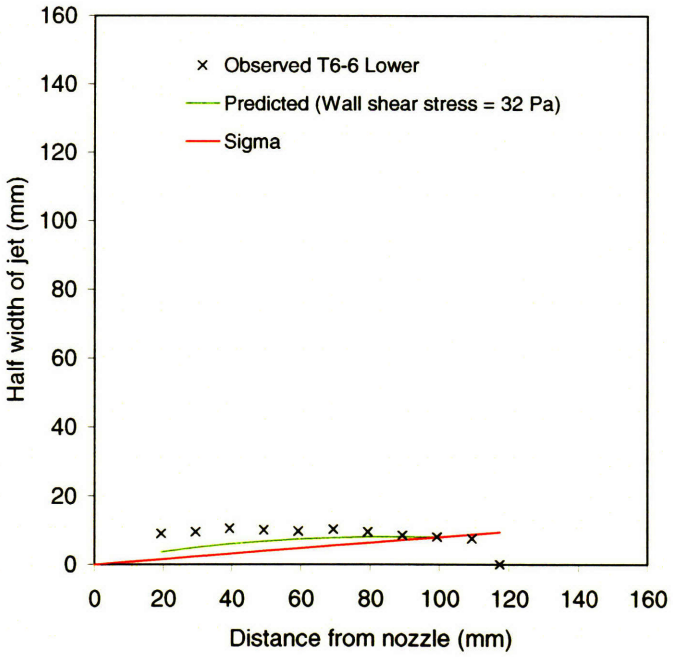

Figure E-8(f). Shape of cut (Specimen T6, Section 6, Lower cut)

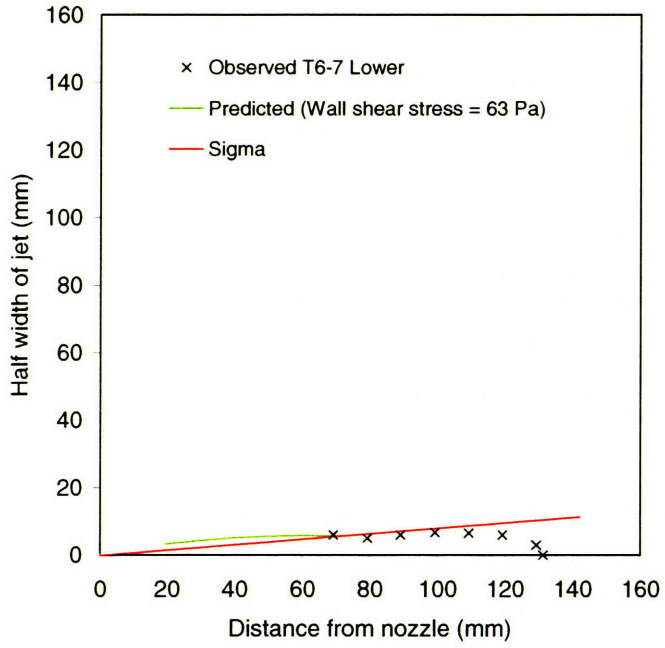

Figure E-8(g). Shape of cut (Specimen T6, Section 7, Lower cut)

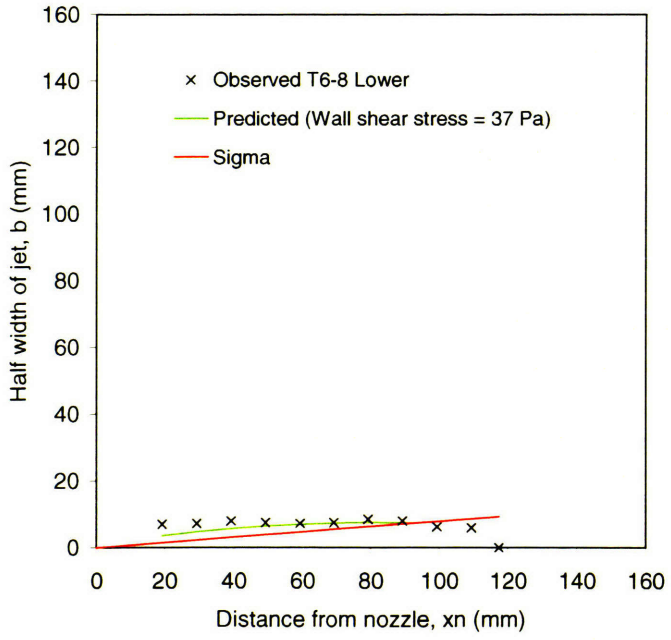

Figure E-8(h). Shape of cut (Specimen T6, Section 8, Lower cut)

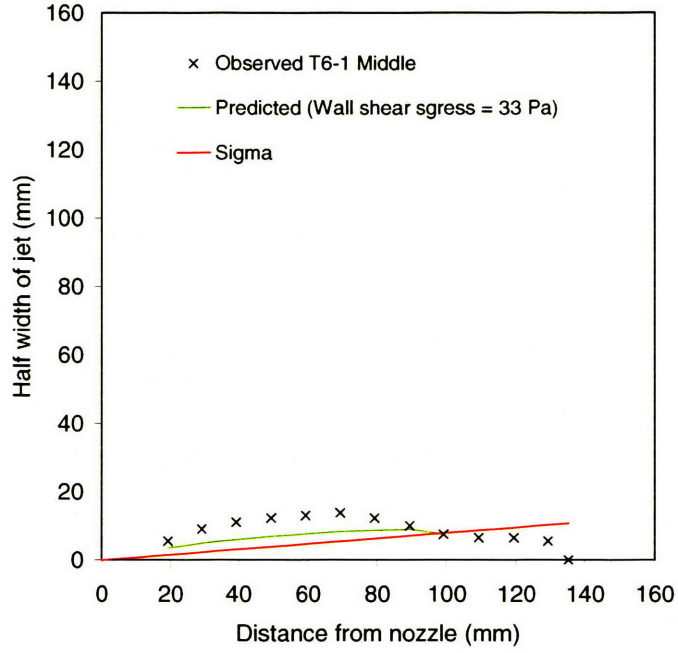

Figure E-9(a). Shape of cut (Specimen T6, Section 1, Middle cut)

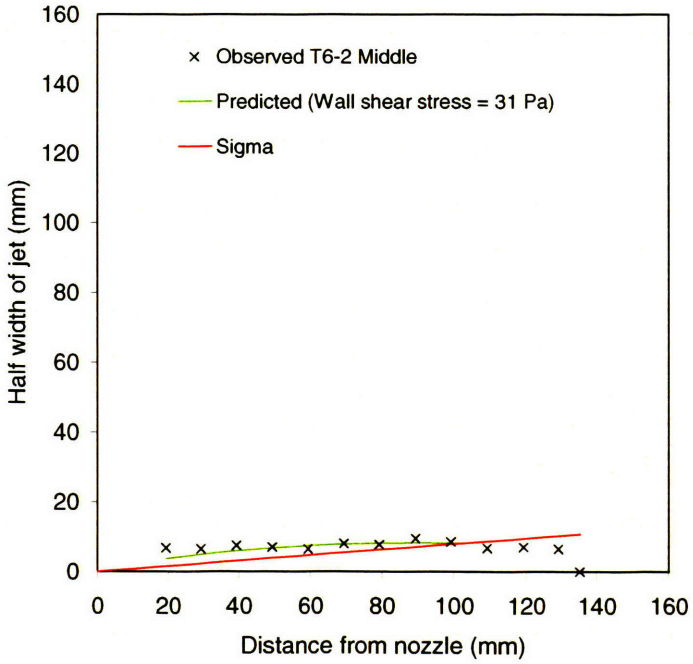

Figure E-9(b). Shape of cut (Specimen T6, Section 2, Middle cut)

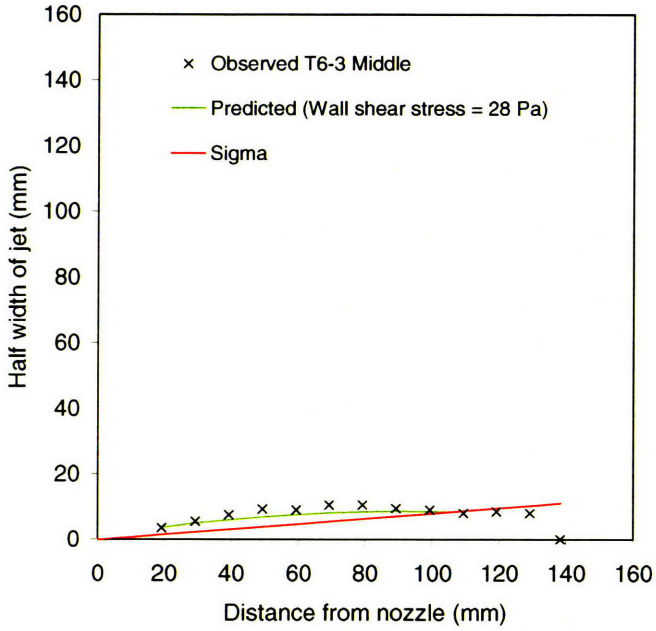

Figure E-9(c). Shape of cut (Specimen T6, Section 3, Middle cut)

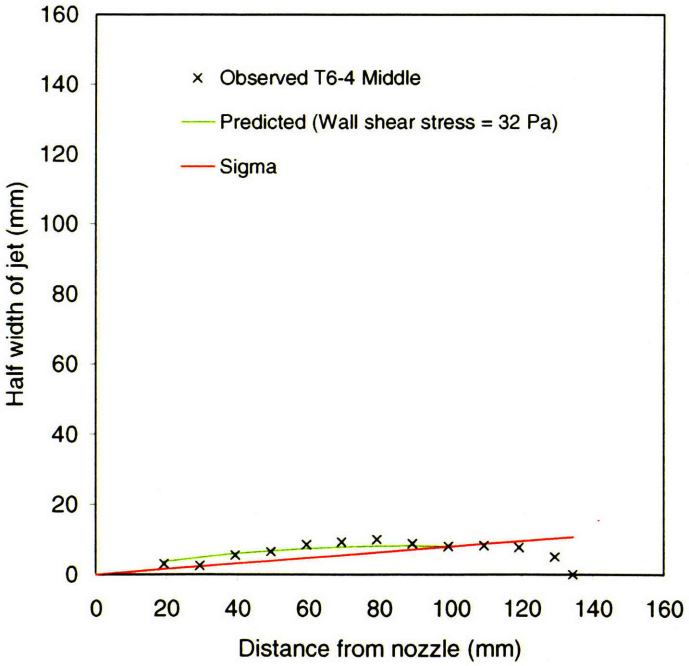

Figure E-9(d). Shape of cut (Specimen T6, Section 4, Middle cut)

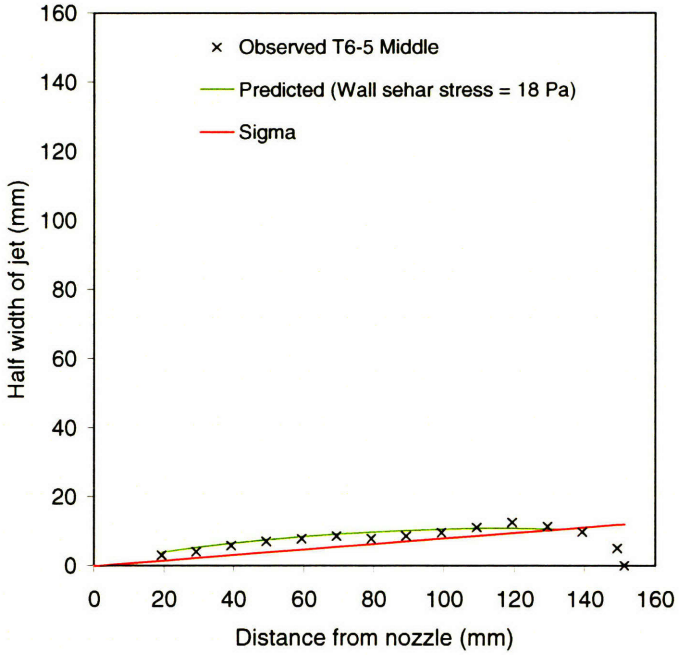

Figure E-9(e). Shape of cut (Specimen T6, Section 5, Middle cut)

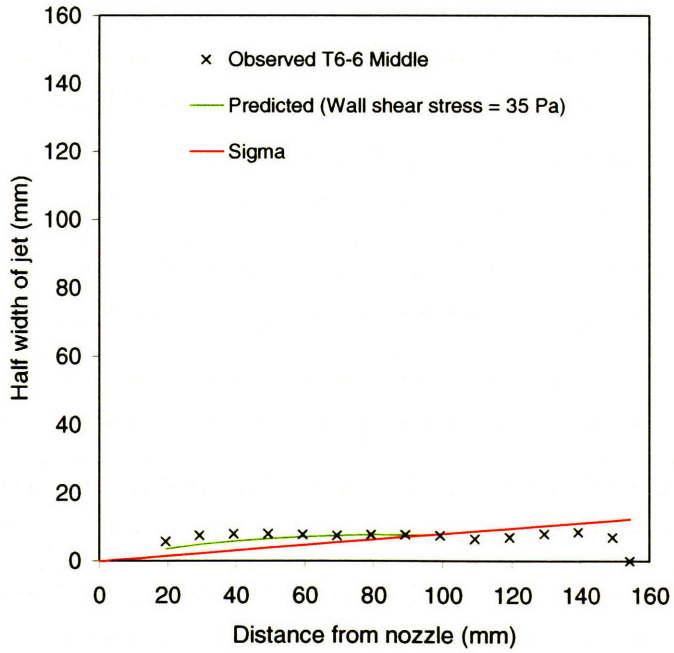

Figure E-9(f). Shape of cut (Specimen T6, Section 6, Middle cut)

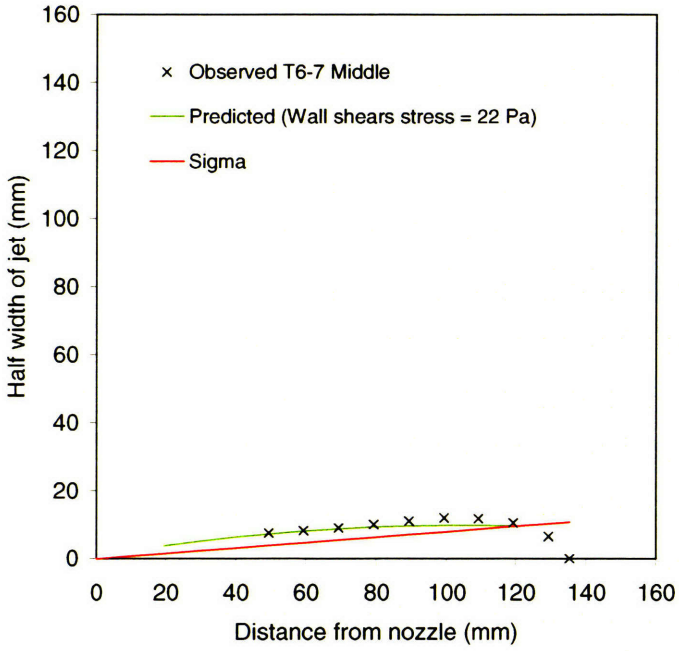

Figure E-9(g). Shape of cut (Specimen T6, Section 7, Middle cut)

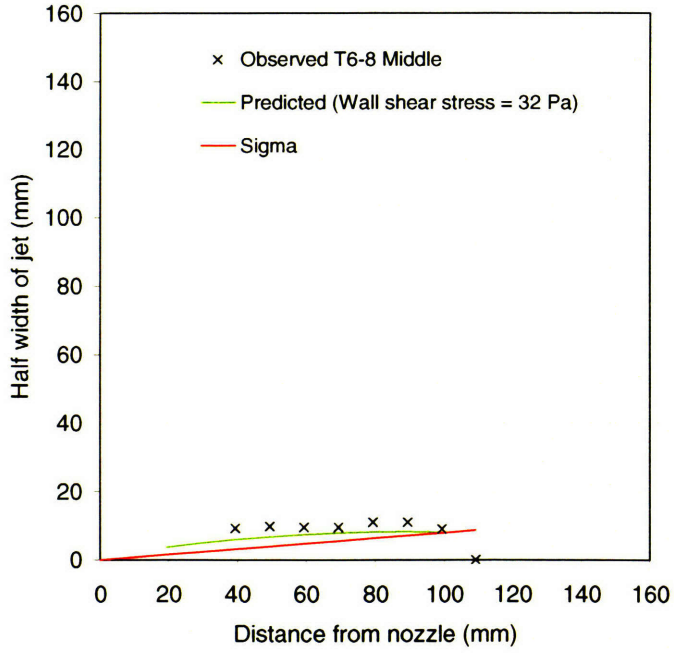

Figure E-9(h). Shape of cut (Specimen T6, Section 8, Middle cut)

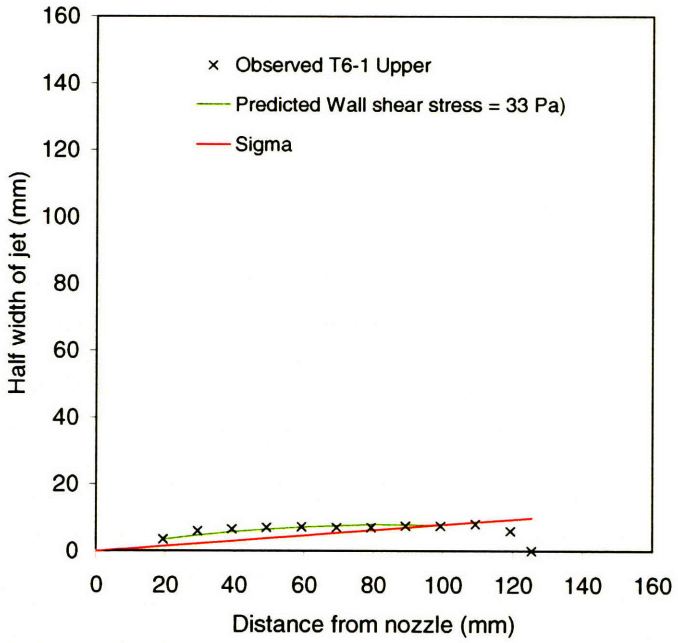

Figure E-10(a). Shape of cut (Specimen T6, Section 1, Upper cut)

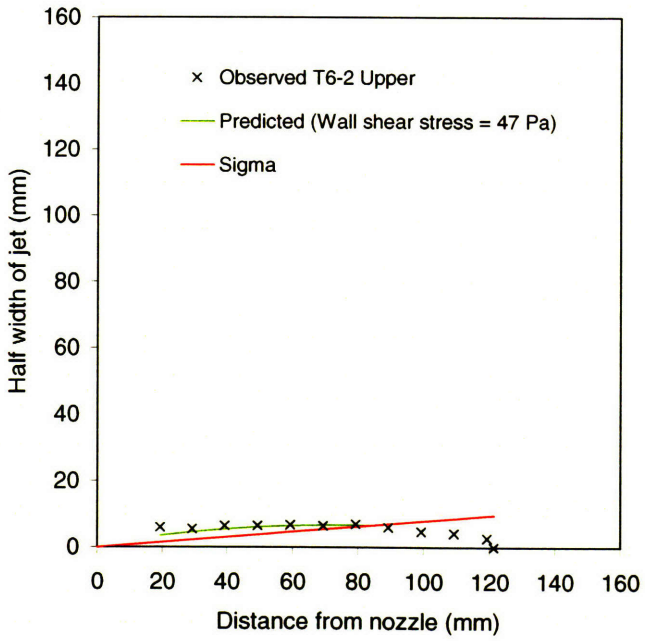

Figure E-10(b). Shape of cut (Specimen T6, Section 2, Upper cut)

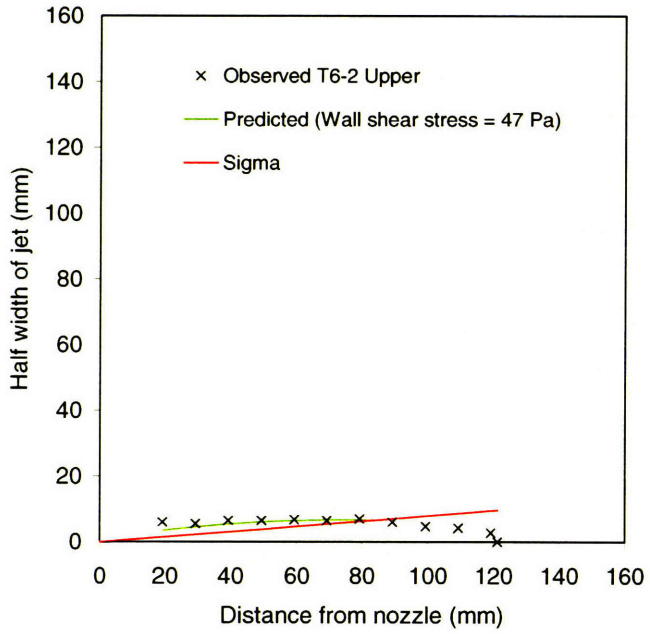

Figure E-10(c). Shape of cut (Specimen T6, Section 3, Upper cut)

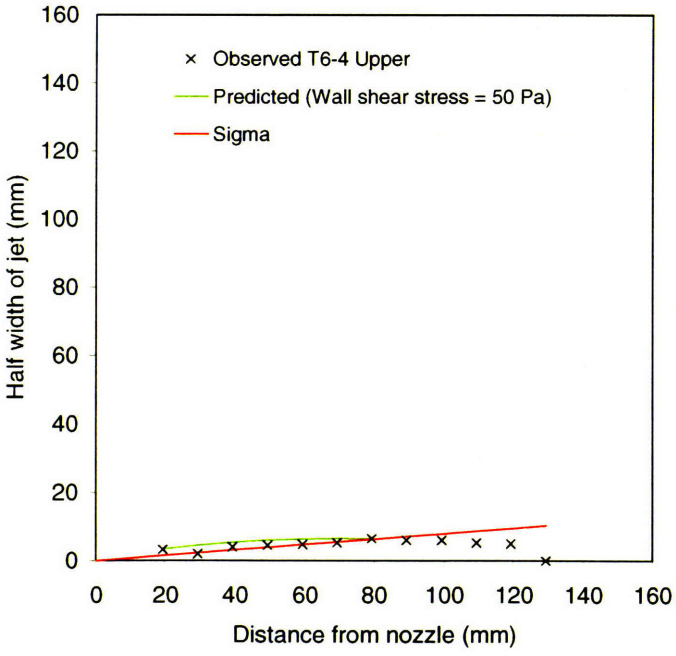

Figure E-10(d). Shape of cut (Specimen T6, Section 4, Upper cut)

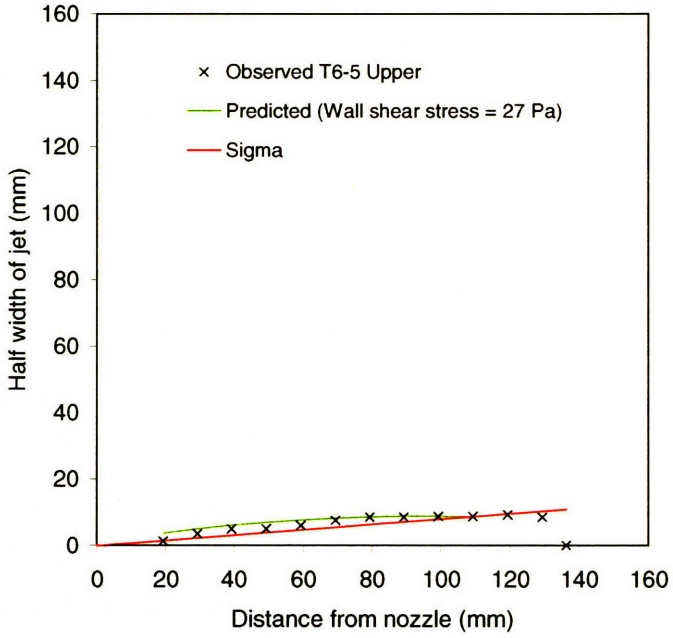

Figure E-10(e). Shape of cut (Specimen T6, Section 5, Upper cut)

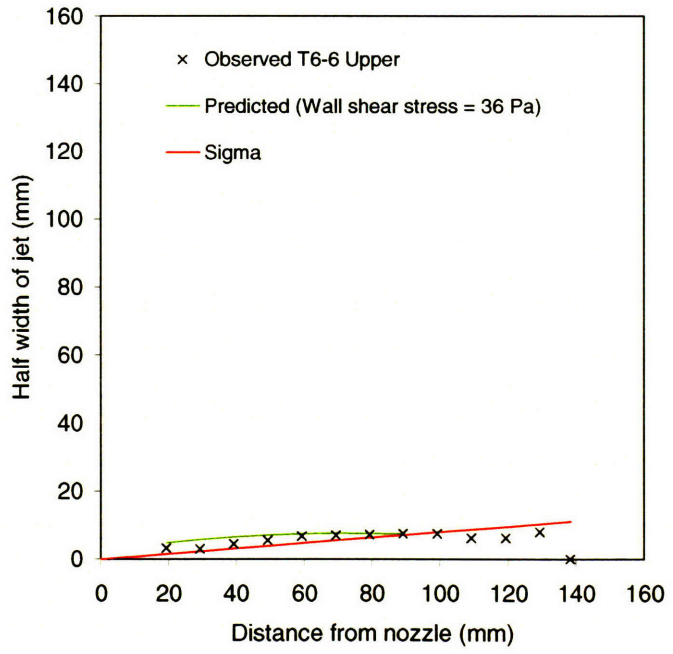

Figure E-10(f). Shape of cut (Specimen T6, Section 6, Upper cut)

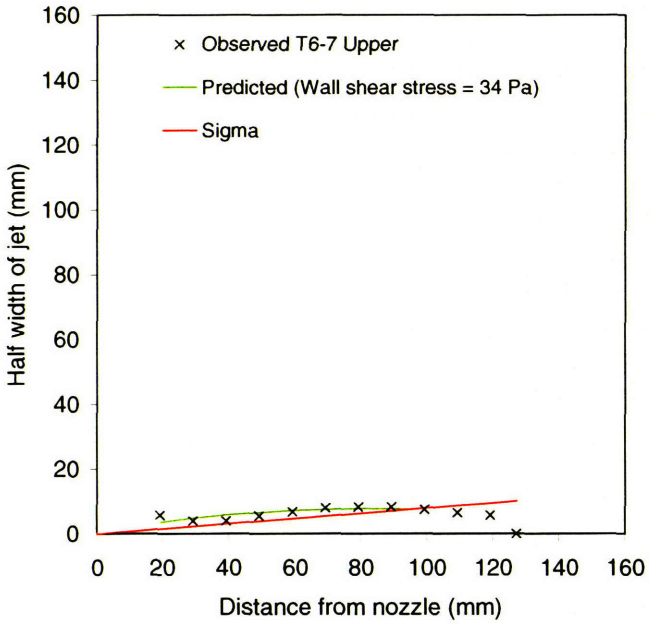

Figure E-10(g). Shape of cut (Specimen T6, Section 7, Upper cut)

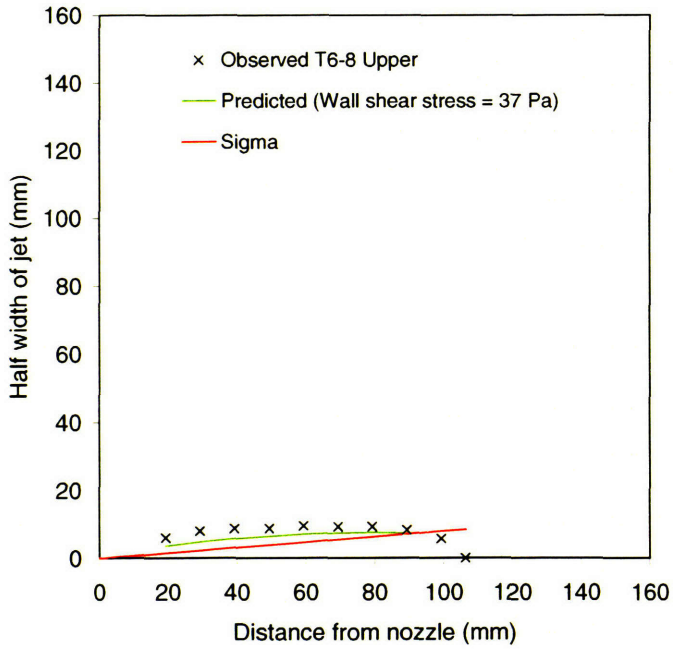

Figure E-10(h). Shape of cut (Specimen T6, Section 8, Upper cut)

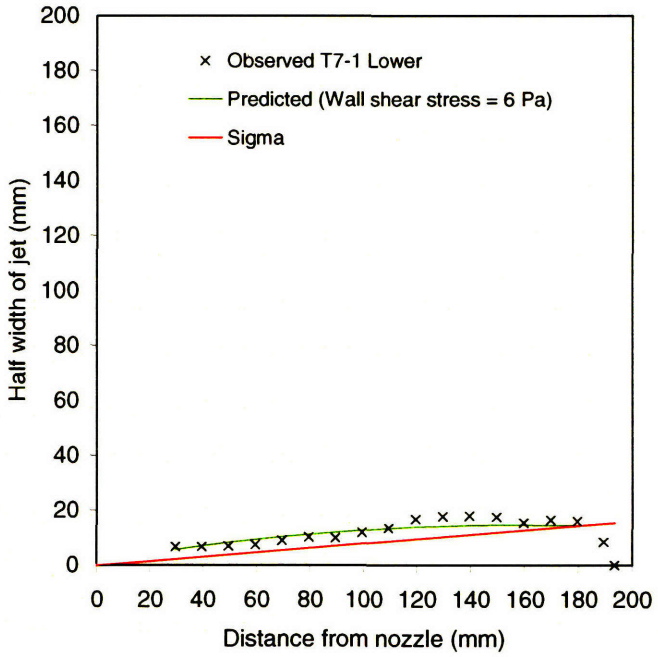

Figure E-11(a). Shape of cut (Specimen T7, Section 1, Lower cut)

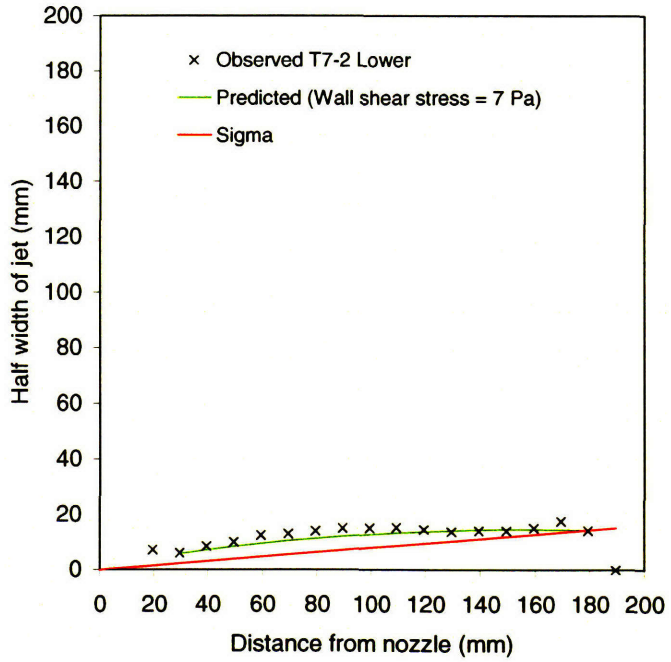

Figure E-11(b). Shape of cut (Specimen T7, Section 2, Lower cut)

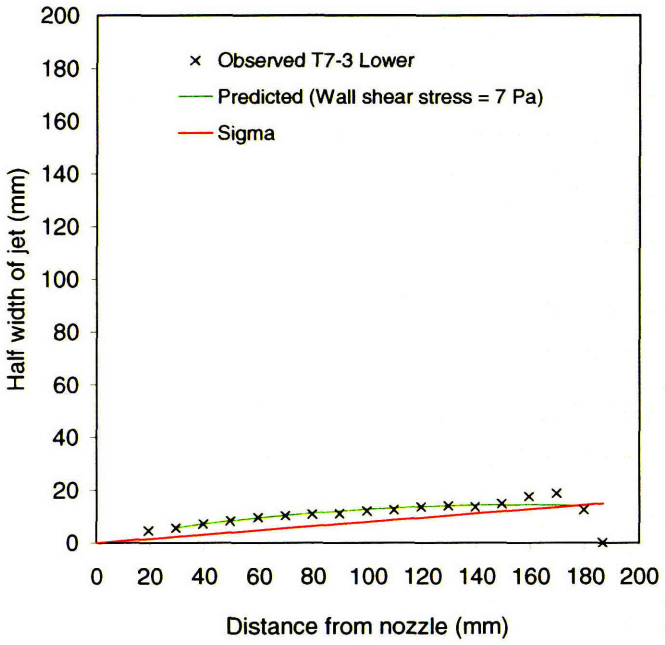

Figure E-11(c). Shape of cut (Specimen T7, Section 3, Lower cut)

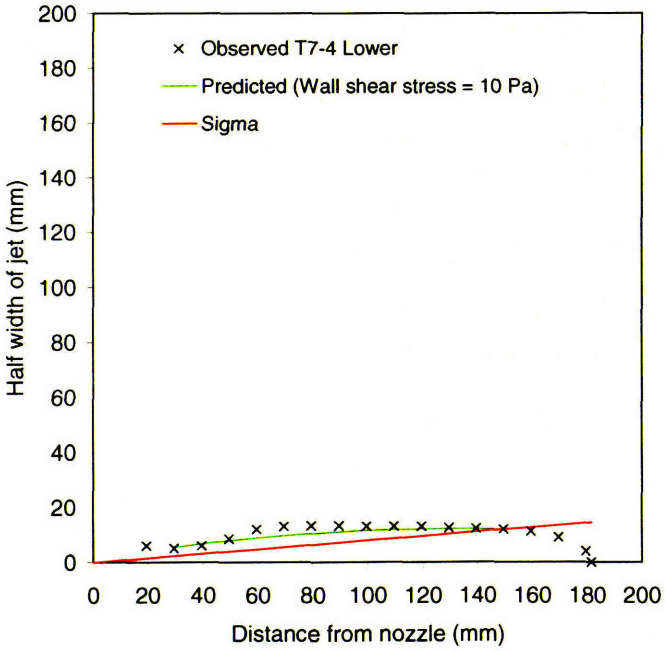

Figure E-11(d). Shape of cut (Specimen T7, Section 4, Lower cut)

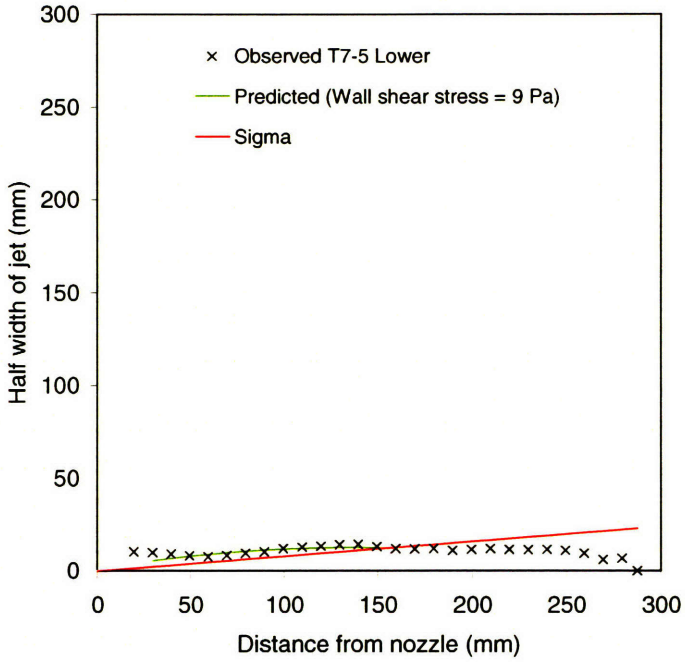

Figure E-11(e). Shape of cut (Specimen T7, Section 5, Lower cut)

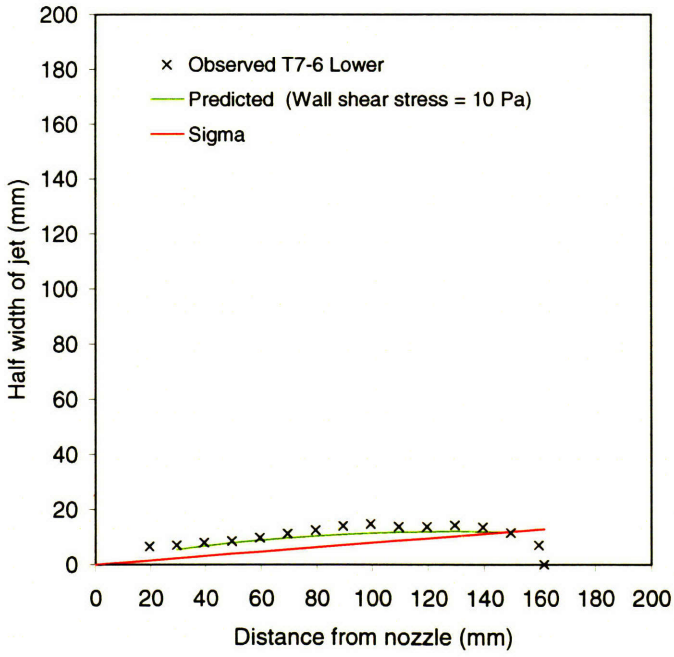

Figure E-11(f). Shape of cut (Specimen T7, Section 6, Lower cut)

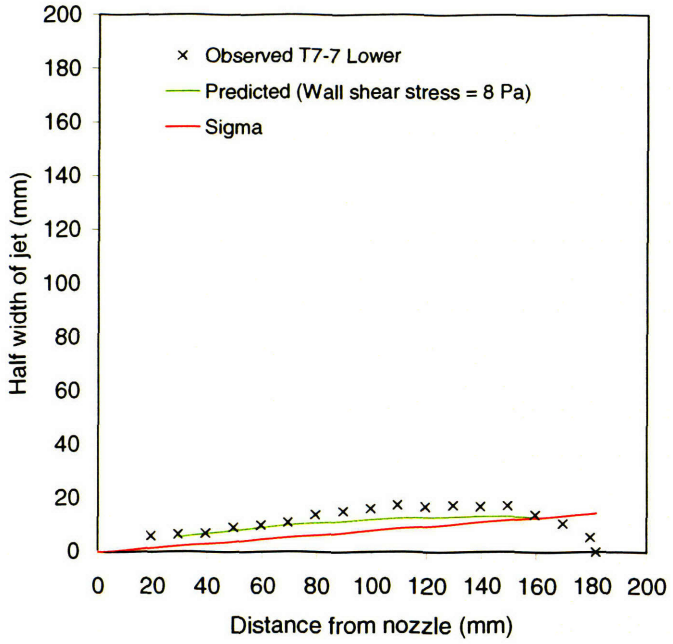

Figure E-11(g). Shape of cut (Specimen T7, Section 7, Lower cut)

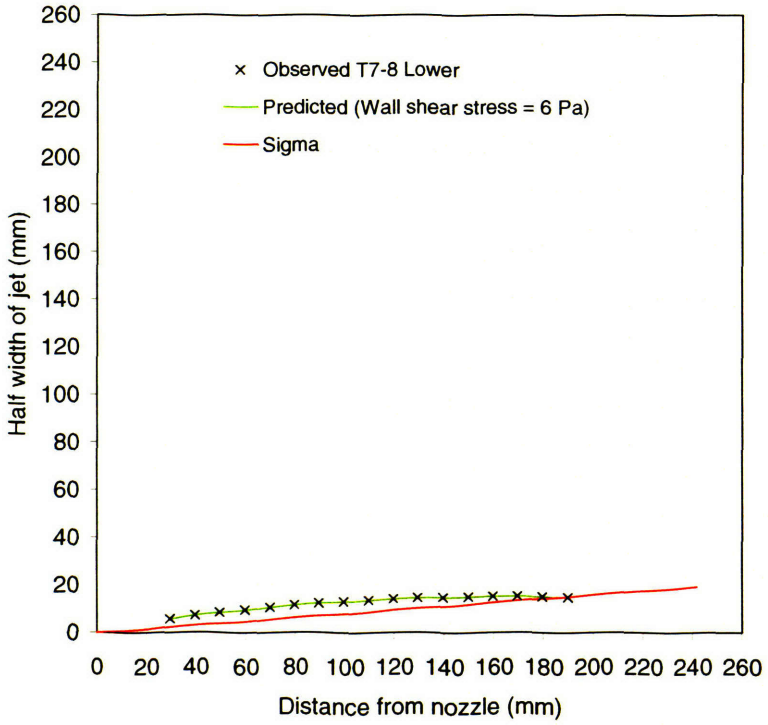

Figure E-11(h). Shape of cut (Specimen T7, Section 8, Lower cut)

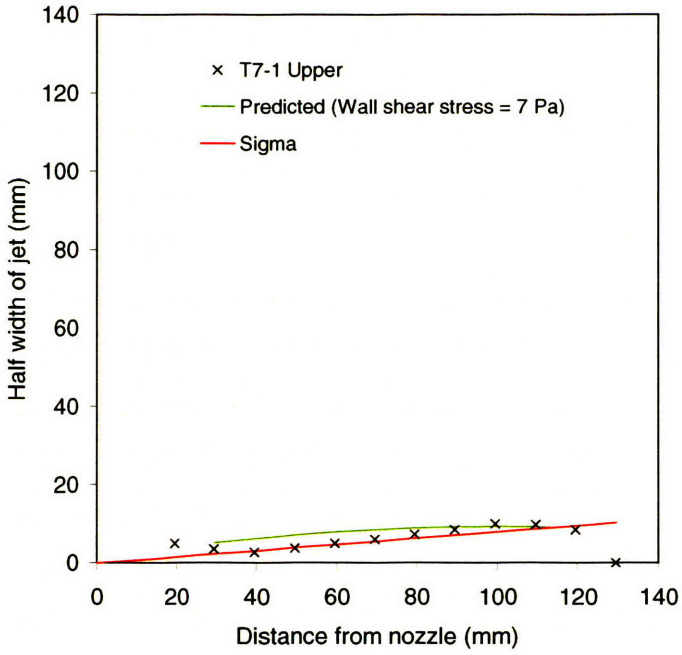

Figure E-12(a). Shape of cut (Specimen T7, Section 1, Upper cut)

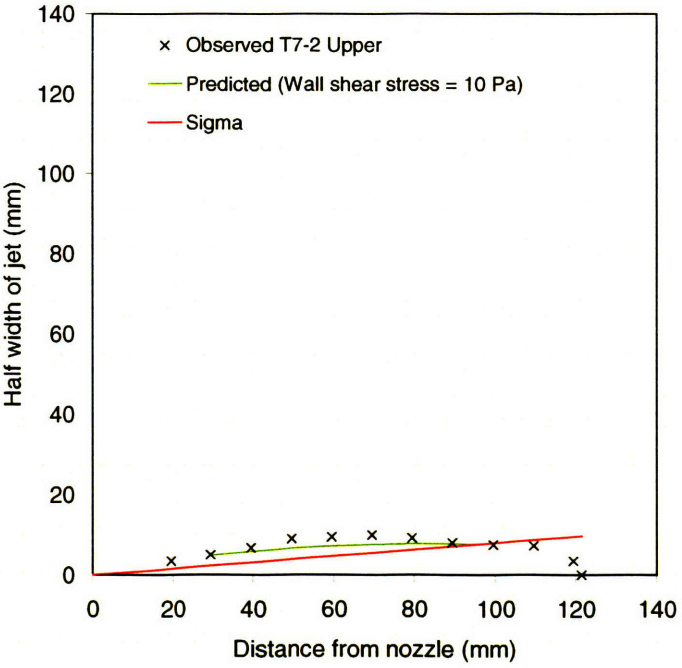

Figure E-12(b). Shape of cut (Specimen T7, Section 2, Upper cut)

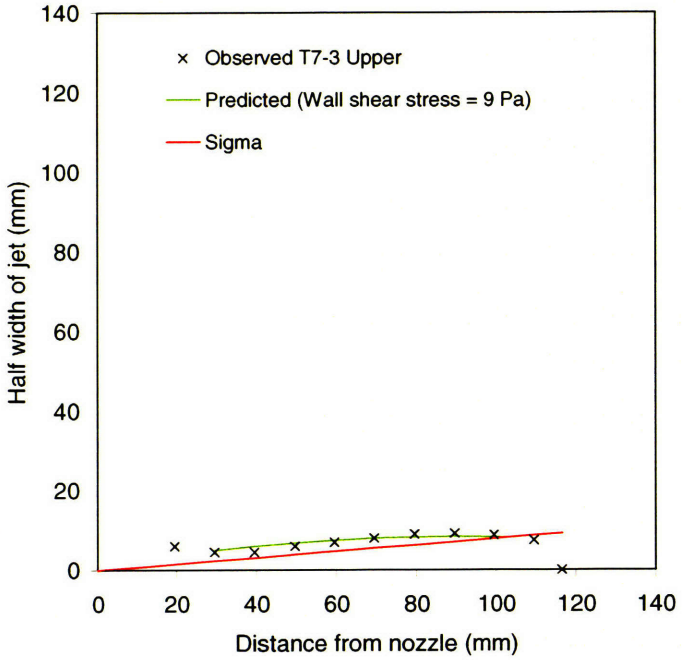

Figure E-12(c). Shape of cut (Specimen T7, Section 3, Upper cut)

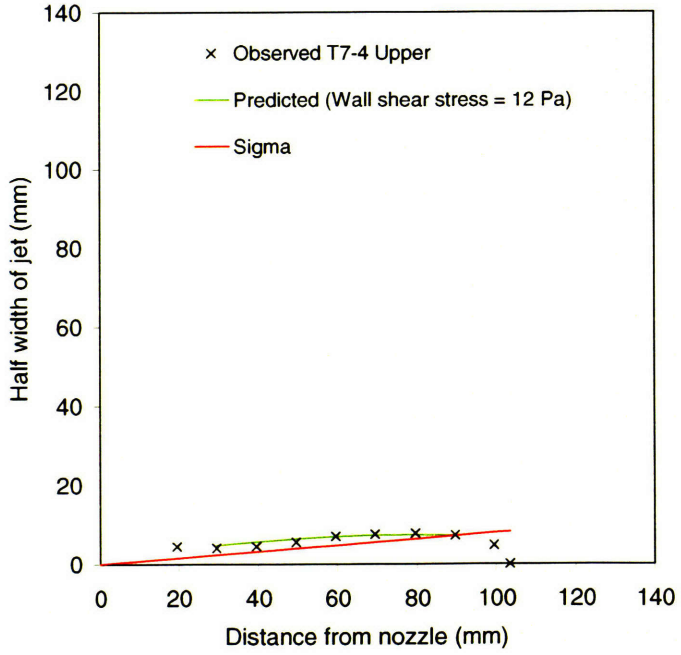

Figure E-12(d). Shape of cut (Specimen T7, Section 4, Upper cut)

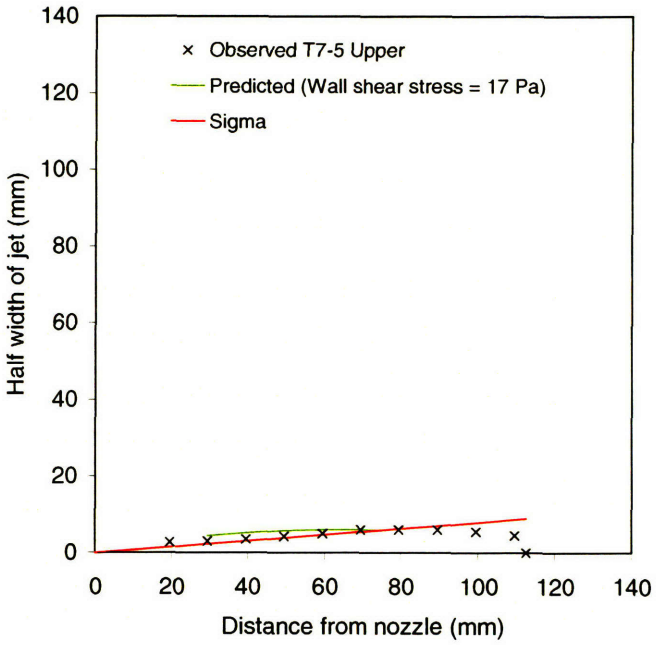

Figure E-12(e). Shape of cut (Specimen T7, Section 5, Upper cut)

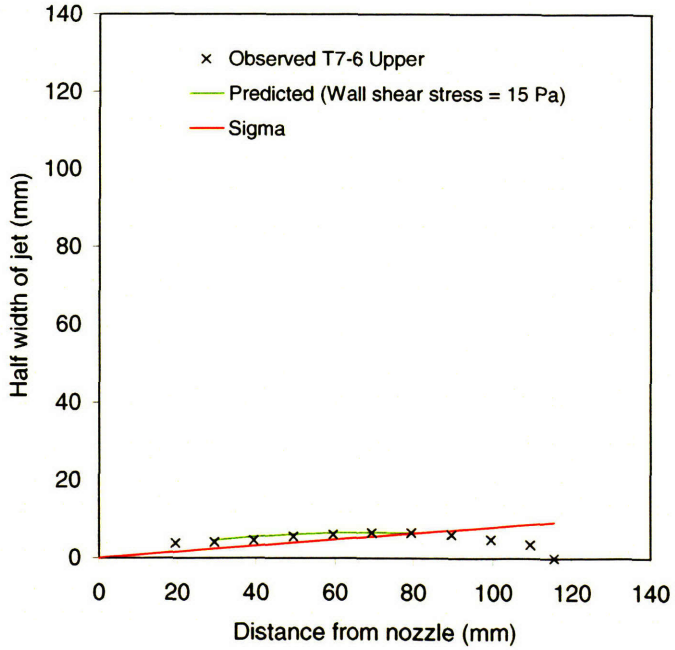

Figure E-12(f). Shape of cut (Specimen T7, Section 6, Upper cut)

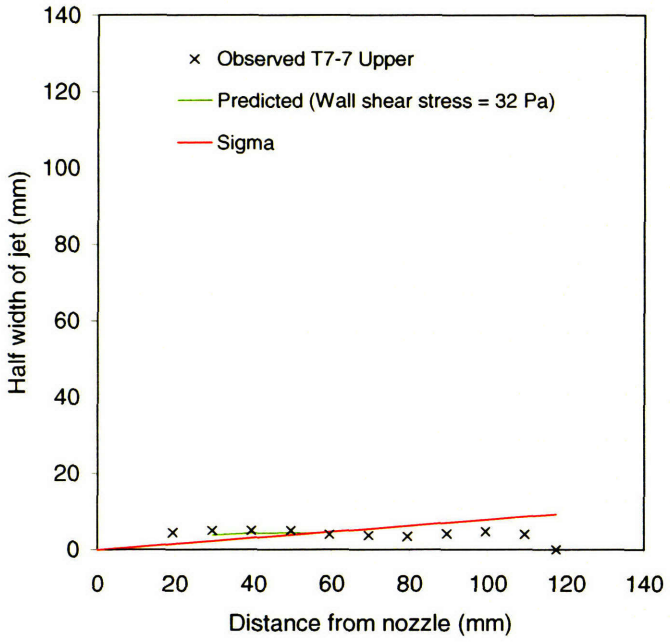

Figure E-12(g). Shape of cut (Specimen T7, Section 7, Upper cut)

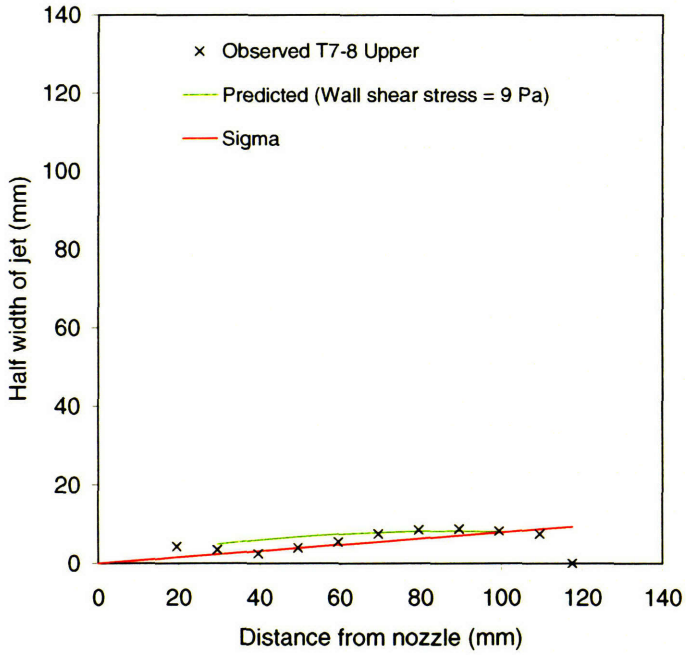

Figure E-12(h). Shape of cut (Specimen T7, Section 8, Upper cut)

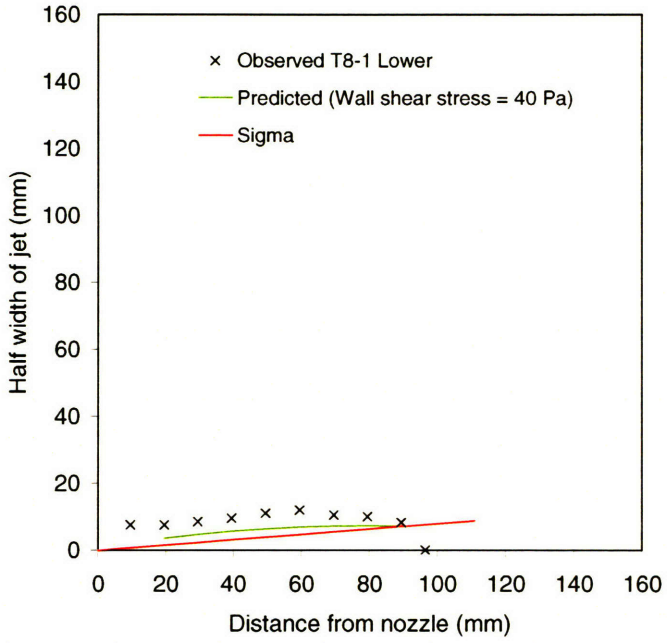

Figure E-13(a). Shape of cut (Specimen T8, Section 1, Lower cut)

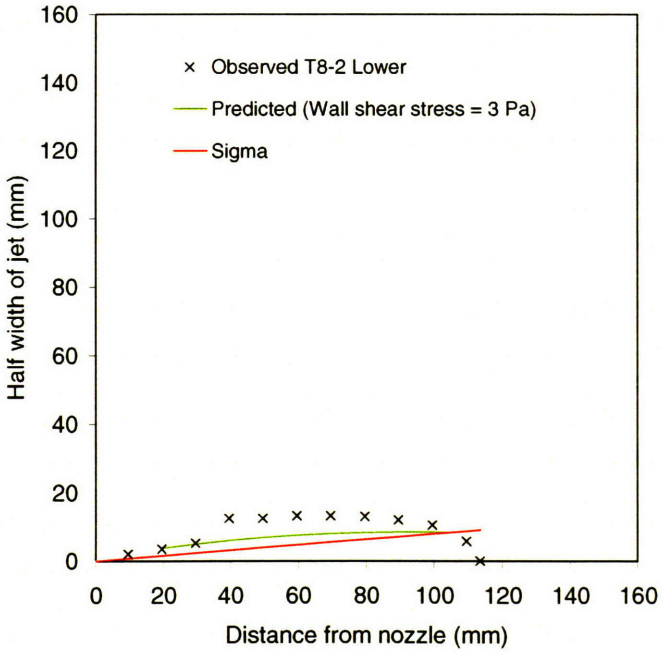

Figure E-13(b). Shape of cut (Specimen T8, Section 2, Lower cut)

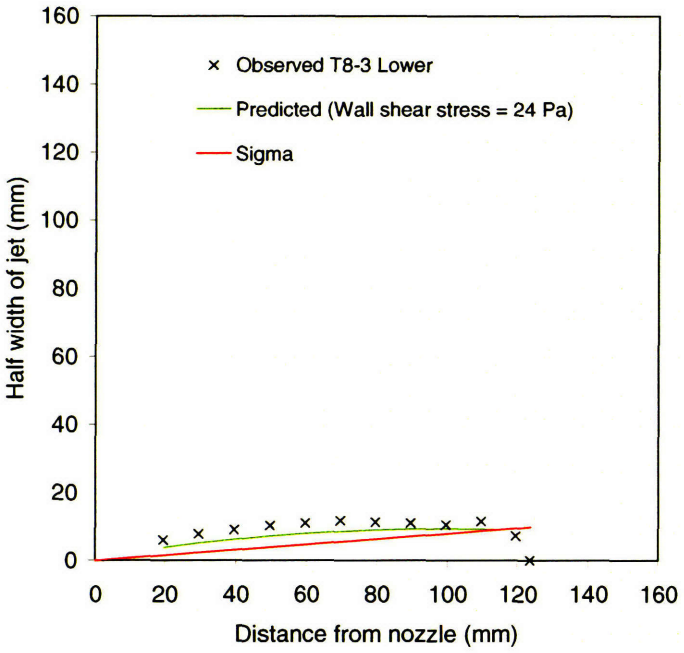

Figure E-13(c). Shape of cut (Specimen T8, Section 3, Lower cut)

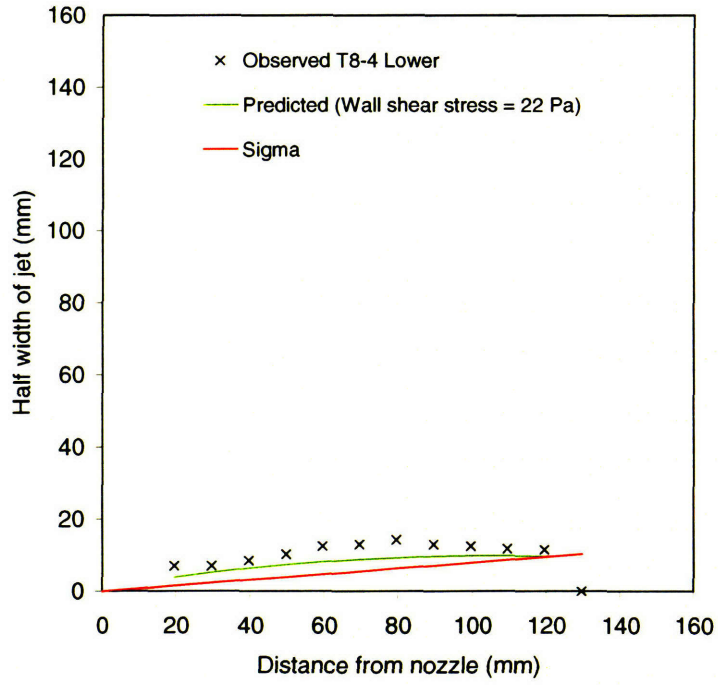

Figure E-13(d). Shape of cut (Specimen T8, Section 4, Lower cut)

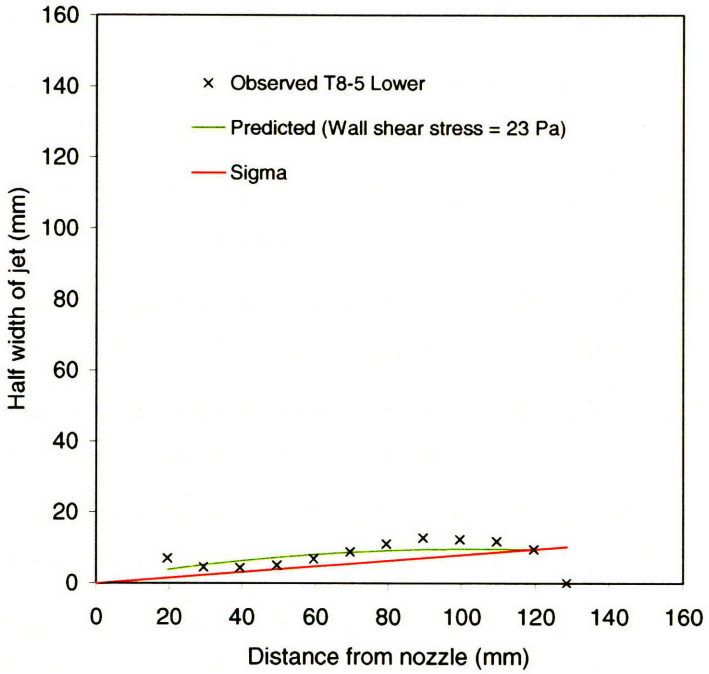

Figure E-13(e). Shape of cut (Specimen T8, Section 5, Lower cut)

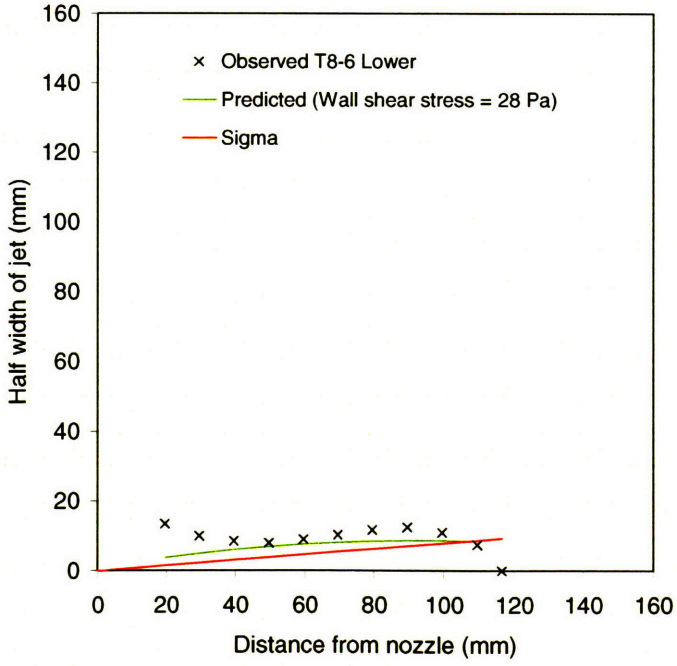

Figure E-13(f). Shape of cut (Specimen T8, Section 6, Lower cut)

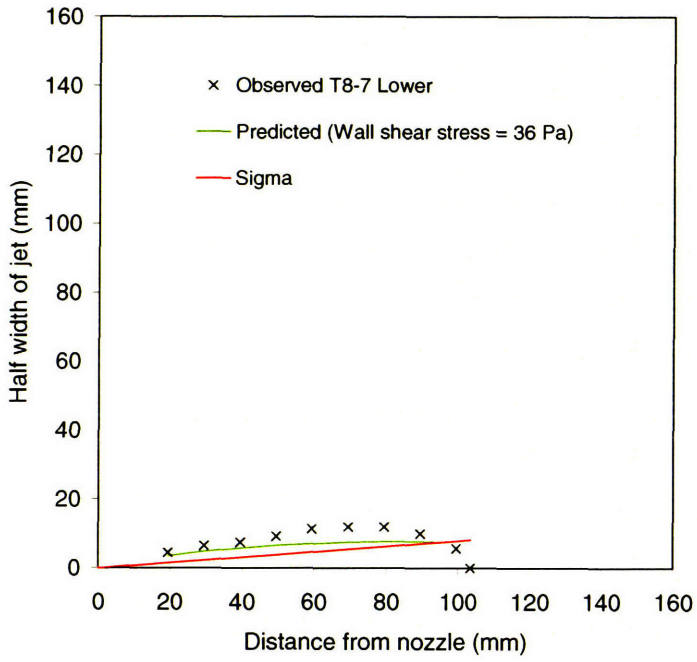

Figure E-13(g). Shape of cut (Specimen T8, Section 7, Lower cut)

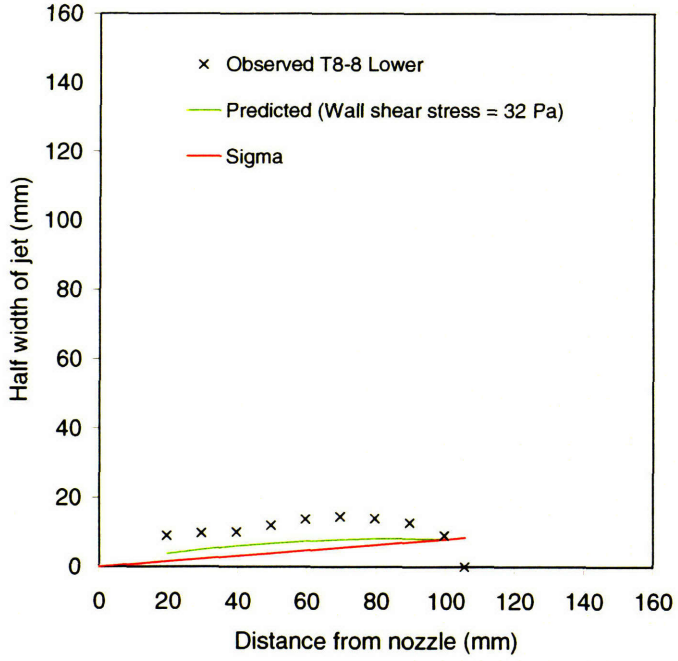

Figure E-13(h). Shape of cut (Specimen T8, Section 8, Lower cut)

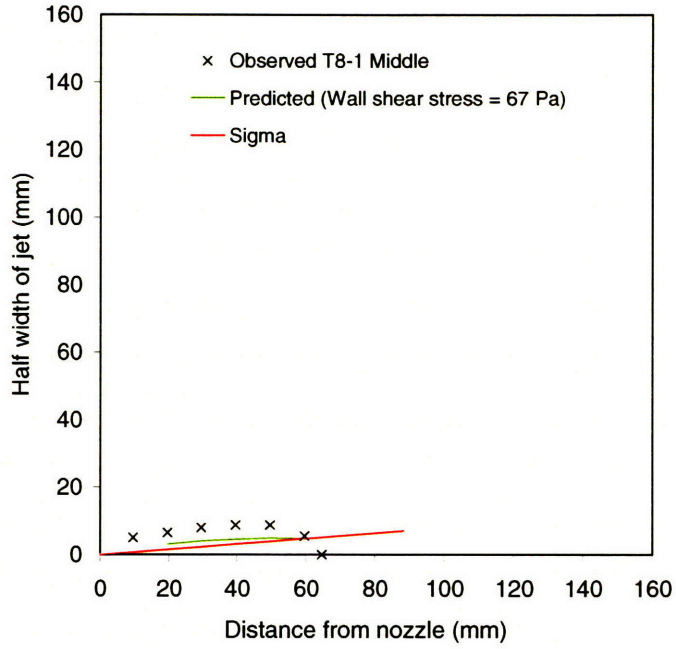

Figure E-14(a). Shape of cut (Specimen T8, Section 1, Middle cut)

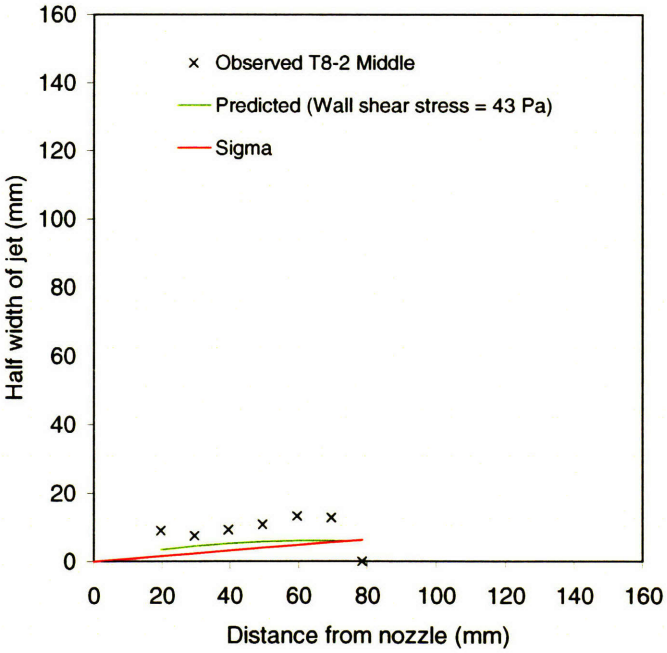

Figure E-14(b). Shape of cut (Specimen T8, Section 2, Middle cut)

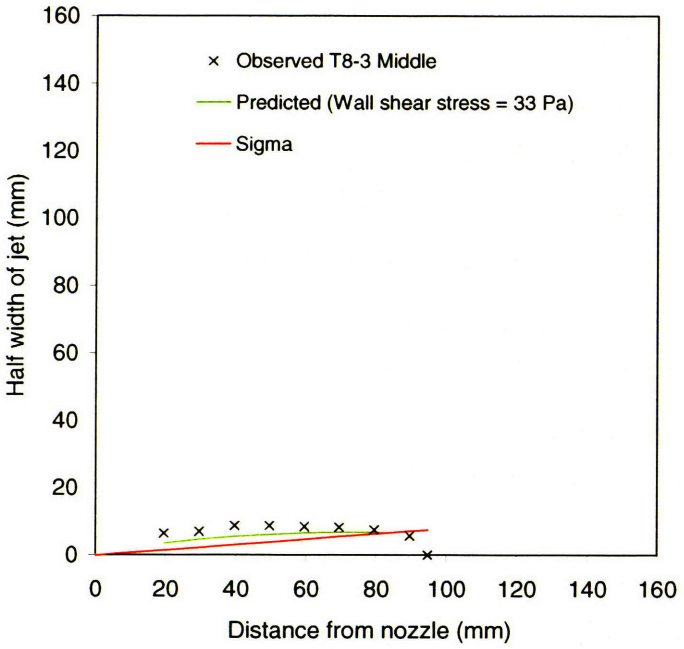

Figure E-14(c). Shape of cut (Specimen T8, Section 3, Middle cut)

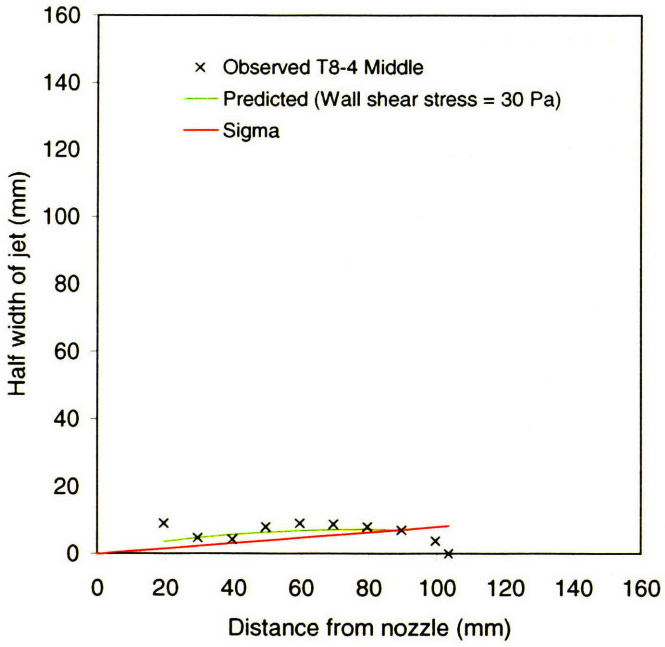

Figure E-14(d). Shape of cut (Specimen T8, Section 4, Middle cut)

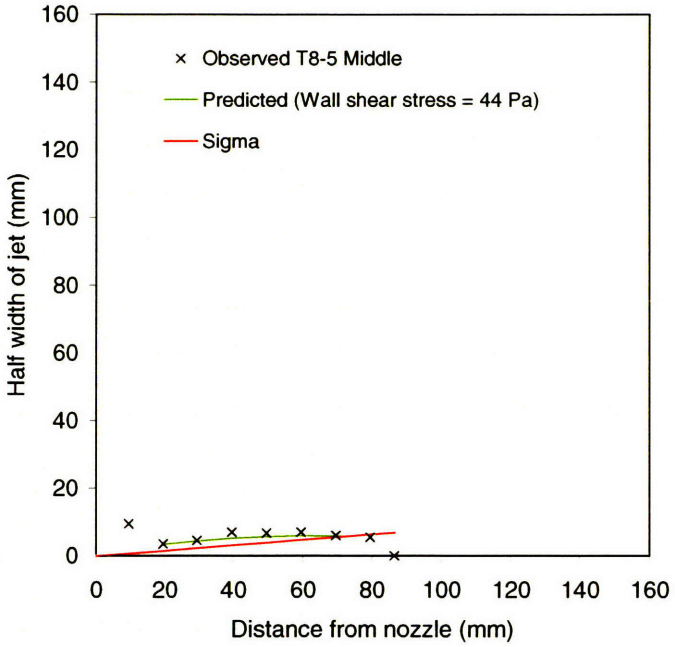

Figure E-14(e). Shape of cut (Specimen T8, Section 5, Middle cut)

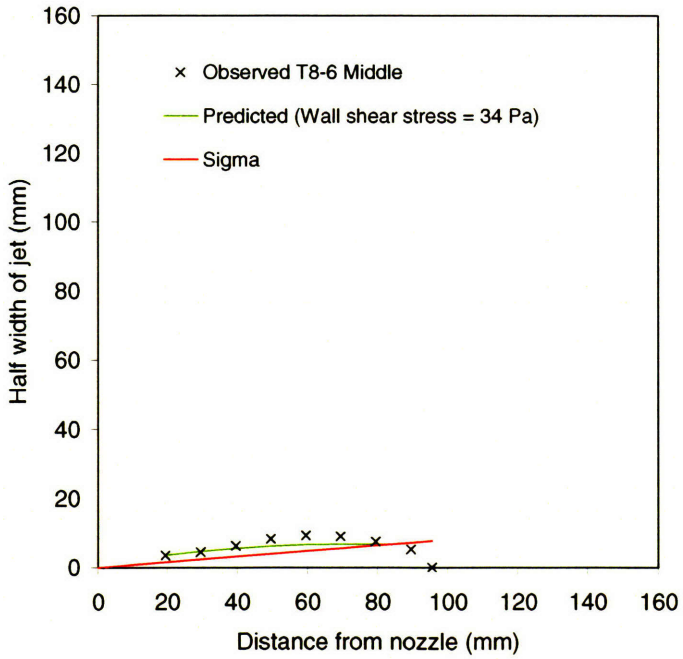

Figure E-14(f). Shape of cut (Specimen T8, Section 6, Middle cut)

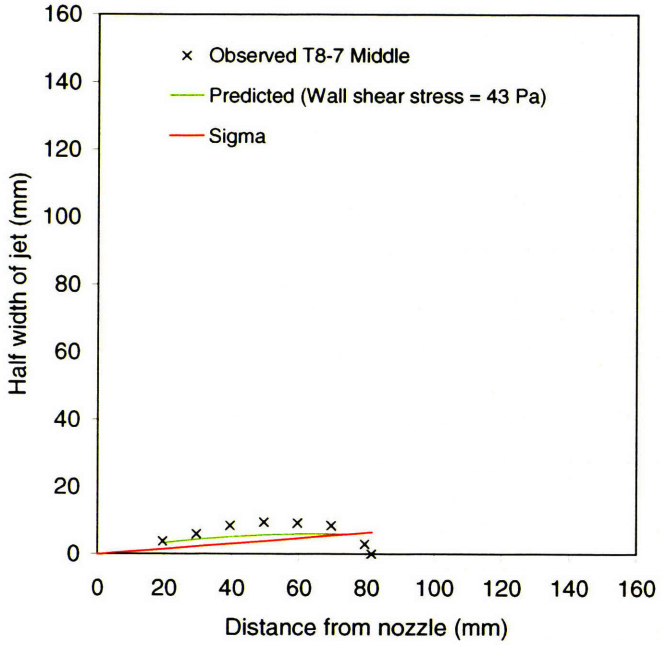

Figure E-14(g). Shape of cut (Specimen T8, Section 7, Middle cut)

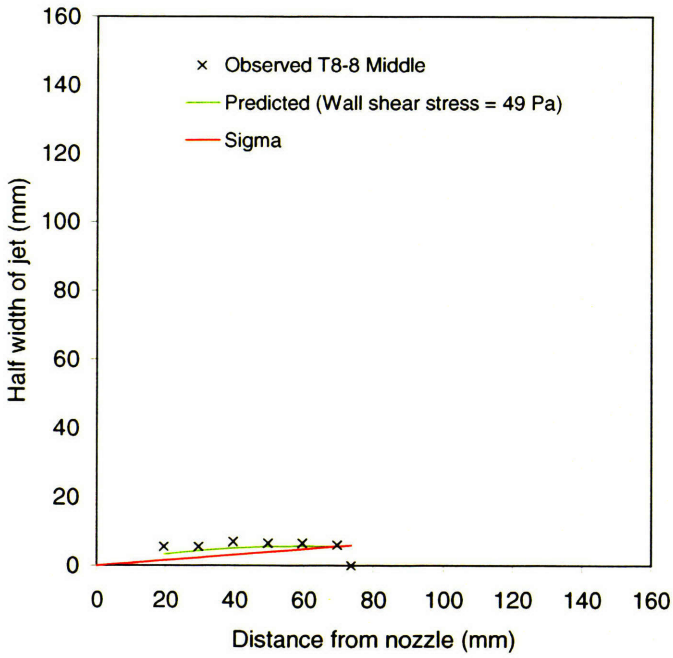

Figure E-14(h). Shape of cut (Specimen T8, Section 8, Middle cut)

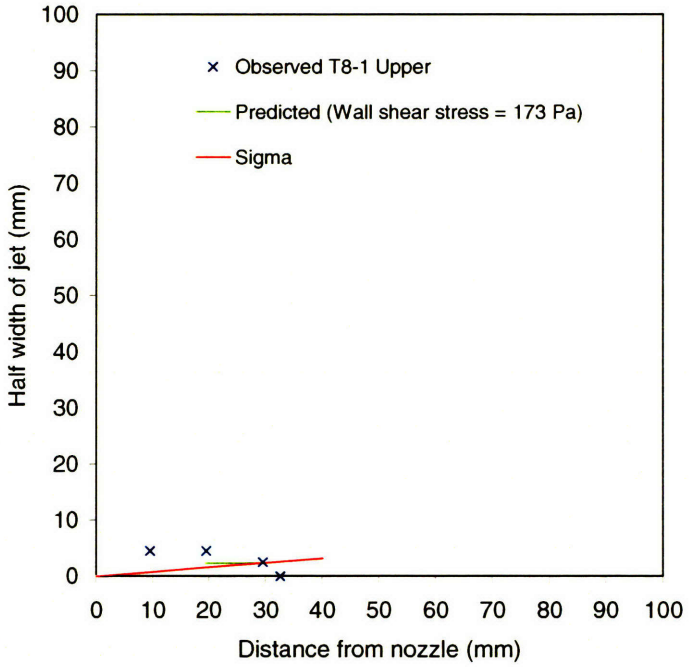

Figure E-15(a). Shape of cut (Specimen T8, Section 1, Upper cut)

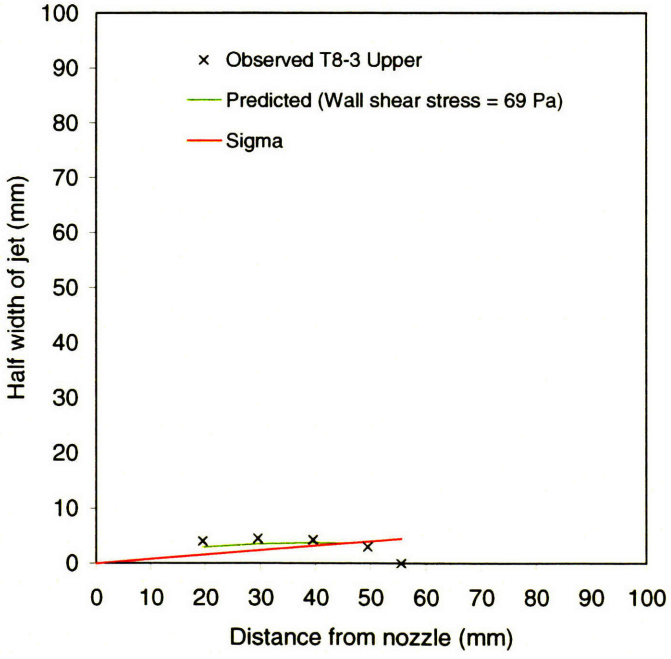

Figure E-15(b). Shape of cut (Specimen T8, Section 3, Upper cut)

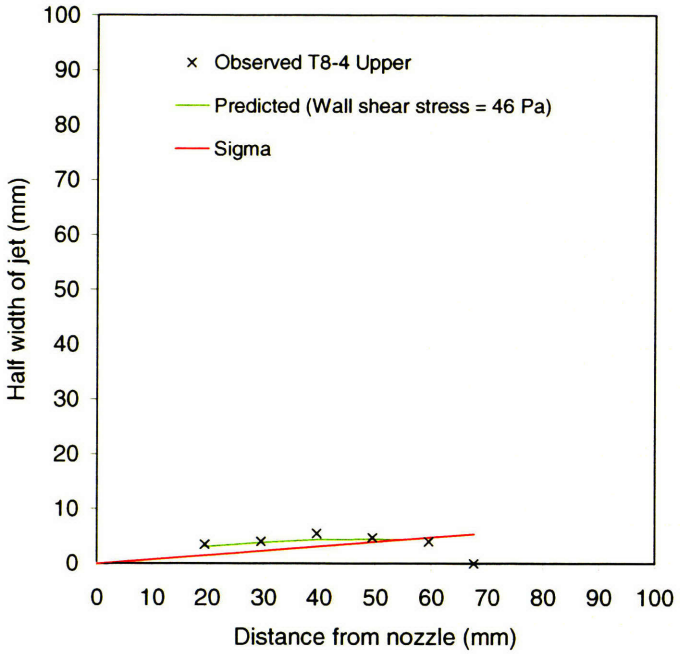

Figure E-15(c). Shape of cut (Specimen T8, Section 4, Upper cut)

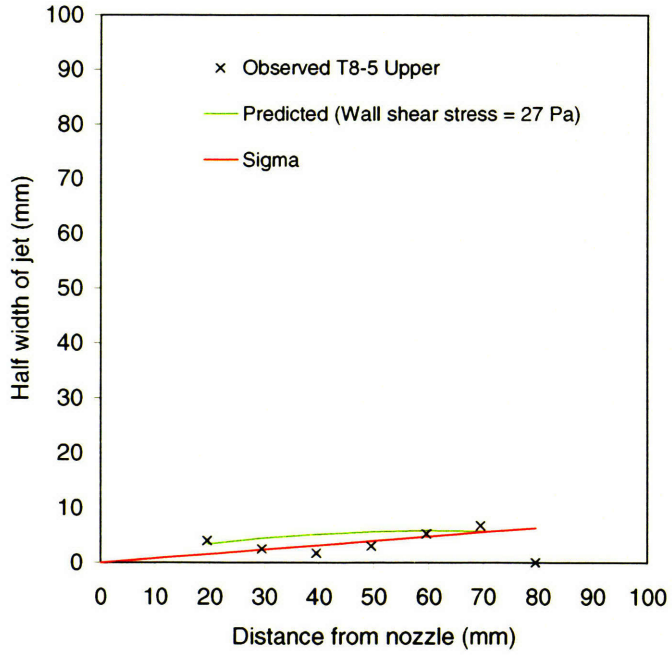

Figure E-15(d). Shape of cut (Specimen T8, Section 5, Upper cut)

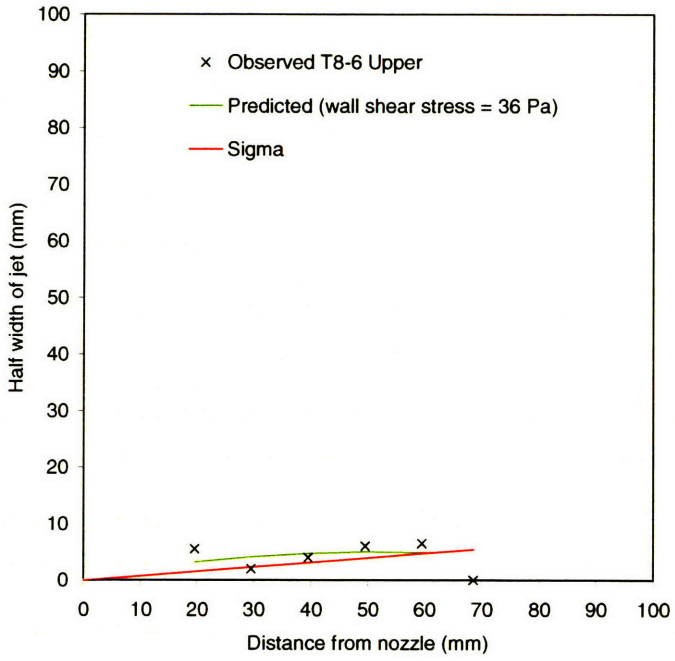

Figure E-15(e). Shape of cut (Specimen T8, Section 6, Upper cut)

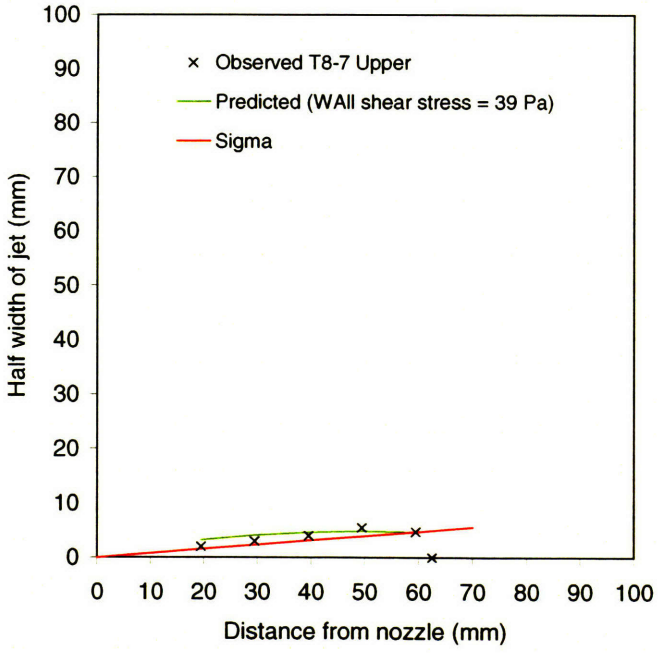

Figure E-15(f). Shape of cut (Specimen T8, Section 7, Upper cut)

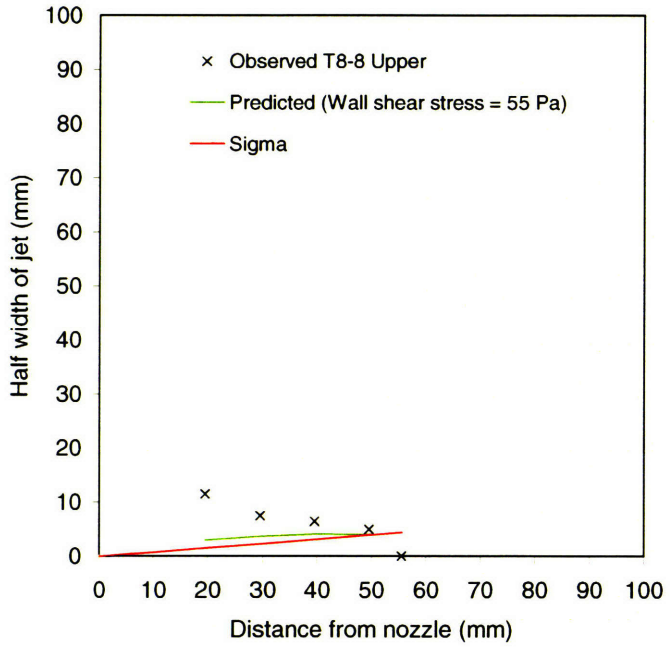

Figure E-15(g). Shape of cut (Specimen T8, Section 8, Upper cut)

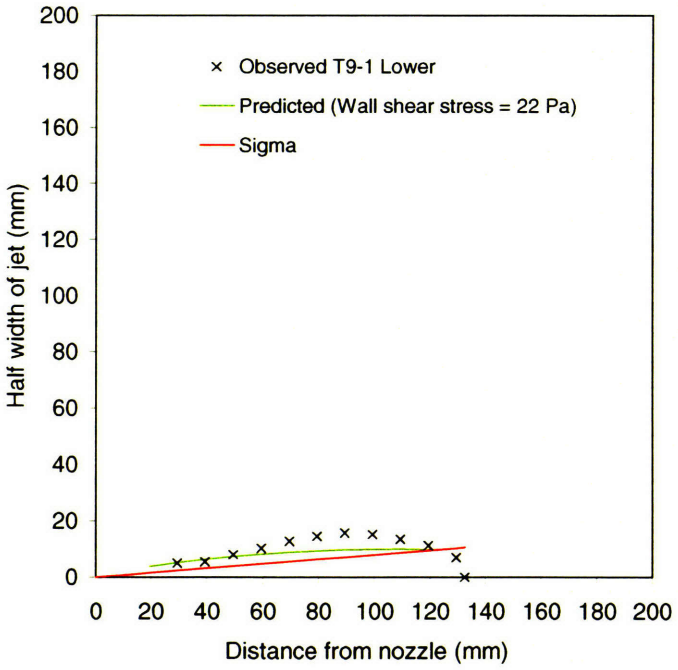

Figure E-16(a). Shape of cut (Specimen T9, Section 1, Lower cut)

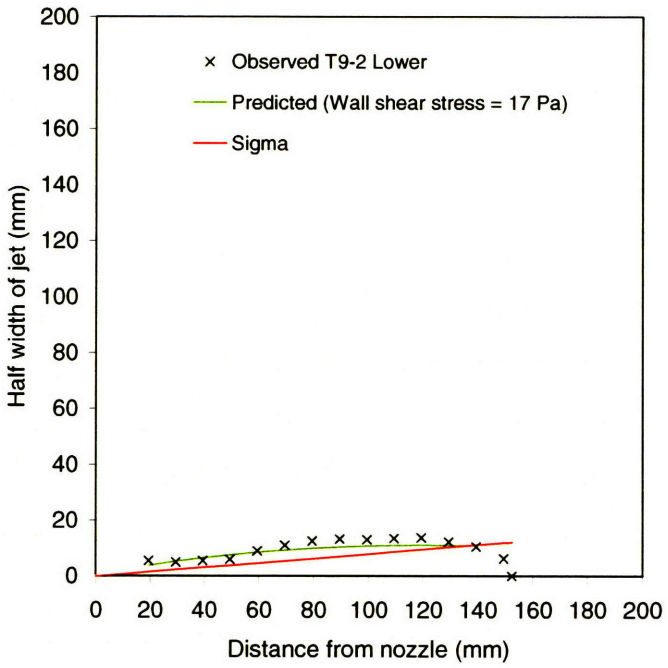

Figure E-16(b). Shape of cut (Specimen T9, Section 2, Lower cut)

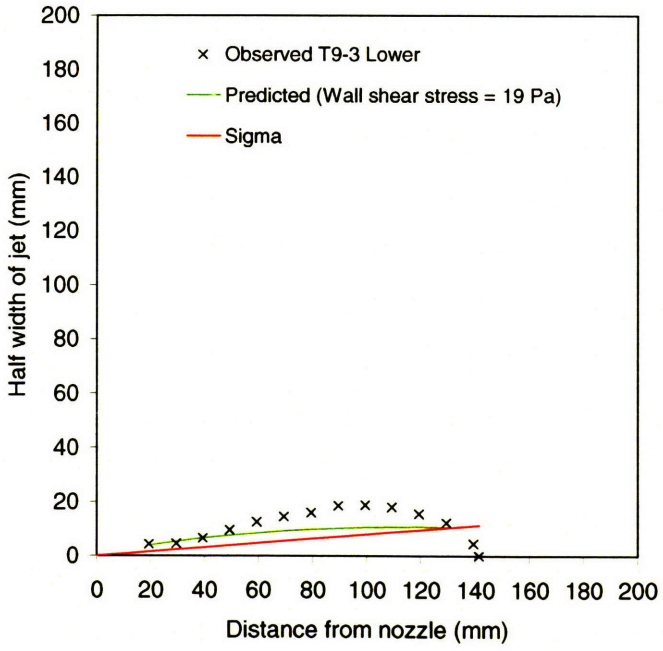

Figure E-16(c). Shape of cut (Specimen T9, Section 3, Lower cut)

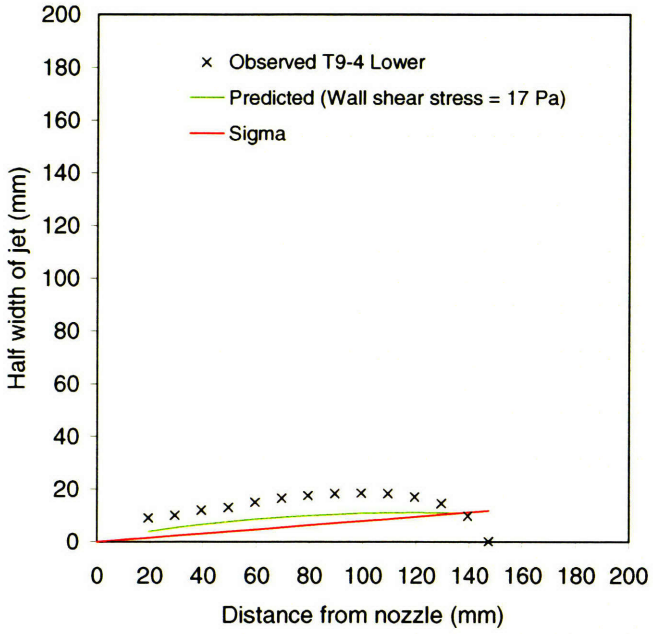

Figure E-16(d). Shape of cut (Specimen T9, Section 4, Lower cut)

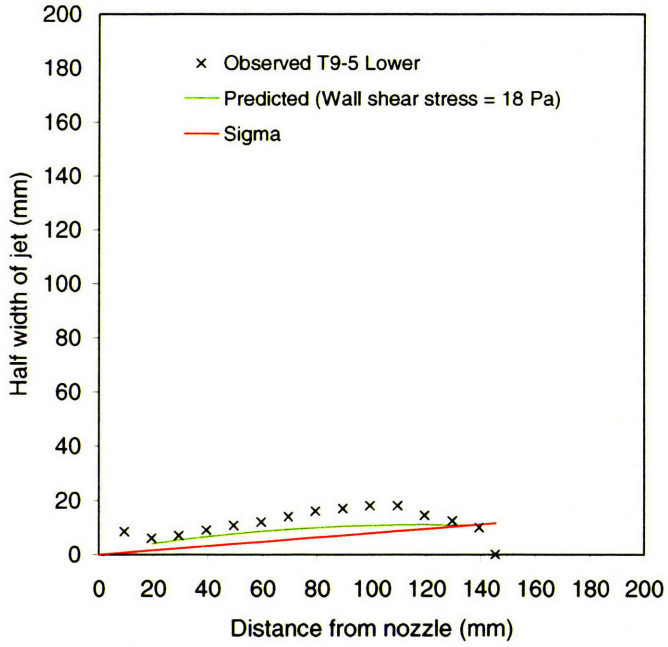

Figure E-16(e). Shape of cut (Specimen T9, Section 5, Lower cut)

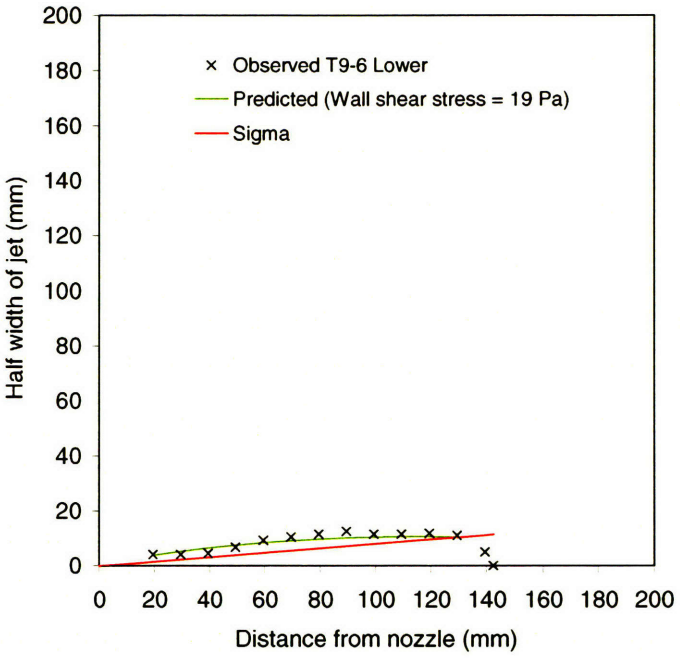

Figure E-16(f). Shape of cut (Specimen T9, Section 6, Lower cut)

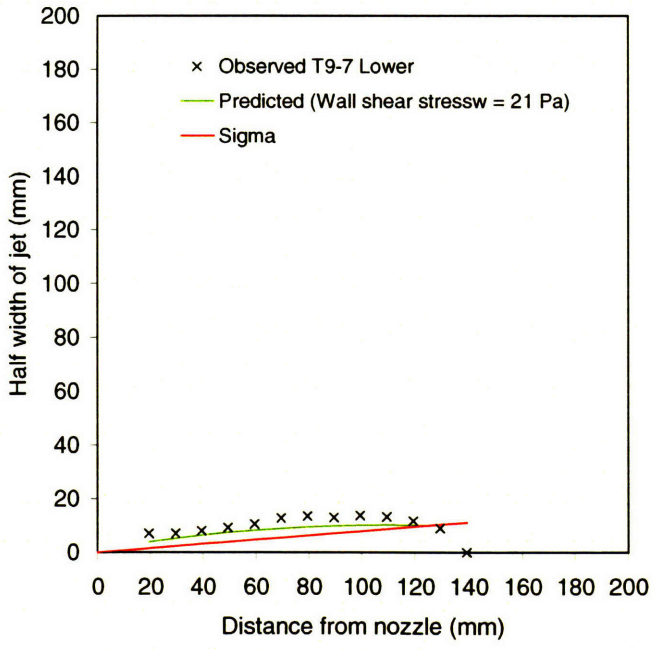

Figure E-16(g). Shape of cut (Specimen T9, Section 7, Lower cut)

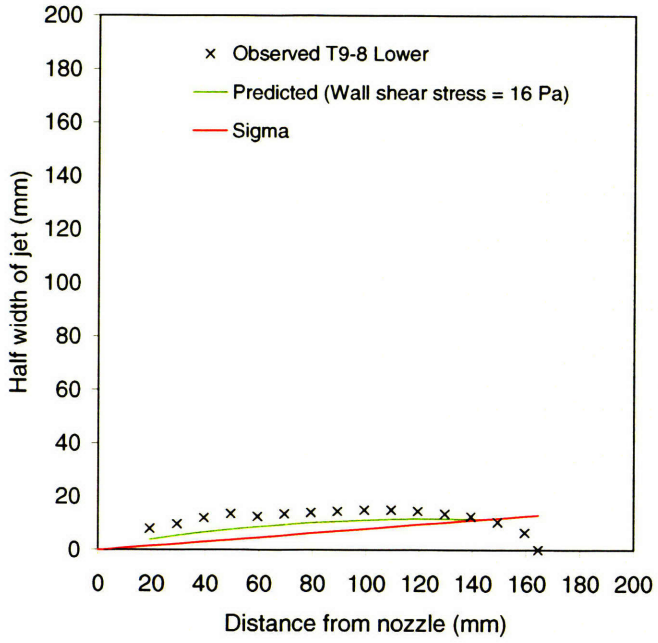

Figure E-16(h). Shape of cut (Specimen T9, Section 8, Lower cut)

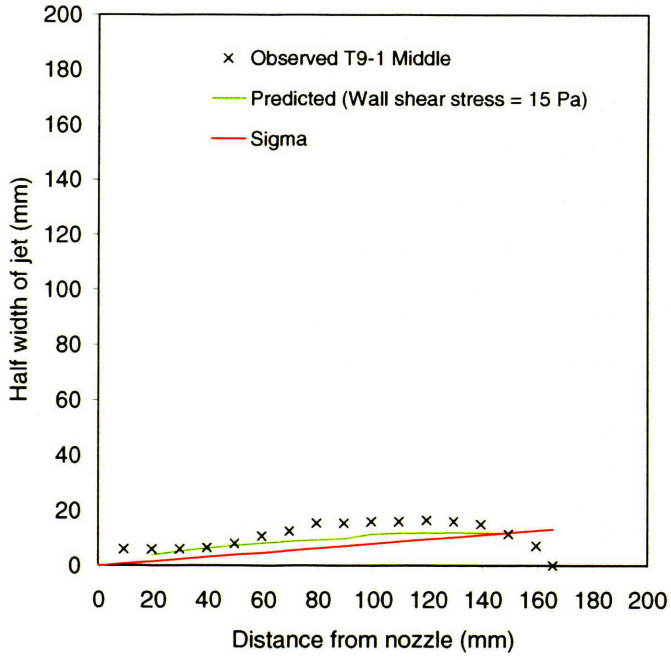

Figure E-17(a). Shape of cut (Specimen T9, Section 1, Middle cut)

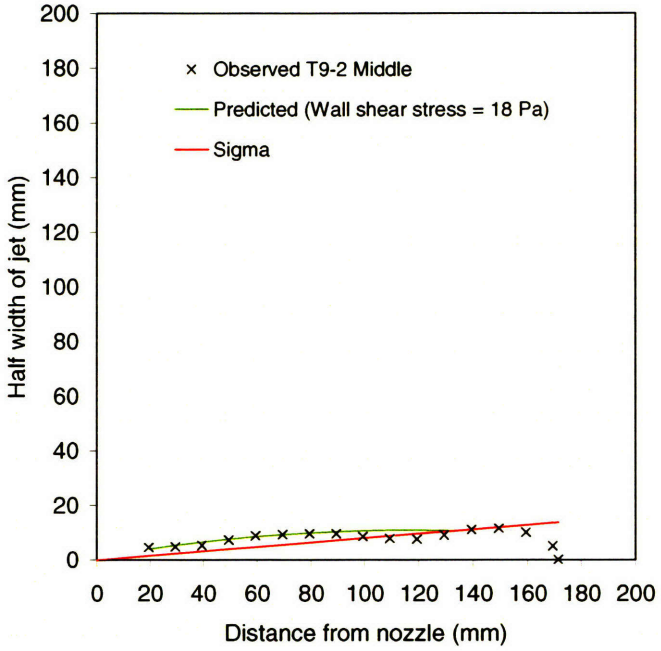

Figure E-17(b). Shape of cut (Specimen T9, Section 2, Middle cut)

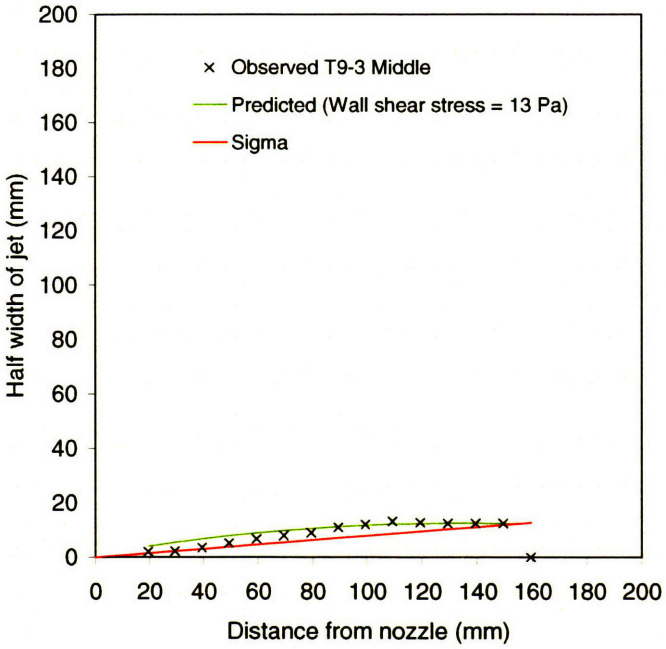

Figure E-17(c). Shape of cut (Specimen T9, Section 3, Middle cut)

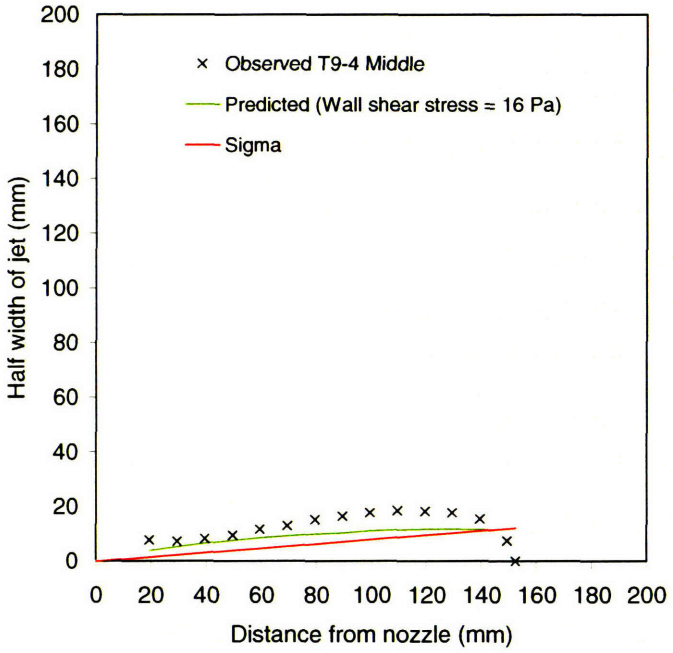

Figure E-17(d). Shape of cut (Specimen T9, Section 4, Middle cut)

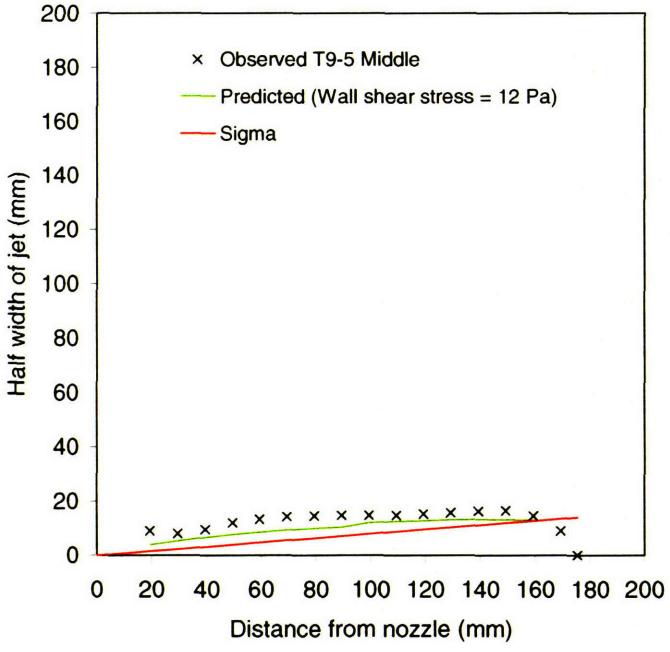

Figure E-17(e). Shape of cut (Specimen T9, Section 5, Middle cut)

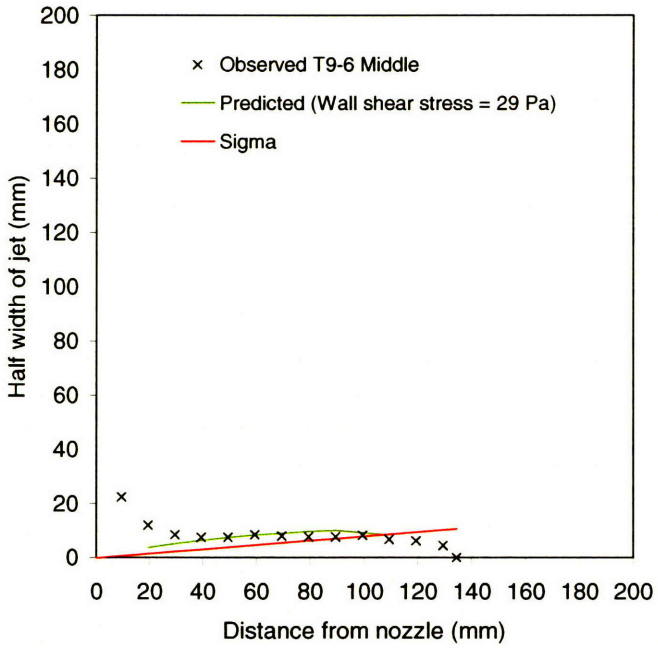

Figure E-17(f). Shape of cut (Specimen T9, Section 6, Middle cut)

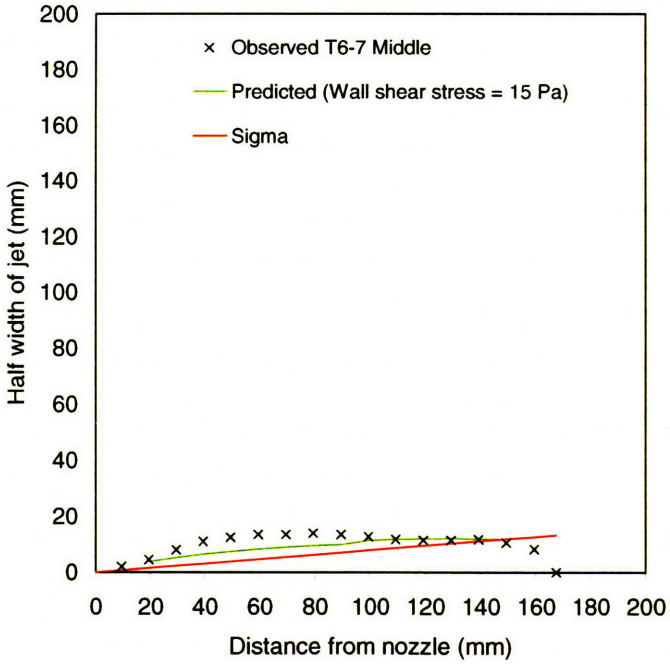

Figure E-17(g). Shape of cut (Specimen T9, Section 7, Middle cut)

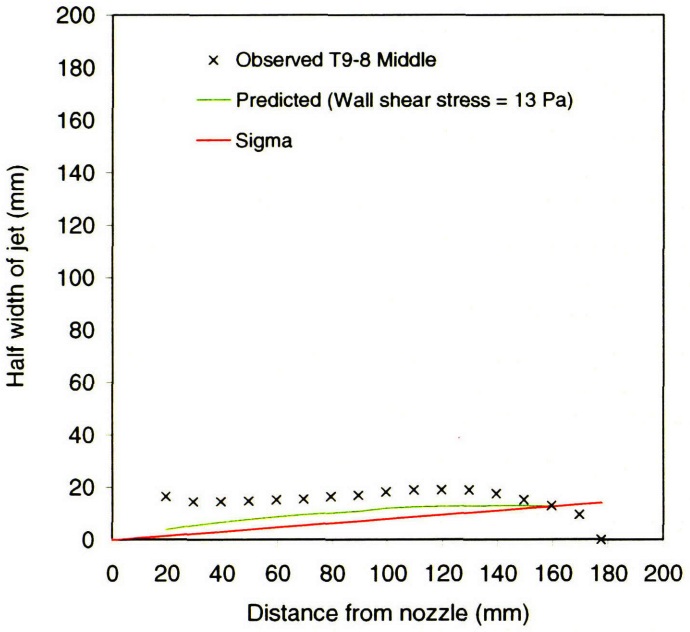

Figure E-17(h). Shape of cut (Specimen T9, Section 8, Middle cut)

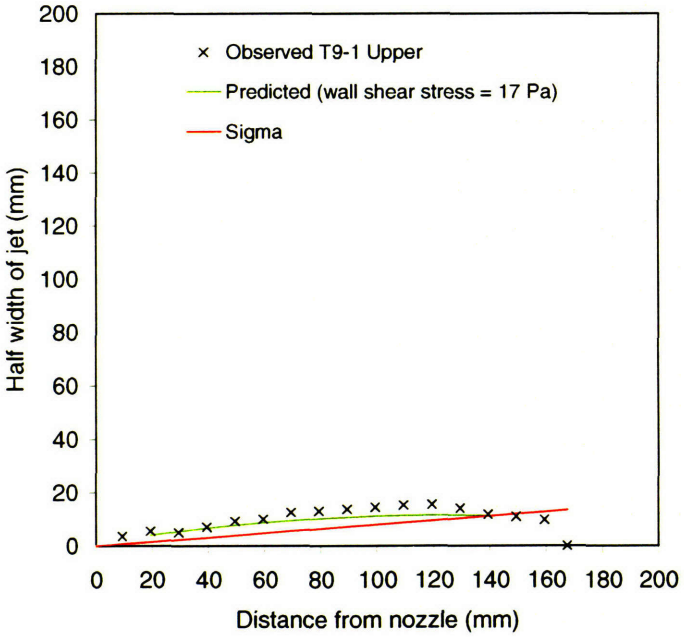

Figure E-18(a). Shape of cut (Specimen T9, Section 1, Upper cut)

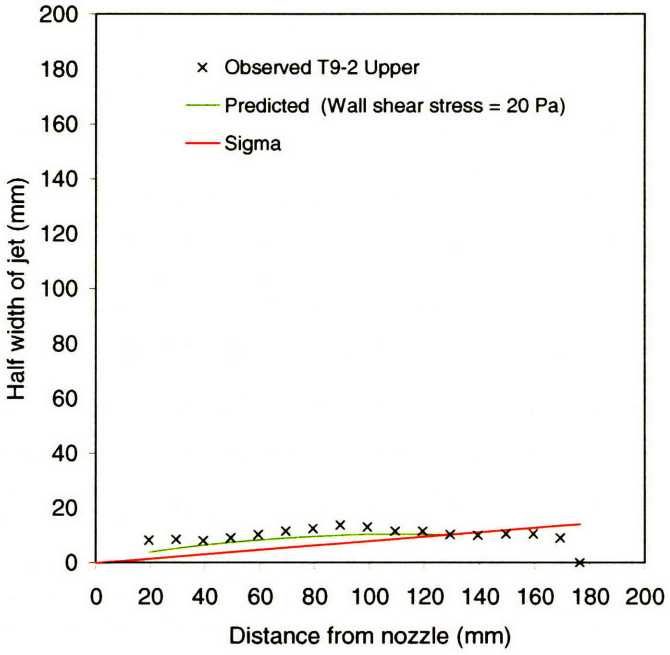

Figure E-18(b). Shape of cut (Specimen T9, Section 2, Upper cut)

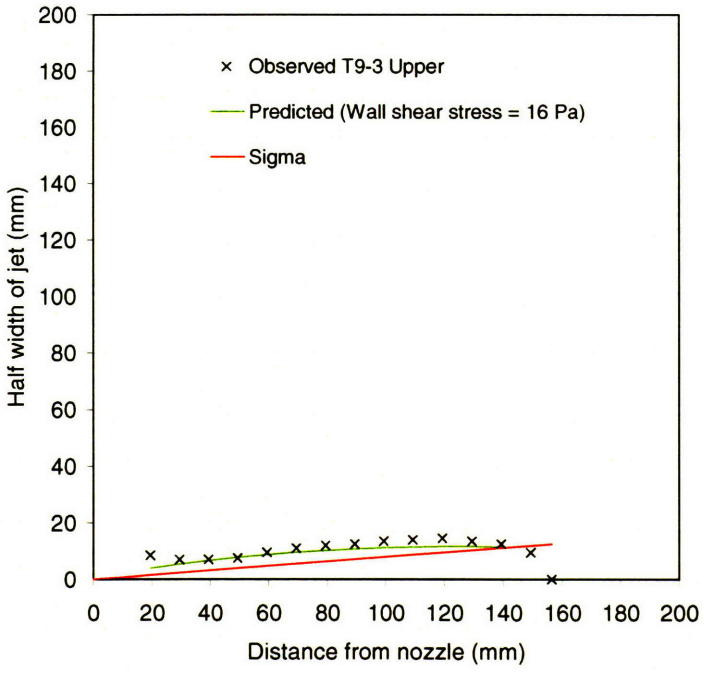

Figure E-18(c). Shape of cut (Specimen T9, Section 3, Upper cut)

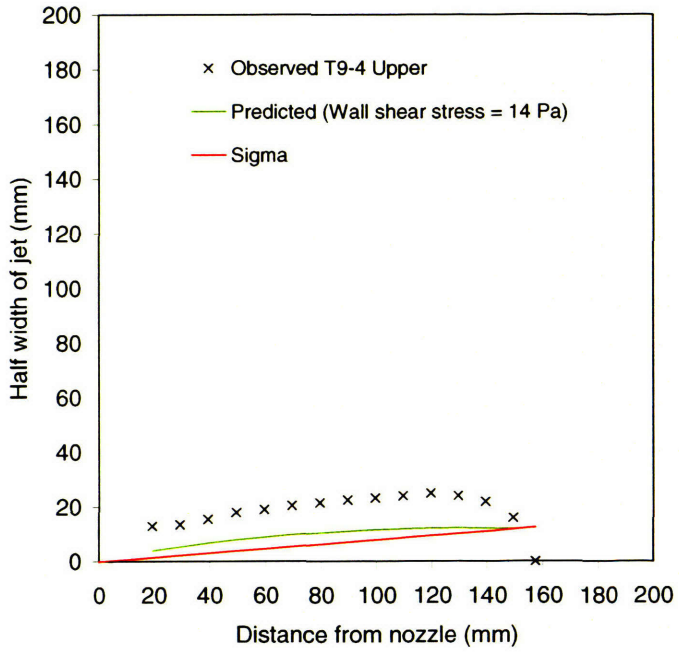

Figure E-18(d). Shape of cut (Specimen T9, Section 4, Upper cut)

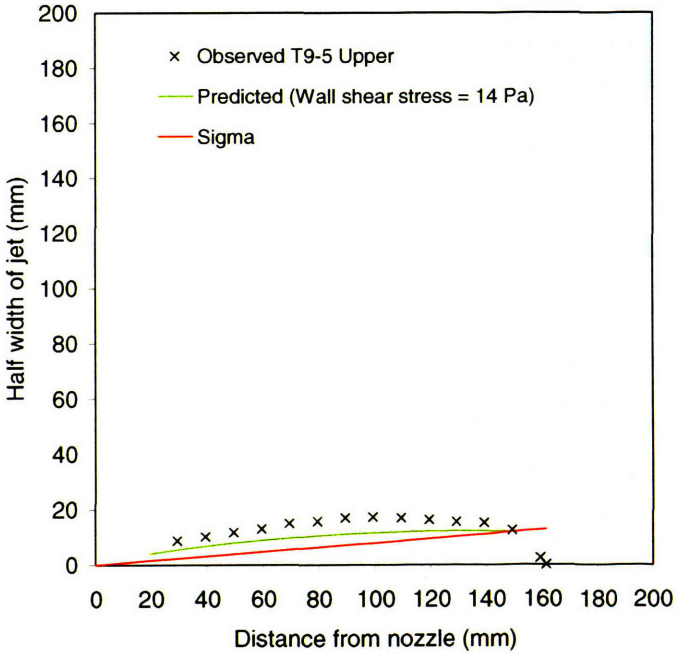

Figure E-18(e). Shape of cut (Specimen T9, Section 5, Upper cut)

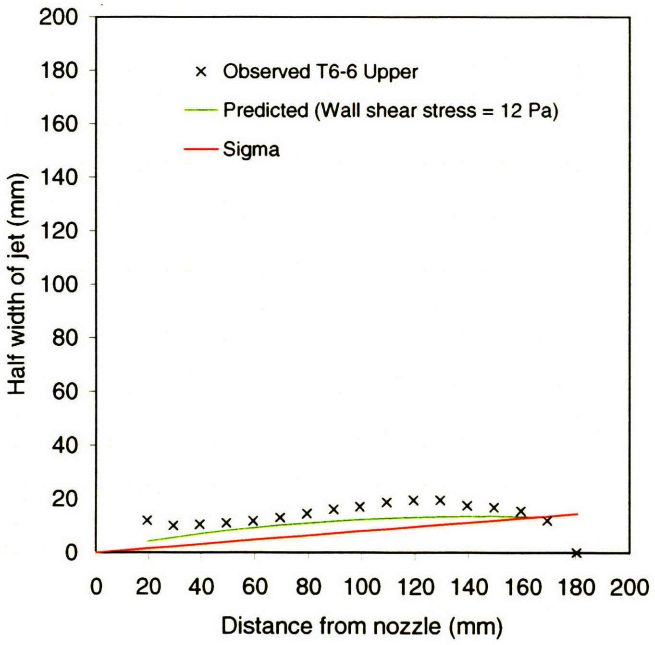

Figure E-18(f). Shape of cut (Specimen T9, Section 6, Upper cut)

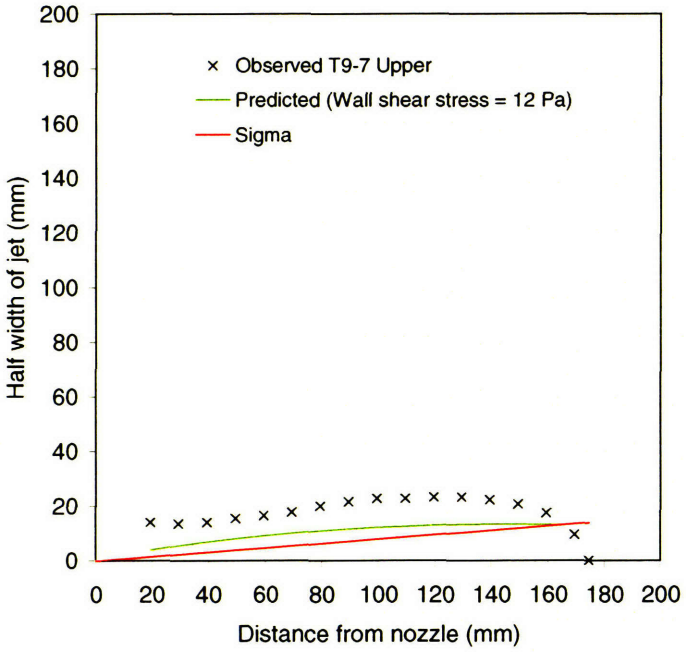

Figure E-18(g). Shape of cut (Specimen T9, Section 7, Upper cut)

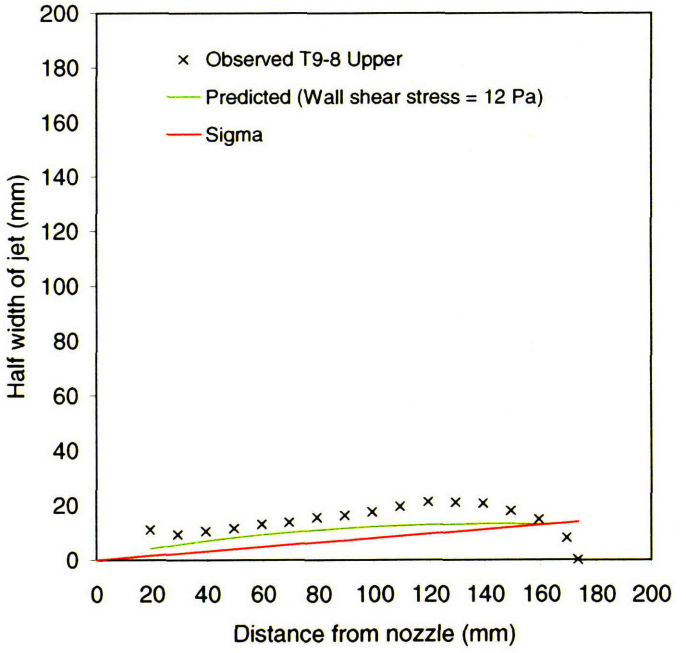

Figure E-18(h). Shape of cut (Specimen T9, Section 8, Upper cut)

APPENDIX F

SUMMARY OF PARAMETERS AT EQUILIBRIUM POINT

Table F-1. Interpreted parameters at equilibrium point for Specimen T2

Cut level	Sect.	Equilibrium point		Centerline velocity	Velocity at r_s	Reynold's Number	Shear stress coef.	Wall shear stress		
		x_s (mm)	r_s (mm)	v_{xc} (m/s)	v_{xr} (m/s)	R_x	c_f	τ_w (Pa)	Mean (Pa)	Std dev (Pa)
Upper	T2-1	151.8	12.1	7.7	4.7	3.94	0.00106	15	12.9	2.6
	T2-2	182.9	14.6	6.4	3.9			10		
	T2-3	157.6	12.6	7.4	4.5			14		
	T2-4	141.2	11.3	8.3	5.0			17		
	T2-5	158.1	12.7	7.4	4.5			13		
	T2-6	164.2	13.1	7.1	4.3			13		
	T2-7	194.4	15.6	6.0	3.6			9		
	T2-8	168.1	13.5	6.9	4.2			12		
Middle	T2-1	134.2	10.7	8.7	5.3	3.94	0.00106	19	20.3	4.5
	T2-2	133.0	10.6	8.8	5.3			19		
	T2-3	119.2	9.5	9.8	5.9			24		
	T2-4	140.2	11.2	8.3	5.1			17		
	T2-5	126.3	10.1	9.2	5.6			21		
	T2-6	126.2	10.1	9.3	5.6			21		
	T2-7	109.5	8.8	10.7	6.5			28		
	T2-8	157.8	12.6	7.4	4.5			13		
Lower	T2-1	138.4	11.1	8.4	5.1	3.94	0.00106	18	21.5	7.8
	T2-2	135.5	10.8	8.6	5.2			18		
	T2-3	145.5	11.6	8.0	4.9			16		
	T2-4	130.3	10.4	9.0	5.4			20		
	T2-5	93.5	7.5	12.5	7.6			38		
	T2-6	120.3	9.6	9.7	5.9			23		
	T2-7	113.4	9.0	10.3	6.3			26		
	T2-8	160.3	12.8	7.3	4.4			13		

Table F-2. Interpreted parameters at equilibrium point for Specimen T3

Cut level	Sect.	Equilibrium point		Centerline velocity	Velocity at r_s	Reynold's Number	Shear stress coef.	Wall shear stress		
		x_s (mm)	r_s (mm)	v_{xc} (m/s)	v_{xr} (m/s)	R_x	c_f	τ_w (Pa)	Mean (Pa)	Std dev (Pa)
Upper	T3-1	61.3	4.9	8.4	5.1	1.74	0.00159	26	47.0	17.0
	T3-2									
	T3-3	50.0	4.03	10.3	6.3	1.74	0.00159	39		
	T3-4	43.3	3.5	11.9	7.2	1.74	0.00159	53		
	T3-5						0.00159			
	T3-6	36.2	2.9	14.3	8.6	1.74	0.00159	75		
	T3-7	43.7	3.5	11.8	7.2	1.74	0.00159	52		
	T3-8	52.0	4.2	9.9	6.0	1.74	0.00159	37		
Middle	T3-1	79.9	6.4	9.1	5.5	2.46	0.00134	26	49.1	20.7
	T3-2	72.7	5.8	10.0	6.1	2.46	0.00134	31		
	T3-3	60.8	4.9	12.0	7.3	2.46	0.00134	45		
	T3-4	61.6	4.9	11.9	7.2	2.46	0.00134	44		
	T3-5	42.4	3.4	17.3	10.5	2.46	0.00134	94		
	T3-6	60.6	4.9	12.0	7.3	2.46	0.00134	45		
	T3-7	56.9	4.6	12.8	7.8	2.46	0.00134	51		
	T3-8	53.7	4.3	13.6	8.2	2.46	0.00134	57		
Lower	T3-1	108.1	8.6	8.3	5.0	3.01	0.00121	19	53.1	36.9
	T3-2	80.0	6.4	11.2	6.8	3.01	0.00121	35		
	T3-3	111.5	8.9	8.0	4.9	3.01	0.00121	18		
	T3-4	76.4	6.1	11.7	7.1	3.01	0.00121	38		
	T3-5	61.3	4.9	14.6	8.8	3.01	0.00121	60		
	T3-6	41.5	3.3	21.5	13.1	3.01	0.00121	131		
	T3-7	55.1	4.4	16.3	9.8	3.01	0.00121	74		
	T3-8	67.1	5.4	13.3	8.1	3.01	0.00121	50		

Table F-3. Interpreted parameters at equilibrium point for Specimen T4

Cut level	Sect.	Equilibrium point		Centerline velocity	Velocity at r_s	Reynold's Number	Shear stress coef.	Wall shear stress		
		x_s (mm)	r_s (mm)	v_{xc} (m/s)	v_{xr} (m/s)	R_x	c_f	τ_w (Pa)	Mean (Pa)	Std dev (Pa)
Middle	T4-1*									
	T4-2*									
	T4-3*									
	T4-4*									
	T4-5*									
	T4-6*									
	T4-7A*									
	T4-8*									
	T4-1A	194.3	15.5	4.6	2.8	2.85	0.00124	6	6.5	0.7
	T4-1B	1.88.0	15.0	4.7	2.9	2.85	0.00124	7		
Lower	T4-1	132.1	10.6	5.0	3.0	2.07	0.00146	8	8.4	2.0
	T4-2	141.8	11.4	4.7	2.8	2.08	0.00146	7		
	T4-3	133.8	10.7	4.9	3.0	2.07	0.00146	8		
	T4-4	131.2	10.5	5.0	3.1	2.07	0.00146	8		
	T4-5	121.1	9.7	5.4	3.3	2.06	0.00146	10		
	T4-6	150.0	12.0	4.4	2.7	2.09	0.00146	6		
	T4-7A	113.4	9.1	5.8	3.5	2.04	0.00146	11		
	T4-8	111.7	8.9	5.9	3.6	2.04	0.00146	12		
	T4-1A	135.5	10.8	4.9	3.0	2.07	0.00146	8		
	T4-1B	141.6	11.3	4.4	2.7	1.98	0.00146	6		

*Collapsed, no data was obtained

Table F-4. Interpreted parameters at equilibrium point for Specimen T6

Cut level	Sect.	Equilibrium point		Centerline velocity	Velocity at r_s	Reynold's Number	Shear stress coef.	Wall shear stress		
		x_s (mm)	r_s (mm)	v_{xc} (m/s)	v_{xr} (m/s)	R_x	c_f	τ_w (Pa)	Mean (Pa)	Std dev (Pa)
Upper	T6-1	98.6	7.9	11.1	6.7	3.35	0.00115	33	37.6	7.5
	T6-2	83.3	6.7	13.2	8.0	3.28	0.00116	47		
	T6-3	93.7	7.5	11.7	7.1	3.33	0.00115	37		
	T6-4	80.6	6.5	13.6	8.2	3.27	0.00116	50		
	T6-5	109.4	8.8	10.0	6.1	3.38	0.00114	27		
	T6-6	94.0	7.5	11.6	7.1	3.33	0.00115	36		
	T6-7	96.6	7.7	11.3	6.9	3.34	0.00115	34		
	T6-8	92.9	7.4	11.8	7.2	3.32	0.00115	37		
Middle	T6-1	98.1	7.9	11.2	6.8	3.34	0.00115	33	28.9	5.9
	T6-2	10.20	8.2	10.7	6.5	3.36	0.00115	31		
	T6-3	106.1	8.5	10.3	6.3	3.37	0.00114	28		
	T6-4	100.4	8.0	10.9	6.6	3.35	0.00115	32		
	T6-5	133.4	10.7	8.2	5.0	3.44	0.00113	18		
	T6-6	95.3	7.6	11.5	7.0	3.33	0.00115	35		
	T6-7	121.4	9.7	3.9	5.5	3.41	0.00114	22		
	T6-8	100.5	8.0	10.9	6.6	3.35	0.00115	32		
Lower	T6-1	111.3	8.9	9.8	6.0	3.39	0.00114	26	31.4	13.9
	T6-2	131.0	10.5	8.4	5.1	3.43	0.00113	28		
	T6-3	118.3	9.5	9.3	5.6	3.40	0.00114	23		
	T6-4	121.9	9.8	9.0	5.4	3.41	0.00114	21		
	T6-5	123.2	9.9	8.9	5.4	3.42	0.00114	21		
	T6-6	99.8	8.0	11.0	6.7	3.35	0.00115	32		
	T6-7	72.1	5.8	15.2	9.2	3.22	0.00117	63		
	T6-8	92.9	7.4	11.8	7.2	3.32	0.00115	37		

Table F-5. Interpreted parameters at equilibrium point for Specimen T7

Cut level	Sect.	Equilibrium point		Centerline velocity	Velocity at r_s	Reynold's Number	Shear stress coef.	Wall shear stress		
		x_s (mm)	r_s (mm)	v_{xc} (m/s)	v_{xr} (m/s)	R_x	c_f	τ_w (Pa)	Mean (Pa)	Std dev (Pa)
Upper	T7-1	114.5	9.2	4.3	2.6	1.54	0.00169	7	13.9	8.0
	T7-2	96.2	7.7	5.2	3.1	1.51	0.00171	10		
	T7-3	103.6	8.3	4.8	2.9	1.52	0.00170	9		
	T7-4	90.1	7.2	5.5	3.3	1.50	0.00172	12		
	T7-5	75.3	6.0	6.6	4.0	1.46	0.00174	17		
	T7-6	81.0	6.5	6.1	3.7	1.48	0.00173	15		
	T7-7	66.7	4.5	8.9	5.4	1.39	0.00178	32		
	T7-8	101.5	8.1	4.9	3.0	1.52	0.00170	9		
Lower	T7-1	181.6	14.5	4.7	2.9	2.75	0.00127	6	7.9	1.6
	T7-2	179.2	14.3	4.8	2.9	2.75	0.00127	7		
	T7-3	177.0	14.2	4.9	2.9	2.74	0.00127	7		
	T7-4	149.9	12.0	5.7	3.5	2.72	0.00127	10		
	T7-5	155.4	12.4	5.6	3.4	2.72	0.00127	9		
	T7-6	147.9	11.8	5.8	3.5	2.71	0.00127	10		
	T7-7	162.7	13.0	5.3	3.2	2.73	0.00127	8		
	T7-8	186.7	14.9	4.6	2.8	2.75	0.00127	6		

Table F-6. Interpreted parameters at equilibrium point for Specimen T8

Cut level	Sect.	Equilibrium point		Centerline velocity	Velocity at r_s	Reynold's Number	Shear stress coef.	Wall shear stress		
		x_s (mm)	r_s (mm)	v_{xc} (m/s)	v_{xr} (m/s)	R_x	c_f	τ_w (Pa)	Mean (Pa)	Std dev (Pa)
Upper	T8-1	29.9	2.4	20.5	12.4	1.4	0.0018	173	63.6	50.1
	T8-2								45.3	14.9
	T8-3	45.4	3.6	13.5	8.2	1.6	0.0017	69		
	T8-4	55.1	4.4	11.1	6.7	1.7	0.0016	46		
	T8-5	71.3	5.7	8.6	5.2	1.7	0.0016	27		
	T8-6	61.9	5.0	9.9	6.0	1.7	0.0016	36		
	T8-7	59.5	4.8	10.3	6.2	1.7	0.0016	39		
	T8-8	50.8	4.1	12.0	7.3	1.7	0.0016	55		
Middle	T8-1	60.2	4.8	14.7	8.9	2.5	0.0013	67	42.9	11.7
	T8-2	74.6	6.0	11.9	7.2	2.6	0.0013	43		
	T8-3	84.3	6.7	10.5	6.4	2.7	0.0013	33		
	T8-4	88.7	7.1	10.0	6.1	2.7	0.0013	30		
	T8-5	73.2	5.9	12.1	7.3	2.6	0.0013	44		
	T8-6	83.5	6.7	10.6	6.4	2.6	0.0013	34		
	T8-7	74.5	6.0	11.9	7.2	2.6	0.0013	43		
	T8-8	69.8	5.6	12.7	7.7	2.6	0.0013	49		
Lower	T8-1	90.5	7.2	12.2	7.4	3.3	0.0012	40	29.4	6.4
	T8-2	104.3	8.4	10.6	6.4	3.4	0.0011	30		
	T8-3	115.2	9.2	9.6	5.8	3.4	0.0011	24		
	T8-4	121.2	9.7	9.1	5.5	3.4	0.0011	22		
	T8-5	119.3	9.6	9.2	5.6	3.4	0.0011	23		
	T8-6	106.8	8.5	10.3	6.3	3.4	0.0011	28		
	T8-7	95.4	7.6	11.5	7.0	3.3	0.0012	36		
	T8-8	100.2	8.0	11.0	6.7	3.4	0.0012	32		

Table F-7. Interpreted parameters at equilibrium point for Specimen T9

Cut level	Sect.	Equilibrium point		Centerline velocity	Velocity at r_s	Reynold's Number	Shear stress coef.	Wall shear stress		
		x_s (mm)	r_s (mm)	v_{xc} (m/s)	v_{xr} (m/s)	R_x	c_f	τ_w (Pa)	Mean (Pa)	Std dev (Pa)
Upper	T9-1	141	11	8	5	3.6	0.0011	15	12.9	2.6
	T9-2	129	10	9	5	3.5	0.0011	10		
	T9-3	143	11	8	5	3.6	0.0011	14		
	T9-4	151	12	7	5	3.6	0.0011	17		
	T9-5	151	12	7	5	3.6	0.0011	13.4		
	T9-6	166	13	7	4	3.6	0.0011	12.5		
	T9-7	165	13	7	4	3.6	0.0011	9		
	T9-8	162	13	7	4	3.6	0.0011	12		
Middle	T9-1	148	12	8	5	3.4	0.0011	19	20.3	4.5
	T9-2	134	11	8	5	3.5	0.0011	19		
	T9-3	156	12	7	4	3.6	0.0011	24		
	T9-4	145	12	8	5	3.5	0.0011	17		
	T9-5	162	13	7	4	3.6	0.0011	21		
	T9-6	108	9	10	6	3.5	0.0011	21		
	T9-7	149	12	8	5	3.5	0.0011	28		
	T9-8	160	13	7	4	3.6	0.0011	13		
Lower	T9-1	123	10	9	6	3.5	0.0011	18	21.5	7.8
	T9-2	137	11	8	5	3.5	0.0011	18		
	T9-3	132	11	9	5	3.5	0.0011	16		
	T9-4	137	11	8	5	3.5	0.0011	20		
	T9-5	138	11	8	5	3.5	0.0011	38		
	T9-6	130	10	9	5	3.5	0.0011	23		
	T9-7	126	10	9	5	3.5	0.0011	26		
	T9-8	144	12	8	5	3.5	0.0011	13		

APPENDIX G

SUMMARY OF CASE HISTORY DATA

Table G-1a. Jet grouting field trial data (after Davie et al. 2003)

Column No.	Length exhumed (m)	Nozzles		Grouting Pressure P_t (bar)	Rotation speed R_r (rpm)	Withdrawal rate L_r (cm/min)	Water-cement ratio	With precutting	Measured column diameter D (mm)
		No.	Diameter d_n (mm)						
I-PT-1				55		25			653
I-PT-2				50		25			660
I-PT-3				55		25			684
I-PT-4				50		35			468
I-PT-5				55		35			549
I-PT-6				50		25			605
I-PT-7	2 to 3	2	1.8	55	20	25	1.0	Yes	573
I-PT-8				50		35			525
I-PT-9				55		35			573
I-PT-10				47.5		30			565
I-PI-11				50		35			565
I-PT-12				55		40			541
I-PT-13				52		35			605
II-1						30			588
II-2						27.5			614
II-3						27.5	1.0		468
II-4*						35			528
II-5*						30			509
II-6*						27.5	———		557
II-7						30			512
II-8						27.5			530
II-9	2 to 3	2	1.8	50	20	27.5		Yes	493
II-10*						35			533
II-11*						30			568
II-12*						27.5	1.25		547
II-13*						35			482
II-14*						35			471
II-15*						40			563
II-16*						40			560
II-17*						40			455
III-1a						25			621
III-1b						35			613
III-2a						25			643
III-2b						35			639
III-3a						25			626
III-3b	2 to 3	2	1.8	55	50	35	1.5	Yes	652
III-4a						25			606
III-4b						35			639
III-5a						25			637
III-5b						35			645

*These trials were carried out using two stages of pre-cutting with water prior to the jet grouting pass. All other trials used only one stage of pre-cutting.

Soil description:
Stiff brown slightly gravelly and sandy clay, s_u = 65 kPa, γ = 18 kN/m^3, w_L = 60 to 85 %, w_p = 20 %, I_p = 40 to 65 %, w_n = 30 to 50 %

Table G-1b. Precutting data for jet grout trial (after Davie et al. 2003)

Column No.	Rotation speed R_s (rpm)	Stage 1 Pre-cutting (downward)		Stage 2 Pre-cutting (upward)	
		Water Pressure P_i (bar)	Traverse speed v_t (cm/min)	Water Pressure P_i (bar)	Traverse speed v_t (cm/min)
I-PT-1	20	5	250		
I-PT-2		15			
I-PT-3		15			
I-PT-4		15			
I-PT-5		15			
I-PT-6		25			
I-PT-7		25			
I-PT-8		25			
I-PT-9		25			
I-PT-10		5			
I-PI-11		5			
I-PT-12		5			
I-PT-13		5			
II-1	20	35	40		
II-2		35	50		
II-3		35	60		
II-4		15	200	35	40
II-5		15	200	35	50
II-6		15	200	35	60
II-7		35	40		
II-8		35	50		
II-9		35	60		
II-10		15	200	35	40
II-11		15	200	35	50
II-12		15	200	35	60
II-13		15	200	35	100
II-14		15	200	35	60
II-15		15	200	35	40
II-16		15	200	35	50
II-17		15	200	35	100
III-1a	20	40	50		
III-1b					
III-2a					
III-2b					
III-3a					
III-3b					
III-4a					
III-4b					
III-5a					
III-5b					

Table G-2. Jet grouting field trial data (after Durgunoglu et al. 2003)

Column No.	Length exhumed (m)	Nozzles		Grouting Pressure P_i (bar)	Rotation speed R_r (rpm)	Withdrawal rate L_s (cm/min)	Water-cement ratio	With precutting	Measured column diameter D (mm)
		No.	Diameter d_n (mm)						
3/F	3	2	2.0	500	20	48	1.0	No	550 to 600
4/G	3	2	2.2	500	20	50	1.0	No	550 t600
8/P	6	2	2.0	550	50	43	1.5	Yes*	650 to 760

* precutting details not published

Soil description:
Alluvial deposits, predominantly slightly cemented micaceous silt with interbedded sandy gravels and clays, I_p = 10 to 20 %, s_u = 50 kPa (indicated as assumed in paper)

Table G-3. Jet grouting field trial data (after Duzceer and Golkap, 2003)

Column No.	Length exhumed (m)	Nozzles		Grouting Pressure P_i (bar)	Rotation speed R_r (rpm)	Withdrawal rate L_s (cm/min)	Water-cement ratio	With precutting	Measured column diameter D (mm)
		No.	Diameter d_n (mm)						
TT-1	3 to 3.5	2	2.4	500	15	45	1.0	No	793
TT-2						46			823
TT-4						44			918
TT-6						42			787

Soil description:
Stiff yellowish brown clay, SPT N = 10 blows/0.3m, γ = 18.8 kN/m^3, s_u = 20 kPa, and soft gray silty clay, SPT N= 2 blows/0.3m, γ = 17.5 kN/m3, s_u = 25 kPa.

Table G-4. Jet grouting field trial data (after Samano et al. 1999)

Column No.	Length exhumed (m)	Nozzles		Grouting Pressure P_i (bar)	Rotation speed R_r (rpm)	Withdrawal rate Ls (cm/min)	Water-cement ratio	With precutting	Measured column diameter D (mm)
		No.	Diameter d_n (mm)						
2	2.5	3	2.0	460	30	50	1.0	No	1030
3				240					840
4				120					630
5	2.5	3	2.0	460	20	33	1.0	No	1110
6				240					920
7				120					710

Soil description:
Soft highly plastic clay, w_n = 100 to 400 %, s_u = 8 to 12 kPa